Shaped beam scattering by an eccentric particle and Rainbow properties of spheroids

Jiajie Wang

THESIS

Submitted to

***Xidian University, China**

***Institut National des Sciences Appliquées de Rouen, France**

To obtain

China-France Joint PhD

in

Discipline: *PHYSICS*

Speciality: *Energy*

by

WANG Jiajie

Shaped beam scattering by an eccentric particle and Rainbow properties of spheroids

Defense date: 24.09.2011

Members of the jury:

Reviewers:

Bai Jintao	Professor, Northwest University, Xi'an, China
Liu Weidong	Professor, National Univeristy of Defense Technology, China
Wang Fei	Professor, Zhejiang University, Hangzhou, China

Examiners:

Wu Zhensen	Professor, Xidian University, Xi'an, China
Gérard Gouesbet	Emeritus Professor, INSA de Rouen, France
Xu Jiadong	Professor, Northwestern Polytechnical University, Xi'an, China
Guo Lixin	Professor, Xidian University, Xi'an, China
Han Xiang'e	Professor, Xidian University, Xi'an, China
Gérard Gréhan	Director of Research, CORIA, UMR 6614, CNRS, France
Yiping Han	Professor, Xidian University, Xi'an, China

中国西安电子科技大学
法国国家科学应用研究院鲁昂分院
（中法联合培养）

博 士 研 究 生 学 位 论 文

偏心粒子对有形波束散射及椭球粒子的彩虹特性

作者姓名：　汪加洁

导师姓名：　韩一平　教授　（中国）

Gérard Gréhan 主任研究员（法国）

Gérard Gouesbet 教授（法国）

二零一一年九月

Acknowledgements

This thesis is a direct fruit of a Joint PhD project between UMR 6614/CORIA[1], CNRS[2]-Université et INSA de Rouen[3], France and XiDian University, Xi'an, China, which is supported by the French Embassy in China.

I am most grateful to my supervisory committee for their guidance, continuing encouragement and unyielding support both in my academic work and in my daily life.

I am deeply grateful to my supervisor, Professor Yiping Han in Xidian University, Xi'an, China, for her excellent guidance and enthusiastic encouragement during my PhD studies. The freedom she gave me has boosted my interests in light scattering field. And it is through her recommendation that I was awarded the chance to pursue my education abroad in the well-known laboratory CORIA, France. This education experience will benefit me all through my academic life.

I want to especially express sincere gratitude to my supervisor in France, Dr. Gérard Gréhan and Professor Gérard Gouesbet, their creative ideas and excellent insight into the physical phenomenon have brought me to the higher level of thinking in the research. I'm very grateful to Dr. Gérard Gréhan, for his logical instruction with dynamic thoughts, very patient help and the academic freedom he provided to this research. Furthermore, the finance support he found for me permits me to concentrate on my research during my extra stay in France. Special respects are shown to Professor Gérard GOUESBET, who has been retired but still be very active in the academic field with higher level enthusiasms. I am also very appreciation for his carefulness and patience in helping me modifying the manuscripts of the journal papers.

Thanks are also due to the reviewers and examiners of my thesis, Professor Weidong Liu, Professor Jingtao Bai, Professor Fei Wang in Zhejiang University, Professor Zhensen Wu, Professor Xu Jiadong, Professor Lixin Guo, Professor Xiang'e Han in XiDian University, for many useful suggestions regarding my thesis, which make my thesis better to present my work. I would express my respect for them for their high scientific competence, their carefulness in reading the manuscript and their very precious comments.

I would like to acknowledge Professor Garo Annie, Dr. Meunier-guttin-cluzel Siegfried and Professor Kuangfang Ren for their constructive discussion in my work. Thanks are also due to Ms. Yaoyuan Shi, Ms. Yaling Jin, Mr. Annian He in Xidian University, Ms. Nathalie FOUET in CORIA and Ms. Beaulieu in CROUS of Haute-Normandie, without their warmhearted aids, I can hardly work so efficiently in my PhD during a relatively short time.

I would like to thank all the colleagues in CORIA and School of Science in XiDian University who have helped me for the preparation of my thesis. In particular, thanks are due to my friends: Huangyong Zhang, Guoxia Han, Zhiwei cui, Wenjuan Zhao, Lu Han, Zhengjun Li, Sawitree Saengkaew, Damien Bonin, Saïd Idlahcen, Patcharaporn Lorturn, Yijia Yuan, Siqian Liu, Jiesheng Min for their support and encouragement throughout my

thesis, Special thanks is dedicated to my wife Yumin Sun, for her warmly support all through my thesis and her help in check my thesis text.

Finally, I would like to acknowledge the supports for this thesis from the French Embassy in China, the Natural Science Foundation of China (No.60771039) and the European Regional Development Fund.

****

1. CORIA : Complexe de Recherche Interprofessionnel en Aérotherochimie;
2. CNRS : Centre National de la Recherche Scientifique;
3. INSA : Institut National des Sciences Appliquées;

Résumé: Diffusion d’un faisceau modelé par un particule excentrique et propriétés arc-en-ciel du sphéroïdes

Deux pièces de travail sont inclus dans cette thèse. La première partie analyse l'interaction d'une sphère excentrique avec un faisceau incident quelconque forme au sein de l'généralisé la théorie de Lorenz-Mie (GLMT). Distributions de contrôle interne, près de la surface, loin des champs dispersés zone ainsi que le comportement de la morphologie dépendant résonances (MDR) dans une sphère excentrique éclairée par un faisceau focalisé gaussien sont analysés. Dans la seconde partie, en utilisant le EBCM, les propriétés de diffusion de lumière autour de l'angle arc pour un ensemble de sphéroïdes dans des orientations aléatoires éclairé par une onde plane sont étudiés. En comparant les paramètres extraits de ces paramètres originaux utilisés dans les expériences de simulation, la sensibilité de la technique d'arc de la sphéricité des gouttelettes non est quantifiée.

Mots-clés： GLMT Faisceau modelé Particule excentrique EBCM Sphéroïdes Technique d'arc-en-ciel

Abstract: Shaped beam scattering from an eccentric particle and rainbow properties of spheroids

Two parts of work are included in this thesis. The first part analyses the interaction of an eccentric particle with an arbitrary incident shaped beam within the generalized Lorenz-Mie theory (GLMT). Distributions of internal, near-surface, far-zone scattered fields as well as the behavior of morphology-dependent resonances (MDRs) in an eccentric sphere illuminated by a focused Gaussian beam are analyzed. In the second part, by using the EBCM, light scattering properties around the rainbow angle for an ensemble of spheroids in random orientations illuminated by a plane wave are studied. By comparing the extracted parameters with those original parameters used in the simulation experiments, the sensitivity of the rainbow technique to the non-sphericity of droplets is quantified.

Key word： GLMT Shaped Beam Eccentric particle EBCM Spheroids Rainbow technique

摘要：偏心粒子对有形波束散射及椭球粒子的彩虹特性

本论文围绕偏心球粒子（散射目标内部组成成分分布不均匀情况下的物理模型）对任意方向入射有形波束的散射问题以及椭球粒子（散射目标外表面发生形变情况下的物理模型）的彩虹特性展开相关研究。本论文的主要研究工作和成果在于：

推导了任意方向入射有形波束的波束因子在任意直角坐标系之间相互转换的一般关系式。基于广义洛伦兹米理论(Generalized Lorenz-Mie Theory,GLMT)，详细推导了偏心球粒子对任意方向入射有形波束散射问题的求解。基于理论推导结果，利用FORTRAN语言编写了一套用于求解偏心球粒子电磁(光)波波束散射问题的程序。以广泛应用的高斯激光波束为例，从数值上研究了偏心球粒子在有形波束照射下偏心球粒子的远场、表面近场和内场三维空间电磁强度的分布情况。研究了偏心球粒子在汇聚高斯波束激发下的光学振荡特性。

基于扩展边界条件法(Extended Boundary Condition Method, EBCM)，数值模拟了取向随机任意分布的椭球粒子群在不同粒径分布和不同椭球率分布下对平面波的散射特性，分析了彩虹角附近远场散射场的强度空间分布情况。对模拟实验中得到的椭球粒子的彩虹信号数据进行了反演。将反演所得粒子参数和实际用于数值模拟实验的粒子参数进行对比，研究分析了椭球粒子对彩虹技术中粒子粒径分布、复折射率大小等参数反演精度的影响。

关键词： 广义洛伦兹米理论 有形波束 偏心球粒子 扩展边界条件法 椭球粒子 彩虹技术

Table of Contents

目 录

第一部分 偏心粒子的波束散射

第二部分 椭球粒子彩虹特性研究

第一章 绪论

§1.1 论文选题背景及意义

本论文依托于中法国际合作项目研究课题“Optical characterization of shape and thermo-chemical composition of biodiesel droplets in flames”，是由法国驻华大使馆资助。论文的选题还来源于国家自然科学基金项目(60771039)“光镊中光势阱的研究”以及欧盟国际区域发展基金项目“Interreg Iva-C5: Cross-Chanel Center for Low Carbon Combustion”。主要研究了偏心粒子、椭球粒子等对任意方向入射有形波束的散射特性。为激光对微粒的探测、诊断以及操纵技术提供关键的理论支持和实际指导。

粒子对电磁波（光波）波束散射特性的研究对于分析粒子的结构形状、组成成分、粒径大小和作用性质等等都具有重要作用。电磁（光）波已经在自动化工农业过程中[1-3]（如研磨煤粉和液体燃料的燃烧过程、流体高压喷雾的雾化过程、金属粉末和医药药用粉末的生产过程等等），宇宙悬浮颗粒的探测[4]、生物医学诊断[5]、大气环境监测和微波遥感等多个领域有着重要的实际应用。如表1-1所示，为了加强对相关工农业产品生产过程以及产品质量的监测，根据具体情况和具体要求的不同，我们需要对直径大小从亚微米到毫米量级范围内的微小粒子（尘埃、液滴、沙粒、生物细胞、烟雾等）的成分、浓度、速度、温度以及尺寸大小及分布等进行快速、准确的测量。

为了实现对上述各种参数的测量，基于光散射理论的光学测量技术源于其非直接接触测量、准确、快速等优点而一直受到各行业科研人员和工程技术人员的青睐。特别是自激光问世以来，不论是工程应用测量技术，还是相关光散射理论的研究都有了突破性的进展，科研人员已经开发出了适用各种不同情况和条件的测量方法和仪器设备。例如基于弹性光散射的粒度分析测量技术，包括相多普勒测量技术、消光法测量、彩虹技术、干涉成像技术等等。这些技术已经在生物物理学、多相流、燃烧过程、流体力学、化工、环保等研究中有了极其广泛的应用[6]。例如在化石燃料的燃烧过程中，通过对各种燃烧生成物组成的颗粒体系对激光波束散射信号的测量，我们可以研究燃料雾化的质量好坏以及燃料燃烧的程度和利用效率。采用激光作为光源对多粒子散射体系进行测量还有许多重要的用途，例如应用在研究颗粒系，如水雾，标准溶液等对激光束散射特性的基础上形成的全域彩虹测量技术就可以测量颗粒系的粒径分布和温度大小；而在大气环境科学中，

我们已经利用激光雷达作为通讯、探测的手段，基于大气中的气溶胶悬浮粒子、云层中的雨滴等对电磁光波的散射和吸收作用所产生的散射谱和吸收谱，实现了大气质量，天气变化情况的实时监测和有效预报。在生物医药学中，由于特定生物细胞组织成分，病变细胞等对电磁光波有不同的散射和吸收作用，从而实现不同细胞组织以及病理的非接触式识别和诊断；在化工行业中，对输送物料的多相流的浓度和速度进行非直接接触的测量，另外在激光相多普勒技术中，研究粒子的形状、尺寸、折射率分布和粒子运动的速度等都具有重要的意义。

表1.1 电磁（光）波对小粒子测量在工农业质量控制上的广泛应用

主要应用领域	主要目标和作用
燃烧	煤粉、化石液体燃料在燃烧室中粒径和速度的测量
喷雾	测量雾化液滴的粒径和浓度，改进喷雾装置的设计
医药、医疗	医药药用粉末的生产过程的监控，药物作用的检测
涂料工业，金属粉末的生产	控制和检测颗粒生产的过程，主要是颗粒大小的变化
污染控制	控制和检测发动机，锅炉燃烧过程中污染颗粒的排放
食品生产	控制食品的口感和质地，如速溶咖啡生产的监控
大气监测	天气预报，灾害防治，监测云层中液滴粒径的分布
农业	杀虫剂，农药等的喷洒

作为上述各种光学测量技术的理论基础，研究各种粒子的光散射特性一直是国际上持续关注的重要研究课题之一。通过对激光波束在复杂颗粒系中散射和传输特征的研究又能够反过来促进激光在已知和更多未知领域中的改进和应用开拓，因此研究粒子对激光束的散射有着重要的理论价值和实际应用前景。

在理论方法上，分析各种规则和不规则形状粒子电磁（光）散射的方法有许多。按照粒子的直径大小与入射波波长的比值可将待研究的散射体分为：瑞利区的小粒子($\mathrm{d} < 0.1\lambda$)，几何光学区的大粒子($10\lambda < d$)，以及谐振区与入射波长大小相比拟的粒子($0.1\lambda < d < 10\lambda$)。求解瑞利区小粒子散射问题的方法主要有：瑞利近似、玻恩近似、WKB近似等；求解几何光学区大粒子散射的方法主要有：几何绕射理论(GTD)、物理光学法(PO)、物理绕射理论(PTD)、几何光学法(GO)、一致绕射理论(UTD)以及等效电磁流法等；而求解谐振区散射问题的方法有：分离变量法(SVM)，扩展边界法(EBCM，又称T矩阵法或零场法)、微扰法、时域有限差分法(FDTD)、有限元法(FEM)、矩量法(MOM)，点匹配法(PMM)等。在分析粒子电磁散射的问题时，各种计算方法都有其各自的优缺点，并在其适用领域获得了迅速的发展。例如分离变量法主要适用于精确求解各种表面形状规则粒子的散射问

题，包括球形，圆柱形，椭球形粒子等，而微扰法局限于粒子几何形状有较小形变的情况，扩展边界法则可以求解非规则任意形状粒子的散射问题，特别适合于旋转对称形粒子的计算。本文的研究目的是针对燃烧过程中高压喷雾细小液滴参数测量、光镊操纵实验中微小粒子与高汇聚激光之间相互作用而展开的，其中所研究的粒子大小处于散射谐振区，因此本文主要采用分量变量法和扩展边界条件法来研究对象粒子的散射特性。

在以往小粒子散射的问题中，球形粒子被广泛用数值建模和分析上。然而为了进一步表征粒子复杂的内部结构，提高各种现有光学测量仪器的精度和探测技术的适用范围，从理论模型上对各种规则和非规则粒子对电磁（光）波的散射进行研究是一个必要的课题，并且从这些研究中发现新的光学现象，开拓出新的光学测量技术。因此非均匀球形粒子的散射问题的建模和研究成为近年来光散射研究的重点和热点。本论文在此研究背景下选题为微小粒子对电磁（光）波波束散射问题的研究。具体研究了偏心球粒子（球形粒子内部介质非均匀分布模型）对任意方向入射有形波束的散射问题以及椭球粒子（球形粒子外表面形变模型）对彩虹信号的影响以及对微粒相关参数测量精度的影响。

§1.2 偏心粒子散射的研究现状

自从人们开始关注小粒子的光波散射特性以来，由于球形粒子在数值建模和分析上所具有的特殊的空间对称性，它被广泛应用在相关散射问题的描述上。关于各向同性介质组成的均匀球形粒子对平面电磁波的散射问题，分别由Lorenz[7]于1890年和Mie[8]于1908年基于麦克斯韦方程组，获得了均匀球形粒子对平面波散射的的解析解，形成了著名的洛伦兹米理论(Lorenz-Mie theory, LMT)。经过一个多世纪的理论研究和实验验证，均匀球形粒子电磁散射各个相关方面都已经有了比较系统和完善的的研究。洛伦兹米理论被广泛应用在由均匀介质组成的细小微粒的散射问题中，能够取得较好的预测结果。该理论在科学研究的发展过程中扮演了很重要的角色。然而随着光测量和光操纵技术应用范围的不断增大，科学研究的对象也在不断发生多样性的变化，比如细胞质非均匀分布的血红细胞，含细胞核的动物细胞等等。为了更加准确地描述粒子的结构及散射特性，使光散射理论预测结果更加精确，科学工作者逐渐开始在合适的情况下引入双层甚至多层球散射模型。

Aden和Kerker[9]在1951首先开始对同心球粒子与平面电磁波之间相互作用问题进行研究。而后Kerker[10]在其1969发表的著作中将双层同心球散射模型推广到多层球的电磁散射模型，并给出了计算多层球电磁散射系数的矩阵公式。在多层球电磁散射模型的建立之后发现该问题的数值收敛性不好。特别是在分层数较多的

情况下，不仅数值计算的效率大大减慢，更会出现严重的收敛性问题。为了预测多层球粒子这种典型模型的散射特性，之后的更多研究主要集中到数值算法的改进上。围绕多层球粒子模型散射的数值求解问题，Toon等人[11]、Bohren等人[12]这方面做了大量相关工作。特别值得一提的是吴振森和王一平[13]在1991年提出了一种计算多层球散射场的改进数值方法，使得可计算模拟的球形粒子的尺寸参数和层数都得到了很大的提高。此迭代算法之后被Johnson[14]加以完善，实现了模拟球形粒子每一层中的电磁场强度的分布。在实验测量和验证方面，Hightower等人[15]利用细微玻璃球为内核，在其表面浸置甘油丙三醇的粒子对平面波的散射进行了相关实验。实验中发现当甘油涂覆层厚度仅为几百纳米的情况下，他们所得散射实验数据和利用Aden和Kerker的同心球模型散射理论所预测结果能够很好地吻合，从而第一次从实验上验证了同心球模型对平面波散射理论的精确性。之后Ray等人[16]和Kaiser等人[17]分别利用不同液体介质，比如丙三醇液滴外面加覆邻苯二甲酸二甲酯溶液，进行了相关实验，他们所得实验数据也和双层同心球三理论预测结果吻合的比较一致。

但是我们需要认识到，不管是Hightower等人实验中使用的玻璃球涂覆丙三醇，还是Ray等人使用的非相容性不同液体，因为所用两种介质之间都存在一定的密度差异，根据流体力学的相关理论，由于重力的原因，密度较大的介质会趋向于移向密度较小介质的底部，从而必然使得试验中使用的同心球模型转化成偏心球模型。因此，在Hightower等人的实验中发现只有在外涂覆层厚度仅为几百纳米的情况下，实验数据才能和同心球散射模型的理论预测结果实现较好的吻合。而当外层涂覆厚度超过入射波波长大小时，实验所得数据与同心球模型理论预测结果相差较大。另外，在Secker等人[18]对含核球形粒子光散射的实验中，他们对直径大小为20um左右含空气气泡的油酸液滴的图像进行了显微摄影。从他们发布的图像中我们不难发现，油酸内的空气气泡由于重力原因会不断向上运动到油酸液滴的顶部，从而证实了实验中所用液滴更加接近偏心双层球粒子。在近期Tu和Ray[19]所进行的实验中，他们发现即使是涂覆层厚度很小的情况下，由于重力原因，完美的同心球也几乎是不存在的。因此在此实验结果下，建立偏心球模型，研究偏心球粒子对入射电磁（光）波的散射特性已经越来越成为当下科学工作者的研究重点和兴趣所在。

由于数学推导的复杂性，关于偏心球粒子散射问题的理论研究是在数学相关理论的发展基础上发展起来的。为了研究偏心球粒子的电磁波散射问题，其中一个关键问题是如何将空间中任意一点的电磁场分量分别在不同的坐标系中表示。Friedman和Russek[20]在1954年发表的论文中首次给出了标量球谐函数的平移加法定理，基于此加法定理，我们可以将电磁波在不同坐标系下用各自的球谐波函数展开所得的展开系数联立起来，从而开启了研究偏心球粒子的电磁散射问题的序

幕。之后Stein[21]和Cruzan[22]先后分别修正了Friedman和Russek在公式推导过程中的几处偏差，重新给出了矢量球面波函数加法定理的推导过程和结果。为了更加有效地用于电磁散射问题的求解，Bobbert和Vlieger[23],Mackowski[24]分别给出了求解平移展开因子的两种不同迭代数值方法，大大加快了迭代求解的速度。平移加法定理的发表为偏心粒子以及多粒子体系的相关研究提供了必要的数学工具。

1979年，Fikioris和Uzunoglu[25]首先对偏心球粒子与电磁波之间相互作用进行了研究。基于分离变量法，他们推导求解了偏心球对平面电磁波散射问题的解析解，给出了相关平面波散射系数的解析表达式，并初步探讨了探测球形粒子内部非均匀杂质的方法。由于当时计算机计算水平低下，Fikioris和Uzunoglu只给出了内核小球子微小偏心位移下的近似数值结果。直到1992年，Borghese等人[26, 27]重新推导了偏心球对平面电磁波的散射求解方程并将单核偏心球散射模型扩展到多核偏心球的散射模型。他们发现不同于均匀球粒子和同心球粒子，偏心球粒子的散射强度在空间分布上不再具有普遍的球对称性，并且在散射强度分量中会引起很强的极化效果，这些数值结果都将为偏心球粒子相关参数的检测，比如偏心度、内核大小等，提供依据。为了研究平面上悬浮尘埃粒子的沉积和清除方法，Fuller[28]从理论上推导了多核偏心球粒子对平面波的散射求解问题，同时他对单核偏心球粒子内部的环形光学谐振腔的光学谐振特性作了探索性研究[29]。他发现偏心球内核的存在将会引起大球内谐振模频率的偏移。基于扩展边界法，Videen等人[30]从理论上对内核为任意形状的偏心球粒子的平面波散射问题进行了推导和求解，Ngo等人[31, 32]进一步研究了偏心球对任意方向入射平面波的散射问题，并给出了FORTRAN计算程序。该程序可以对散射场、后向散射强度、消光系数等进行数值模拟与分析，一定程度上促进了偏心球粒子散射问题的研究。针对球形天线涂覆多层介质涂层的情况，Lim和Lee[33]建立并研究了多层偏心球形粒子对平面电磁波的散射特性，并给出了三层涂层情况下数值模拟结果。

就目前我们所查到的文献来看，文献中研究偏心球散射问题时大多数是以平面电磁波作为外加激励源的。然而自从上个世纪60年代激光的发明以来，激光光束已经成为绝大多数光学测量仪器和技术中的首选光源，例如激光相多普勒仪就是基于移动粒子对激光光束的散射原理，从而得到粒子的形状，尺寸，运动速度等相关信息。因此研究粒子对激光波束的散射是近几年的一个研究热点，Davis[34]在1979年提出了高斯波束用平面波角谱来展开的数学形式，为研究粒子的波束散射提供了一种途径。从1982年开始，Gouesbet、Grehan等人[35]基于Davis的展开结果，利用Bromwich公式深入推导了有形波束对均匀球的散射情况，提出了广义洛伦兹米理论，给出了高斯波束用球矢量波函数展开的表达式，并给出了其展开系数的三种数值计算方法。经过近30年的研究发展，广义洛伦兹米理论已经成为研究规则形状粒子（如球形粒子[36, 37]，柱形粒子[38, 39]，椭球粒子[40, 41]等等）与任意

有形电磁波束（如高斯波束[36]，椭球形波束[42]等）之间相互作用的重要理论方法。Barton[43]导出了TEM_{00}高斯波束电磁场分量的高阶近似表达式，采用分离变量法分别研究了球形粒子、椭球粒子、无限长圆柱对高斯光束的散射强度的分布。Khaled[44]等人研究了同心球在离轴高斯波束中散射强度的数值计算，并研究了离轴高斯波束不同位置对同心球中谐振模式能量耦合的影响。吴振森、郭立新等人[37]于1997年提出了多层球对平面波和波束散射的改进算法，大大拓展了多层球粒子的尺寸参量和分层数。

随着波束散射问题研究的逐步深入，2000年，Gouesbet和Grehan[45]将广义洛伦兹米理论应用到了偏心球粒子对波束散射的研究中，从理论上推导了散射方程和求解过程，但没有给出具体的数值模拟及分析。最近韩国霞等人[46, 47]和颜兵等人[48, 49]分别推导了高斯波束斜入射到偏心球表面情况下散射问题的求解问题，给出了高斯波束沿不同方向照射偏心球情况下散射强度角分布和消光截面的相关数值结果，并对偏心球与高聚焦高斯光之间的相互作用的梯度力做了详细的研究。但是对于偏心球粒子内场和近场的研究目前还没有相关报道。

综上所述，我们不难发现，自从Fikioris和Uzunoglu首先开始研究偏心球粒子的散射问题以来已有30年的研究历史，但是由于数学推导以及数值计算上的难度，目前对于偏心球粒子的研究仍处于发展阶段，特别是对电磁波（激光）波束的散射研究才刚刚开始，主要以下几个方面的重点问题需要研究：

第一：在激光光源成为试验室标准配置光源的情况下，从理论上系统地研究偏心球粒子和各种有形光束之间的相互作用是一个关键的问题。而其中首要的问题是如何从理论上去正确描述以任意入射方向照射到粒子上的任意形状的电磁波束。比如在光镊操纵系统中，为了更加有效地实现微小粒子的稳定捕获和操纵，除了常用的高斯激光外，贝塞尔光束等其他形状的强聚焦激光也经常被用来当作操纵光源，因此对高斯波束等任意方向入射的有形波束的展开描述是我们研究的一个重点。

第二：理论模拟终究是为了实际测量或者开发新的测量技术而服务的，因此我们需要系统的对偏心球粒子和有形光束之间的相互作用结果进行系统的研究，包括远场，近场以及内场电磁场强度的空间分布的研究。并尝试从各个角度探讨如何从数值模拟结果中有效地提取信息，为探测偏心球粒子的各种参数提供新的测量手段。

第三：根据我们对现已发表的程序以及数值结果的分析来看，即使在平面波的照射下，现有理论和程序在数值计算上仍然存在较大的适用局限性。特别是在偏心度较大的情况下，目前的程序只能对尺寸参数在50以下的偏心球粒子进行正确预测。这个在没有得到解决的数值收敛性问题大大限制了该理论在相关测量技术上的应用，如：彩虹技术，傅里叶干涉成像技术等。因此，如何从数值计算上

如何去改善提高程序的适用性，提高计算适用范围成为本文的一个讨论重点。

§1.3 椭球粒子散射的研究现状

与球形粒子模型相比，椭球模型在很多情况下更加接近于一些实际存在的粒子。比如当流体通过高压喷头进入高压燃烧室时，由于空气阻力的作用，雾化的小液滴在雾化初期以及破裂成更小液滴期间更多的是呈现椭球形状。气象观测和诸多实验结果都已证实下落过程中的大多数雨滴的形状也呈椭球形。又如在光镊操作系统中对一些生物细胞进行拉伸试验，此时的生物细胞也更加接近椭球形。椭球粒子为科研工作者提供了研究非球形粒子对电磁散射的最有效模型之一，因此从理论上详细研究椭球形粒子的散射特性在实际应用中有着非常重要的指导意义。但是由于椭球波函数的表述形式十分复杂，给理论推导以及数值计算带来了诸多困难，特别是对电磁场边界条件的处理更为困难，因此研究发表的文献相对于球形粒子的研究就相对少的多。

关于椭球形粒子对平面波的散射，Asano等人[50, 51]基于分离变量法，提出了一种处理椭球粒子电磁场边界条件的理论方法，较好的解决了椭球边界条件问题。该方法之后被许多文献所引用，是一种公认的研究椭球形粒子对平面波散射的重要方法。在有形波束的照射下，Barton[52, 53]对椭球形粒子的近场散和内场的电磁强度分布做了较为详细的分析。但是相对于Asano的方法而言，他的理论方法无法给出高斯波束在椭球坐标系中的展开形式，并且他通过积分方法来处理边界条件，是一种近似方法，在计算中会带来一定的数值误差。为了分析球形粒子外形形变对相关测量的影响，韩一平等人[54, 55]对Asano等人的理论方法进行了重新推导，纠正了Asano在其文献中对边界条件推导过程中的部分错误结果，修改了若干错误参数，给出了正确结果。并且在GLMT理论框架内详细研究了椭球对正入射高斯波束的散射。张华永等人[56]利用球矢量波函数的旋转加法定理，推导了椭球粒子对任意方向入射下高斯波束的散射情况，并将理论研究拓展到对双层甚至多层椭球的电磁波束散射的研究上去。徐峰等人[41, 57]基于GLMT理论框架，研究了高聚焦高斯波束与椭球之间的相互作用，计算了椭球所受的光梯度力和旋转扭矩的大小。最近，他还利用Debye级数展开方法[58]对椭球粒子进行了分析，对所得散射结果给出了更加清晰的物理解释。从目前所发表的数值结果来看，利用分离变量法对椭球光散射的预测仍然在尺寸参数上存在很大的限制，阻碍了对大尺寸粒子计算的应用。而另一方面，基于扩展边界条件方法[59]，又称T矩阵法或者空场方法（Null-field method）[60]，对椭球粒子的计算已经可以达到150以上[61]。

扩展边界条件法是由Waterman[62]于1971年首次提出，该理论由于能够对非球形粒子进行计算预测而备受关注。特别是在诸如椭球、圆柱粒子等一类轴旋转对

称粒子散射问题的预测计算上，该方法比其他数值计算方法，如FDTD, MOM等在计算速度上要快几个量级。经过近40年的不断发展和完善，它已经成为目标散射领域最有效的方法之一[59, 60]。由于该方法在求解过程中需要对入射波束和散射电磁场之间的传输矩阵（Transition Matrix, T矩阵）进行求逆，当椭球粒子的椭球率过大，或者尺寸参数过大时，将导致传输矩阵的严重病态化，对能够计算的椭球粒子散射结果的尺寸参数有很大的限制。但是经过Mishchenko[63]、Wielaard[64]等多位科研人员的研究，这个限制已经大大得到缓解，因此为本论文中研究较大尺寸粒子的彩虹现象提供了理论工具。Hackman[65]，Schulz等人[66]基于椭球矢量波函数，用EBCM求解方法研究了椭球粒子对平面波的散射问题。然而椭球矢量波函数自身的数值求解收敛性较弱，导致该方法对较大尺寸参数椭球粒子散射问题的数值求解依然存在收敛性不强的问题。

Mishchenko等人[67, 68]首先将EBCM应用于空间取向随机任意的一群不相关粒子的散射问题上，推导了适用于旋转对称粒子的散射表达式，并且还给出了相应的Fortran程序，大大推动了EBCM方法在多粒子体系散射问题上的应用。Skaropoulos等人[69]也对旋转对称的多粒子散射体系进行了系统推导，通过将散射矩阵的解析表达式用一般球谐函数的级数来展开，加速了传输矩阵的求解，并重点研究了具有特殊偏向的一群粒子对平面波的散射情况。本论文中我们将基于电磁场分量的球矢量波函数展开，推导了散射单体对电磁波散射的EBCM解法，重点研究了椭球粒子对标准彩虹信号的影响以及一群取向随机任意的椭球粒子对全域彩虹信号的影响。

§1.4 论文主要内容和结构安排

根据研究对象的不同，本论文的具体研究内容可以分成以下两个部分：第一部分是在广义洛伦兹米理论框架内对偏心球粒子与有形波束之间相互作用的研究；第二部分是利用扩展边界条件法分析了椭球粒子的彩虹信号以及椭球粒子对彩虹技术中参数反演精度的影响。本论文章节结构的安排如下：

第一章：绪论。结合国内外对偏心球粒子和椭球粒子电磁(光)波散射方面的最新发展状况，介绍了本论文选题的相关背景以及进行该研究的实际意义，并给出了本论文主要完成的工作以及主要创新点。

第二章：任意入射有形波束的球矢量波函数展开。简单介绍了广义洛伦兹米理论(Generalized Lorenz-Mie Theory, GLMT)的最新进展，详细介绍了球矢量波函数的旋转加法定理和平移加法定理，给出了任意方向入射有形波束用球矢量波函数展开的数学表达式，推导了波束因子在任意直角坐标系之间相互转换的一般关系式关系。以轴对称波束为例，给出了轴对称波束的波束因子在任意直角坐标系

之间相互转换的简化解析表达式，可直接用于数值计算。任意方向入射有形波束在任意直角坐标系中的展开是求解各种规则和非规则粒子对有形波束散射问题的关键点和难点，本章内容为多种电磁（光）波散射解析理论，如广义洛伦兹米理论，扩展边界条件方法(Extended Boundary Conditions Method, EBCM)的有形波束散射问题提供了必需的工具。

第三章：偏心球粒子的波束散射。基于GLMT，结合球矢量波函数的平移加法定理，详细推导了偏心球粒子在有形波束任意方向照射下散射问题的求解过程。基于论文的理论推导，利用FORTRAN计算语言编写了一套可用于模拟仿真有形波束照射下偏心球散射远场，近场和内场电磁强度三维空间分布的程序。在将所写程序和已有程序的数值结果进行对比验证的基础上，本章分析了偏心球内核粒子相对大小、偏心距、波束入射方向等因素对远场散射特性的影响。

第四章：偏心球粒子内场和近场分析。本章利用直角坐标系与球坐标系的相互转换关系式，推导了有形波束任意方向入射情况下，偏心球粒子散射近场和内场场强空间分布的计算表达式。在对所得公式和相应程序进行充分数值验证的条件下，给出了高斯波和平面波沿不同方向照射偏心球粒子时，偏心球粒子内场和近场电磁强度分布的相关算例和结果分析。

第五章：偏心球粒子光学谐振的研究。研究了偏心球粒子在强汇聚高斯波束激发下的光学形态谐振模特性。通过数值模拟计算偏心球粒子的后向散射强度和微分消光截面随粒子尺寸参数变化谱，研究了内核小球粒子在不同相对尺寸大小，不同偏心度下对偏心球中形态共振模谐振位置和谐振振幅的影响。给出了强汇聚离轴高斯波和平面波照射下，偏心球粒子在谐振以及非谐振情况下内场强度的空间分布特性。

第六章：扩展边界条件法。基于等效原理，利用扩展边界条件法，推导了各向同性和各向异性散射目标的散射传输矩阵。针对多粒子散射体系，基于单次散射模型，推导了取向随机任意粒子群对平面波散射的解析解。通过将散射矩阵中各个元素的解析表达式用一般球函数的级数来展开，大大提高了散射问题的数值求解速度。本章的相关理论推导将为下一章的研究提供理论基础。

第七章：椭球粒子的彩虹特性。本章在光散射理论的框架内介绍了彩虹现象的形成原理以及彩虹测量技术的开发过程，对传统标准彩虹技术和最近逐步发展完善的全域彩虹技术的优点以及局限性做了简单介绍。针对标准彩虹信号易受液滴粒子表面非球形形变影响的问题，基于椭球粒子模型，利用扩展边界条件法，论文模拟了方向随机任意分布的椭球粒子群在不同粒径分布和不同椭球率分布下对平面波的散射特性，特别分析了彩虹角附近远场散射场的强度空间分布情况。利用基于Nussenzveig球形粒子散射理论对模拟得到的椭球粒子的彩虹信号进行参数反演，将反演所得粒子参数和实际用于数值模拟实验的粒子参数进行对比，分

析了椭球粒子对彩虹技术中粒子粒径分布，复折射率大小等参数反演精度的影响。

第八章：论文总结和展望。主要对全文进行总结并提出一些需要进一步研究的问题。

§1.5 本文特色及创新之处

本文基于广义米理论研究了偏心球粒子对任意方向入射有形波束的电磁散射问题，并且利用扩展边界条件法分析了椭球粒子的彩虹信号以及椭球粒子对彩虹技术中参数反演精度的影响。本论文主要完成了以下几点原创性工作：

1. 基于有形波束的球矢量波函数展开式，利用球矢量波函数的旋转加法定理和平移加法定理，推导了任意方向入射有形波束的波束因子在任意直角坐标系之间相互转换的一般关系式。以轴对称波束为例，给出了轴对称波束的波束因子在任意坐标系下的简化解析表达式，可直接用于数值计算编程。分析了波束因子区域近似法与直角坐标系旋转变换关系之间的兼容性和局限性问题，对区域近似法的应用起到补充和修正的作用。相关结果主要集中在论文第二章进行阐述，并且已经以一个系列的形式发表在Optics Communications杂志上[70-74]。
2. 详细推导了偏心球粒子对任意方向入射有形波束散射问题的求解过程，基于理论推导结果，利用FORTRAN计算语言编写了一套可用于模拟仿真有形波束照射下偏心球散射远场，近场和内场电磁强度三维空间分布的程序。
3. 研究了偏心球粒子波束散射的远区电磁场强的三维空间分布，并且首次研究了偏心球粒子散射的近场和内场的强度分布情况，讨论了高斯波束束腰半径，高斯波束入射方向，偏心内核心距离，偏心内核相对尺寸参数大小等因素对远区的散射场分布、近场和内场的分布的影响。相关成果主要在论文的第三章和第四章进行阐述，并且已经发表在Journal of the Optical Society of America A杂志上[75]。
4. 研究了汇聚离轴高斯波束激发下偏心介质球内的光学振荡模的产生和分布情况。通过数值模拟计算偏心球粒子的后向散射强度和微分消光截面随粒子尺寸参数变化谱，研究了内核小球粒子在不同相对尺寸大小、不同偏心度下对偏心球中光学振荡模谐振位置和谐振振幅的影响。数值仿真了强汇聚高斯波束和平面波照射下，偏心球处于谐振情况下的和非谐振条件下内场强度分布的不同。此结果有助于拓展复杂光学微腔在光电器件，生物细胞检测方面的应用。相关成果主要在论文第五章进行阐述，并且已经发表在Journal of the Optical Society of America A杂志上[76]。
5. 针对彩虹信号易受液滴粒子表面非球形形变影响的问题，基于椭球粒子散射模型，利用扩展边界条件法，模拟了方向随机任意分布的椭球粒子群在不同粒径

分布和不同椭球率分布下对平面波的散射特性，特别分析了彩虹角附近远场散射场的强度空间分布情况。基于Nussenzveig球形粒子散射理论对模拟得到的椭球粒子的彩虹信号进行参数反演，将反演所得粒子参数和实际用于数值模拟实验的粒子参数进行对比，分析了椭球粒子对彩虹技术中粒子粒径分布，复折射率大小等参数反演精度的影响。相关成果主要在论文第七章进行阐述，并且已经发表在Experiment in Fluids杂志上[77]。

第一部分 偏心粒子的波束散射

为了从数学角度来描述和研究各种规则和不规则粒子与电磁（光）波之间相互作用的物理机理，建立一个恰当的数学模型是解决问题的关键一步。在以往关于粒子光散射的相关研究中，人们经常将微小粒子抽象模拟成由各向同性均匀介质组成的球形粒子。而这种最简单、最理想的模型在一些情况下也是对许多问题的提供一个很好的近似解。随着数学工具的不断发展以及实验仪器设备精度的不断提高，目标光散射的研究在理论和应用两方面都取得了巨大的发展。为了提高理论仿真对实际测量情况的预测，用于理论分析研究的散射粒子模型逐渐从最初的均匀球演变成内部非均匀分布的多层球粒子、偏心球粒子，外表面形状形变情况下的椭球、圆柱等模型。

在许多实际的大气环境或人造的实验环境中，我们经常会遇到那些不能简单地被视为内部均匀分布或者同心多层的粒子。比如在粉末状速溶咖啡的生产过程中，其中一个流程是利用喷雾的方式将已经煮好并加以浓缩的咖啡液用高压的喷嘴高速地喷出来，让水分在空气中迅速蒸发掉而得到粉末状的咖啡颗粒。为了得到粉末颗粒大小合适、口感最好的咖啡产品，就需要在这个工业流程中对咖啡喷雾的浓度、粒度大小以及温度高低加以监测。从流体力学的理论来看，由于咖啡颗粒和水溶液之间较大的密度差异，这种咖啡喷雾中的细小液滴已经不能简单地被视为同心双层球粒子来处理。又比如生物组织中的单核细胞、大气中的气溶胶颗粒、含有气泡的玻璃微球，水滴包裹的冰核等等，这些粒子的内核除了拥有和主粒子完全不同的光学特性外，主粒子和内核之间都有明显的密度差异，使得内核粒子可能随机地存在于粒子内部空间的不同位置，呈现出明显的偏心特征。从相关实验测量结果中我们也发现，实验中所得到的这类偏心粒子的光散射特性与用分层同心粒子模型理论预测的数值结果有很大的不同。为了更加精确的描述和预测这类偏心粒子的光散射特性，满足科学实践和工业生产中对粒子直径，浓度等参数精确检测的需要，开展偏心粒子对电磁（光）波散射特性的相关研究已经成为近年来国际上的重要课题之一。

另一方面，除了上述电磁（光）波与偏心粒子之间相互作用的研究外，偏心粒子模型在声学共振谐振腔体的研究上也是一个热点问题。如Leung等[78]利用入射场和散射场的叠加近似计算了小扰动球附近区域的声场，而Curzon和Plant[79]利用拉普拉斯方程的不规则解来计算了球形扰动体附近的紊流问题。徐德龙等人[80]在微扰理论的框架内，推导了偏心内核小球引起球形谐振腔的共振频率偏移的表达式，研究了偏心球的各种几何参数与共振频率偏移量之间的关系曲线。最近

Hasheminejad和Mirzaei[81]利用严格的分离变量法重新研究了偏心球三维谐振腔内声波的传播特性。本文由于研究目的的不同，主要着眼于偏心球对电磁波束的散射的研究，但同时也能够给偏心球对其他波束，如声波，的散射和共振研究提供理论指导。

本论文第一部分主要包括第二章到第五章的相关内容。其中第二章中对任意有形波束在任意直角坐标系中的数学展开做了系统的研究分析，相关理论推导结果已经以一个系列的形式发表在Optics Communications上[70-74]，其中主要结论在第二章内容中都有体现。该章节内容也为后面章节的研究提供了必需的理论方法。在第三章中我们基于广义洛伦兹米理论，对偏心球与有形波束之间的散射做了详细的理论推导，并且用FORTRAN语言对理论推导进行编程求解。第四章中我们利用所编写的程序，对偏心球的近场和内场特性进行了数值模拟和结果分析，第三和第四章的相关成果已经发表在JOSA A杂志上[75]。在第五章中我们对偏心球的光学振荡特性进行了数值模拟和结果分析，相关成果已经发表在JOSA A杂志上[76]。

第二章 任意入射有形波束的球矢量波函数展开

本章简单介绍了广义洛伦兹米理论(GLMT)的进展状况。在广义洛伦兹米理论的框架内，利用球矢量波函数在共原点旋转直角坐标系下的旋转加法定理和在平行坐标系下的平移加法定理，将任意方向入射的有形波束在任意直角坐标系下用球矢量波函数展开，推导了波束因子(Beam Shape Coefficients, BSCs)在不同坐标系之间相互转换的一般关系式。以轴对称波束为例，给出了轴对称波束波束因子在任意直角坐标系下相互转换的简化解析表达式，可直接用于数值计算编程。最后以应用最广泛的高斯激光波束为例，给出了可直接用于数值计算的波束因子的数学表达式。分析了波束因子与坐标系旋转变换之间的兼容性和局限性问题，对区域近似法的应用起到补充和修正的作用。

§2.1 广义洛伦兹米理论

关于由各向同性介质组成的均匀球粒子对平面电磁波的散射问题，分别由Lorenz[7]于1890年和Mie[8]于1908年基于麦克斯韦方程组进行了严格求解，获得了各个电磁场散射分量空间分布的解析表达式，形成了经典的洛伦兹米理论(Lorenz-Mie theory, LMT)。 自从1964年第一台激光器的诞生以来，激光便以其高单色性，强相干性，高强度等特点被广泛应用到材料加工，通信传输，粒径测量等领域。而正是伴随着激光的发明和应用，各种光学测量技术才有了里程碑式的发展和应用。如今在绝大多数的光学测量技术和仪器设备中，激光都由于其本身所具有的特性被选作激励光源，因此科研人员对激光与散射体之间相互作用的研究一直有着浓厚的兴趣并一直是国际上的研究热点课题之一。与平面波的传播方式不同，在传播截面上，激光光束的空间能量分布不均匀，其能量空间分布的特点依赖于激光器工作的具体模式。比如应用广泛的氦氖激光器在TEM_{00}模式下工作时，它所发生出来的激光的截面能量分布呈现标准的高斯分布，因此也被称为高斯光。当散射体与有形波束发生相互作用时，产生的散射场的空间分布不仅依赖于散射体自身的性质和有形波束的性质，而且还依赖于散射体处在激光波束的具体空间位置。为了使数值仿真实验更加符合实际应用问题，我们需要从理论上分析激光灯有形电磁波束与粒子之间的散射问题。而其中最关键，也是最困难的问题之一是如何使在不同的坐标系中来描述各种有形电磁波束。

通常我们可以将有形电磁波束分解成分波(Partial Waves)或者是子平面波(Partial Plane Waves)的级数叠加，展开的级数的振幅和相位由一组展开系数来表示，

又称之为波束因子。其中应用最为广泛的方法是由Gouesbet和Grehan等人[35]提出的广义洛伦兹米理论(Generalized Lorenz-Mie theory, GLMT)。广义洛伦兹米理论将有形电磁波束分解成不同振幅和相位大小分波的级数叠加，然后通过分离变量法，在与各种不同形状粒子相对应的坐标系中求解出电磁场方程的精确解。经历近30年的发展和应用后，在多位科学研究者的不断完善下，它已经成为用来描述和计算有形电磁波束与各种规则粒子之间相互作用的最重要理论方法之一。较最初提出的广义洛伦兹米理论而言，该理论在各种有形波束的展开方面和各种典型粒子散射问题的研究拓展上有很大的发展。1982年，Gouesbet和Grehan发表的广义洛伦兹米理论是针对高斯波束对球形粒子散射问题的研究。在有形波束的散射问题上，Barton[43]对高阶高斯波TEM_{mn}进行了研究分析，Loic[82]，韩一平[83]对脉冲激光波束的散射问题进行了研究，任宽芳[42]对椭球波束(Laser-sheet beam)的函数展开进行了研究。在各种形状粒子的研究拓展上，Gouesbet和Grehan[84]、Barton[85]、Lock[86]、吴振森[37]等人对球型粒子、多层球粒子有过广泛的研究。Barton[52]、韩一平[40]、张华永[56]等人主要对椭球粒子的散射进行了研究。对于更多GLMT近30年来更为的具体发展细节，该方法处理问题的优势和局限性，请参考Gouesbet和Grehan最近出版的专著[84]。

如上所述，在粒子对波束散射问题求解的过程中最关键，也是最困难的问题之一是如何利用数学方法在特定坐标系下描述任意入射的有形波束，并在相应的坐标系下求解相对应的波束因子，为有形波束散射问题的求解提供必须的数学工具。下来我们基于球矢量波函数，解决有形波束在任意坐标系下的展开问题，为粒子对波束散射问题的求解提供理论基础。

§2.2 球矢量波函数的加法定理

§2.2.1 球矢量波函数的定义

自1935年Hansen第一次提出球矢量波函数理论之后，该理论被广泛应用于各种波的描述及散射理论的研究中，例如洛伦兹米理论，广义洛伦兹米理论，EBCM方法等等。下面我们简单介绍球矢量波函数的推导，并给出了本文使用的球矢量波函数的定义。

在无源、均匀、各向同性媒质中，略去时间谐波因子$\exp(iwt)$，时谐电磁场的电场分量和磁场分量分别满足以下相同的矢量微分方程：

$$\begin{aligned}\nabla^2\mathbf{E}+k^2\mathbf{E}=0\\ \nabla^2\mathbf{H}+k^2\mathbf{H}=0\end{aligned} \tag{2-1}$$

其中有色散关系式 $k^2=\omega^2\mu\varepsilon+i\sigma\mu\omega$，而 ε， μ， σ 分别为媒质的介电常数，磁导率和电导率；波传播波数 $k=(2\pi/\lambda)n$， λ 为电磁波在自由空间的波长， n 为媒质相对于自由空间的相对折射率。

根据麦克斯韦理论，电磁波的电场分量 $\mathbf{E}$ 和磁场分量 $\mathbf{H}$ 之间还存在有以下关系式：

$$\mathbf{E}=\frac{i\omega\mu}{k^2}\nabla\times\mathbf{H},\qquad \mathbf{H}=\frac{1}{i\omega\mu}\nabla\times\mathbf{E} \tag{2-2}$$

将矢量微分方程式(2-1)放到特定坐标系中求解，比如球坐标系中，我们可以将其分解为三个独立分量的标量方程，但求解过程相对困难。为了求解(2-1)式的方程，Stratton[87]先在数学上引入了标量函数 ψ 和任一常矢量 $\mathbf{r}$，然后由标量波函数构造出满足(2-1)式方程的三个矢量波函数解：

$$\begin{aligned}\mathbf{L}&=\nabla\psi\\ \mathbf{M}&=\nabla\times(\mathbf{r}\psi)\\ \mathbf{N}&=k^{-1}\cdot\nabla\times\mathbf{M}\end{aligned} \tag{2-3}$$

其中 $\mathbf{r}$ 即为任一常矢量，在实际推导中它可取作单位矢量。

标量波函数 ψ 函数满足相应于(2-1)式的标量微分方程：

$$\nabla^2\psi+k^2\psi=0 \tag{2-4}$$

在与任意直角坐标系 $Oxyz$ 相对应的球坐标系 (R,θ,φ) 中，(2-4)式可写为：

$$\frac{1}{R^2}\frac{\partial}{\partial R}(R^2\frac{\partial\psi}{\partial R})+\frac{1}{R^2\sin\theta}\frac{\partial}{\partial\theta}(\sin\theta\frac{\partial\psi}{\partial\theta})+\frac{1}{R^2\sin^2\theta}\frac{\partial^2\psi}{\partial\phi^2}+k^2\psi=0 \tag{2-5}$$

采用分离变量法求解该偏微分方程，所得特征解为：

$$\psi_{mn}=z_n(kr)P_n^m(\cos\theta)\exp(im\varphi) \tag{2-6}$$

其中 $z_n(kR)$ 为四类球贝塞尔函数 $j_n(kR)$， $y_n(kR)$， $h_n^{(1)}(kR)$， $h_n^{(2)}(kR)$ 中的任意一个， $P_n^m(\cos\theta)$ 为第一类连带勒让德函数。

将在球坐标系中求解得到的标量波函数 ψ_{mn} 表达式(2-6)代入式(2-3)即可得到与之相对应的三个矢量球谐波函数 $\mathbf{L}_{nm}$， $\mathbf{M}_{nm}$， $\mathbf{N}_{nm}$：

$$\mathbf{M}_{nm}^{(j)}(kr,\theta,\varphi)=(-1)^m[im\pi_n^m(\cos\theta)\mathbf{i}_\theta-\tau_n^m(\cos\theta)\mathbf{i}_\varphi]z_n(kr)\exp(im\varphi) \tag{2-7}$$

$$\begin{aligned}\mathbf{N}_{nm}^{(j)}(kr,\theta,\varphi)=(-1)^m\Big\{&\frac{n(n+1)}{kr}z_n(kr)\,P_n^m(\cos\theta)\mathbf{i}_r\\&+\frac{1}{kr}\frac{d[rz_n(kr)]}{dr}[\tau_n^m(\cos\theta)\mathbf{i}_\theta+im\pi_n^m(\cos\theta)\mathbf{i}_\varphi]\Big\}\exp(im\varphi)\end{aligned} \tag{2-8}$$

$$\mathbf{L}_{nm}^{(j)}(kr,\theta,\varphi)=(-1)^m k\left\{\frac{dz_n(kr)}{d(kr)}P_n^m(\cos\theta)\mathbf{i}_r + \frac{z_n(kr)}{kr}[\tau_n^m(\cos\theta)\mathbf{i}_\theta + im\pi_n^m(\cos\theta)\mathbf{i}_\varphi]\right\}\exp(im\varphi) \tag{2-9}$$

其中 $P_n^m(\cos\theta)$，$\tau_n^m(\cos\theta)$，$\pi_n^m(\cos\theta)$ 分别为连带勒让德函数以及两个连带勒让德角函数，它们的具体数学定义和表达式，以及详细的数值求解方法请查看附录A。另外在附录A中我们还分别提供了归一化的连带勒让德函数以及两个归一化的连带勒让德角函数 $\widetilde{P_n^m}(\cos\theta)$，$\widetilde{\tau_n^m}(\cos\theta)$，$\widetilde{\pi_n^m}(\cos\theta)$ 的具体定义。

可以证明三个球矢量波函数彼此之间线性无关，并且在球坐标系中满足两两正交关系，构成了一个完备的正交集。因此，任意满足式(2-1)的矢量波函数均可用 $\mathbf{L}_{nm}$，$\mathbf{M}_{nm}$，$\mathbf{N}_{nm}$ 的线性叠加来表示。在许多情况下，比如发散的无源电磁场，其展开式中只包含 $\mathbf{M}_{nm}$，$\mathbf{N}_{nm}$ 两个分量，而本论文所研究的波束散射问题均属于该类情况。

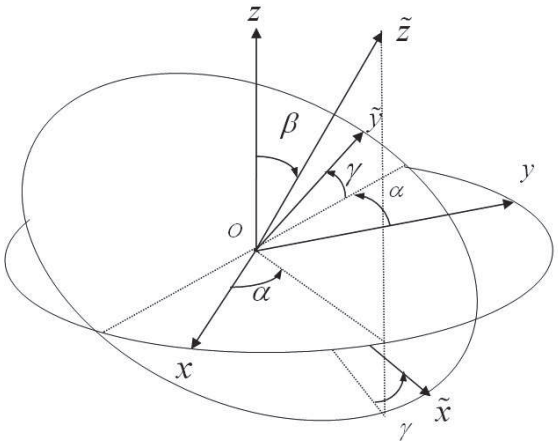

图2.1 共原点直角坐标系之间通过欧拉角进行相互转换

§2.2.2 欧拉角的定义

假定有任意两个共原点的直角坐标系，分别用标注 *Oxyz* 和 *Oxỹz̃* 来表示。它们对应的球坐标系分别用 (r,θ,φ) 和 $(r,\tilde{\theta},\tilde{\varphi})$ 来表示。通过对坐标轴的旋转变换，我们可以建立起两个坐标系之间的相互转换关系，该旋转过程通常用欧拉角 (α,β,γ) 来描述。

关于两个共原点的直角坐标系之间通过欧拉角 (α,β,γ) 进行的旋转过程，Edmonds[88]在他的专著中给出了详细的论述，之后的多名科研工作者包括Mishchenko，Doicu，韩一平等人都沿用了这个描述。首先我们规定旋转方向满足右手螺旋关系的方向为正旋转方向，满足左手螺旋关系的为负旋转方向。具体旋

转过程分如图2.1所示，可以分成以下三个步骤：

1. 以坐标系 $Oxyz$ 中的 z 轴为中心旋转轴进行旋转，旋转角度 $\alpha\,(0\le\alpha\le 2\pi)$，从而得到坐标系 $Ox_\alpha y_\alpha z_\alpha$。

2. 以坐标系 $Ox_\alpha y_\alpha z_\alpha$ 中的 y_α 轴为中心旋转轴进行旋转，旋转角度 $\beta\,(0\le\alpha\le\pi)$，从而得到坐标系 $Ox_\beta y_\beta z_\beta$。

3. 以坐标系 $Ox_\beta y_\beta z_\beta$ 中的 z_β 轴为中心旋转轴进行旋转，旋转角度 $\gamma\,(0\le\alpha\le\pi)$，从而得到坐标系 $Ox_\gamma y_\gamma z_\gamma$，就是最后的旋转坐标系 $O\tilde{x}\tilde{y}\tilde{z}$。

值得注意的一点是，$\tilde{z}$ 轴在 $Oxyz$ 系中的球坐标 (r,θ,φ) 即为：(r,β,α)

§2.2.3　球矢量波函数的旋转加法定理

两个共原点的直角坐标系可以通过欧拉角 (α,β,γ) 旋转相互联系起来，基于这两个不同坐标系的球矢量波函数之间的相互转换关系称为球矢量波函数的旋转加法定理，这个定理将为有形波束在不同坐标系中的展开提供关键数学工具。下面我们对这个定理进行简单描述：

在任意一组共原点的旋转坐标系中，基于不同坐标系的连带勒让德函数之间有转换关系式：

$$P_n^m(\cos\theta)\exp(im\varphi)=\sum_{s=-n}^{n}\rho(m,s,n)P_n^s(\cos\tilde{\theta})\exp(is\tilde{\varphi}) \tag{2-10}$$

其中：

$$\rho(m,s,n)=\exp(is\gamma)u_{sm}^n(\beta)\exp(im\alpha) \tag{2-11}$$

$$\begin{aligned}u_{sm}^n(\beta)=&\left[\frac{(n+s)!(n-s)!}{(n+m)!(n-m)!}\right]^{1/2}\\&\times\sum_{\sigma}(-1)^{n-s-\sigma}\binom{n+m}{n-s-\sigma}\binom{n-m}{\sigma}(\cos\frac{\beta}{2})^{2\sigma+s+m}(\sin\frac{\beta}{2})^{2n-2\sigma-s-m}\end{aligned} \tag{2-12}$$

对于有共同原点的一组坐标系，空间中的任意一点在各个坐标系中都具有相等的径向坐标值 r，因此将关系式(2-10)两边同乘以 $z_n(kr)$，并进行梯度运算，之后乘以相同的单位矢径 $\hat{\mathbf{r}}$，可得到以下等式：

$$\nabla[z_n(kr)P_n^m(\cos\theta)e^{im\varphi}]\times\hat{\mathbf{r}}=\sum_{s=-n}^{n}\{\rho(m,s,n)\nabla[z_n(kr)P_n^s(\cos\tilde{\theta})e^{is\tilde{\varphi}}]\times\hat{\mathbf{r}}\} \tag{2-13}$$

将等式(2-13)对比标量波函数 ψ_{nm} 的定义式(2-6)，我们可以得到：

$$\nabla\psi_{nm}\times\hat{\mathbf{r}}=\sum_{s=-n}^{n}\{\rho(m,s,n)\nabla\widetilde{\psi_{ns}}\times\hat{\mathbf{r}}\} \tag{2-14}$$

根据Stratton由标量波函数构造矢量球谐函数的定义，我们可以得到：

$$\mathbf{M}_{mn}(kr)=\nabla\times(\mathbf{r}\psi_{mn})=\nabla\psi_{mn}\times\mathbf{r} \tag{2-15}$$

对比以上两式，我们即可得到波矢量球函数的旋转加法定理：

$$\mathbf{M}_{mn}(kr,\theta,\varphi)=\sum_{s=-n}^{n}\rho(m,s,n)\mathbf{M}_{sn}(kr,\tilde{\theta},\tilde{\varphi}) \tag{2-16}$$

为了提高数值计算的稳定性以及对相应的推导过程加以简化，在这里我们引入Wigner-d函数。Wigner-d函数是一类在量子力学、分子化学中经常遇到的数学函数，能够很方便地用来表征一组坐标系之间通过旋转建立起来的相互关系。Wigner-d函数的其中一个数学表达形式为：

$$\begin{aligned}d_{sm}^{(n)}(\beta)=&(-1)^{n-m}\sqrt{(n+s)!(n-s)!(n+m)!(n-m)!}\\&\times\sum_{\sigma}(-1)^{\sigma}\frac{(\cos\frac{\beta}{2})^{2\sigma+s+m}(\sin\frac{\beta}{2})^{2n-2\sigma-s-m}}{\sigma!(n-s-\sigma)!(n-m-\sigma)!(s+m+\sigma)!}\end{aligned} \tag{2-17}$$

将Wigner-d函数的表达式与 u_{sm}^{n} 的表达式(2-12)进行比较，我们可以得到：

$$d_{sm}^{(n)}(\beta)=(-1)^{m+s}u_{sm}^{n} \tag{2-18}$$

更多关于Wigner-d函数的表达式，递推运算关系，以及它与连带勒让德函数之间的关系请参照附录A。

基于以上的数学推导，结合本论文对球矢量波函数的定义，我们可以得到以下球矢量波函数的旋转加法定理：

$$\mathbf{M}_{mn}(kr,\theta,\varphi)=\sum_{s=-n}^{n}H_{mn}^{s}(\alpha,\beta,\gamma)\mathbf{M}_{sn}(kr,\tilde{\theta},\tilde{\varphi}) \tag{2-19}$$

其中

$$H_{mn}^{s}(\alpha,\beta,\gamma)=(-1)^{m+s}e^{is\gamma}d_{sm}^{(n)}(\beta)e^{im\alpha} \tag{2-20}$$

依照相似的数学运算过程，我们可以得到另外一个球矢量波函数 $\mathbf{N}_{mn}(kr)$ 的旋转转换关系：

$$\mathbf{N}_{mn}(kr,\theta,\varphi)=\sum_{s=-n}^{n}H_{mn}^{s}(\alpha,\beta,\gamma)\mathbf{N}_{sn}(kr,\tilde{\theta},\tilde{\varphi}) \tag{2-21}$$

§2.2.4　球矢量波函数的平移加法定理

在目标电磁散射相关问题的求解过程中，如果研究对象是多个粒子体系，我们需要把满足每个粒子的边界条件的各个电磁场统一到某个粒子所在的特定的坐标系里去，此过程中就将涉及到电磁场电磁分量在几个坐标系之间相互转换的问

题。借助球矢量波函数的平移加法定理，我们就可以实现电磁场分量在相互平行的不同坐标系中的表示，为相关问题的边界条件求解提供数学工具。

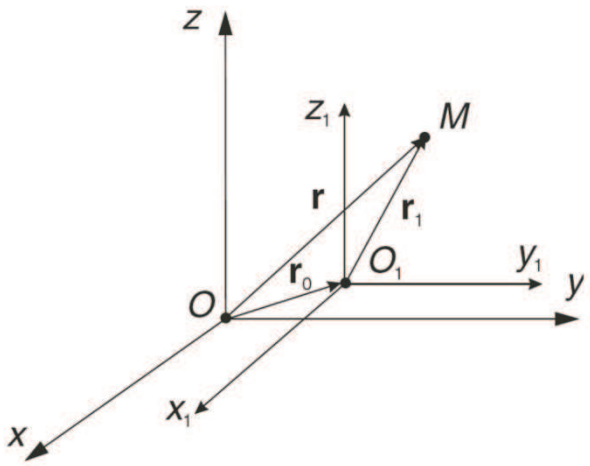

图2.2 直角坐标系的平行移动示意图

球矢量波函数的加法定理最初于1961年由Stein[21]推导和论述，而其中最为困难的问题是对加法定理展开系数的求解。经过多位科学工作者几十年来的的研究，目前对于矢量球谐函数加法定理展开系数的求解主要有以下几种代表性的算法：(I) 间接迭代求解方法。该方法最初由Stein[21]提出，并由Mackowski[24]、Chew[89]等人加以改进，使得计算更为方便。它利用迭代方法先求解得到标量球谐函数的平移系数，然后通过矢量平移系数和标量球谐函数平移系数之间的关系式，来求解得到矢量球谐函数加法定理的平移系数。(II) Wigner 3*jm*符号算法。1962年Cruzan[22]对加法定理进行了重新推导和论述，通过引进递推公式代替了Stein推导中的多项式表达式，提出由Wigner 3*jm*符号可以直接得到矢量传输系数的解析表达形式的计算方法，给出了球矢量波函数平移加法定理的较为简洁的形式。其后，Bruning和Lo[90, 91]将这一结果进行了简化。Tsang等人[92]进一步得到了便于计算机计算的表达形式。(III)基于快速计算Gaunt系数的算法。Xu[93]对加法定理的系数进行了较为系统的研究，提出了通过直接计算Gaunt系数来求解平移系数的算法，并将其广泛应用到对多粒子散射的问题求解中[94]。下面我们简单介绍矢量球谐函数的平移加法定理。

如图2.2所示，任意两个平行的直角坐标系分别用 $Oxyz$ 和 $O_1x_1y_1z_1$ 来表示，其中坐标系 $O_1x_1y_1z_1$ 的原点 O_1 在坐标系 $Oxyz$ 中的位置用矢量 $\mathbf{r}_0$ 来表示。假设空间中存在任意一点 M，它在直角坐标系 $Oxyz$ 和 $O_1x_1y_1z_1$ 中的位置分别用 $\mathbf{r}$ 和 $\mathbf{r}_1$ 来表示。我们有以下简单的关系式：$\mathbf{r}=\mathbf{r}_0+\mathbf{r}_1$。

对于一般的坐标系平移情况，矢量球谐函数的平移加法定理表示为：

$$\begin{aligned}\mathbf{M}_{mn}^{(j)}(k\mathbf{r})&=\sum_{\nu=1}^{\infty}\sum_{\mu=-\nu}^{\nu}[A_{\mu\nu}^{mn,p}(k\mathbf{r}_0)\mathbf{M}_{\mu\nu}^{(j)}(k\mathbf{r}_1)+B_{\mu\nu}^{mn,p}(k\mathbf{r}_0)\mathbf{N}_{\mu\nu}^{(j)}(k\mathbf{r}_1)]\\\mathbf{N}_{mn}^{(j)}(k\mathbf{r})&=\sum_{\nu=1}^{\infty}\sum_{\mu=-\nu}^{\nu}[B_{\mu\nu}^{mn,p}(k\mathbf{r}_0)\mathbf{M}_{\mu\nu}^{(j)}(k\mathbf{r}_1)+A_{\mu\nu}^{mn,p}(k\mathbf{r}_0)\mathbf{N}_{\mu\nu}^{(j)}(k\mathbf{r}_1)]\end{aligned}\tag{2-22}$$

其中 $A_{\mu\nu}^{mn,p}$，$B_{\mu\nu}^{mn,p}$ 为平移系数。

对于平移方向只沿坐标系 z 轴方向移动的特殊平移方式，式(2-22)中的双重叠加运算退化成一重叠加运算：

$$\begin{aligned}\mathbf{M}_{mn}^{(j)}(k\mathbf{r})&=\sum_{\nu=1}^{\infty}[A_{m\nu}^{mn,p}(k\mathbf{r}_0)\mathbf{M}_{m\nu}^{(j)}(k\mathbf{r}_1)+B_{m\nu}^{mn,p}(k\mathbf{r}_0)\mathbf{N}_{m\nu}^{(j)}(k\mathbf{r}_1)]\\\mathbf{N}_{mn}^{(j)}(k\mathbf{r})&=\sum_{\nu=1}^{\infty}[B_{m\nu}^{mn,p}(k\mathbf{r}_0)\mathbf{M}_{m\nu}^{(j)}(k\mathbf{r}_1)+A_{m\nu}^{mn,p}(k\mathbf{r}_0)\mathbf{N}_{m\nu}^{(j)}(k\mathbf{r}_1)]\end{aligned}\tag{2-23}$$

对于收敛性正则球谐函数，我们有：

$$\begin{aligned}\mathbf{M}_{mn}^{(1)}(k\mathbf{r})&=\sum_{\nu=1}^{\infty}[A_{m\nu}^{mn,1}(k\mathbf{r}_0)\mathbf{M}_{m\nu}^{(1)}(k\mathbf{r}_1)+B_{m\nu}^{mn,1}(k\mathbf{r}_0)\mathbf{N}_{m\nu}^{(1)}(k\mathbf{r}_1)]\\\mathbf{N}_{mn}^{(1)}(k\mathbf{r})&=\sum_{\nu=1}^{\infty}[B_{m\nu}^{mn,1}(k\mathbf{r}_0)\mathbf{M}_{m\nu}^{(1)}(k\mathbf{r}_1)+A_{m\nu}^{mn,1}(k\mathbf{r}_0)\mathbf{N}_{m\nu}^{(1)}(k\mathbf{r}_1)]\end{aligned}\tag{2-24}$$

对于发散性球谐函数，在 $r_1\geq r_0$ 的情况下，我们有：

$$\begin{aligned}\mathbf{M}_{mn}^{(3,4)}(k\mathbf{r})&=\sum_{\nu=1}^{\infty}[A_{m\nu}^{mn,1}(k\mathbf{r}_0)\mathbf{M}_{m\nu}^{(3,4)}(k\mathbf{r}_1)+B_{m\nu}^{mn,1}(k\mathbf{r}_0)\mathbf{N}_{m\nu}^{(3,4)}(k\mathbf{r}_1)]\\\mathbf{N}_{mn}^{(3,4)}(k\mathbf{r})&=\sum_{\nu=1}^{\infty}[B_{m\nu}^{mn,1}(k\mathbf{r}_0)\mathbf{M}_{m\nu}^{(3,4)}(k\mathbf{r}_1)+A_{m\nu}^{mn,1}(k\mathbf{r}_0)\mathbf{N}_{m\nu}^{(3,4)}(k\mathbf{r}_1)]\end{aligned}\tag{2-25}$$

在 $r_1<r_0$ 的情况下，我们有：

$$\begin{aligned}\mathbf{M}_{mn}^{(3,4)}(k\mathbf{r})&=\sum_{\nu=1}^{\infty}[A_{m\nu}^{mn,(3,4)}(k\mathbf{r}_0)\mathbf{M}_{m\nu}^{(1)}(k\mathbf{r}_1)+B_{m\nu}^{mn,(3,4)}(k\mathbf{r}_0)\mathbf{N}_{m\nu}^{(1)}(k\mathbf{r}_1)]\\\mathbf{N}_{mn}^{(3,4)}(k\mathbf{r})&=\sum_{\nu=1}^{\infty}[B_{m\nu}^{mn,(3,4)}(k\mathbf{r}_0)\mathbf{M}_{m\nu}^{(1)}(k\mathbf{r}_1)+A_{m\nu}^{mn,(3,4)}(k\mathbf{r}_0)\mathbf{N}_{m\nu}^{(1)}(k\mathbf{r}_1)]\end{aligned}\tag{2-26}$$

对于平移系数的 $(A_{m\nu}^{mn,p},B_{m\nu}^{mn,p})$ 的递推迭代求解方法，详细细节请具体参考附录B。

§ 2.3 任意入射有形波束的展开

§2.3.1 有形波束的Bromwich描述和波束因子的定义

在麦克斯韦方程的基础上，Gouesbet等人[36]利用Bromwich标量势对入射波束的电磁场分量进行表征，完成了对电磁场分量空间分布的描述。任意入射有形波

束的Bromwich标量势满足以下偏微分方程：

$$\frac{\partial^2 U}{\partial r^2}+\frac{1}{r^2\sin\theta}\frac{\partial}{\partial\theta}(\sin\theta\frac{\partial U}{\partial\theta})+\frac{1}{r^2\sin^2\theta}\frac{\partial^2 U}{\partial\varphi^2}+k^2U=0 \tag{2-27}$$

采用分离变量法求解以上方程，得到两个特征解的表达式分别为：

$$U_{TM}^{i}=\frac{E_0}{k}\sum_{n=1}^{\infty}\sum_{m=-n}^{n}c_n^{pw}g_{n,TM}^{m}\psi_n(kr)P_n^{|m|}(\cos\theta)\exp(im\varphi) \tag{2-28}$$

$$U_{TE}^{i}=\frac{H_0}{k}\sum_{n=1}^{\infty}\sum_{m=-n}^{n}c_n^{pw}g_{n,TE}^{m}\psi_n(kr)P_n^{|m|}(\cos\theta)\exp(im\varphi) \tag{2-29}$$

其中k为介质中波传播的波数，$\psi_n(kr)=krj_n(kr)$ 为Ricatti-Bessel函数。$g_{n,TM}^{m}, g_{n,TE}^{m}$ 为待求的两组波束因子，c_n^{pw} 为平面波因子：

$$c_n^{pw}=\frac{1}{k}(-i)^{n+1}\frac{2n+1}{n(n+1)} \tag{2-30}$$

这两组不相关的特征解分别对应电磁波中的横磁波 $H_r=0$ (Transverse magnetic wave, TM wave)分量和横电波 $E_r=0$ (Transverse electric wave, TE wave)分量。基于电磁场Bromwich标量势的两个特征解，利用电磁波束各个电磁场分量与标量势之间的相互关系，我们就可以求得电磁场分量的具体数学表达式。例如对于电磁波中的TM波，我们有：

$$E_{r,TM}=\frac{\partial^2 U_{TM}}{\partial r^2}+k^2U_{TM},\quad E_{\theta,TM}=\frac{1}{r}\frac{\partial^2 U_{TM}}{\partial r\partial\theta},\quad E_{\varphi,TM}=\frac{1}{r\sin\theta}\frac{\partial^2 U_{TM}}{\partial r\partial\varphi} \tag{2-31}$$

$$H_{\theta,TM}=\frac{i\omega\varepsilon}{r\sin\theta}\frac{\partial U_{TM}}{\partial\varphi},\quad H_{\varphi,TM}=-\frac{i\omega\varepsilon}{r}\frac{\partial U_{TM}}{\partial\theta} \tag{2-32}$$

将Bromwich标量势 U_{TM} 的表达式(2-28)代入求解关系式(2-31)-(2-32)就可以得到电磁波中横磁波的各个电磁分量。同样的方法，利用Bromwich标量势 U_{TE} 的表达式经过类似求解过程就可以得到电磁波中横电波的各个电磁场分量。将电磁场分量的数学表达式对比球矢量波函数 $\mathbf{M}_{mn}(k\mathbf{r}), \mathbf{N}_{mn}(k\mathbf{r})$ 的定义式进行简化，可以得到入射有形波束的电场分量和磁场分量表达式为：

$$\mathbf{E}^{i}=E_0\sum_{n=1}^{\infty}\sum_{m=-n}^{n}kc_n^{pw}(-1)^{(m-|m|)/2}\frac{(n-m)!}{(n-|m|)!}[-ig_{n,TE}^{m}\mathbf{M}_{mn}(k\mathbf{r})+g_{n,TM}^{m}\mathbf{N}_{mn}(k\mathbf{r})] \tag{2-33}$$

$$\mathbf{H}^{i}=-\frac{kE_0}{i\omega\mu}\sum_{n=1}^{\infty}\sum_{m=-n}^{n}kc_n^{pw}(-1)^{(m-|m|)/2}\frac{(n-m)!}{(n-|m|)!}[-ig_{n,TE}^{m}\mathbf{N}_{mn}(k\mathbf{r})+g_{n,TM}^{m}\mathbf{M}_{mn}(k\mathbf{r})] \tag{2-34}$$

从展开式(2-33)-(2-34)可以看出，通过将入射电磁波束的电磁场分量分解成各阶球矢量波函数的叠加，从而实现任意有形波束的数学描述。在物理意义上，我们将这些不同阶数的球谐函数分量称为分波，而它们的振幅强度由复系数 $g_{n,TM}^{m}, g_{n,TE}^{m}$，即波束因子的绝对值大小来表征。

§2.3.2 任意入射有形波束的展开

利用GLMT可以对常见规则粒子与有形波束的散射问题进行系统的求解和分析。它基于分离变量法，在与散射粒子形状相对应的坐标系中通过应用边界条件来求解有形波束的散射问题。例如对于球形粒子中，基于球矢量波函数 $\mathbf{M}_{mn}(k\mathbf{r}),\mathbf{N}_{mn}(k\mathbf{r})$ 之间的线性无关和相互正交关系，我们可以将任意无源发散的电磁场分量用球矢量波函数 $\mathbf{M}_{mn}(k\mathbf{r}),\mathbf{N}_{mn}(k\mathbf{r})$ 来展开，它们的振幅强度由波束因子 $g_{n,TM}^{m},g_{n,TE}^{m}$ 的绝对值来决定。相类似的，在柱坐标系下，任意无源发散电磁场分量都可以用相应的柱矢量波函数 $\mathbf{M}_{m\lambda}(kr),\mathbf{N}_{m\lambda}(kr)$ 来唯一展开，得到相应柱坐标系下的波束因子。在椭球坐标系下，也可以利用矢量椭球波函数 $\mathbf{M}_{mn}(c,\eta,\zeta,\varphi),\mathbf{N}_{mn}(c,\eta,\zeta,\varphi)$ 来展开相应的电磁波。下面我们基于球矢量波函数，讨论任意入射有形波束在任意直角坐标系下的数学展开问题，这种波束展开形式可以应用到GLMT，EBCM等多种理论方法中去解决波束散射问题。

通常把入射波束的电磁场分量用第一类球矢量波函数展开：

$$\mathbf{E}^{i}=E_{0}\sum_{n=1}^{\infty}\sum_{m=-n}^{n}a_{mn}\mathbf{M}_{mn}(k\mathbf{r})+b_{mn}\mathbf{N}_{mn}(k\mathbf{r}) \tag{2-35}$$

$$\mathbf{H}^{i}=-\frac{kE_{0}}{i\omega\mu}\sum_{n=1}^{\infty}\sum_{m=-n}^{n}a_{mn}\mathbf{N}_{mn}(k\mathbf{r})+b_{mn}\mathbf{M}_{mn}(k\mathbf{r}) \tag{2-36}$$

将上面的式子与式(2-33)-(2-34)进行比较，我们可以得出展开系数 a_{mn},b_{mn} 与波束因子 $g_{n,TM}^{m},g_{n,TE}^{m}$ 之间具有以下关系式：

$$b_{mn}=kc_{n}^{pw}(-1)^{(m-|m|)/2}\frac{(n-m)!}{(n-|m|)!}g_{n,TM}^{m} \tag{2-37}$$

$$a_{mn}=-ikc_{n}^{pw}(-1)^{(m-|m|)/2}\frac{(n-m)!}{(n-|m|)!}g_{n,TE}^{m} \tag{2-38}$$

因此，如果计算得到波束因子 $g_{n,TM}^{m},g_{n,TE}^{m}$ 的值，就可以根据 a_{mn},b_{mn} 和波束因子 $g_{n,TM}^{m},g_{n,TE}^{m}$ 之间的相互关系，得到特定坐标系下有形波束的展开数学表达式。

由于有形波束的波束因子的求解比较困难，现有的一般做法是在合适的取向上建立波束坐标系，比如沿对称波束的对称轴建立z轴，让波束在坐标系中具备一定的对称条件，然后将有形波束在波束坐标系中展开，求解对应的波束因子，最后再求解其他相关坐标系(旋转坐标系，平行坐标系)下波束因子的值。关于有形波束在波束坐标系中的展开，Gouesbet等人[95]先后给出了积分法、有限级数法和区域近似法等三种计算方法来求解波束因子 $g_{n,TM}^{m},g_{n,TE}^{m}$。在此基础上，下面我们将利用球矢量波函数的旋转加法定理和平移加法定理，探讨任意球直角坐标下波束因子的具体求解方法，实现任意入射有形波束的电磁分量在任意直角坐标下展开。

假设有任意两个共原点的直角坐标系 $Oxyz$ 和 $O\tilde{x}\tilde{y}\tilde{z}$，他们之间通过欧拉角 (α,β,γ) 可以实现相互旋转转换。在直角坐标系 $Oxyz$ 下，有形波束可以用球矢量波函数展开成以下形式：

$$\mathbf{E}^i = E_0 \sum_{n=1}^{\infty} \sum_{m=-n}^{n} a_{mn}\mathbf{M}_{mn}(k\mathbf{r}) + b_{mn}\mathbf{N}_{mn}(k\mathbf{r}) \tag{2-39}$$

$$\mathbf{H}^i = -\frac{kE_0}{i\omega\mu} \sum_{n=1}^{\infty} \sum_{m=-n}^{n} a_{mn}\mathbf{N}_{mn}(k\mathbf{r}) + b_{mn}\mathbf{M}_{mn}(k\mathbf{r}) \tag{2-40}$$

利用球矢量波函数的旋转加法定理，将式(2-19)和(2-21)代入入射波束的展开式(2-39)-(2-40)中，就得到旋转坐标系 $O\tilde{x}\tilde{y}\tilde{z}$ 下有形波束的球矢量波函数展开。以电场分量为例，可以得到：

$$\mathbf{E}^i = \sum_{n=1}^{\infty} \sum_{m=-n}^{n} \sum_{s=-n}^{n} H_{mn}^{s}(\alpha,\beta,\gamma)[a_{mn}\mathbf{M}_{sn}(kr,\tilde{\theta},\tilde{\varphi}) + b_{mn}\mathbf{N}_{sn}(kr,\tilde{\theta},\tilde{\varphi})] \tag{2-41}$$

将标注 m 与 s 相互替换，整理之后：

$$\mathbf{E}^i = \sum_{n=1}^{\infty} \sum_{m=-n}^{n} \widetilde{a_{mn}}\mathbf{M}_{mn}(kr,\tilde{\theta},\tilde{\varphi}) + \widetilde{b_{mn}}\mathbf{N}_{mn}(kr,\tilde{\theta},\tilde{\varphi}) \tag{2-42}$$

其中展开系数为：

$$\widetilde{a_{mn}} = \sum_{s=-n}^{n} H_{sn}^{m}(\alpha,\beta,\gamma) a_{sn} \tag{2-43}$$

$$\widetilde{b_{mn}} = \sum_{s=-n}^{n} H_{sn}^{m}(\alpha,\beta,\gamma) b_{sn} \tag{2-44}$$

将式(2-37)-(2-38)代入式(2-43)-(2-44)，我们就建立起旋转坐标系 $O\tilde{x}\tilde{y}\tilde{z}$ 下有形波束波束因子 $\widetilde{g_{n,X}^{m}}$ 与非旋转坐标系 $Oxyz$ 下有形波束波束因子 $g_{n,X}^{m}$ 之间相互转换的一般关系式：

$$\widetilde{g_{n,X}^{m}} = \mu_{mn} \sum_{s=-n}^{n} \frac{H_{sn}^{m}(\alpha,\beta,\gamma)}{\mu_{sn}} g_{n,X}^{s} \tag{2-45}$$

其中有：

$$\mu_{mn} = (-1)^{(m-|m|)/2} \frac{(n-|m|)!}{(n-m)!} \tag{2-46}$$

$$H_{mn}^{s}(\alpha,\beta,\gamma) = (-1)^{m+s} e^{is\gamma} d_{sm}^{(n)}(\beta) e^{im\alpha} \tag{2-47}$$

§2.3.3　任意入射轴对称波束的展开

波束是以很小的发散角向某个特定方向上定向传输的波的形式。人们最为熟

悉的激光光束就是一种空间定向传播的电磁波束。此外，利用波导天线定向传输的微波波束，使用扩音器定向播放的声波波束都是典型波束形式。下面我们介绍一类能量在空间传播截面上成轴对称分布的波束，比如说高斯波束，贝塞尔波束等，称为轴对称波束。下面就通过以轴对称波束为例来对波束的球矢量波函数展开中波束因子求解方法进行具体的分析。

§2.3.3.1 在轴轴对称波束的展开

假设矢量**S**为任意有形波束的坡印廷矢量，它沿任意直角坐标系 x, y, z 三个坐标轴分别有 S_x, S_y, S_z 等三个分量。假设该波束传播方向沿 z 轴传播，首先我们定义当且仅当坡印廷矢量沿传播方向 z 轴的分量 $S_z(\theta=0)$ 不等于零的波束称为一般波束(Generic beams)。下面的讨论都将在一般波束的范围内考虑。进一步，我们定义旋转对称波束是一类在波束自身坐标系中，该波束的坡印廷矢量沿传播方向 z 轴的分量 S_z 的变化大小与方位角 φ 无关，更为确切的，这类波束称为在轴轴对称波束。这类波束的波束因子具有以下简单形式[96]：

$$g_n^m = 0, \quad |m| \neq 1 \tag{2-48}$$

$$g_{n,TM}^1 = \frac{1}{K} g_{n,TM}^{-1} = -i\varepsilon g_{n,TE}^1 = \frac{i\varepsilon}{K} g_{n,TE}^{-1} = \frac{g_n}{2} \tag{2-49}$$

其中参数 ε 只是一个表征能流方向的量，当能流方向沿正 z 轴时，ε 取-1；当能流方向沿负 z 轴时，ε 取+1。参数K为一个表征波束极化状态的实数，具体的取值将和实际选用的坐标系有关。特别的，当坡印廷矢量沿传播方向 x 轴的分量 S_x 正比于 $\cos\varphi$ 时，有 $K=\pm 1$。

将等式(2-48)以及(2-49)代入有形波束波束因子坐标系之间旋转变换的一般关系式(2-45)，即可得到在轴轴对称波束的波束因子在共原点旋转坐标系之间相互转换的关系式：

$$\widetilde{g_{n,X}^m} = \mu_{mn}\left[\frac{H_{1n}^m(\alpha,\beta,\gamma)}{\mu_{1n}} g_{n,X}^1 + \frac{H_{-1n}^m(\alpha,\beta,\gamma)}{\mu_{-1n}} g_{n,X}^{-1}\right] \tag{2-50}$$

其中有：

$$\mu_{1n} = (-1), \quad \mu_{-1n} = \frac{1}{n(n+1)} \tag{2-51}$$

$$H_{1n}^m(\alpha,\beta,\gamma) = (-1)^{m+1} e^{im\gamma} d_{m1}^n(\beta) e^{i\alpha} \quad H_{-1n}^m(\alpha,\beta,\gamma) = (-1)^{m-1} e^{im\gamma} d_{m-1}^n(\beta) e^{-i\alpha} \tag{2-52}$$

根据附录A中对各个基本函数的推导，有A.24和A.25：

$$\sqrt{\frac{(n-m)!}{(n+m)!}}\left[\tau_n^m(\cos\beta) + m\pi_n^m(\cos\beta)\right] = -\sqrt{n(n+1)} d_{m1}^n(\beta) \tag{2-53}$$

$$\sqrt{\frac{(n-m)!}{(n+m)!}}\left[\tau_n^m(\cos\beta)-m\pi_n^m(\cos\beta)\right]=\sqrt{n(n+1)}d_{m-1}^n(\beta) \tag{2-54}$$

将等式(2-53)和(2-54)代入式子(2-52)，我们可以得到：

$$H_{1n}^m(\alpha,\beta,\gamma)=(-1)^{m+1}e^{im\gamma}d_{m1}^n(\beta)e^{i\alpha} \tag{2-55}$$

$$H_{-1n}^m(\alpha,\beta,\gamma)=(-1)^{m-1}e^{im\gamma}d_{m-1}^n(\beta)e^{-i\alpha} \tag{2-56}$$

将等式(2-55)-(2-56)连同等式(2-51)代入式子(2-50)，我们可以得到轴对称波束在轴情况下波束因子在共原点旋转坐标系之间相互转换的简化解析表达式：

$$\begin{aligned}\widetilde{g_{n,X}^m}&=(-1)^{m+1}(-1)^{\frac{m-|m|}{2}}e^{im\gamma}\\&\left\{m\pi_n^m(\cos\beta)[e^{-i\alpha}g_{n,X}^{-1}-e^{i\alpha}g_{n,X}^{1}]-\tau_n^m(\cos\beta)[e^{-i\alpha}g_{n,X}^{-1}+e^{i\alpha}g_{n,X}^{1}]\right\}\end{aligned} \tag{2-57}$$

§ 2.3.3.2　离轴轴对称波束的展开

对于波束因子 $g_{n,TM}^m$, $g_{n,TE}^m$ 的计算，Grehan和Gouesbet等人[97]前后提出了积分法、有限级数展开法、区域近似法等三种计算方法。任宽芳[98]将积分法和区域近似法相结合，提出了适用性更广，计算更为灵活的积分区域近似法。 在求得在轴波束波束因子的基础上，Doicu等[99]利用球矢量波函数的平移加法定理推导了离轴波束波束因子的计算公式。张华永等[100]也对这种平移加法定理求解有形波束波束因子的方法进行了分析。在所提到的这些求解方法中，区域近似法以其计算速度快，收敛性好，具有明确的物理意义而得到广泛应用。兼顾论文的系统性，下面我们就分别对平移加法定理求解法和区域近似法进行介绍，为离轴波束波束因子的求解提供理论基础。

A. 平移加法定理求解法

如图2.2所示，有任意两个相互平行的直角坐标系分别用 $Oxyz$ 和 $O_1x_1y_1z_1$ 来表示，其中坐标系 $O_1x_1y_1z_1$ 的原点 O_1 在坐标系 $Oxyz$ 中的位置用矢量 $\mathbf{r}_0$ 来表示。假设空间中存在任意一点 M ，它在直角坐标系 $Oxyz$ 和 $O_1x_1y_1z_1$ 中的位置分别用 $\mathbf{r}$ 和 $\mathbf{r}_1$ 来表示。我们有以下简单的关系式： $\mathbf{r}=\mathbf{r}_0+\mathbf{r}_1$ 。在直角坐标系 $Oxyz$ 中我们可以把入射波束的电磁场分量用球矢量波函数展开：

$$\mathbf{E}^i=E_0\sum_{n=1}^{\infty}\sum_{m=-n}^{n}a_{mn}\mathbf{M}_{mn}(k\mathbf{r})+b_{mn}\mathbf{N}_{mn}(k\mathbf{r}) \tag{2-58}$$

$$\mathbf{H}^i=-\frac{kE_0}{i\omega\mu}\sum_{n=1}^{\infty}\sum_{m=-n}^{n}a_{mn}\mathbf{N}_{mn}(k\mathbf{r})+b_{mn}\mathbf{M}_{mn}(k\mathbf{r}) \tag{2-59}$$

利用矢量球谐函数的平移定理：

$$\begin{aligned}\mathbf{M}_{mn}^{(1)}(k\mathbf{r})&=\sum_{\nu=1}^{\infty}\sum_{\mu=-\nu}^{\nu}[A_{\mu\nu}^{mn,1}(k\mathbf{r}_0)\mathbf{M}_{\mu\nu}^{(1)}(k\mathbf{r}_1)+B_{\mu\nu}^{mn,1}(k\mathbf{r}_0)\mathbf{N}_{\mu\nu}^{(1)}(k\mathbf{r}_1)]\\\mathbf{N}_{mn}^{(1)}(k\mathbf{r})&=\sum_{\nu=1}^{\infty}\sum_{\mu=-\nu}^{\nu}[B_{\mu\nu}^{mn,1}(k\mathbf{r}_0)\mathbf{M}_{\mu\nu}^{(1)}(k\mathbf{r}_1)+A_{\mu\nu}^{mn,1}(k\mathbf{r}_0)\mathbf{N}_{\mu\nu}^{(1)}(k\mathbf{r}_1)]\end{aligned}\tag{2-60}$$

将式(2-60)代入式(2-58)-(2-59)，并将 $\mu\nu$ 和 mn 分别调换，我们可以得到：

$$a'_{mn}=\sum_{uv}a_{uv}A_{mn}^{\mu\nu,1}+b_{uv}B_{mn}^{\mu\nu,1},\qquad b'_{mn}=\sum_{uv}a_{uv}B_{mn}^{\mu\nu,1}+b_{uv}A_{mn}^{\mu\nu,1}\tag{2-61}$$

其中 a'_{mn}，b'_{mn} 为平移之后坐标系下有形波束的展开系数。将式(2-61)代入式(2-37)-(2-38)即可得到有形波束在平移坐标系下展开的波束因子，在此不加累述。

另外在求得在轴有形波束波束因子的前提下，根据球矢量波函数与椭球矢量波函数、球矢量波函数与圆柱矢量波函数之间的相互转换关系，我们即可以求得有形波束波束因子在椭球坐标系、圆柱坐标系下的表达式[100]。

B． 区域近似法求解

虽然在求得在轴波束波束因子的前提下，利用平移加法定理能够有效求得离轴波束波束因子。但是特别值得一提的是，Gouesbet等人[101]提出的区域近似法以其计算速度快，收敛性好，具有明确的物理意义而得到更为广泛的应用。下面我们就用区域近似法来求解任意方向入射有形波束在任意坐标系下的波束因子。利用区域近似法求解波束因子一般可分成以下几个步骤[101]：

第一：将电场径向分量 $E_r(r,\theta,\varphi)$ 和磁场径向分量 $H_r(r,\theta,\varphi)$ 分别分离成 m 阶分量波束 E_r^m 和 H_r^m。其中 m 为方位角模数，因此该分离过程类似于将有形波束在方位角方向上分解成 m 个子波。

$$\begin{pmatrix}E_r\\H_r\end{pmatrix}=\sum_{m=-\infty}^{m=+\infty}\begin{pmatrix}E_r^m\\H_r^m\end{pmatrix}\tag{2-62}$$

第二：将以上各阶分量波束 E_r^m 和 H_r^m 中的平面波分量分离出来。

$$\begin{pmatrix}E_r^m\\H_r^m\end{pmatrix}=\left[\begin{pmatrix}E_0\\H_0\end{pmatrix}\exp(-ikr\cos\theta)\exp(im\varphi)\sin\theta\right]\begin{pmatrix}E_{r,-}^m\\H_{r,-}^m\end{pmatrix}\tag{2-63}$$

我们可以得到不再依赖于 φ 变量的振幅分量 $E_{r,-}^m$ 和 $H_{r,-}^m$。

第三：将 $E_{r,-}^m$ 和 $H_{r,-}^m$ 进行区域近似化。即在球坐标系中，将边界上的点到 z 轴的距离参量 $r\sin\theta$ 用 $L^{1/2}$ 来代替，并将极角 θ 取定为 $\pi/2$。其中有：

$$L=(n+1/2)^2-(|m|+1/2)^2\tag{2-64}$$

第四：最后将以上所得运算结果乘上归一化因子 Z_n^m 进行归一化：

$$Z_n^m = (\frac{-i}{L^{1/2}})^{|m|-1} \tag{2-65}$$

即可得到离轴波束在任意平行坐标系下的波束因子 $g_{n,TM}^m, g_{n,TE}^m$。将波束因子 $g_{n,TM}^m, g_{n,TE}^m$ 的表达式代入式(2-45)即可得到离轴轴对称波束在任意坐标系下展开的波束因子。为了更加具体地分析轴对称波束在任意坐标系下的展开，下面我们以高斯波束为例来阐述任意坐标下波束因子的求解。

§2.3.4 任意入射高斯波束的展开

上面我们讨论了轴对称波束波束因子在任意直角坐标系下转换求解的一般关系式。从等式(2-48)-(2-49)不难发现，当 $(\varepsilon, K) = (-1, +1)$ 时，轴对称波束波束因子的数值大小刚好和束腰处沿 x 轴极化的在轴高斯波束的波束因子具有一样的取值：

$$g_{n,TM}^1 = g_{n,TM}^{-1} = ig_{n,TE}^1 = -ig_{n,TE}^{-1} = \frac{g_n}{2} \tag{2-66}$$

即高斯波束是一种典型的轴对称波束，它还是激光出射能量分布最为普遍的模式之一，下面就对高斯波束的具体展开和波束因子的求解进行详细的分析。

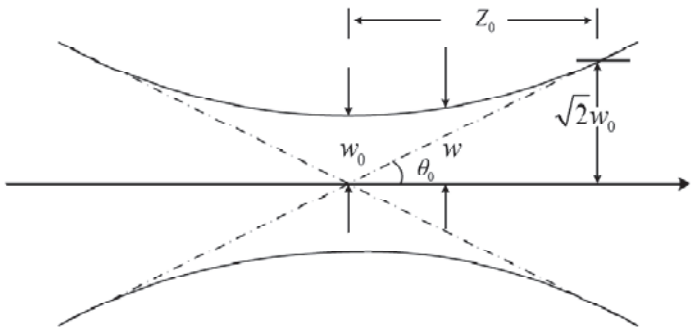

图2.3 高斯波束传播空间传播截面图

§ 2.3.4.1 高斯波束的描述

电磁波在无源空间内传播时满足Hermitz方程：

$$\nabla^2 \mathbf{E} + k^2 \mathbf{E} = 0 \tag{2-67}$$

通过求解方程可以发现，平面波、球面波以及柱面波都是它的特征解。但是高斯波不是电磁场Hermitz方程的精确解，而是在缓变振幅近似下的一个近似解。高斯波束是指传播路径上横向截面强度分布符合高斯型函数的波束的统称。

如图2.3所示为高斯波束传播截面图。它的电场分量表达式为：

$$E(r,z)=\frac{E_0\omega_0}{\omega(z)}\exp[-\frac{r^2}{\omega^2(z)}]\exp\left\{-i[k(\frac{r^2}{R(z)}+z)-\psi(z)]\right\} \tag{2-68}$$

其中 ω_0 为束腰半径， $\omega(z)$ 为坐标 z 处的波束宽度， $R(z)$ 为等相面曲率半径， $\psi(z)$ 为相位因子：

$$\omega(z)=\omega_0\sqrt{1+(z/z_0)^2},\psi(z)=\tan^{-1}(\frac{z}{z_0}) \tag{2-69}$$

其中 z_0 为共焦参数，也称瑞利长度：

$$z_0=\frac{1}{2}k\omega_0^2 \tag{2-70}$$

基模高斯波束TEM_{00}是激光器最普遍的工作模式，也是电磁波定向传播最基本的能量空间分布形式。下面我们以基模高斯波束TEM_{00}为例来说明高斯波束在任意坐标系中的展开。如图2.4所示，一束束腰半径为 ω_0 的单色近轴高斯波波束沿坐标系 O_guvw 中 w 轴的正方向传播，时间因子为 $\exp(i\omega t)$，其中 ω 为角频率。束腰中心与坐标系原点 O_g 重合，电磁波电场分量沿 u 轴正方向极化。有另一个与 O_guvw 坐标系平行的直角坐标系 $Oxyz$，其中 O_guvw 坐标系原点 O_g 在坐标系 $Oxyz$ 中的坐标为 (x_0,y_0,z_0)。最后，旋转直角坐标系 $O\tilde{x}\tilde{y}\tilde{z}$ 是通过坐标系 $Oxyz$ 的在欧拉角 (α,β,γ) 的旋转来达到的。

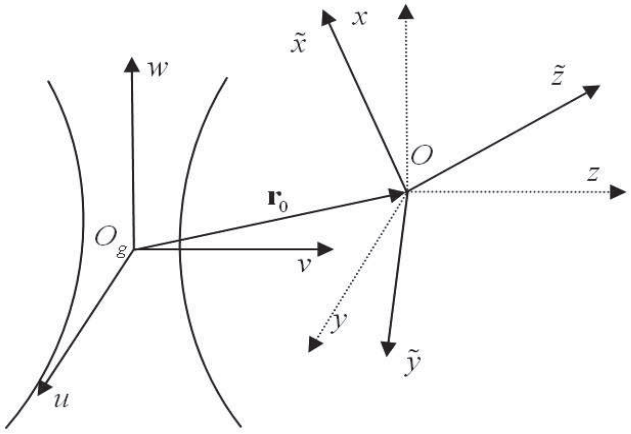

图2.4 高斯波束在任意直角坐标系中的描述

§ 2.3.4.2 在轴高斯波束的数学描述

在波束坐标系 O_guvw 中，Davis[34]把近轴高斯波束展开成多阶子波的级数，每阶子波近似满足麦克斯韦方程，从而较好地解决了波束展开的数学描述问题。在最低阶时，入射高斯波束在直角坐标系 O_guvw 中的电磁场分量的表达式如下所示：

$$
\begin{aligned}
E_u^i(u,v,w) &= E_0\Psi_0\exp(-ikw)\\
E_v^i(u,v,w) &= 0\\
E_w^i(u,v,w) &= -\frac{2Qu}{l}E_u^i(u,v,w)
\end{aligned}
\tag{2-71}
$$

$$
\begin{aligned}
H_u^i(u,v,w) &= 0\\
H_v^i(u,v,w) &= H_0\Psi_0\exp(-ikw)\\
H_w^i(u,v,w) &= -\frac{2Qv}{l}H_v^i(u,v,w)
\end{aligned}
\tag{2-72}
$$

其中 E_0 是束腰中心处电场的幅度，磁场的幅度可由以下关系式得到：

$$
H_0 = E_0\sqrt{\frac{\varepsilon_0}{\mu_0}} \tag{2-73}
$$

$$
\Psi_0 = iQ\exp\left(-\frac{iQ(u^2+v^2)}{\omega_0^2}\right),\quad Q=\frac{1}{i+2(z-z_0)/l} \tag{2-74}
$$

l 为衍射长度： $l = k\omega_0^2$

§ 2.3.4.3　离轴高斯波束的数学描述

对于两个相互平行的坐标系 $Oxyz$ 和坐标系 O_guvw，其坐标轴 Ox 平行于 Ou，其它各个坐标轴也都相互平行，O_guvw 坐标原点 O_g 在坐标系 O_pxyz 中的坐标是 (x_0,y_0,z_0)。令：

$$
w = z - z_0,\quad u = x - x_0,\quad v = y - y_0 \tag{2-75}
$$

将式(2-75)代入到在轴高斯波束表达式(2-71)-(2-72)中就可以等到离轴高斯波束的在直角坐标下的相应表达式：

$$
\begin{aligned}
E_x &= E_0\psi_0\exp(-ik(z-z_0))\\
E_y &= 0\\
E_z &= -\frac{2Q}{l}(x-x_0)E_x
\end{aligned}
\tag{2-76}
$$

$$
\begin{aligned}
H_x &= 0\\
H_y &= H_0\psi_0\exp(-ik(z-z_0))\\
H_z &= -\frac{2Q}{l}(y-y_0)H_y
\end{aligned}
\tag{2-77}
$$

其中有：

$$
\psi_0 = iQ\exp\left(-iQ(\frac{x^2+y^2}{\omega_0^2})\right),\quad Q=\frac{1}{i+2(z-z_0)/l} \tag{2-78}
$$

通过简单的投影关系，我们就可以在球坐标系中得到入射波的各个分量：

$$\begin{aligned} E_r &= E_0\psi_0[\cos\varphi\sin\theta(1-\frac{2Q}{l}r\cos\theta)+\frac{2Q}{l}x_0\cos\theta]\exp(K) \\ E_\theta &= E_0\psi_0[\cos\varphi(\cos\theta+\frac{2Q}{l}r\sin^2\theta)-\frac{2Q}{l}x_0\cos\theta]\exp(K) \\ E_\varphi &= -E_0\psi_0\sin\varphi\exp(K) \end{aligned} \tag{2-79}$$

$$\begin{aligned} H_r &= H_0\psi_0[\sin\varphi\sin\theta(1-\frac{2Q}{l}r\cos\theta)+\frac{2Q}{l}y_0\cos\theta]\exp(K) \\ H_\theta &= H_0\psi_0[\sin\varphi(\cos\theta+\frac{2Q}{l}r\sin^2\theta)-\frac{2Q}{l}y_0\sin\theta]\exp(K) \\ H_\varphi &= H_0\psi_0\cos\varphi\exp(K) \end{aligned} \tag{2-80}$$

其中：

$$K=-ik(r\cos\theta-z_0)\qquad Q=1/(i+\frac{2(r\cos\theta-z_0)}{l}) \tag{2-81}$$

$$\begin{aligned} \psi_0 &= \psi_0^0\psi_0^\varphi \\ \psi_0^0 &= iQ\exp(-iQ\frac{r^2\sin^2\theta}{\omega_0^2})\exp(-iQ\frac{x_0^2+y_0^2}{\omega_0^2}) \\ \psi_0^\varphi &= \exp[\frac{2iQ}{\omega_0^2}r\sin\theta(x_0\cos\varphi+y_0\sin\varphi)] \end{aligned} \tag{2-82}$$

§2.3.4.4　高斯波束的球矢量波函数展开

我们知道，对于直角坐标系下高斯波束各个电磁分量的数学描述表达式只是麦克斯韦方程的近似解，并不严格满足麦克斯韦方程。然而利用区域近似法对高斯波束进行级数展开，得到的高斯波束的级数展开式却是能够完全满足麦克斯韦方程，是麦克斯韦方程的严格解[102, 103]。

应用2.3节所述区域近似法求解波束因子，我们可以得到离轴高斯波束用球矢量波函数展开的波束因子 $g_{n,TM}^m$, $g_{n,TE}^m$ 的求解表达式：

$$\begin{pmatrix} g_{n,TM}^m \\ g_{n,TE}^m \end{pmatrix} = Z_n^m\exp(ikz_0)iQ_+\exp[-iQ_+(\frac{\rho_n}{\omega_0})^2]\exp(-iQ_+\frac{x_0^2+y_0^2}{\omega_0})\frac{1}{2}(\sum_{j_+=m}^{jp}\Psi_{jp}\pm\sum_{j_-=m}^{jp}\Psi_{jp}) \tag{2-83}$$

$$Q=\frac{1}{i+2(z-z_0)/l}\qquad Q_+=Q(z=0)=\frac{1}{i-(2z_0/l)} \tag{2-84}$$

$$\rho_n=L^{1/2}\frac{\lambda}{2\pi} \tag{2-85}$$

$$\Psi_{jp}=(\frac{iQ_{+}r\sin\theta}{\omega_0^2})^j\frac{(x_0-iy_0)^{j-p}(x_0+iy_0)^p}{(j-p)!\,p!} \tag{2-86}$$

$$\sum^{jp}=\sum_{j=0}^{\infty}\sum_{p=0}^{j}\qquad j_{+}=j+1-2p\qquad j_{-}=j-1-2p$$

特例一：在轴高斯波束。此时有 $x_0=y_0=0$，将其带入式(2-86)，即可得到 $\boldsymbol{\psi}_{jp}=0$ 以及 $\boldsymbol{\psi}_{00}=1$。经过简单运算：

$$\begin{pmatrix} g_{n,TM}^m \\ ig_{n,TE}^m \end{pmatrix}=\frac{1}{2}g_n,\quad |m|=1 \tag{2-87}$$

$$g_n=\exp[-(\frac{\rho_n}{\omega_0})^2] \tag{2-88}$$

特例二：平面波情况。当高斯波束的束腰半径 $\omega_0\to\infty$ 时，高斯波束退化成平面波，此时有： $g_n=1$，则：

$$\begin{pmatrix} g_{n,TM}^m \\ ig_{n,TE}^m \end{pmatrix}=\frac{1}{2} \tag{2-89}$$

将高斯波束波束因子 $g_{n,TM}^m, g_{n,TE}^m$ 的求解表达式代入式(2-45)或者(2-50)，我们就可以得到该波束波束因子在任意坐标系下的表达式。

特别的，将式(2-87)-(2-88)代入式(2-45)或者(2-50)，我们可以得到在轴高斯波束波束因子在任意直角坐标系下的一般表达式：

$$\widetilde{g_{n,TM}^m}=(-1)^m(-1)^{(m-|m|)/2}\frac{(n-|m|)!}{(n+m)!}g_n\bullet e^{im\gamma}[\sin\alpha\bullet im\pi_n^m(\cos\beta)+\cos\alpha\tau_n^m(\cos\beta)] \tag{2-90}$$

$$\widetilde{g_{n,TE}^m}=(-1)^{m+1}(-1)^{(m-|m|)/2}\frac{(n-|m|)!}{(n+m)!}g_n\bullet e^{im\gamma}[\cos\alpha\bullet im\pi_n^m(\cos\beta)-\sin\alpha\tau_n^m(\cos\beta)] \tag{2-91}$$

以上这种求解任意坐标系下有形波束波束因子的方法，根据所用方法的前后数学运算过程，我们将其命名为RL方法。即先在波束坐标系下用区域近似法求解非旋转坐标系下的波束因子（L过程），然后通过坐标系旋转关系（R过程）得到旋转坐标系下的波束因子。为了反映该求解过程，方便和下面所得结果进行比较，我们定义： $\widetilde{\widetilde{g_{n,X}^m}}=\widetilde{g_{n,X}^m}$。即 $\widetilde{\widetilde{g_{n,X}^m}}$ 是用RL-过程求解得到的波束因子。

下面我们将会看到，利用区域近似法求解波束因子（L过程）的过程与波束因子在坐标轴之间的旋转变换关系（R过程）是不兼容的。即我们不能先在直角坐标系下对电磁波波束的各个电磁分量进行旋转变换（R过程），然后再对其在旋转坐标系中应用区域近似法求解（L过程）。下面我们以用有形波束的最特殊情况为例，平面波波束因子的求解，来对以上结论加以论述。

当高斯波束的束腰半径趋于无限大时，高斯波即退化成平面波，此时波束在

波束自身的直角坐标系下电磁分量表达式为：

$$E_x = \exp(-ikz) \qquad E_y = E_z = 0 \tag{2-92}$$

经过欧拉角的旋转，我们可以得到旋转坐标系下电磁波分量：

$$\begin{aligned} E_{\tilde{x}} &= \cos\alpha\cos\beta\exp(-ikz) \\ E_{\tilde{y}} &= -\sin\alpha\exp(-ikz) \\ E_{\tilde{z}} &= \cos\alpha\sin\beta\exp(-ikz) \end{aligned} \tag{2-93}$$

根据简单的投影关系，可得电磁场电矢量分量在球坐标系下的径向分量为：

$$E_r = [\sin\tilde{\theta}(\cos\alpha\cos\beta\cos\tilde{\varphi} - \sin\alpha\sin\tilde{\varphi}) + \cos\alpha\sin\beta\cos\tilde{\theta}]\exp(-ikz) \tag{2-94}$$

根据区域近似法的求解过程，我们有：

$$E_r^{loc} = E_r(\tilde{\theta} = \frac{\pi}{2}) = [\cos\alpha\cos\beta\frac{e^{j\tilde{\varphi}} + e^{-j\tilde{\varphi}}}{2} - \sin\alpha\frac{e^{j\tilde{\varphi}} - e^{-j\tilde{\varphi}}}{2}]\overline{\exp(-ikz)} \tag{2-95}$$

这里我们用符合“$\overline{X}$”来表示对表达式“X”进行区域近似算法运算，即将距离$r\sin\theta$用$L^{1/2}$来代替，并将极角θ取定为$\pi/2$，其中L的表达式如式(2-64)所示。

将式(2-95)中的z变量用旋转之后球坐标系下的坐标$\tilde{x},\tilde{y},\tilde{z}$来表示，我们可以得到：

$$\overline{\exp(-ikz)} = \exp(-iR\sin\beta\cos\tilde{\varphi}) \tag{2-96}$$

对于变量$\tilde{\varphi}$，$\overline{\exp(-ikz)}$是一个以2π为周期变化的函数，将其作傅里叶变换：

$$\overline{\exp(-ikz)} = \sum_{l=-\infty}^{\infty}\frac{A_l}{2\pi}e^{il\tilde{\varphi}} \tag{2-97}$$

在等式(2-96)和(2-97)上同时加载运算符$\int_0^{2\pi}d\tilde{\varphi}e^{-im\tilde{\varphi}}$，我们可以得到：

$$\int_0^{2\pi}d\tilde{\varphi}e^{iB\cos\tilde{\varphi}-im\tilde{\varphi}} = \sum_{l=-\infty}^{\infty}\int_0^{2\pi}d\tilde{\varphi}\frac{A_l}{2\pi}e^{i(l-m)\tilde{\varphi}} = \begin{cases} 0, & l \neq m \\ A_m, & l = m \end{cases} \tag{2-98}$$

其中我们已令$B = -R\sin\beta$

另外我们有：

$$J_n(x) = \frac{i^{-n}}{2\pi}\int_0^{2\pi}e^{i(x\cos\theta + n\theta)}d\theta \tag{2-99}$$

将(2-99)带入等式(2-98)，我们可得：

$$A_m = \frac{2\pi}{i^m}J_{-m}(B) \tag{2-100}$$

则有：

$$\overline{\exp(-ikz)} = \sum_{m=-\infty}^{\infty}i^m J_m(B)e^{im\tilde{\varphi}} \tag{2-101}$$

将式(2-101)代入电矢量表达式(2-95)，我们可以得到：

$$\bar{E}_r = \sum_{m=-\infty}^{\infty} i^{m+1} e^{im\tilde{\varphi}} [f_- J_{m+1}(B) - f_+ J_{m-1}(B)] \tag{2-102}$$

其中有：$f_- = (\cos\alpha\cos\beta + i\sin\alpha)/2$，$f_+ = (\cos\alpha\cos\beta - i\sin\alpha)/2$

则可得LR方法下求解所得波束因子为：

$$\overline{\widetilde{g^m_{n,TM}}} = (\frac{-i}{L^{1/2}})^{|m|-1} i^{m+1} [f_- J_{m+1}(-L^{1/2}\sin\beta) - f_+ J_{m-1}(-L^{1/2}\sin\beta)] \tag{2-103}$$

很明显利用此LR方法求得的波束因子 $\overline{\widetilde{g^m_{n,TM}}}$ 和RL方法求得的波束因子 $\widetilde{\overline{g^m_{n,TM}}}$ 不相等。由于RL方法已经经过多种途径的验证，包括理论对比和实验对比，因此可以认定LR方法不适用于任意方向入射有形波束波束因子的求解。

§2.4 任意入射高斯波束的波束因子

下面我们利用2.3节中波束因子的转换定理来求解任意入射高斯波束的波束因子：

$$\widetilde{g^m_{n,X}} = \mu_{mn} \sum_{s=-n}^{n} \frac{H^m_{sn}(\alpha,\beta,\gamma)}{\mu_{sn}} g^s_{n,X} \tag{2-104}$$

其中有：

$$\mu_{mn} = (-1)^{(m-|m|)/2} \frac{(n-|m|)!}{(n-m)!}$$

$$H^m_{sn}(\alpha,\beta,\gamma) = \sqrt{\frac{(n-m)!(n+s)!}{(n+m)!(n-s)!}} e^{is\alpha} (-1)^{m+s} d^{(n)}_{sm}(\beta) e^{im\gamma}$$

在数值计算过程中做简单变换：

$$\widetilde{g^m_{n,X}} = \sum_{s=0}^{n} \frac{\mu_{mn}}{1+\delta_{0s}} \left[\frac{H^m_{sn}(\alpha,\beta,\gamma)}{\mu_{sn}} g^s_{n,X} + \frac{H^m_{-sn}(\alpha,\beta,\gamma)}{\mu_{-sn}} g^{-s}_{n,X} \right] \tag{2-105}$$

将式(2-104)代入式(2-105)：

$$\begin{aligned} \widetilde{g^m_{n,X}} = \sum_{s=0}^{n} \frac{1}{1+\delta_{0s}} (-1)^{m+s} (-1)^{\frac{(m-|m|)}{2}} \sqrt{\frac{(n-|m|)!(n+s)!}{(n+|m|)!(n-s)!}} \\ \times \left[e^{im\gamma} e^{is\alpha} d^n_{ms} g^s_{n,X} + (-1)^s e^{im\gamma} e^{-is\alpha} d^n_{m-s} g^{-s}_{n,X} \right] \end{aligned} \tag{2-106}$$

通过求解Wigner-d函数，我们可以得到旋转坐标系下的波束因子。

为了验证推导的正确性，我们将所得结果与已发表数据进行比较[104]。在表2.1中我们计算了波长为 $\lambda = 0.5145\mu m$，束腰半径为 $\omega_0 = 10.0\mu m$，束腰中心位置坐标 $x_0 = y_0 = 0.5\omega_0$，$z_0 = 0.5s$，$s = 8.1885E-03$ 的离轴高斯波束分别在正入射（欧拉角 $\alpha = \beta = \gamma = 0.0^\circ$）以及斜入射（欧拉角 $\alpha = \gamma = 0.0^\circ$，$\beta = 60.0^\circ$）时波束因子的数

值结果。其中表中在欧拉角（$\alpha=\beta=\gamma=0.0^\circ$）时的数值结果和文献中[104]给出的结果完全一致。

表2.1 离轴高斯波束任意方向入射时波束因子的数值结果

波束因子	$g_{n,TM}^{m}(\alpha=\beta=\gamma=0.0^\circ)$	$g_{n,TM}^{m}(\alpha=\gamma=0.0^\circ,\beta=60.0^\circ)$
g_1^{-1}	(-6.14427E-02, -2.96953E-01)	(5.7801E-02, 2.82976E-01)
g_1^{0}	(4.854417E-03, -1.04614E-03)	(-4.2087E-02, -1.80031E-01)
g_1^{1}	(-6.14650E-02, -2.96948E-01)	(5.77785E-02, 2.8298E-01)
g_2^{-2}	(-1.47481E-03, -9.51931E-04)	(-9.66254E-03, -4.1728E-02)
g_2^{-1}	(-6.14147E-02, -2.96917E-01)	(-4.7399E-02, -2.43079E-01)
g_2^{0}	(1.45603E-02, -3.13778E-03)	(0.11888, 0.514614)
g_2^{1}	(-6.147664E-02 -2.96903E-01)	(-4.7021E-02 -2.41613E-01)
g_2^{2}	(-9.51827E-04, 1.474874E-03)	(-1.01512E-02, -4.4041E-02)

§2.5 小结

本章首先介绍了用于描述激光波束与目标之间电磁散射相互作用的广义洛伦兹米理论。在GLMT理论中，其中最关键、也是最困难的问题之一是如何在特定坐标系下对有形波束进行合适的数学展开描述。在广义洛伦兹米理论的框架内，利用球矢量波函数在共原点旋转直角坐标系下的旋转加法定理和在平行坐标系下的平移加法定理，将任意方向入射的有形波束在任意直角坐标系下用球矢量波函数展开，推导了波束因子在不同坐标系之间相互转换的一般关系式。以轴对称波束为例，给出了轴对称波束波束因子在任意直角坐标系下相互转换的简化解析表达式，可直接用于数值计算编程。最后以应用最广泛的高斯激光波束为例，给出了可直接用于数值计算的波束因子的数学表达式。

任意入射有形波束在球矢量波函数下展开的求解是研究非均匀粒子、非球形粒子散射问题的关键。解决这个理论难点，为后续相关散射问题的求解提供必须的理论工具。这部分的理论推导工作为后续章节，偏心球粒子对任意方向入射有形波束的散射以及多粒子的相干散射问题奠定了必须的基础。

第三章 偏心球粒子的波束散射

基于上一章中对任意方向入射有形波束的球矢量波函数展开，本章在GLMT理论框架内，利用球矢量波函数的平移加法定理，推导并求解了偏心球粒子对任意方向入射有形波束的散射方程。基于本章的理论推导结果，利用FORTRAN计算语言编写了一套可用于模拟仿真有形波束照射下偏心球散射远场、表面近场和内场电磁强度三维空间分布的程序。在对程序进行充分验证的基础上，分析了偏心球内核粒子相对大小、偏心距、波束入射方向等因素对远场散射特性的影响。对于偏心球内场和表面近场的详细分析将在下一章展开讨论。

§3.1 引言

在对粒子粒径大小分布、速度矢量场、组成成分等参数进行激光探测的过程中，我们需要对采集的散射信号进行理论解释和信息提取，即参数的反演。而实现精确参数反演的前提是建立合理贴切的物理模型。对于自然界中生物细胞或者孢子，大气中的烟、雾、冰雹等，大气或者液体中的悬浮粒子、粉体工业中的复合粉体颗粒等，这类微粒最显著的特点就是含有微小的内核。由于同心球粒子的几何对称性，国内外众多学者起初都将这种模型作为含核粒子相关散射特性研究的理论模型，在很多情况下也能取得很好的模拟预测结果。而实际上，内核粒子和大球粒子之间普遍存在较大密度差异，由于重力原因，内核粒子将经常呈现明显的偏心特性。因此相比同心球来说，利用含有偏心核的球形粒子模型(本文中简称为偏心球粒子)来模拟诸如生物细胞、气溶胶颗粒、人造用于军事目的的孢子甚至细菌等更为贴切。

Fikioris和Uzunoglu[25]、Broghese[26, 27]和Fuller等人[28, 29]分别对偏心球粒子的平面波散射问题进行了理论分析。Ngo和Videen等人[31, 32]基于EBCM方法将单核偏心球推广到任意形状的偏心内核以及多内核的情况，给出了计算程序，推动了偏心球散射研究的发展。然而在更多的实际测量过程和实验中，如利用强汇聚激光波束对微小粒子进行操控的光镊实验中，在利用激光干涉条纹对粒子进行探测的激光干涉成像光学系统中，在利用光学全息技术对粒子特性进行研究的系统中，我们都利用激光波束而非平面波作为激励光源。这些实际应用和操作要求对偏心球粒子在激光等有形波束照射下的散射特性进行深入的研究。Gouesbet等人[45]于2000年首先提出并研究了偏心球粒子的波束散射问题，在GLMT框架内推导了偏心球粒

子对沿对称轴入射的有形波束的散射方程，但没有给出数值分析。最近，颜兵等人[49, 105]在GLMT的理论框架内，利用积分区域近似法求解波束因子，从数值上实现了偏心球粒子对在轴高斯波束散射的模拟计算，对粒子的远场散射特性和波束作用在粒子上的辐射力进行了分析。韩国霞等人[47, 106]利用区域近似法，分析了离轴高斯波束对偏心球粒子的散射情况，但是也主要对粒子的远场散射特性以及光束对粒子的辐射力进行了分析。根据文献的检索结果，对汇聚激光波束照射下偏心球粒子的内场和近场电磁强度分布还没有相关报道。

相对于球形粒子的空间任意对称性，偏心球粒子的单轴对称性是这类粒子的最大特点。当波束沿不同方向入射时，偏心球粒子的散射特性将表现出很大差异性，因此研究偏心球在波束任意入射时的散射特性对实际测量具有重要的指导意义。下面我们在GLMT理论框架内研究了偏心球粒子对任意方向入射有形波束的散射问题，推导了偏心球粒子对任意入射有形波束的散射方程。并以应用最为广泛的高斯波束为例，模拟分析了不同粒子参数和入射波束参数对偏心球粒子远场散射特性的影响。

§ 3.2 偏心球粒子的波束散射

§3.2.1　散射模型的建立

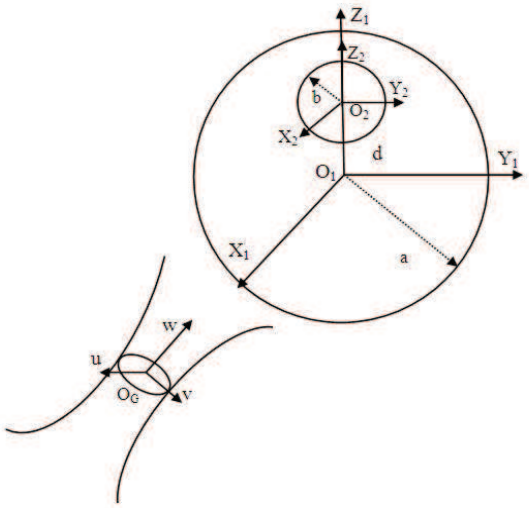

图3.1 任意方向入射偏心球粒子的模型示意图

对于偏心球粒子来说，单轴对称性是这类粒子的最大特点，如图3-1所示为含核粒子模型对有形波束散射问题的示意图。为了便于理论模型的建立和数值模拟的研究，我们充分利用模型的单轴对称性，在大球上建立坐标系$O_1x_1y_1z_1$，并让内

核小球球心位于z_1轴上。另外，在内核小球上建立与一个与大球坐标系$O_1x_1y_1z_1$相平行的内球坐标系$O_2x_2y_2z_2$。大球坐标系和内球坐标系相对应的球坐标系分别用(r_1,θ_1,φ_1)和(r_2,θ_2,φ_2)来表示。两球球心之间的距用d表示：

$$x_2=x_1,\quad y_2=y_1,\quad z_2=z_1-d \tag{3-1}$$

根据有形波束自身所具有的空间分布特点，一般以波束的传播方向为轴建立波束坐标系O_guvw，波束沿w轴传播。原点O_g在$O_1x_1y_1z_1$坐标系中的坐标值为(x_0,y_0,z_0)。从上面的描述可以知道，若将波束坐标系O_guvw按照欧拉角(α,β,γ)进行旋转，我们可以得到平行于$O_1x_1y_1z_1$的坐标系$O_g\tilde{x}\tilde{y}\tilde{z}$，将坐标系$O_g\tilde{x}\tilde{y}\tilde{z}$沿矢量$(x_0,y_0,z_0)$进行平移，我们就可以得到$O_1x_1y_1z_1$坐标系。

如上所述，我们建立了以大球坐标系为主的全局坐标系$O_1x_1y_1z_1$，以内核小球坐标系为辅助的局部坐标系$O_2x_2y_2z_2$，以及以波束的传播方向为轴建立的波束坐标系O_guvw。

§3.2.2　大球坐标系下散射方程的建立

选定大球坐标系$O_1x_1y_1z_1$作为求解问题的全局坐标系。在全局坐标系中，将任意入射有形波束的电磁场分量用球矢量波函数展开：

$$\mathbf{E}^{inc}=E_0\sum_{n=1}^{\infty}\sum_{m=-n}^{n}a_{nm}\mathbf{M}_{nm}^{(1)}(k_0\mathbf{r}_1)+b_{nm}\mathbf{N}_{nm}^{(1)}(k_0\mathbf{r}_1) \tag{3-2}$$

$$\mathbf{H}^{inc}=-\frac{kE_0}{i\omega\mu}\sum_{n=1}^{\infty}\sum_{m=-n}^{n}a_{nm}\mathbf{N}_{nm}^{(1)}(k_0\mathbf{r}_1)+b_{nm}\mathbf{M}_{nm}^{(1)}(k_0\mathbf{r}_1) \tag{3-3}$$

其中展开系数$\left(a_{mn},b_{mn}\right)$和波束因子$\left(g_{n,TM}^{m},g_{n,TE}^{m}\right)$具有以下关系式：

$$b_{mn}=kc_n^{pw}(-1)^{(m-|m|)/2}\frac{(n-m)!}{(n-|m|)!}g_{n,TM}^{m} \tag{3-4}$$

$$a_{mn}=-ikc_n^{pw}(-1)^{(m-|m|)/2}\frac{(n-m)!}{(n-|m|)!}g_{n,TE}^{m} \tag{3-5}$$

类似于入射波束的数学展开，我们将散射场$\mathbf{E}^{sca}$在坐标系$O_1x_1y_1z_1$中用第四类球矢量波函数表示为：

$$\mathbf{E}^{sca}=E_0\sum_{n=1}^{\infty}\sum_{m=-n}^{n}c_{nm}\mathbf{M}_{nm}^{(4)}(k_0\mathbf{r}_1)+d_{mn}\mathbf{N}_{nm}^{(4)}(k_0\mathbf{r}_1) \tag{3-6}$$

$$\mathbf{H}^{sca}=-\frac{kE_0}{i\omega\mu}\sum_{n=1}^{\infty}\sum_{m=-n}^{n}d_{nm}\mathbf{N}_{nm}^{(4)}(k_0\mathbf{r}_1)+c_{nm}\mathbf{M}_{nm}^{(4)}(k_0\mathbf{r}_1) \tag{3-7}$$

位于大球内表面和内核外表面之间环形区域内的电磁场是由向外辐射的电磁

场分量和向内传播的电磁场分量的叠加，我们用第三类和第四类球矢量波函数将其电磁场展开表示为：

$$\mathbf{E}^{int1}=E_0\sum_{n=1}^{\infty}\sum_{m=-n}^{n}e_{nm}\mathbf{M}_{nm}^{(3)}(k_1\mathbf{r}_1)+f_{mn}\mathbf{N}_{nm}^{(3)}(k_1\mathbf{r}_1)+v_{nm}\mathbf{M}_{nm}^{(4)}(k_1\mathbf{r}_1)+h_{mn}\mathbf{N}_{nm}^{(4)}(k_1\mathbf{r}_1) \tag{3-8}$$

$$\mathbf{H}^{int1}=-\frac{kE_0}{i\omega\mu}\sum_{n=1}^{\infty}\sum_{m=-n}^{n}f_{nm}\mathbf{M}_{nm}^{(3)}(k_1\mathbf{r}_1)+e_{mn}\mathbf{N}_{nm}^{(3)}(k_1\mathbf{r}_1)+h_{nm}\mathbf{M}_{nm}^{(4)}(k_1\mathbf{r}_1)+v_{mn}\mathbf{N}_{nm}^{(4)}(k_1\mathbf{r}_1) \tag{3-9}$$

在大球表面应用电磁场边界条件，即要求电磁波在球表面上的切向分量连续：

$$\begin{aligned} E_\theta^{int1}|_{r_1=a}&=E_\theta^{inc}|_{r_1=a}+E_\theta^{sca}|_{r_1=a} & H_\theta^{int1}|_{r_1=a}&=H_\theta^{inc}|_{r_1=a}+H_\theta^{sca}|_{r_1=a}\\ E_\varphi^{int1}|_{r_1=a}&=E_\varphi^{inc}|_{r_1=a}+E_\varphi^{sca}|_{r_1=a} & H_\varphi^{int1}|_{r_1=a}&=H_\varphi^{inc}|_{r_1=a}+H_\varphi^{sca}|_{r_1=a}\end{aligned} \tag{3-10}$$

经过简单运算，我们可以得到：

$$a_{nm}\psi_n(k_0a)+c_{nm}\psi_n(k_0a)=\frac{k_0}{k_1}[e_{nm}\xi_n(k_1a)+v_{nm}\varsigma_n(k_1a)] \tag{3-11}$$

$$a_{nm}\psi_n'(k_0a)+c_{nm}\varsigma_n'(k_0a)=e_{nm}\xi_n'(k_1a)+v_{nm}\varsigma_n'(k_1a) \tag{3-12}$$

$$b_{nm}\psi_n(k_0a)+d_{nm}\varsigma_n(k_0a)=f_{nm}\xi_n(k_1a)+h_{nm}\varsigma_n(k_1a) \tag{3-13}$$

$$b_{nm}\psi_n'(k_0a)+d_{nm}\varsigma_n'(k_0a)=\frac{k_0}{k_1}[f_{nm}\xi_n'(k_1a)+h_{nm}\varsigma_n'(k_1a)] \tag{3-14}$$

其中 $\psi_n(r),\ \xi_n(r),\ \varsigma_n(r)$ 为各类Riccati-Bessel函数：

$$\psi_n(r)=rj_n(r),\ \xi_n(r)=rh_n^{(1)}(r),\ \varsigma_n(r)=rh_n^{(2)}(r) \tag{3-15}$$

而 $\psi_n'(r),\xi_n'(r),\varsigma_n'(r)$ 分别是对各类Riccati-Bessel函数的求导。

至此，我们已经在全局坐标系下建立起一组散射方程，要得到相关散射问题的解，我们还需要在内核小球的局部坐标系下建立相应的散射方程来联立求解散射系数。

§3.2.3　内核坐标系下散射方程的建立

类似于全局坐标系下散射方程的建立过程，我们可以在内核小球的局部坐标系下建立相应的散射方程。在局部坐标系下，将位于大球内表面和内核外表面之间环形区域内的电磁场分量用第三类和第四类球矢量波函数将其展开为：

$$\mathbf{E}^{int1}=E_0\sum_{n=1}^{\infty}\sum_{m=-n}^{n}r_{nm}\mathbf{M}_{nm}^{(3)}(k_1\mathbf{r}_2)+s_{mn}\mathbf{N}_{nm}^{(3)}(k_1\mathbf{r}_2)+t_{nm}\mathbf{M}_{nm}^{(4)}(k_1\mathbf{r}_2)+u_{mn}\mathbf{N}_{nm}^{(4)}(k_1\mathbf{r}_2) \tag{3-16}$$

$$\mathbf{H}^{int1}=\frac{-kE_0}{i\omega\mu}\sum_{n=1}^{\infty}\sum_{m=-n}^{n}s_{nm}\mathbf{M}_{nm}^{(3)}(k_1\mathbf{r}_2)+r_{mn}\mathbf{N}_{nm}^{(3)}(k_1\mathbf{r}_2)+u_{nm}\mathbf{M}_{nm}^{(4)}(k_1\mathbf{r}_2)+t_{mn}\mathbf{N}_{nm}^{(4)}(k_1\mathbf{r}_2) \tag{3-17}$$

内核小球内的电磁场用第一类球矢量波函数表示为：

$$\mathbf{E}^{int2} = E_0 \sum_{n=1}^{\infty} \sum_{m=-n}^{n} p_{nm} \mathbf{M}_{nm}^{(1)}(k_2 \mathbf{r}_2) + q_{mn} \mathbf{N}_{nm}^{(1)}(k_2 \mathbf{r}_2) \tag{3-18}$$

$$\mathbf{H}^{int2} = -\frac{kE_0}{i\omega\mu} \sum_{n=1}^{\infty} \sum_{m=-n}^{n} q_{nm} \mathbf{M}_{nm}^{(1)}(k_2 \mathbf{r}_2) + p_{mn} \mathbf{N}_{nm}^{(1)}(k_2 \mathbf{r}_2) \tag{3-19}$$

在内核小球表面应用电磁场边界条件：

$$\begin{aligned} E_\theta^{int1}|_{r_2=b} &= E_\theta^{int2}|_{r_2=b} \qquad & H_\theta^{int1}|_{r_2=b} &= H_\theta^{int2}|_{r_2=b} \\ E_\varphi^{int1}|_{r_2=b} &= E_\varphi^{int2}|_{r_2=b} \qquad & H_\varphi^{int1}|_{r_2=b} &= H_\varphi^{int2}|_{r_2=b} \end{aligned} \tag{3-20}$$

经过简单运算，我们可以得到：

$$p_{nm}\psi_n(k_2 b) = \frac{k_2}{k_1}[r_{nm}\xi_n(k_1 b) + t_{nm}\varsigma_n(k_1 b)] \tag{3-21}$$

$$p_{nm}\psi_n'(k_2 b) = r_{nm}\xi_n'(k_1 b) + t_{nm}\varsigma_n'(k_1 b) \tag{3-22}$$

$$q_{nm}\psi_n(k_2 b) = s_{nm}\xi_n(k_1 b) + u_{nm}\varsigma_n(k_1 b) \tag{3-23}$$

$$p_{nm}\psi_n'(k_2 b) = \frac{k_2}{k_1}[s_{nm}\xi_n'(k_1 b) + u_{nm}\varsigma_n'(k_1 b)] \tag{3-24}$$

联立以上方程，消去系数 $p_{nm,}\ q_{nm}$，我们可以得到：

$$Q_n^r = \frac{r_{nm}}{t_{nm}} = \frac{k_1\varsigma_n'(k_1 b)\psi_n(k_2 b) - k_2\varsigma_n(k_1 b)\psi_n'(k_2 b)}{k_2\xi_n(k_1 b)\psi_n'(k_2 b) - k_1\xi_n'(k_1 b)\psi_n(k_2 b)} \tag{3-25}$$

$$Q_n^s = \frac{s_{nm}}{u_{nm}} = \frac{k_2\varsigma_n'(k_1 b)\psi_n(k_2 b) - k_1\varsigma_n(k_1 b)\psi_n'(k_2 b)}{k_1\xi_n(k_1 b)\psi_n'(k_2 b) - k_2\xi_n'(k_1 b)\psi_n(k_2 b)} \tag{3-26}$$

在偏心球粒子的内核是理想导体的情况下，例如在金属导体表面有一层不均匀的涂覆层，那么由于导体的屏蔽作用，其内部深处不存在电磁场内场，此时对应的内核小球表面的边界条件为：

$$\begin{aligned} E_\theta^{int1}|_{r_2=b} &= 0 \qquad & H_\theta^{int1}|_{r_2=b} &= 0 \\ E_\varphi^{int1}|_{r_2=b} &= 0 \qquad & H_\varphi^{int1}|_{r_2=b} &= 0 \end{aligned} \tag{3-27}$$

经过类似的运算过程，我们可以得到：

$$Q_n^r = \frac{r_{nm}}{t_{nm}} = -\frac{\varsigma_n'(k_1 b)}{\xi_n'(k_1 b)} \tag{3-28}$$

$$Q_n^s = \frac{s_{nm}}{u_{nm}} = -\frac{\varsigma_n(k_1 b)}{\xi_n(k_1 b)} \tag{3-29}$$

至此，通过应用各个边界面上的边界条件，我们已经分别在全域坐标系和局部坐标系下建立起了两组散射方程，但是对于两个不同坐标系下的方程，我们需

要利用相应的工具将其联立起来求解，而球矢量波函数的平移加法定理为我们提供了这个的工具。

§3.2.4 散射系数的求解

为了将全局坐标系和局部坐标系中分别建立起来的散射方程组相联立，利用球矢量波函数的平移加法定理，将两组散射系数统一到同一坐标系中。对于发散性球谐函数，在 $r_2 \geq |d|$ 的条件下，我们有：

$$\begin{aligned}\mathbf{M}_{mn}^{(3,4)}(k\mathbf{r}_2) &= \sum_{\nu=1}^{\infty}[A_{m\nu}^{mn,1}(kd)\mathbf{M}_{m\nu}^{(3,4)}(k\mathbf{r}_1) + B_{m\nu}^{mn,1}(kd)\mathbf{N}_{m\nu}^{(3,4)}(k\mathbf{r}_1)] \\ \mathbf{N}_{mn}^{(3,4)}(k\mathbf{r}_2) &= \sum_{\nu=1}^{\infty}[B_{m\nu}^{mn,1}(kd)\mathbf{M}_{m\nu}^{(3,4)}(k\mathbf{r}_1) + A_{m\nu}^{mn,1}(kd)\mathbf{N}_{m\nu}^{(3,4)}(k\mathbf{r}_1)]\end{aligned} \tag{3-30}$$

将式(3-30)代入局部坐标系下环形区域电磁场的展开式(3-16)和(3-17)中，然后将所得表达式和全局坐标系下的展开式(3-8)和(3-9)进行比较，我们可以得到：

$$e_{nm} = \sum_{\nu=1}^{\infty} r_{\nu m} A_{mn}^{m\nu} + s_{\nu m} B_{mn}^{m\nu} \tag{3-31}$$

$$f_{nm} = \sum_{\nu=1}^{\infty} s_{\nu m} A_{mn}^{m\nu} + r_{\nu m} B_{mn}^{m\nu} \tag{3-32}$$

$$v_{nm} = \sum_{\nu=1}^{\infty} t_{\nu m} A_{mn}^{m\nu} + u_{\nu m} B_{mn}^{m\nu} \tag{3-33}$$

$$h_{nm} = \sum_{\nu=1}^{\infty} u_{\nu m} A_{mn}^{m\nu} + t_{\nu m} B_{mn}^{m\nu} \tag{3-34}$$

将等式(3-31)-(3-34)连同等式(3-25)-(3-26)一起代入方程组(3-11)-(3-14)，可以得到：

$$\begin{aligned}a_{nm}\psi_n(k_0a) + c_{nm}\varsigma_n(k_0a) = \frac{k_0}{k_1}\sum_{\nu=1}^{\infty} & t_{\nu m} A_{mn}^{m\nu}[\varsigma_n(k_1a) + Q_\nu^r \xi_n(k_1a)] \\ & + u_{\nu m} B_{mn}^{m\nu}[\varsigma_n(k_1a) + Q_\nu^s \xi_n(k_1a)]\end{aligned} \tag{3-35}$$

$$\begin{aligned}a_{nm}\psi_n'(k_0a) + c_{nm}\varsigma_n'(k_0a) = \sum_{\nu=1}^{\infty} & t_{\nu m} A_{mn}^{m\nu}[\varsigma_n'(k_1a) + Q_\nu^r \xi_n'(k_1a)] \\ & + u_{\nu m} B_{mn}^{m\nu}[\varsigma_n'(k_1a) + Q_\nu^s \xi_n'(k_1a)]\end{aligned} \tag{3-36}$$

$$\begin{aligned}b_{nm}\psi_n(k_0a) + d_{nm}\varsigma_n(k_0a) = \sum_{\nu=1}^{\infty} & t_{\nu m} B_{mn}^{m\nu}[\varsigma_n(k_1a) + Q_\nu^r \xi_n(k_1a)] \\ & + u_{\nu m} A_{mn}^{m\nu}[\varsigma_n(k_1a) + Q_\nu^s \xi_n(k_1a)]\end{aligned} \tag{3-37}$$

$$b_{nm}\psi_n'(k_0a)+d_{nm}\varsigma_n'(k_0a)=\frac{k_0}{k_1}\sum_{v=1}^{\infty}t_{vm}B_{mn}^{mv}[\varsigma_n'(k_1a)+Q_v^r\xi_n'(k_1a)]$$
$$+u_{vm}A_{mn}^{mv}[\varsigma_n'(k_1a)+Q_v^s\xi_n'(k_1a)] \tag{3-38}$$

入射波束的展开系数a_{mn},b_{mn}可以通过波束因子$g_{n,TM}^m,g_{n,TE}^m$的求解而得到，联立以上式子，消去散射系数c_{nm},d_{nm}，我们可以得到：

$$a_{nm}\gamma_n=\sum_{v=1}^{\infty}t_{vm}T_{mn}^{mv,1}+u_{vm}U_{mn}^{mv,1} \tag{3-39}$$

$$b_{nm}\gamma_n=\sum_{v=1}^{\infty}t_{vm}T_{mn}^{mv,2}+u_{vm}U_{mn}^{mv,2} \tag{3-40}$$

其中有

$$\gamma_n=k_1[\psi_n(k_0a)\varsigma_n'(k_0a)-\psi_n'(k_0a)\varsigma_n(k_0a)] \tag{3-41}$$

$$T_{mn}^{mv,1}=A_{mn}^{mv}\{k_0\varsigma_n'(k_0a)[\varsigma_n(k_1a)+Q_v^r\xi_n(k_1a)]-k_1\varsigma_n(k_0a)[\varsigma_n'(k_1a)+Q_v^r\xi_n'(k_1a)]\} \tag{3-42}$$

$$U_{mn}^{mv,1}=B_{mn}^{mv}\{k_0\varsigma_n'(k_0a)[\varsigma_n(k_1a)+Q_v^s\xi_n(k_1a)]-k_1\varsigma_n(k_0a)[\varsigma_n'(k_1a)+Q_v^s\xi_n'(k_1a)]\} \tag{3-43}$$

$$T_{mn}^{mv,2}=B_{mn}^{mv}\{k_1\varsigma_n'(k_0a)[\varsigma_n(k_1a)+Q_v^r\xi_n(k_1a)]-k_0\varsigma_n(k_0a)[\varsigma_n'(k_1a)+Q_v^r\xi_n'(k_1a)]\} \tag{3-44}$$

$$U_{mn}^{mv,2}=A_{mn}^{mv}\{k_1\varsigma_n'(k_0a)[\varsigma_n(k_1a)+Q_v^s\xi_n(k_1a)]-k_0\varsigma_n(k_0a)[\varsigma_n'(k_1a)+Q_v^s\xi_n'(k_1a)]\} \tag{3-45}$$

利用矩阵求解法，如LU分解法，Gaussian分解法等，联立求解以上方程组，就可以计算得到环形区域中的内场系数t_{nm},u_{nm}。将内场系数t_{nm},u_{nm}代入式(3-35)-(3-38)，就可以得到外场散射系数c_{nm},d_{nm}。

§3.2.5　偏心球粒子散射场的求解

根据空间探测点距离被探测偏心球粒子的远近来分，散射场主要分为近场和远场两个区域。在粒子表面附近的近场分布由入射波的电磁场分量和散射波的电磁场分量两部分叠加组成。在$r_1>>r_0$条件下，散射电磁波的径向电磁场分量可以忽略，散射波变成横波传播形式。下面我们将对偏心球形粒子的散射电磁场的空间分布进行数值分析。与颜兵[48]、韩国霞等人[46]所做研究不同，这里主要针对空间的三维散射场进行研究分析，为实际探测的信号提供理论依据。

在全局坐标系中，粒子对波束散射电磁场用球矢量波函数表示为:

$$\mathbf{E}^{sca}=\sum_{n=1}^{\infty}\sum_{m=-n}^{n}c_{nm}\mathbf{M}_{nm}^{(4)}(k_0\mathbf{r}_1)+d_{nm}\mathbf{N}_{nm}^{(4)}(k_0\mathbf{r}_1) \tag{3-46}$$

将球矢量波函数的具体展开式(3-7)和(3-8)代入到式(3-46)中，得到电磁场电场分量的表达式如下所示，这些表达式可直接用于数值计算：

$$E_r^{sca}=\sum_{n=1}^{\infty}\sum_{m=-n}^{n}(-1)^m d_{nm}h_n^{(2)}(k_0r_1)\frac{n(n+1)}{k_0r_1}\widetilde{P_n^m}(\cos\theta)\exp(im\varphi) \tag{3-47}$$

$$\begin{aligned}E_\theta^{sca}=&\sum_{n=1}^{\infty}\sum_{m=-n}^{n}(-1)^m\left\{c_{nm}h_n^{(2)}(k_0r_1)im\widetilde{\pi_n^m}(\cos\theta)\right.\\&\left.+\frac{1}{k_0r_1}d_{nm}\frac{d(r_1h_n^{(2)}(k_0r_1))}{dr_1}\widetilde{\tau_n^m}(\cos\theta)\right\}\exp(im\varphi)\end{aligned} \tag{3-48}$$

$$\begin{aligned}E_\varphi^{sca}=&\sum_{n=1}^{\infty}\sum_{m=-n}^{n}(-1)^m\left\{-c_{nm}h_n^{(2)}(k_0r_1)\widetilde{\tau_n^m}(\cos\theta)\right.\\&\left.+\frac{1}{k_0r_1}d_{nm}\frac{d(r_1h_n^{(2)}(k_0r_1))}{dr_1}im\widetilde{\pi_n^m}(\cos\theta)\right\}\exp(im\varphi)\end{aligned} \tag{3-49}$$

在远场区域下，满足$r_1>>r_0$的客观条件，与切向分量相比，此时电磁场的径向分量可以忽略，散射电磁波退化成横波传播形式。利用汉克函数的远场近似表达式：

$$h_n^{(2)}(kr)\sim i^{n+1}\frac{e^{-ikr}}{kr},\quad \frac{dh_n^{(2)}(kr)}{d(kr)}\sim i^n\frac{e^{-ikr}}{kr} \tag{3-50}$$

可以得到以下近似表达式：

$$kr\bullet h_n^{(2)}(kr)\sim i^{n+1}e^{-ikr},\quad \frac{d[kr\bullet h_n^{(2)}(kr)]}{d(kr)}\sim i^n e^{-ikr} \tag{3-51}$$

将式(3-51)代入场强分量表达式(3-47)-(3-49)，我们可以得到：

$$E_r^{sca}=0 \tag{3-52}$$

$$E_\theta^{sca}=\frac{ie^{-ikr}}{kr}\sum_{n=1}^{\infty}\sum_{m=-n}^{n}[c_{nm}im\widetilde{\pi_n^m}(\cos\theta)-d_{nm}\widetilde{\tau_n^m}(\cos\theta)]i^{n+1}(-1)^m\exp(im\varphi) \tag{3-53}$$

$$E_\varphi^{sca}=\frac{e^{-ikr}}{kr}\sum_{n=1}^{\infty}\sum_{m=-n}^{n}[-c_{nm}\widetilde{\tau_n^m}(\cos\theta)+d_{nm}m\widetilde{\pi_n^m}(\cos\theta)]i^{n+1}(-1)^m\exp(im\varphi) \tag{3-54}$$

散射电磁场的振幅大小可以用矩阵表示为：

$$\begin{pmatrix}I_\theta\\I_\varphi\end{pmatrix}=\frac{\lambda^2}{4\pi^2r^2}\begin{pmatrix}|S_1|^2\\|S_2|^2\end{pmatrix} \tag{3-55}$$

其中：

$$S_2=\sum_{n=1}^{\infty}\sum_{m=-n}^{n}[c_{nm}m\widetilde{\pi_n^m}(\cos\theta)-d_{nm}\widetilde{\tau_n^m}(\cos\theta)]i^{n+1}(-1)^m\exp(im\varphi) \tag{3-56}$$

$$S_1=\sum_{n=1}^{\infty}\sum_{m=-n}^{n}[c_{nm}\widetilde{\tau_n^m}(\cos\theta)-d_{nm}m\widetilde{\pi_n^m}(\cos\theta)]i^{n+1}(-1)^m\exp(im\varphi) \tag{3-57}$$

§3.3 程序编写与验证

基于前面几节的理论推导，我们利用Fortran语言编程求解了偏心球粒子对任意入射有形波束的散射问题。在程序的编写过程中，我们将波束因子的计算和散射问题的求解这两个过程独立开来，这样在所写程序的基础上，只需要更换不同的波束因子，就可以实现任意有形波束对偏心球粒子的散射。相对于Ngo发布的程序，我们的程序主要有以下几个不同和创新：

1. 引入了有形波束作为激励源。通过数值求解波束的波束因子，实现了偏心球粒子对任意方向入射有形波束散射问题的求解。而平面波则作为有形波束的一种最简单的特殊情况被包括在内；

2. 推导并编写了用于预测仿真有形波束照射下偏心球粒子内场，表面近场以及远场三维空间电磁散射强度分布的程序，拓展了程序的应用范围。

3. 优化了Riccati-Bessel函数、连带Legendre函数等基本函数的计算，利用Mackowski给出的迭代公式数值求解球矢量波函数平移加法定理中的平移系数，提高了程序的稳健性；

4. 利用FORTRAN90语言编程程序，提高了程序的可移植性和可读性；

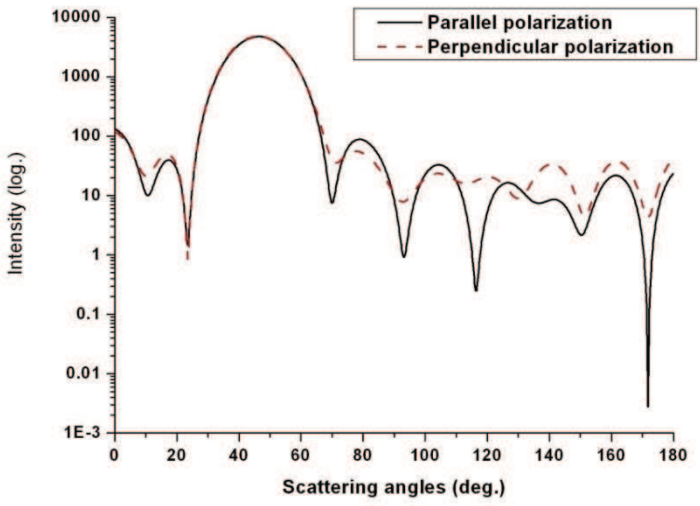

图3.2 平面波照射下偏心球粒子的散射强度随散射角度分布图

在利用所写程序对各种情况进行数值模拟和预测之前，我们先将所写的程序通过和已公开发表的数据进行比较来进行验证。其中的一个特殊例子是当入射波束的束腰半径远大于粒子直径时，高斯波束对粒子的散射结果将与平面波的散射结果一致。Ngo[32]研究了偏心球粒子对斜入射平面波的散射问题并且在其论文中发表了几组数据。这里我们选取最具有代表性的一组参数进行对比：大球半径为

$a=0.925\mu\mathrm{m}$，内核小球半径为$b=0.525\mu\mathrm{m}$，两球球心之间的距离为$d=0.25\mu\mathrm{m}$，大球的复折射率为$m=1.33-0.0i$，内核小球的复折射率为$m=1.75-0.0i$，用波长为$\lambda=0.6328\mu\mathrm{m}$，束腰半径$\omega_0=20.0\mu\mathrm{m}$的高斯波束以入射角$\theta=45^\circ$照射到粒子表面，波束的束腰中心位于全局坐标系原点$x_0=y_0=z_0=0.0$处。在此情况下，我们得到粒子的微分散射系数等于微分消光系数为$Q_{ext}=Q_{sca}=3.2555690$，其结果和Ngo给出的结果完全一致。另外我们这里还给出了偏心球粒子散射强度随散射角度分布图，如图3.2所示。

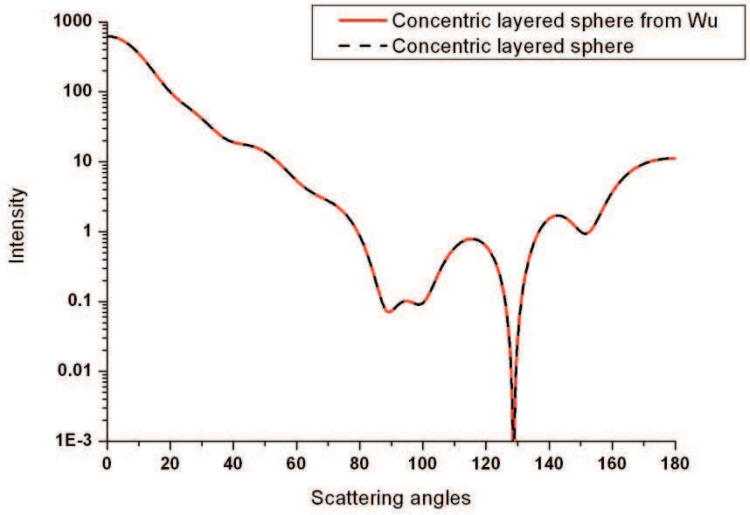

图3.3 同心球粒子在高斯波照射下散射强度随散射角度分布图

对本论文所写程序进行验证的另外一个特例是同心球粒子的散射结果对比。当两球球心之间的距离$d=0$时，偏心球粒子退化为同心球形粒子。为验证本文理论及程序的正确性，我们将所写程序对同心球粒子散射结果与同心球粒子的GLMT计算结果[37]作了比较。如图3.3中，我们计算了偏心球粒子在$d=0$时的散射强度随散射角分布并与双层球的GLMT计算结果进行了比较。其中大球、内核小球的半径及折射率分别为$a=1.0\mu\mathrm{m}, b=0.5\mu\mathrm{m}$，$m=1.33-0.0i$，$m=1.55-0.0i$，入射波束为波长为$\lambda=0.6328\mu\mathrm{m}$，束腰半径为$\omega_0=0.75\mu m$的高斯波束，波束的束腰中心全局位于坐标系原点$x_0=y_0=z_0=0.0$处，入射角为零，即正入射，欧拉角为$\alpha=\beta=\gamma=0.0^\circ$。由图3.3可见，本程序所计算的同心双层球对高斯波束的散射结果与已发表的双层球的GLMT的结果吻合很好。

另外，韩国霞等人[106]和颜兵等人[105]分别对高斯波入射下偏心球粒子的远场散射特性作了数值分析。颜兵等人给出了在轴高斯波入射的情况分析，而韩国霞等人给出了更为一般的离轴高斯波入射情况下的数值结果。这里我们将本论文程序所得结果和韩国霞等人的计算结果进行对比。其中大球、内核小球的半径及复折射率分别为$a=1.0\mu\mathrm{m}, b=0.5\mu\mathrm{m}$，$m=1.33-0.0i, m=1.55-0.0i$，两球球心之间

的距离为 $d=0.25\mu\mathrm{m}$。入射波束为波长为 $\lambda=0.6328\mu\mathrm{m}$，束腰半径为 $\omega_0=1.0\mu m$ 的高斯波束，以欧勒角为 $\beta=45^\circ$， $\alpha=\gamma=0.0^\circ$ 方向入射。如图3.4所示，我们给出了入射波束束腰中心位于坐标系 $x_0=y_0=z_0=0.0$ 和 $x_0=y_0=z_0=0.5\mu m$ 两种情况下的散射结果。从两个图的对比中可以发现，虽然所得结果在前向和后向散射方向上的强度有些差别，但两者结果之间特征吻合的较好。

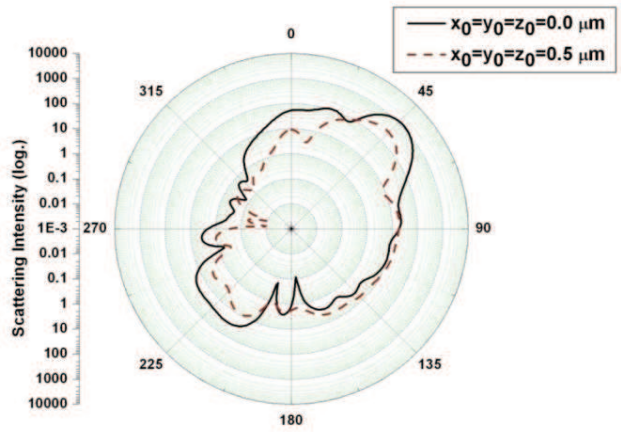

（a）本论文程序计算所得偏心球粒子波束散射强度极坐标分布

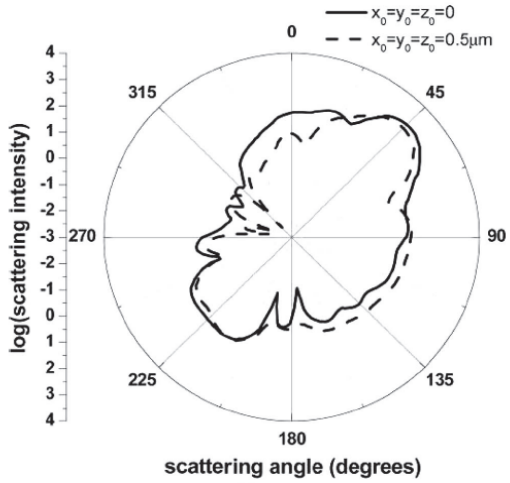

（b）文献[106]给出偏心球粒子波束散射强度极坐标分布

图3.4 偏心球粒子在高斯波照射下散射强度随散射角度分布图

§3.4 偏心球粒子散射场的空间分布

在传统的光散射信号的测量中，我们一般采用单个或若干个可移动的光电感应器对其进行收集，如光电倍增管，光电二极管等。这种测量方法能够满足对球形粒子等形状在某些特定方向上有对称关系的粒子的散射信号的采集。随着对非球形粒子的深入研究，人们发现非球形粒子散射信号的空间对称性一般情况下不复存在，为了得到准确的散射信号，我们通常需要更加繁琐的进行多次测量。但

是随着计算机特别是高分辨率CCD或CMOS等光电传感器件的发展，二维光电测量阵列已经成为光学测量实验室中的标准配置仪器。充分利用这种测量设备及其测量手段，已经使得非球形粒子的形变大小、多粒子散射强度分布、显微数字全息测速度、生物医学诊断等许多领域测量得到很大发展。因此在理论上，我们也需要对粒子光束散射的空间强度分布进行二维甚至三维的计算和预测。

§3.4.1 偏心球粒子远场散射场的三维空间分布

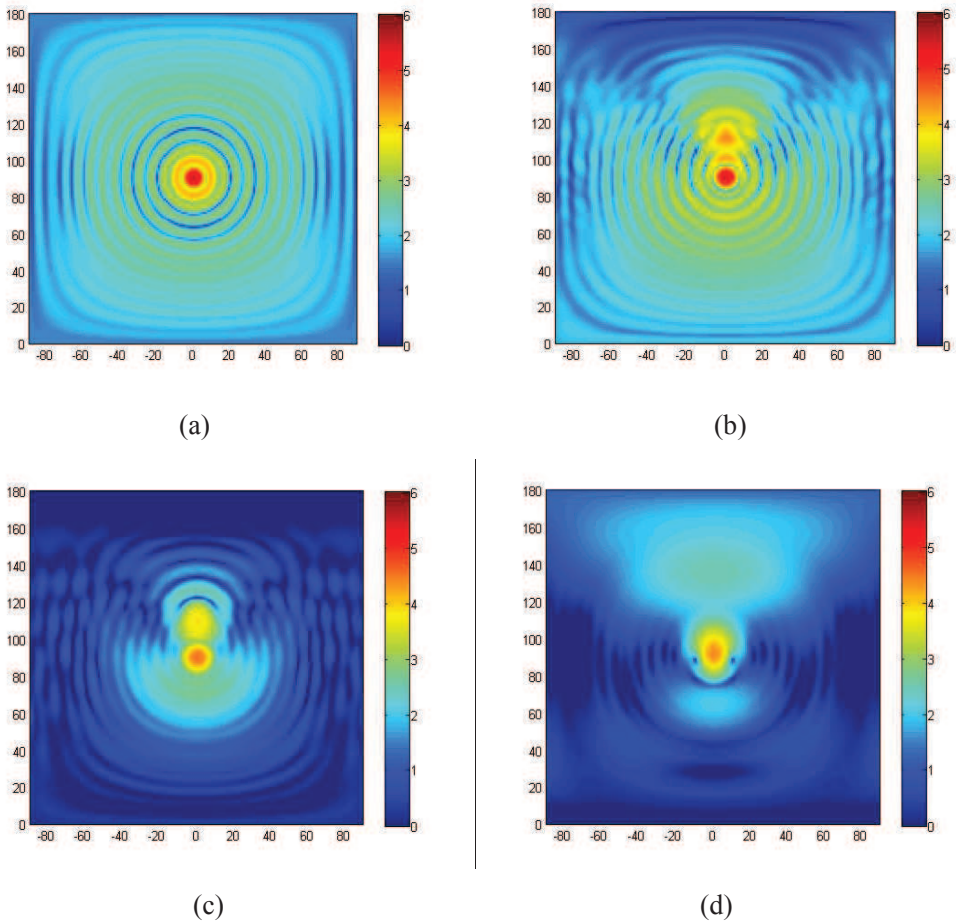

(a) (b)

(c) (d)

图3.5 水滴包含微小玻璃球组成的偏心球粒子在高斯波照射下远场散射强度的三维空间分布图，其中横轴坐标为散射方位角φ，纵轴坐标为散射极角θ。 (a) 平面波正入射同心球粒子 (b) 平面波90度斜入射偏心球粒子 (c) 高斯波90度斜入射偏心球粒子 (d) 离轴高斯波90度入射同心球粒子

Secker等人[18]在2000年针对由于重力作用而发生外表面形变的液滴以及被杂质污染的非均匀液滴的光学特性做了初步探索性的研究实验，之后Videen等人[107]对该实验中的相关结果从理论上进行了分析。利用偏心球的数学模型，Prabhu等人[108]在2001年进一步从理论上研究了由油酸包裹水滴组成的偏心球粒子在平面波

照射下的三维空间远场散射强度分布。然而在高斯波束照射下，偏心球粒子散射场的空间分布不仅仅取决于偏心球粒子自身的性质（尺寸参数、复折射率等），还将受到入射波束各种参数（束腰半径大小、束腰中心位置、入射方向等）的调制和影响。下面我们对高斯波束入射到被水层（复折射率为1.33-0.0i）覆盖的小玻璃球（复折射率为1.5-0.0i）上的情况加以分析。大球粒子的半径为3.0μm。一束电矢量沿z轴方向极化的高斯波束沿x轴正方向照射在偏心球粒子上。一个半径大小为1.5μm的内核小球粒子位于z轴上，初始状态下内核小球球心与大球球心重合。

在束腰半径为50μm的高斯波束，即近似平面波的照射下，偏心球粒子的远场散射强度三维空间分布如图3.5(a)所示。图中横轴坐标为散射方位角φ,纵轴坐标为散射极角θ。将内核小球粒子沿z轴正方向逐渐移动到两球心距离d=1.0μm的位置，此时偏心球的远场散射强度三维空间分布如图3.5(b)所示。从图中我们可以发现在内核小球粒子空间镜面对称的位置上出现了一个亮斑，这个亮斑作为一个相干光源与大球球心位置的另外一个相干光源发现相互干涉，形成了美丽的蝴蝶图案。该数值模拟结果和Secker等人[18]所得实验结果一致。保持内核小球粒子的位置不变，逐渐缩小高斯波束的束腰半径至$\omega_0 = 2.0\mu m$，此时偏心球的远场散射强度三维空间分布如图3.5(c)所示。从图中我们发现发现，随着入射波束束腰半径的减小，偏心球远场散射的干涉条纹愈加明显。这是因为在汇聚高斯波束照射下，更多的入射光透过大球外表面与内核小球发生相互作用，增强了内核小球的散射场，使得内核小球粒子产生的相干光源的强度更加接近于大球的球心处的相干光源而发生更加明显的干涉现象。保持束腰半径为$\omega_0 = 2.0\mu m$的高斯波束的照射，我们将内核小球粒子沿z轴方向逐渐移动回到大球球心，在这个过程中我们可以观察到类似于平面波照射下不断变化的干涉图像。并且我们可以发现，在此情况下随着内核小球粒子的移动，干涉条纹的空间频率也在不断变化，充分说明了两球心之间间距对干涉条纹的空间频率大小有重要影响。最后我们将高斯波束的束腰中心从$x_0 = y_0 = z_0 = 0.0\mu m$移动到$x_0 = y_0 = 0.0\mu m,\ z_0 = 2.0\mu m$的位置，我们在图3.5(d)中画出了此时偏心球（同心球）在离轴高斯波束照射下远场散射强度三维空间分布。限于图片展示的局限性，我们已将以上所述过程所对应的散射强度空间分布图以动态电影的形式展现出来，请参考文献[75]。

从图3.5可以发现，不论是在平面波还是在高斯波的照射下，由于偏心球内核小球的散射作用所产生的相干光源都将和大球球心所在处的相干光源在外场发生干涉，并形成特定的蝴蝶图案。由于该蝴蝶图案的具体形式和空间干涉频率会受到内核小球相对尺寸大小和三维空间位置的影响，因此如果将此干涉条纹用二维光电探测器件加以采集和处理，将为偏心球粒子的相关测量提供重要依据。下面我们就从实验测量的角度来模拟仿真偏心球外场的干涉现象。

§3.4.2 偏心球粒子远场散射场空间分布的局部特性

§ 3.4.2.1 光电传感器的空间位置描述

如图3.6所示，一束激光波束沿全局坐标系 *OXYZ* 的负 *Z* 轴向正 *Z* 轴传播，波束电磁场的电矢量分量沿 *X* 轴方向极化。我们用一个正方形二维光电传感器，比如CCD和CMOS器件，作为干涉等图像信息的记录介质，就可以进行数字全息理论、技术以及其在粒子场中的应用等展开研究。该测量装置较常用在多分散性粒子的探测系统中，比如在高压喷雾的研究系统中被用来测量和表征各个粒子之间的相对距离和间隔，间接测量出喷雾液滴的蒸发速率以及液体雾化的效果。对于后续的图像处理，将分别涉及到小波变换方法、菲涅耳变换方法、卷积方法和傅立叶变换方法等研究在轴和离轴数字全息系统3D粒子场的再现算法和理论，以数字聚焦和层析技术获得3D物场的再现图像，这些内容将不再本章中涉及，但可以作为以后的工作来加以研究。

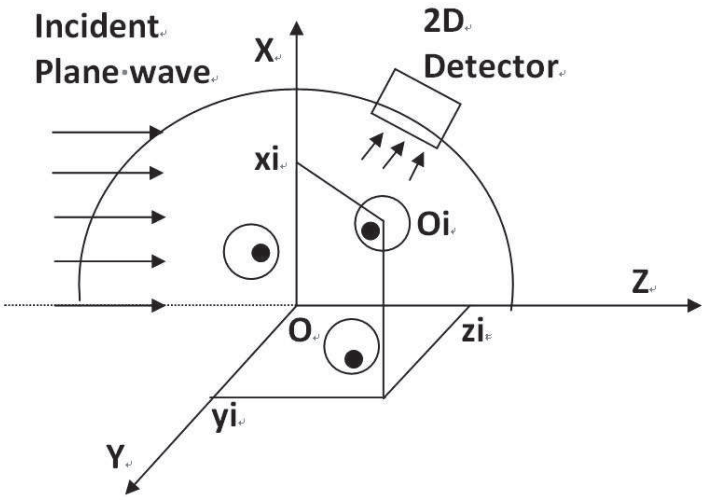

图3.6 粒子散射场局部图像测量实验示意图

首先我们需要对二维光电信号探测器上的每一个像元尺寸在全局坐标系 *OXYZ* 中的位置进行描述。假设点A是正方形探测器的中心点，那么矢量 $\overrightarrow{OA}$ 就是探测中心线。探测中心线 $\overrightarrow{OA}$ 与坐标轴 *OZ* 之间的夹角称为探测角度，用 θ_{m} 来表示。探测器的探测范围可以用最大和最小探测角度 $\theta_{\max}$ 和 $\theta_{\min}$ 来表示，它们与探测角度 θ_{m} 之间有以下简单的关系式：$\theta_{\mathrm{m}}=(\theta_{\max}+\theta_{\min})/2$。

建立适当的坐标系，使得探测中心线 $\overrightarrow{OA}$ 与探测器的探测面刚好垂直。那么 $\overrightarrow{OA}$ 的模值大小就是坐标原点到探测器的距离。则A点在全局坐标系中的坐标为：

（$R\cos\theta_m$ $R\sin\theta_m$），假设M点是探测面上沿xoz平面上与探测器相交直线上的一点，其坐标为(x, 0, z)，那么我们有：

$$\overrightarrow{AM}=(x-R\sin\theta_m, z-R\cos\theta_m) \tag{3-58}$$

由于探测中心线$\overrightarrow{OA}$与探测器的探测面刚好垂直，那么向量$\overrightarrow{OA}$向量$\overrightarrow{AM}$的乘积为零，可以得到：

$$\overrightarrow{OA}\bullet\overrightarrow{AM}=R(z\cos\theta_m+x\sin\theta_m)-R^2=0 \tag{3-59}$$

则有：

$$z\cos\theta_m+x\sin\theta_m=R \tag{3-60}$$

根据探测器探测角度的限定，我们可以得到：

$$x_i=\tan\theta_{\min}z_i \qquad x_f=\tan\theta_{\max}z_f \tag{3-61}$$

从而得到：

$$z_i=\frac{R}{\cos\theta_m+\sin\theta_m\tan\theta_{\min}} \qquad z_f=\frac{R}{\cos\theta_m+\sin\theta_m\tan\theta_{\max}} \tag{3-62}$$

光电传感器上每一个像元所收集的信号强度大小对应于垂直于探测面的电磁场强度大小。因此我们将通过对每个像元处的Poynting矢量的计算来确定采集到的信号强度：

$$\boldsymbol{S}=\frac{1}{2}Re\left[\mathbf{E}^{\mathrm{t}}\bullet\mathbf{H}^{\mathrm{t}*}\right] \tag{3-63}$$

§3.4.2.2　偏心球粒子的引入和描述

在对偏心球粒子进行描述之前，我们先将下面要使用到的三个直角坐标系加以说明。第一个为全局坐标系$OXYZ$，用于对入射波束的描述，并引入探测器的相对空间位置。第二个坐标系为局部坐标系$oxyz$，其坐标原点和偏心球粒子大球的球心P重合，在全局坐标系中的坐标为(x_p, y_p, z_p)。局部坐标系的各个坐标轴与全局坐标系的相应坐标轴相互平行，可以通过将全局坐标系$OXYZ$进行平移得到。第三个坐标系为旋转粒子坐标系$O\tilde{x}\tilde{y}\tilde{z}$。它是由局部坐标系$oxyz$经过欧拉角$(\alpha,\beta,\gamma)$的旋转得到。

选取探测器平面上任意一点D，它在全局坐标系中的坐标为(x_d, y_d, z_d)。则向量$\overrightarrow{PD}$在局部坐标系中可以表示为$(x_d-x_p, y_d-y_p, z_d-z_p)$。

$$\overrightarrow{PD}=x_{loc\_t}\hat{x}+y_{loc\_t}\hat{y}+z_{loc\_t}\hat{z} \tag{3-64}$$

其中：$x_{loc\_t}=x_d-x_p, y_{loc\_t}=y_d-y_p,\ z_{loc\_t}=z_d-z_p$

经过简单的旋转变换，我们可以得到向量$\overrightarrow{PD}$在旋转粒子坐标系$O\tilde{x}\tilde{y}\tilde{z}$中的表示为：

$$\overrightarrow{PD}=x_{loc}\hat{x}'+y_{loc}\hat{y}'+z_{loc}\hat{z}' \tag{3-65}$$

其中：

$$\begin{bmatrix}x_{loc}\\ y_{loc}\\ z_{loc}\end{bmatrix}=\mathrm{R}\begin{bmatrix}x_{loc\_t}\\ y_{loc\_t}\\ z_{loc\_t}\end{bmatrix}$$

$$\mathrm{R}=\begin{bmatrix}\cos\gamma & \sin\gamma & 0\\ -\sin\gamma & \cos\gamma & 0\\ 0 & 0 & 1\end{bmatrix}\begin{bmatrix}\cos\beta & 0 & -\sin\beta\\ 0 & 1 & 0\\ \sin\beta & 0 & \cos\beta\end{bmatrix}\begin{bmatrix}\cos\alpha & \sin\alpha & 0\\ -\sin\alpha & \cos\alpha & 0\\ 0 & 0 & 1\end{bmatrix} \tag{3-66}$$

然后即可得到探测单元在旋转坐标系中的球坐标表示：

$$r=\sqrt{(x_d-x_p)^2+(y_d-y_p)^2+(z_d-z_p)^2} \tag{3-67}$$

$$\theta=\arccos\left(z_{loc}/R_{loc}\right)\quad \varphi=\arctan\left(y_{loc}/x_{loc}\right) \tag{3-68}$$

§3.4.2.3　散射系数的对称关系

在旋转坐标系中，如第二章等式(2-42)所示，我们可以将任意入射有形波束用球矢量波函数表示为：

$$\mathbf{E}^i=E_0\sum_{n=1}^{\infty}\sum_{m=-n}^{n}\widetilde{a_{mn}}\mathbf{M}_{mn}(k\mathbf{r})+\widetilde{b_{mn}}\mathbf{N}_{mn}(k\mathbf{r}) \tag{3-69}$$

其中有：

$$\mathbf{M}_{nm}^{(j)}(kr,\theta,\varphi)=(-1)^m[im\pi_n^m(\cos\theta)\mathbf{i}_\theta-\tau_n^m(\cos\theta)\mathbf{i}_\varphi]z_n(kr)\exp(im\varphi) \tag{3-70}$$

$$\begin{aligned}\mathbf{N}_{nm}^{(j)}(kr,\theta,\varphi)=(-1)^m\Bigg\{&\frac{n(n+1)}{kr}z_n(kr)P_n^m(\cos\theta)\mathbf{i}_r\\&+\frac{1}{kr}\frac{d[rz_n(kr)]}{dr}[\tau_n^m(\cos\theta)\mathbf{i}_\theta+im\pi_n^m(\cos\theta)\mathbf{i}_\varphi]\Bigg\}\exp(im\varphi)\end{aligned} \tag{3-71}$$

类似于式(2-37)-(2-38)，有形波束在旋转坐标系下的展开因子$\left(\widetilde{a_{mn}},\widetilde{b_{mn}}\right)$和波束因子$\left(\widetilde{g_{n,TM}^m},\widetilde{g_{n,TE}^m}\right)$之间有关系式：

$$\widetilde{b_{mn}} = E_0 k c_n^{pw} (-1)^m (-1)^{(m-|m|)/2} \frac{(n-m)!}{(n-|m|)!} \widetilde{g_{n,TM}^m} \tag{3-72}$$

$$\widetilde{a_{mn}} = -ikc_n^{pw} (-1)^m (-1)^{(m-|m|)/2} \frac{(n-m)!}{(n-|m|)!} \widetilde{g_{n,TE}^m} \tag{3-73}$$

关于旋转坐标系中任意有形波束波束因子的求解我们已经在第二章中给出了具体推导过程，这里我们引用关于高斯基本模TEM_{00}的波束因子具体表达式：

$$\widetilde{g_{n,TM}^m} = (-1)^m (-1)^{(m-|m|)/2} \frac{(n-|m|)!}{(n+m)!} g_n \bullet e^{im\gamma} [\sin\alpha \bullet im\pi_n^m(\cos\beta) + \cos\alpha\tau_n^m(\cos\beta)] \tag{3-74}$$

$$\widetilde{g_{n,TE}^m} = (-1)^{m+1} (-1)^{(m-|m|)/2} \frac{(n-|m|)!}{(n+m)!} g_n \bullet e^{im\gamma} [\cos\alpha \bullet im\pi_n^m(\cos\beta) - \sin\alpha\tau_n^m(\cos\beta)] \tag{3-75}$$

将式(3-74)-(3-75)代入式(3-72)-(3-73)，我们可以得到：

$$\widetilde{b_{mn}} = E_0 k c_n^{pw} \frac{(n-m)!}{(n+m)!} g_n \bullet e^{im\gamma} [\sin\alpha \bullet im\pi_n^m(\cos\beta) + \cos\alpha\tau_n^m(\cos\beta)] \tag{3-76}$$

$$\widetilde{a_{mn}} = iE_0 k c_n^{pw} \frac{(n-m)!}{(n+m)!} g_n \bullet e^{im\gamma} [\cos\alpha \bullet im\pi_n^m(\cos\beta) - \sin\alpha\tau_n^m(\cos\beta)] \tag{3-77}$$

为了简化数值计算，我们引入归一化连带Legendre函数:

$$\widetilde{P_n^m}(\cos\theta) = \sqrt{\frac{2n+1}{2}\frac{(n-m)!}{(n+m)!}} P_n^m(\cos\theta) = c_n^m P_n^m(\cos\theta) \tag{3-78}$$

考虑到：

$$P_n^{-m}(\cos\theta) = (-1)^m \frac{(n-m)!}{(n+m)!} P_n^m(\cos\theta) \tag{3-79}$$

则有:

$$\widetilde{P_n^{-m}}(\cos\theta) = (-1)^m \widetilde{P_n^m}(\cos\theta) \tag{3-80}$$

那么即可将入射有形波束用归一化的矢量球谐函数表示为：

$$\mathbf{E}^i = E_0 \sum_{n=1}^{\infty} \sum_{m=-n}^{n} (\widetilde{a_{mn}})_N \mathbf{M}_{mn}(k\mathbf{r})_N + (\widetilde{b_{mn}})_N \mathbf{N}_{mn}(k\mathbf{r})_N \tag{3-81}$$

$$\mathbf{M}_{nm}^{(j)}(kr,\theta,\varphi)_N = (-1)^m [im\widetilde{\pi_n^m}(\cos\theta)\mathbf{i}_\theta - \widetilde{\tau_n^m}(\cos\theta)\mathbf{i}_\varphi] z_n(kr)\exp(im\varphi) \tag{3-82}$$

$$\begin{aligned}\mathbf{N}_{nm}^{(j)}(kr,\theta,\varphi)_N = (-1)^m \Bigg\{ & \frac{n(n+1)}{kr} z_n(kr) \widetilde{P_n^m}(\cos\theta)\mathbf{i}_r \\ & + \frac{1}{kr}\frac{d[rz_n(kr)]}{dr} [\widetilde{\tau_n^m}(\cos\theta)\mathbf{i}_\theta + im\widetilde{\pi_n^m}(\cos\theta)\mathbf{i}_\varphi] \Bigg\} \exp(im\varphi)\end{aligned} \tag{3-83}$$

上式中我们引入了下标”N”来表征归一化的球矢量波函数，则有:

$$\begin{aligned}\mathbf{M}_{nm}^{(j)}(kr,\theta,\varphi)_N &= c_n^m\mathbf{M}_{nm}^{(j)}(kr,\theta,\varphi)\\ \mathbf{N}_{nm}^{(j)}(kr,\theta,\varphi)_N &= c_n^m\mathbf{N}_{nm}^{(j)}(kr,\theta,\varphi)\end{aligned} \tag{3-84}$$

因此可以得到波束的展开因子：

$$\begin{aligned}(\widetilde{a_{mn}})_N &= \widetilde{a_{mn}}/c_n^m = i\frac{2E_0kc_n^{pw}g_n}{2n+1}\bullet e^{im\gamma}[\cos\alpha\bullet im\widetilde{\pi_n^m}(\cos\beta)-\sin\alpha\widetilde{\tau_n^m}(\cos\beta)]\\ (\widetilde{b_{mn}})_N &= \widetilde{b_{mn}}/c_n^m = \frac{2E_0kc_n^{pw}g_n}{2n+1}\bullet e^{im\gamma}[\sin\alpha\bullet im\widetilde{\pi_n^m}(\cos\beta)+\cos\alpha\widetilde{\tau_n^m}(\cos\beta)]\end{aligned} \tag{3-85}$$

当$\alpha=0.0$或者$\alpha=\pi$，我们可以得到关系式：

$$(\widetilde{a_{-mn}})_N = e^{-2im\gamma}(-1)^{m+1}\widetilde{a_{mn}} \qquad (\widetilde{b_{-mn}})_N = e^{-2im\gamma}(-1)^m\widetilde{b_{mn}} \tag{3-86}$$

通过一些简单的数学运算，我们可以得到：

$$(\widetilde{c_{-mn}})_N = e^{-2im\gamma}(-1)^{m+1}\widetilde{c_{mn}} \qquad (\widetilde{d_{-mn}})_N = e^{-2im\gamma}(-1)^m\widetilde{d_{mn}} \tag{3-87}$$

当$\alpha=\pi/2$或者$\alpha=3\pi/2$时，我们可以得到关系式：

$$(\widetilde{a_{-mn}})_N = e^{-2im\gamma}(-1)^m\widetilde{a_{mn}} \qquad (\widetilde{b_{-mn}})_N = e^{-2im\gamma}(-1)^{m+1}\widetilde{b_{mn}} \tag{3-88}$$

同样通过类似的数学运算，我们可以得到：

$$(\widetilde{c_{-mn}})_N = e^{-2im\gamma}(-1)^m\widetilde{c_{mn}} \qquad (\widetilde{d_{-mn}})_N = e^{-2im\gamma}(-1)^{m+1}\widetilde{d_{mn}} \tag{3-89}$$

在数值计算中使用上述的对称关系式将会大大提高程序的计算效率。

§3.4.2.4 散射光强的计算

在旋转粒子坐标系中，通过散射问题的求解，我们可以求得粒子散射场在球坐标系下的6个电磁场分量。根据直角坐标系与球坐标系之间的相互转换关系，我们得到散射场在直角坐标系下各个方向的分量为：

$$\begin{bmatrix}E_x'\\E_y'\\E_z'\end{bmatrix}=\begin{bmatrix}\cos\tilde{\varphi}\sin\tilde{\theta} & \cos\tilde{\varphi}\cos\tilde{\theta} & -\sin\tilde{\varphi}\\ \sin\tilde{\varphi}\sin\tilde{\theta} & \sin\tilde{\varphi}\cos\tilde{\theta} & \cos\tilde{\varphi}\\ \cos\tilde{\theta} & -\sin\tilde{\theta} & 0\end{bmatrix}\begin{bmatrix}E_r'\\E_\theta'\\E_\varphi'\end{bmatrix} \tag{3-90}$$

通过与欧拉角旋转$(-\gamma,-\beta,-\alpha)$,可以将旋转粒子坐标系转换到未旋转的局部坐标系，得到电磁场6个分量在局部坐标系下的表达式：

$$\begin{bmatrix}E_x\\E_y\\E_z\end{bmatrix}=R'\begin{bmatrix}E_x'\\E_y'\\E_z'\end{bmatrix} \tag{3-91}$$

其中有：

$$R' = \begin{bmatrix} \cos\alpha & -\sin\alpha & 0 \\ \sin\alpha & \cos\alpha & 0 \\ 0 & 0 & 1 \end{bmatrix} \begin{bmatrix} \cos\beta & 0 & \sin\beta \\ 0 & 1 & 0 \\ -\sin\beta & 0 & \cos\beta \end{bmatrix} \begin{bmatrix} \cos\gamma & -\sin\gamma & 0 \\ \sin\gamma & \cos\gamma & 0 \\ 0 & 0 & 1 \end{bmatrix} \tag{3-92}$$

在不同的光测量技术中，例如彩虹技术、离轴全息技术等，需要在不同的散射角度来收集散射信号。利用以下转换关系可以将电磁场分量投影到任意散射角度的探测面上去：

$$\begin{bmatrix} E_{xd} \\ E_{yd} \\ E_{zd} \end{bmatrix} = \begin{bmatrix} \cos\theta_m & 0 & -\sin\theta_m \\ 0 & 1 & 0 \\ \sin\theta_m & 0 & \cos\theta_m \end{bmatrix} \begin{bmatrix} E_x \\ E_y \\ E_z \end{bmatrix} \tag{3-93}$$

求得电磁场所有的电磁分量后，就可以根据式(3-63)来对Poynting矢量进行计算，从而来确定散射信号强度的大小。

§3.4.2.5　多粒子散射强度的叠加

忽略散射体系中粒子之间的多次散射，自由空间中任意一点P的总电磁场强度就是所有粒子散射强度在该点的相干叠加。对各个粒子散射波的各个电磁场分量的复振幅进行叠加：

$$V_w^{\mathrm{t}} = \sum_{j=1}^{N} Y_w^{\mathrm{s},j} \tag{3-94}$$

其中N为测量空间单元中粒子的总数。V代表电场分量E或者磁场分量H的矢量和。W代表电磁场沿直角坐标系中x, y或z方向上的分量。Y代表各个粒子散射场中电场分量E或者磁场分量H。

基于以上的理论推导和分析，本论文编写了计算多粒子散射强度分布的程序。该程序的主要特点有：

1. 任意一个粒子的直径、复折射率、空间位置都可以随意定义。

2. 光电信号传感器可以放置在空间的任意位置。因此可以对彩虹技术、离轴全息技术等进行预测分析。

3. 被探测粒子与探测器之间的位置可以任意定义。因此不管是近场分布还是远场散射分布都可以进行预测。

§3.4.2.6　数值结果与分析

虽然本论文所写程序可以对多粒子散射体系的散射结果进行预测，但是这里我们只对单个粒子的数值结果进行举例说明，针对偏心球粒子的散射强度空间分布的特点进行分析，而多个粒子的散射结果只需要利用式(3.91)进行相干叠加即可得到。由于只涉及单个散射粒子，我们不防假定这个粒子的球心位置位于全局坐

标系的原点O上。

(a) 直径为D=10μm的液滴

(b) 直径为D=6μm的玻璃球

(c) 球粒子分别散射之后振幅的叠加

(d) 同心球粒子的散射结果

图3.7 平面波入射下粒子远场散射图案。(a) 水滴粒子 (b) 玻璃球粒子 (c) 水滴和玻璃球散射强度的矢量叠加 (d) 水滴包裹玻璃球组成的同心球粒子。入射波波长为0.532μm, 极化方式为TM极化，散射信号采集角度为30至50度。水滴的复折射率为m=1.33-0.0i, 玻璃球的复折射率为m=1.5-0.0i

为了通过对比来研究非均匀粒子散射图像的特点，论文首先分别对均匀球粒子及同心球粒子的散射图像进行了模拟计算，该过程同时也构成了对所写程序的验证。如图3.7所示，我们分别对平面波照射下水滴、玻璃球、以及由水滴包裹微小玻璃球组成的同心球产生的散射条纹图案进行了模拟计算。入射平面波波长为0.532μm，极化方式为TM极化，水滴的直径大小为D=10μm，复折射率m=1.33-0.0i，玻璃球的直径大小为D=6μm，复折射率m=1.5-0.0i，光电传感器的信号采集角度涵盖从30度到50度的范围，像素阵列为512*512， 散射信号采集点距离水滴R=1m。将图3.7a和图3.7b进行对比，我们很容易发现，随着粒子粒径的增大，在信号采集角度内的条纹的频率增加。我们将图3.7a和图3.7b的信号相互叠加平均后得到图3.7c，而图3.7d则是内球为直径大小为D=6μm的玻璃球，外球为直径大小为D=10μm

的水滴组成的同心球的散射结果。从图3.7c和图3.7d中都可以看出，不管是合成图案还是同心球散射强度图中都包含有两个频率的干涉条纹，其中的高频率条纹来自于大球粒子，而较小频率的条纹来自于较小尺寸的内核粒子。将图3.7c和图3.7d进行对比，我们可以看出同心球粒子的散射条纹图案与两个小球合成散射强度之间的存在巨大差异。

(a) 偏心球内核沿z轴移动d=1.0μm

(b) 偏心球内核沿x轴移动d=1.0μm

(c) 偏心球内核沿y轴移动d=0.50μm

(d) 偏心球内核沿y轴移动d=1.0μm,

图3.8 平面波入射水滴包裹玻璃球的偏心球粒子产生的远场散射图案。入射波波长为0.532μm, 极化方式为TM极化，信号采集角度30至50度。大球液滴的直径大小为D=10μm,复折射率为m=1.33-0.0i, 内核玻璃球的直径大小为D=6μm,复折射率为m=1.5-0.0i

为了研究偏心球粒子的散射特性以及探测偏心球内核粒子相对于大球球心的三维偏移，我们模拟计算了偏心球粒子的干涉条纹图案。如图3.8所示，我们对由玻璃球作为内核小球，水滴作为大球的偏心球粒子在平面波照射下散射产生的条纹图案分别进行了模拟计算，其中内核小球的球心相对于大球球心的空间位置用直角坐标系下的偏移量(x, y, z)来表示。入射平面波波长为0.532μm, 平面波极化方式为TM极化，水滴的直径为D=10μm,复折射率m=1.33-0.0i, 内核玻璃球的直径为D=2μm,复折射率m=1.5-0.0i, 光电传感器的信号采集空间角度涵盖从30度到50度的范围，像素阵列为512*512, 散射信号采集点距离水滴R=1m。

从图3.7可以看出，同心球粒子的散射条纹仍然为一系列的同心散射圆环。而对于内核粒子相对于大球粒子有一个偏移的偏心球粒子有将会有怎样的新的特性？如图3.8所示，当内核小球粒子沿直角坐标系的x轴或者z轴移动时，偏心球的散射强度图案仍然为一组同心圆环。而当内核粒子沿y轴方向移动时，光电传感器采集的散射强度图案可以看出是由两个不同位置的相干光源干涉叠加的结果，并且移动的距离越大，相干图像的角度也越大。这是因为当二维光电传感器的中心点位于x-z平面上，如果内核粒子沿x轴或者z轴，甚至沿x-z平面上的任意方向移动时，由内核粒子散射产生的相干光源与大球球心位置的相干光源到达传感器时的角度差异很小，而当内核小球粒子沿y轴移动时，两等效相干光源之间有明显的偏心距离，在相互作用时就产生复杂的干涉图案。偏心内核移动的距离越大，两个相干光源到达光电传感器的角度就越大，所采集的散射图像受到的影响也越大。

§3.5 小结

基于任意入射有形波束的球矢量波函数展开，本章在GLMT理论框架内对偏心球粒子与有形波束之间相互作用的散射问题进行了求解。利用球矢量波函数的平移加法定理，推导并求解了偏心球粒子对任意方向入射有形波束的散射方程。基于本章的理论推导结果，利用FORTRAN计算语言编写了一套可用于模拟仿真有形波束照射下偏心球散射远场，近场和内场电磁强度三维空间分布的程序。在对程序进行充分验证的基础上，分析了偏心球内核粒子相对大小、两球心距离、波束入射方向等因素对远场散射特性的影响。对于偏心球粒子内场和近场的详细分析将在下一章展开。

第四章 偏心球粒子内场和近场分析

在GLMT理论框架内，推导并求解了偏心球粒子对任意方向入射有形波束的散射方程。利用FORTRAN90编写了一套可用于模拟仿真有形波束照射下偏心球散射远场，近场和内场电磁强度三维空间分布的程序。在第三章我们已经分析了有形波束入射下偏心球粒子远场的散射特性。利用直角坐标系与球坐标系的相互转换关系式，本章推导了有形波束任意方向入射情况下，偏心球粒子散射近场和内场场强空间分布的计算表达式。在对所得到的公式和相应程序进行了数值验证的条件下,给出了高斯波和平面波沿不同方向照射偏心球粒子时，偏心球粒子内场和近场电磁强度分布的相关算例和结果分析。

§4.1 引言

相对于均匀球粒子或者椭球粒子，偏心球粒子与电磁（光）波之间的相互作用更加复杂。为了清楚认识复杂粒子与有形电磁波束之间相互作用的物理机理，深入了解和分析偏心球内部发生的非可积哈密顿光学混沌现象[109, 110]，本章对偏心球粒子在汇聚高斯波束照射下偏心球粒子的内场和表面近场强度分布进行了计算和模拟，本章结果将为我们实际的探测提供重要的指导信息。

在这种光学混沌背景下，球形腔体内的光学谐振特性将受到很大影响，比如光学谐振模式的分离[111]，某些谐振模式被加强从而诱发激光出射现象[112]，由于内核小球粒子与大球内壁之间复杂的相互作用而产生新的光学谐振模式[109]，将这些光学谐振特性加以激发和诱导，将有可能加强或者抑制某些非线性光学现象的产生，例如受激拉曼散射，受激布里渊散射等等。Kerker[10],Barber和Hill等人[113]先后对平面波入射情况下，均匀球型、椭球型粒子的近场和内场做了详细的分析。Barton等人[43, 52, 85]则对高斯波束任意方向入射情况下，均匀球型、椭球型粒子散射的近场和内场做了详细的分析。基于GLMT理论，我们在第三章已经详细推导了偏心球粒子对任意方向入射有形波束散射问题的求解，本章我们就偏心球对任意方向入射有形波束散射的近场和内场的强度分布进行分析研究，以应用广泛的基模高斯激光为例，对汇聚激光波束与偏心球粒子的相互作用进行研究，给出了一些具体的数值案例。并对入射波波束束腰半径、入射方向、内核小球相对尺寸、偏心距等参数对散射强度分布的影响进行讨论。

§4.2 理论推导

根据第三章相关的理论推导，我们可以得到偏心球粒子各个场电磁分量的具体表达式。然而由于电场强度的平方与电磁场强度称正比，因此可以用电场强度的平方更加方便地来表征电磁场强度的空间分布，即强度计算的表征参量为：

$$I=\frac{\mathbf{E}\bullet\mathbf{E}^{*}}{\left|E_0\right|^2} \tag{4-1}$$

其中 **E** 是空间中任意一点电磁场的电矢量分量, E_0 为入射电磁波电场分量的振幅值。在以下的计算中，为计算方便，我们假定入射电磁波电场分量的振幅值为单位值1。

§4.2.1 内场强度的数学表达式

对于偏心球粒子而言，它的内场分布包括以下两个部分：(I) 内核小球内部的场强；(II) 内核小球外表面和大球粒子内表面围成环形区域内的场强；由第三章的理论分析可知，在内核小球的局部坐标系下，我们可以将环形区域内的电场用矢量球谐函数表示为：

$$\mathbf{E}^{\mathrm{int1}}=\sum_{n=1}^{\infty}\sum_{m=-n}^{n} r_{nm}\mathbf{M}_{nm}^{(3)}(k_1\mathbf{r}_2)+s_{nm}\mathbf{N}_{nm}^{(3)}(k_1\mathbf{r}_2)+t_{nm}\mathbf{M}_{nm}^{(4)}(k_1\mathbf{r}_2)+u_{nm}\mathbf{N}_{nm}^{(4)}(k_1\mathbf{r}_2) \tag{4-2}$$

将球矢量波函数的具体数学表达式(2-7)-(2-8)代入到式(4-2)中，我们可以得到电矢量各个分量的具体计算式子：

$$E_r^{\mathrm{int1}}=\sum_{n=1}^{\infty}\sum_{m=-n}^{n}(-1)^m[s_{nm}h_n^{(1)}(k_1r_2)+u_{nm}h_n^{(2)}(k_1r_2)]\frac{n(n+1)}{k_1r_2}\widetilde{P_n^m}(\cos\theta)\exp(im\varphi) \tag{4-3}$$

$$\begin{aligned}E_\theta^{\mathrm{int1}}=\sum_{n=1}^{\infty}\sum_{m=-n}^{n}(-1)^m\Big\{&[r_{nm}h_n^{(1)}(k_1r_2)+t_{nm}h_n^{(2)}(k_1r_2)]im\widetilde{\pi_n^m}(\cos\theta)\\&+\frac{1}{k_1r_2}[s_{nm}\frac{d(r_2h_n^{(1)}(k_1r_2))}{dr_2}+u_{nm}\frac{d(r_2h_n^{(2)}(k_1r_2))}{dr_2}]\widetilde{\tau_n^m}(\cos\theta)\Big\}\exp(im\varphi)\end{aligned} \tag{4-4}$$

$$\begin{aligned}E_\varphi^{\mathrm{int1}}=\sum_{n=1}^{\infty}\sum_{m=-n}^{n}(-1)^m\Big\{&[-r_{nm}h_n^{(1)}(k_1r_2)-t_{nm}h_n^{(2)}(k_1r_2)]\widetilde{\tau_n^m}(\cos\theta)\\&+\frac{1}{k_1r_2}[s_{nm}\frac{d(r_2h_n^{(1)}(k_1r_2))}{dr_2}+u_{nm}\frac{d(r_2h_n^{(2)}(k_1r_2))}{dr_2}]im\widetilde{\pi_n^m}(\cos\theta)\Big\}\exp(im\varphi)\end{aligned} \tag{4-5}$$

同样的，在内核小球的局部坐标系里面，我们可以将内核小球内部的场强用矢量球谐函数表示为：

$$\mathbf{E}^{\text{int}2}=\sum_{n=1}^{\infty}\sum_{m=-n}^{n}p_{nm}\mathbf{M}_{nm}^{(1)}(k_1\mathbf{r}_2)+q_{nm}\mathbf{N}_{nm}^{(1)}(k_1\mathbf{r}_2) \tag{4-6}$$

将矢量球谐函数的具体数学表达式(2-7)-(2-8)代入到式(4-6)中，就可以得到电场分量表达式为：

$$E_r^{\text{int}1}=\sum_{n=1}^{\infty}\sum_{m=-n}^{n}(-1)^m q_{nm}j_n(k_2r_2)\frac{n(n+1)}{k_2r_2}\widetilde{P_n^m}(\cos\theta)\exp(im\varphi) \tag{4-7}$$

$$\begin{aligned}E_\theta^{\text{int}1}=\sum_{n=1}^{\infty}\sum_{m=-n}^{n}(-1)^m\Big\{&p_{nm}j_n(k_2r_2)im\widetilde{\pi_n^m}(\cos\theta)\\&+q_{nm}\frac{1}{k_2r_2}\frac{d(r_2j_n(k_2r_2))}{dr_2}\widetilde{\tau_n^m}(\cos\theta)\Big\}\exp(im\varphi)\end{aligned} \tag{4-8}$$

$$\begin{aligned}E_\varphi^{\text{int}1}=\sum_{n=1}^{\infty}\sum_{m=-n}^{n}(-1)^m\Big\{&-p_{nm}j_n(k_2r_2)\widetilde{\tau_n^m}(\cos\theta)\\&+q_{nm}\frac{1}{k_2r_2}\frac{d(r_2j_n(k_2r_2))}{dr_2}im\widetilde{\pi_n^m}(\cos\theta)\Big\}\exp(im\varphi)\end{aligned} \tag{4-9}$$

§4.2.2　近场散射强度的数学表达式

粒子表面的近场由入射电磁波和散射电磁波两部分矢量叠加组成。在系统全局坐标系中，散射电磁波的电场和磁场分量可以用球矢量波函数分别表示为：

$$\mathbf{E}^{sca}=\sum_{n=1}^{\infty}\sum_{m=-n}^{n}c_{nm}\mathbf{M}_{nm}^{(4)}(k_0\mathbf{r}_1)+d_{nm}\mathbf{N}_{nm}^{(4)}(k_0\mathbf{r}_1) \tag{4-10}$$

将球矢量波函数的具体展开数学表达式(2-7)-(2-8)代入到式(4-10)中，得到电场分量表达式：

$$E_r^{sca}=\sum_{n=1}^{\infty}\sum_{m=-n}^{n}(-1)^m d_{nm}h_n^{(2)}(k_0r_1)\frac{n(n+1)}{k_0r_1}\widetilde{P_n^m}(\cos\theta)\exp(im\varphi) \tag{4-11}$$

$$\begin{aligned}E_\theta^{sca}=\sum_{n=1}^{\infty}\sum_{m=-n}^{n}(-1)^m\Big\{&c_{nm}h_n^{(2)}(k_0r_1)im\widetilde{\pi_n^m}(\cos\theta)\\&+d_{nm}\frac{1}{k_0r_1}\frac{d[r_1h_n^{(2)}(k_0r_1)]}{dr_1}\widetilde{\tau_n^m}(\cos\theta)\Big\}\exp(im\varphi)\end{aligned} \tag{4-12}$$

$$\begin{aligned}E_\varphi^{\text{int}1}=\sum_{n=1}^{\infty}\sum_{m=-n}^{n}(-1)^m\Big\{&-c_{nm}h_n^{(2)}(k_0r_1)\widetilde{\tau_n^m}(\cos\theta)\\&+d_{nm}\frac{1}{k_0r_1}\frac{d(r_1h_n^{(2)}(k_0r_1))}{dr_1}im\widetilde{\pi_n^m}(\cos\theta)\Big\}\exp(im\varphi)\end{aligned} \tag{4-13}$$

§4.3 偏心球内场和近场的数值分析

从文献检索的结果来看，对于均匀球粒子在平面波或者有形波束照射下粒子内场和近场强度空间分布的研究已经有大量的报道。但是对于偏心球粒子的内场和近场场强分布的研究还没有报道。本节基于4.2节中的理论分析，着重讨论了任意方向入射有形波束与偏心球粒子相互作用下粒子散射场强的空间分布情况，给出了高斯波任意方向入射下偏心球粒子内场和近场强度分布的情况。该研究对粒子内部结构的探测和识别，对激光在雾、霭、云层中的传播和传热等物理机制的理解有着实际的参考和重要指导价值。

§4.3.1 程序的数值对比和验证

为了验证本论文程序的正确性，我们重复了相关文献中给出的几个数值模拟实验。将本论文程序计算所得的结果和所发表的相关数据进行对比，得到了一致的结果。如图4.1a所示，我们给出尺寸参数为20，复折射率为 $m=1.5-0.0i$ 的均匀球粒子对平面波的散射情况下近场和内场的场强沿 z 轴方向的强度分布。平面波的振幅设定为单位强度1。图中的坐标值大小已经针对小球的直径大小做了归一化处理。我们的计算结果和由Barber和Hill[113]所得的数据完全一致。其中用于检查的数据点主要有-2.5, -1.0, 1.0和-2.5。他们相对应的数值分别为0.87081, 1.4987, 59.2146, 3.2682。

§4.3.2 在轴高斯波束入射分析

本节我们模拟计算了一个被介质水（复折射率为 $m=1.33-0.0i$ ）非均匀覆盖的微小玻璃球（复折射率为 $m=1.5-0.0i$ ）分别在平面波和高斯波照射下内场和表面近场场强的空间分布情况。波长为 $\lambda=0.6283\mu m$ 的电磁波束沿 z 轴传播，其电矢量分量沿 x 方向极化。对于高斯波入射情况，我们设定其束腰半径为 $\omega_0=1.6\mu m$ ，其大小小于大球的半径 $a=2.0\mu m$ 而大于内核小球的半径 $b=1.0\mu m$ 。

如图4.1和图4.2所示，我们分别给出了偏心球粒子在平面波以及汇聚高斯波束照射下沿 z 轴一维方向和在 $x-z$ 二维平面上内场和表面近场强度大小的空间分布。在模拟计算偏心球粒子在一个截面上的强度分布时，我们先建立一个截面分割区间为 $2r/a\times 2r/a$ ，即在一个以粒子半径为标准进行归一化的空间截面上进行分析。由于电磁波束在其传播方向上的变化比其他方向要快，因此在波束正入射情况下，我们沿 z 轴方向设置计算200个点，而沿 x 轴或者 y 轴为100个点就已经足够表征强

度的变化情况。但是当波束倾斜入射到粒子上时，那么我们将在两个方向上都计算200个点，如图4.3和图4.4中的模拟计算。值得注意的是，在模拟计算内场的过程中如果所用空间点数过多，那么在靠近原点处会因为贝塞尔函数中的变量值比模数值小太多而使得的数值计算出现不稳定。

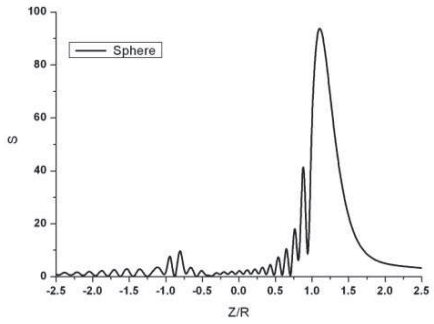

(a)

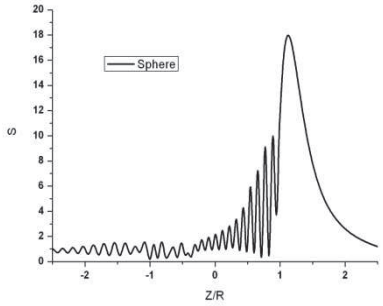

(e)

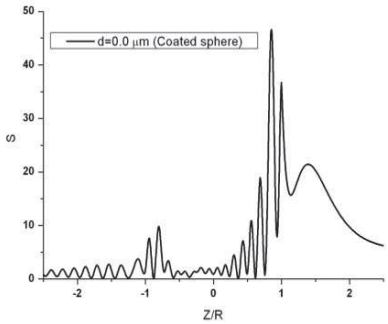

(b)

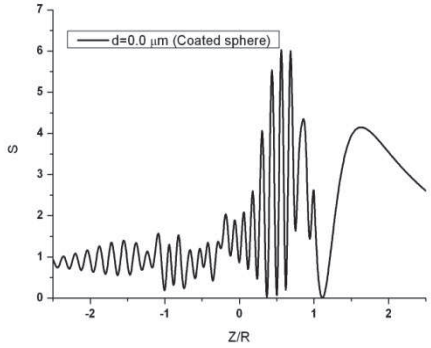

(f)

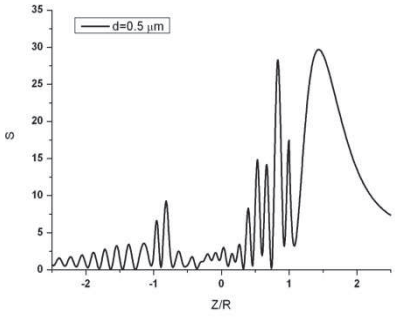

(c)

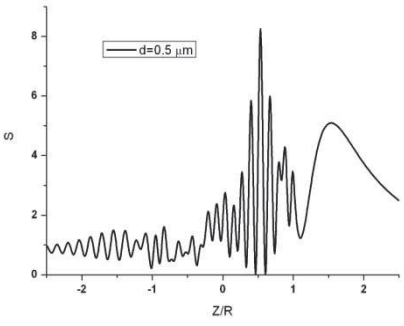

(f)

图4.1 偏心球粒子内场强度沿z轴的分布情况：(a,b,c) 平面波照射下，(d,e,f) 汇聚高斯波束照射下。内核小球粒子和大球的半径分别为 $a=2.0\mu m$ ， $b=1.0\mu m$ ，两球球心之间的距离为 $d=0.5\mu m$

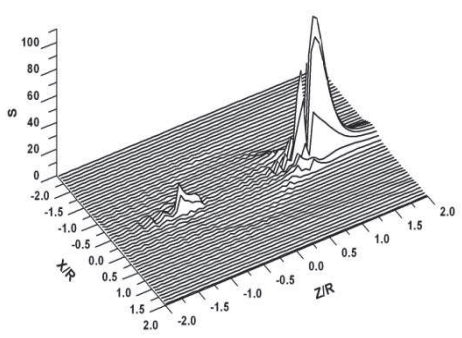

(a)

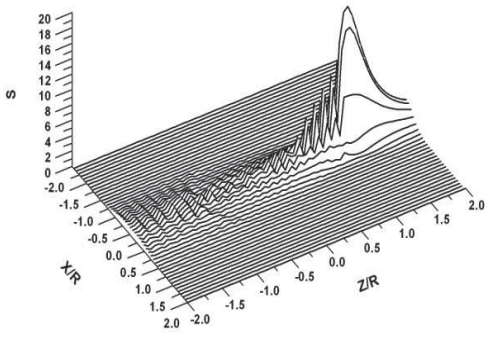

(d)

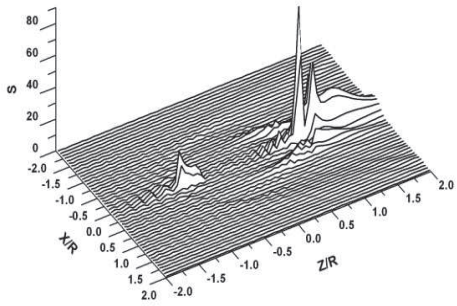

(b)

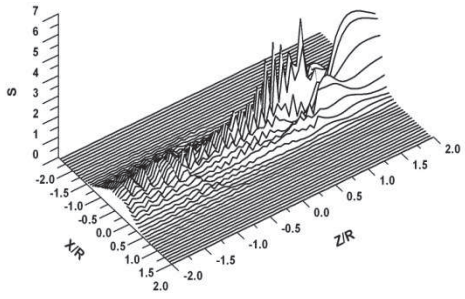

(e)

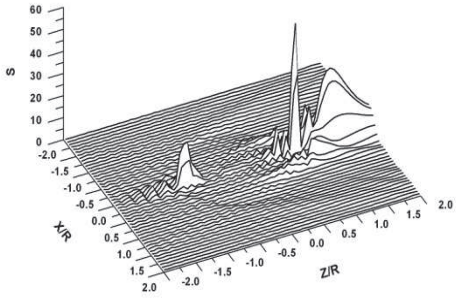

(c)

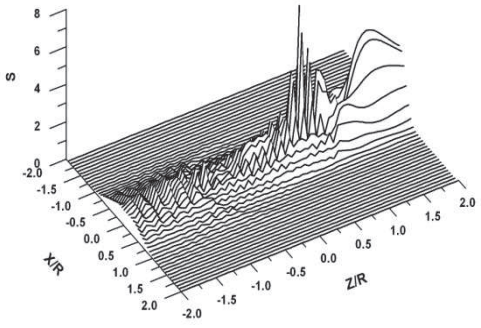

(f)

图4.2 偏心球粒子内场强度在x-z平面上的分布情况：(a,b,c) 平面波照射下，(d,e,f) 汇聚高斯波束照射下。内核小球粒子和大球的半径分别为 $a=2.0\mu m$ 和 $b=1.0\mu m$，两球球心之间的距离为 $d=0.5\mu m$

从图4.1(a)中我们可以看出，在平面波的照射下，均匀球形粒子散射的前向投影区域内有一个强度高达入射波强度100倍以上的高强度能量聚焦点。但是这个高强度的能量聚焦点的强度会由于偏心内核的散射作用而大大减小，如图4.1(b,c)。另外，当利用汇聚高斯光照射时，这个高强度点的强度也会被大大削弱，如图4.1d所示。在进一步的研究中发现，高斯波束的束腰半径越小，这个聚焦点的相对强度大小也越小。因此我们可以断定这个高强度汇聚点的产生主要是由于球形粒子表面对电磁波的汇聚作用，这样的效果类似于光学系统中的透镜对可见光的汇聚作用。

图4.1中的另外一个显著的特点是，在平面波的照射下，偏心球内场强度分布在后向有一个小的强度峰值点。但是在高汇聚高斯波的照射下，偏心球内场分布中的这个强度峰值点会消失不见。从几何光学的角度来看，这个强度极值点是由于大球内表面对经过若干次全反射光波的汇聚作用而形成的。而本文利用严格解析方法得到的数值结果也验证和支持了这个观点，即这个后向强度极值点是由离大球球心较远的离轴子波经过全反射汇聚作用形成的。

从图4.2中我们除了可以找出各种图4.1中发现的散射特性，还可以清楚的看出电磁波束在偏心球粒子内部的主要能流传播方向。这对于粒子的能流辐射和传播的理解有重要的意义。

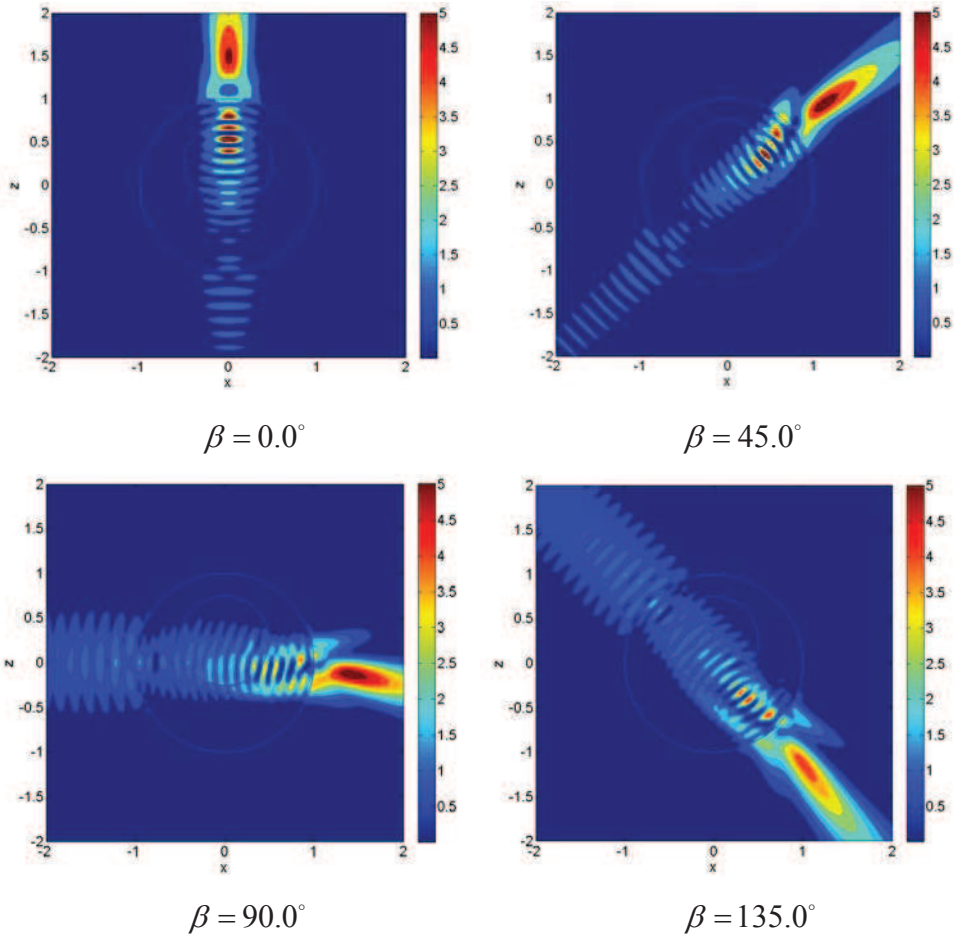

图4.3 任意方向入射在轴高斯波束照射下，偏心球粒子内场强度在x-z平面上的分布情况。内核小球粒子和大球的半径分别为 $a = 2.0\mu m$ 和 $b = 1.0\mu m$，两球球心之间的距离为 $d = 0.5\mu m$

为了进一步研究汇聚高斯波在偏心球粒子中的传播特性，我们在图4.3中给出了高斯波任意方向入射下，偏心球粒子内场和近场强度的分布情况。偏心球粒子两球心之间的距离为 $d = 0.5\mu m$，一束束腰半径为 $\omega_0 = 0.8a$ 的高斯波束以欧拉角 $\alpha = \gamma = 0.0^\circ$，$\beta$ 为变量入射到偏心球粒子上，束腰中心的位置为 $x_0 = y_0 = z_0 = 0.0$，即在轴入射，其他参数和图4.1相同。从图4.3中可以看出，当高斯波束斜入射到偏心球粒子时，散射粒子的空间球对称性被破坏，造成了内场强度和近场强度的非对称性分布。透射到大球内部的波束中有一部分能量由于内核小球粒子的散射作用而产生能流分流作用，这部分能量在偏心球粒子内部和主能流电磁场发生相互干涉，出射后在外场产生了一个较大的散射旁瓣，这个特性将为粒子内部结构的探测和分辨提供重要的指导意义。

§4.3.3　离轴高斯波束入射分析

在图4.4中，我们以高斯波波束的束腰中心位置为变量，进一步分析了偏心球粒子对离轴高斯光的散射特性。偏心球粒子两球心之间的距离用 $d=0.5\mu m$，一束束腰半径为 $\omega_0=0.8a$ 的高斯波束以欧拉角 $\alpha=\gamma=0.0^\circ$，$\beta=90.0^\circ$ 入射到偏心球粒子上，束腰中心的位置为 $x_0=y_0=0.0$，z_0 为变量。如图所示，根据内核粒子与入射高斯光束腰中心相对空间位置的不同，我们所得到的内场强度分布有很大的不同。当高斯波束束腰中心距离内核小球粒子很近时，透射到大球内部的电磁波受到内核粒子强烈的散射作用而使得内场和近场的电磁场强度分布更加分散。

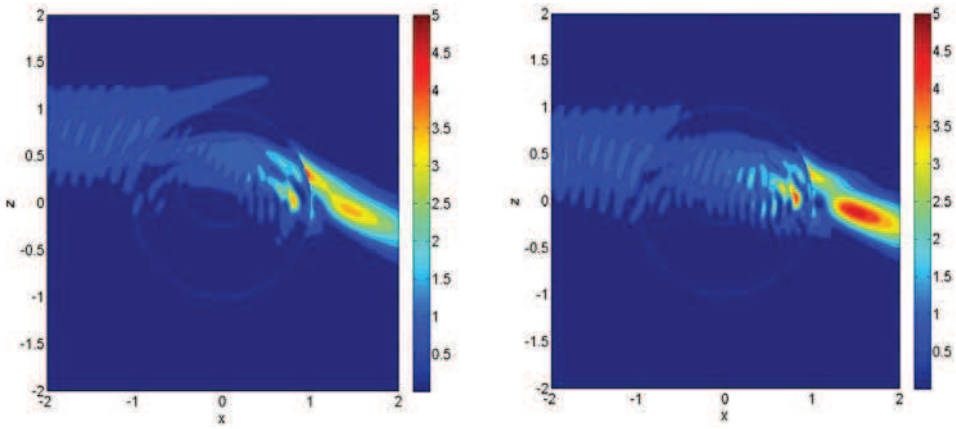

$z_0=1.0a$　　$z_0=0.5a$

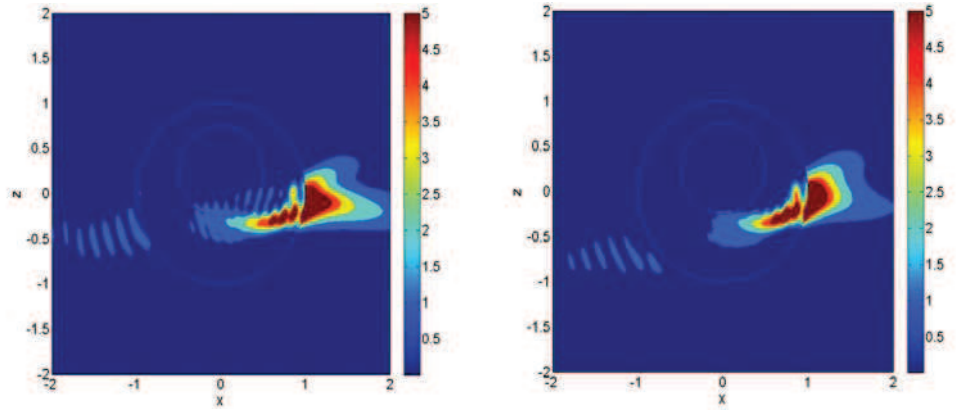

$z_0=-0.5a$　　$z_0=-1.0a$

图4.4　离轴高斯光斜入射情况下，偏心球粒子内场强度在x-z平面上的分布情况。内核小球粒子和大球的半径分别为 $a=2.0\mu m$ 和 $b=1.0\mu m$，两球球心之间的距离为 $d=0.5\mu m$

§4.4 小结

基于第二章和第三章中相关的理论推导，本章利用电磁场分量在直角坐标系与球坐标系之间相互转换的数学关系式，推导了有形波束任意方向入射情况下，偏心球粒子表面近场和内场场强空间分布的计算表达式。利用FORTRAN90计算语言编写了模拟仿真偏心球粒子有形波束散射下近场和内场场强空间分布的程序。在对所得公式和所写程序进行数值验证的条件下，本章给出了高斯波和平面波沿不同方向照射偏心球粒子时，偏心球内场和近场强度大小空间分布的相关算例和结果分析。这部分的研究将对清楚认识复杂粒子与汇聚电磁波束之间相互作用的物理机理，为实际光学探测提供重要的指导信息。

第五章 偏心球粒子光学谐振的研究

研究了偏心球粒子在强汇聚高斯波束激发下的光学谐振特性。通过数值模拟偏心球粒子的后向散射强度和微分消光截面随粒子尺寸参数的变化谱，研究了内核小球粒子在不同相对尺寸大小、不同偏心度下对偏心球中光学谐振模的谐振位置和谐振振幅的影响。给出了强汇聚离轴高斯波和平面波照射下，偏心球粒子在谐振及非谐振情况下内场强度的空间分布。此研究将对复杂光学微腔在光电转换器件设计、生物细胞探测等方面的应用有重要指导作用。

§5.1 偏心球光学谐振的研究现状

虽然声波、光波等在球形表面能够产生共振这样一个有趣的现象在一个世纪以前就已经引起了Lord Rayleigh的注意，但是仅仅是在1964年激光的发明之后，该现象及相关理论才在科学研究的领域上有了长足的发展。现代微细加工技术的发展，以及材料制备手段的突破，为具有微小尺度的介质微腔的制备和应用提供了必需的要素和手段，使得基于回音壁模式的光学微腔振荡成为多个领域的研究热点。特别是最近10年来，由于光学谐振模式极高的品质因数和极小的模式体积，已经使得基于光学微腔谐振的技术被广泛应用到微小粒子性质测量、光电器件的高度集成、腔量子电动力学以及量子信息处理等多领域的理论和实验研究中去[114]。

现代微小介质谐振腔内的光学谐振现象(Morphology-dependent resonances, MDRs)是由Ashkin[115]等人在用高汇聚激光对微小介质小球进行光辐射压力测量的实验中首次发现的。不久之后，该实验中所得的相关结果就在Mie-Debey理论框架下得到了高精度数值模拟的证实[116]。由于MDRs中各个谐振模的谐振位置和模式宽度对谐振粒子的尺寸参数及复折射率的变化相当敏感，基于光学谐振现象的光学测量技术很快被广泛开发出来用于对微小粒子的各种光学特性进行测量[2, 117]。比如利用高分辨率的光谱仪，通过对粒子弹性光学散射谱[118]或者非弹性光学散射谱[119]中MDRs谐振模的位置和宽度进行精确测量，不仅可以得到粒子的绝对粒径和复折射率大小，还可以间接得到液滴等各种粒子的遇热挥发以及遇冷沉淀变化速率。这些参数对于液滴的雾化，特别是燃烧环境中液滴各种参数变化的表征有着相当重要的作用。

不论是在平面波照射下还是在汇聚高斯波照射下，对于均匀介质小球中MDRs的研究已经有了大量的报道[1]。在粒子随尺寸参数变化的各种光学谱中，如消光谱，后向散射强度谱等等，MDRs的各阶谐振模会以尖锐的极值形式表现出来。在均匀

球形谐振情况下，我们可以用一组模数(n,m,l)来特定表征任意一个谐振模式的谐振峰。其中n是沿小球圆周变化的角度模数，它的数值为沿圆周强度极值数目的一半；l为径向模数，它的数值指代强度场沿径向方向极值的数目。m为方位模数，在均匀球的振荡中，由于球形粒子的任意一个直径都可以作为它的一个对称轴，因此它的方位角模数m彻底退化成了一个相同的合成模值。但是这个合成模值将会由于球形粒子表面的形变[120-122]或者球形粒子内部介质的不均匀分布[31, 111, 123]而发生分离。

从技术发展的角度来看，均匀介质小球构成的光学微腔是目前应用最为广泛的微腔之一。对于具有圆对称的球形微腔或者微盘谐振腔，它们缺乏定向的能量输出，因此人们只能通过消逝波耦合等形式来实现能量的输出利用。然而这种耦合模式的效率很低，为了实现大功率的耦合输出，通过改变谐振腔的形状来破坏微盘的对称性，从而打破方位模数m的合成模式，就有可能实现内部能量高效率定向输出。韩一平[120]，Mishchenko等人[121]对椭球型介质光学微腔进行了相关研究，结果表明在纵横比不是很大的情况下，谐振模的谐振位置会随着椭球纵横比的增大而发生单调偏移。然而在纵横比比例较大的情况下[122]，不仅会发生光学谐振模m的分解，也有可能会发生光路的定向输出，即激光的产生。中科院黄永箴课题组对非对称光学微腔做了大量的工作[124]。比如他们利用正方形微腔实现了双端口激光器的调制，适用于光子集成回路上同时驱动两个光学器件，或是应用于光学信号的处理和输出。

除了通过改变微腔的外表面几何形状来实现激光的定向输出，在这里我们给出了另外一种可能产生激光定向输出的模型装置，即偏心球模型。在这种模型中，当内核小球偏心地向大球表面贴近时，大球内壁和小球外壁组成的圆环空间是一个特殊的谐振腔，光波在这个圆环形谐振腔内传播将会出现复杂的光学混沌现象。一方面，内核小球的偏心移动有可能导致均匀大球内原有光学谐振模的消逝或者分解，从而使得原有MDRs的高品质因子不复存在，将会严重影响非线性光学过程，如受激拉曼散射，受激布里渊散射等的发生。另一方面，这种光学混沌现象也有可能使得入射光在内核小球和大球的相互作用下产生新的光学谐振模，使激光的定向耦合输出成为可能。在对偏心球粒子的相关研究文献中，诸如MDRs谐振模宽度变宽、激光出射等有趣的现象都已有相关报道。Gouesbet等人[109, 110, 125]利用几何光学方法（射线追踪法）对这个模型进行了细致的分析，对这种非对称环形微腔可能存在的谐振模式进行了深入的探讨。Mazumder等人[126]对介质球中内含一个偏心内核的情况分别用EBCM方法和微扰法就偏心核折射率的变化对MDRs的谐振位置和品质因数大小的影响进行了研究。他们发现随着偏心核折射率的增大，MDRs的谐振位置在尺寸参数的标征上呈单调递减。Fuller等人[29]则发现如果偏心内核小球的位置位于大球前向聚焦点附近时，有可能会引起MDRs谐振位置的偏移。

Leung等人[123]研究了一个大介质球包含众多小介质球时的散射情况。在这种情况下，由于整个散射体系失去原有的球形对称，将导致MDRs的分裂，从而丢失球形谐振腔原有的高品质因子。Rao和Gupta[111]在对一个大介质球包含一个小介质球时的情况进行研究时，也同样得出了类似的结果。从文献的查阅来看，对于偏心球MDRs的研究都是集中在平面波的照射情况下，下面我们在GLMT严格解析理论的框架内，对激光照射下偏心球的光学谐振情况进行进一步的研究分析，将为相关领域的工程研究提供重要的指导意义。

§ 5.2 汇聚激光激励下偏心球粒子的光学谐振特性

§5.2.1 程序的数值对比和验证

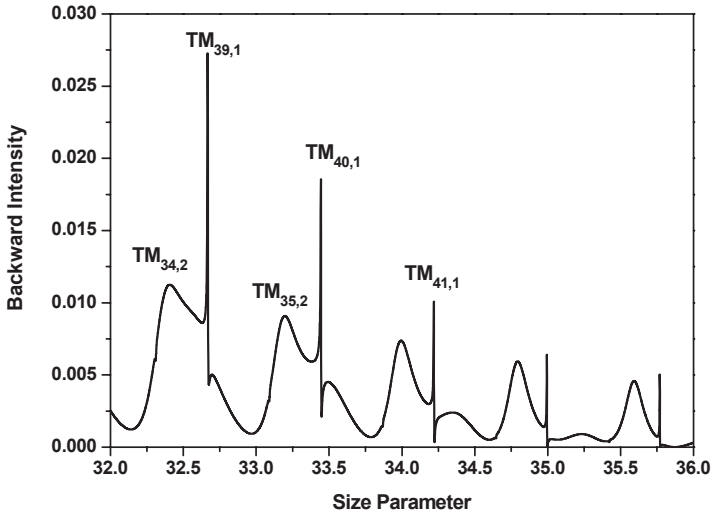

图5.1 同心球粒子在离轴高斯波束照射下的后向散射强度谱。内外小球的半径比为r=0.7R. 激光波束束腰中心位置坐标为 $x_0 = z_0 = 0.0\mu m$， $y_0 = 2.93357\mu m$

除了在各类散射谱中能够观察到MDRs的变化和特性，我们也可以在某个具体的方向上，利用粒子的散射强度谱来研究MDRs。实际上，相对于其他散射区域来说，后向散射区域的散射背景强度更加弱小，因此在后向区域的散射强度谱中将会观察到更加明显的谐振现象。Barber和Hill从数值上分析了平面波照射下均匀小球粒子在后向的散射强度的谐振特性，并给出了相关数值以供参考对比。Khaled等人[127, 128]研究了高斯波照射下，均匀球粒子和同心球粒子在后向的散射强度谐振特性。为了验证本论文程序的正确性，我们重复了以上文献提到的几个数值模拟

实验，将所得结果和已发表的相关数据进行了对比，得到了一致的结果。下面我们给出了对比验证实验中比较有代表性的一个例子，即同心球在高斯波束照射下后向散射强度谐振的数值结果。

同心球是偏心球的两球心距离 $d=0.0\mu m$ 情况下的特例。完全采用Khaled等人[128]在文献中所给的相关参数，即内核小球与大球的半径比为 $r=0.7R$，内核小球和大球的复折射率分别为为 $m_1=1.5-0.0i$， $m_2=1.36-0.0i$。一束束腰半径为 $\omega_0=1.0\mu m$，波长为 $\lambda=0.532\mu m$ 的高斯波束沿 z 轴正方向传播，其束腰中心处电磁波的电矢量分量沿x轴方向极化，其束腰中心位置为 $x_0=z_0=0.0\mu m$，$y_0=2.93357\mu m$。如图5.1所示，我们计算模拟了同心双层球尺寸参数 kr 在32到36区间上变化时的微分消光截面谱和后向散射强度谱，仿真中采用尺寸参数步长为 $\Delta x=1.0\times10^{-5}$。所得结果与文献中的结果吻合完全一致。比较有趣的是，在这种情况下只有TM谐振模被激发。另外在图5.3中我们将会发现，当高斯波束沿 x 轴方向移动时，即波束的束腰中心位置为 $y_0=z_0=0.0\mu m$， $x_0=2.93357\mu m$，时，将只有TE谐振模被激发。

§5.2.2 离轴高斯激光平行入射下光学谐振的研究

在程序经过相关比较和验证的情况下，下面我们计算并给出了高斯波束照射偏心球时，粒子微分散射截面谱和后向散射强度谱的一些数值算例，并对其中的一些特性和现象进行分析和阐述。

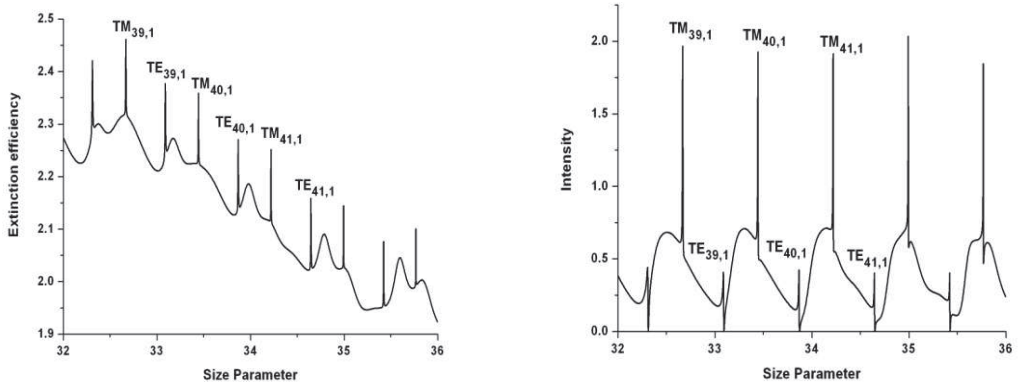

图5.2 平面波照射下，同心球粒子的微分消光系数谱和后向散射强度谱。内外小球的半径比为 $r=0.7R$. 平面波入射角为 0.0°

下面所给出数值模拟算例所用高斯波束除特别说明外均沿 z 轴正方向传播，电磁波电矢量分量在束腰中心处沿 x 轴方向极化，其束腰中心位置位于 $y_0=z_0=0.0$，x_0 为变量。当 $x_0=0.0\mu m$ 时为在轴入射情况，反之则为离轴入射情况。在已经发

表的文献中提到，当汇聚高斯激光波束在轴入射时不能有效激发谐振模式的产生，而我们的数值模拟结果也进一步证实了这一结论。因此在下面的研究中我们将利用离轴高斯激光波束作为激励源对偏心球粒子进行照射，研究MDRs谐振模的变化特点。当激光波长为 $\lambda = 0.532\mu m$ 时，我们选取选取波束中心位置 $x_0 = 2.93357\mu m$，这个离轴波束中心的位置刚好对应于均匀球粒子中谐振模式 $TE_{41,1}\,(n = 41,\ l = 1)$ 产生时大球粒子的半径大小。内核小球的复折射率为 $m_1 = 1.5 - 0.0i$ 对应于玻璃或者石英，外球折射率为 $m_2 = 1.36 - 0.0i$ 对应于乙醇。

上面已经提到，相对于其他散射区域来说，因为后向散射区域的散射背景强度更加弱，所以在这个区域内更容易观察到散射强度的谐振现象。如图5.2所示，我们计算了同心球对束腰半径为 $\omega_0 = 100\mu m$ 的高斯波束，即平面波照射下微分消光截面谱和后向散射强度谱。和汇聚高斯波束入射下的情况不同，在平面波的照射下，我们不仅可以看到TE模谐振，也可以看到TM模谐振会同时被激发。将5.2(b)与5.2(a)进行对比，我们不难发现，相对于微分消光谱，TM谐振模在后向散射方向上特别明显，更易于观察。同样的，在进一步的仿真实验中我们发现，如果波束的电矢量分量沿y轴方向极化，TE谐振模在后向散射方向上将表现的更加明显。

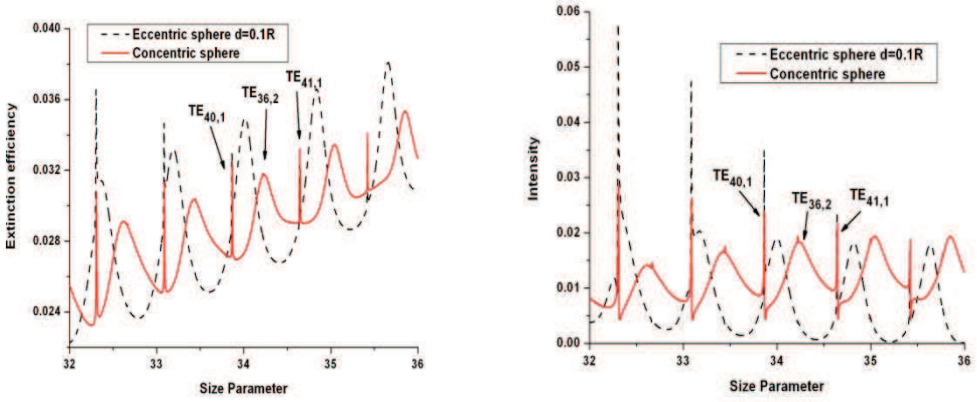

图5.3 高斯波束照射下，偏心球粒子和同心球粒子的微分消光系数谱以及后向散射强度谱的比较。偏心球两球心间的距离为d=0.1R。内外小球的半径比为r=0.7R. 高斯波入射角为0.0°。激光波束束腰中心位置坐标为 $y_0 = z_0 = 0.0\mu m$， $y_0 = 2.93357\mu m$

在图5.3中我们计算模拟了偏心球粒子的尺寸参数在32到36区间上的微分散射截面谱和后向散射强度谱，仿真中采用计算步长为 $\Delta x = 1.0\times10^{-5}$。其中内核小球和大球的半径比为 $r = 0.7R$。从图5.3中我们可以发现，当内核小球的球心相对于大球球心有一个微小的位置偏移时，这里取 $d = +0.1R$，偏心球的MDRs一阶谐振模的谐振位置基本上没有什么变化，而二阶谐振模的谐振位置则发生了比较大的偏移。这是因为在谐振情况下，从小球的内场径向强度分布来看，一阶振荡的峰值位置较二阶振荡的峰值位置更加靠近小球表面，因此二阶振荡受到偏心小球的影

响更大。

同时我们从图5.3中，特别是图5.3(b)中可以发现，在高斯波束的照射下，一阶谐振模的峰值大小随着粒子尺寸参数的变化呈现出单调减少的趋势。这个结果可以用区域近似原理来进行合理的解释。在此理论中，用矢量球谐函数展开的n阶子波束对应于一束距离粒子球心$(n+1/2)(\lambda/2\pi)$的光束。因此当我们用汇聚激光波束照射粒子时，取决于激光波束的能量分布和束腰中心的具体位置，只有特定模式的谐振模能够被明显激发表现出来。对于图5.3中所有高斯波束的束腰中心位置沿x轴移动距离$a=2.93357\mu m$，这个距离对应于谐振模式$TE_{41,1}$产生时大球粒子的半径大小，因此使得模式$n=41$附近的谐振模被加强激发。值得一提的是，并不是模式$n=41$本身，而是比其低一些的模式通过耦合得到了最大的能量。这是因为当汇聚激光中心稍微位于粒子外表面之外时，内场能量才能最高效率地耦合到谐振模式中去[44]。

不管是同心球还是偏心球，在高斯波束照射下所得的散射系数都正比于平面波照射下所得的散射系数，因此不论是在平面波还是高斯波的照射下，粒子谐振模式的谐振位置将不变。这个结果我们通过将图5.3和图5.2中同心球谐振模式进行比较即可得到验证。我们在前面已经提到，对于均匀球粒子或者同心球粒子，我们可以用一组模数(n,m,l)来特定表征任何一个谐振模式的谐振峰，比如说谐振模式$TE_{41,1}$代表了散射系数c_{nm}在模式$n=41,\ l=1$时有极值出现。然而对于偏心球粒子，我们从数值上发现，每一个谐振峰对应于多个模数n的极值，因此我们不能简单的沿用均匀球粒子或者同心球粒子情况下对谐振峰的传统标识，该问题还需要在后面做进一步的研究。

由于激光的加热作用，加上乙醇本身的强挥发特性，偏心球外面包裹的乙醇液体层会逐渐变薄。为了模拟仿真这种情况下的光学谐振特性，我们取内核小球和大球的半径比例为$r=0.92R$，两球心之间的距离为$d=0.04R$，其他参数均与图5.3中相同进行计算模拟。如图5.4所示，我们给出了离轴高斯波正入射到偏心球粒子和同心球粒子情况下消光谱以及后向散射强度谱的比较。

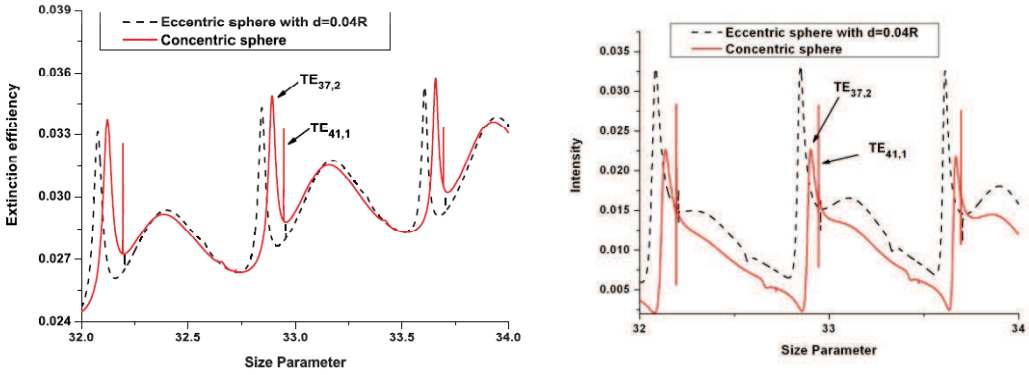

图5.4 高斯波束照射下，偏心球粒子和同心球粒子的微分消光系数谱以及后向散射强度谱的比较。偏心球两球心间的距离为d=0.04R。内外小球的半径比为r=0.92R. 高斯波束入射角为 0.0°。激光波束束腰中心位置坐标为 $y_0 = z_0 = 0.0\mu m$， $y_0 = 2.93357\mu m$

对比图5.3我们可以看出，在图5.4中虽然内核粒子的球心仅仅有 $d = 0.04R$ 的位置偏移，但它的一阶光学振荡($l = 1$)发生谐振的位置较 $r = 0.7R$ 发生了较大的偏移。与图5.3中的情况类似，由于二阶振荡发生的空间位置和内核小球有更多的重叠，因此二阶振荡比一阶振荡受到偏心小球的影响更大，发生谐振时的位置偏移也更多。比较值得关注的是，当内核小球粒子有 $d = 0.04R$ 的位置偏移时，一阶振荡的振幅比起相同内外球半径比的同心球粒子而言有很大的降低，这意味着与同心球粒子相比，偏心球内一阶振荡的能量更容易被耦合到内核小球粒子里面去。

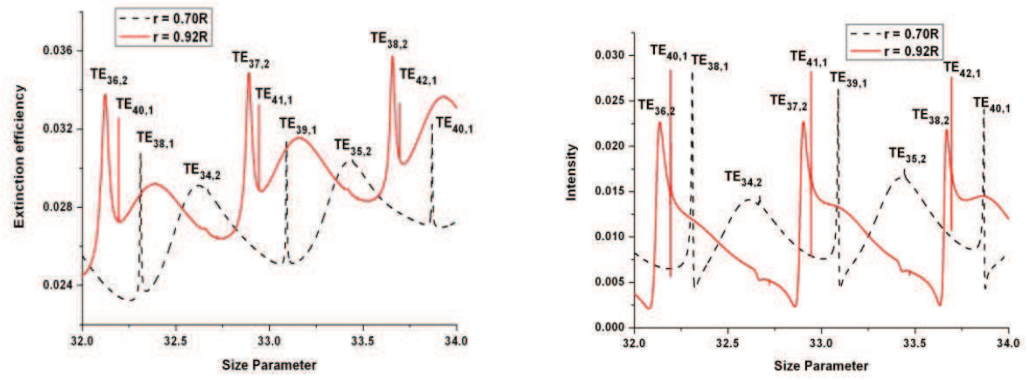

图5.5 高斯波束照射下，两个内外球半径比大小不同的同心球粒子的微分消光系数谱以及后向散射强度谱的比较。高斯波入射角为 0.0°

最后我们在图5.5中给出了高斯波束照射下内核小球与大球半径比例分别为0.7和0.92两种情况下同心球粒子散射的微分消光截面谱和后向散射强度谱。从图中容易看出，当内核小球和大球半径比例增大后，一阶振荡和二阶振荡的谐振位置和品质因子的大小的都受到很大的影响。二阶谐振受内核小球的影响要比一阶

谐振大，这是因为一阶谐振对应的能量峰值更加贴近大球的外表面，因此受内层球尺寸变化的影响较小。

§5.2.3　离轴高斯激光斜入射下光学谐振的研究

Rao和Gupta[111]研究了平面波照射下，偏心球粒子的光学振荡特性。他们发现当平面波正入射偏心球粒子时，即入射角为零度的情况下，由于散射体系在方位角方向上的球对称性，偏心球光学振荡中的方位角模数 m 不会分解。在本论文上一节对偏心球的光学振荡特性进行数值仿真和分析的结果也表明当汇焦高斯激光平行照射偏心球时，偏心球光学振荡中的方位角模数 m 也不会发生分解。然而当波束斜入射到偏心球粒子上时，粒子的整个散射体系将失去原有的球对称性，从而有可能会导致MDRs中方位角模数 m 的分解，丢失原本存在的高品质因子。在这一节，我们将重点对汇聚激光斜入射下偏心球的光学谐振进行相关的数值研究。

在本节的相关模拟计算中，我们假定波束的入射方向为90度，在此情况下，对于确定的两球心之间的距离，偏心球粒子相对于入射波束的非对称度达到最大。即一束束腰中心处电矢量分量沿z轴极化的高斯波束沿x轴方向传播，束腰中心的位置为 $x_0 = y_0 = 0.0\mu m$ ， $z_0 = 2.93357\mu m$.

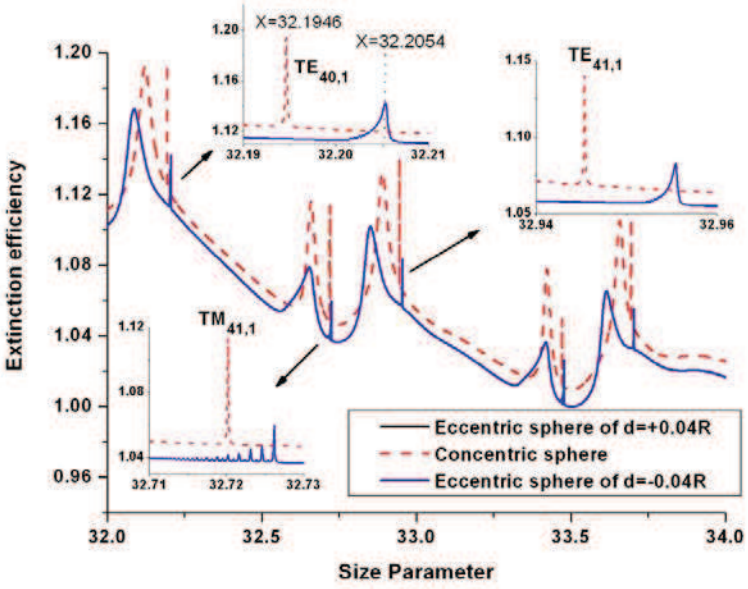

图5.6 平面波照射下，同心球粒子和偏心球粒子的微分消光系数谱的比较。内外小球的半径比为r=0.92R。偏心球两球心间的距离为d=0.04R。平面波入射角为90.0度

在图5.6中，我们给出了平面波照射下同心球粒子和偏心球粒子的消光谱的比较。内外球的半径比为r=0.92R。从图中可以看出，那些有较高品质因子的振荡模式都发生了模式分离现象。通过图中放大的小窗口我们可以发现，在这种情况下

TM振荡模要比TE振荡模更容易发生模式分离。

在汇聚高斯波束斜入射情况下，我们在图5.7给出了 $r=0.7R$，不同偏心距大小情况下的微分消光截面谱比较。图5.8中则给出了偏心球粒子内外球半径比例为 $r=0.92R$，不同偏心距大小情况下的微分消光截面谱比较。

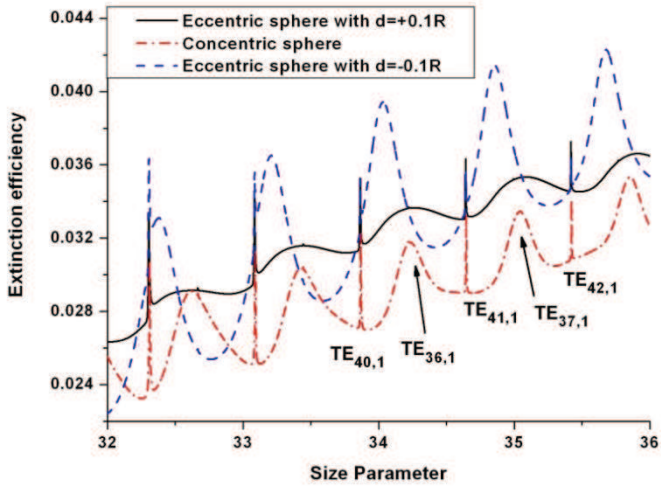

图5.7 高斯波束照射下，不同偏心度大小的偏心球粒子的微分消光系数谱的比较。内外小球的半径比为r=0.7R.

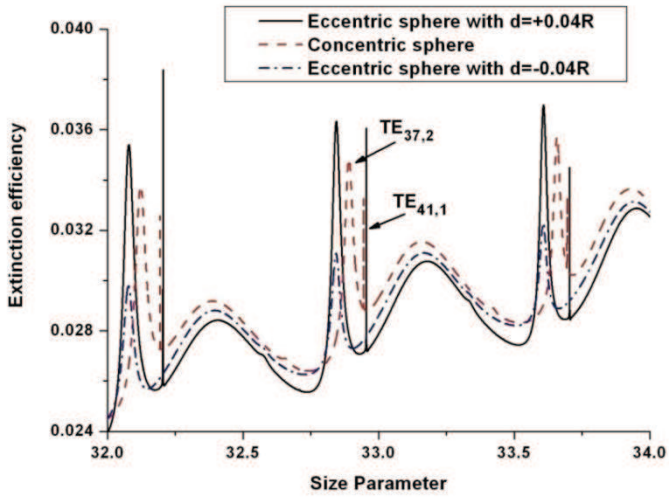

图5.8 高斯波束照射下，不同偏心度大小的偏心球粒子的微分消光系数谱的比较。内外小球的半径比为r=0.92R.

与平面波照射下不同的是，汇聚高斯波束斜入射下我们在偏心球粒子的微分消光截面谱中看到振荡模式的分离现象。当内外球半径比例 $r=0.7R$ 时，内核小球较小的偏心移动对一阶振荡的影响较小，而对二阶振荡的影响很大。而当内外球半径比例 $r=0.92R$ 时，一阶和二阶振荡都受到很大的影响。比较值得注意的是，

当内核小球从距离高斯波束较远的地方 $d=-0.04R$ 到 $d=0.0R$ 再到 $d=+0.04R$ 逐步靠近高斯波束的束腰中心位置时，一阶和二阶振荡的振幅逐步增大。

§5.2.4 离轴高斯激光照射下偏心球粒子内场的强度分布

由上面的分析可以看出，和平面波的照射下的情况不同，在汇聚高斯光的激励下，偏心球粒子的微分散射截面谱中的光学振荡模式并没有出现分离。为了进一步深入研究这种振荡模式的具体情况，我们对偏心球内场强度大小空间分布做了模拟计算。

如图5.9所示，分别对平面波照射和离轴汇聚高斯波照射两种情况下，我们展示了偏心球粒子在非振荡情况，完整振荡模式情况和非完整振荡模式情况下不同的内场分布情况。

对于非光学振荡情况下，偏心球粒子在离轴汇聚高斯波束照射下的内场分布（图5.9d）与在平面波的照射下的内场分布（图5.9a）有很大的不同，这主要是由于不同入射波束在传播截面上能量分布不同而造成的。在完整光学振荡情况下，平面波照射下偏心球粒子的内场沿大球表面分布有一系列强度极值，而最大的极值分别在散射前向和后向两个方向上（图5.9b）。通过更加深入的分析我们可以发现，对于任意一个谐振模式 $TE_{n,l}$ 将在x-z平面以z轴为对称轴，在每一边都将有 n 个极值。而在汇聚高斯波束的照射下，这些分离的极值点以一个实心的环形强度带来呈现。在平面波的斜入射情况下，偏心球的光学振荡模式将在方位角模数上发生分离。从图5.9c中我们可以发现，此时偏心球粒子的内场沿大球表面分布的一系列强度极值中最大的极值已经不在位于散射前向和后向两个方向上，而是分别像其他方向发生偏移。我们虽然不能从偏心球粒子的微分消光谱中观察到光学振荡模式模数的分离现象，但是从偏心球粒子的内场强度的分布中，我们发现此时内场强度的极大值也已经不再位于散射前向和后向两个方向上，而是类似与平面波照射喜爱分别向其他方向发生偏移，从而暗示了汇聚高斯波束照射下，偏心球粒子的光学振荡模式模数也发生了分离。

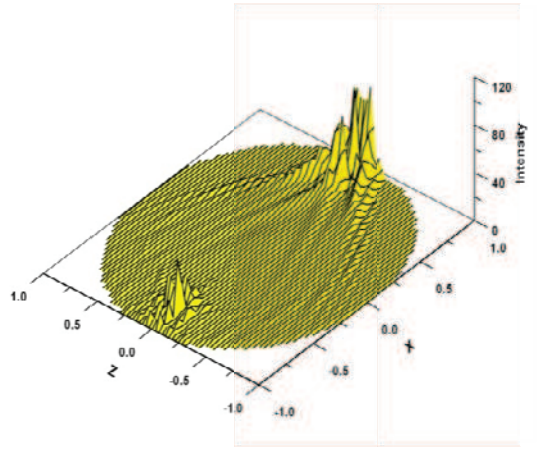

(a) 非谐振情况x=32.19

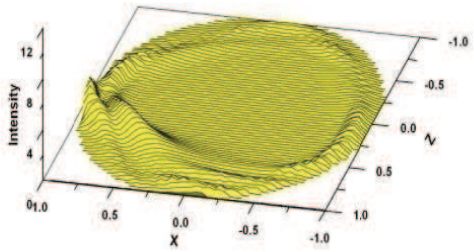

(d) 非谐振情况x=32.19

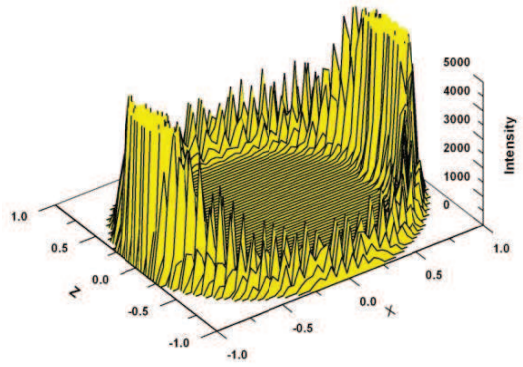

(b) 完整谐振情况x=32.1946

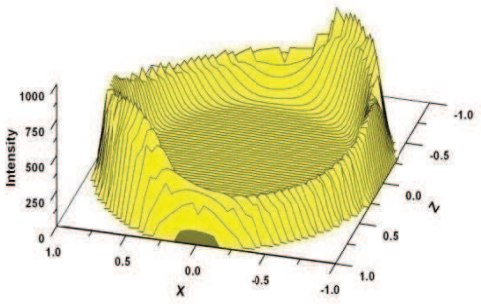

(e) 完整谐振情况x=32.1946

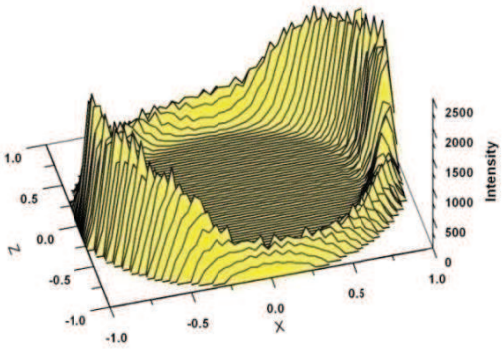

(c) 非完整谐振情况x=32.2054

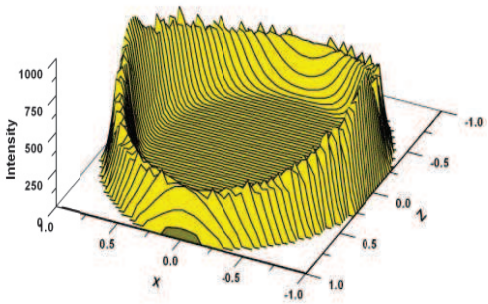

(f) 非完整谐振情况x=32.2054

图5.9 平面波(a,b,c)和高斯波束照射下(d,e,f)偏心球粒子内场强度分布情况。(a,d) 偏心球粒子处于非谐振情况下d=-0.04R；(b,e) 同心球粒子的处于完整的谐振情况下；(c,f) 偏心球粒子处于非完整谐振情况下d=0.04R

§5.3 小结

从当前的发展来看，均匀介质小球构成的光学微腔是目前应用最为广泛的微腔之一。然而，当均匀介质小球中被掺入其他杂质或出现气泡造成空缺时，介质球的光学振荡性质将会因为构成腔体介质的不均匀而受到影响。本章在GLMT理论框架内，研究了偏心球粒子在任意方向入射的离轴汇聚高斯波束激励下的光学振荡特性。通过对微分消光谱和后向散射强度谱的仿真和分析，研究了偏心球粒子的各种几何参数对光学振荡特性的影响。给出了离轴高斯波和平面波照射下，偏心球粒子在谐振以及非谐振情况下内场强度的空间分布图。

与均匀球形粒子和多层同心球一样，偏心球内部光学谐振模式的谐振位置不会因为入射波束束腰半径等参数的改变而发生变化。与斜入射平面波的激励情况不同，在汇聚高斯光的照射下，我们不能在偏心球粒子微分消光谱中观察到光学谐振模数 m 的分解。但是，通过对偏心球内场强度空间分布的仿真我们可以看到，和斜入射平面波的激励一样，在斜入射汇聚高斯光的照射下，偏心球内部原本对称分布的电磁能量被打破，能量分布也发生了明显的方向偏转，表明光学谐振模数 m 也发生了分解。

第二部分 椭球粒子彩虹特性研究

基于光散射理论的光学测量技术具有高精度、非接触以及实时动态测量等优势，最适于各种精密测量和运动测量，在航空航天工业和农业等多个领域中的应用中具有十分重要的作用和意义。比如它的非接触性，通过分析目标散射结果进行测量，不会对目标的结构特性和运动特性带来任何干扰，并且在某些特殊条件下，如高温、高压条件下的燃烧环境，光学的非接触性测量使其成为燃烧检测的最佳方法之一。又比如说液体燃料在进入汽缸之后的雾化过程，工业上用喷雾进行冷却，农业上的雾化农药、浇灌，以及人们日常食用的速溶咖啡的制造过程等等，为了实现生产过程以及产品质量的的监控，就需要对喷雾液滴粒子的相关参数进行测量，包括粒径分布、温度大小以及运动速度进行测量。另外，将相关实验数据加以分析、统计和总结，还可以为复杂物理过程的模型建立，如流体计算程序CFD，FLUENT，燃烧仿真程序LES，DNS等，提供更加准确的数据验证，进而研究更加复杂的物理现象和过程。

从测量技术发展的角度来看，基于粒子光散射理论的光测量技术之所以能够得到广泛的开发和应用，主要得益于激光技术的发展以及微弱信号检测技术的提高。激光因具有良好的单色性、强相干性以及高强度能量等特性而逐渐成为光探测技术中的首选光源。激光在小粒子体系中传播时会发生散射现象，散射光的强度角分布、偏振特性、光谱特性等都与散射目标本身的结构和性质密切相关，通过对散射光相关参量的测量，就可以反演出散射体本身结构和性质的多种信息。

目前已发展了多种测量粒子尺寸大小及浓度的光测量方法，能够满足不同情况下及时、准确、直观的测量需要。比如动态光散射法(Dynamic Light Scattering, DLS)、光子相关光谱测量(Photon Correlation Spectroscopy, PCS)、显微镜法、高速摄影法等等。本论文主要围绕谐振区粒子（微米量级和亚毫米量级）的测量展开，该范围内粒子相关测量的方法也很丰富，如消光法[4, 129, 130]、相多普勒法[131]、彩虹技术[131-135]等等。其中消光法[4, 129, 130]（或称全散射法）依据单次散射理论，根据入射光通过被测粒子群的透射率谱分布来反演小粒子的尺寸分布（粒子的数密度比较小），在粒度测量的许多领域被广泛采用。该方法优点具有测量速度快、视场大的特定。但是，该方法对大粒子尺寸的测量与反演的能力较为有限。比较成熟的测量技术如激光多普勒测速仪(Laser Doppler Velocimetry, LDV)和粒子成像测速(Particle Imaging Velocimetry, PIV)能够用来测量粒子的速度，但是对粒子粒径大小的测量却无能为力。将LDV技术进行改进升级，利用从光散射信号中提取出来的相位信号来反演粒子的大小，这个仪器称为相多普勒仪(Phase Doppler

Anemometry, PDA)。相多普勒仪(PDA)作为激光多普勒仪的新一代测量仪器，从二十世纪八十年代中开始得到了飞速发展和广泛应用。它可以同时测量粒子的速度快慢和粒径大小，为多相流、燃烧、喷雾过程的研究提供了有力的测试工具。利用相多普勒仪进行粒子折射率、粒子表面曲率等特性的测量也在研究当中。一般的相多普勒测量仪能够很好地测量10 μm 以上均匀粒子的尺寸分布，但是对于折射率（或温度）大小的测量精度就不是很理想。源于杨氏干涉原理，激光相干成像(Interferometric Laser Imaging for Droplet Sizing，ILIDS)，又称为粒子相干成像(Interferometric Particle Imaging, IPI)利用干涉条纹图像测量来测量较大范围内粒子粒径的大小分布，精度可达光波波长级。这个技术是基于被照射粒子上的反射光线和一阶折射光线之间在前向相干的所产生的干涉条纹来对表征粒子的性质，如粒径大小和速度。根据其工作原理可以看出，这个方法的限制在于只能用于透明球形粒子的测量。并且和其他的成像技术一样，这个方法受困于多幅干涉图像的重叠相加，在粒子密度较大的情况下误差相对会比较大。

高压喷雾过程中液滴各种参数的测量和表征一直是个极为关键且难以准确测量的问题。利用上述的PIV，PDA，ILIDS等技术和仪器能够对飞行的喷雾液滴的速度、粒径分布以及几何形状进行较为准确的测量，对液滴的雾化效果和传输变化形态的研究起到了重要的作用，然而这些技术却对液滴的温度测量无能为力。然而为了准确描述燃烧过程中燃料液滴粒子的加热和挥发作用，为高效率燃烧器的合理设计以及实现低污染排放提供数据支持，就必须对液滴的温度分布以及液滴化学组成成分进行测量。和其他测温方法相比，彩虹技术不仅能够高精度测量液滴的温度大小，还能够通过复折射率的测量来反演液滴的化学组成成分，为燃烧过程的精确数学建模起到重要基础作用[136, 137]。

类似于ILIDS的测量原理，彩虹技术(Rainbow technique)是利用不同阶数散射光之间的相干信息，比如彩虹角的位置和Airy峰的间距，来对球形粒子、柱形粒子的粒径分布、折射率（温度）大小等参数进行精确的测量。飞速发展的光散射理论和计算程序可以精确计算均匀或者非均匀球形粒子和柱形粒子散射光强度角分布，为改进和扩展这一测量技术的测量范围提供了有力工具。彩虹技术根据测量对象的不同和实验装置的差异，可以分成标准彩虹测量技术(Standard Rainbow technique)和全域彩虹测量技术(Global Rainbow technique)两种。

在标准彩虹测量技术中，我们通常使用二维光电传感器来记录单个液滴粒子对电磁（光）波光散射的电磁强度角分布。该电磁强度角分布图和粒子的粒径大小、粒子复折射率以及入射电磁波的性质有着密切的关系。在标准彩虹信号中，各个光强度峰值之间的距离包含有粒径大小的信息，而彩虹角的具体位置则可以用来确定粒子折射率的大小，从而推算出粒子平均温度的大小。一般情况下，由于单个粒子外表面形变会给彩虹信号带来很大的偏差，标准彩虹技术不太适应于

非球型粒子参数的测量。

为了消除液滴粒子外表面形变对彩虹信号的影响，van Beeck等人[138]提出了全域彩虹技术。从实验测量装置的搭建来看，全域彩虹技术和标准彩虹技术之间最大的不同是在标准彩虹技术技术中需要通过加载空间滤波器来选择性地对单个液滴的彩虹信号进行采集。而全域彩虹技术中则去除了这个空间滤波器，使的信号采集的对象从单个液滴拓展到了一群液滴粒子。从实验搭建和测量原理来看，全域彩虹技术的测量原理更加类似于自然界中彩虹现象的形成原理。然而全域彩虹技术的提出是建立在随机任意分布的非球形粒子对彩虹信号带来的影响不大这样的假设前提下的，为了验证液滴粒子外表面形变对全域彩虹测量带来的影响，以椭球粒子为模型，我们分别从实验[134]和理论[77]两个方面对该假设进行了系统分析。本论文的具体工作在于从理论和数值的角度研究椭球粒子的彩虹信号特性以及其对全域，相关结果发表在Experiment in Fluids上[77]。

从上面的介绍我们也可以看出，各个光测量技术都有其自身的优点和相应的局限性。而在实际的测量过程中，为了同时测量待测粒子的粒径分布、折射率大小以及速度矢量等多个参数，仅仅利用单一的技术或方法进行测量往往是不够的。因此我们经常需要将两种或多种方法相结合起来进行测量，例如利用PDA和彩虹技术相结合的方法来进行粒子尺寸和折射率的测量[139]。

第六章 扩展边界条件法

基于等效原理，利用扩展边界条件法(Extended Boundary Condition Method, EBCM)，推导了各向同性和各向异性散射目标的散射传输矩阵。针对多粒子散射体系，采用单次散射物理模型，推导了空间取向随机任意分布粒子群对平面波散射的解析解。通过将散射矩阵中各个元素的解析表达式用一般球函数的级数来展开，有效提高了散射问题的数值求解效率。本章的理论推导将为下一章的研究提供理论基础。

§6.1 引言

非规则目标对电磁（光）波的散射问题在大气科学和遥感[140]，光镊捕获和操纵[141]等多个学科和领域里的有着广泛的研究。在诸多求解算法中，扩展边界条件法是求解非规则粒子散射问题最有效的方法之一。从理论上来说，利用扩展边界条件法可求解任意形状目标的电磁波散射问题。特别的，当散射目标具有沿某个特定对称轴旋转对称的几何形状时，例如球形粒子、椭球粒子、圆柱粒子等散射体，在它们的散射问题求解过程中所对应的散射传输矩阵的计算积分与方位角无关，大大简化了其积分运算量，使得该方法的数值运算速度较其它几种计算非规则目标散射问题的数值方法，比如时域有限差分法(FDTD)、矩量法(MOM)、离散多极子法(DDA)等，要快好几个量级。另外，扩展边界条件法已经能够对尺寸参数在150以上的非球形粒子进行散射特性的预测[68]，将谐振区散射问题的求解范围上限和几何光学区大粒子散射问题的下限无缝衔接起来，消除了求解谐振区域这个区间上限范围内非规则粒子散射问题的空挡。

扩展边界条件法(Extended Boundary Condition Method, EBCM)，又称作零场方法(Null Field Method)或者T-矩阵法(Transition matrix method, T-matrix method)。该方法最早由Waterman[62]提出，利用扩展边界条件的方法，将入射电磁波和散射电磁波在一个包含散射微粒的外接曲面上分别利用合适的矢量波函数来展开，然后用散射传输矩阵的形式来描述展开系数之间满足的线性传输关系。此后大量文献讨论了该理论方法的改进以及其在各种复杂散射问题中的相关应用问题[59, 60, 113]。

§6.2 单体目标散射

§6.2.1 等效原理

扩展边界条件方法是将入射电磁波和散射电磁波在一个包含散射微粒的外接曲面上利用合适的矢量波函数来展开，然后用散射传输矩阵的形式来描述展开系数之间满足的线性传输关系。为了得到散射场、入射场及散射体内场之间的关系，我们需要利用等效源原理(Field Equivalence Principle)将实际电磁场的激励源在电磁场问题求解的边界上转换为等效电磁流元的辐射问题。

假设S为任意一个闭合曲面，它将整个介质空间分为内部和外部两部分，使得曲面S外为无源区，而所有的电磁激励源都位于曲面S内部。如图6.1(A)所示，根据场的等效定理：以曲面S为边界的无源空间的场可以在该曲面上引入电流元及磁流元来等效实际空间中（曲面S内部）的电磁激励源分布。如果位于S内部的激励源在整个空间所产生的场是 $(\mathbf{E}_s, \mathbf{H}_s)$，则在曲面S上我们可以用等效电磁流 $(\mathbf{E}_s \times \hat{n}, \hat{n} \times \mathbf{H}_s)$ 来表征这些S内部的激励源，即曲面S外的散射场 $(\mathbf{E}_s, \mathbf{H}_s)$ 是由电磁流 $(\mathbf{E}_s \times \hat{n}, \hat{n} \times \mathbf{H}_s)$ 激发产生的。其中 $\hat{n}$ 为曲面S上的外法向矢量。由于曲面S外的电磁场分布完全由边界条件决定，则S内的场可为任意值，不防设其为零场，等效结果如示意图6.1(B)所示。

类似的，考虑如图6.1(C)所示，设曲面S外有一系列的源 $(-\mathbf{J}_i, -\mathbf{M}_i)$ 在自由空间中产生电磁场 $(-\mathbf{E}_i, -\mathbf{H}_i)$，利用等效原理，我们可以得到如图6.2(D)所示的等效结果，即曲面S以外的激励源可用曲面S上的等效电磁流元来代替，这些等效流元在S内部产生的电磁场用 $(-\mathbf{E}_i, -\mathbf{H}_i)$ 表示，而在曲面S外的场强为任意值，不妨设为零场。相对于总的散射问题，这些场被计为负的入射场。

将图6.1(B)和图6.1(D)所示的两个子问题相叠加得到图6.1(E)所示问题，有：

$$\mathbf{J}_+ = \hat{n} \times (\mathbf{H}_i + \mathbf{H}_s), \quad \mathbf{M}_+ = (\mathbf{E}_i + \mathbf{E}_s) \times \hat{n} \tag{6-1}$$

在图6.1(E)中引入一系列的激励源 $(\mathbf{J}_i, \mathbf{M}_i)$，该激励源产生等效入射场 $(\mathbf{E}_i, \mathbf{H}_i)$，等效结果如图6.1(F)所示。其中 $(\mathbf{E}_i + \mathbf{E}_s, \mathbf{H}_i + \mathbf{H}_s)$ 即曲面S外部的总场。至此我们可以看出，曲面S外部的激励源与电磁场分布都与图6.1(A)中的初始问题相同，只是此时散射目标被一系列等效表面电磁流取代。这些表面电磁流元在曲面S外所激发的场就是待求散射场，在曲面S内产生的是负的入射场。

根据等效原理，我们可以将电场分量表示为：

$$\mathbf{E}^s(\mathbf{r}) = \nabla \times \int_s (\hat{n} \times \mathbf{E}_+) g(kR) dS - \nabla \times \nabla \times \int_s \frac{1}{i\omega\varepsilon_0} (\hat{n} \times \mathbf{H}_+) g(kR) dS \tag{6-2}$$

在曲面S内部区域：

$$0=\mathbf{E}_i(kr)+\nabla\times\int_s(\hat{n}\times\mathbf{E}_+)g(kR)dS-\nabla\times\nabla\times\int_s\frac{1}{i\omega\varepsilon_0}(\hat{n}\times\mathbf{H}_+)g(kR)dS \tag{6-3}$$

其中 $g(kR)$ 是自由空间的格林函数：

$$g(kR)=\frac{\exp(ikR)}{4\pi R},\qquad R=|\mathbf{r}-\mathbf{r}'| \tag{6-4}$$

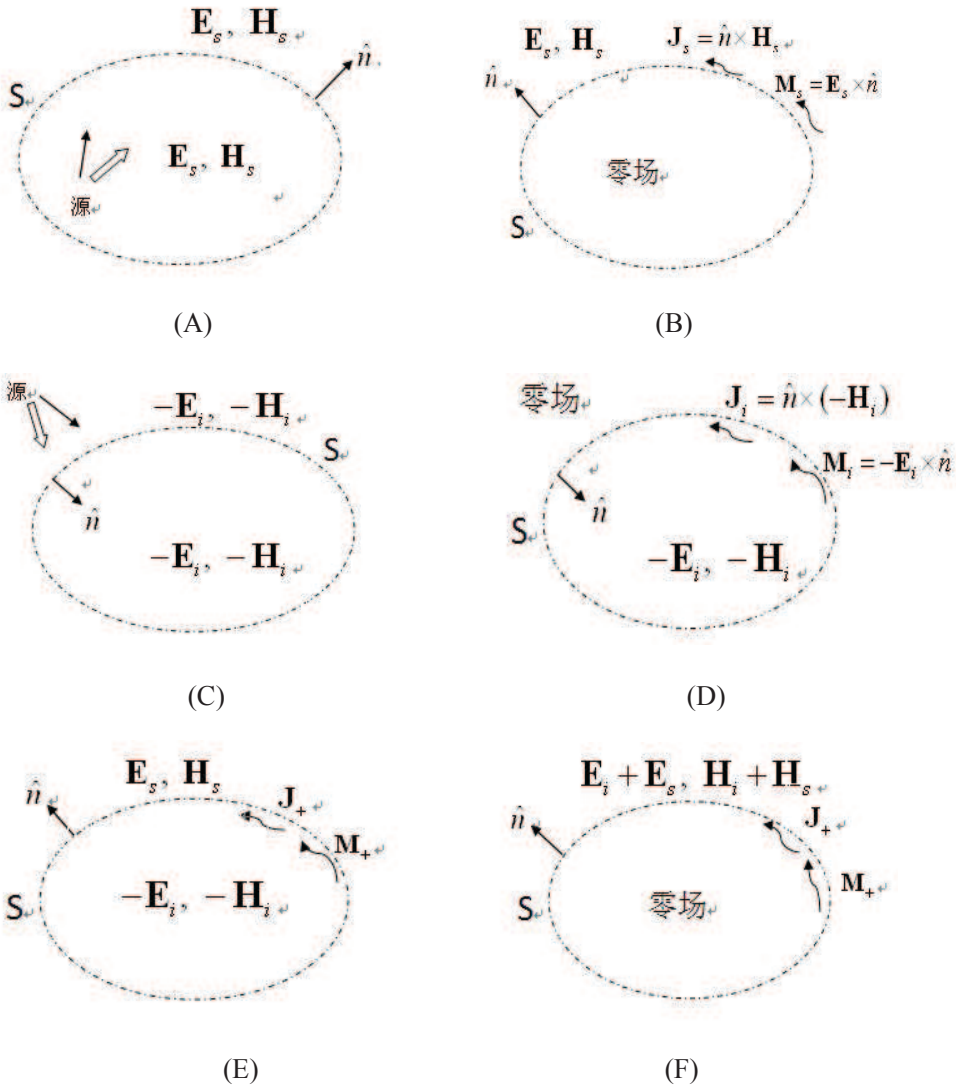

图6.1 等效原理示意图

式(6-3)中的积分项可以展开为：

$$(\hat{n}\times\mathbf{E}_+)g(kR)=(\hat{n}\times\mathbf{E}_+)\bullet\mathbf{G},\qquad(\hat{n}\times\mathbf{H}_+)g(kR)=(\hat{n}\times\mathbf{H}_+)\bullet\mathbf{G} \tag{6-5}$$

其中 $\mathbf{G}$ 为并矢格林函数。

§6.2.2 各向同性介质目标的散射问题

如图6.2所示，有一被曲面S包围的体积为V的任意形状散射体，设V_{in}为散射体内接球内部区域，V_{out}为散射体外接球的外部区域。内接球为散射体内，中心在原点的最大的球，外接球为包含散射体且球心在原点处最小的球。

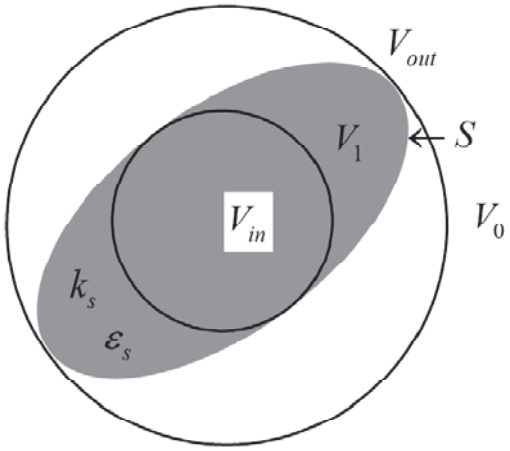

图6.2 扩展边界条件法示意图

在球坐标系下，对于任何由均匀各向同性介质组成的目标的电磁散射问题，我们可以把入射场、散射场以及内场分别用球矢量波函数来展开：

$$\mathbf{E}^{i}(\mathbf{r})=\sum_{n=1}^{\infty}\sum_{m=-n}^{n}\left[a_{nm}\mathbf{M}_{nm}^{(1)}(k\mathbf{r})+b_{nm}\mathbf{N}_{nm}^{(1)}(k\mathbf{r})\right] \tag{6-6}$$

$$\mathbf{E}^{s}(\mathbf{r})=\sum_{n=1}^{\infty}\sum_{m=-n}^{n}\left[c_{nm}\mathbf{M}_{nm}^{(3)}(k\mathbf{r})+d_{nm}\mathbf{N}_{nm}^{(3)}(k\mathbf{r})\right] \tag{6-7}$$

$$\mathbf{E}^{\mathrm{int}}(\mathbf{r})=\sum_{n=1}^{\infty}\sum_{m=-n}^{n}\left[f_{nm}\mathbf{M}_{nm}^{(1)}(k_s\mathbf{r})+g_{nm}\mathbf{N}_{nm}^{(1)}(k_s\mathbf{r})\right] \tag{6-8}$$

其中：$k=k_0 n$，$k_s=k_0 n_s$，k_0是电磁波在真空中传播时的波数，n_s是散射目标内部介质的复折射系数，n是粒子周围介质的复折射系数。

假设入射场源来自外接球之外，当位置矢量r位于在V_{in}内时，则S面上所有点的位置矢量都有$r'>r$，则有：

$$\begin{pmatrix}a_{nm}\\ b_{nm}\end{pmatrix}=-ik\int_s dS\hat{n}\times i\omega\mu\mathbf{H}_{+}\bullet\begin{bmatrix}\mathbf{M}_{-mn}^{(3)}(k\mathbf{r})\\ \mathbf{N}_{-mn}^{(3)}(k\mathbf{r})\end{bmatrix}-ik^2\int_s dS\hat{n}\times\mathbf{E}_{+}\bullet\begin{bmatrix}\mathbf{N}_{-mn}^{(3)}(k\mathbf{r})\\ \mathbf{M}_{-mn}^{(3)}(k\mathbf{r})\end{bmatrix} \tag{6-9}$$

当r位于在V_{out}外时，曲面S上的所有点的位置矢量都有$r'<r$：

$$\begin{pmatrix}c_{nm}\\ d_{nm}\end{pmatrix}=ik\int_s dS\hat{n}\times i\omega\mu\mathbf{H}_{+}\bullet\begin{bmatrix}\mathbf{M}_{-mn}^{(1)}(k\mathbf{r})\\ \mathbf{N}_{-mn}^{(1)}(k\mathbf{r})\end{bmatrix}+ik^2\int_s dS\hat{n}\times\mathbf{E}_{+}\bullet\begin{bmatrix}\mathbf{N}_{-mn}^{(1)}(k\mathbf{r})\\ \mathbf{M}_{-mn}^{(1)}(k\mathbf{r})\end{bmatrix} \tag{6-10}$$

根据Morse和Feshbach给出的球矢量波函数与格林函数的关系：

$$\mathbf{G}_0(\mathbf{r},\mathbf{r}')=ik\sum_{n=1}^{\infty}\sum_{m=-n}^{n}(-1)^m\begin{cases}\mathbf{M}_{-mn}^{(3)}(k\mathbf{r}')\times\mathbf{M}_{mn}^{(1)}(k\mathbf{r})+\mathbf{N}_{-mn}^{(3)}(k\mathbf{r}')\times\mathbf{N}_{mn}^{(1)}(k\mathbf{r}) & r>r'\\ \mathbf{M}_{-mn}^{(1)}(k\mathbf{r}')\times\mathbf{M}_{mn}^{(3)}(k\mathbf{r})+\mathbf{N}_{-mn}^{(1)}(k\mathbf{r}')\times\mathbf{N}_{mn}^{(3)}(k\mathbf{r}) & r<r'\end{cases} \tag{6-11}$$

从式(6-11)可以看出，实际上只有内接球内部和外接球外部的区域是格林函数的收敛区间。因此虽然扩展边界条件法可以求解任意形状目标的散射问题，但是对散射体内场电磁强度分布的预测方面有它的不足之处。

根据电磁散射问题边界条件的线性关系，我们可以在散射目标的入射场、散射场以及内场的展开系数之间建立如下的线性等式：

$$\begin{bmatrix}a_{nm}\\ b_{nm}\end{bmatrix}=Q\bullet\begin{bmatrix}f_{nm}\\ g_{nm}\end{bmatrix}\qquad\qquad\begin{bmatrix}c_{n,m}\\ d_{n,m}\end{bmatrix}=-RgQ\bullet\begin{bmatrix}f_{n,m}\\ g_{n,m}\end{bmatrix} \tag{6-12}$$

定义散射传输矩阵：

$$\begin{bmatrix}c_{n,m}\\ d_{n,m}\end{bmatrix}=T\bullet\begin{bmatrix}a_{n,m}\\ b_{n,m}\end{bmatrix} \tag{6-13}$$

其中：

$$T=-RgQ\bullet Q^{-1} \tag{6-14}$$

有：

$$Q=\begin{pmatrix}Q^{11} & Q^{12}\\ Q^{21} & Q^{22}\end{pmatrix}$$

$$Q^{(1,1)}=J^{(1,2)}+n_sJ^{(2,1)} \tag{6-15}$$

$$Q^{(1,2)}=J^{(2,2)}+n_sJ^{(1,1)} \tag{6-16}$$

$$Q^{(2,1)}=J^{(1,1)}+n_sJ^{(2,2)} \tag{6-17}$$

$$Q^{(2,2)}=J^{(2,1)}+n_sJ^{(1,2)} \tag{6-18}$$

而其中有：

$$J_{mn,m'n'}^{1,1}=(-1)^m\int_s\mathbf{M}_{m'n'}^{(1)}(k_s\mathbf{r})\times\mathbf{M}_{-mn}^{(3)}(k\mathbf{r})\bullet\hat{n}dS \tag{6-19}$$

$$J_{mn,m'n'}^{1,2}=(-1)^m\int_s\mathbf{M}_{m'n'}^{(1)}(k_s\mathbf{r})\times\mathbf{N}_{-mn}^{(3)}(k\mathbf{r})\bullet\hat{n}dS \tag{6-20}$$

$$J_{mn,m'n'}^{2,1}=(-1)^m\int_s\mathbf{M}_{m'n'}^{(1)}(k_s\mathbf{r})\times\mathbf{N}_{-mn}^{(3)}(k\mathbf{r})\bullet\hat{n}dS \tag{6-21}$$

$$J_{mn,m'n'}^{2,2}=(-1)^m\int_s\mathbf{N}_{m'n'}^{(1)}(k_s\mathbf{r})\times\mathbf{N}_{-mn}^{(3)}(k\mathbf{r})\bullet\hat{n}dS \tag{6-22}$$

利用同样的方法，将以上各式中的 $\mathbf{M}_{mn}^{(3)}$ 和 $\mathbf{N}_{mn}^{(3)}$ 分别替换成 $\mathbf{M}_{mn}^{(1)}$ 和 $\mathbf{N}_{mn}^{(1)}$，就可以得到 RgQ 的相应求解积分表达式。

如果散射目标的表面形状能够在球坐标系中用数学解析表达式表示出来，那么上面的积分式子就可以展开为：

$$J_{mn,m'n'}^{1,1}=(-1)^m\int_0^{2\pi}d\phi\int_0^{\pi}d\theta\mathbf{M}_{m'n'}^{(1)}\left(k_s\mathbf{r}(\theta,\phi)\right)\times\mathbf{M}_{-mn}^{(3)}\left(k\mathbf{r}(\theta,\phi)\right)\bullet\left[\frac{\partial\mathbf{r}}{\partial\theta}\times\frac{\partial\mathbf{r}}{\partial\phi}\right] \tag{6-23}$$

类似的我们可以得到J矩阵的其他式子。

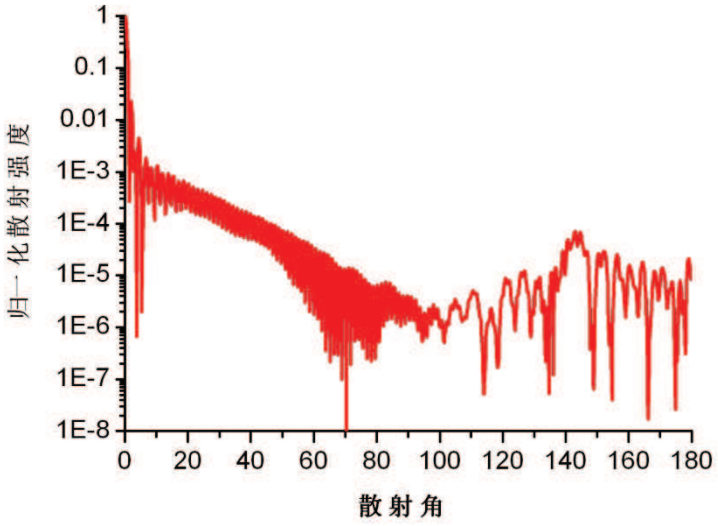

图6.3 扁椭球粒子（椭球率为0.97）的归一化强度角分布图，粒子的等面积尺寸参数为150

例如有一个以z轴为旋转对称轴的旋转椭球粒子，对应的半长轴用b表示，它在x轴和y轴上的半长轴为a，其直角坐标系下的方程为：

$$\frac{x^2+y^2}{a^2}+\frac{z^2}{b^2}=1 \tag{6-24}$$

定义椭球粒子的椭球率为 b/a。如果 $a>b$，我们习惯将之称为扁椭球，例如人体的血红细胞就可以用扁椭球模型来表征；如果 $a<b$，我们将之称为长椭球，例如人的脑袋模型。通过坐标转换，我们即可得到椭球粒子在相应球坐标系下的方程为：

$$r(\theta)=\left(\frac{\sin^2\theta}{a^2}+\frac{\cos^2\theta}{b^2}\right)^{-1/2} \tag{6-25}$$

很明显，从式(6-25)可以看出，由于椭球粒子沿z轴的旋转对称性使得积分式与方位角无关，这在数值计算中将大大加速传输矩阵的计算。如图6.3所示，我们给出了一个椭球率为0.97的扁椭球粒子的归一化强度角分布图，粒子的等面积尺寸参数为150。

对于旋转对称非球形粒子的散射计算，由于扩展边界条件法的运算速度较其他几种用于计算非规则粒子散射问题的数值方法，比如FDTD，DDA等，要快好几个量级，因此大量的应用文献都集中在研究这些具有旋转对称形状的目标方面。然而经过不断的改进，扩展边界法在计算非旋转对称目标散射问题上也得到了广泛的应用。下面就以立方体粒子为例，来说明扩展边界条件方法在求解非旋转对称目标散射问题上的应用和处理方法。

立方体粒子由6个相同的面组成，较旋转对称目标而言，它最大的特点就是各个面之间有一条突变边界，这使得求解传输矩阵过程中的J矩阵中关于方位角变量φ的积分式子不连续。对于这种情况，Kahnert等人[142]对用来处理这种突变边界情况的两种方法做了总结和比较，并且分析了特定情况下使用的优劣。Laitinen和Lumme[143]认为在任何散射问题中，所谓的突变边界只不过是局部附近的点在特定方向上的的曲率半径要远远小于特定的尺度，而这个特定尺度的大小依赖于散射粒子的实际尺寸参数，而没有必要硬性地认为这点的曲率半径为零。因此他将立方体的表面几何形状用以下这样一系列的连续的平滑函数来近似展开表示：

$$r(\theta,\varphi)\approx a_{00}+\sum_{l=1}^{l_{\max}}\sum_{k=0}^{l}a_{kl}d_{0k}^{l}(\theta)\cos(k\varphi) \tag{6-26}$$

从式(6-26)可以看出，由于立方体粒子的方位对称性，所以没有$\sin(k\varphi)$因子的出现。当$l_{\max}=0$时，它所表示的是一个标准的球形粒子；而随着$l_{\max}$的逐渐增大，这个式子继而不断趋向于立方体粒子的形状。利用这种思想，就可以避开传输矩阵积分中方位角参数不连续的问题。此处理方法可以扩展应用到计算任意星形粒子的散射问题上去。不同的是，Barber和Hill[113]，以及Mishchenko等人[59]则在各个不连续的角分区间分别使用高斯积分，使得积分式在各个分区间内连续性成立，最终完成总的积分，这个方法可以得到良好的收敛结果。

其实在涉及到立方体粒子散射问题之前，Mishchenko等人在用扩展边界条件方法计算有限圆柱体散射问题的时候就已经处理过这种偏微分不连续的情况，正如上述第二种方法，将高斯积分分别在$[0,\theta_0]$，$[\theta_0,\pi/2]$，$[\pi/2,\pi-\theta_0]$，$[\pi-\theta_0,\pi]$四个分区间上应用，从而形成一个整体的积分计算。而立方体的情况与有限圆柱体之间最大的不同点在于：φ角分别在0，90，180和270度上为极点，而θ角虽然仅有一个极点存在，但是这个极点的位置却依赖于相应的φ。因此必须将θ作为内部变量因子先进行积分，然后对相应的φ角进行积分。

如图6.4所示我们是用扩展边界条件计算一个立方体粒子平面波照射下的微分散射截面随散射角的特性曲线。微分散射截面的具体定义如式(6-68)所示。

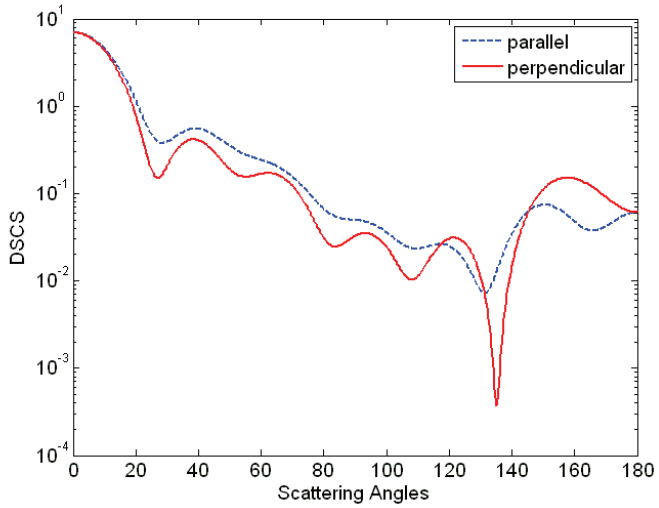

图6.4 立方体粒子在平面波照射下微分散射截面的角分布图。入射波波长为0.6283μm，粒子的边长大小为1μm

§6.2.3 各向异性介质目标的散射问题

从以上利用扩展边界条件法对各向同性介质目标散射问题的推导可以看出，为了建立散射场与入射场之间的传输矩阵，我们需要借助它们与粒子内场之间的线性关系，因此利用该方法求解散射问题首先需要对粒子的内场进行展开和表述。与各向同性介质目标不同的是，各向异性介质目标内场不能简单地用正则化的球矢量波函数展开。根据麦克斯韦方程，下面以磁化等离子体组成的散射体为例，我们给出了一组类球矢量波函数来对各向异性介质的内场进行波函数展开。

§ 6.2.3.1 各向异性目标内场的展开

电磁场在无源且均匀的等离子体中的传播满足以下麦克斯韦方程：

$$\begin{aligned} \nabla\times\mathbf{E} &= ik_0\mathbf{B} \qquad & \nabla\times\mathbf{H} &= -ik_0\mathbf{D} \\ \nabla\bullet\mathbf{B} &= 0 \qquad & \nabla\bullet\mathbf{B} &= 0 \end{aligned} \tag{6-27}$$

并且满足以下色散关系：

$$\mathbf{D} = \overline{\overline{\varepsilon}}\mathbf{E} \qquad \mathbf{B} = \overline{\overline{\mu}}\mathbf{H} \tag{6-28}$$

其中 $\overline{\overline{\varepsilon}}, \overline{\overline{\mu}}$ 是介电常数矩阵和磁导率矩阵。这里我们假定有一个沿z轴的外加磁场，那么磁化等离子体就有一个各向同性的介电常数 $\overline{\overline{\mu}}$ 和一个磁导率矩阵 $\overline{\overline{\varepsilon}}$，分别由以下所示：

$$\overline{\overline{\varepsilon}} = \begin{bmatrix} \varepsilon & i\varepsilon_g & 0 \\ -i\varepsilon_g & \varepsilon & 0 \\ 0 & 0 & \varepsilon_z \end{bmatrix} \qquad \overline{\overline{\mu}} = \mu \tag{6-29}$$

其中 $\varepsilon = 1 - \frac{w_p^2}{w^2 - w_e^2}$；$\varepsilon_g = -\frac{w_e}{w}\frac{w_p^2}{(w^2 - w_e^2)}$；$\varepsilon_z = 1 - \frac{w_p^2}{w^2}$；以及 w, w_e, w_p 分别为等离子体频率、等离子体旋转频率以及等离子体角频率。

从另一个角度来看，我们有另外一个色散关系：

$$\mathbf{E} = \overline{\overline{\kappa}} \bullet \mathbf{D} \qquad \mathbf{H} = \overline{\overline{\nu}} \bullet \mathbf{B} \tag{6-30}$$

其中：

$$\overline{\overline{\kappa}} = \begin{bmatrix} \kappa & i\kappa_g & 0 \\ -i\kappa_g & \kappa & 0 \\ 0 & 0 & \kappa_z \end{bmatrix} \quad ; \quad \overline{\overline{\nu}} = \mu^{-1} \tag{6-31}$$

磁导率矩阵 $\overline{\overline{\varepsilon}}$ 和这里的 $\overline{\overline{\kappa}}$ 存在以下关系：

$$\kappa = \frac{\varepsilon}{\varepsilon^2 - \varepsilon_g^2}; \quad \kappa_g = \frac{-\varepsilon_g}{\varepsilon^2 - \varepsilon_g^2}; \quad \kappa_z = \frac{1}{\varepsilon_z} \tag{6-32}$$

通过反傅里叶变换，电磁场分量可用平面波分量的积分形式表示：

$$\mathbf{X}(\mathbf{r}) = \int \mathbf{x}(\mathbf{k}) e^{i\mathbf{k}\bullet\mathbf{r}} dV(\mathbf{k}) \tag{6-33}$$

其中**X(r)**表示 E，H，D和B中的任意一个分量，X(k)则表示E，H，D，B相应的傅里叶变换分量，k是波数。利用以下的定义式：

$$\nabla \times \mathbf{X}(\mathbf{r}) = j\int k \times \mathbf{x}(\mathbf{k}) e^{j\mathbf{k}\bullet\mathbf{r}} dV(\mathbf{k}) \tag{6-34}$$

我们可以将麦克斯韦方程式子(6-27)以及色散关系式(6-30)变换为：

$$\mathbf{k} \times \mathbf{E} = k_0 \mathbf{B} \qquad \mathbf{k} \times \mathbf{H} = -k_0 \mathbf{D} \tag{6-35}$$

$$\mathbf{k} \bullet \mathbf{B} = 0 \qquad \mathbf{k} \bullet \mathbf{D} = 0 \tag{6-36}$$

$$\mathbf{E} = \overline{\overline{\kappa}} \mathbf{D} \qquad \mathbf{H} = \overline{\overline{\nu}} \mathbf{B} \tag{6-37}$$

我们把这个问题放到一个球坐标系中去考虑，对应的坐标分量为 $(\mathbf{e}_r, \mathbf{e}_\theta, \mathbf{e}_\varphi)$，其中波矢量 $\mathbf{k}$ 可以表示为 $\mathbf{k} = k \bullet \mathbf{e}_r$，用 $(\mathrm{A}_r, \mathrm{A}_\theta, \mathrm{A}_\varphi)$ 表示矢量 $A(r, \theta, \varphi)$ 的各个分量，我们可以将色散关系在直角坐标系和球坐标系中通过以下关系矩阵 $\Re$ 来实现相互转换：

$$\begin{pmatrix} A_x \\ A_y \\ A_z \end{pmatrix} = \begin{bmatrix} \cos\varphi\sin\theta & \cos\varphi\cos\theta & -\sin\varphi \\ \sin\varphi\sin\theta & \sin\varphi\cos\theta & \cos\varphi \\ \cos\theta & -\sin\theta & 0 \end{bmatrix} \begin{pmatrix} \mathrm{A}_r \\ \mathrm{A}_\theta \\ \mathrm{A}_\varphi \end{pmatrix} = \Re \begin{pmatrix} \mathrm{A}_r \\ \mathrm{A}_\theta \\ \mathrm{A}_\varphi \end{pmatrix} \tag{6-38}$$

在球坐标系中，式(6-35)和(6-36)转换为：

$$\begin{pmatrix} \mathrm{E}_\theta \\ \mathrm{E}_\varphi \end{pmatrix} = \mu(\frac{k_0}{k})^2 \begin{pmatrix} \mathrm{D}_\theta \\ \mathrm{D}_\varphi \end{pmatrix} \qquad \mathrm{D}_r = 0 \tag{6-39}$$

式(6-37)为：

$$\begin{pmatrix} \mathrm{E}_r \\ \mathrm{E}_\theta \\ \mathrm{E}_\varphi \end{pmatrix} = \begin{bmatrix} \lambda_{r\theta} & \lambda_{r\varphi} \\ \lambda_{\theta\theta} & \lambda_{\theta\varphi} \\ \lambda_{\alpha\theta} & \lambda_{\varphi\varphi} \end{bmatrix} \begin{pmatrix} \mathrm{D}_\theta \\ \mathrm{D}_\varphi \end{pmatrix} \tag{6-40}$$

其中有：

$$\overline{\overline{\kappa}}_k = \Re^T \overline{\overline{\kappa}} \Re = \begin{bmatrix} \kappa\sin^2\theta + \kappa_z\cos^2\theta & (\kappa-\kappa_z)\sin\theta\cos\theta & i\kappa_g\sin\theta \\ (\kappa-\kappa_z)\sin\theta\cos\theta & \kappa\cos^2\theta + \kappa_z\sin^2\theta & i\kappa_g\cos\theta \\ -i\kappa_g\sin\theta & -i\kappa_g\cos\theta & \kappa \end{bmatrix} = \begin{bmatrix} \lambda_{rr} & \lambda_{r\theta} & \lambda_{r\varphi} \\ \lambda_{\theta r} & \lambda_{\theta\theta} & \lambda_{\theta\varphi} \\ \lambda_{\varphi r} & \lambda_{\varphi\theta} & \lambda_{\varphi\varphi} \end{bmatrix} = \overline{\overline{\lambda}}$$

式(6-39)和(6-40)构成了均匀介质中D_θ和D_φ的特征方程:

$$\begin{bmatrix} \lambda_{\theta\theta}-\lambda & \lambda_{\theta\varphi} \\ \lambda_{\varphi\theta} & \lambda_{\varphi\varphi}-\lambda \end{bmatrix} \begin{pmatrix} \mathrm{D}_\theta \\ \mathrm{D}_\varphi \end{pmatrix} = 0 \qquad \lambda = \mu(\frac{k_0}{k})^2 \tag{6-41}$$

通过求解以上特征方程，我们可以得到两个特征值$k_{1,2}$以及对应的特征向量$\mathbf{V}_{1,2}$：

$$\mathbf{V}_1 = f\hat{e}_\theta + \hat{e}_\varphi \qquad \mathbf{V}_2 = (\hat{e}_\theta + f\hat{e}_\varphi) \tag{6-42}$$

$$k_{1,2} = k_0\sqrt{\mu/\lambda_{1,2}} \qquad \lambda_{1,2} = \frac{1}{2}(\lambda_{\theta\theta}+\lambda_{\varphi\varphi} \pm D) \tag{6-43}$$

$$D = \sqrt{(\lambda_{\theta\theta}-\lambda_{\varphi\varphi})^2 - 4\lambda_{\theta\varphi}^2} \qquad f = -2\lambda_{\theta\varphi}/(\lambda_{\theta\theta}-\lambda_{\varphi\varphi}-D) \tag{6-44}$$

对于一个磁化等离子体，我们有：

$$D = \sqrt{(\lambda_{\theta\theta}-\lambda_{\varphi\varphi})^2 - 4\lambda_{\theta\varphi}^2} = \sqrt{(\kappa-\kappa_z)^2\sin^4\theta + 4\kappa_g^2\cos^2\theta} \tag{6-45}$$

对于$D>0$，我们有$\lambda_1 \neq \lambda_2$，因此两个特征向量是不相关的。特征方程(6-41)的任意一个特征解都可以表示成以上两个特征向量的线性叠加。我们将电位移矢量在一个球面上用两个未知的标量函数的积分形式展开得到：

$$\mathbf{D(r)} = \int_\Omega \left[\mathrm{D}_1(\theta,\varphi)\mathbf{V}_1(\mathbf{e}_r,\mathbf{e}_\theta,\mathbf{e}_\varphi)e^{ik_1\mathbf{e}_r\cdot\mathbf{r}} + \mathrm{D}_2(\theta,\varphi)\mathbf{V_2}(\mathbf{e}_r,\mathbf{e}_\theta,\mathbf{e}_\varphi)e^{ik_2\mathbf{e}_r\cdot\mathbf{r}} \right] d\Omega \tag{6-46}$$

其中D_1，D_2是以θ和φ为变量的待解的两个标量函数。

为了能够描述散射体内部电磁场分量分布的数学表达展开式，我们引入矢量球谐函数，为了数值计算的简便，我们定义为：

$$\begin{aligned}\mathbf{m_{mn}}(\theta,\varphi)&=[im\pi_n^{|m|}(\theta)\mathbf{e}_\theta-\tau_n^{|m|}(\theta)\mathbf{e}_\varphi]e^{im\varphi}\\ \mathbf{n_{mn}}(\theta,\varphi)&=[\tau_n^{|m|}(\theta)\mathbf{e}_\theta+im\pi_n^{|m|}(\theta)\mathbf{e}_\varphi]e^{im\varphi}\\ \mathbf{p_{mn}}(\theta,\varphi)&=P_n^{|m|}e^{im\varphi}\mathbf{e}_r\end{aligned}\tag{6-47}$$

其中 $(\mathbf{e}_r,\mathbf{e}_\theta,\mathbf{e}_\varphi)$ 是位置矢量 $\mathbf{r}$ 的球坐标系分量， $\pi_n^{|m|}(\theta),\tau_n^{|m|}(\theta)$ 为角函数，可以用连带Legendre函数表示为：

$$\pi_n^{|m|}(\theta)=\frac{P_n^m(\cos\theta)}{\sin\theta}\qquad\tau_n^{|m|}(\theta)=\frac{d}{d\theta}P_n^m(\cos\theta)\tag{6-48}$$

由于球矢量波函数的正交性，我们可以将任意电磁场展开成矢量球谐函数的级数展开。并且从式(6-39)可以看出问题中 D_r 分量为零，因此 $\mathbf{p_{mn}}$ 将在下面的分析中略去。其他两个切向分量满足以下关系式：

$$\mathbf{e}_r\times\mathbf{m}_{mn}=\mathbf{n}_{mn}\qquad\mathbf{e}_r\times\mathbf{n}_{mn}=-\mathbf{m}_{mn}\tag{6-49}$$

因此电矢量位移可以展开为：

$$\mathrm{D}_1(\theta,\varphi)\mathbf{V}_1(\theta,\varphi)+\mathrm{D}_2(\theta,\varphi)\mathbf{V_2}(\theta,\varphi)=-\varepsilon\sum_{n=1}^{\infty}\sum_{m=-n}^{n}\frac{1}{4\pi i^{n+1}}[-ic_{mn}\mathbf{m_{mn}}(\theta,\varphi)+d_{mn}\mathbf{n_{mn}}(\theta,\varphi)]\tag{6-50}$$

经过一些简单直接的数学运算，我们可以得到：

$$\begin{aligned}\mathrm{D}_1&=-\varepsilon\left(\frac{1}{1-f^2}\right)\sum_{n=1}^{\infty}\sum_{m=-n}^{n}\frac{1}{4\pi i^{n+1}}\{c_{mn}[m\tau_n^{|m|}(\theta)(-f)+i\tau_n^{|m|}(\theta)]+d_{mn}[\tau_n^{|m|}(\theta)(-f)+im\pi_n^{|m|}(\theta)]\}e^{im\varphi}\\ \mathrm{D}_2&=-\varepsilon\left(\frac{1}{1-f^2}\right)\sum_{n=1}^{\infty}\sum_{m=-n}^{n}\frac{1}{4\pi i^{n+1}}\{c_{mn}[m\pi_n^{|m|}(\theta)+i\tau_n^{|m|}(\theta)(-f)]+d_{mn}[\tau_n^{|m|}(\theta)+im\pi_n^{|m|}(\theta)(-f)]\}e^{im\varphi}\end{aligned}\tag{6-51}$$

考虑到(6-40)以及(6-46)-(6-51),我们可以得到散射体内部电磁场分量的准球谐函数展开式：

$$\begin{aligned}\mathbf{E}(\mathbf{r})&=\sum_{n=1}^{\infty}\sum_{m=-n}^{n}[c_{mn}\mathbf{X}_{mn}^e(\mathbf{r})+d_{mn}\mathbf{Y}_{mn}^e(\mathbf{r})]\\ \mathbf{H}(\mathbf{r})&=-j\sqrt{\frac{\varepsilon}{\mu}}\sum_{n=1}^{\infty}\sum_{m=-n}^{n}[c_{mn}\mathbf{X}_{mn}^h(\mathbf{r})+d_{mn}\mathbf{Y}_{mn}^h(\mathbf{r})]\end{aligned}\tag{6-52}$$

其中 $\mathbf{X}_{mn}^{e,h}$， $\mathbf{Y}_{mn}^{e,h}$ 为新推导的准球谐函数：

$$\begin{aligned}\mathbf{X}_{mn}^{e,h}(\mathbf{r})&=\int_\Omega\left(-\frac{1}{1-f^2}\right)[A_{mn}\mathbf{w}_1^{e,h}e^{ik_1\mathbf{e}_r\cdot\mathbf{r}}+B_{mn}\mathbf{w}_2^{e,h}e^{ik_2\mathbf{e}_r\cdot\mathbf{r}}]dS(\Omega)\\ \mathbf{Y}_{mn}^{e,h}(\mathbf{r})&=\int_\Omega\left(-\frac{1}{1-f^2}\right)[A'_{mn}\mathbf{w}_1^{e,h}e^{ik_1\mathbf{e}_r\cdot\mathbf{r}}+B'_{mn}\mathbf{w}_2^{e,h}e^{ik_2\mathbf{e}_r\cdot\mathbf{r}}]dS(\Omega)\end{aligned}\tag{6-53}$$

$$A_{mn} = m\pi_n^{|m|}(\theta)(-f) + i\tau_n^{|m|}(\theta) \qquad A'_{mn} = im\pi_n^{|m|}(\theta)(-f) + \tau_n^{|m|}(\theta) \tag{6-54}$$

$$B_{mn} = m\pi_n^{|m|}(\theta) + i\tau_n^{|m|}(\theta)(-f) \qquad B'_{mn} = im\pi_n^{|m|}(\theta) + \tau_n^{|m|}(\theta)(-f) \tag{6-55}$$

$$\begin{aligned} \mathbf{w}_1^e &= \varepsilon\left\{[(\lambda_{r\theta}f + \lambda_{r\varphi})]\mathbf{e}_r + \lambda_1 \bullet \mathbf{v}_1\right\} \qquad \mathbf{w}_1^h = \sqrt{\lambda_1\varepsilon}(f\hat{e}_\varphi - \hat{e}_\theta) \\ \mathbf{w}_2^e &= \varepsilon\left\{[(\lambda_{r\theta} + \lambda_{r\varphi}f)]\mathbf{e}_r + \lambda_2 \bullet \mathbf{v}_2\right\} \qquad \mathbf{w}_2^h = \sqrt{\lambda_2\varepsilon}(\hat{e}_\varphi - f\hat{e}_\theta) \end{aligned} \tag{6-56}$$

从上面的推导可以看出，这些表达式可以看成单轴各向异性介质电磁场分量的补充。通过将磁导率矩阵中的非对角线元素设置为零，我们可以得到单轴各向异性介质的表达式。

$$k_g = 0 \to \lambda_{\theta\varphi} = \lambda_{\varphi\theta} = 0 \;\rightarrow\; f = 0 \;\rightarrow\; \mathbf{V}_1 = \hat{e}_\alpha, \mathbf{V}_2 = \hat{e}_\beta \tag{6-57}$$

因此我们得到：

$$\begin{aligned} \mathrm{D}_2 = \mathrm{D}_\theta &= -\varepsilon\sum_{n=1}^{\infty}\sum_{m=-n}^{n}\frac{1}{4\pi i^{n+1}}[c_{mn}m\pi_n^{|m|}(\theta) + d_{mn}\tau_n^{|m|}(\theta)]e^{im\varphi} \\ \mathrm{D}_1 = \mathrm{D}_\varphi &= -\varepsilon\sum_{n=1}^{\infty}\sum_{m=-n}^{n}\frac{1}{4\pi i^{n+1}}j[c_{mn}\tau_n^{|m|}(\theta) + d_{mn}m\pi_n^{|m|}(\theta)]e^{im\varphi} \end{aligned} \tag{6-58}$$

以上表达式和文献[60]中给出的单轴各向异性介质表达式完全一样，从而也支持了我们推导的正确性。

§6.2.3.2 扩展边界条件法求解

结合上面内场的表达式，以下我们将用扩展边界条件法来求解磁化等离子体各向异性目标的散射问题。粒子表面用S表示，它将散射体分成内部区域 D_{int} 和外部区域 D_{ext}。自由空间中的介电常数和电导率分别为 ε_0 和 μ_0。

首先，我们可将入射场和散射场用矢量球谐函数展开成以下级数：

$$\mathbf{E}_{inc}(\mathbf{r}) = \sum_{n=1}^{\infty}\sum_{m=-n}^{n}[f_{mn}\mathbf{M}_{mn}^{(1)}(k_s\mathbf{r}) + g_{mn}\mathbf{N}_{mn}^{(1)}(k_s\mathbf{r})] \tag{6-59}$$

$$\mathbf{E}_{sca}(\mathbf{r}) = \sum_{n=1}^{\infty}\sum_{m=-n}^{n}[a_{mn}\mathbf{M}_{mn}^{(3)}(k_s\mathbf{r}) + b_{mn}\mathbf{N}_{mn}^{(3)}(k_s\mathbf{r})] \tag{6-60}$$

其中 $k_s = k_0\sqrt{\varepsilon_s\mu_s}$ 为周围各向同性介质的波数。$a_{mn}, b_{mn}, f_{mn}, g_{mn}$ 分别为入射场和散射场的展开系数。

在散射目标表面应用电磁场的边界条件：

$$\begin{aligned} \hat{\mathbf{n}}\times\mathbf{E}_{inc} - \hat{\mathbf{n}}\times\mathbf{E}_{sca} &= \hat{\mathbf{n}}\times\mathbf{E}_{\text{int}} \\ \hat{\mathbf{n}}\times\mathbf{H}_{inc} - \hat{\mathbf{n}}\times\mathbf{H}_{sca} &= \hat{\mathbf{n}}\times\mathbf{H}_{\text{int}} \end{aligned} \tag{6-61}$$

即可得到入射场和散射场之间的传输矩阵：

$$\begin{bmatrix} f_{mn} \\ g_{mn} \end{bmatrix} = T \begin{bmatrix} a_{mn} \\ b_{mn} \end{bmatrix} \tag{6-62}$$

$$T = -Q_{gyro}^{11}(Q_{gyro}^{31})^{-1} \tag{6-63}$$

其中 Q_{gyro}^{31} 矩阵在 $\mu = \mu_s = \mu_0$ 时为：

$$Q_{gyro}^{31} = \begin{pmatrix} P_{mnm'n'}^3 & R_{mnm'n'}^3 \\ S_{mnm'n'}^3 & U_{mnm'n'}^3 \end{pmatrix} \tag{6-64}$$

$$\begin{pmatrix} P_{mnm'n'}^3 \\ R_{mnm'n'}^3 \\ S_{mnm'n'}^3 \\ U_{mnm'n'}^3 \end{pmatrix} = \begin{pmatrix} i\frac{k_s^2}{\pi}\int_s (\hat{\mathbf{n}}\times\mathbf{X}_{m'n'}^e)\bullet\mathbf{N}_{mn}^{(3)} + \sqrt{\frac{\varepsilon}{\varepsilon_s}}(\hat{\mathbf{n}}\times\mathbf{X}_{m'n'}^h)\bullet\mathbf{M}_{mn}^{(3)}dS \\ i\frac{k_s^2}{\pi}\int_s (\hat{\mathbf{n}}\times\mathbf{Y}_{m'n'}^e)\bullet\mathbf{N}_{mn}^{(3)} + \sqrt{\frac{\varepsilon}{\varepsilon_s}}(\hat{\mathbf{n}}\times\mathbf{Y}_{m'n'}^h)\bullet\mathbf{M}_{mn}^{(3)}dS \\ i\frac{k_s^2}{\pi}\int_s (\hat{\mathbf{n}}\times\mathbf{X}_{m'n'}^e)\bullet\mathbf{M}_{mn}^{(3)} + \sqrt{\frac{\varepsilon}{\varepsilon_s}}(\hat{\mathbf{n}}\times\mathbf{X}_{m'n'}^h)\bullet\mathbf{N}_{mn}^{(3)}dS \\ i\frac{k_s^2}{\pi}\int_s (\hat{\mathbf{n}}\times\mathbf{Y}_{m'n'}^e)\bullet\mathbf{M}_{mn}^{(3)} + \sqrt{\frac{\varepsilon}{\varepsilon_s}}(\hat{\mathbf{n}}\times\mathbf{Y}_{m'n'}^h)\bullet\mathbf{N}_{mn}^{(3)}dS \end{pmatrix} \tag{6-65}$$

Q_{gyro}^{11} 矩阵可以直接将 Q_{gyro}^{31} 中的 $\mathbf{M}_{mn}^{(3)}$ 和 $\mathbf{N}_{mn}^{(3)}$ 分别替换成 $\mathbf{M}_{mn}^{(1)}$ 和 $\mathbf{N}_{mn}^{(1)}$ 来得到。

在远场条件下 我们可以得到 $\mathbf{M}_{mn}(k_s\mathbf{r})$ 和 $\mathbf{N}_{mn}(k_s\mathbf{r})$ 的近似表达式：

$$\begin{aligned} \mathbf{M}_{mn}^{(3)}(k_s\mathbf{r}) &= \frac{\exp(ikr)}{kr}\{(-i)^{n+1}\mathbf{m}_{mn}(\theta,\varphi) + O(\frac{1}{r})\} \\ \mathbf{N}_{mn}^{(3)}(k_s\mathbf{r}) &= \frac{\exp(ikr)}{kr}\{(-i)^{n}\mathbf{n}_{mn}(\theta,\varphi) + O(\frac{1}{r})\} \end{aligned} \tag{6-66}$$

将式(6-66)代入式(6-59)我们可以得到：

$$\lim_{r\to\infty}\mathbf{E}_s(\mathbf{r}) == \frac{\exp(ik_s r)}{k_s r}[E_{s\theta}\hat{\theta} + E_{s\varphi}\hat{\varphi}] \tag{6-67}$$

其中 $E_{s\theta}$ 和 $E_{s\varphi}$ 为电场分量在远区场的切向分量。

另外在雷达遥感中，我们最感兴趣的一个参量是雷达散射截面，定义为：

$$\sigma_{RCS} = \lim_{r\to\infty} 4\pi r^2 \frac{|E_{sca}|^2}{|E_{inc}|^2} = \frac{4\pi}{k_s^2}\left\{\frac{|E_{s\theta}|^2}{|E_{inc}|^2} + \frac{|E_{s\varphi}|^2}{|E_{inc}|^2}\right\} \tag{6-68}$$

§6.2.3.3 数值结果

根据前面相应的理论推导，我们用FORTRAN语言对散射问题实现了编程求解。假设入射波是一个沿z轴传播的平面波，其电矢量沿x轴方向极化。

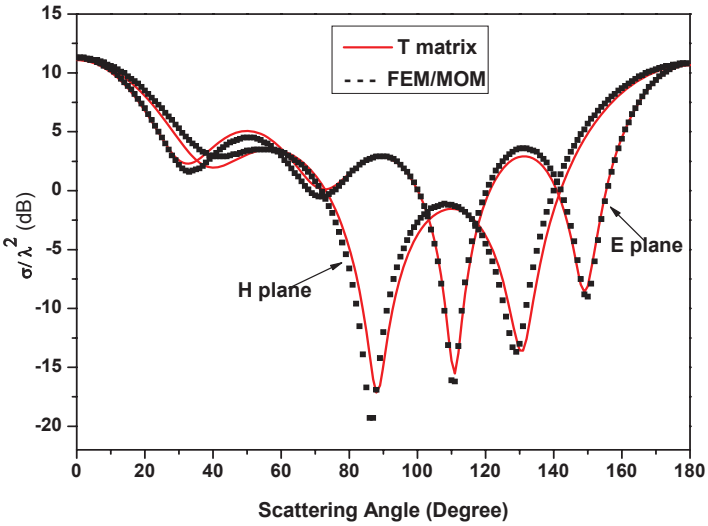

图6.5 雷达散射截面(RCSs)随散射角 θ 的变化.实线为EBCM方法计算结果，虚线为FEM/MoM混合方法计算结果。磁化等离子体的计算参数分别为 $k_0 r=\pi$， $\varepsilon=5.3495\varepsilon_0$，$\varepsilon_z=7.0\varepsilon_0$。

首先，为了验证程序，我们设置 $\varepsilon_g=0$，小球的尺寸参数为 $k_0 r=\pi$，其它介电常数分布为 $\varepsilon=5.3495\varepsilon_0$， $\varepsilon_z=7.0\varepsilon_0$。在这种情况下，我们已经将散射体的材料从磁化等离子体退化成单轴介质。将本论文所得的雷达散射截面结果与Doicu专著中所提供的程序[60]进行对比，所得结果完全吻合。

另外，我们还将本论文所得结果与有限元/矩量(FEM/MoM)混合方法所得结果进行比较，所得结果如图6.5所示。在图6.5中，我们分别用EBCM方法和有限元/矩量(FEM/MoM)混合方法计算了磁化等离子体球的雷达散射截面(RCSs)。磁化等离子体球的参数分别为 $k_0 r=0.5$， $\varepsilon=5\varepsilon_0$， $\varepsilon_g=-\varepsilon_0$， $\varepsilon_z=7\varepsilon_0$。从图中可以看出，两者结果符合的很好，从而进一步表明了以上理论推导及所编写程序的正确性。

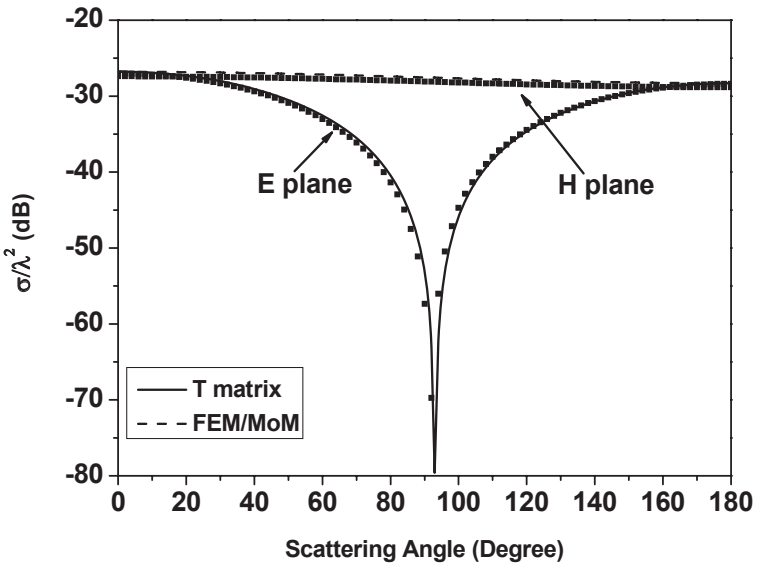

图6.6 雷达散射截面(RCSs)随散射角 θ 的变化。实线为EBCM方法计算结果，虚线为FEM/MoM混合方法计算结果。磁化等离子体的计算参数分别为 $k_0 r = 0.5$，$\varepsilon = 5\varepsilon_0$，$\varepsilon_g = -\varepsilon_0$，$\varepsilon_z = 7\varepsilon_0$

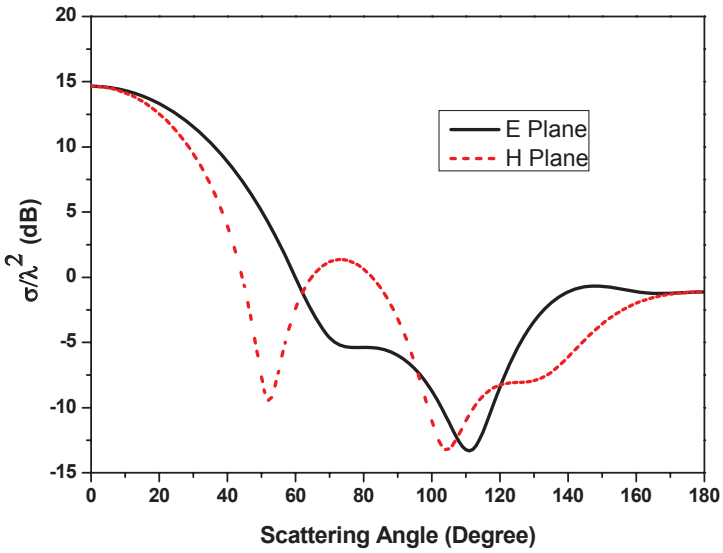

图6.7 雷达散射截面 (RCSs) 随散射角 θ 的变化。实线为E-plane计算结果，H-plane计算结果。磁化等离子体的计算参数分别为 $k_0 r = \pi$， $\varepsilon = 5.3495\varepsilon_0$， $\varepsilon_g = -2\varepsilon_0$， $\varepsilon_z = 7\varepsilon_0$

在图6.6中，我们用EBCM方法计算了磁化等离子体球的雷达散射截面(RCSs)的又一个算例。磁化等离子体球的参数分别为 $\varepsilon = 5\varepsilon_0$， $k_0 r = \pi$， $\varepsilon = 5.3495\varepsilon_0$，$\varepsilon_g = -2\varepsilon_0$， $\varepsilon_z = 7\varepsilon_0$。比较算例2中的参数，算例6.7中的尺寸参数要大的多。

§6.3 多目标体系的散射问题

扩展边界条件法之所以能在非规则形状目标的电磁散射问题的研究中获得广泛的应用，其中一个重要原因是由于传输矩阵的计算只依赖于目标本身的性质，包括粒子大小、形状、方向、组成成分等，而与入射场的性质无关。因此对于求解一个散射单体的电磁散射问题，我们只需要计算一次传输矩阵，就可以重复用来计算散射体的各种散射特性。这个优点在光镊实验中对于非规则粒子的捕获力及扭矩的数值仿真中得到很好的体现，因为只需要计算一次粒子散射的传输矩阵，就可以计算出粒子位于光镊中各个不同空间位置处所受到的捕获力和扭矩的大小，为实际实验操作和改进提供重要的理论依据。另一方面，由于扩展边界条件法是一种解析和数值方法相结合的电磁求解方法，其潜在的解析运算能力可以大大提高数值计算效率，为电磁散射问题求解中提供很好的辅助作用，该优势在对具有旋转对称形状的单体散射问题的求解上已经得到了很好的体现。在实际测量中，除了对单体散射的研究之外，我们还经常需要对多粒子体系进行探测，下面采用单次散射模型，推导了空间取向随机任意的多粒子的散射问题的扩展边界条件法的求解过程。

Mishchenko等人[67]将扩展边界条件法应用于取向随机的一群不相关粒子的散射问题上，推导了适用于旋转对称粒子群的散射表达式，并且还给出了相应的程序，大大推动了该方法在多粒子体系散射问题上的应用。Skaropoulos等人[69]也对旋转对称的多粒子散射体系进行了系统推导，通过将散射矩阵的解析表达式用一般球谐函数的级数来展开，加速了传输矩阵的求解，并重点研究了具有特定偏向的一群粒子对平面波的散射情况。这里我们基于前一节扩展边界条件法对单体散射问题的求解，推导了应用于随机取向的粒子群对平面波的散射。

A．单个粒子的散射矩阵

假设入射平面波的入射角度为 (θ,φ)，那么入射面为 z 轴与入射方向 $\hat{n}$ 所组成的平面。

$$\mathbf{E}_i(\mathbf{r})=(E_\theta^i\hat{\theta}_i+E_\varphi^i\hat{\varphi}_i)\exp(i\mathbf{k}_i\bullet\mathbf{r}) \tag{6-69}$$

在远区场，散射场退化成横波，其数学表达式为：

$$\mathbf{E}_s(\mathbf{r})=E_\theta^s\hat{\theta}_s+E_\varphi^s\hat{\varphi}_s \tag{6-70}$$

那么散射矩阵可以定义为：

$$\begin{pmatrix}E_\theta^s\\E_\varphi^s\end{pmatrix}=\frac{\exp(ikr)}{r}S(\hat{n}_s,\hat{n}_i)\begin{pmatrix}E_\theta^i\\E_\varphi^i\end{pmatrix} \tag{6-71}$$

其中散射矩阵 $S(\hat{n}_s,\hat{n}_i)$ 的值取决于散射粒子的特性，包括大小、形状、组成成分以及粒子空间取向。

除了像上面一样使用线性极化基来表示外，我们还可以用一组圆极化基来表示：

$$E_{+1}=\frac{1}{\sqrt{2}}(E_\theta+iE_\varphi),\qquad E_{-1}=\frac{1}{\sqrt{2}}(E_\theta-iE_\varphi) \tag{6-72}$$

$$\begin{pmatrix}E_{+1}\\E_{-1}\end{pmatrix}=\mathbf{P}\begin{pmatrix}E_\theta\\E_\varphi\end{pmatrix},\qquad \mathbf{P}=\frac{1}{\sqrt{2}}\begin{bmatrix}1 & i\\1 & -i\end{bmatrix} \tag{6-73}$$

那么单个粒子的散射矩阵可用圆极化基表示为：

$$\begin{aligned}\mathbf{C}(\hat{n}_s,\hat{n}_i)&=\mathbf{P}\mathbf{S}(\hat{n}_s;\hat{n}_i)\mathbf{P}^{-1}=\begin{bmatrix}C_{+1+1} & C_{+1-1}\\C_{-1+1} & C_{-1-1}\end{bmatrix}\\&=\begin{bmatrix}S_{11}-iS_{12}+iS_{21}+S_{22} & S_{11}+iS_{12}+iS_{21}-S_{22}\\S_{11}-iS_{12}-iS_{21}-S_{22} & S_{11}+iS_{12}-iS_{21}+S_{22}\end{bmatrix}\end{aligned} \tag{6-74}$$

B．单个粒子的米勒矩阵

单个粒子的米勒矩阵用线性极化基表示为：

$$\mathbf{I}_S^{sca}=\frac{1}{r^2}Z^S(\hat{n}_s,\hat{n}_i,\alpha,\beta,\gamma)\mathbf{I}_S^{inc} \tag{6-75}$$

其中 $\mathbf{I}_s,\mathbf{I}_i$ 分别为入射场和散射场的斯托克斯参数 $\mathbf{I}=[I\ \ Q\ \ U\ \ V]^T$：

$$I=E_\theta E_\theta^*+E_\varphi E_\varphi^*\qquad Q=E_\theta E_\theta^*-E_\varphi E_\varphi^* \tag{6-76}$$

$$U=-E_\theta E_\varphi^*-E_\varphi E_\theta^*\qquad V=i(E_\varphi E_\theta^*-E_\theta E_\varphi^*) \tag{6-77}$$

其中T表示转置，而*表示取共轭。

单个粒子的米勒矩阵用圆极化基表示为：

$$\mathbf{I}_C^{sca}=\frac{1}{r^2}Z^C(\hat{n}_s,\hat{n}_i,\alpha,\beta,\gamma)\mathbf{I}_C^{inc} \tag{6-78}$$

$$Z^C(\hat{n}_s,\hat{n}_i,\alpha,\beta,\gamma)=\begin{bmatrix}C_{-1-1}C_{+1+1}^* & C_{-1+1}C_{+1+1}^* & C_{-1-1}C_{+1-1}^* & C_{-1+1}C_{+1-1}^*\\C_{+1-1}C_{+1+1}^* & C_{+1+1}C_{+1+1}^* & C_{+1-1}C_{+1-1}^* & C_{+1+1}C_{+1-1}^*\\C_{-1-1}C_{-1+1}^* & C_{-1+1}C_{-1+1}^* & C_{-1-1}C_{-1-1}^* & C_{-1+1}C_{-1-1}^*\\C_{+1-1}C_{-1+1}^* & C_{+1+1}C_{-1+1}^* & C_{+1-1}C_{-1-1}^* & C_{+1+1}C_{-1-1}^*\end{bmatrix} \tag{6-79}$$

其中 $\mathbf{I}_C^{sca},\mathbf{I}_C^{inc}$ 分别为入射场和散射场的斯托克斯参数 $\mathbf{I}_C=[I_2\ \ I_0\ \ I_{-0}\ \ I_{-2}]^T$：

$$I_2=E_{-1}E_{+1}^*=(Q+iU)/2\qquad I_0=E_{+1}E_{+1}^*=(I+V)/2 \tag{6-80}$$

$$I_{-0}=E_{-1}E_{-1}^*=(I-V)/2\qquad I_{-2}=E_{+1}E_{-1}^*=(Q-iU)/2 \tag{6-81}$$

以上两种表示方式之间有以下转换关系式：

$$Z^S(\hat{n}_s;\hat{n}_i)=\mathbf{A}^{-1}Z^C(\hat{n}_s,\hat{n}_i)\mathbf{A} \tag{6-82}$$

其中有：

$$\mathbf{A}=\frac{1}{2}\begin{bmatrix}0&1&i&0\\1&0&0&1\\1&0&0&-1\\0&1&-i&0\end{bmatrix}\qquad \mathbf{A}^{-1}=\begin{bmatrix}0&1&1&0\\1&0&0&1\\-i&0&0&i\\0&1&-1&0\end{bmatrix} \tag{6-83}$$

C．多粒子群的米勒矩阵

对于一个微小体元中取向随机任意的粒子群，其米勒矩阵等于所有粒子的矩阵平均值的总和：

$$\mathbf{Z}(\hat{n}_s;\hat{n}_i)=N<\mathbf{Z}(\hat{n}_s;\hat{n}_i;\alpha,\beta,\gamma)> \tag{6-84}$$

$$\begin{aligned}<\mathbf{Z}(\hat{n}_s;\hat{n}_i;\alpha,\beta,\gamma)>=&\int_0^{2\pi}d\alpha\int_0^{\pi}\sin\beta d\beta\int_0^{2\pi}d\gamma\\&\times\mathbf{Z}(\hat{n}_s;\hat{n}_i;\alpha,\beta,\gamma)p(\alpha,\beta,\gamma)\end{aligned} \tag{6-85}$$

其中 $p(\alpha,\beta,\gamma)$ 是群粒子的取向随机分布函数，它们有以下的归一化等式：

$$\int_0^{2\pi}d\alpha\int_0^{\pi}\sin\beta d\beta\int_0^{2\pi}d\gamma p(\alpha,\beta,\gamma)=1 \tag{6-86}$$

D．粒子群的散射矩阵

多粒子体系散射的散射矩阵是通过其米勒矩阵来定义的：

$$F(\theta_s)=\frac{4\pi}{C_{sca}}<\mathbf{Z}(\theta_s;0,0,0)> \tag{6-87}$$

其中 C_{sca} 为微分散射系数：

$$C_{sca}=2\pi\int_0^{\pi}\sin\theta_s d\theta<Z_{11}(\theta_s;0,0,0)> \tag{6-88}$$

$Z_{11}(\theta_s;0,0,0)$ 为米勒矩阵的第一个元素且满足以下归一化条件：

$$\frac{1}{2}\int_0^{\pi}\sin\theta_s d\theta F_{11}(\theta_s)=1 \tag{6-89}$$

我们需要注意的是，这里的散射矩阵是定义在散射平面上的。需要通过以下转换关系将其转换到全局坐标系中：

$$<\mathbf{Z}(\hat{n}_s;\hat{n}_i;\alpha,\beta,\gamma)>=\frac{C_{sca}}{4\pi}L(\pi-\sigma_2)F(\theta_s)L(-\sigma_1) \tag{6-90}$$

其中：

$$L(\theta)=\begin{bmatrix}1 & 0 & 0 & 0\\ 0 & \cos 2\theta & \sin 2\theta & 0\\ 0 & -\sin 2\theta & \cos 2\theta & 0\\ 0 & 0 & 0 & 1\end{bmatrix} \tag{6-91}$$

对于一群微观上取向随机任意，宏观上具有镜面对称的粒子，其散射矩阵矩阵具有以下表达形式：

$$F(\theta)=\begin{bmatrix}a_1 & b_1 & 0 & 0\\ b_1 & a_2 & 0 & 0\\ 0 & 0 & a_3 & b_2\\ 0 & 0 & -b_2 & a_4\end{bmatrix} \tag{6-92}$$

$$F^C(\theta)=\frac{1}{2}\begin{bmatrix}a_2+a_3 & b_1+ib_2 & b_1-ib_2 & a_2-a_3\\ b_1+ib_2 & a_1+a_4 & a_1-a_4 & b_1-ib_2\\ b_1-ib_2 & a_1-a_4 & a_1+a_4 & b_1+ib_2\\ a_2-a_3 & b_1-ib_2 & b_1+ib_2 & a_2+a_3\end{bmatrix} \tag{6-93}$$

由于通过圆极化基表示的散射矩阵中的元素可以展开成一般球谐函数的级数表示：

$$F_{kl}^C(\theta_S^{sca})=\sum_{s=\max(|k|,|l|)}^{\infty} g_{kl}^s P_{kl}^s(\cos\theta_S^{sca}) \tag{6-94}$$

其中 $P_{kl}^s(\cos\theta)$ 一般性球谐函数。

其展开系数由积分等式求得：

$$g_{kl}^s=\frac{2s+1}{2}\int_{-1}^{1} d(\cos\theta_S^{sca})F_{kl}^C(\theta_S^{sca})P_{kl}^s(\cos\theta_S^{sca}) \tag{6-95}$$

那么相应于线性基表示下的散射矩阵中的元素，我们有：

$$a_1(\theta)=\sum_{s=0}^{\infty} a_1^s P_{00}^s(\cos\theta) \tag{6-96}$$

$$a_2(\theta)+a_3(\theta)=\sum_{s=2}^{\infty}(a_2^s+a_3^s)P_{22}^s(\cos\theta) \tag{6-97}$$

$$a_2(\theta)-a_3(\theta)=\sum_{s=2}^{\infty}(a_2^s-a_3^s)P_{2-2}^s(\cos\theta) \tag{6-98}$$

$$a_4(\theta)=\sum_{s=0}^{\infty} a_4^s P_{00}^s(\cos\theta) \tag{6-99}$$

$$b_1(\theta)=\sum_{s=2}^{\infty} b_1^s P_{02}^s(\cos\theta) \tag{6-100}$$

$$b_2(\theta)=\sum_{s=2}^{\infty} b_2^s P_{02}^s(\cos\theta) \tag{6-101}$$

其中：

$$\begin{aligned} a_1^s &= g_{00}^s + g_{0-0}^s \\ a_2^s &= g_{22}^s + g_{2-2}^s \\ a_3^s &= g_{22}^s - g_{2-2}^s \\ a_4^s &= g_{00}^s - g_{0-0}^s \\ b_1^s &= 2\,\mathrm{Re}\, g_{02}^s \\ b_2^s &= 2\,\mathrm{Im}\, g_{02}^s \end{aligned} \tag{6-102}$$

这样即将散射矩阵中的元素展开成一般球谐函数的级数的表示方式，这种解析方法的将较大提高数值计算的效率。

§6.4 小结

基于等效原理，利用扩展边界条件法推导了各向同性和各向异性散射单体的散射传输矩阵。给出了旋转对称椭球、正方体粒子、等离子体球等散射单体的散射数值结果，通过数值对比，验证了论文中理论推导和程序的正确性和有效性。针对多粒子散射体系，采用单次散射模型，推导了空间取向随机任意粒子群对平面波散射的解析解。通过将散射矩阵中各个元素的解析表达式用一般球函数的级数来展开，能够较大提高散射问题的数值求解效率。本章的相关理论推导将为下一章的研究提供理论基础。

第七章 椭球粒子的彩虹特性

为了提高产品的利用效率，在诸多的工农业生产过程中，我们需要对产品进行细化，如液体燃料在内燃机中的高压雾化过程、农药大面积喷洒时的雾化过程等等。在这些过程中为保证产品细化的质量，我们需要对雾化液滴的各种参数进行实时检测，其中主要包括液滴的粒径大小、温度大小、蒸发速率、移动速率等等。由于测量装置简单、测量精度高、实时性强等优点，彩虹技术已经在多个领域的在线检测和线下验证中受到越来越多的关注和应用。不同于直接利用散射光强度绝对值大小进行反演的光学测量技术，彩虹技术通过对彩虹角空间位置的测量来反演液滴粒子的尺寸分布和温度大小，具有较强的噪音抵抗力，能够应用在比如高温高压等复杂环境下。

本章在光散射理论的框架内介绍了彩虹现象的形成原理以及彩虹测量技术的最新开发进展，对传统标准彩虹技术和最近逐步发展完善的全域彩虹技术的优点以及局限性做了简单介绍。针对彩虹信号易受液滴粒子外表面形变影响的问题，采用椭球粒子模型，利用扩展边界条件法，模拟了空间取向随机任意分布的椭球粒子群在不同粒径分布和不同椭球率分布下对平面波的散射特性，特别分析了彩虹角附近远场散射场的空间分布情况。利用基于Nussenzveig球形粒子散射理论对模拟实验中椭球粒子的彩虹信号进行参数反演，将反演所得粒子参数和实际用于数值模拟实验的粒子参数进行对比，分析了椭球粒子对彩虹技术中粒子粒径分布、复折射率大小等参数反演精度的影响。

§7.1 彩虹现象和彩虹技术

§7.1.1 彩虹现象产生原理

雨后长虹，如雾似梦。

彩虹是大自然中一个神奇而美丽的光学现象。在阳光的照耀下，我们经常可以在雷阵雨过后，异或是在飞流直下的瀑布或者人造喷泉旁边，见到迷人的彩虹。如果空气质量较好，我们还可能有幸欣赏到漂亮的双层彩虹，如图7.1所示。对于第一阶彩虹，壮观的拱形彩带从内到外可以大致区分出紫色、蓝色、绿色、黄色、橙色以及红色，而第二阶彩虹的颜色排布顺序正好和第一阶彩虹的颜色排布顺序相反。在两阶彩虹中间，有一个较为深色的暗带，为了纪念这个暗带的发现者亚

历山大，通常我们把它称为亚历山大暗带。彩虹这个美丽的光学现象在过去数百年的时间里几乎是不可避免的引起了无数物理学家和数学家的研究兴趣。在过去漫长的研究过程中，人们发现彩虹的形成实际上是由于大气中的小水滴或者小冰晶对太阳光的散射作用引起的。

图7.1 自然界中拍摄到的双层彩虹现象

早在1611年，Dominis首先从粒子对光学散射的角度给出了彩虹产生的理论解释。这个理论之后很快被Descartes加以发展并首次在实验室中得到证实。Descartes利用反射定律、折射定律等几何光学原理，研究和描述了光线入射到单个球形水滴后的传播途径，并较为成功地解释了光线由大量水滴散射所形成的初级彩虹的原因。对于彩虹现象产生的本质原因的解释最重要的进展之一是在1802年Yong基于著名的杨氏双缝实验，提出了光的相干性原理。根据光的相干性原理，结合惠更斯的波动光学理论，他得出了两束平行光线在无限远处会由于它们之间的相位差而产生干涉相消或干涉加强的结论，从而对彩虹的形成原理进行了较为系统的阐述。

根据光学相干原理，在同一波前局部光强振幅保持不变的假设下，Airy于1838年利用惠更斯-菲涅耳原理及菲涅耳积分给出了一种解释彩虹现象产生的理论，称为Airy理论。Airy理论可以预测彩虹变化的趋势以及彩虹的振荡分布，但是由于该理论是建立在几何光学的基础上的近似理论，因此依然不能获得叠加在Airy曲线上实际存在的高频振荡分量。根据Airy理论，在通过球形粒子散射所形成的彩虹中，光束相干产生的低频分量分布的间隔仅仅取决于球形粒子的直径大小，而与粒子的折射率无关。同时由几何光学获得的彩虹角位置仅仅取决于粒子的折射率实部，与粒子的直径无关。但实际上粒子的直径变化也会引起彩虹角空间位置的变化。

对于Airy理论适用范围的探究，Van de Hulst[144]，van Beeck[145]，韩香娥[146]等人都对其做了相应的验证和探索。

针对用于解释彩虹现象成因的各种近似理论，Van de Hulst[144]在他的专著中（修订本）对它们相应的适用范围进行了较为系统的诠释。对于尺寸参数大于5000的液滴，在0.628μm波长下相当于半径为0.5mm大小的液滴，Airy理论可以对彩虹角的位置给出准确的预测。对于尺寸参数大于2000的液滴，利用惠更斯积分方法可以得到比Airy理论更为准确的预测结果。对于尺寸参数介于30至2000之间的粒子，Airy理论或者惠更斯积分方法虽然都可以用来粗略估计散射强度的分布，但是由于该理论方法都是在几何光学的基础上建立起来的，因此所给出的理论解释只是近似解。特别对于尺寸参数低于30的粒子，只有严格的Lorenz-Mie理论才能给出精确解并能从电磁波散射的角度对彩虹现象给予合理全面的解释。

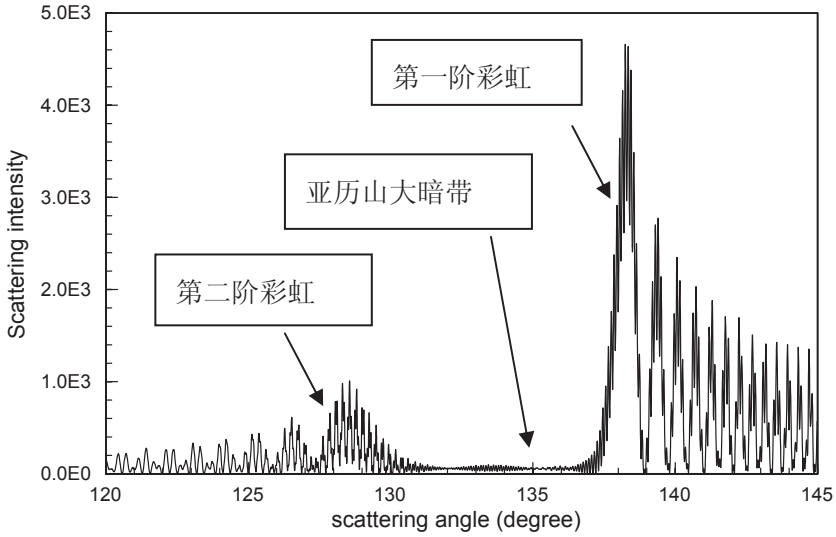

图7.2 均匀球粒子在平面波照射下，第一阶和第二阶彩虹附近散射强度分布图。粒子直径大小为d=600μm，复折射率为m=1.33-0.0i,入射波波长为λ=0.6328μm

从Lorenz-Mie理论出发，我们不仅能够获得叠加在彩虹低频分量上的高频结构，而且可以对高阶彩虹进行合理解释，因此Lorenz-Mie理论成为研究彩虹现象的最重要的方法之一。如图7.2所示，我们给出了一个均匀球粒子在平面波照射下一阶和二阶彩虹附近散射强度分布图。对于球形水滴粒子而言，一阶彩虹主峰位置位于138度左右，而二阶彩虹主峰位置位于128度左右。在图7.3中，我们给出了一阶彩虹附近更为详细的散射强度分布图。从图中可以看出，除了代表彩虹图案变化大趋势的低频分量外，还可以观察到叠加在低频分量上的高频震荡分量。

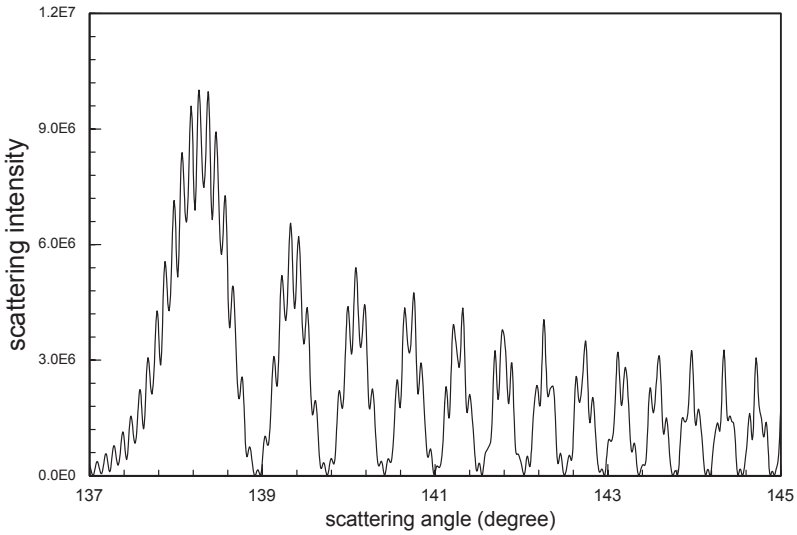

图7.3 均匀球粒子在平面波照射下，第一阶彩虹附近的散射强度分布图。粒子直径大小为d=600μm，复折射率为m=1.33-0.0i, 入射波波长为λ=0.6328μm

著名的Lorenz-Mie理论为我们提供了解决平面电磁波与均匀球形粒子之间相互作用的方法。然而几乎在所有的光学测量技术中，激光由于其本身所具有的良好特性而被选择作为激励光源。实际上，正是随着激光的发明和应用，光学测量技术才有了广泛的关注和应用。激光具有良好的单色性，准直性好，以及很强的光学相干性。因此人们对激光与粒子的相互作用所产生的性质感兴趣。为了更加符合实际应用和满足实际预测的需要，Gouesbet和Grehan等人[36]于1988年提出了广义Lorenz-Mie理论(GLMT)来描述和计算任意波形的电磁波束和各种规则粒子之间的相互作用。基于GLMT，利用离轴高斯波束散射可以模拟不同位置入射的光束对彩虹结构的贡献。van Beeck[145]在他的博士论文中利用一束或两束从粒子不同位置入射的高斯波束作为激励光源，模拟并验证了一阶彩虹和二阶彩虹形成机理。至此，对于球形粒子散射产生彩虹现象的研究已经相对比较完善，而基于彩虹现象发展起来的彩虹测量技术则处于发展阶段，并在更多领域开始得到越来越多的关注。

§7.1.2 标准彩虹技术

虽然对彩虹现象产生原理的理论研究已经有好几个世纪了，但是直到1988年，彩虹技术（又称标准彩虹技术，Standard Rainbow Technique）才由Roth等人[147, 148]第一次提出用来对粒子的相关参数进行测量。该技术可以同时实现液滴粒径分布和温度大小的测量。

与自然界中彩虹现象的产生不同，实验室利用单色激光光源替代自然太阳光

作为探测光源，通过单个或者多个液滴对激光光束的散射来而形成单色彩虹结构。更确切的说，实验室所得到的是单色光条纹状强度分布，并没有色彩的混合和叠加。通过观察单个液滴对单色激光散射所产生的散射强度角分布图样，在实验室里我们不仅可以精确的研究初级彩虹，而且可以研究二级甚至更高阶彩虹。Walker[149]利用He-Ne激光器研究了水和其它液体的前13级彩虹。从理论上讲，彩虹存在着无限多级，但级数越高，图样就变的越宽，越暗，这也是我们在自然界中难以观察到一阶和二阶彩虹以外更高阶彩虹的原因所在。

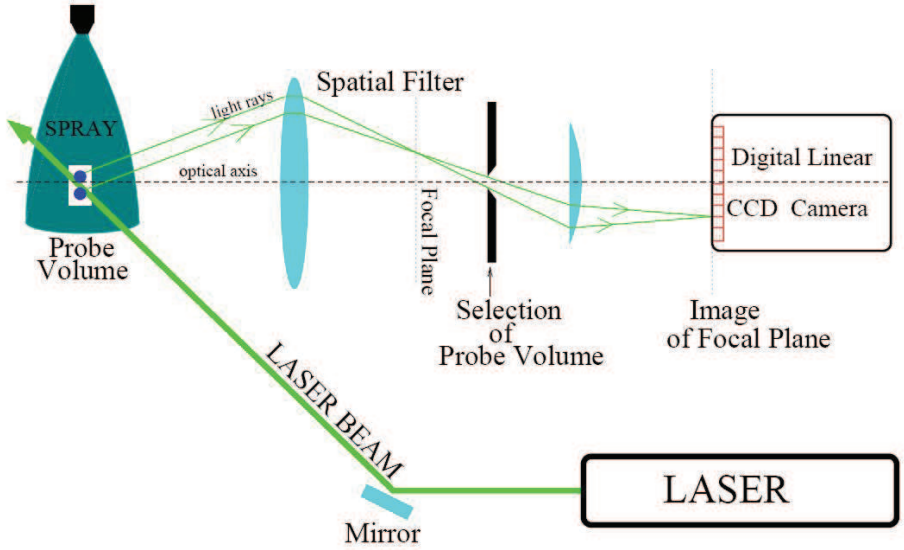

图7.4 彩虹测量技术实验装置搭建示意图

标准彩虹测量技术的实验装置搭建比较简单，装置的示意图和实验室实物图分别如图7.4和7.5所示。在这套装置中，主要包括了以下几个组成部分：(I) 液滴（液柱，喷雾）的产生装置。一般这个装置的主要部分会配备对液体温度进行调节的功能。比如在法国CORIA的实验室里面，装置可以将水滴的温度恒定于5^0C到80^0C之间的某个特定温度。液滴的平均粒径大小将由液体的流速、喷嘴的大小、振动频率等因素来控制。(II) 普通半导体激光器产生的激光光束就可作为实验装置的激励源。一方面，一个功率在毫瓦级的激光器所提供的激光光束就可以用作激励源进行相关测量实验。另一方面，由于散射目标对连续激光和脉冲激光散射特性上的较大差异，目前也有科研人员利用飞秒级的钛-蓝宝石激光器作激励源，对彩虹技术的应用范围进行拓展。(III) 彩虹信号的采集记录部分。激光光束与液滴相互作用后，其彩虹角附近位置的远场散射强度先由一个大孔径的透镜来采集。采集的光强度信号用一个空间滤波器加以过滤，选取单个液滴散射的散射彩虹信号。被选择的信号在经过第二个透镜的反傅里叶变换后用一个放在透镜焦平面上的二维平面光电传感器接收。如图7.6所示是CCD收集到的典型标准彩虹信号。(IV) 最后一步是基于各种彩虹解释的相关理论，如Airy理论，GLMT理论等，对CCD等

二维光电探测器采集的彩虹图像信号进行信息处理就可以反演出液滴的粒径分布、折射率大小等相关测量参数。

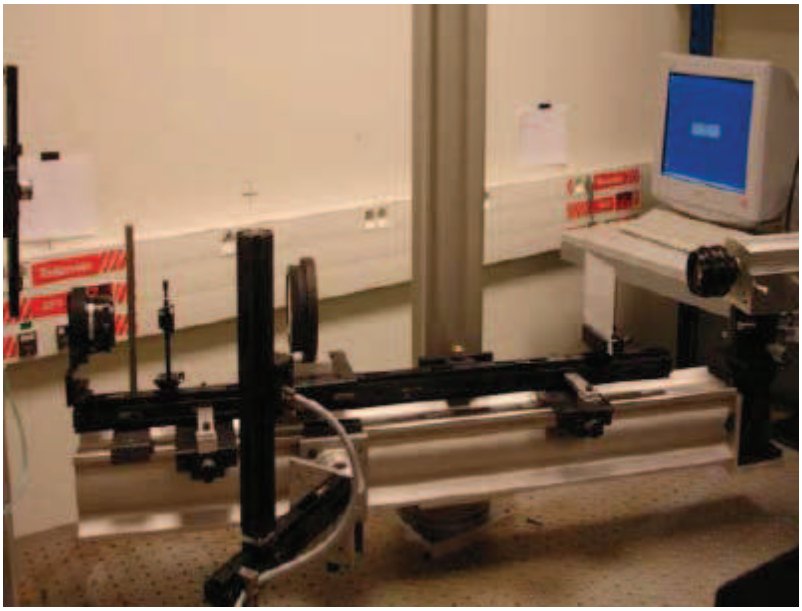

图7.5 彩虹测量技术实验室装置搭建实物图（文献[134]）

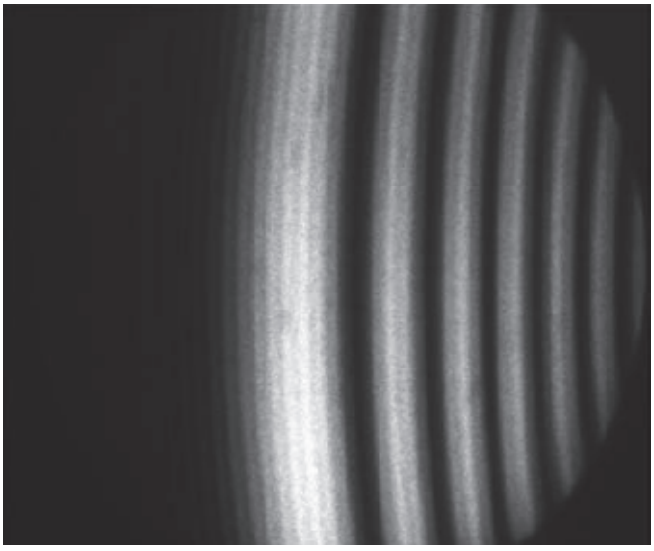

图7.6 二维光电探测仪器采集的典型标准彩虹信号

§7.1.3 全域彩虹技术

自从1988年Roth等人[147]第一次提出利用彩虹技术（现在称为标准彩虹技术）用以测量液体喷雾的相关参数以来，由于该技术实验装置简单、测量精度高、实时性强等优点，它在各种工农业生产的监测过程中上已经开始受到广泛应用。但是和其他测量技术一样，它自身也存在一定的局限性，将影响其测量精度。其中

最主要的因素有液滴粒子内部温度的非均匀性[150, 151]和液滴外表面的形变[132, 152]。韩香娥[146]分别从理论和实验两方面研究了具有温度梯度液柱的彩虹现象，姜会芬[153]详细推导了无限长非均匀介质圆柱对任意方位斜入射平面波的散射理论，并分析了非均匀（多层）球粒子的彩虹特性，Saengkaew等人[154]对非均匀（多层）球粒子的彩虹特性做了研究，大大提供了彩虹技术对粒子参数的反演精度。而液滴粒子外表面的形变对彩虹信号的影响以及对后续参数反演精度的影响尤为突出。为了消除液滴表面形变对彩虹测量精度的影响，van Beeck等人[138] 于1999年首次提出了全域彩虹技术(Global Rainbow Technique, GRT)。

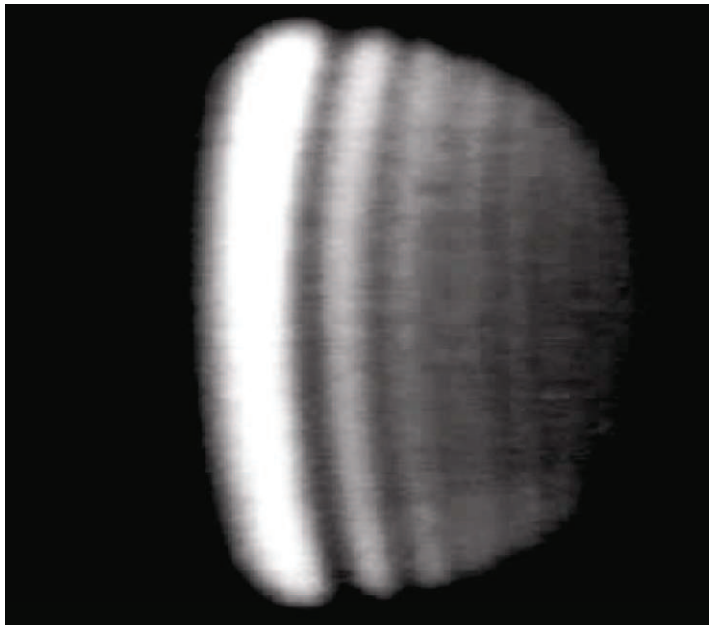

图7.7 二维光电探测仪器采集到的典型的全域彩虹信号

在实验测量装置的搭建上，全域彩虹技术和标准彩虹技术之间最大的不同是标准彩虹技术中需要在两个透镜之间加载空间滤波器来选择性地对单个液滴的散射信号进行采集。而全域彩虹技术中则去除了这个空间滤波器，使的信号采集的对象从单个液滴拓展到了一群液滴粒子。从实验搭建和测量原理来看，全域彩虹技术的测量原理更加接近于自然界中彩虹现象的形成原理。然而全域彩虹技术的提出是建立在随机任意分布的非球形粒子对全域彩虹信号带来的影响不大这样的假设前提下的。因为不同粒径大小但组成成分相同的球形粒子所产生的彩虹角位置不变，通过叠加效应准确的平均彩虹角位置将从由非球型粒子所产生的散射背景里面凸显出来。为了验证全域彩虹技术所基于的假设性是否普遍成立以及分析液滴粒子外表面非球形形变对全域彩虹测量带来的影响，我们以椭球粒子为模型，分别从实验[134]和理论[77]两个方面对该假设进行了分析。作为该研究工作的一部分，下面我们主要从理论和数值分析的角度，选取椭球粒子作为研究对象，研究椭球粒子的全域彩虹信号特点。

§7.2 椭球粒子彩虹信号的理论分析

§7.2.1 椭球粒子的标准彩虹信号

在利用彩虹技术对粒子相关参数进行测量的实验中，有诸多因素可能会影响到实验中反演结果的精度，比如说液体形状的非球形形变、液滴内部温度的非均匀梯度变化、彩虹信号中的高频振荡分量干扰等等。而其中液滴外表面的形变对彩虹信号的影响是最难以预测的因素之一，因此在传统标准彩虹技术中经常需要对非球形粒子的彩虹信号进行过滤和排除来提高测量的精度。

由于液体表面张力的原因，高速喷入空气中的雾化液滴会逐渐变成球形，因此很多文献在讨论激光光束被液滴粒子散射产生彩虹信号的问题时，经常将液滴粒子简化为球形粒子。事实上，水滴在下落过程中，由于空气阻力、自身重力等各方面因素的作用，它的形状更加接近于椭球。

对于平面波照射下非球形粒子彩虹信号的研究，早在1910年，Möebius就在纯几何光学方法的基础上，利用椭球模型对由于粒子外表面形变而引起的几何彩虹角位置的偏移进行了讨论，并给出了椭球粒子彩虹角偏移随椭球率大小变化的预测公式。但是由于他没有考虑光的相互干涉，因此该公式只能给出初级彩虹图案中几何彩虹角的近似位置变化，而不能预测次级彩虹条纹的出现。Marston[155]则最早开始从实验上来研究和观察了椭球的彩虹现象。

假设入射平面波的传播方向与直角坐标系z轴夹角为α，入射光线经过一次内反射后,能够出现彩虹现象的出射光线与入射光线的最小夹角为θ_{rg},该角又称为球形粒子的几何彩虹角。借助几何光学射线追踪法可以得到θ_{rg}与入射角τ_{rg}之间的相互关系。对于球形粒子,它们之间的关系表达式为:

$$\theta_{rg} = 4\tau'_{rg} - 2\tau_{rg} \tag{7-1}$$

$$\sin\tau_{rg} = \sqrt{\frac{n^2-1}{3}} \tag{7-2}$$

$$n\cos\tau'_{rg} = \cos\tau_{rg} \tag{7-3}$$

其中n是粒子折射率与周围介质折射率之比。在椭球粒子的椭球率接近于1，即粒子球形形状变化不大的情况下，球形粒子几何彩虹角和椭球形粒子几何彩虹角的差别：

$$\Delta\theta_{rg} = 16\left(\frac{b-a}{b+a}\right)\frac{\cos\tau_{rg}}{n}\sin^3\left(\arccos\left(\frac{\cos\tau_{rg}}{n}\right)\right)\cos(\theta_{rg}-2\alpha) \tag{7-4}$$

虽然Möebius公式不能预测粒子外表面形变带给其他干涉分量的影响，但是它

给我们一个非球形偏差所带来影响大小的感性认识。

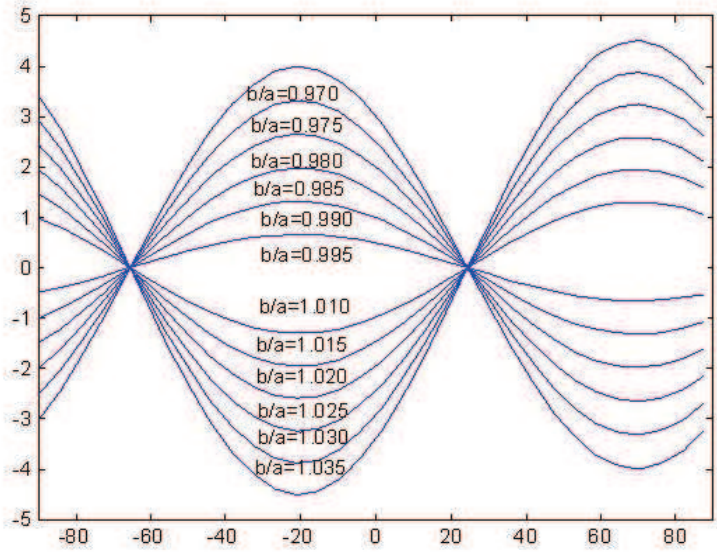

图7.8 Möebius公式对彩虹角位置偏差随椭球粒子椭球率变化的预测

如图7.8所示，我们根据等式(7-4)给出了Möebius的预测结果。从图中可以看出，形状上与球形粒子偏差3%的椭球型粒子，如$b/a=1.03$，彩虹角的空间位置偏差可达4^0左右。

关于粒子非球形偏差对彩虹信号所带来的影响，van Beeck[145]用几何光学加惠更斯-菲涅耳表面积分的混合方法进行了研究。从Möebius公式预测的结果来看，彩虹角位置的偏移大小只和椭球率以及入射波的入射角有关，而与椭球粒子的尺寸大小无关。但是van Beeck所得数值结果告诉我们，彩虹角位置的偏移大小同样依赖于粒子尺寸大小的变化。韩一平等人[152]在GLMT严格理论的框架下对该问题进行了分析，并和Möebius所得到的结果进行了对比，所得结果基本一致。最近，徐峰等人[58]利用Debye级数方法研究了椭球粒子的散射问题，通过从级数中分离出p=2阶散射信号，分析了粒子非球形偏差给彩虹角位置变化带来的影响。李祥震等人[156]利用几何光学射线追迹法研究了平面波以任意方向入射到均匀椭球粒子上时一阶几何光学彩虹角分布。

从文献中基于各种不同理论方法所得的数值分析结果来看，对于单个粒子来说，无论是彩虹角的空间位置还是彩虹图案本身的结构都会因为粒子外表面形状的非球形偏差而带来很大的变化。基于扩展边界条件方法(EBCM)，我们重新对上述结果进行了验证并得到了一致的结果。

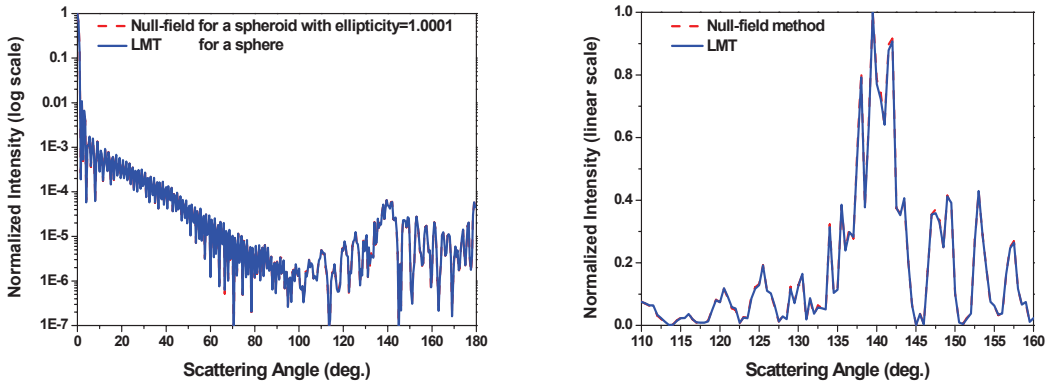

(a) 强度角分布图　　(b) 彩虹角附近强度角分布图

图7.9 球形粒子归一化强度角分布图: LMT方法计算结果（实线）与EBCM方法计算结果（虚线）的对比。粒子的尺寸参数为150

首先为了验证我们EBCM程序的正确性和适用范围，如图7.9所示，我们分别用EBCM和Lorenz-Mie理论计算了一个球形粒子对平面波的散射情况。如图所示，在这种情况下，由两种方法计算所得的归一化角强度分布图完全吻合。

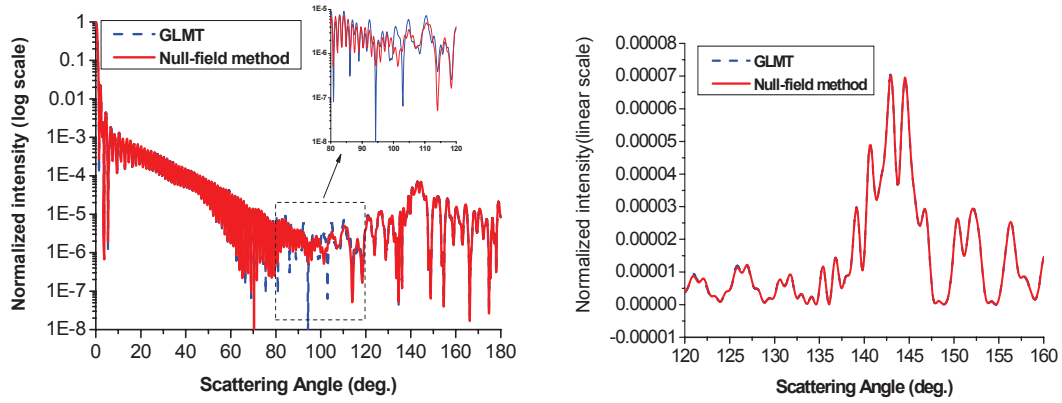

(a) 散射强度角分布图以及90°附近强度分布图　　(b) 彩虹角附近强度分布图

图7.10 扁椭球粒子（椭球率为0.97）的归一化强度角分布图: GLMT方法计算结果（虚线）与EBCM方法计算结果（实线）的对比。粒子的等面积尺寸参数为150

GLMT方法经过多年的发展，同样能对椭球粒子光散射特性进行预测[40, 41]。因此为了进一步验证EBCM程序的可靠性，如图7.10所示，我们分别用GLMT和EBCM计算了一个长椭球粒子对平面波的散射情况。椭球的椭球率为0.97,它的旋转对称轴方向由欧拉角α，β，γ来确定，这里欧拉角α，β，γ均为0°。如图所示，除了在散射角90°附近有些偏差，由两种方法计算所得的椭球粒子归一化强度的角度分布图基本吻合。而这个在散射角90°附近的偏差主要是由GLMT数值计算不稳定造成的

[40]，目前该问题的进一步研究也是本学科的一个重要的待解决问题。然后这个数值不稳定性对彩虹角附近的散射强度分布没有什么影响，如图7.10b所示，两种方法所得结果完全一致，因此将对彩虹角位置的预测不会产生影响。

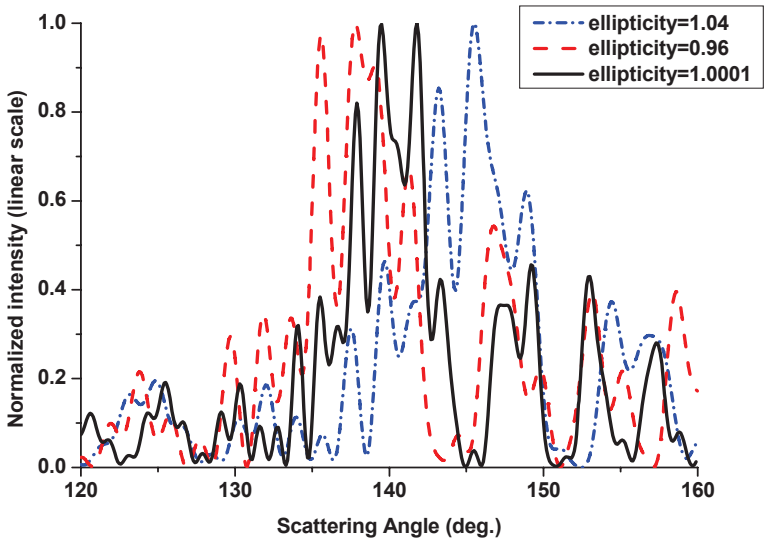

图7.11 EBCM方法计算不同椭球率的椭球粒子散射的归一化强度角分布图。粒子的等面积尺寸参数为150

基于EBCM，如图7.11所示，我们给出了不同椭球率椭球粒子在彩虹角附近归一化散射强度的角分布图。各个椭球粒子的等面积尺寸参数均为150。该结果进一步证实了粒子外表面形变对标准彩虹信号的剧烈影响。

§7.2.2　椭球粒子的全域彩虹信号

从上一节的分析可以看出，对于单个粒子来说，无论是彩虹角的空间位置还是彩虹信号图案本身结构都会受到粒子非球形偏差而带来的剧烈变化，因此基于球形粒子光散射理论，对外表面有非球形形变粒子参数的彩虹信号进行相关参数的反演将会产生较大误差。为了减少粒子形变给测量结果带来的误差，提高被探测粒子参数的精度，van Beeck等人提出全域彩虹技术(Global Rainbow Technique, GRT)，利用一群方向随机任意分布的粒子所产生的合成彩虹信号来进行参数反演[134]。

如同自然界中彩虹现象的形成原理一样，全域彩虹信号是由一群粒子各自在彩虹角附近的光散射强度的叠加所产生的稳定的合成彩虹图案。这个彩虹信号主要由两部分信号叠加组成，一部分光散射强度来自于球形粒子散射信号的叠加，因为不同粒径大小但具有相同组成成分的球形粒子对波束散射所产生的彩虹角位

置不变，通过叠加效应，准确的彩虹角位置将从散射体系的散射背景里面凸显出来。另外一部分信号来自于方向任意分布的非球形粒子在彩虹角附近的光散射强度，由于粒子取向的随机任意性，它们在彩虹角附近的光散射强度将呈现一个均匀的杂波背景，从而使得合成彩虹信号对粒子的外表面形变的变得相对不敏感。

虽然全域彩虹信号不会像标准彩虹信号那样对极易受到粒子外表面非球形形变的影响，但是并没有充分的研究表明粒子的外表面形变不会给粒子粒径分布和内部平均温度大小等参数的反演带来误差。为了验证全域彩虹技术最初理论假设的正确性以及确定该技术的适用范围，Vetrano[157]利用全域彩虹技术对两种互不相融液体的混合液进行了测量，初步验证了全域彩虹测量技术的有效性。但是由于该研究对象的不稳定性和可控性不强，该实验并没有给出较为一般和定量的验证结果。为此，我们以椭球粒子为模型，分别从实验[134]和理论[77]两个方面对全域彩虹技术中液滴粒子外表面非球形形变的敏感度进行了探索和研究。以下我们主要从理论和数值上研究了椭球粒子对彩虹技术参数反演准确度的影响。

从相关文献的报道和内部交流来看，目前基于GLMT计算任意方向椭球粒子散射强度角分布的程序还存在尺寸参数过大时不收敛的问题[41, 158]，然而基于EBCM方法已经能够对尺寸参数超过150的椭球粒子的散射特性进行准确预测，因此这里我们选用EBCM方法来对一群椭球粒子产生的全域彩虹信号进行数值模拟和分析。

§7.2.2.1　相同椭球率椭球粒子群的全域彩虹信号

本节中我们模拟计算了几种椭球率相同但空间取向随机任意分布的椭球粒子群在平面波照射下的散射特性，重点分析了彩虹角附近全域彩虹信号的强度分布。用于模拟仿真的椭球粒子的等表面积尺寸参数为100，在波长为0.6283μm的平面波参照下，粒子的直径约为20μm。粒子的复折射率为1.33-0.0i。

图7.12和图7.13中所示的是取向随机任意但椭球率相同的椭球粒子群对平面波散射在彩虹角附近的归一化强度角分布图。从图7.12中可以看出，对于一群外表面形变不大的非球形粒子，我们可以得到稳定的合成彩虹图案。但是相对于球形粒子所产生的彩虹信号，取向随机任意分布的椭球粒子群所产生的一阶彩虹的主峰位置向较小散射角度偏移。除主峰以外，一阶彩虹的次峰会随着粒子椭球率的增大而逐渐淹没在背景信号里。同时我们可以看到，由于椭球粒子的空间取向任意随机分布，彩虹图案上的高阶分量会由于光强度的叠加效果而逐渐消失。因为这样一个特点，全域彩虹技术比起标准彩虹技术更适用于20μm以下小粒径液滴相关参数的测量。通过图7.13中对具有相同形变率的长椭球和扁椭球的全域彩虹图像的对比，我们可以看出，相对于扁椭球粒子，长椭球粒子群对高频分量具有更强的抑制作用。

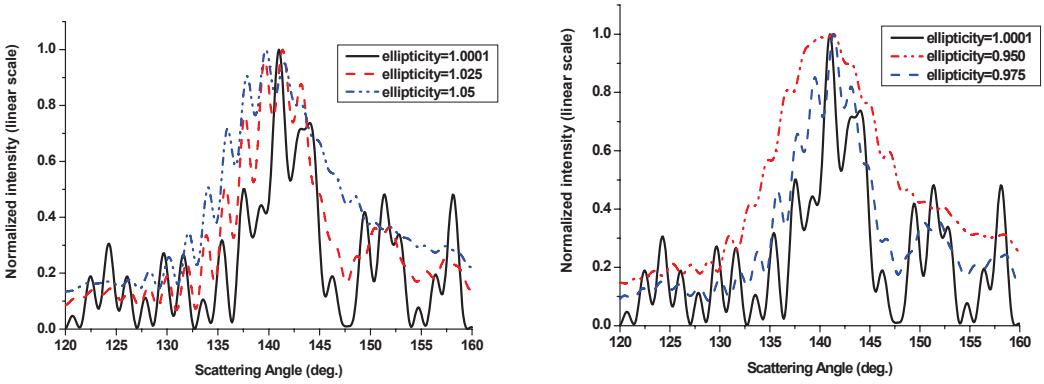

(a) 扁椭球粒子群散射　　(b) 长椭球粒子群散射

图7.12 椭球粒子群对平面波散射在彩虹角附近的归一化强度角分布图。每个椭球群中的椭球粒子具有相同的等面积尺寸参数为100，且具有相同的椭球率，但粒子空间取向任意分布

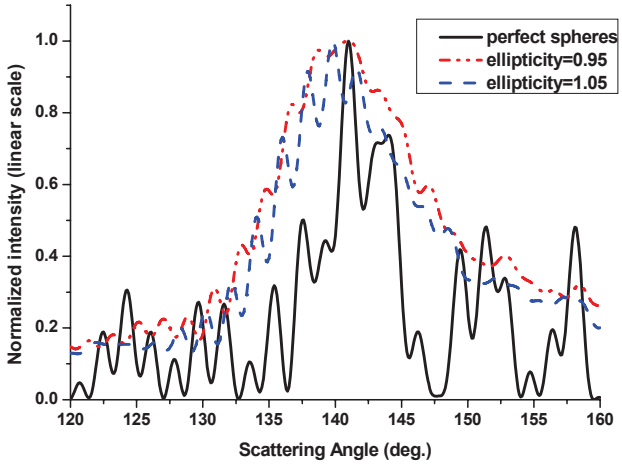

图7.13 等表面积尺寸参数的球形粒子群，长椭球粒子群（椭球率为0.95），扁椭球粒子群（椭球率为1.05）对平面波散射在彩虹角附近的归一化强度角分布图

§ 7.2.2.2　不同椭球率椭球粒子群的全域彩虹信号

上一节我们对椭球率相同但空间取向随机任意的椭球粒子群对平面波散射所得全域彩虹信号做了模拟分析。在本节中，我们将对不同椭球率取向随机任意的椭球粒子群对平面波散射产生的全域彩虹图案进行分析。椭球粒子具有相等的等表面积尺寸参数为100，粒子的椭球率在区间[0.9 1.1]上满足高斯正态分布且空间取向取向任意随机分布。粒子的复折射率为1.33-0.0i。

如图7.14所示的是椭球率呈高斯分布的椭球粒子群对平面波散射在彩虹角附近光散射的归一化强度角分布图。图7.14a中椭球粒子群椭球率的均值为1.00，标

准差分别为0.00, 0.01和0.02的椭球粒子群。而图7.14b中椭球粒子群椭球率的均值为0.97，标准差分别为0.00，0.01和0.02。从图7.14中可以看出，在椭球粒子椭球率均值不变的情况下，随着椭球率标准差的增加，一阶彩虹主峰的空间位置变化不大，但是主峰的半宽度逐渐变大。通过对图7.14(a)和图7.14(b)中彩虹信号图案的对比，我们可以发现对于形变率较大的椭球粒子群，椭球率分布标准差的大小对椭球粒子的合成彩虹图案的影响不大。

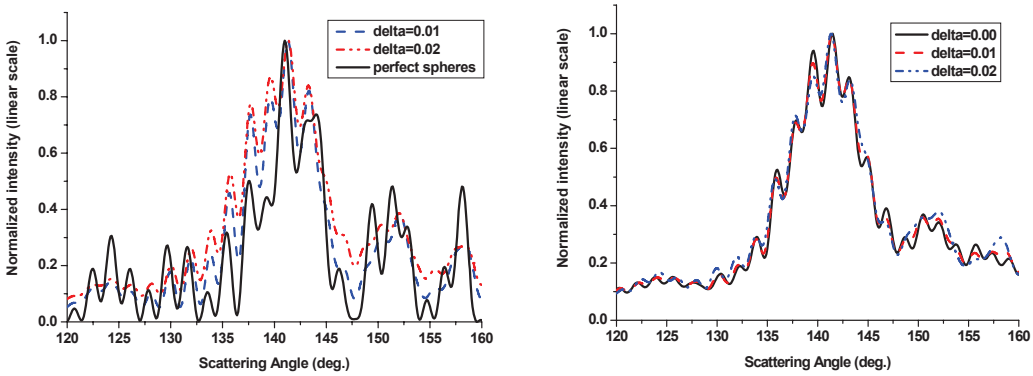

(a) 椭球率均值为1.00　　(b) 椭球率均值为0.97

图7.14 取向随机任意椭球粒子群对平面波散射在彩虹角附近归一化强度角分布图。椭球粒子的椭球率满足高斯正态分布。

§7.3 椭球粒子全域彩虹信号的反演

从上一节对椭球粒子彩虹信号的分析可以看出，相对于粒子外表面形变对标准彩虹信号的影响，粒子外表面形变对全域彩虹信号的影响不大。虽然全域彩虹信号不像标准彩虹信号那样极易受到粒子外表面形变的剧烈影响，但是粒子外表面形变是否将给粒子粒径分布、平均温度大小的反演带来影响？会产生多大的影响？为了回答以上问题，在本节中，我们对利用椭球粒子为模型仿真得到的全域彩虹信号进行参数反演，从数值上定量地分析粒子外表面形变大小对全域彩虹技术在液滴粒径大小分布、平均温度测量上所带来的影响大小。

从全域彩虹技术的提出以来，为了实现被探测粒子相关参数的精确反演，近几年来逐步提出了一些较为稳健的反演方法[151, 157]。Saengkaew和Grehan[151]在对包括广义米理论，Debye级数方法，Airy理论，CAM理论(Complex Angular Momentum theory)等多种彩虹预测理论进行数值分析对比的基础上，综合考虑模型计算精度和反演参数的速度，采用Nussenzveig提出的CAM散射理论，结合经验修正参数，利用非负最小二乘法(Non-Negative Square Least method, NNSL)算法编写了稳健快速的粒子参数反演计算程序。下面我们就用该反演程序对利用椭球粒子为模型模拟

仿真得到的全域彩虹信号进行参数反演。

§7.3.1 相同椭球率椭球粒子群的参数反演

对于取向随机任意但具有相同椭球率的水雾液滴群（折射率为1.33）在平面波照射下产生的全域彩虹信号进行参数反演，我们可以得到粒子粒径分布和折射率大小的反演结果分别如图7.15和表格7-1所示。用于仿真实验的液滴的等表面积尺寸参数为100，在波长为0.628μm的入射波参照下相当于直径大小为20μm的粒子。如图7.15所示，随着粒子椭球率的逐渐增大，在粒径反演的过程中将会出现越来越多的“虚粒子”。这个反演结果和我们在验证实验中所的结果一致[134]。通过数值模拟，我们可以发现，当粒子的椭球率超过3%以后，这些“虚粒子”开始在反演粒径结果中占据主要比例。

表7-1 反演所得折射率大小随椭球粒子椭球率均值大小变化统计表（标准差为0.0）

椭球率	1.01	1.02	1.03	1.04	1.05
折射率大小	1.3287	1.3278	1.3241	1.3198	1.3135
椭球率	0.99	0.98	0.97	0.96	0.95
折射率大小	1.3272	1.3291	1.3245	1.3191	1.3136

从表格7-1可以发现，即使全部散射微粒为椭球粒子，椭球率的大小变化对折射率反演结果的影响也并不严重。但是值得注意的是反演所得数值和实际用于仿真彩虹信号的数值之间的误差将随着椭球率的增大而增加。和预期结果相对一致，全域彩虹技术对于一群空间取向随机任意具有同等大小形变率的长椭球粒子和扁椭球粒子进行测量时所得反演结果类似。这个结果和Asano[51]对小粒径椭球粒子进行散射特性研究时所得到的结果相一致。

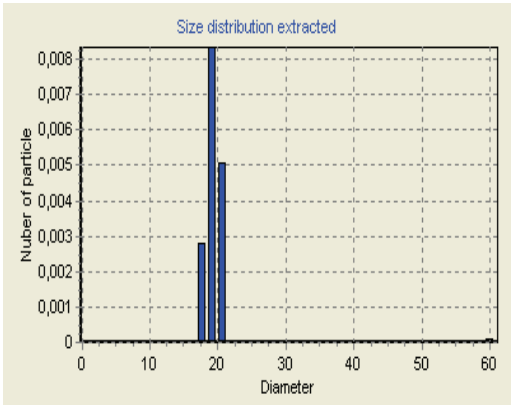

椭球率为0.99

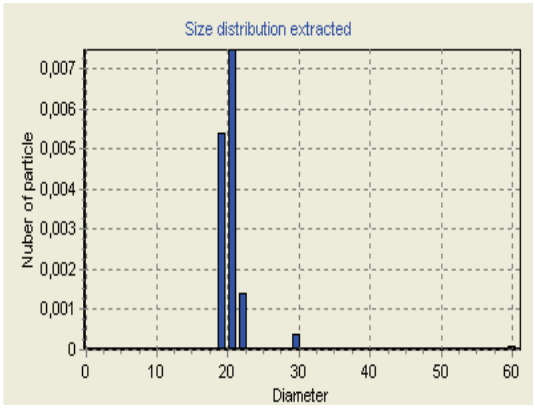

椭球率为1.01

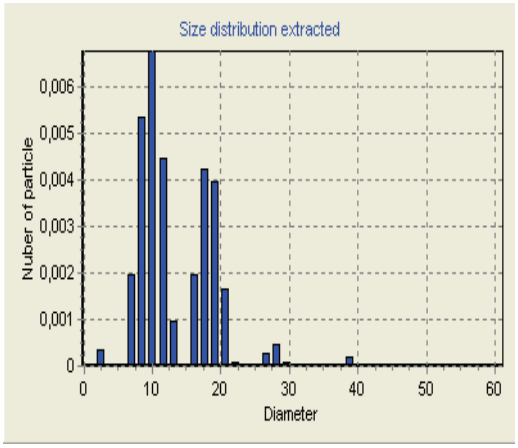

椭球率为0.97

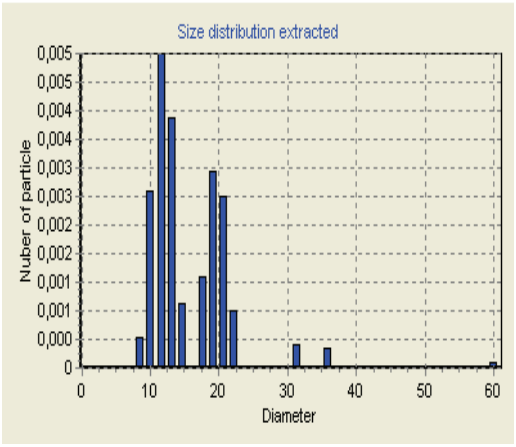

椭球率为1.03

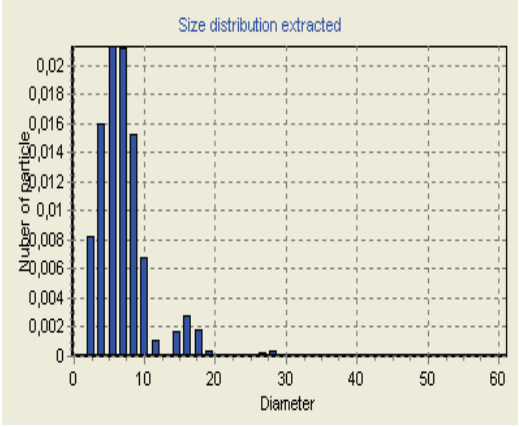

椭球率为0.95

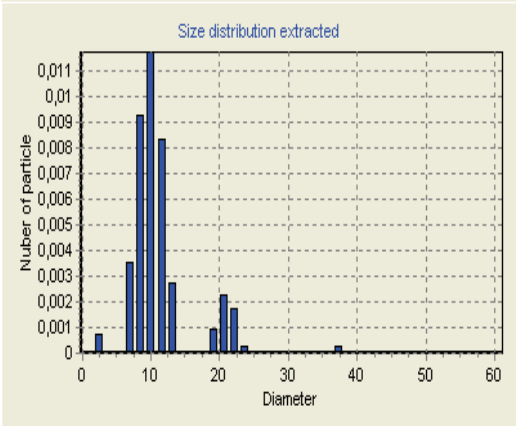

椭球率为1.05

图7.15 对水雾液滴群产生的全域彩虹信号进行粒径反演所得的反演结果。液滴粒子实际的等表面积直径为20μm，具有固定的椭球率大小但粒子取向随机任意

§7.3.2 不同椭球率椭球粒子群的参数反演

对取向随机任意且椭球率大小不相同的水雾液滴群（折射率大小为1.33-0.0i）

在平面波照射下产生的全域彩虹信号进行参数反演，如图7.16和表格7-(2,3,4)所示，我们给出了粒子粒径大小和折射率大小的反演结果。

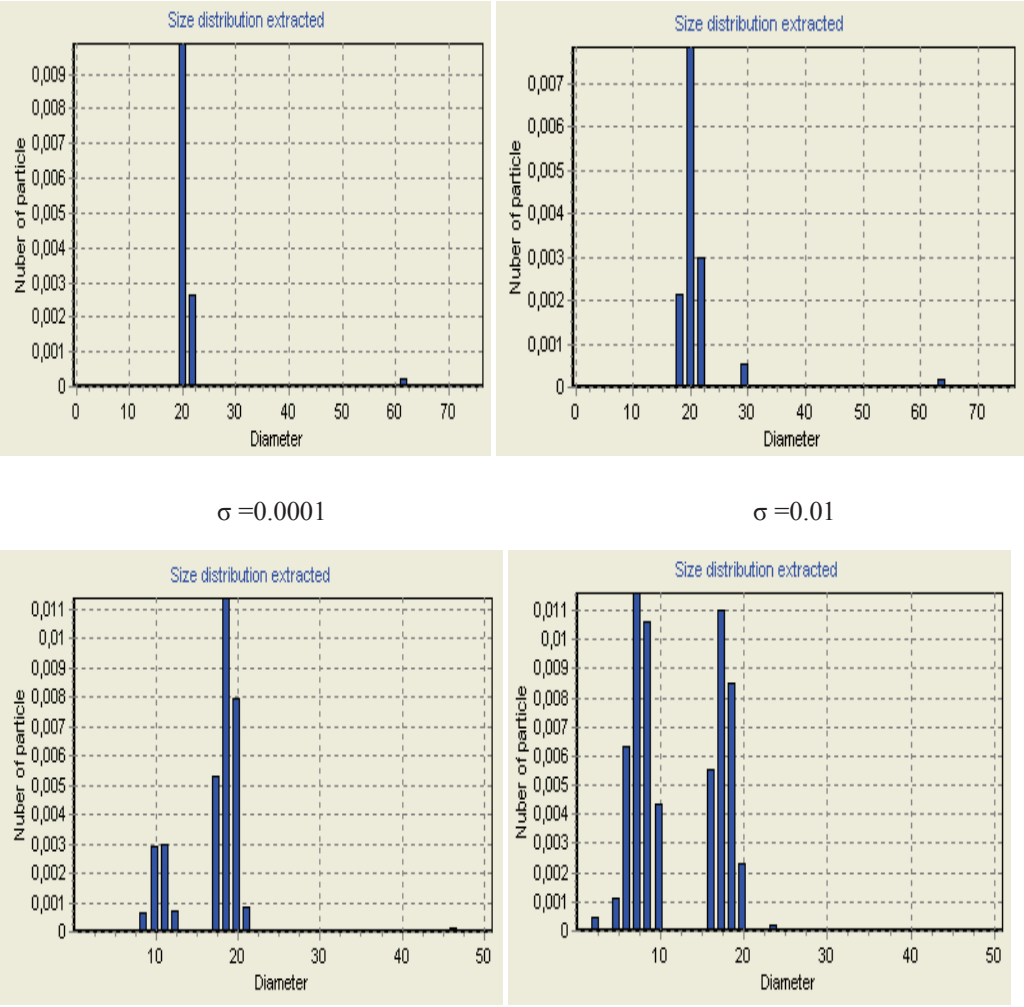

图7.16. 对椭球水雾液滴群所产生的全域彩虹信号进行粒径反演所得到的反演结果。液滴粒子的等表面积直径为20μm，椭球率分布满足高斯正态分布，均值为1.00，σ为标准差。

其中液滴的等表面积尺寸参数为100，在波长为0.628μm的入射波参照下相当于直径为20μm的粒子。粒子的椭球率在[0.9 1.1]区间内满足高斯正态分布，粒子外表面形变大小由椭球率的均值来决定，均值越接近于1.0，椭球粒子就越接近于球形粒子。而各个粒子之间形状的差异性则由椭球率均方差来决定，方差越小，粒子之间形状越接近。

表7-2 反演所得折射率大小随椭球粒子椭球率标准差变化统计表（均值为1.0）

分布标准差	0.01	0.015	0.02	0.025	0.030
折射率	1.3288	1.3273	1.3261	1.3248	1.3232

表7-3 反演所得折射率大小随椭球粒子椭球率大小的变化统计表（标准差为0.01）

椭球率	1.01	1.02	1.03	1.04	1.05
折射率	1.3276	1.3255	1.3233	1.3202	1.3135
椭球率	0.99	0.98	0.97	0.96	0.95
折射率	1.3283	1.3255	1.3223	1.3181	1.3121

表格7-4反演所得折射率大小随椭球粒子椭球率变化统计表

	椭球率均值 1.03	椭球率均值 1.0001	椭球率均值 0.97
标准差0.001	1.3241	1.3294	1.3245
标准差0.01	1.3233	1.3288	1.3223
标准差0.02	1.3205	1.3261	1.3205

在图7.16中，粒子椭球率均值为1.00，当椭球率的高斯分布方差较小时，如σ=0.01，通过反演算法所得到的粒子参数和实际数值几乎相同。随着方差的逐步增大，在粒子粒径大小的反演过程中将会出现越来越多的“虚粒子”。当粒子的椭球率方差超过3%之后，这些“虚粒子”开始在粒径反演结果中占据主要比例。与此同时，从表格7-2中我们可以发现，反演所得液滴粒子的折射率会随着椭球率方差的增大而小于实际值的方向偏离实际值。

表格7-3中则给出了对椭球率分布均值不同，方差大小为0.01的水雾液滴群（折射率为1.33）产生的全域彩虹信号进行参数反演所得折射率大小的反演结果。在表格7-4中给展示的是椭球率分布均值和方差大小均不同的水雾液滴群（折射率为1.33）产生的全域彩虹信号进行参数反演所得折射率大小的反演结果。

上面我们对液滴粒子折射率的反演结果随粒子外表面形变大小变化的规律做了统计，利用液体折射率大小和温度高低之间的关系，就可以得到液体温度的大小和分布。对于一些常用液体，比如说水、乙醇、甲醇等，已经在相关文献中给出了特定的线性关系。对于复杂的混合液体，也可以在实验室里利用较为常用的多频谱折射率测量仪来确定他们之间关系。一般来说，液滴的折射率大小会随着温度的变化而呈单调的线性变化。因此我们通过对液滴折射率的测量就可以得到温度大小。

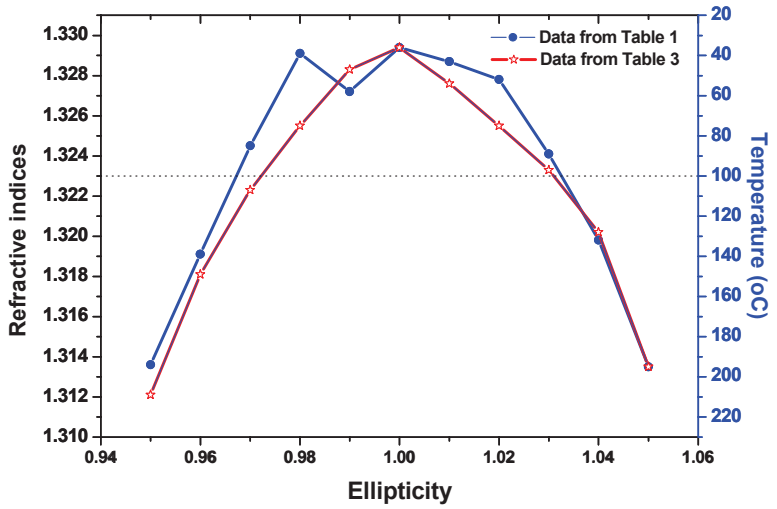

图7.17 表格7-3和表格7-1中反演所得折射率（温度）大小随椭球率变化的比较

对于水介质，通过对表格7-3和表格7-1中数据的对比，我们将折射率随椭球率的变化情况在图7.17中表现出来。另外根据Harvey等人[159]给出的水介质温度和折射率大小的对应关系，我们也将相应的温度大小表述在图7.17右边的纵坐标上。从图中可以看出，一旦椭球粒子的椭球率超出[0.97 1.03]的范围区间，实验中反演出来的折射率就会太小，对应于不合理的温度大小，这个结果可以作为实验中相关测量的一个判断标准。即如果在实验中反演出不合理的温度值，那么就很可能是由于椭球粒子椭球率过大，即液滴粒子外表面形变过大所造成的测量误差。同时图7.17也告诉我们，反演得到的折射率大小会随着椭球率方差的增大而向小于实际值的方向偏离实际值。这个结论也得到表格7-4中数据的支持。

§7.4 小结

在粒子光散射理论框架内，本章介绍了彩虹现象的形成原理以及光学彩虹测量技术的开发，分别对标准彩虹技术和全域彩虹技术的优点以及局限性做了简单分析。针对彩虹技术易受液滴外表面形变影响的问题，本章以椭球粒子为模型，利用扩展边界条件法，模拟了取向随机任意分布的椭球粒子群在不同粒径分布和不同椭球率分布下对平面波的散射特性，特别分析了彩虹角附近远场散射场的空间分布情况。基于Nussenzveig球形粒子平面波散射理论对模拟得到的椭球粒子的彩虹信号数据进行参数反演，将反演所得粒子参数和实际用于数值模拟实验的粒子参数进行对比，分析了椭球粒子对彩虹技术中粒子粒径分布、复折射率大小等参数反演精度的影响。

第八章 论文总结和展望

本论文选题为偏心粒子与电磁（激光）波束之间相互作用以及椭球粒子彩虹特性的研究。按照研究对象来分，本论文内容主要包括以下两个主要部分：(I) 在广义米理论(GLMT)框架内系统地研究了偏心球粒子与任意入射有形波束之间的相互作用；(II) 在扩展边界条件法(EBCM)理论框架内研究了椭球粒子的彩虹信号以及对彩虹技术参数反演精度的影响。下面我们就本论文的主要研究工作和结论做个总结：

第一：任意入射有形波束用矢量波函数展开问题的求解是研究非均匀粒子、非球形粒子对波束散射问题的关键，也是解决问题的难点。本论文基于有形波束的球矢量波函数展开式，利用球矢量波函数的旋转加法定理和平移加法定理，推导了任意方向入射有形波束的波束因子在任意直角坐标系之间相互转换的一般关系式。以轴对称波束为例，给出了轴对称波束波束因子在任意直角坐标系下相互转换的简化解析表达式，可直接用于数值计算编程。该部分的研究内容为本论文后续问题的求解，以及任意非均匀粒子、非球形粒子对波束散射问题的求解提供了理论基础。

第二：基于GLMT理论，详细推导了偏心球粒子模型对任意入射有形波束散射问题的求解。基于本论文的理论推导结果，利用FORTRAN语言编写了一套用于求解偏心球粒子电磁(光)波波束散射问题的程序。

第三：研究了偏心球粒子对高斯波束散射情况下偏心球粒子的远场、表面近场和内场三维空间电磁强度的分布情况。此研究结果对深入认识复杂粒子与波束之间相互作用，对粒子内部结构的探测和识别，粒子内部各种非线性光学现象的产生等提供重要的理论指导。

第四：研究了偏心球粒子在汇聚高斯波束激发下的光学谐振特性。分析了内核小球粒子在不同相对尺寸大小、不同偏心度下对偏心球中谐振模谐振位置和谐振振幅的影响。此研究将对复杂光学微腔在光电转换器件，生物细胞探测等方面的应用有指导作用。

第五：利用EBCM方法，模拟了空间取向随机任意分布的椭球粒子群在不同粒径分布和不同椭球率分布下对平面波的散射特性，特别分析了椭球粒子彩虹角附近散射场的空间分布情况。基于Nussenzveig球形粒子散射理论对模拟实验中得到的椭球粒子彩虹信号进行参数反演，将反演所得粒子参数和用于数值模拟实验的粒子参数进行对比，分析了椭球粒子对彩虹技术中粒子粒径分布、复折射率大小等参数反演精度的影响。

复杂粒子与有形波束之间相互作用的理论研究在粒子粒度测量与分析、粒子三维速度场还原的理论基础等诸多领域里有着广泛的应用。本论文基于前人的研究基础，在相关理论和数值研究方面开展了相应的工作并取得了一定的创新成果，针对本研究课题的工作进展和应用潜力，下一步的研究工作可以主要围绕以下几个方面进行：

第一：本论文对偏心球粒子在有形波束照射下粒子的内场、表面近场以及远场的强度分布做了理论研究并给出了相应的数值结果和分析。在后续的工作中，有两个方面的内容可以做进一步深入的研究：(I)偏心球粒子对于椭圆高斯波束、高阶Hermite-Gaussian波束的散射情况，将会呈现新的散射特性。(II)对于多层偏心球粒子的研究，结合不同的材料涂层，其散射特性的变化也有必要进行分析。

第二：本论文在GLMT框架下编写了有形波束对偏心球粒子散射问题的求解程序。然而在内核小球粒子平移距离较大情况下，球矢量波函数的平移加法定理在数值计算上仍然存在收敛不足的问题，目前本论文所写程序对能够计算和分析的偏心粒子的尺寸参数还有一定的限制。因此，如何从数值计算和算法上对程序进行优化和改进将是一个很值得研究的方向。

第三：本论文从理论上较全面地分析了偏心球粒子的内场、表面近场以及远场散射特性，这些结果对偏心球粒子或者多粒子散射体系中三维空间场和速度场的探测和还原、粒子内部结构的探测和识别、粒子内部各种非线性光学现象的产生提供重要的指导作用。因此结合本论文的数值实验结果，进一步探索偏心粒子在实际测量和识别中的应用将是下一步的重要工作。

第四：本论文分析了椭球粒子的彩虹信号特性以及椭球粒子在彩虹技术参数反演中对粒子粒径分布、复折射率大小等参数反演精度的影响，发现全域彩虹技术能够有效降低粒子外表面形变对粒子参数反演精度的影响。为了进一步提高彩虹技术的测量精度，下一步的研究工作主要有两方面：一方面是从理论上去建立更为准确的反演模型和反演算法，另一方面则是从实验的角度去开拓更为有效的彩虹信号采集和筛选方法。

致 谢

本论文依托中法合作研究课题“Optical characterization of shape and thermo-chemical composition of biodiesel droplets in flames”，是由法国驻华大使馆资助，为中法联合培养博士研究生项目。该项目旨在加强中法两国之间的国际交流与合作，充分结合中法双方实验室不同研究领域或方向上的优秀科研资源，带动相关领域，特别是交叉学科研究的发展。因此该博士论文是中国西安电子科技大学(Xidian University, China)和法国国家应用科学研究院鲁昂分院(INSA de Rouen, France)合作完成的成果。该博士论文选题还来源于国家自然科学基金项目(60771039)“光镊中光势阱的研究”，以及欧盟国际区域发展基金项目“Interreg Iva-C5: Cross-Chanel Center for Low Carbon Combustion”。

本论文能够顺利完成，首先要感谢我的中国导师韩一平教授。自从2006年进入实验室以来，正是在她的悉心指导下我才逐步进入学术研究的领域。韩老师以其敏捷的思维和深刻的洞察力直接启发和帮助我，她开放式的指导方式让我在电磁和激光探测研究领域的前沿中可以自由寻找自己感兴趣的研究方向。另外也正是通过韩老师的大力引荐，我才有幸能够去法国CORIA这个优秀的研究所学习，使我学到了很多终生难忘的教益。

我要特别感谢我的法国导师Gérard Gréhan和Gérard Gouesbet教授。Gréhan老师扎实的理论功底、严谨的治学态度以及不受约束的科研思维让我领略了做学术的张弛有度和做科研的乐趣。Gouesbet老师虽然早在几年前就已经退休了，但是他在学术上仍然保持着高度的活跃，他敏捷的思维和高涨的科研热忱让我对学术研究产出出更多的兴趣。特别要感谢Gouesbet老师对我每一篇杂志文章不厌其烦的修改。

其次，我要感谢西安电子科技大学理学院和CORIA研究所的诸位老师。尤其感谢吴振森教授、葛德彪教授、韩香娥教授、郭立新教授等几位老师，从2002年本科开始我就是在他们的指导和感染下逐渐成长起来的。他们扎实的理论功底、严谨的治学态度以及极强的敬业精神，无不给我留下深刻的印象。还要感谢Garo Annie老师、Meunier-guttin-cluzel Siegfried老师、任宽芳老师等在学术上对我的指导和帮助，和他们的讨论让我受益匪浅。还要感谢靳亚玲老师、何安年老师、史耀媛老师、上诺曼底CROUS的Beaulieu女士等人在生活和学习上给予我无私的帮助与鼓励，有了她们的帮助才使得我的研究能够得以顺利进行。

感谢我的朋友张华永、韩国霞、崔志伟、赵文娟、韩璐、李正军、Sawitree Saengkaew、Damien Bonin、Patcharaporn Lorturn、袁怡佳、闵皆昇、刘斯倩、蒋克丽等人给予我学术及生活上的诸多帮助。

最后，我要感谢我的妻子孙毓敏对我的支持和帮助，特别是在本论文的校准上给予我很大的帮助，使得我的论文得以顺利完成。

参考文献

[1] Barber, P.W. and R.K. Chang, *Optical effects associated with small particles*. Advanced series in Applied Physics, ed. S. Ramaseshan. Vol. 1. 1988: World Scientific.

[2] Chen, G., M.M. Mazumder, R.K. Chang, et al., Laser diagnostics for droplet characterization: Application of morphology dependent resonances. Progress in Energy and Combustion Science, 1996. **22**: p. 163-188.

[3] Gouesbet, G. and G. Grehan, *Optical particle sizing: Theory and Practice*. 1988: Plenum Publishing Co.,N.Y.

[4] Quinten, M., U. Kreibig, T. Henning, et al., Wavelength-dependent optical extinction of carbonaceous particles in atmospheric aerosols and interstellar dust. Appl. Opt., 2002. **41**: p. 7102-7113.

[5] Meyer, R.A., Light scattering from red blood ghosts: sensitivity of angular dependent structure to membrane thickness and refractive index. Appl. Opt., 1977. **16**: p. 2036-2037.

[6] Frohn, A. and N. Roth, *Dynamics of Droplets*. 2000: Springer-Verlag.

[7] Lorenz, L., Lysbevaegelsen i og uden for en af plane Lysbolger belyst Kugle. Videnskabernes Selskabs Skrifter, 1890. **6**: p. 2-62.

[8] Mie, G., Beitrage zur Optik truben Medien speziell kolloidaler Metalosungen. Annalen der Physik, 1908. **25**: p. 377–452.

[9] Aden, A.L. and M. Kerker, Scattering of electromagnetic wave from concentric sphere. J. Appl. Phys., 1951. **22**: p. 1242-1246.

[10] Kerker, M., *The scattering of light and other electromagnetic radiation*. 1969, New York: Academic.

[11] Toon, O.B. and T.P. Ackerman, Algorithm for the calculation of scattering by stratified sphere. Appl. Opt., 1981. **20**: p. 3657-3660.

[12] Bohren, C.F. and D.R. Huffman, *Absorption and Scattering of Light By Small Particles*. 1983, New York: Wiley.

[13] Wu, Z.S. and Y.P. Wang, A new algorithm for electromagnetic scattering of multilayered sphere. Journal of Electronics, 1993. **10**: p. 235-242.

[14] Johnson, B.R., Light scattering by a multilayered sphere. Appl. Opt., 1996. **35**(18): p. 3286-3296.

[15] Hightower, R.L., C.B. Richardson, H.B. Lin, et al., Measurement of scattering of light from layered microspheres. Opt. Lett., 1988. **13**: p. 946-948.

[16] Ray, A.K., B. Devakottai, A. Souyri, et al., Evaporation characteristics of droplets coated with immiscible layers of nonvolatile liquids. Langmuir, 1991. **7**: p. 525-531.

[17] Kaiser, T., G. Roll, and G. Schweiger, Investigation of coated droplets in an optical trap: Raman-scattering, elastic-light-scattering and evaporation characteristics. Appl. Opt., 1996. **35**: p. 1-7.

[18] Secker, D.R., P.H. Kaye, R.S. Greenaway, et al., Light scattering from deformed droplets and droplets with inclusions. I. Experimental results. Appl. Opt., 2000. **39**: p. 5023-5030.

[19] Tu, H.H. and A.K. Ray, Investigation of concentrically and eccentrically layered droplets by light scattering. Appl. Opt., 2006. **45**(29): p. 7652-7656.

[20] Friedman, B. and J. Russek, Addition theorems for spherical waves. Quarterly of Applied Mathematics, 1954. **12**: p. 13-23.

[21] Stein, S., Addition theorems for spherical wave functions. Sylvania Electronic Systems, 1961. **XIX**(1): p. 15-24.

[22] Cruzan, O.R., Translational addition theorems for spherical vector wave functions. Quarterly of Applied Mathematics, 1962. **20**: p. 33-44.

[23] Bobbert, P.A. and J. Vlieger, Light scattering by a sphere on a substrate. Physica A, 1986. **137**: p. 209-241.

[24] Mackowski, D.W., Analysis of radiative scattering from multiple sphere configurations. Proceedings of the Royal society of London, 1991. **433**: p. 599-614.

[25] Fikioris, J.G. and N.K. Uzunoglu, Scattering from an eccentrically stratified dielectric sphere. J. Opt. Soc. Am. A, 1979. **69**: p. 1359-1366.

[26] Borghese, F., P. Denti, R. Saija, et al., Optical properties of spheres containing a spherical eccentric inclusion. J. Opt. Soc. Am. A, 1992. **9**: p. 1327-1335.

[27] Borghese, F., P. Denti, R. Saija, et al., Optical properties of spheres containing several spherical inclusions. Appl. Opt., 1994. **33**: p. 484-493.

[28] Fuller, K.A., Scattering and absorption by inhomogeneous spheres and sphere aggregates. SPIE Proc., 1993. **1862**: p. 249-257.

[29] Fuller, K.A., Morphology-dependent resonances in eccentrically stratified sphere. Opt. Lett., 1994. **19**: p. 1272-1274.

[30] Videen, G., D. Ngo, P. Chylek, et al., Light scattering from a sphere with an irregular inclusion. J. Opt. Soc. Am. A, 1995. **12**: p. 922-928.

[31] Ngo, D. and R.G. Pinnick, Suppression of scattering resonances in inhomogeneous microdroplets. J. Opt. Soc. Am. A, 1994. **11**: p. 1352-1359.

[32] Ngo, D., G. Videen, and P. Chylek, A FORTRAN code for the scattering of EM waves by a sphere with a nonconcentric spherical inclusion. Comput. Phys. Commun., 1996. **99**: p.

94-112.

[33] Lim, K. and S.S. Lee, Analysis of electromagnetic scattering from an eccentric multilayered sphere. IEEE Transactions on antennas and propagation, 1995. **43**(11): p. 1325-1328.

[34] Davis, L.W., Theory of electromagnetic beam. Phys. Rev. A, 1979. **19**: p. 1177-1179.

[35] Gouesbet, G. and G. Grehan, Sur la generalisation de la theorie de Lorenz-Mie. J. Opt. Paris, 1982. **13**(2): p. 97-103.

[36] Gouesbet, G., B. Maheu, and G. Grehan, Light scattering from a sphere arbitrarily located in a Gaussian beam, using a Bromwich formulation. J. Opt. Soc. Am. A, 1988. **5**: p. 1427-1443.

[37] Wu, Z.S., L.X. Guo, K.F. Ren, et al., Improved algorithms for electromagnetic scattering of plane waves and shaped beams by multilayered spheres. Appl. Opt., 1997. **36**(21): p. 5188-5198.

[38] Gouesbet, G., Interaction between an infinite cylinder and an arbitrary-shaped beam. Appl. Opt., 1997. **36**: p. 4292-4304.

[39] Mees, L., K.F. Ren, G. Grehan, et al., Scattering of a Gaussian beam by an infinite cylinder with arbitrary location and arbitrary orientation, numerical results. Appl. Opt., 1999. **38**: p. 1867-1876.

[40] Han, Y.P., G. Grehan, and G. Gouesbet, Generalized Lorenz-Mie theory for a spheroidal particle with off-axis Gaussian-beam illumination. Appl. Opt., 2003. **42**: p. 6621-6629.

[41] Xu, F., K.F. Ren, G. Gouesbet, et al., Generalized Lorenz-Mie theory for an arbitrary oriented, located, and shaped beam scattered by homogeneous spheroid. J. Opt. Soc. Am. A, 2007. **24**: p. 119-131.

[42] Ren, K.F., G. Grehan, and G. Gouesbet, Evaluation of laser-sheet beam shape coefficients in generalized Lorenz-Mie theory by use of a localized approximation. J. Opt. Soc. Am. A, 1994. **11**(7): p. 2072-2079.

[43] Barton, J.P., Electromagnetic-field calculation for a sphere illuminated by a higher-order Gaussian beam. I. Internal and near-field effect. Appl. Opt., 1997. **36**: p. 1303-1311.

[44] Khaled, E.E.M., S.C. Hill, and P.W. Barber, Internal electric energy in a spherical particle illuminated with a plane wave or off-axis Gaussian beam. Appl. Opt., 1994. **33**: p. 524-532.

[45] Gouesbet, G. and G. Grehan, Generalized Lorenz-Mie theory for a sphere with an eccentrically located spherical inclusion. J. Mod. Optic., 2000. **47**: p. 821-837.

[46] Han, G.X., Study on the interaction of arbitrarily incident Gaussian beam with eccentric sphere and bi-sphere, in *School of Science*. 2009, *Xidian University*: Xi'an.

[47] Han, G.X. and Y.P. Han, Radiation force of a sphere with an eccentric inclusion illuminated by a laser beam. ACTA Physica SINICA, 2009. **58**: p. 6167-6173.

[48] Yan, B., X.E. Han, and K.F. Ren, Scattering of a shaped beam by a spherical particle with an

eccentric spherical inclusion. J. Opt. A: Pure Appl. Opt., 2009. **11**(1): p. 015705.

[49] Yan, B. and X.E. Han, Radiation trapping forces acting on eccentric sphere in Gaussian beam ACTA Optica Sinica, 2009. **29**(6): p. 1691-1696.

[50] Asano, S. and G. Yamamoto, Light scattering by a spheroid particle. Appl. Opt., 1975. **14**: p. 29-49.

[51] Asano, S., Light scattering properties of spheroidal particles. Appl. Opt., 1979. **18**: p. 712-723.

[52] Barton, J.P., Internal and near-surface electromagnetic fields for a spheroidal particle with arbitrary illumination. Appl. Opt., 1995. **34**: p. 5542-5551.

[53] Barton, J.P., Internal and near-surface electromagnetic fields for an absorbing spheroidal particle with arbitrary illumination. Appl. Opt., 1995. **34**: p. 6471-8473.

[54] Han, Y.P. and Z.S. Wu, The expansion coefficients of a spheroidal particle illuminated by Gaussian beam. IEEE Transactions on Antennas and Propagation, 2001. **49**: p. 615-620.

[55] Han, Y.P., Scattering of a spheroidal particle illuminated by Gaussian beam, in *School of Science*. 2000, *Xidian Univerisity*: Xi'an.

[56] Zhang, H.Y. and Y.P. Han, Scattering by a confocal multilayered spheroidal particle illuminated by an axial Gaussian beam. IEEE Transactions on antennas and propagation, 2005. **53**: p. 1514-1518.

[57] Xu, F., J.A. Lock, G. Gouesbet, et al., Radiation torque exerted on a spheroid: analytical solution. Phys. Rev. A, 2008. **78**: p. 013843.

[58] Xu, F., J.A. Lock, and C. Tropea, Debye series for light scattering by a spheroid. J. Opt. Soc. Am. A, 2010. **27**(4): p. 671-686.

[59] Mishchenko, M.I., J.W. Hovenier, and L.D. Travis, *Light scattering by nonspherical particles : theory, measurements, and applications*. 2000: Academic Press.

[60] Doicu, A., T. Wriedt, and Y.A. Eremin, *Light Scattering by Systems of Particles. Null-Field Method with Discrete Sources: Theory and Programs*. 2006: Springer Science+Business Media, New York, USA.

[61] Schuh, R. and T. Wriedt, Computer programs for light scattering by particles with inclusions. J. Quant. Spectrosc. Radiat. Transfer, 2001. **70**: p. 715-723.

[62] Waterman, P.C., Symmetry, unitarity and geometry in electromagnetic scattering. Phys. Rev. , 1971. **3**: p. 825-839.

[63] Mishchenko, M.I., Light scattering by size-shape distributions of randomly oriented axially symmetric particles of a size comparable to a wavelength. Appl. Opt., 1993. **32**(24): p. 4652-66.

[64] Wielaard, D.J., M.I. Mishchenko, A. Macke, et al., Improved T-matrix computations for

large, nonabsorbing and weakly absorbing nonspherical particles and comparison with geometrical-optics approximation. Appl. Opt., 1997. **36**(18): p. 4305-4313.

[65] Hackman, R.H., Development and application of the spheroidal coordinate based T matrix solution to elastic wave scattering. Radio Science, 1994. **29**: p. 1035-1049.

[66] Schulz, F.M., K. Stamnes, and J.J. Stamnes, Scattering of electromagnetic wave by spheroidal particles: a novel approach exploiting the T matrix computed in spheroidal coordinates. Applied Optics, 1998. **37**: p. 7875-7896.

[67] Mishchenko, M.I., Light scattering by randomly oriented axially symmetric particles. J. Opt. Soc. Am. A, 1991. **8**(6): p. 871-882.

[68] Mishchenko, M.I. and L.D. Travis, Capabilities and limitations of a current fortran implementation of the T-matrix method for randomly oriented, rotationally symmetric scatterers. J. Quant. Spectrosc. Radiat. Transfer, 1998. **60**(3): p. 309-324.

[69] Skaropoulos, N.C. and H.W. Russchenberg, Light scattering by arbitrarily oriented rotationally symmetric particles. J. Opt. Soc. Am. A, 2002. **19**(8): p. 1583-91.

[70] Gouesbet, G., J.J. Wang, and Y.P. Han, Transformations of spherical beam shape coefficients in generalized Lorenz-Mie theories through rotations of coordinate systems. I. General formulation. Opt. Commun., 2010. **283**: p. 3218-3225.

[71] Wang, J.J., G. Gouesbet, and Y.P. Han, Transformations of spherical beam shape coefficients in generalized Lorenz-Mie theories through rotations of coordinate systems. II. Axisymmetric beams. Opt. Commun., 2010. **283**: p. 3226-3234.

[72] Gouesbet, G., J.J. Wang, and Y.P. Han, Transformations of spherical beam shape coefficients in generalized Lorenz-Mie theories through rotations of coordinate systems. III. Special Euler angles. Opt. Commun., 2010. **283**: p. 3235-3243.

[73] Gouesbet, G., J.A. Lock, J.J. Wang, et al., Transformations of spherical beam shape coefficients in generalized Lorenz-Mie theories through rotations of coordinate systems. V. Localized beam models. Opt. Commun., 2011. **284**: p. 411-417.

[74] Gouesbet, G., J.J. Wang, Y.P. Han, et al., Transformations of spherical beam shape coefficients in generalized Lorenz-Mie theories through rotations of coordinate systems. IV. Plane waves. Opt. Commun., 2011. **283**: p. 3244-3254.

[75] Wang, J.J., G. Gouesbet, Y.P. Han, et al., Study of scattering from a sphere with an eccentrically located spherical inclusion by generalized Lorenz-Mie theory: internal and external field distribution. J. Opt. Soc. Am. A, 2011. **28**: p. 24-39.

[76] Wang, J.J., G. Gouesbet, G. Grehan, et al., Morphology-dependent resonances in an eccentrically layered sphere illuminated by a tightly focused off-axis Gaussian beam: parallel and perpendicular beam incidence. J. Opt. Soc. Am. A 2011. **28**: p. 1849-1859.

[77] Wang, J.J., G. Gréhan, Y.P. Han, et al., Numerical study of global rainbow technique: sensitivity to non-sphericity of droplets. Experiments in Fluids, 2011. **51**: p. 149-159.

[78] Leung, E., C.P. Lee, and N. Jacobi, Resonance frequency shift of and acoustic chamber containing a rigid sphere. J. Acoutic. Soc. Am., 1982. **72**: p. 615-620.

[79] Curzon, F.L. and D. Plant, Using perturbed resonance frequencies to study eigenmodes of an acoustic resonator. Am. J. Phys., 1986. **54**: p. 367-372.

[80] Xu, D.L., X.M. Wang, Y.J. Song, et al., Acoustic resonance calculation of spherical resonance cavity caused by an eccentric sphere. Journal of Daqing Petroleum Institute, 2002. **26**(1): p. 18-20.

[81] Hasheminejad, S.M. and Y. Mirzaei, Exact 3D elasticity solution for free vibrations of eccentric hollow sphere. Journal of Sound and Vibration, 2010. **330**: p. 229-244.

[82] Mees, L., G. Gouesbet, and G. Grehan, Transient internal and scattered fields from a multi-layered sphere illuminated by a pulsed laser. Opt. Commun., 2009. **282**: p. 4189-4193.

[83] Han, Y.P., L. Mees, K.F. Ren, et al., Far scattered field from a spheroid under a femtosecond pulsed illumination in a generalized Lorenz-Mie theory framework. Opt. Commun., 2004. **231**: p. 71-77.

[84] Gouesbet, G. and G. Grehan, *Generalized Lorenz-Mie Theories*. 2011: Springer.

[85] Barton, J.P., D.R. Alexander, and S.A. Schaub, Internal and near-surface electromagnetic fields for a spherical particle irradiated by a focused laser beam. J. Appl. Phys., 1988. **64**: p. 1632-1639.

[86] Lock, J.A. and G. Gouesbet, Generalized Lorenz-Mie theory and applications. J. Quant. Spectrosc. Radiat. Transfer, 2009. **110**: p. 800-807.

[87] Stratton, J.A., *Electromagnetic theory*. 1941: New-York, London: McGraw-Hill Book Company.

[88] Edmonds, A.R., *Angular momentum in quantum mechanics*. 1957: Princeton University Press.

[89] Chew, W.C., *Waves and Field in Inhomogeneous Media*. 1990: IEEE Press.

[90] Bruning, J.H. and Y.T. Lo, Multiple scattering of EM waves by spheres part I: multipole expansion and ray optical solution. IEEE Transactions on antennas and propagation, 1971. **19**: p. 378-390.

[91] Bruning, J.H. and Y.T. Lo, Multiple scattering of EM waves by spheres part II: numerical and experimental results. IEEE Transactions on antennas and propagation, 1971. **19**: p. 391-400.

[92] Tsang, L., J.A. Kong, and R.T. Shin, *Theory of Microwave Remote Sensing* 1985, New York: John Wiley & Sons.

[93] Xu, Y.L., Calculation of the addition coefficients in electromagnetic multisphere scattering theory. Journal of Computational Physics, 1996. **127**: p. 285-298.

[94] Xu, Y.L., Efficient evaluation of vector translation coefficients in multiparticle light scattering theories. Journal of Computational Physics, 1997. **139**: p. 137-165.

[95] Gouesbet, G., G. Grehan, and B. Maheu, Computations of the gn coefficients in the generalized Lorenz-Mie theory using three different methods. Appl. Opt., 1988. **27**: p. 4874-4883.

[96] Gouesbet, G., Partial-wave expansions and properties of axisymmetric light beams. Appl. Opt., 1996. **35**(9): p. 1543-1555.

[97] Gouesbet, G., J.A. Lock, and G. Grehan, Generalized Lorenz-Mie theories and description of electromagnetic arbitrary shaped beams: localized approximations and localized beam models. Journal of Quantitative Spectroscopy and Radiative Transfer, 2011. **12**: p. 1-27.

[98] Ren, K.F., G. Gouesbet, and G. Grehan, Integral Localized Approximation in Generalized Lorenz-Mie Theory. Appl. Opt., 1998. **37**(19): p. 4218-4225.

[99] Doicu, A. and T. Wriedt, Computation of the beam-shape coefficients in the generalized Lorenz-Mie theory by using the translational addition theorem for spherical vector wave functions. Appl. Opt., 1997. **36**(13): p. 2971-2978.

[100] Zhang, H.Y. and Y.P. Han, Addition theorem for the spherical vector wave functions and its application to the beam shape coefficients. J. Opt. Soc. Am. B, 2008. **25**(2): p. 255-260.

[101] Gouesbet, G., G. Grehan, and B. Maheu, Localized interpretation to compute all the coefficients gmn in the generalized Lorenz-Mie theory. J. Opt. Soc. Am. A, 1990. **7**(6): p. 998-1007.

[102] Lock, J.A. and G. Gouesbet, Rigorous justification of the localized approximation to the beam-shape coefficients in generalized Lorenz-Mie theory. I. On-axis beams. J. Opt. Soc. Am. A, 1994. **11**(9): p. 2503-2515.

[103] Gouesbet, G. and J.A. Lock, Rigorous justification of the localized approximation to the beam-shape coefficients in generalized Lorenz-Mie theory. II. Off-axis beams. J. Opt. Soc. Am. A, 1994. **11**(9): p. 2516-2525.

[104] Ren, K.F., G. Grehan, and G. Gouesbet, Localized Approximation of Generalized Lorenz-Mie Theory: Faster algorithm for computations of beam shape coefficients. Part. Part. Syst. Char., 1992. **9**(1-4): p. 144-150.

[105] Yan, B., X.e. Han, K.F. Ren, et al., Light scattering of Gaussian beam from an eccentrically stratified dielectric sphere and application. ACTA Photonica Sinica, 2009. **38**(5): p. 1268-1273.

[106] Han, G.X., Y.P. Han, J.Y. Liu, et al., Scattering of an eccentric sphere arbitrarily located in a

shaped beam. J. Opt. Soc. Am. B, 2008. **25**(12): p. 2064-2072.

[107] Videen, G., W. Sun, Q. Fu, et al., Light scattering from deformed droplets and droplets with inclusions. II. Theoretical treatment. Appl. Opt., 2000. **39**: p. 5031-5039.

[108] Prabhu, D.R., M. Davies, and G. Videen, Light scattering calculations from oleic-acid droplets with water inclusions. Optics Express, 2001. **8**(6): p. 308-313.

[109] Gouesbet, G., S.M. Guttin-Cluzel, and G. Grehan, Periodic orbits in Hamiltonian chaos of the annular billiard. Phys. Rev. E, 2001. **65**: p. 016212.

[110] Gouesbet, G., S.M. Guttin-Cluzel, and G. Grehan, Morphology-dependent resonances and/or whispering gallery modes for a two-dimensional dielectric cavity with an eccentrically located circular inclusion, a Hamiltonian point of view with Hamiltonian (optical) chaos. Opt. Commun., 2002. **203**: p. 223-242.

[111] Rao, V.S.C.M., Gupta, and S. Dutta, Broken azimuthal degeneracy with whispering gallery modes of microspheres. J. Opt. A: Pure Appl. Opt., 2005. **7**: p. 279-285.

[112] Essien, M., R.L. Armstrong, and J.B. Gillespie, Lasing emission from an evaporating layered microdroplet. Opt. Lett., 1993. **18**(10): p. 762-4.

[113] Barber, P.W. and S.C. Hill, *Light scattering by particles: computational methods*. Advanced Series in Applied Physics, v. 2. 1990: World Scientific. 261.

[114] Spillane, S.M., T.J. Kippenberg, and K.J. Vahala, Ultralow-threshold Raman laser using a spherical dielectric microcavity. Nature, 2002. **415**: p. 621-623.

[115] Ashkin, A. and J.M. Dziedzic, Observation of resonances in the radiation pressure on dielectric spheres. Phys. Rev. Lett, 1977. **38**: p. 1351-1354.

[116] Chylek, P., J.T. Kiehl, and M.K.W. Ko, Optical levitation and partial-wave resonance. Phys. Rev. A, 1978. **18**: p. 2229-2233.

[117] Ducastel, J., Etude des resonances morphologiquement dependantes et application a la caracterisation de microparticules en milieu diphasique. 2007, *Institut National des Sciences Appliquees de Rouen, FRANCE*.

[118] Chylek, P., B. Ramaswamy, A. Ashkin, et al., Simultaneous determination of refractive index and size of spherical dielectric particles from light scattering data. Appl. Opt., 1983. **22**: p. 2302-2307.

[119] Tzeng, H.M., K.F. Wall, M.B. Long, et al., Evaporation and condensation rates of liquid droplets deduced from structure resonances in the fluorescence spectra. Opt. Lett., 1984. **9**: p. 273-275.

[120] Han, Y.P., L. Mees, G. Gouesbet, et al., Resonant spectra of a deformed spherical microcavity. J. Opt. Soc. Am. B, 2006. **23**: p. 1390-1397.

[121] Mishchenko, M.I. and A.A. Lacis, Morphology-dependent resonances of nearly spherical

particles in random orientation. Appl. Opt., 2003. **20**: p. 5551-5556.

[122] Chen, G., R.K. Chang, S.C. Hill, et al., Frequency splitting of degenerate spherical cavity mode: stimulated Raman scattering spectrum of deformed droplets. Opt. Lett., 1991. **16**: p. 1269-1271.

[123] Leung, P.T., S.W. Ng, and K.M. Pang, Morphology-dependent resonances in dielectric spheres with many tiny inclusions. Opt. Lett., 2002. **27**: p. 1749-1751.

[124] Huang, Y.-Z., K.-J. Che, Y.-D. Yang, et al., Directional emission InP/GaInAsP square-resonator microlasers. Opt. Lett., 2008. **33**(19): p. 2170-2172.

[125] Gouesbet, G., S.M. Guttin-Cluzel, and G. Grehan, Generalized Lorenz-Mie Theory for a Sphere with an Eccentrically Located Inclusion, and Optical Chaos. Part. Part. Syst. Char., 2001. **18**: p. 190-195.

[126] Mazumder, M.M., S.C. Hill, and P.W. Barber, Morphology-dependent resonances in inhomogeneous spheres: comparison of the layered T-matrix method and the time-independent perturbation method. J. Opt. Soc. Am. A, 1992. **9**: p. 1844-1853.

[127] Khaled, E.E.M., S.C. Hill, P.W. Barber, et al., Near-resonance excitation of dielectric spheres with plane waves and off-axis Gaussian beams. Appl. Opt., 1992. **31**(9): p. 1166-1169.

[128] Khaled, E.E.M., S.C. Hill, and P.W. Barber, Light scattering by a coated sphere illuminated with a Gaussian beam. Appl. Opt., 1994. **33**: p. 3308-3314.

[129] Novick, V.J., Use of series light extinction cells to determine aerosol number concentration. Aerosol Science and Technology, 1988.

[130] Hu, K., J.J. Wang, and Y.P. Han. *Measurement of soot concentration by light extinction method*. in *The Sixth Northwest Academic Conference on Computational Physics, China*. 2008.

[131] Durst, F., A. Melling, and J.H. Whiteiaw, *Principles and Practice of Laser Dropper Anemometry*. 1976, New York: Academic Presss.

[132] van Beeck, J.P. and M.L. Riethmuller, Rainbow phenomena applied to the measurement of droplet size and velocity and to the detection of nonsphericity. Appl. Opt., 1996. **35**(13): p. 2259-66.

[133] Hom, J. and N. Chigier, Rainbow refractometry: simultaneous measurement of temperature, refractive index, and size of droplets. Appl. Opt., 2002. **41**(10): p. 1899-907.

[134] Saengkaew, S., G. Godard, J.B. Blaisot, et al., Experimental analysis of global rainbow technique: sensitivity of temperature and size distribution measurements to non-spherical droplets. Exp. Fluids, 2009. **47**: p. 839-848.

[135] van Beeck, J.P., T. Grosges, and M.G. De Giorgi, Global rainbow thermometry assessed by Airy and Lorenz-Mie theories and compared with phase Doppler anemometry. Appl. Opt.,

2003. **42**(19): p. 4016-22.

[136] Bertoli, C. and C.M. Migliaccio, A finite conductivity model for diesel spray evaporation computations. Int. J. Heat and Fluid Flow, 1999. **20**: p. 552-561.

[137] Castanet, G., M. Lebouche, and F. Lemoine, Heat and mass transfer of combustiing monodisperse droplets in a linear stream. Int. J. Heat Mass Transfer, 2005. **48**: p. 3261-3275.

[138] van Beeck, J.P., D. Giannoulis, L. Zimmer, et al., Global rainbow thermometry for droplet-temperature measurement. Opt. Lett., 1999. **24**(23): p. 1696-8.

[139] Wilms, J., Global rainbow refractometry with a selective imaging method. Part. Part. Syst. Char., 2008. **25**: p. 39-48.

[140] Havemann, S. and A.J. Baran, Extension of T-matrix to scattering of electromagnetic plane waves by non-axisymmetric dielectric particles: application to hexagonal ice cylinders. Journal of Quantitative Spectroscopy and Radiative Transfer, 2000. **70**: p. 139-158.

[141] Nieminen, T.A., N.R. Hechenberg, and H.R. Dunlop. *Computational modelling of optical tweezers*. in *Proc. SPIE*. 2004.

[142] Kahnert, F.M., J.J. Stamnes, and K. Stamnes, Application of the extended boundary condition method to particles with sharp edges: a comparison of two surface integration approaches. Appl. Opt., 2001. **40**(18): p. 3101-9.

[143] Laitinen, H. and K. Lumme, T-matrix method for general star-shaped particles: first results. J. Quant. Spectrosc. Radiat. Transfer, 1998. **60**(3): p. 325-334.

[144] van de Hulst, H.C., *Light Scattering by Small Particles*. 1982: Peter Smith Pub Inc.

[145] Van Beeck, J.P., Rainbow phenomena: development of a laser-based, non-intrusive technique for measuring droplet size, temperature and velocity. 1997, *Technische Universiteit Eindhoven*.

[146] Han, X.E., Study of refractometry of rainbow and applications to the measurement of instability and temperature gradient of a liquid jet. 2000, *Universite de Rouen*: Rouen.

[147] Roth, N., K. Anders, and A. Frohn. *Simultaneous measurement of temperature and size of droplets in the micrometric range*. in *7th International Congress on Optical in Flow and Particle Diagnostic*. 1988. U.S.A.

[148] Roth, N., K. Anders, and A. Frohn, Simultaneous measurement of temperature and size of droplets in the micrometric range. Journal of Laser Applications, 1990. **2**: p. 37-42.

[149] Walker, J.D., Multiple rainbows from single drops of water and other liquids. Am. J. Phys., 1976. **44**: p. 421-433.

[150] Anders, K., N. Roth, and A. Frohn. *Theoretical and experimental studies of the influence of internal temperature gradients on rainbow refractometry*. in *4th International Congress on Optical Particle Sizing*. 1995. Germany.

[151] Saengkaew, S., Development of novel Global rainbow technique for characterizing spray generated by ultrasonic nozzle. 2005, *Universite de Rouen*.

[152] Han, Y.P., L. Mees, K.F. Ren, et al., Scattering of light by spheroids: the far field case. Opt. Commun., 2002. **210**(1-2): p. 1-9.

[153] Jiang, H.F., On Characteristics of Light Scattering by Inhomogeneous Particles and Measurement of Refractive Index Profile, in *School of Science*. 2007, *Xidian University*: Xi'an.

[154] Saengkaew, S., T. Charinpanitkul, H. Vanisri, et al., Rainbow refractrometry on particles with radial refractive index gradients. Experiments in Fluids, 2007. **43**(4): p. 595-601.

[155] Marston, P.L., Cusp diffraction catastrophe from spheroids: generalized rainbows and inverse scattering. Opt. Lett., 1985. **10**(12): p. 588-590.

[156] Li, X.Z. and X.e. Han, Rainbow angle analysis of a homogeneous spheroid. Journal of Xidian University, 2010. **37**(4): p. 731-736.

[157] Vetrano, M.R., J.P. van Beeck, and M.L. Riethmuller, Global rainbow thermometry: improvements in the data inversion algorithm and validation technique in liquid-liquid suspension. Appl. Opt., 2004. **43**(18): p. 3600-7.

[158] Han, Y.P., Y. Zhang, H.Y. Zhang, et al., Scattering of typical particles by beam shape in oblique illumination. J. Quant. Spectrosc. Radiat. Transfer, 2009. **110**: p. 1375-1381.

[159] Harvey, A.H., J.S. Gallagher, and J. Sengers, Revised formulation for the refractive index of water and stream as a function of wavelength, temperature and density. J. Phys. Chem. Ref. Data, 1998. **27**: p. 761-774.

攻读博士期间从事的科研项目及发表的文章

一． 参加的科研项目

中法合作项目：中法联合培养博士研究生项目，法国驻华大使馆资助

项目名称：“Optical characterization of shape and thermo-chemical composition of biodiesel droplets in flames”

(2008－2011)

中国：国家自然科学基金面上项目(No.60771039)

项目名称：“光镊中光势阱的研究”

(2008－2010)

中国教育部“新世纪优秀人才支持计划”(NECT－04－0949)

项目名称：“脉冲激光器在线探测非球形颗粒尺寸和浓度”

(2005－2007)

法国：欧盟区域发展基金项目

项目名称：“Interreg Iva-C5: Cross-Chanel Center for Low Carbon Combustion”

(2009－2012)

二． 攻读博士期间已投及已发表的论文

1. **J.J. Wang**, G. Gouesbet, G. Gréhan, Y.P. Han, S. Saengkaew. Morphology-dependent resonances in an eccentrically layered sphere illuminated by a tightly focused Gaussian beam, JOSA A. Vol.28, pp1849-1859, (2011)
2. **J.J. Wang**, G. Gréhan, Y.P. Han, S. Saengkaew, G. Gouesbet. Numerical study of global rainbow technique: sensitivity to non-sphericity of droplets, Experiments in Fluids, Vol.51, pp.149-159 DOI: 10.1007/s00348-010-1036-4, (2011)
3. **J.J. Wang**, G. Gouesbet, Y.P. Han, G. Gréhan. A study of scattering from a sphere with an eccentrically located spherical inclusion by generalized Lorenz-Mie theory. Internal and External field distribution, JOSA A. Vol. 28. pp. 24-39 (2011)
4. **J.J. Wang**, G. Gouesbet, Y.P. Han. Transformations of spherical beam shape coefficients in generalized Lorenz-Mie theories through rotations of coordinate systems. II. Axisymmetric beams, Optics Communication. Vol. 283. pp.

3226-3234 (2010)

5. G. Gouesbet, **J.J. Wang**, Y.P. Han. Transformations of spherical beam shape coefficients in generalized Lorenz-Mie theories through rotations of coordinate systems. I. General formulation. Optics Communication. Vol. 283. pp. 3218-3225 (2010)
6. G. Gouesbet, **J.J. Wang**, Y.P. Han. Transformations of spherical beam shape coefficients in generalized Lorenz-Mie theories through rotations of coordinate systems. III Special Euler angles. Optics Communication. Vol. 283. pp. 3235-3243 (2010)
7. G. Gouesbet, **J.J. Wang**, Y.P. Han. Transformations of spherical beam shape coefficients in generalized Lorenz-Mie theories through rotations of coordinate systems. IV. Plane waves. Optics Communication. Vol. 283. pp. 3244-3254 (2010)
8. G. Gouesbet, J.A. Lock, **J.J. Wang**, G. Gréhan. Transformations of spherical beam shape coefficients in generalized Lorenz-Mie theories through rotations of coordinate systems. V. localized beam models. Optics Communication. Vol. 284. pp. 411-417 (2011)
9. 胡坤，**汪加洁**，韩一平，“消光法对煤烟粒子浓度的研究”；第六届西北地区计算物理学术会议(2008)

Morphology-dependent resonances in an eccentrically layered sphere illuminated by a tightly focused off-axis Gaussian beam: parallel and perpendicular beam incidence

J. J. Wang,[1,2,*] G. Gouesbet,[1] G. Gréhan,[1] Y. P. Han,[2] and S. Saengkaew[1]

[1]*Laboratoire d'Electromagnétisme des Systèmes Particulaires (LESP), Unité Mixte de Recherche (UMR) 6614 du Centre National de la Recherche Scientifique (CNRS), COmplexe de Recherche Interprofessionnel en Aérothermochimie (CORIA), Université de Rouen, et Institut National des Sciences Appliquées (INSA) de Rouen, BP12, avenue de l'université, technopôle du Madrillet, 76801 Saint-Etienne-du Rouvray, France*

[2]*School of Science, Xidian University, 710071 Xi'an, China*

**Corresponding author: jiajie.wang@coria.fr*

Received May 24, 2011; accepted July 13, 2011;
posted July 18, 2011 (Doc. ID 148104); published August 22, 2011

Following the recent results in generalized Lorenz–Mie theory concerning the description of an arbitrary shaped electromagnetic beam propagating in an arbitrary orientation, a theoretical investigation of morphology-dependent resonances (MDRs) excited in a sphere with an eccentrically located spherical inclusion illuminated by a tightly focused Gaussian beam is presented. Calculations of extinction efficiency spectra and backward-scattering intensity spectra are made for different locations and radii of the inclusion with respect to the host sphere. Exemplifying field distributions inside of the scatterer under both off-resonance and on-resonance conditions are exhibited. The influences of the relative size of the inclusion with respect to the host sphere and of the separation distance between the two sphere centers on the positions and on the amplitudes of the MDRs peaks are studied. As are the cases for spheres and concentrically multilayered spheres, the resonance positions of MDRs in an eccentrically layered sphere are located at the same size parameter for Gaussian beam illumination and for plane-wave illumination. In contrast with the lift of azimuthal modes m degeneracy in MDR peaks for an eccentric sphere illuminated obliquely by a plane wave, we display a kind of lift that cannot be observed in extinction efficiency spectra with an oblique illumination of a tightly focused Gaussian beam. Nevertheless, asymmetric distributions of the internal field inside of the eccentric sphere at resonance conditions are observed both with an oblique illumination of a tightly focused beam and with an oblique illumination of a plane-wave illumination. Interpretation from a perspective of the localization principle is applied to the simulation results.

OCIS codes: 260.2110, 140.3430.

1. INTRODUCTION

Morphology-dependent resonances (MDRs) generated by a spherical surface are believed to be first described by Lord Rayleigh a century ago, but only after the invention of laser did they start to have more scientific relevance, and it is only during the past three decades that there has been a substantial move toward extensive practical applications. MDRs were first observed in radiation pressure experiments on dielectric spheres while levitating a droplet by a tightly focused laser beam [1]. Numerical simulations carried out with high resolution by using the Mie–Debye theory were given very soon after [2], and remarkable agreement with the experimental observations of MDRs was shown. Because of the fact that the positions and the widths of MDRs are highly sensitive to the size parameter and to the refractive index of the scatterers (in particular droplets), MDR-related optical techniques, based on the properties of MDR peaks in elastic scattering spectra [3] or in inelastic scattering spectra [4], were introduced to detect various properties of droplets. With extensive investigations in the past decades [5,6], a reliable optical tool for optical particle characterization is now available. Relying on the precise measurement of the positions and of the widths of the MDR peaks by high-resolution spectroscopy, absolute sizes of spheres can be obtained to a precision of 1 part in 10^5. By measuring the wavelength shift of MDR peaks in the scattering spectrum, evaporation and condensation rates of droplets can be obtained.

MDRs in a dielectric sphere have been studied extensively for both plane-wave illumination and Gaussian beam illumination. They exhibit themselves in the form of sharp spikelike features in the plots of various scattering characteristics versus size parameter. Recalling the MDR labeling convention, one resonance excited in a homogeneous sphere can be identified by its state of polarization and by three so-called quantum numbers l, n, and m. The mode order l is associated with the radial function and indicates the number of intensity peaks in the radial distribution of the field inside of the sphere. The mode number n is one of the classical quantization numbers for the angular momentum, which coincides with half the number of intensity maxima along the perimeter of the sphere. For a perfect sphere, there is no particular quantization axis, which leads to the fact that the resonance frequencies do not depend on mode m, therefore corresponding to a degeneracy in m for the resonances. Nevertheless, the degeneracy in m

mode can be lifted by a nonconcentric perturbation inside of the scatterer [6–9] or by a deformation in the outer surface of the particle [10–12].

The present study is more particularly devoted to the analysis of the influence of a perturbation inside the particle on MDR properties. More specifically, the scattering model of a sphere with an eccentrically located spherical inclusion is studied in this paper, a geometry that has also been analyzed by several groups. Indeed, as we know, the analysis of MDR properties has attracted much attention particularly because the MDRs can significantly enhance internal field intensities with ultrahigh quality factors (Qs) of MDRs that can reach 10^8, enabling nonlinear optical processes such as fluorescence, stimulated Raman scattering (SRS), and stimulated Brillouin scattering (SBS) to occur in droplets with a relatively low level of pumping power. Nevertheless, such high Qs of MDRs can be greatly influenced by nonconcentric perturbation inside of the droplet. Numerous interesting observations, such as spectral line broadening and laser emission, have been reported. In the analysis of resonance locations and Qs of MDRs in an inhomogeneous sphere with a small perturbation in refractive index carried out by Mazumder *et al.* [13], an increase in the refractive index in a nonconcentric spherical region inside the larger sphere leading to a decrease of resonance frequencies was reported. Fuller [14] discovered that a spectral shift of the resonance peak might be brought up when the inclusion is located in the forward hot spot of the host sphere. Furthermore, predicted by Leung *et al.* [8], MDRs in a dielectric sphere with many tiny inclusions may split into multiplets because of the loss of spherical symmetry and manifest themselves as broadened spectral lines in the scattering cross section. Similar results were also presented by Rao *et al.* [9] in considering a system of an inclusion sphere embedded in a larger sphere.

Because of the fact that all of the previous theoretical analysis of MDR behaviors in a host sphere containing an eccentric spherical inclusion (in short, an eccentric sphere, with variants) was carried out in the case of plane-wave illumination, our motivation in this paper is to study the properties of MDRs excited in an eccentric sphere with illumination by a tightly focused Gaussian beam. This scattering model under study is of great interest because, when the inclusion inside of the host sphere approaches the rim of the host sphere, then, on one hand, some MDRs may be suppressed or even annihilated by the embedded inclusion resulting in a loss of the high Qs, which may block the phenomena of SRS, SBS, and so on. But, on the other hand, some MDRs might be extensively enhanced due to the complex optical interaction between the spherical inclusion and the host sphere, which form a dielectric annular billiard, which can possibly be used as a quantum chaotic model of a micro-optical resonator [15,16]. Under favorable circumstances, these highly enhanced MDRs can be manipulated to realize an efficient coupling to the external medium in a specific orientation, leading to potential practical applications in novel light transition devices, compact laser cavities, high-sensitivity biosensors as well as microparticle characteristics [17,18].

Within the framework of the generalized Lorenz–Mie theory (GLMT), the scattering problem of an eccentric sphere illuminated by an arbitrary shaped beam was originally studied by Gouesbet and Gréhan [19], however, only in a formal way, without any numerical results. Numerical results for far-zone field distribution were given later by Han *et al.* [20] and Yan *et al.* [21]. By virtue of the recent theoretical results in the GLMT concerning the description of an arbitrary shaped beam in an arbitrary orientation [22–26], numerical results for spatial distributions of external and internal fields under off-resonance conditions have been recently presented [27]. In the present paper, the properties of MDRs excited in an eccentric sphere under illumination by tightly focused beams are studied. Corresponding results for plane-wave illumination are also presented for the sake of comparison. These calculations will provide insights for the understanding of previously reported experimental observations as well as providing guidelines for future experiments in biological observation and particle characterization.

The body of the present paper is organized as follows. In Section 2, we briefly present a theoretical treatment for the scattering problem of an eccentric sphere illuminated by an arbitrary shaped electromagnetic beam in an arbitrary orientation in the framework of the GLMT. In Section 3, a tightly focused Gaussian beam in the fundamental mode (TEM_{00}) is specifically considered for numerical illustration. The behaviors of MDRs excited in an ethanol sphere with a glass inclusion are analyzed under parallel and oblique illuminations of an off-axis Gaussian beam. Some results and discussions are summarized in Section 4, which also serves as a conclusion.

2. THEORETICAL ANALYSIS BY THE GLMT

A. Definition of the Problem

The geometry of the specific scattering problem under study is illustrated in Fig. 1. The host sphere is attached to a global Cartesian coordinate system $(O_1X_1Y_1Z_1)$, and its corresponding spherical coordinates are designated as $(r_1, \theta_1, \varphi_1)$. A spherical inclusion is embedded in the host sphere. It is attached to an inclusion coordinate system $(O_2X_2Y_2Z_2)$ whose corresponding spherical coordinates are designated as $(r_2, \theta_2, \varphi_2)$. The three axes in the inclusion coordinate

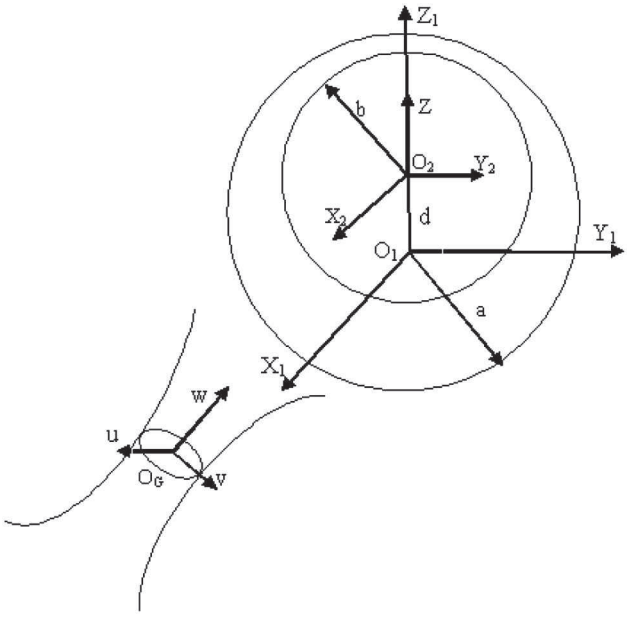

Fig. 1. Scattering geometry of the problem under study.

system are parallel to the corresponding axes in the global coordinate system, respectively.

Without any loss of generality, the center of the inclusion is located on the z axis of the global coordinate system. The center–center separation distance being designated by d, we have

$$x_2 = x_1, \qquad y_2 = y_1, \qquad z_2 = z_1 - d. \tag{1}$$

The radii of the host sphere and of the inclusion are a and b, respectively. The complex refractive index and wavenumber of the surrounding medium are m_0 and k_0, respectively. The corresponding parameters for the host sphere are m_1 and k_1 and for the inclusion m_2 and k_2.

The scattering model in Fig. 1 is illuminated by an arbitrary shaped beam propagating along the w axis in the beam coordinate system $OgUVW$. The coordinates of its origin Og with respect to the global coordinate system $(O_1X_1Y_1Z_1)$ are denoted as (x_0, y_0, z_0). The frame system $(O_1X_1Y_1Z_1)$ can be obtained from the beam coordinate system (O_gUVW) by rotations through Euler angles (α, β, γ) [22–26] followed by a translation of (x_0, y_0, z_0) and vice versa. The time-dependence factor reading as $\exp(jwt)$ is assumed, where w is the angular frequency. This term will be omitted from all formulae for the sake of conciseness.

B. Solutions

As already mentioned, the theoretical treatment to the scattering of a sphere with an eccentrically located spherical inclusion illuminated by an arbitrary shaped beam was originally presented by Gouesbet and Gréhan [19]. Afterward, Han *et al.* [20] and Yan *et al.* [21] also studied this problem and analyzed the scattered field in the far zone. Both the external field and internal field intensity distributions at off-resonance conditions were very recently presented by Wang *et al.* [27]. Therefore, we will not focus on these derivations but only recall some expressions useful for the sequel.

In the global coordinate system, an arbitrary shaped beam in an arbitrary orientation illuminating the host sphere may be expressed in terms of vector spherical wave functions (VSWFs) with two sets of expansion coefficients a_{nm} and b_{nm} according to

$$\mathbf{E}^{\text{inc}} = \sum_{n=1}^{\infty} \sum_{m=-n}^{+n} a_{nm}\mathbf{M}_{nm}^{(1)}(k_0\mathbf{r}_1) + b_{nm}\mathbf{N}_{nm}^{(1)}(k_0\mathbf{r}_1), \tag{2}$$

in which the field strength E_0 has been set equal to unity. Furthermore, the relationship between the expansion coefficients a_{nm}, b_{nm} on one hand and the more traditional beam shape coefficients $g_{n,X}^{m}$ on the other hand is available from [28] and will be provided in the sequel.

Similarly, the scattered field may be expanded using the spherical Bessel functions of the fourth kind (in the VSWFs):

$$\mathbf{E}^{\text{sca}} = \sum_{n=1}^{\infty} \sum_{m=-n}^{+n} c_{nm}\mathbf{M}_{nm}^{(4)}(k_0\mathbf{r}_1) + d_{nm}\mathbf{N}_{nm}^{(4)}(k_0\mathbf{r}_1). \tag{3}$$

The main field in the annular zone between the surface of the host sphere and that of the inclusion may be expressed using the spherical Bessel functions of the third and the fourth kind in the global coordinates system, indicating a superposition of incoming and outcoming partial waves:

$$\mathbf{E}^{\text{int1}} = \sum_{n=1}^{\infty} \sum_{m=-n}^{+n} e_{nm}\mathbf{M}_{nm}^{(3)}(k_1\mathbf{r}_1) + f_{nm}\mathbf{N}_{nm}^{(3)}(k_1\mathbf{r}_1) + v_{nm}\mathbf{M}_{nm}^{(4)}(k_1\mathbf{r}_1) + h_{nm}\mathbf{N}_{nm}^{(4)}(k_1\mathbf{r}_1). \tag{4}$$

In the inclusion coordinate system, the main field can be expanded as

$$\mathbf{E}^{\text{int1}} = \sum_{n=1}^{\infty} \sum_{m=-n}^{+n} r_{nm}\mathbf{M}_{nm}^{(3)}(k_1\mathbf{r}_2) + s_{nm}\mathbf{N}_{nm}^{(3)}(k_1\mathbf{r}_2) + t_{nm}\mathbf{M}_{nm}^{(4)}(k_1\mathbf{r}_2) + u_{nm}\mathbf{N}_{nm}^{(4)}(k_1\mathbf{r}_2), \tag{5}$$

and the internal field inside the inclusion can be represented as

$$\mathbf{E}^{\text{int2}} = \sum_{n=1}^{\infty} \sum_{m=-n}^{+n} p_{nm}\mathbf{M}_{nm}^{(1)}(k_2\mathbf{r}_2) + q_{nm}\mathbf{N}_{nm}^{(1)}(k_2\mathbf{r}_2). \tag{6}$$

In order to obtain the solutions to the scattering problem, the expansion coefficients of the fields can be related by application of the boundary conditions at the sphere surface $r_1 = a$ and at the inclusion surface $r_2 = b$. It is worth noticing that the VSWFs in the global coordinate system in Eq. (4) and those in the inclusion coordinate system Eq. (5) are different and they can be related by applying translational addition theorems of VSWFs; please refer to [19,27] for more details.

The extinction cross sections can be obtained by a similar procedure as for a spherical particle [29], but they are given as

$$C_{\text{ext}} = \frac{\lambda^2}{\pi}\text{Re}\left[\sum_{n=1}^{\infty}\sum_{m=-n}^{+n}\frac{2n+1}{n(n+1)}\frac{n+|m|!}{n-|m|!} \times (c_{nm}a_{nm}^{*} + d_{nm}b_{nm}^{*})\right]. \tag{7}$$

The normalized differential scattering cross section is given by

$$\sigma_{\text{sca}} = \frac{|\mathbf{E}^{\text{sca}}|^2}{\pi a^2}. \tag{8}$$

C. Beam Shape Coefficients for an Arbitrary Shaped Beam in an Arbitrary Orientation

In the GLMT, the electromagnetic components of the illuminating beam are described by multipole expansions over a set of basis functions. The expansion coefficients are expressed versus fundamental coefficients, usually denoted as $g_{n,X}^{m}$ [X is transverse electric (TE) or transverse magnetic (TM), with n from 1 to ∞, m from $-n$ to n], known as beam shape coefficients (BSCs). These BSCs are used to express electromagnetic fields of laser beams in expanded forms, for use in GLMTs, or in other light scattering approaches, such as the extended boundary condition method. Their calculations form the key issue, and the most difficult one, when dealing with a GLMT. Initiated by Han *et al.* [30,31], a systematic analysis was made recently concerning the transformation of BSCs through rotations of coordinate systems, and corresponding results are published in a series of papers [22–26], providing us with

a new tool for further studies, especially in cases of nonspherical or composite scatterers.

The relationships between the expansion coefficients a_{nm}, b_{nm} on one hand and the BSCs $\tilde{g}^m_{n,X}$ on the other hand read as [22]

$$a_{nm} = -ikc_n^{pw}(-1)^m(-1)^{\frac{m-|m|}{2}}\frac{(n-m)!}{(n-|m|)!}\frac{\tilde{g}^m_{n,\mathrm{TE}}}{c_n^m}, \tag{9}$$

$$b_{nm} = kc_n^{pw}(-1)^m(-1)^{\frac{m-|m|}{2}}\frac{(n-m)!}{(n-|m|)!}\frac{\tilde{g}^m_{n,\mathrm{TM}}}{c_n^m}, \tag{10}$$

in which c_n^{pw} are plane-wave coefficients reading as [29]

$$c_n^{pw} = \frac{1}{k}(-i)^{n+1}\frac{2n+1}{n(n+1)}. \tag{11}$$

According to the transformation theorem for BSCs in spherical coordinates [22], the tilde-decorated BSCs $\tilde{g}^m_{n,X}$ in a rotated system are expressed versus the BSCs $g^m_{n,X}$ in another system, called the unrotated system, as

$$\tilde{g}^m_{n,X} = \mu_{nm}\sum_{s=-n}^{n}\frac{H^m_{sn}}{\mu_{ns}}g^s_{n,X}, \tag{12}$$

where

$$\mu_{nm} = (-1)^m(-1)^{\frac{m-|m|}{2}}\frac{(n-|m|)!}{(n-m)!}, \tag{13}$$

$$H^m_{sn} = (-1)^{n+s}\frac{(n-m)!}{(n-s)!}e^{im\gamma}e^{is\alpha}\sum_{\sigma}(-1)^{\sigma}\binom{n+s}{n-m-\sigma}\binom{n-s}{\sigma} \times\left(\cos\frac{\beta}{2}\right)^{2\sigma+m+s}\left(\sin\frac{\beta}{2}\right)^{2n-2\sigma-m-s}, \tag{14}$$

in which (α,β,γ) are Euler angles bringing the unrotated system to the rotated system, whose definitions could be found in [22–26].

With decades of effort devoted to the description of an arbitrary shaped beam, the BSCs of an arbitrary shaped beam in the unrotated coordinate system $g^m_{n,X}$ can be evaluated by several methods, sharing various degrees of time running efficiency, or of flexibility, which are described in detail in a very recent book with computation programs by Gouesbet and Gréhan [32]. In our computer program, the modified localized approximation method [33], which was rigorously justified by Gouesbet and Lock [34,35], is applied to evaluate the BSCs in the unrotated coordinate system due to the fact that it provides the most efficient method, with regard to computational time, by orders of magnitude with respect to other methods such as by using quadratures [36]. It is also the most appealing from a physical point of view because it provides many physical insights on the interpretation of beam models [37].

3. NUMERICAL RESULTS AND DISCUSSIONS

MDRs will exhibit themselves in the form of supernarrow spikelike features in the plots of various scattering characteristics versus size parameter, such as extinction efficiency spectra. They can also be observed in scattered intensity spectra at a specific orientation. Actually, the resonances become in general more pronounced with increasing scattering angles since the scattered intensity is greatly reduced in the backscattering direction. Nevertheless, it is worthy to mention that some of the resonances can vanish at the scattering angle of 90° because the associated Legendre functions are equal to zero for certain modes n [38].

In this section, simulations concerning the MDRs excited by a focused Gaussian beam or a plane wave are made by using a homemade code [27] within the framework of the GLMT. The correctness of the code has already been checked in several ways, including by comparing results with those obtained from a widely used code published by Ngo *et al.* [39] and with published research data [20,40].

Exemplifying results about extinction efficiency spectra and normalized differential scattering cross sections in a specific direction are displayed in the following. Because of the fact that the normalized differential scattering cross sections calculated by using Eq. (8) are proportional to the intensity, it is conveniently referred to as intensity in the present paper. The case of a focused fundamental Gaussian beam (TEM_{00} mode) illuminating an ethanol sphere (having a real refractive index equal to 1.36) with an eccentrically located spherical glass inclusion (having a real refractive index equal to 1.50) is simulated. This model can be regarded as a glass bead covered inhomogeneously with an ethanol coating illuminated by a laser beam. The wavelength of the laser beam is assumed to be $\lambda = 0.532\,\mu$m, and the beam waist radius is $w_0 = 1.0\,\mu$m. Furthermore, a plane wave can be obtained by setting w_0 to be much larger than the radius of the host sphere, say, $w_0 = 100R$. The amplitude of the beam at its focal point is set to be unity without any loss of generality.

A. Parallel Illumination by an Off-Axis Gaussian Beam

Previous observations [41] in experiments and results in numerical calculations of the light scattered by a homogeneous sphere or a concentric sphere illuminated by a Gaussian beam show that the excitation of MDRs depends significantly on the focal center position and the polarization of the incident beam [40,42,43]. As the beam is shifted farther away from the particle center, the fraction of the incident energy coupled into the sphere at resonance first increases and then decreases [40]. Electromagnetic energy is most efficiently coupled into MDRs when a laser beam is focused near the edge of a particle. Results in our simulations also support these mentioned conclusions. Thus, for exemplifying results, an off-axis Gaussian beam, which is aligned at the edge of the scatterer, is applied as an excitation source to excite MDRs. The Gaussian beam is assumed to propagate in the z-axis direction with its electric vector polarized along the x axis at its waist center. The focal center of the Gaussian beam is shifted along the x axis to a constant distance $a = 2.93357\,\mu$m relative to the center of the droplet, which corresponds to the radius of an ethanol sphere when the $\mathrm{TE}_{41,1}$ ($n = 41$, $l = 1$) resonance is excited.

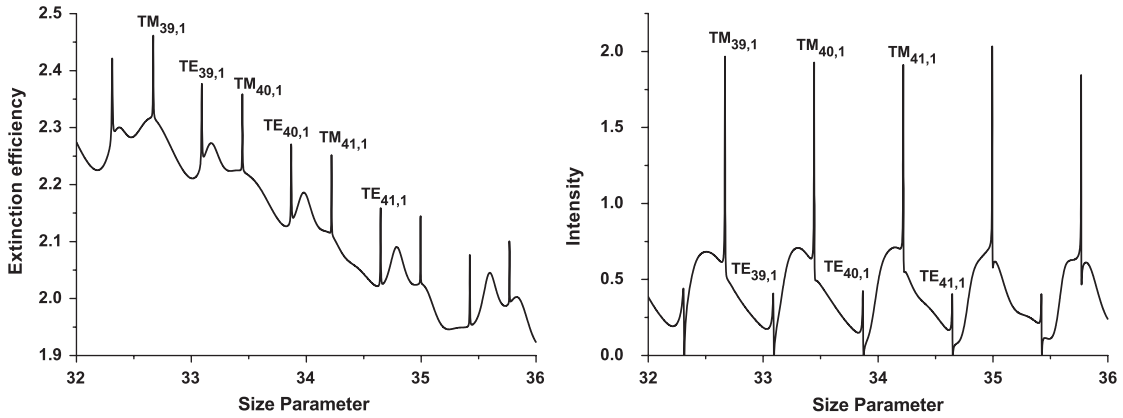

(a) Extinction efficiency spectrum (b) Backward intensity spectrum

Fig. 2. Extinction efficiency spectrum and backward intensity spectrum for a concentric sphere. The radius of the inclusion is $r = 0.7R$, plane-wave illumination with incidence angle 0.0°.

With plane-wave illumination, extinction efficiency and scattered intensity at scattering angle 180° are shown in Fig. 2 for a concentric sphere as a function of size parameter. The radius of the host sphere is denoted by R, and the radius of the inclusion is specified as a ratio of the host sphere radius $r = 0.7R$. Both TE and TM resonances are visible in Fig. 2. It is obvious that the resonances in the backscattering direction [Fig. 2(b)] are much more pronounced than those in the extinction efficiency spectrum [Fig. 2(a)].

With Gaussian beam illumination, comparisons of extinction efficiency and of scattered intensity at scattering angle 180° as a function of size parameter are shown in Fig. 3 for a concentric sphere and an eccentric sphere. The radius of the inclusion is $r = 0.7R$. The displacement of the inclusion with respect to the host sphere center is designated as a center–center separation distance $d = 0.1R$ for the eccentric sphere. In Fig. 3, both the first-order ($l = 1$) and the second-order ($l = 2$) resonances are clearly visible. Compared with plane-wave illumination, only TE resonances can be seen in Fig. 3 with Gaussian beam illumination. A similar calculation shows that only TM resonances can be seen if the Gaussian beam shifts along the y axis instead of along the x axis. This is agreement with the fact that only tangential components of the electromagnetic field can be sufficiently coupled into the resonances. For a concentric sphere or a multilayered sphere, the scattered field coefficients with an illumination of arbitrary shaped beam in the framework of the GLMT are actually proportional to the corresponding scattered field coefficients with a plane-wave illumination in the Lorenz–Mie theory (LMT) [44]; thus, the MDRs found in Fig. 3 for the concentric sphere are located at the same positions as those in Fig. 2.

As we can see from Fig. 2, especially from Fig. 2(b), the amplitudes of the first-order resonance peaks $l = 1$ are not changed a lot under a plane-wave illumination in the limited size parameter range shown in Fig. 2. Nevertheless, the amplitudes of the first-order resonance peaks decrease monotonically under the focused Gaussian beam illumination, which can be observed in Fig. 3, particularly in Fig. 3(b). This can be explained by invoking the localization principle [37,45], according to which the nth partial wave is associated with a bunch of rays passing through a radial position $(n + 1/2)(\lambda/2\pi)$ from the scatterer center, where λ is the wavelength. Thus, only certain resonances can be strongly excited by a focused laser beam depending greatly on the shape pattern as well as on the focal center location of the laser beam. For the simulations in this paper, the focal center of the Gaussian beam is shifted along the x axis with $a = 2.93357\,\mu$m, which corresponds to the $TE_{41,1}$ resonance, so that resonances modes around $n = 41$ are more pronounced. It is interesting to find that the most enhanced resonances are

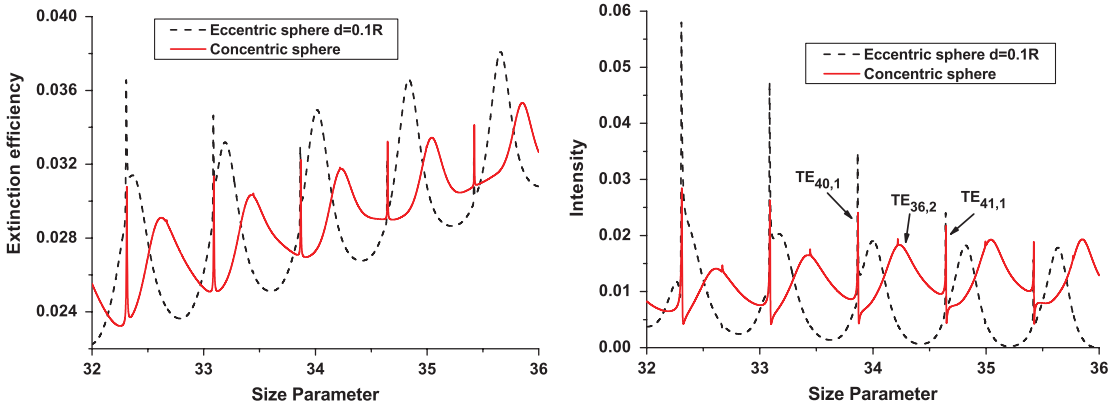

(a) Extinction efficiency spectrum (b) Backward intensity spectrum

Fig. 3. (Color online) Comparison of extinction efficiency spectra and of backward intensity spectra for a concentric sphere and an eccentric sphere ($d = 0.1R$), respectively. The radius of the inclusion is $r = 0.7R$, Gaussian beam illumination with incidence angle 0.0°.

for the modes a little bit smaller than $n = 41$. This is agreement with the result that the fraction of the internal energy is most efficiently coupled to the resonances when the focused beam center is located slightly outside of the particle [40].

Compared with the concentric sphere, the second-order resonances ($l = 2$) in the eccentric sphere with a separation distance $d = 0.1R$ are greatly affected by the shift of the inclusion. Nevertheless, the first-order resonances ($l = 1$) are little affected. This is reasonable because, for an inclusion with $r = 0.7R$, a small displacement of the inclusion $d = 0.1R$ cannot affect the first-order resonances efficiently because they are closer to the rim of the particle. As has been mentioned above, each resonance in a sphere or a concentric sphere can be identified by its state of polarization and two quantum numbers n, l and does not depend on mode m, such as the label $TE_{41,1}$ indicates the resonance is predominantly in the c_{nm} coefficients at quantum numbers $n = 41$, $l = 1$. Nevertheless, the resonances in an eccentric sphere cannot be labeled like this. This is due to the fact that each resonance in the eccentric sphere is contributed by several n modes instead of a single n mode, which was also mentioned by Rao *et al.* [9]. Thus, all the resonances in an eccentric sphere are not labeled in the figures of this paper.

Heated by the laser beam or by any possible heating method, such as by putting it close to a hot iron wall, the ethanol coating would become thinner because of evaporation. Accordingly, in Fig. 4, the radius of the inclusion is specified as $r = 0.92R$ to indicate a very thin film of ethanol coating. A center–center separation distance $d = 0.04R$ is assumed. The other parameters are exactly the same than the ones used in Fig. 3. Compared with the case when $r = 0.7R$ with $d = 0.1R$, the positions of the first-order resonances shift much more in Fig. 4 when $r = 0.92R$, even with a smaller displacement of the inclusion $d = 0.04R$. Similar to the behavior in Fig. 3, the second-order resonances in Fig. 4 are also much more affected than the first-order resonances. This is because more energy from the second-order modes overlap with the core region. It is interesting to find that the amplitudes of the first-order resonances decrease a lot in the eccentric sphere with $d = 0.04R$ compared to that in the concentric sphere, which may be due to the fact that the electromagnetic energy at the first-order resonances is more efficiently coupled into the inclusion in the eccentric sphere than in the concentric sphere.

Furthermore, with Gaussian beam illumination, extinction efficiency and backscatter intensity are plotted in Fig. 5 as a function of size parameter for a concentric sphere of $r = 0.7R$ and for a concentric sphere of $r = 0.92R$. It is obvious that, as the relative radius of the inclusion with respect to the host sphere increases, both the first-order and second-order resonances shift dramatically. And the second-order resonances are significantly enhanced.

B. Oblique Illumination by an Off-Axis Gaussian Beam

As reported by Rao *et al.* [9], with a parallel illumination by a plane wave, that is to say, when the wave travels along the z axis in our case, which indicates the incidence angle is zero, the degeneracy in mode m is not lifted for an eccentric sphere. This is reasonable because the symmetry of the scatterer is not broken in the azimuthal direction with regard to the incident direction of plane wave. Indeed, we have shown in Subsection 3.A that the degeneracy in mode m is also not lifted with a parallel illumination by an off-axis Gaussian beam.

In the following calculations, the incidence angle of the Gaussian beam is assumed to be 90°, in which case the asymmetry of an eccentric sphere reaches the largest extent for a fixed center–center separation distance d. More specifically, the Gaussian beam is assumed to propagate in the x-axis direction with its electric vector polarized in the z axis at its waist center. The focal center of the Gaussian beam is situated on the z axis with a constant distance $z_0 = 2.93357\,\mu$m.

With a plane-wave illumination, as we can see from Fig. 6, splitting in MDRs are observed for modes having sufficiently high Qs. More detailed information for single resonance peaks can be obtained in the insets. It shows that the TM resonance peaks are more easily lifted than the TE resonance peaks.

With a tightly focused Gaussian beam illumination, extinction efficiency as a function of size parameter for an eccentric sphere of $r = 0.7R$ with different displacements of the inclusion is shown in Fig. 7, and that for an eccentric sphere of $r = 0.92R$ with different displacements of the inclusion is shown in Fig. 8. In contrast with the case of a plane-wave illumination, splitting in resonance peaks are not observed in the extinction efficiency spectrum for the focused Gaussian beam illumination. For the eccentric sphere with $r = 0.7R$ in Fig. 7,

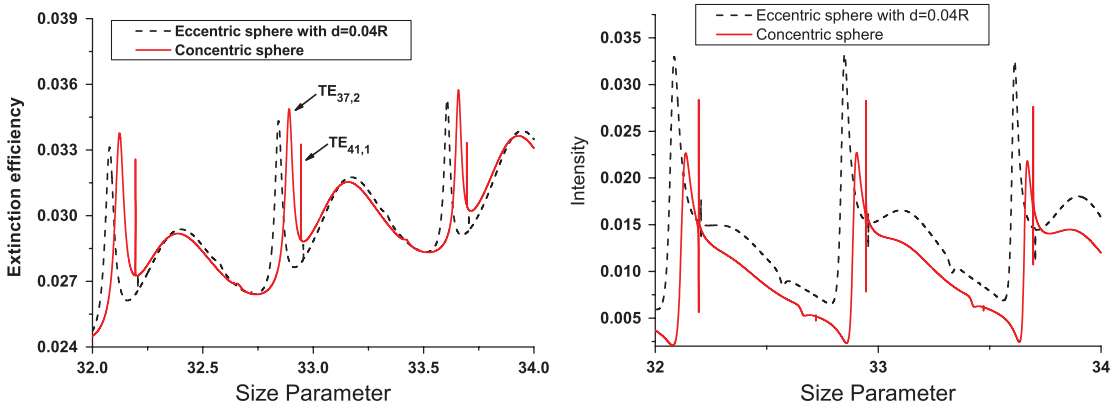

(a) Extinction efficiency spectrum (b) Backward intensity spectrum

Fig. 4. (Color online) Comparison of extinction efficiency spectra and of backward intensity spectra for a concentric sphere and an eccentric sphere ($d = 0.04R$), respectively. The radius of the inclusion is $r = 0.92R$, Gaussian beam illumination with incidence angle 0.0°.

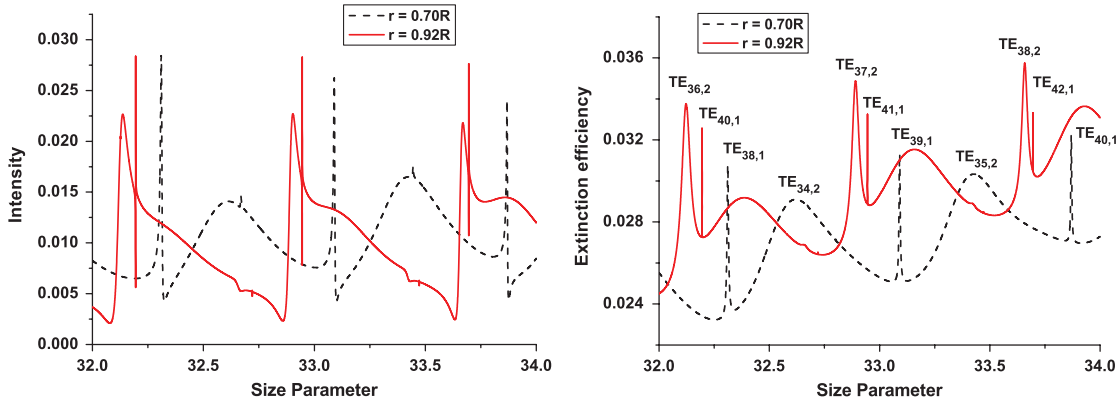

(a) Extinction efficiency spectrum (b) Backward intensity spectrum

Fig. 5. (Color online) Comparison of extinction efficiency spectra and of backward intensity spectra for concentric spheres of $r = 0.7R$ and of $r = 0.92R$, respectively. Gaussian beam illumination with incidence angle 0.0°.

the effects on the second-order resonances due to the eccentric shift of inclusion are very significant, while there is much less influence on its first-order resonances. For the eccentric sphere with $r = 0.92R$ in Fig. 8, all the amplitudes of first-order and second-order resonances are enhanced step by step as the inclusion approaches the symmetric axis of the Gaussian beam from $d = -0.04R$ to $d = 0.0$ and then to $d = +0.04R$. It is interesting to find that the first-order resonances are greatly suppressed for $d = -0.04R$ while the first-order resonances are greatly enhanced for $d = +0.04R$.

Furthermore, as for spheres or concentrically multilayered spheres [44], the scattered field coefficients for eccentric spheres with an illumination of arbitrary shaped beam in the framework of the GLMT are also proportional to the corresponding scattered field coefficients with a plane-wave illumination; thus, the MDRs found in Fig. 6 for the eccentric sphere are located at the same positions as those in Fig. 8.

C. Internal Field Distribution

In contrast with the behaviors of MDRs with a plane-wave illumination, splittings in the resonance peaks are not observed in the extinction efficiency spectrum with a tightly focused Gaussian beam illumination. To provide additional information with regard to the pattern of the MDRs, plots of internal field distributions for some resonances are presented.

Even though the magnitude and the phase for each partial wave component of the electromagnetic field can be determined from the GLMT formalism, a useful visualization of the field distribution can be obtained by plotting the normalized source function as a function of spatial position. The normalized source function is defined as

$$S = |\mathbf{E}|^2/|E_0|^2, \tag{15}$$

where $\mathbf{E}$ is the electric vector of the internal or external field and E_0 is the electric field strength of the incident field, which is assumed to be unity. To emphasize the internal distribution, the external field intensities are suppressed to zero in the

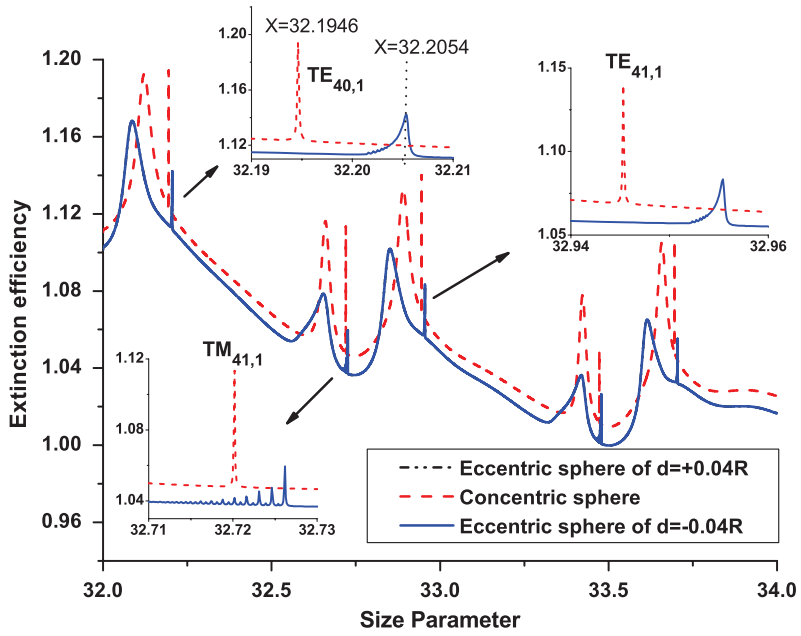

Fig. 6. (Color online) Comparison of extinction efficiency spectra for a concentric sphere and eccentric spheres ($d = 0.04R$, $d = -0.04R$). The radius of the inclusion is $r = 0.92R$, plane-wave illumination with incidence angle 90.0°.

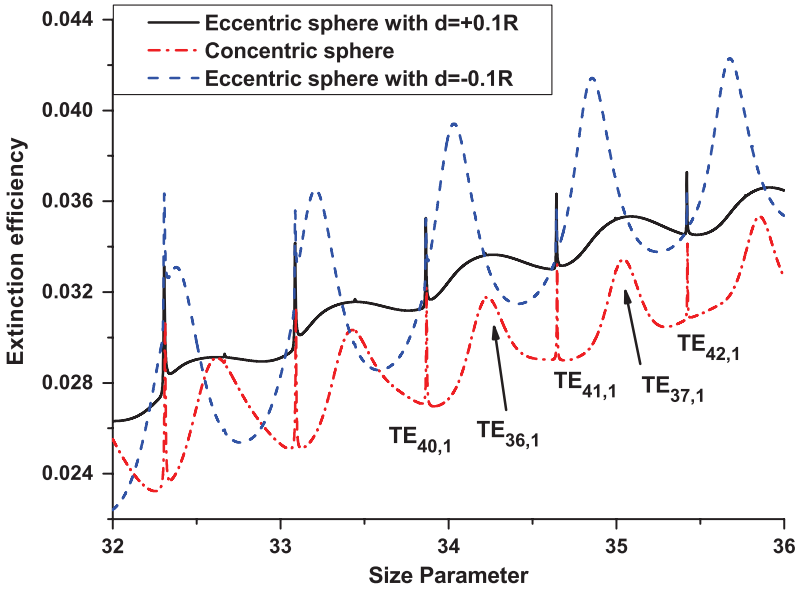

Fig. 7. (Color online) Comparison of extinction efficiency spectra for eccentric spheres of $r = 0.7R$ with different center–center separation distances illuminated by a Gaussian beam.

subsequent figures, and the spatial coordinates are normalized by the host sphere radius.

Calculations of internal field distribution for an off-resonance case, a complete resonance case in a concentric sphere, and a broken-resonance case in an eccentric sphere are shown in Figs. 9(a)–9(c), respectively, for a plane-wave illumination and in Figs. 9(d)–9(f), respectively, for a tightly focused Gaussian beam illumination. Parameters used in Figs. 9(a)–9(c) are the same as the ones used in Fig. 6, and parameters used in Figs. 9(d)–9(f) are the same as the ones used in Fig. 8.

For a plane-wave illumination, a picture of an off-resonance case at size parameter $x = 32.19$ for the eccentric sphere is plotted in the transverse x–z plane in Fig. 9(a). Figure 9(b) is the $TE_{40,1}$ resonance occurring in the concentric sphere at size parameter $x = 32.1946$. The largest enhancements are near the forward- and backward-scattering directions. Detailed study of the resonance reveals that the $TE_{n,1}$ mode resonance has n peaks in each side of the x–z plane with the z axis as a symmetric axis. Nevertheless, this symmetry is broken if the inclusion is shifted eccentrically to the rim of the host sphere. Figure 9(c) shows the internal field distribution of a broken resonance at size parameter $x = 32.2054$. The largest enhancements are found to be shifted away from the forward- and backward-scattering directions. The intensity peaks around the rim of the sphere become blurred because several m modes contribute to the resonance.

For a tightly focused Gaussian beam illumination, Fig. 9(d) is a plot of internal field distribution for an eccentric sphere with $d = -0.04R$ at off-resonance with size parameter $x = 32.19$. Figure 9(e) shows the $TE_{40,1}$ resonance occurring in an concentric sphere with size parameter $x = 32.1946$. A

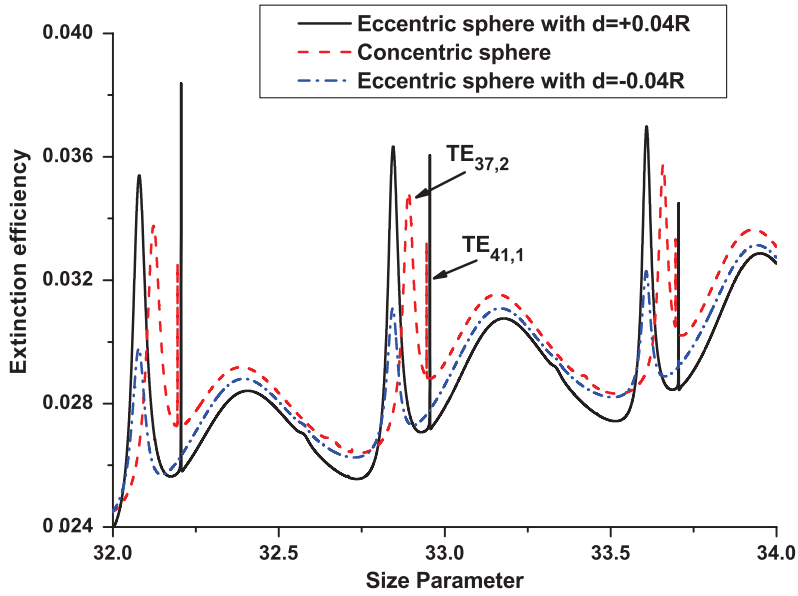

Fig. 8. (Color online) Comparison of extinction efficiency spectra for eccentric spheres of $r = 0.92R$ with different center–center separation distances illuminated by a Gaussian beam.

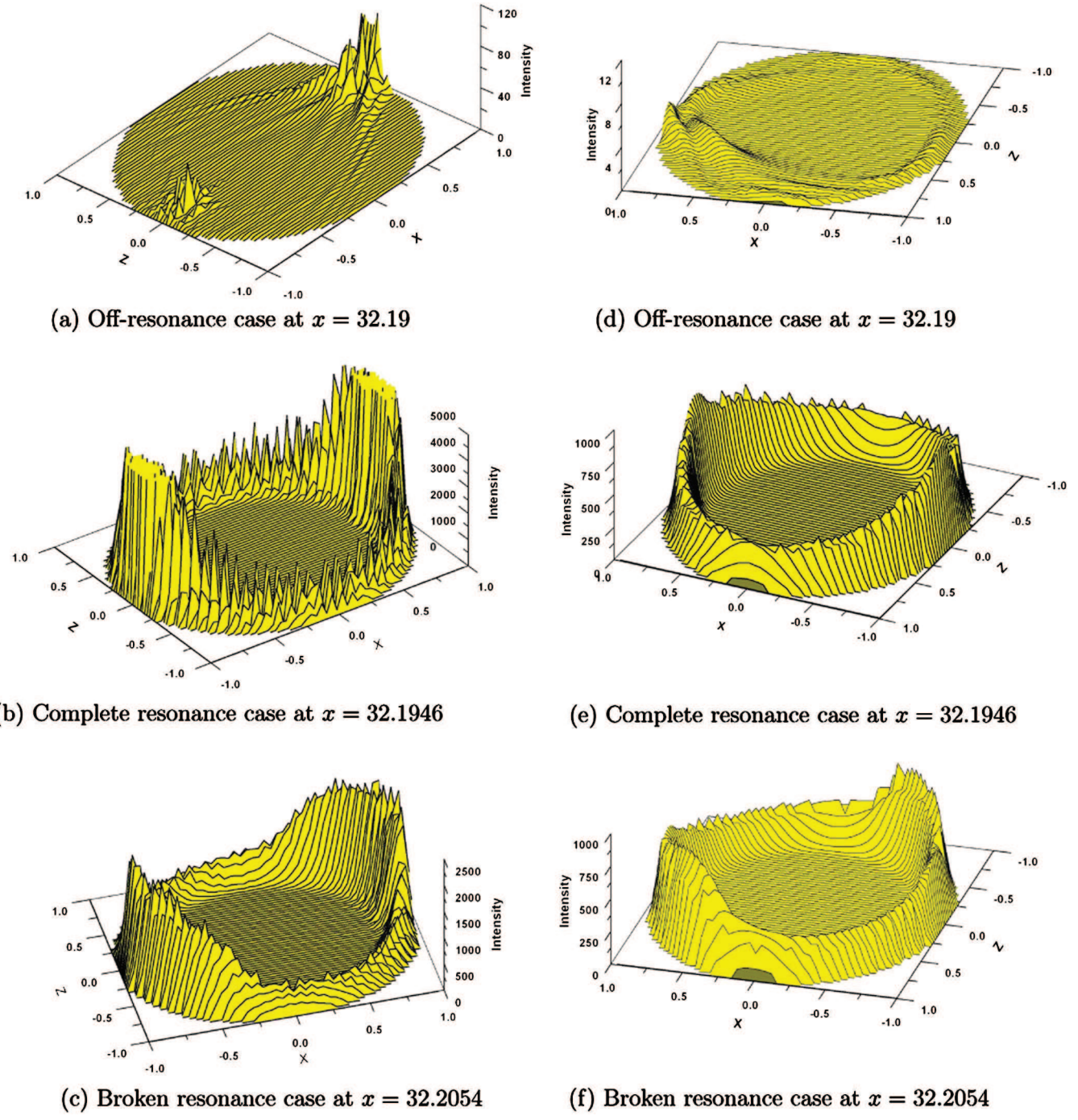

Fig. 9. (Color online) Distributions of internal field for an eccentric sphere illuminated by (a), (b), (c) plane wave and (d), (e), (f) Gaussian beam. (a), (d) off-resonance case with $d = -0.04R$; (b), (e) complete resonance case with $d = 0.0R$, and (c), (f) broken-resonance case with $d = 0.04R$. The radius of the inclusion is $r = 0.92R$. The incident wave propagates along the x axis from negative to positive.

broken-resonance case occurring in an eccentric sphere with size parameter $x = 32.2054$ is presented in Fig. 9(f). For the on-resonance cases in Figs. 9(e) and 9(f), enhancements in the internal intensity are excited near the edge of the host sphere. Different from the pattern of separated peaks observed for the plane-wave illumination in Figs. 9(b) and 9(c), a solid ring formation is displayed for the Gaussian beam illumination. For a concentric sphere, a symmetric formation of the resonance is obtained with greatest field intensities near the forward- and backward-scattering directions. For an eccentric sphere, although the degeneracy of the mode m is not observed in the extinction efficiency spectra, the symmetric formation of the internal field distribution at resonance conditions becomes asymmetric with largest field intensity locations shifted away from the forward- and backward-scattering directions.

4. CONCLUSIONS AND DISCUSSION

Following the recent results in the GLMT concerning the description of an arbitrary shaped beam in an arbitrary orientation [22–27], the properties of MDRs excited in an

ethanol sphere (having a real refractive index equal to 1.36) with an eccentrically located spherical glass inclusion (having a real refractive index equal to 1.50) illuminated by a tightly focused Gaussian beam is studied. Corresponding calculations for plane-wave illumination are also made for the sake of comparison.

As for spheres and concentrically multilayered spheres, since the scattered field coefficients with an illumination by arbitrary shaped beam in the framework of the GLMT are proportional to the corresponding scattered field coefficients with a plane-wave illumination in the LMT, the resonance positions of MDRs in eccentrically layered spheres are equal for laser beam illumination and for plane-wave illumination. With an illumination of a tightly focused Gaussian beam, the positions and the amplitudes of the MDRs peaks excited in an eccentric sphere depend greatly on the relative size of the inclusion with respect to the host sphere and on the separation distance between the two sphere centers. The amplitudes of the MDR peaks are also found to be very sensitive to the relative location and the polarization status of the laser beam. In the simulation of a glass bead covered inhomogeneously with a very thin film of ethanol coating ($r = 0.92R$) illuminated by a Gaussian beam focused at the edge of the particle ($x = 2.93357\,\mu$m), all the first-order ($l = 1$) and second-order ($l = 2$) resonances are found to be enhanced step by step as the inclusion approaches the symmetric axis of the Gaussian beam from $d = -0.04R$ to $d = 0.0$ and then to $d = +0.04R$. It is interesting to find that the first-order resonances are suppressed for $d = -0.04R$ while the first-order resonances are greatly enhanced for $d = +0.04R$ under the tightly focused Gaussian beam illumination. Nevertheless, the extinction efficiency spectra for $d = -0.04R$ and those for $d = +0.04R$ are identical under the plane-wave illumination.

Different from the MDRs with a plane-wave illumination, only certain resonances are strongly excited by a focused laser beam depending greatly on the shape pattern as well as on the location of the focal center of the laser beam. This is easy to understand from the point of view of the localization principle. Indeed, the nth partial wave is associated with a bunch of rays passing through a radial position $(n + 1/2)(\lambda/2\pi)$ from the scatterer center. Thus, for an off-axis illumination by a tightly focused Gaussian beam, only those modes with radial position at or close to the focal center of the Gaussian beam are strongly excited.

With a tightly focused Gaussian beam illumination, splitting of the resonance peaks in the extinction efficiency spectrum is not observed for an eccentric sphere. Looking closely at the absolute value of the BSCs $|g_n^m|$ calculated by using the localization approximation method [46], it is observed that it decreases quickly as $|m|$ increases, and $|g_n^m|$ even vanish except for $|m| = 1$ when the scatterer center is located on the beam axis. Thus the high-order m terms are expected to contribute little to scattering phenomena, and the lift of degeneracy in mode m cannot be observed. Furthermore, instead of exciting only a single angular mode m, several angular modes are excited in the case of an illumination by an off-axis Gaussian beam. Thus, in contrast with the pattern of separated peaks observed in the internal field distribution at resonance condition for a plane-wave illumination, a solid ring formation is displayed for the Gaussian beam illumination. In contrast with the symmetric formation of the internal field distribution at resonance condition for a concentric sphere, asymmetric formation with largest field intensity positions shifted away from the forward- and backward-scattering directions to sideways is observed for an eccentric sphere. It indicates that the degeneracy of m modes is lifted for an eccentric sphere with a tightly focused Gaussian beam, although splitting of the resonance peaks cannot be observed in the extinction efficiency spectra.

ACKNOWLEDGMENTS

The work presented in this paper is supported by the project "Bourses Doctorales en Alternance" between France and China. This work is also partially supported by the European program INTERREG IVa-C5: Cross-Channel Centre for Low Carbon Combustion. The authors thank the reviewers for providing several constructive comments and suggestions to the present paper.

REFERENCES

1. A. Ashkin and J. M. Dziedzic, "Observation of resonances in the radiation pressure on dielectric spheres," Phys. Rev. Lett. **38**, 1351–1354 (1977).
2. P. Chýlek, J. T. Kiehl, and M. K. W. Ko, "Optical levitation and partial-wave resonance," Phys. Rev. A **18**, 2229–2233 (1978).
3. P. Chýlek, B. Ramaswamy, A. Ashkin, and J. M. Dziedzic, "Simultaneous determination of refractive index and size of spherical dielectric particles from light scattering data," Appl. Opt. **22**, 2302–2307 (1983).
4. H.-M. Tzeng, K. F. Wall, M. B. Long, and R. K. Chang, "Evaporation and condensation rates of liquid droplets deduced from structure resonances in the fluorescence spectra," Opt. Lett. **9**, 273–275 (1984).
5. G. Chen, M. M. Mazumder, R. K. Chang, J. C. Swindal, and W. P. Acker, "Laser diagnostics for droplet characterization: application of morphology dependent resonances," Progr. Energy Combust. Sci. **22**, 163–188 (1996).
6. J. Ducastel, "Etude des résonances morphologiquement dépendantes et application à la caractérisation de microparticules en milieu diphasique," Ph.D. thesis (Institut National des Sciences Appliquées de Rouen, 2007).
7. D. Ngo and R. G. Pinnick, "Suppression of scattering resonances in inhomogeneous microdroplets," J. Opt. Soc. Am. A **11**, 1352–1359 (1994).
8. P. T. Leung, S. W. Ng, and K. M. Pang, "Morphology-dependent resonances in dielectric spheres with many tiny inclusions," Opt. Lett. **27**, 1749–1751 (2002).
9. V. S. C. M. Rao and S. D. Gupta, "Broken azimuthal degeneracy with whispering gallery modes of microspheres," J. Opt. A **7**, 279–285 (2005).
10. G. Chen, R. K. Chang, S. C. Hill, and P. W. Barber, "Frequency splitting of degenerate spherical cavity mode: stimulated Raman scattering spectrum of deformed droplets," Opt. Lett. **16**, 1269–1271 (1991).
11. M. I. Mishchenko and A. A. Lacis, "Morphology-dependent resonances of nearly spherical particles in random orientation," Appl. Opt. **42**, 5551–5556 (2003).
12. Y. P. Han, L. Méès, G. Gouesbet, Z. S. Wu, and G. Gréhan, "Resonant spectra of a deformed spherical microcavity," J. Opt. Soc. Am. B **23**, 1390–1397 (2006).
13. M. M. Mazumder, S. C. Hill, and P. W. Barber, "Morphology-dependent resonances in inhomogeneous spheres: comparison of the layered T-matrix method and the time-independent perturbation method," J. Opt. Soc. Am. A **9**, 1844–1853 (1992).
14. K. A. Fuller, "Morphology-dependent resonances in eccentrically stratified sphere," Opt. Lett. **19**, 1272–1274 (1994).
15. G. Gouesbet, S. Meunier-Guttin-Cluzel, and G. Gréhan, "Periodic orbits in Hamiltonian chaos of the annular billiard," Phys. Rev. E **65**, 016212 (2001).
16. M. Hentschel and K. Richter, "Quantum chaos in optical systems: the annular billiard," Phys. Rev. E **66**, 056207 (2002).

17. S. M. Spillane, T. J. Kippenberg, and K. J. Vahala, "Ultralow-threshold Raman laser using a spherical dielectric microcavity," Nature **415**, 621–623 (2002).
18. G. Gouesbet, S. Meunier-Guttin-Cluzel, and G. Gréhan, "Generalized Lorenz–Mie theory for a sphere with an eccentrically located inclusion, and optical chaos," Part. Part. Syst. Charact. **18**, 190–195 (2001).
19. G. Gouesbet and G. Gréhan, "Generalized Lorenz–Mie theory for a sphere with an eccentrically located spherical inclusion," J. Mod. Opt. **47**, 821–837 (2000).
20. G. X. Han, Y. P. Han, J. Y. Liu, and Y. Zhang, "Scattering of an eccentric sphere arbitrarily located in a shaped beam," J. Opt. Soc. Am. B **25**, 2064–2072 (2008).
21. B. Yan, X. Han, and K. F. Ren, "Scattering of a shaped beam by a spherical particle with an eccentric spherical inclusion," J. Opt. A **11**, 015705, 2009.
22. G. Gouesbet, J. J. Wang, and Y. P. Han, "Transformations of spherical beam shape coefficients in generalized Lorenz–Mie theories through rotations of coordinate systems. I. General formulation," Opt. Commun. **283**, 3218–3225 (2010).
23. J. J. Wang, G. Gouesbet, and Y. P. Han, "Transformations of spherical beam shape coefficients in generalized Lorenz–Mie theories through rotations of coordinate systems. II. Axisymmetric beams," Opt. Commun. **283**, 3226–3234 (2010).
24. G. Gouesbet, J. J. Wang, and Y. P. Han, "Transformations of spherical beam shape coefficients in generalized Lorenz–Mie theories through rotations of coordinate systems. III. Special Euler angles," Opt. Commun. **283**, 3235–3243 (2010).
25. G. Gouesbet, J. J. Wang, Y. P. Han, and G. Gréhan, "Transformations of spherical beam shape coefficients in generalized Lorenz–Mie theories through rotations of coordinate systems. IV. Plane waves," Opt. Commun. **283**, 3244–3254 (2010).
26. G. Gouesbet, J. A. Lock, J. J. Wang, and G. Gréhan, "Transformations of spherical beam shape coefficients in generalized Lorenz–Mie theories through rotations of coordinate systems. V. Localized beam models," Opt. Commun. **284**, 411–417 (2011).
27. J. J. Wang, G. Gouesbet, Y. P. Han, and G. Gréhan, "Study of scattering from a sphere with an eccentrically located spherical inclusion by generalized Lorenz–Mie theory: internal and external field distribution," J. Opt. Soc. Am. A **28**, 24–39 (2011).
28. G. Gouesbet, "T-matrix formulation and generalized Lorenz–Mie theories in spherical coordinates," Opt. Commun. **283**, 517–521 (2010).
29. G. Gouesbet, B. Maheu, and G. Gréhan, "Light scattering from a sphere arbitrarily located in a Gaussian beam, using a Bromwich formulation," J. Opt. Soc. Am. A **5**, 1427–1443 (1988).
30. Y. P. Han, H. Y. Zhang, and G. X. Han, "The expansion coefficients of arbitrary shaped beam in oblique illumination," Opt. Express **15**, 735–746 (2007).
31. Y. P. Han, Y. Zhang, H. Y. Zhang, and G. X. Han, "Scattering of typical particles by beam shape in oblique illumination," J. Quant. Spectrosc. Radiat. Transfer **110**, 1375–1381 (2009).
32. G. Gouesbet and G. Gréhan, *Generalized Lorenz–Mie Theories* (Springer, 2011).
33. G. Gouesbet, "Validity of the localized approximation for arbitrary shaped beams in the generalized Lorenz–Mie theory for spheres," J. Opt. Soc. Am. A **16**, 1641–1650 (1999).
34. J. A. Lock and G. Gouesbet, "Rigorous justification of the localized approximation to the beam-shape coefficients in generalized Lorenz–Mie theory. I. On-axis beams," J. Opt. Soc. Am. A **11**, 2503–2515 (1994).
35. G. Gouesbet and J. A. Lock, "Rigorous justification of the localized approximation to the beam-shape coefficients in generalized Lorenz–Mie theory. II. Off-axis beams," J. Opt. Soc. Am. A **11**, 2516–2525 (1994).
36. J. A. Lock, "An improved Gaussian beam scattering algorithm," Appl. Opt. **34**, 559–570 (1995).
37. G. Gouesbet, J. A. Lock, and G. Gréhan, "Generalized Lorenz–Mie theories and description of electromagnetic arbitrary shaped beams: localized approximations and localized beam models," J. Quant. Spectrosc. Radiat. Transfer **112**, 1–27 (2011).
38. P. W. Barber and S. C. Hill, *Light Scattering by Particles: Computational Methods*, Vol. 2 of Advanced Series in Applied Physics (World Scientific, 1990).
39. D. Ngo, G. Videen, and P. Chýlek, "A FORTRAN code for the scattering of EM waves by a sphere with a nonconcentric spherical inclusion," Comput. Phys. Commun. **99**, 94–112 (1996).
40. E. E. M. Khaled, S. C. Hill, and P. W. Barber, "Light scattering by a coated sphere illuminated with a Gaussian beam," Appl. Opt. **33**, 3308–3314 (1994).
41. A. Ashkin and J. M. Dziedzic, "Observation of optical resonances of dielectric spheres by light scattering," Appl. Opt. **20**, 1803–1814 (1981).
42. J. P. Barton, D. R. Alexander, and S. A. Schaub, "Internal fields of a spherical particle illuminated by a tightly focused laser beam: focal point positioning effects at resonance," J. Appl. Phys. **65**, 2900–2906 (1989).
43. E. E. M. Khaled, S. C. Hill, and P. W. Barber, "Internal electric energy in a spherical particle illuminated with a plane wave or off-axis Gaussian beam," Appl. Opt. **33**, 524–532 (1994).
44. F. Onofri, G. Gréhan, and G. Gouesbet, "Electromagnetic scattering from a multilayered sphere located in an arbitrary beam," Appl. Opt. **34**, 7113–7124 (1995).
45. H. C. van de Hulst, *Light Scattering by Small Particles* (Peter Smith, 1982).
46. G. Gouesbet, G. Gréhan, and B. Maheu, "Localized interpretation to compute all the coefficients g_n^m in the generalized Lorenz–Mie theory," J. Opt. Soc. Am. A **7**, 998–1007 (1990).

Exp Fluids (2011) 51:149–159
DOI 10.1007/s00348-010-1036-4

RESEARCH ARTICLE

Numerical study of global rainbow technique: sensitivity to non-sphericity of droplets

Jiajie Wang · Gérard Gréhan · Yiping Han · Sawitree Saengkaew · Gérard Gouesbet

Received: 10 February 2010 / Revised: 21 December 2010 / Accepted: 23 December 2010 / Published online: 12 January 2011

Abstract The measurement of droplet temperature and size distribution in sprays is a difficult task. To reach this aim, the global rainbow technique (GRT) has been developed on the assumption that the synthetic rainbow created by a large number of droplets is insensitive to the non-sphericity of droplets if the droplets' orientations were sufficiently random. In order to test this assumption, numerical as well as experimental analyses of GRT are carried out by our team. As a companion to the work done in experiments, the objective of this work is to quantify the sensitivity of the GRT to the non-sphericity of droplets from a numerical aspect. Light scattering properties around the rainbow angle are investigated by using the Null-field method within a T-matrix formulation, both for a single spheroid in an arbitrary orientation and for an ensemble of spheroids in random orientations illuminated by a plane wave. Refractive index and size distribution of droplets are extracted from simulated global rainbow signals so as to quantify the sensitivity of the GRT to the non-sphericity. Exemplifying results are compiled and presented. Additionally, comparisons between the Null-field method and the generalized Lorenz-Mie theory for spheroids are also provided in this paper.

J. Wang · G. Gréhan (✉) · S. Saengkaew · G. Gouesbet
LESP, UMR 6614/CORIA, CNRS/INSA et Université de ROUEN, 76801 Saint Etienne du Rouvray, France
e-mail: grehan@coria.fr

J. Wang · Y. Han
School of Science, Xidian University, 710071 Xi'an, China
e-mail: wangjj@coria.fr

J. Han
e-mail: yphan@xidian.edu.cn

1 Introduction

Rainbow refractometry has been investigated for over 20 years since the standard rainbow refractometry was presented the first time by Roth et al. (1988, 1990). Both the temperature and the size of droplets can be measured simultaneously. Just as each technique possesses its own advantages and limitations, the measurement accuracy of the rainbow refractometry is also affected by many factors. The most important ones are the refractive index gradients inside the droplets (Saengkaew et al. 2007), the ripple structure on the main rainbow pattern and the non-sphericity of the droplets (Han et al. 2002). The influence of the non-sphericity, which can distort the rainbow pattern, is least understood. During recent years, based on the assumption that the scattering contribution of an ensemble of randomly oriented non-spherical particles to the synthetic rainbow pattern results in a general uniform background, the global rainbow technique (GRT) was developed by van Beeck et al. (1999), which primarily aimed at eliminating the side effects brought in by droplets non-sphericity. This promising technique has already been successively applied to the analysis of water sprays created by flat fan (van Beeck et al. 2001) and measurement of mean temperature of the falling droplets in a large containment vessel (Lemaitre et al. 2006).

In order to optimize the GRT, the assumption that the synthetic rainbow is insensitive to the shape of droplets is tested by our research team recently, both from a numerical aspect and an experimental aspect. As a companion to the work done in experiments (Saengkaew et al. 2009), the objective of this work is to quantify the sensitivity of the GRT to the non-sphericity of droplets from a numerical aspect.

Among those factors that affect the measurement accuracy of rainbow refractometry, the influence of the temperature gradient and ripple structure can be relatively easily quantified by numerical simulations, while the effect of the non-sphericity on the rainbow pattern is more difficult to predict. The influence of the non-sphericity on a single particle was firstly predicted by Möebius (1910). The validity of the Möebius formula has been examined by van Beeck (1997) by using a mixed approach (geometrical optics/Huygens–Fresnel integral) and by Han et al. (2002) in the rigorous framework of generalized Lorenz-Mie theory (GLMT). Xu et al. (2010) also addressed the influence of non-sphericity on rainbow position through separating the $p = 2$ order of scattering by extending the Debye series to spheroidal particles and compared their results with the predictions from Möebius. Similar results were obtained and all of them demonstrated that both the position and the shape of the rainbow pattern for a single particle are very sensitive to the non-sphericity. Due to the spheroid's instinct lower body symmetry compared with a sphere, the location as well as the shape of the rainbow created by a spheroid changes a lot with respect to illumination direction of the incident wave. To our knowledge, in the frame of a rigorous theory, only the shift of rainbow angle as a function of ellipticity was analysed, and a study of rainbow pattern for a single particle in an arbitrary orientation becomes necessary, especially in the analysis of the GRT. Relying on previous works (Barton 1995, 2001; Xu et al. 2007; Han et al. 2003; Han et al. 2009) on developing the GLMT for non-spherical particles, the GLMT provides us with the capability to predict the scattering behaviours for a non-spherical particle with respect to illumination direction of the incident wave. Nevertheless, to our knowledge, the existing programmes within the framework of GLMT for light scattering from a spheroid in an arbitrary orientation still have a limitation in the domain of size parameter at the moment (Xu et al. 2007; Han et al. 2009). More precisely, the programmes are valid for spheroids with size parameter less than 100. On the other hand, this limit has been overcome by using the Null-field method within a T-matrix formulation to deal with particles with size parameter well exceeding 100 (Wielaard et al. 1997). Some comparisons between the results obtained from the Null-field method and those from the GLMT are presented in this paper. It is worth noticing that, for better terminologies and escaping from a misunderstanding between a method and a formulation, we prefer to use the Null-field within a T-matrix formulation terminology instead of T-matrix method (Gouesbet 2010) in this paper.

In the case of an ensemble of non-spherical particles, light scattering properties of randomly oriented, identical spheroids were studied by Asano and Sato (1980) by extending the Lorenz-Mie theory from spheres to spheroids. Mishchenko and Travis (1994a) later analysed light scattering from polydisperse, randomly oriented particles of size comparable to wavelength. In order to study the influence of non-sphericity on the rainbow refractometry technique, light scattering properties near the rainbow angle of relatively large size particles should be further considered. This paper is focused on discussing the light scattering properties of an ensemble of poly-ellipticities, randomly oriented large particles around the rainbow angle.

Since its presentation by Waterman (1971), the Null-field method has been greatly improved and become a powerful tool for computing light scattering by non-spherical particles. It is well known that the inversion procedure of the transition matrix in the Null-field method becomes ill-conditioned easily for particles with large size parameter and/or big ellipticity. Due to the previous efforts of researchers (Mishchenko and Travis 1994b; Wielaard et al. 1997), this limitation has been greatly overcome, which provides us another way to predict the rainbow pattern behaviours and to explore its implication in the GRT measurements. It is worth to mention that, compared with the GLMT, the Null-field method is less efficient in computation time due to the requirement of calculations of integral elements in its T matrix. Nevertheless, by expanding the elements of the scattering matrices in terms of generalized spherical functions analytically (Mishchenko et al. 1999), the cost of computational time by using the Null-field method for an ensemble of particles is greatly reduced and is acceptable. A detailed discussion of Null-field method can be found in the books (Mishchenko et al. 1999; Doicu et al. 2006) and references within and will not be stated here.

This paper is organized as follows. The light scattering properties around the rainbow angle for a single spheroid in an arbitrary orientation are investigated in Sect. 2. In Sect. 3, the light scattering properties for an ensemble of spheroids in random orientations are analysed. The inversion of rainbows signals by using GRT is presented in Sect. 4; corresponding results and deviations are compiled and given. Section 5 contains conclusions and discussions.

2 Scattering by a single spheroid in an arbitrary orientation

To describe the scattering of a non-spherical particle in an arbitrary orientation illuminated by an electromagnetic plane wave, two sets of coordinates are introduced, which are referred to the laboratory frame $L\{x'y'z'\}$ and the particle frame $P\{xyz\}$, respectively. The orientation of the particle with respect to the laboratory frame is specified by three Euler angles of rotation, α, β and γ, which transform

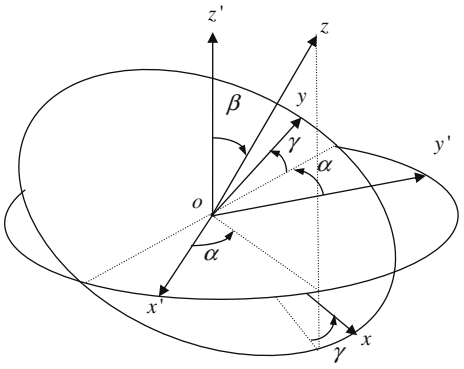

Fig. 1 Rotation of Euler angles (α, β, γ) transforming the laboratory coordinate system L $\{Ox'y'z'\}$ to the particle coordinate system P $\{Oxyz\}$

the laboratory frame into the particle reference frame, corresponding geometric illustration is shown in Fig. 1 with more detailed information available from books published (Mishchenko et al. 1999; Doicu et al. 2006). Furthermore, to characterize the non-sphericity of the spheroids, the ellipticity is defined as the ratio of a spheroid's horizontal length "a" to its vertical length "b", with vertical length "b" as its axis of rotation, similar definitions were used by Han et al. (2002). The ellipticity of the spheroid is given by $e = a/b$, with $e < 1.0$ for a prolate spheroid and $e > 1.0$ for an oblate spheroid. Throughout this paper, the plane wave is assumed to travel along the z′ axis of the laboratory reference frame, and the scattering particles under study are assumed to be water droplets with refractive index equals to 1.330. Moreover, in the computations of this section, the surface-equivalent size parameter of the scattering droplets equals to 150 (corresponding to a diameter equals to about 30 μm for an incident visible wavelength: 0.6283 μm).

First, to validate the code based on the Null-field method, the results calculated by Null-field method for a spheroid with ellipticity equals to 1.0001 are compared with those calculated by Lorenz-Mie theory for a perfect spherical particle. The comparisons of normalized intensities are shown in Fig. 2. The results from the two methods agree with each other very well for the full scattering diagram as well as for the rainbow region.

Relying on previous works on developing the GLMT for spheroids (Xu et al. 2007; Han et al. 2003; Han et al. 2009), the GLMT also provides us the capability to predict the scattering behaviour for spheroids. Thus, the code based on the Null-field method is validated by comparing the scattering results calculated by Null-field method with those calculated by GLMT for spheroids. The scatterer is a prolate spheroid with ellipticity equals to 0.97, whose orientation is specified by Euler angles α, β, γ equal to 0°. Comparisons of normalized intensities are illustrated in

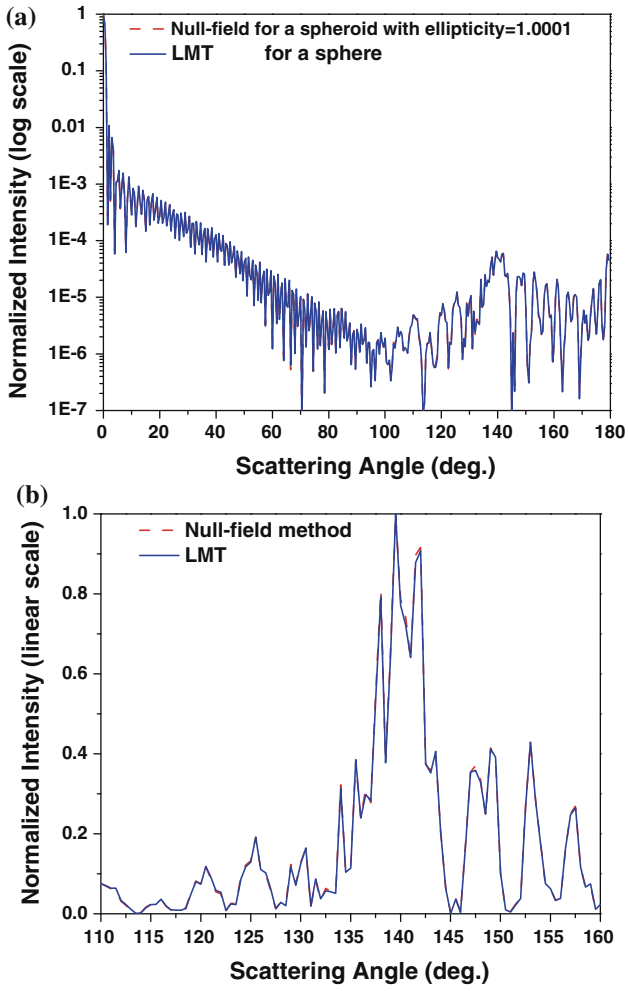

Fig. 2 Comparisons of scattered field intensity diagram calculated by the Null-field method for a spheroid with $a/b = 1.0001$ and by the Lorenz-Mie theory for a perfect sphere with size parameter 150. **a** Full scattering diagram, **b** Details around the rainbow angle

Fig. 3. Figure 3a shows that the results from the two methods coincide with each other in the general picture except a small deviation occurs around the scattering angle 90°. This deviation is caused by a numerical instability, which happens around the scattering angle 90° when we evaluating scattering intensities by GLMT for spheroids with a large particle-size parameter and/or a big ellipticity. This numerical instability has been explained in an earlier paper (Han et al. 2003), and the improvement is under analysis. Nonetheless, we must underline that the instability is not significant around the rainbow angle, a situation that is favourable for rainbow measurements. Figure 3b displays the comparison of the normalized scattered intensities around the rainbow angle calculated by Null-field method and by GLMT. The results from the two methods match each other very well, indicating that both of them are suitable for the rainbow prediction.

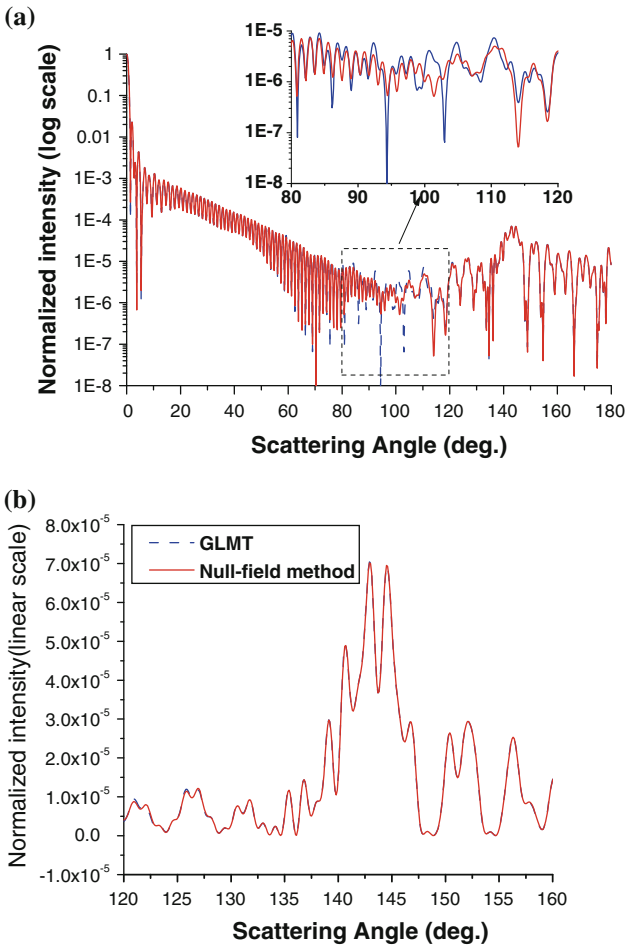

Fig. 3 Comparisons of scattered field intensity diagram calculated by the Null-field method and by the GLMT for a spheroid with ellipticity equals to 0.97 and surface-equivalent size parameter 150. The *solid curve* is obtained by the Null-field method, and the dashed line is obtained by GLMT. The semi-length b is perpendicular to the incident plane wave. **a** General picture and a zoom for details near 90° **b** Details around the rainbow angle

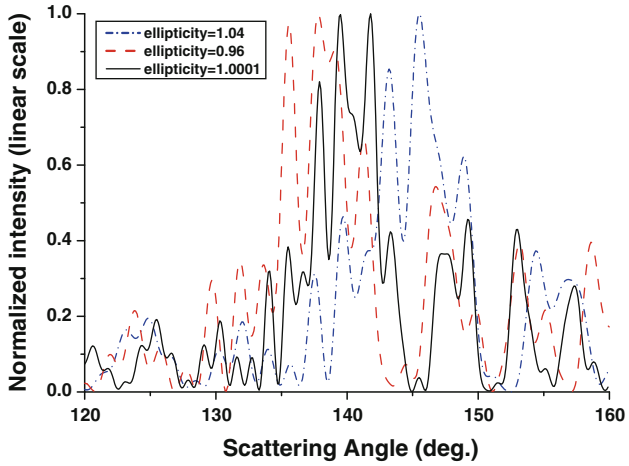

Fig. 4 Normalized scattered intensity diagram around the rainbow angle for a spheroid with surface-equivalent size parameter 150 in a fixed orientation (α, β, γ equal to 0.0°), different ellipticities (0.96, 1.0001, 1.04) are plotted

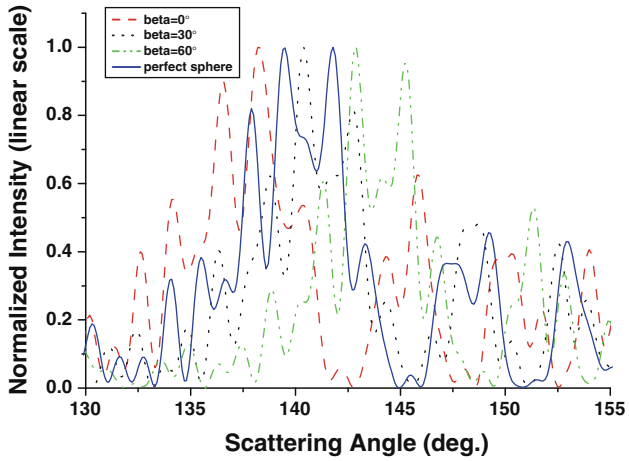

Fig. 5 Normalized scattered field intensity diagram around the rainbow angle for a spheroid with Euler angles $\alpha = 0.0°$, $\gamma = 0.0°$ and different β. The result for a sphere with a same surface-equivalent size parameter 150 is also compiled

On the basis of the validation works above, the Null-field method is applied to check the sensitivity of the rainbow pattern created by an individual particle to its ellipticity. The scattering behaviours of a single spheroid in a fixed orientation with different ellipticities are studied. The Euler angles α, β, γ are equal to 0°, and the particle ellipticity is the parameter. Exemplifying results of normalized intensities are compiled in Fig. 4. A shift of the main peak can be observed with the increase of the ellipticity. The simulation results reveal a general conclusion that both the rainbow position and the shape created by a single non-spherical particle are very sensitive to its ellipticity. Furthermore, the rainbow angle of the primary order rainbow can be obtained by filtering the Fourier transformed intensity diagram, which is calculated by either the GLMT or the Null-field method (Han et al. 2002), corresponding deviations in the filtered intensity for the primary order rainbow can be evaluated by using the Debye series through separating the $p = 2$ order of scattering (Xu et al. 2010).

The behaviour of the rainbow pattern with regard to the change of the particle orientations is investigated in the following. Rainbows created by non-spherical droplets with ellipticity equals to 1.03 and various orientations are discussed. Angular distribution of scattered intensity around the rainbow angle has been computed by Null-field method for a spheroid with Euler angles α, γ equal to 0° and β increasing from 0° to 90° with a step of 10°. Figure 5 compiles some exemplifying results. As the angle β increases from 0° to 90°, the primary rainbow position of

the spheroid shifts slowly from the left side to the right side of the primary rainbow position of its surface-equivalent sphere.

In this section, the code based on the Null-field method is validated by LMT and GLMT. The light scattering properties around the rainbow angle for a spheroid in an arbitrary orientation have been studied by using the Null-field method. Simulation results confirm that a small departure away from perfect sphere can influence both the rainbow location and shape greatly. For particles of the same shape, different orientations also induce large shifts in the rainbow location and big variations in the rainbow shape, which makes it very difficult to find a relationship between the rainbow pattern and the refractive index for an arbitrary oriented non-spherical particle. Nonetheless, the synthetic rainbow obtained by GRT is claimed to be insensitive to the influence of non-sphericity. This claim is analysed and quantified in the next section.

3 Scattering by a group of spheroids in random orientations

On the basis of the results presented in the last section, the rainbow pattern of an individual particle is very sensitive to the non-sphericity, which makes the analysis of the rainbow pattern extremely difficult. To overcome these difficulties, the GRT was developed by van Beeck et al. (1999, 2001). The key point is to extend the investigation from a simple particle to a group of particles. Then, the rainbows created by each droplet in a cloud are added together leading to a stable and clear synthetic rainbow pattern, which can be used to extract a size distribution and a mean refractive index (temperature) of the droplets. The GRT was developed on the assumption that a stable synthetic rainbow can be obtained due to two different intensity summation processes, namely an accumulative summation from rainbows created by spherical droplets, as the rainbow positions are identical for all of them, and a dispersive summation from the rainbows created by randomly oriented non-spherical particles, whose rainbow positions are randomly located then yielding a uniform background, so in this way, the rainbow pattern created by spherical particles is selected out automatically. However, if the assumption of a uniform background is not verified, how does the non-sphericity of droplets affect the results? To test the assumption, the light scattering properties of a group of randomly oriented spheroids are investigated in this section.

As we mentioned, the exiting programmes within the framework of GLMT for light scattering of a spheroid in an arbitrary orientation still have a limitation in the domain of size parameter at the moment (Xu et al. 2007; Han et al. 2009). Nevertheless, this limit has been overcome by using the Null-field method to deal with particles with size parameter well exceeding 100. Thus, the Null-field method is applied in this section for the numerical simulation for an ensemble of spheroids. The basic particle parameters used in the simulations of this section are as follows: the ellipticities are distributed in the range [0.9 1.1], the surface-equivalent size parameter is equal to 100 (corresponding to a diameter equals to about 20 μm for an incident visible wavelength 0.628 μm), and the refractive index equals to 1.330.

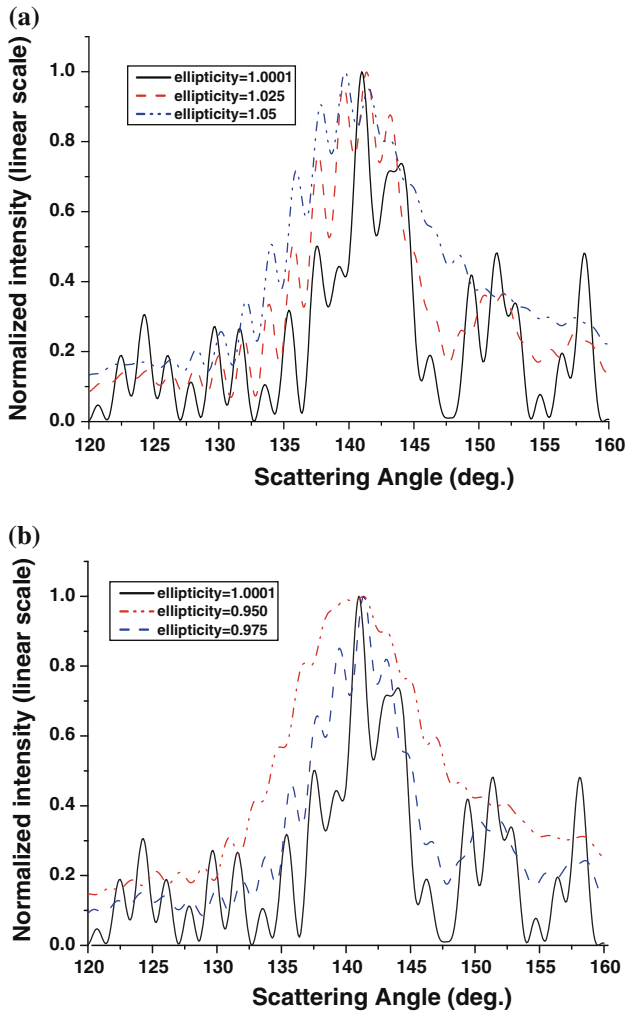

Fig. 6 Normalized scattered intensities around the rainbow angle for randomly oriented spheroids with different ellipticities. **a** Randomly oriented oblate spheroids. **b** Randomly oriented prolate spheroids

3.1 A group of identical spheroids

A group of identical spheroids (spheroids with the same shape) are studied in this subsection. In Fig. 6, angular distribution of scattered intensity around the rainbow angle is displayed for randomly oriented spheroids as a function

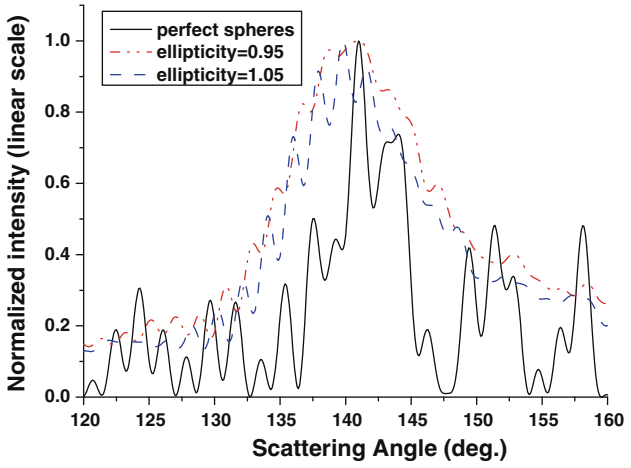

Fig. 7 Comparison of normalized scattered field intensity diagram for **a** prolate spheroids (ellipticity = 0.95); **b** spheres with a same surface-equivalent size parameter; **c** oblate spheroids (ellipticity = 1.05); in random orientations

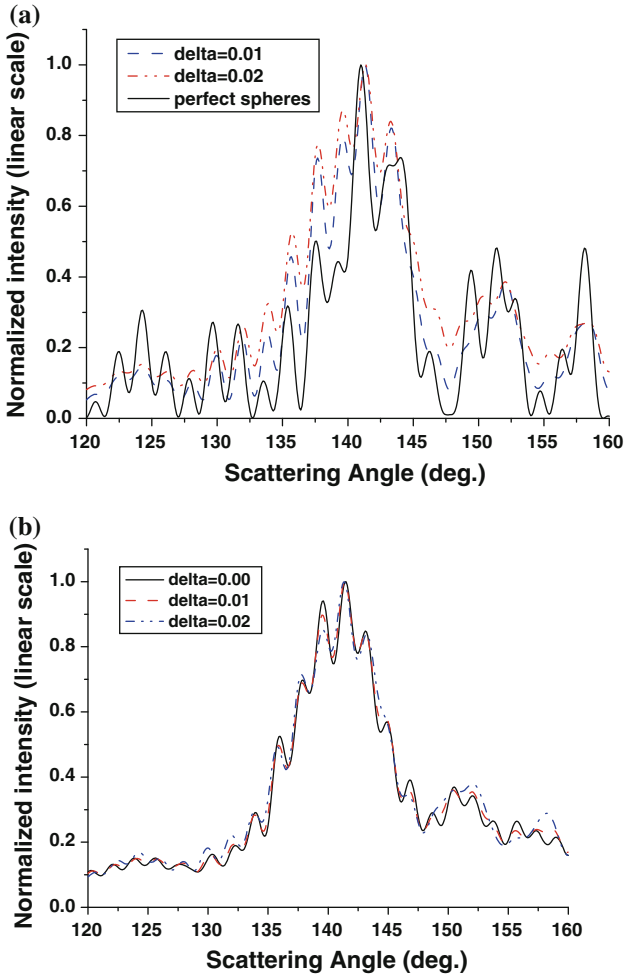

Fig. 8 Normalized scattered field intensity diagram around the rainbow angle for randomly oriented spheroids whose ellipticities satisfy Gauss normal distribution with different dispersions and mean values. **a** Mean value 1.00 with various dispersions **b** Mean value 0.97 with various dispersions

of ellipticity. It shows that, for both oblate (Fig. 6a) and prolate (Fig. 6b) spheroids, a clear and stable synthetic rainbow pattern can be obtained. The angular position of the primary rainbow maximum shifts to smaller angle, as their ellipticities depart away from 1.00. Meanwhile, the half width of the maximum peak of the primary rainbow is broadened. The valley between the first peak and the second peak of the primary rainbow is filled little by little. Furthermore, when the ellipticity departs away further from 1.00, the orientation average effect could eliminate the ripple structure on the primary rainbow. Finally, as is shown in Fig. 7, the average effect due to the random orientations removes the ripple structure for prolate spheroids more efficiently than it does for oblate spheroids.

3.2 A group of spheroids with various ellipticities

In this subsection, a group of water droplets, whose ellipticity distribution satisfies the Gauss normal distribution in the range [0.9 1.1], are taken into consideration.

Figure 8 shows the angular distribution of scattered intensity around the rainbow angle for a group of randomly oriented spheroids whose ellipticity distribution satisfies the Gauss normal distribution. In Fig. 8a, the mean value of their ellipticities is 1.00, and the dispersions are 0.00, 0.01 and 0.02, respectively. In Fig. 8b, the parameters are the same with that in Fig. 8a except that the mean value of their ellipticities is 0.97. The figures tell us that as the dispersion of the ellipticity distribution increases, the angular position of the maximum of the primary rainbow seems to keep steady, the half width of the first peak expands a little, the valley between the first peak and the second peak is filled slowly. Furthermore, a comparison between Fig. 8a, b reveals that the rainbow pattern created by droplets with larger shape deviation (deviation from sphere) is less sensitive to the dispersion of the ellipticity distribution.

4 Practical implications in GRT

It is shown in Sect. 3 that the global rainbow pattern is sensitive to the shape of the scattered particles. In this section, the global rainbow signals obtained from the simulations are used to evaluate the size distribution and temperature of the droplets; the sensitivity of the measurements to the non-sphericity is quantified.

Based on the assumption that a stable synthetic rainbow is created by spherical droplets, several powerful inversion

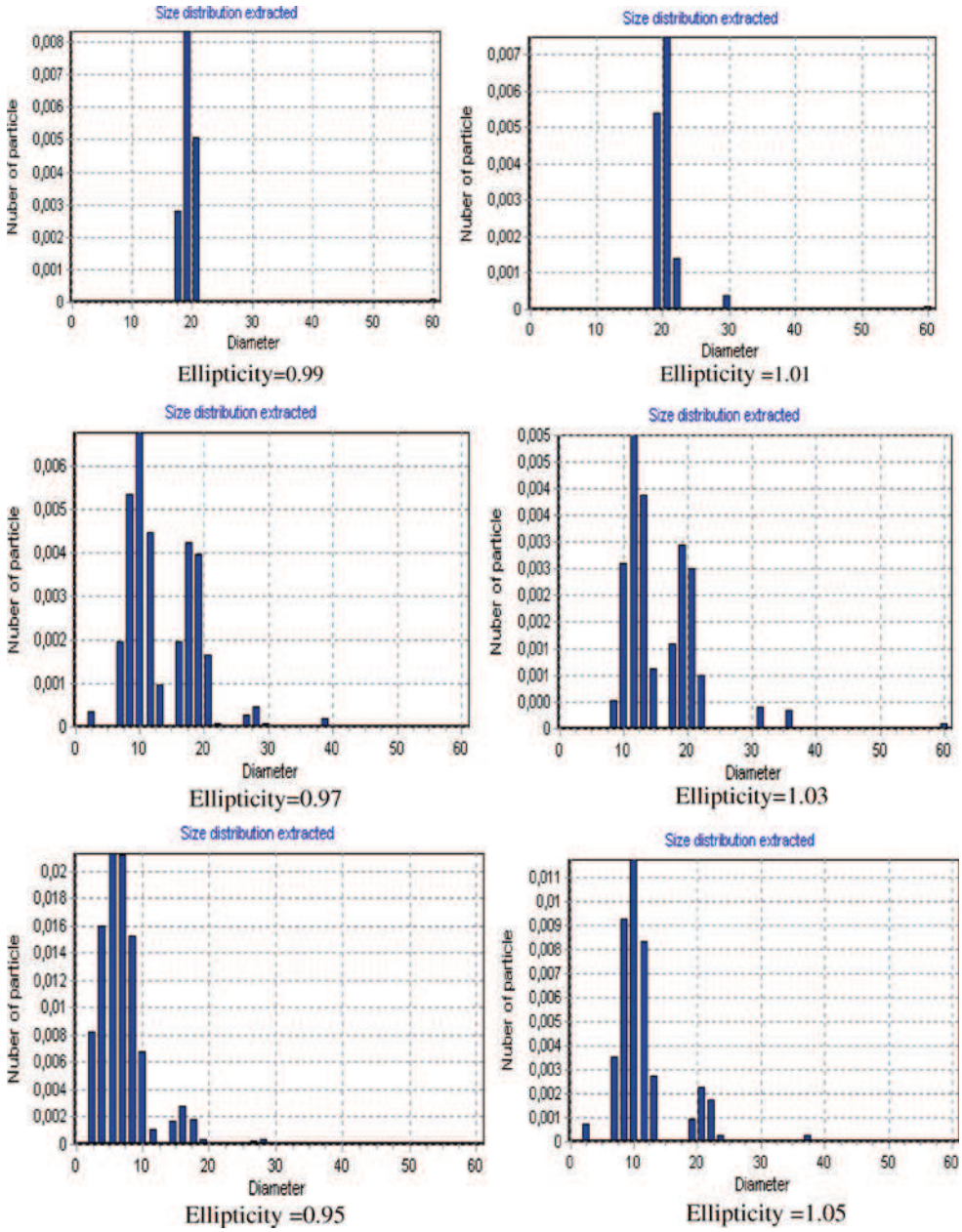

Fig. 9 Typical extracted size distribution for water droplets with a surface-equivalent diameter 20 μm. Ellipticity is the parameter

schemes were developed in the recent years (Vetrano et al. 2004; Saengkaew 2006) in order to deduce the particle parameters (size distribution and refractive index) from the global rainbow signals. In the following, an algorithm (Saengkaew 2006), which is based on the non-negative least *square method combined with a minimization procedure*, is applied to predict the diameter and temperature by fitting the simulated global rainbow signals obtained from the Null-field method for a group of spheroids (samples are presented in the last section) to the simulated results obtained by using Nussenzveig's theory for a group of spheres.

4.1 A group of identical spheroids

Typical inversion results extracted from global rainbow signals created by a group of identical water droplets are shown in Fig. 9 and Table 1. The surface-equivalent size parameter of these spheroids is 100 (corresponding to a diameter equals to about 20 μm for an incident visible wavelength 0.628 μm). The remarkable phenomenon to notice from Fig. 9 is that more and more "spurious small particles" are extracted from the simulated signals, as the shape of the particles departs away from perfect spheres, both when the ellipticity becomes larger and less than 1.0.

Table 1 Extracted refractive indices from simulated signals created by identical spheroids in random orientations with ellipticity as the parameter

Ellipticity	1.01	1.02	1.03	1.04	1.05
Refractive index	1.3287	1.3278	1.3241	1.3198	1.3135
Ellipticity	0.99	0.98	0.97	0.96	0.95
Refractive index	1.3272	1.3291	1.3245	1.3191	1.3136

These predictions are confirmed by the facts we observed in the experiments which we carried out very recently (Saengkaew et al. 2009). Furthermore, the "spurious small particles" even begin to dominate the proportion of the extracted size distribution when the ellipticity of the particles exceeds 1.03 or less than 0.97. Nevertheless, as is shown in Table 1, the influence to the refractive index is less significant. But it is worth to remark that the deviation between the extracted refractive index and the simulation parameter increases as the droplet non-sphericity increases. It is not a surprise to notice that the extracted results for oblate spheroids and for prolate spheroids of the same non-sphericity are similar. Compared to the obvious different behaviour of prolate and oblate spheroid in the analysis of single particle (Fig. 4), there is no more big difference between them when a group of randomly oriented particles are taken into consideration. This agrees with the results found by Asano and Sato (1980) when they analysed particles with smaller size parameter.

4.2 A group of spheroids with various ellipticities

Typical inversion results extracted from global rainbow signals created by a group of water droplets with different mean ellipticities and dispersions (σ) are shown in this subsection. The parameters in Fig. 10 and Table 2 are related to a group of droplets whose ellipticity distribution satisfies the Gauss normal distribution. The mean value is 1.00, and the dispersion is the parameter. When the dispersion is small, the size distribution as well as the refractive index (temperature) is nearly accurate. As the dispersion of the ellipticity distribution increases, the deduced refractive indices move a little to smaller values (Table 2), and the dispersion of the extracted size distribution increases (Fig. 10).

Table 3 are refractive indices extracted from simulated signals created by spheroids with dispersion equals to 0.01

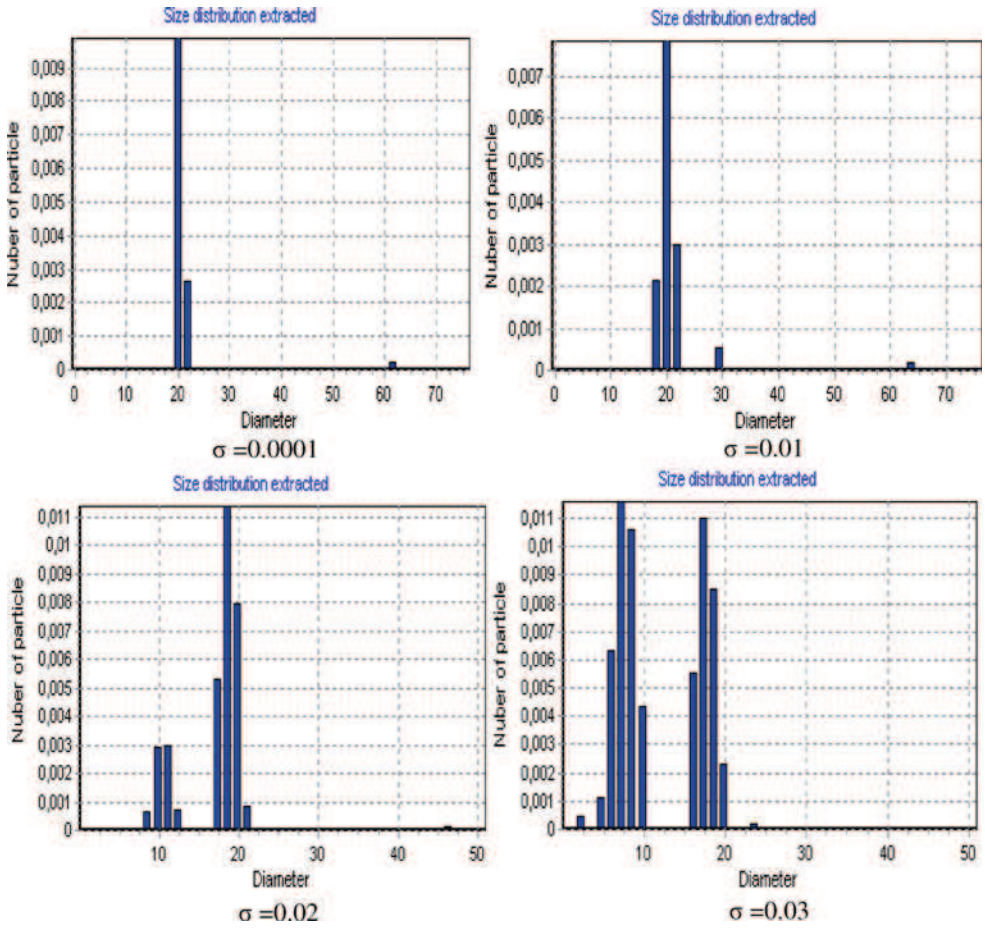

Fig. 10 Typical exacted size distributions for water droplets with a surface-equivalent diameter 20 μm. The dispersions (σ) of the ellipticity distribution is the parameter, while the mean value is a fixed value 1.00

Table 2 Extracted refractive indices from simulated signals created by spheroids with different dispersions of the ellipticity distribution, whose mean value is a fixed value 1.00

Dispersion	0.01	0.015	0.02	0.025	0.030
Refractive index	1.3288	1.3273	1.3261	1.3248	1.3232

Table 3 Extracted refractive indices from simulated signals created by spheroids with different mean values of the ellipticity distribution, whose dispersion is equal to 0.01

Ellipticity	1.01	1.02	1.03	1.04	1.05
Refractive index	1.3276	1.3255	1.3233	1.3202	1.3135
Ellipticity	0.99	0.98	0.97	0.96	0.95
Refractive index	1.3283	1.3255	1.3223	1.3181	1.3121

Table 4 Extracted refractive indices from simulated signals created by spheroids with different mean ellipticities and various dispersions (σ)

	Mean ellipticity = 1.03	Mean ellipticity = 1.0001	Mean ellipticity = 0.97
$\sigma = 0.001$	1.3241	1.3294	1.3245
$\sigma = 0.01$	1.3233	1.3288	1.3223
$\sigma = 0.02$	1.3205	1.3261	1.3205

and different mean values. Table 4 exhibits refractive indices extracted from simulated signals created by spheroids with different mean ellipticities and various dispersions (σ).

Up to this point, only the refractive index has been discussed. However, the temperature of droplets is what we want to determine in the experiments. As we mentioned above, the temperature can be obtained directly according to the relationship between temperature and refractive index for a particular liquid.

For the water droplets used here, in Fig. 11, a comparison between the data from Table 3 and those from Table 1 is shown, along with their corresponding temperatures calculated according to the formulations given by Harvey et al. (1998). It is found that if the spheroids' ellipticity is out of the range [0.97 1.03], the extracted refractive indices are so small that unreasonable temperatures are extracted, which could be regarded as an indicator for experiments. Once an unreasonable temperature is extracted, it tells us that the shape of the particle departs too far away from sphere. The figure also tells us that the deduced refractive indices turn out to be smaller for particles with a larger dispersion of the ellipticity distribution. This conclusion is also supported by the data from Table 4.

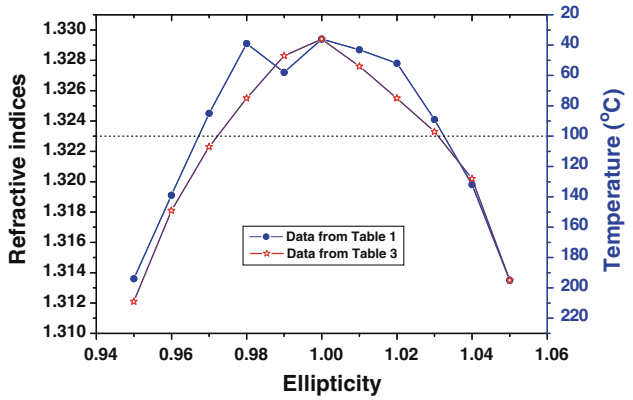

Fig. 11 Comparison of the data from Table 3 and those from Table 1 as a function of ellipticity, temperatures in degree Celsius (°) correspond to the refractive indices are plotted in the *right side*

5 Discussion and conclusion

In the framework of the Null-field method within a T-matrix formulation, the light scattering properties around the rainbow angle are investigated for one spheroid in an arbitrary orientation and for an ensemble of spheroids in random orientations illuminated by a plane wave. Based on the assumption that a stable synthetic rainbow is created by spherical droplets, an algorithm (Saengkaew 2006), which is based on the non-negative least square method, is applied to predict the diameter and temperature by fitting the simulated global rainbow signals obtained from the Null-field method for a group of spheroids to the simulated results obtained by using Nussenzveig's theory for a group of spheres.

For an individual non-spherical droplet, the Null-field method provides us with the capability to simulate rainbows accurately, as confirmed by comparing with the results obtained from the rigorous generalized Lorenz-Mie theory. Simulations show that the rainbow pattern is very sensitive to the particle non-sphericity. This is due to the fact that both the position and shape of the rainbow pattern depend not only on the shape of the particle, but also on its specific orientation, which makes the analysis of the rainbow pattern created by a single non-spherical particle extremely difficult.

In the case of an ensemble of non-spherical droplets in random orientations, a stable and clear global rainbow pattern can always be detected. The global rainbow technique signals generated by a group of droplets do not apparently suffer from the typical problems we encounter in the Standard Rainbow Technique, such as the sensitivity to the ripple structure or the large angle shift due to the non-sphericity of particles. However, it does not mean that the non-sphericity does not influence the prediction accuracy of size distribution and temperature in the measurement.

When the rainbow signals created numerically are processed by an inversion procedure, we can see that as the mean value of the ellipticity distribution increases, larger dispersion in the extracted size distribution and more "spurious small particles" are produced. At the same time, the refractive indices extracted from the simulated signals turn out to be smaller, although it is not significantly influenced. As the dispersion of the ellipticity distribution increases, larger dispersion in the extracted size distribution and relatively smaller refractive indices are found, more "spurious small particles" are also extracted from the simulated signals. These quantified results confirm the experimental observations we previously obtained (Saengkaew et al. 2009).

The physical origin of the small spurious particles extracted by the inversion procedure can be explained. This is due to the fact that the increases of the dispersion and of the mean value of the ellipticity distribution lead to the broadening of the first peak of the primary rainbow and some reduction to its slope. Provided that the rainbow pattern is constructed fully by perfect spherical particles, these phenomena are interpreted to be brought in by a group of smaller water droplets. Consequently, "smaller spurious particles" are produced in the inversion procedure instead of larger spheroids. Meanwhile, the extracted refractive index turns out to be a little smaller than the original parameter. It implies that the presence of the spurious particles can be viewed as an indicator of the refractive index quality. When there is not any spurious particles are extracted, the refractive index measurements can be qualified of nearly exact. Consequently, if spurious particles are extracted, it tells us that the measured temperature is overestimated. Another interesting phenomenon in the simulation is that when the ellipticity of the particle exceeds some kind of range, the extracted refractive indices become so small that unreasonable temperatures are extracted, which could also be regarded as an indicator for experiments. Once an unreasonable temperature is extracted, it tells us that the shape of the particle departs too far away from sphere.

Acknowledgments This paper is a part of work supported by the project "Bourse Doctorales en Alternance" between France and China. This work is also partially supported by the program ASTRA between CNRS and ONERA and by the European Community INTERREG IV-a-C5 program. The authors thank the three anonymous reviewers of our paper for their constructive comments to better present our work.

References

Asano S, Sato M (1980) Light scattering by randomly oriented spheroidal particles. Appl Opt 19:962–974

Barton JP (1995) Internal and near-surface electromagnetic fields for a spheroidal particle with arbitrary illumination. Appl Opt 34:5542–5551

Barton JP (2001) Internal, near-surface, and scattered electromagnetic fields for a layered spheroid with arbitrary illumination. Appl Opt 40:3598–3607

Doicu A, Wriedt T, Eremin YA (2006) Light scattering by systems of particles: null-field with discrete sources-theory and programs. Springer, Berlin

Gouesbet G (2010) T-matrix formulation and generalized Lorenz-Mie theories in spherical coordinates. Opt Commun 283:517–521

Han Y, Méès L, Ren K, Gouesbet G, Wu Z, Gréhan G (2002) Scattering of light by spheroids: the far field case. Opt Commun 210:1–9

Han Y, Gréhan G, Gouesbet G (2003) Generalized Lorenz-Mie theory for a spheroidal particle with off-axis Gaussian-beam illumination. Appl Opt 42:6621–6629

Han Y, Zhang Y, Zhang H, Han G (2009) Scattering of typical particles by beam shape in oblique illumination. J Quant Spectrosc Radiat Transf 110:1375–1381

Harvey AH, Gallagher JS, Sengers J (1998) Revised formulation for the refractive index of water and stream as a function of wavelength, temperature and density. J Phys Chem Ref Data 27:761–774

Lemaitre P, Porcheron E, Gréhan G, Bouilloux L (2006) Development of a global rainbow refractometry technique to measure the temperature of spray droplets in a large containment vessel. Meas Sci Technol 17:1299–1306

Mishchenko MI, Travis LD (1994a) Light scattering by polydispersions of randomly oriented spheroids with sizes comparable to wavelengths of observation. Appl Opt 33:7206–7225

Mishchenko MI, Travis LD (1994b) T-matrix computations of light scattering by large spheroidal particles. Opt Commun 109:16–21

Mishchenko MI, Hovenier JW, Travis LD (1999) Light scattering by nonspherical particle: theory, measurements and applications. Academic, San Diego

Möebius W (1910) Zur Theorie des Regenbogens und ihrer experimentellen Prüfung. Ann Phys (Leipzig) 33:1493–1558

Roth N, Anders K, Frohn A (1988) Simultaneous measurement of temperature and size of droplets in the micrometric range. 7th international congress on optical in flow and particle diagnostic ICALEO 88, L.I.A., Sunnyvale (U.S.A.), 67:294–304

Roth N, Anders K, Frohn A (1990) Simultaneous measurement of temperature and size of droplets in the micrometric range. J Laser Appl 2:37–42

Saengkaew S (2006) Development of novel global rainbow technique for characterizing spray generated by ultrasonic nozzle. Ph.D. dissertation, University of Chulalongkorn (Thailand) and Rouen (France)

Saengkaew S, Charinpanitkul T, Vanisri H, Tanthapanichakoon W, Biscos Y, Garcia N, Lavergne G, Mees L, Gouesbet G, Gréhan G (2007) Rainbow refractrometry on particles with radial refractive index gradients. Exp Fluids 43:595–601

Saengkaew S, Godard G, Blaisot JB, Gréhan G (2009) Experimental analysis of global rainbow technique: sensitivity of temperature and size distribution measurements to non spherical droplets. Exp Fluids 47:839–848

van Beeck J (1997) Rainbow phenomena: development of a laser-based, non-intrusive technique for measuring droplet size, temperature and velocity. Ph.D. Dissertation, Unversity of Eindhoven

van Beeck J, Giannoulis D, Zimmer L, Riethmuller ML (1999) Global rainbow thermometry for droplet temperature measurement. Opt Lett 24:1696–1698

van Beeck J, Zimmer L, Riethmuller ML (2001) Global rainbow thermometry for mean temperature and size measurement of spray droplets, part. Part Syst Charact 18:196–204

Vetrano MR, van Beeck J, Riethmuller ML (2004) Global Rainbow thermometry: improvements in the data inversion algorithm and validation technique in liquid-liquid suspension. Appl Opt 43:3600–3607

Waterman PC (1971) Symmetry, unitarity, and geometry in electromagnetic scattering. Phys Rev 3:825–839

Wielaard DJ, Mishchenko MI, Macke A, Carlson BE (1997) Improved T-matrix computations for large, nonabsorbing and weakly absorbing nonspherical particle and comparison with geometrical-optics approximation. Appl Opt 36:4305–14313

Xu F, Ren K, Gouesbet G, Gréhan G, Cai X (2007) Generalized Lorenz-Mie theory for an arbitrarily oriented, located, and shaped beam scattered by a homogeneous spheroid. J Opt Soc Am A 24:119–131

Xu F, Lock JA, Tropea C (2010) Debye series for light scattering by a spheroid. J Opt Soc Am A 27:671–686

Study of scattering from a sphere with an eccentrically located spherical inclusion by generalized Lorenz–Mie theory: internal and external field distribution

J. J. Wang,[1,2,*] G. Gouesbet,[2] Y. P. Han,[1] and G. Gréhan[2]

[1]*School of Science, Xidian University, Xi'an, China*
[2]*Laboratoire d'Electromagnétisme des Systèmes Particulaires (LESP), Unité Mixte de Recherche (UMR) 6614 du Centre National de la Recherche Scientifique (CNRS), Complexe de Recherche Interprofessionnel en Aérothermochimie (CORIA), Université de Rouen et Institut National des Sciences Appliquées (INSA) de Rouen BP12, avenue de l'université, technôple du Madrillet, 76801, Saint-Etienne-du Rouvray, France*
**Corresponding author: jiajie.wang@coria.fr.*

Received October 19, 2010; accepted November 11, 2010;
posted November 17, 2010 (Doc. ID 136868); published December 22, 2010

Based on the recent results in the generalized Lorenz–Mie theory, solutions for scattering problems of a sphere with an eccentrically located spherical inclusion illuminated by an arbitrary shaped electromagnetic beam in an arbitrary orientation are obtained. Particular attention is paid to the description and application of an arbitrary shaped beam in an arbitrary orientation to the scattering problem under study. The theoretical formalism is implemented in a homemade computer program written in FORTRAN. Numerical results concerning spatial distributions of both internal and external fields are displayed in different formats in order to properly display exemplifying results. More specifically, as an example, we consider the case of a focused fundamental Gaussian beam (TEM_{00} mode) illuminating a glass sphere (having a real refractive index equal to 1.50) with an eccentrically located spherical water inclusion (having a real refractive index equal to 1.33). Displayed results are for various parameters of the incident electromagnetic beam (incident orientation, beam waist radius, location of the beam waist center) and of the scatterer system (location of the inclusion inside the host sphere and relative diameter of the inclusion to the host sphere).

OCIS codes: 140.0140, 260.2110, 290.0290.

1. INTRODUCTION

The well-known Lorenz–Mie theory (LMT) [1] provides a rigorous way to describe the electromagnetic scattering interaction between a linearly polarized plane wave and a homogeneous spherical particle described by its diameter d and its complex refractive index m. Since the advent of the laser, the interaction of a focused laser beam with different kinds of particles has become a most interesting topic, with applications spread in a variety of fields including particle sizing, Raman scattering diagnostics, optical manipulation, and design of new optics devices. To meet the requirements of these new practical situations, the LMT has been generalized after the name of generalized Lorenz–Mie theory (GLMT) mainly from two perspectives: (i) arbitrary laser beam and (ii) particle shape, with recent reviews by Lock and Gouesbet [2] and by Gouesbet [3]. The GLMT extends the LMT, from the first perspective, to deal with the scattering problem of particles illuminated by an arbitrary laser beam [4–7] instead of a continuous plane wave, which is the case in the LMT framework. Another version to arbitrary shaped beam, equivalent to GLMT, could be found in [8]. The GLMT was also extended to deal with cases of nonspherical and/or composite scatterers from the second perspective, relying on the method of separation of variables (SVM) in various orthogonal coordinate systems [9–12].

For an arbitrary shaped beam, an issue of significance concerns the orientation of the beam with respect to the scatterer. The consideration of arbitrary orientation is compulsory in the case of GLMTs for cylinders and has been implemented, both in circular cylindrical and in elliptical cylindrical coordinates, e.g., [9,13–15] and references therein. In the case of spherical coordinates with spherical particles possessing a complete spherical symmetry (homogeneous spheres, or concentric layered spheres), the concept of arbitrary orientation, more precisely of arbitrary direction (that is to say without accounting for the direction of polarization), is irrelevant since any diameter of the scatterer can be regarded as an axis of symmetry. Any direction of propagation then does belong to the parallel illuminations, including on-axis incident case [16] and off-axis incident case [17]. However, in spherical coordinates, with spherical particles which do not possess a complete spherical symmetry, such as for the case of a spherical particle hosting an eccentric spherical inclusion, we may have to distinguish between parallel and oblique illuminations and relate beam shape coefficients in various coordinate systems obtained, one from the other, by a rotation of coordinates. These issues of oblique illumination and of the transformations of spherical beam shape coefficients through rotations of coordinate systems have been thoroughly investigated recently by us with results that can be found in [18–24]. These recent results obtained in the GLMT framework provide a new tool for the description of illuminating arbitrary beams, including the special case of plane waves, and are implemented in the present paper.

With regard to the shape of the scatterer, the wave scattering problem defined by a host homogeneous sphere embedding an eccentrically located inclusion (or several inclusions) has

attracted much interest in recent years in both electromagnetic- and acoustic-oriented literatures [10,25–30]. This is partially due to the fact that particles or fluid droplets with smaller inclusions are very common in our daily life as well as in the research for industry or environment concerns. For instance, many small particles, such as natural biological spores or cells, possibly artificial biological spores or cells for military purposes, and aerosols in the atmosphere could be regarded as spheres with concentric or eccentric inclusions. Also, fluid droplets with small inclusions such as medicinal sprays or daily cosmetics could be modeled as spherical particles with inclusions as well [31–34].

The associated scattering problem has been studied by using various methods, such as the separation of variables method [10,25], the order of scattering approach [26,27], and the extended boundary condition method (EBCM) [28,35], which is also named null-field method [29]. Nevertheless, most of the previous literature dealt with the case of plane wave illumination. After the introduction of a GLMT for the problem under study by Gouesbet and Gréhan [10], numerical results have been provided by Han *et al.* [36] and Yan *et al.* [37]. Nevertheless, only far-field scattering results were presented in [36,37]. In the present paper, spatial distributions of external and internal fields, including scattered field in the far zone, near-surface field outside of the host sphere and internal field inside the host sphere, are analyzed extensively and systematically by taking advantage of the new aforementioned computational tool [20–24].

One of the purposes of our present work is to cast some light on light-scattering-related experimental or industrial applications such as in particle characterization or identification techniques [31,33,34]. Indeed, as we know, light scattering methods provide ideal means for *in situ* particle characterization or identification, because of their fast responses and nondestructiveness.

Traditionally, light scattering measurements are made with a single, possibly movable, detector, or with a limited number of fixed detectors. Sometimes, such simple facilities might be sufficient due to the inherent symmetries in the scattered field patterns created by particles sharing a high enough level of symmetry, such as spherical particles or axisymmetric particles exhibiting some specific orientations. However, for the study of nonspherical or nonhomogeneous particles, such as the ones investigated in the present paper, in cases where symmetries in the scattered field distribution are broken, more elaborate spatial detections might be required. With improved instrumentation, such as wide application of intensified charge-coupled device cameras, researchers are able to employ two-dimensional angular optical scattering as a tool for analyzing such particle systems [31,38]. Along with the applications of new facilities in the measurements, a knowledge of spatial distributions of the energy intensity is also required in theoretical processing, especially when the symmetry of the scattering pattern is broken, this being an issue that we keep in mind in the present paper.

Another motivation of our study lies on the expected future detection of optical (Hamiltonian) chaos features depicted in [39–41], which might be associated with the destruction and splitting of morphology-dependent resonances (MDRs) [27,42,43]. Such features are associated with the increase of complexity of the optical interactions between the eccentrically located inclusion and the host sphere, generated by a loss of spherical symmetry. The curved surfaces of the particle system together with the discontinuity of the complex refractive index at the interface of two different media influence the spatial distribution of the field intensities both in the internal and external regions. In this paper, spatial distributions of the internal and near-surface fields for the scattering system under study in off-resonance conditions are presented for the first time, with the expectation that the numerical results given here would contribute to the understanding of multiple scattering interactions between closely spaced particles or between different parts of a scattering system.

The body of the present paper is organized as follows. In Section 2, we present a theoretical treatment for the scattering problem of a sphere with an eccentrically located spherical inclusion illuminated by an arbitrary shaped electromagnetic beam in an arbitrary orientation in the framework of GLMT. Particular attention is paid to the description and application of an arbitrary shaped beam in an arbitrary orientation to the problem under study. In Section 3, the case of a focused Gaussian beam in the fundamental mode (TEM_{00}) is specifically considered for numerical illustration. Spatial distributions of both internal and external fields, including scattered field in the far zone, near-surface field outside of the host sphere and internal field inside the host sphere, are presented for various parameters of the incident electromagnetic beam and of the scatterer system. Some discussions are presented in Section 4, which serves as a conclusion as well.

2. THEORETICAL TREATMENT BY GLMT

A. Definition of the Problem

The geometry of the specific scattering problem under study is illustrated in Fig. 1. The host sphere is attached to a global Cartesian coordinate system $(O_1X_1Y_1Z_1)$, and its corresponding spherical coordinates are designated as $(r_1, \theta_1, \varphi_1)$. A spherical inclusion is embedded in the host sphere. It is attached to an inclusion coordinate system $(O_2X_2Y_2Z_2)$, whose corresponding spherical coordinates are designated as $(r_2, \theta_2, \varphi_2)$. The three axes in the inclusion coordinate system

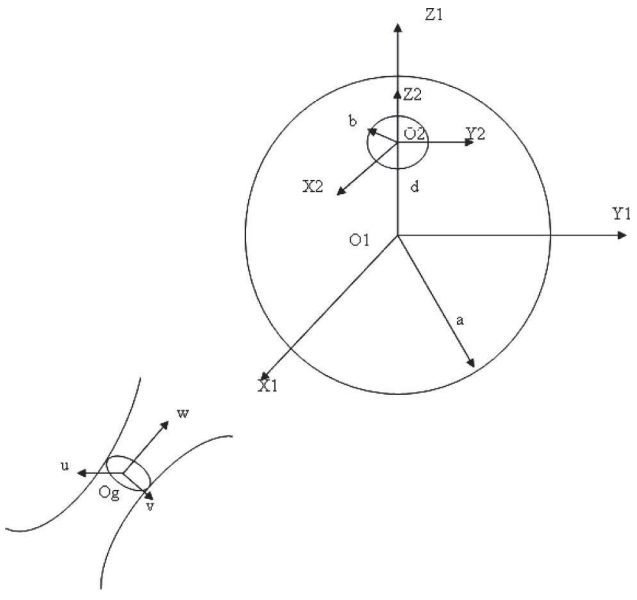

Fig. 1. Scattering geometry of the problem under study.

are parallel to the corresponding axes in the global coordinate system, respectively.

Without any loss of generality, the center of the inclusion is located on the z axis of the global coordinate system. The center–center separation distance is designated by d; we have

$$x_2 = x_1, \qquad y_2 = y_1, \qquad z_2 = z_1 - d. \tag{1}$$

The radii of the host sphere and of the inclusion are a and b, respectively. The complex refractive index and wavenumber of the surrounding medium are m_0 and k_0, the corresponding parameters for the host sphere are m_1 and k_1, and for the inclusion, m_2 and k_2.

The scattering model in Fig. 1 is illuminated by an arbitrary shaped beam propagating along the w axis in the beam coordinate system O_gUVW. The coordinates of its origin O_g with respect to the global coordinate system $(O_1X_1Y_1Z_1)$ are denoted as (x_0, y_0, z_0). The frame system $(O_1X_1Y_1Z_1)$ can be obtained from the beam coordinate system (O_gUVW) by rotations through Euler angles (α, β, γ) [20–23] followed by a translation of (x_0, y_0, z_0), and vice versa. In this paper, a focused Gaussian beam propagating along the w axis with beam waist center located in the origin of the beam coordinate system O_gUVW is specified for numerical illustration. The time-dependence factor reading as $\exp(jwt)$ is assumed, where w is the angular frequency. This term will be omitted from all formulas for the sake of conciseness.

B. Vector Spherical Wave Functions

The vector spherical wave functions (VSWFs) used in this paper are a little different from the ones used in [20,44] by a normalization factor and also by the fact that we have interchanged the indices n and m, i.e., $\mathbf{M}_{nm}^{(j)}$ instead of $\mathbf{M}_{mn}^{(j)}$ and similarly for $\mathbf{N}_{nm}^{(j)}$. Nevertheless, the interchanges of orders n and m in subscripts occur only superficially in appearance for the purpose of consistency in the paper, which will not change their original meanings. They read as

$$\mathbf{M}_{nm}^{(j)} = (-1)^m [im\tilde{\pi}_n^m(\cos\theta)\mathbf{i}_\theta - \tilde{\tau}_n^m(\cos\theta)\mathbf{i}_\varphi] z_n(kr)\exp(im\varphi), \tag{2}$$

$$\begin{aligned}\mathbf{N}_{nm}^{(j)} = (-1)^m \Bigg\{ & \frac{n(n+1)}{kr} z_n(kr)\tilde{P}_n^m(\cos\theta)\mathbf{i}_r \\ & + \frac{1}{kr}\left[\frac{d}{dr} r z_n(kr)\right]\tilde{\tau}_n^m(\cos\theta)\mathbf{i}_\theta \\ & + \frac{1}{kr}\left[\frac{d}{dr} r z_n(kr)\right] im\tilde{\pi}_n^m(\cos\theta)\mathbf{i}_\varphi \Bigg\} \exp(im\varphi),\end{aligned} \tag{3}$$

in which $\mathbf{i}_r$, $\mathbf{i}_\theta$, and $\mathbf{i}_\varphi$ are standard unit vectors associated with the coordinates r, θ, and φ, respectively, of a spherical coordinate system (r, θ, φ), k is the wavenumber in the considered medium, $z_n(kr)$ designates any spherical Bessel function $(j_n, y_n, h_n^{(1)}, h_n^{(2)})$, and $\tilde{\pi}_n^m$ and $\tilde{\tau}_n^m$ designate the normalized generalized Legendre functions according to

$$\tilde{\pi}_n^m(\cos\theta) = \frac{\tilde{P}_n^m(\cos\theta)}{\sin\theta}; \qquad \tilde{\tau}_n^m(\cos\theta) = \frac{d}{d\theta}\tilde{P}_n^m(\cos\theta). \tag{4}$$

$\tilde{P}_n^m(\cos\theta)$ is the fully normalized associated Legendre function, which is normalized from the associated Legendre functions $P_n^m(\cos\theta)$:

$$\tilde{P}_n^m(\cos\theta) = c_n^m P_n^m(\cos\theta), \tag{5}$$

where c_n^m is a normalization factor:

$$c_n^m = (-1)^m \sqrt{\frac{2n+1}{2}\frac{(n-m)!}{(n+m)!}}, \tag{6}$$

and the associated Legendre functions $P_n^m(\cos\theta)$ read as

$$P_n^m(\cos\theta) = (-1)^m(\sin\theta)^m \frac{d^m P_n(\cos\theta)}{(d\cos\theta)^m}. \tag{7}$$

C. Solutions

The theoretical treatment to scattering from a sphere with an eccentrically located spherical inclusion illuminated by an arbitrary shaped beam was originally presented by Gouesbet and Gréhan [10]. Afterward, Han *et al.* [36] and Yan *et al.* [37] also studied this problem. Here, we will not focus on these derivations but recall some expressions necessary for the sequel.

In the global coordinate system, an arbitrary shaped beam in an arbitrary orientation illuminating the host sphere may be expressed in terms of VSWFs with two sets of expansion coefficients a_{nm} and b_{nm}:

$$\mathbf{E}^{\text{inc}} = \sum_{n=1}^{\infty}\sum_{m=-n}^{+n} a_{nm}\mathbf{M}_{nm}^{(1)}(k_0\mathbf{r}_1) + b_{nm}\mathbf{N}_{nm}^{(1)}(k_0\mathbf{r}_1), \tag{8}$$

in which the field strength E_0 has been set equal to unity. Furthermore, the relationship between the expansion coefficients a_{nm} and b_{nm} on one hand and the more traditional beam shape coefficients $g_{n,X}^m$ on the other hand is available from [44] and will be provided in the sequel.

Similarly, the scattered field may be expanded using the spherical Bessel functions of the fourth kind:

$$\mathbf{E}^{\text{sca}} = \sum_{n=1}^{\infty}\sum_{m=-n}^{+n} c_{nm}\mathbf{M}_{nm}^{(4)}(k_0\mathbf{r}_1) + d_{nm}\mathbf{N}_{nm}^{(4)}(k_0\mathbf{r}_1). \tag{9}$$

The main field in the annular zone between the surface of the host sphere and that of the inclusion may be expressed using the spherical Bessel functions of the third and the fourth kind in the global coordinates system, indicating a superposition of incoming and outcoming partial waves:

$$\begin{aligned}\mathbf{E}^{\text{int1}} = & \sum_{n=1}^{\infty}\sum_{m=-n}^{+n} e_{nm}\mathbf{M}_{nm}^{(3)}(k_1\mathbf{r}_1) + f_{nm}\mathbf{N}_{nm}^{(3)}(k_1\mathbf{r}_1) \\ & + v_{nm}\mathbf{M}_{nm}^{(4)}(k_1\mathbf{r}_1) + h_{nm}\mathbf{N}_{nm}^{(4)}(k_1\mathbf{r}_1).\end{aligned} \tag{10}$$

In [10], Eqs. (11) and (12), the choice has been made to use the first and fourth kinds of VSWFs instead , indicating superposition of waves incident on the inclusion and of waves scattered from the inclusion.

The incident coefficients a_{nm} and b_{nm} and the scattered coefficients c_{nm} and d_{nm} can then be related to the expansion coefficients e_{nm}, f_{nm}, v_{nm}, and h_{nm} by applying the

well-known boundary conditions at the main sphere surface $r_1 = a$, according to which the tangential components of the electric and magnetic field would be continuous across the sphere surface.

The same procedure is then implemented in the inclusion coordinate system, which relates the expansion coefficients r_{nm}, s_{nm}, t_{nm}, and u_{nm} of the main field,

$$\mathbf{E}^{\text{int1}} = \sum_{n=1}^{\infty}\sum_{m=-n}^{+n} r_{nm}\mathbf{M}_{nm}^{(3)}(k_1\mathbf{r}_2) + s_{nm}\mathbf{N}_{nm}^{(3)}(k_1\mathbf{r}_2) + t_{nm}\mathbf{M}_{nm}^{(4)}(k_1\mathbf{r}_2) + u_{nm}\mathbf{N}_{nm}^{(4)}(k_1\mathbf{r}_2), \tag{11}$$

to the expansion coefficients p_{nm}, and q_{nm} of the internal field inside the inclusion,

$$\mathbf{E}^{\text{int2}} = \sum_{n=1}^{\infty}\sum_{m=-n}^{+n} p_{nm}\mathbf{M}_{nm}^{(1)}(k_2\mathbf{r}_2) + q_{nm}\mathbf{N}_{nm}^{(1)}(k_2\mathbf{r}_2), \tag{12}$$

by applying the well-known boundary conditions at the inclusion surface $r_2 = b$.

In order to obtain the solutions to the scattering problem, translational addition theorems of VSWFs [45,46] should be applied to the main field so as to relate its expansion coefficients e_{nm}, f_{nm}, v_{nm}, andh_{nm} in the global coordinate system with those r_{nm}, s_{nm}, t_{nm}, and u_{nm} in the inclusion coordinate system. Relevant translational coefficients of the vector addition theorem as well as those of the scalar addition theorem have been discussed in the literature, e.g., [29,47,48], and are given in Appendix A.

As a summary, in the global coordinate system, the expansion coefficients that describe the scattered field, c_{nm} and d_{nm}, and the expansion coefficients that describe the main field, e_{nm}, f_{nm}, v_{nm}, and h_{nm}, can be related to the expansion coefficients that describe the incident field a_{nm} and b_{nm} by application of the boundary conditions, according to which the tangential components of the electric and magnetic field would be continuous across the sphere surface. Similarly, in the inclusion coordinate system, the expansion coefficients which describe the inclusion internal field, p_{nm} and q_{nm}, can be related to the expansion coefficients describing the main field, r_{nm}, s_{nm}, t_{nm}, and u_{nm}, by application of the corresponding boundary conditions at the surface of the spherical inclusion. The solutions to the scattering problem can then be readily reached by applying translational addition theorems of VSWFs to the main field; see [10] for details.

D. Beam Shape Coefficients for an Arbitrary Shaped Beam in an Arbitrary Orientation

In the GLMT, the electromagnetic components of the illuminating beam are described by multipole expansions over a set of basis functions. The expansion coefficients are expressed versus fundamental coefficients, usually denoted as $g_{n,X}^m$ (X is TE, transverse electric, or TM, transverse magnetic, with n from 1 to ∞, m from $-n$ to n), known as beam shape coefficients (BSCs). These BSCs are used to express electromagnetic fields of laser beams in expanded forms, for use in GLMTs, or in other light scattering approaches such as the EBCM. Their calculations form the key issue, and the most difficult one, when dealing with a GLMT. Initiated by Han *et al.* [18,19], a systematic analysis was made recently concerning the transformation of BSCs through rotations of coordinate systems, and corresponding results are published in a series of papers [20–24], providing us a new tool for further studies, especially in cases of nonspherical or composite scatterers.

The relationships between the expansion coefficients a_{nm}, b_{nm} on one hand, and the BSCs $\tilde{g}_{n,X}^m$ on the other hand read as [44]

$$a_{nm} = -ikc_n^{pw}(-1)^m(-1)^{\frac{m-|m|}{2}}\frac{(n-m)!}{(n-|m|)!}\frac{\tilde{g}_{n,\text{TE}}^m}{c_n^m}, \tag{13}$$

$$b_{nm} = kc_n^{pw}(-1)^m(-1)^{\frac{m-|m|}{2}}\frac{(n-m)!}{(n-|m|)!}\frac{\tilde{g}_{n,\text{TM}}^m}{c_n^m}, \tag{14}$$

in which c_n^{pw} are plane wave coefficients reading as [4]

$$c_n^{pw} = \frac{1}{k}(-i)^{n+1}\frac{2n+1}{n(n+1)}. \tag{15}$$

With respect to the corresponding equations in [44], the following modifications have been introduced: (i) the field strength E_0 has again been set equal to unity, (ii) the coefficient c_n^m has been introduced as a consequence of the fact that we use a slightly different definition for the VSWFs [see Subsection 2.B], and (iii) the BSCs are tilde-decorated to indicate that they are valid in a rotated system.

According to the transformation theorem for BSCs in spherical coordinates [20], the tilde-decorated BSCs $\tilde{g}_{n,X}^m$ in a rotated system are expressed versus the BSCs $g_{n,X}^m$ in another system, called the unrotated system, as

$$\tilde{g}_{n,X}^m = \mu_{nm}\sum_{s=-n}^{n}\frac{H_{sn}^m}{\mu_{ns}}g_{n,X}^s, \tag{16}$$

where

$$\mu_{nm} = (-1)^m(-1)^{\frac{m-|m|}{2}}\frac{(n-|m|)!}{(n-m)!}, \tag{17}$$

$$H_{sn}^m = (-1)^{n+s}\frac{(n-m)!}{(n-s)!}e^{im\gamma}e^{is\alpha}\sum_{\sigma}(-1)^{\sigma}\binom{n+s}{n-m-\sigma}\binom{n-s}{\sigma} \times\left(\cos\frac{\beta}{2}\right)^{2\sigma+m+s}\left(\sin\frac{\beta}{2}\right)^{2n-2\sigma-m-s}, \tag{18}$$

in which (α, β, γ) are Euler angles bringing the unrotated system to the rotated system, whose definitions could be found in any of the references [20–24].

With decades of efforts devoted to the description of an arbitrary shaped beam, the BSCs of an arbitrary shaped beam in the unrotated coordinate system can be evaluated by several methods, sharing various degrees of time running efficiency, or of flexibility, namely by using quadratures [49], finite series [50], localized approximations generating localized beam models [6], or by a hybrid method taking advantage of both quadratures and of a localized approximation, named the integral localized approximation [51]. The evaluation of BSCs has also been investigated by relying on addition theorems for translations of coordinate systems, an approach originally introduced by Doicu and Wriedt [52] and also used by Zhang and Han [53]. In our computer program, the Modified Localized Approximation method [6,54], which was rigorously justified by Gouesbet

and Lock [16,17], is applied to evaluate the BSCs in the unrotated coordinate system due to the fact that it provides the most efficient method, with regard to computational times, by orders of magnitude with respect to other methods, such as by using quadratures [55]. It is also the most appealing from a physical point of view because it provides many physical insights on the interpretation of beam models.

In order to describe an arbitrary shaped beam in an arbitrary orientation, the BSCs in the rotated coordinate system have to be evaluated.

Two different ways have been explored to deal with the use of a localization procedure associated with a rotation, namely, a rotation–localization (RL) procedure in which we first apply a localization operator and afterward rotate, and a localization–rotation procedure, in which we first rotate and afterward apply a localization procedure, with details presented in [24]. It has been surprising to uncover that the operations of rotation and localization do not commute, not only for non-Maxwellian beams, but also for Maxwellian beams, in particular, for even a plane wave. Therefore, at the present time, in order to obtain a localized beam model under an arbitrary orientation, one has to use the RL procedure as we have used in this paper. That is to say, after obtaining the BSCs of an arbitrary shaped beam in the unrotated coordinate system by the Modified Localized Approximation method [6,16,17,54], the transformation theorem for BSCs [20–24] is applied to obtain a localized beam model in a rotated system in terms of the localized beam model in the unrotated system.

E. External Near-Surface and Internal Fields

Even though the magnitude and the phase for each component of the electromagnetic field can be determined from the GLMT formalism discussed in this paper, a useful visualization of the electromagnetic field distribution can be obtained by plotting the normalized source function as a function of spatial position. The normalized source function is defined as

$$S = |\mathbf{E}|^2/|E_0|^2, \tag{19}$$

where $\mathbf{E}$ is the electric (internal or external) field and E_0 is the electric field strength of the incident field, which is assumed to be unity in this paper.

1. Internal Field

Inserting Eqs. (2) and (3) into Eq. (11), expressions for evaluating the main internal field in the annular area can be obtained:

$$\mathbf{E}_r^{\mathrm{int1}} = \sum_{n=1}^{\infty}\sum_{m=-n}^{+n}(-1)^m[s_{nm}h_n^{(1)}(k_1r_2) + u_{nm}h_n^{(2)}(k_1r_2)] \times \frac{n(n+1)}{k_1r_2}\tilde{P}_n^m(\cos\theta)\exp(im\varphi), \tag{20}$$

$$\mathbf{E}_\theta^{\mathrm{int1}} = \sum_{n=1}^{\infty}\sum_{m=-n}^{+n}(-1)^m\left\{[r_{nm}h_n^{(1)}(k_1r_2) + t_{nm}h_n^{(2)}(k_1r_2)]im\tilde{\pi}_n^m \times(\cos\theta) + \frac{1}{k_1r_2}\left[s_{nm}\frac{d(r_2h_n^{(1)}(k_1r_2))}{dr_2} + u_{nm}\frac{d(r_2h_n^{(2)}(k_1r_2))}{dr_2}\right]\tilde{\tau}_n^m(\cos\theta)\right\}\exp(im\varphi), \tag{21}$$

$$\mathbf{E}_\varphi^{\mathrm{int1}} = \sum_{n=1}^{\infty}\sum_{m=-n}^{+n}(-1)^m\left\{[-r_{nm}h_n^{(1)}(k_1r_2) - t_{nm}h_n^{(2)}(k_1r_2)]\tilde{\tau}_n^m \times(\cos\theta) + \frac{1}{k_1r_2}\left[s_{nm}\frac{d(r_2h_n^{(1)}(k_1r_2))}{dr_2} + u_{nm}\frac{d(r_2h_n^{(2)}(k_1r_2))}{dr_2}\right]im\tilde{\pi}_n^m(\cos\theta)\right\}\exp(im\varphi). \tag{22}$$

Similarly, the main internal field could also be evaluated in the global coordinate system by using Eq. (10).

Also, the expressions for calculating the internal field inside the inclusion can be obtained:

$$\mathbf{E}_r^{\mathrm{int1}} = \sum_{n=1}^{\infty}\sum_{m=-n}^{+n}(-1)^m q_{nm}\frac{j_n(k_2r_2)}{k_2r_2}n(n+1)\tilde{P}_n^m(\cos\theta)\exp(im\varphi), \tag{23}$$

$$\mathbf{E}_\theta^{\mathrm{int1}} = \sum_{n=1}^{\infty}\sum_{m=-n}^{+n}(-1)^m\left\{p_{nm}j_n(k_2r_2)im\tilde{\pi}_n^m(\cos\theta) + q_{nm}\frac{1}{k_2r_2}\frac{d(r_2j_n(k_2r_2))}{dr_2}\tilde{\tau}_n^m(\cos\theta)\right\}\exp(im\varphi), \tag{24}$$

$$\mathbf{E}_\varphi^{\mathrm{int1}} = \sum_{n=1}^{\infty}\sum_{m=-n}^{+n}(-1)^m\left\{-p_{nm}j_n(k_2r_2)\tilde{\tau}_n^m(\cos\theta) + q_{nm}\frac{1}{k_2r_2}\frac{d(r_2j_n(k_2r_2))}{dr_2}im\tilde{\pi}_n^m(\cos\theta)\right\}\exp(im\varphi). \tag{25}$$

2. External Near-Surface Field

The external near-surface field is a summation of the incident field and the scattered field. The intensity of the incident shaped beam can be evaluated either by using analytical expressions in closed form (see [4]) or by using expressions in expanded form from Eq. (8), which is applied in our simulations in this paper. The approach for calculations of the scattered field in the near zone is very similar to that used in the calculation of the internal field. The only significant difference lies in the number of summation terms. In the evaluation of scattered field, the number of terms taken into account is fixed at a cut-off number related with the size parameter of the host sphere. While in the evaluation of internal intensity distribution, a fewer number of summation terms for smaller radii than the fixed cut-off number have to be taken into account.

The expressions for calculating the scattered field in the near zone are given:

$$\mathbf{E}_r^{\mathrm{sca}} = \sum_{n=1}^{\infty}\sum_{m=-n}^{+n}(-1)^m d_{nm}\frac{h_n^{(2)}(k_0r_1)}{k_0r_1}n(n+1)\tilde{P}_n^m(\cos\theta) \times\exp(im\varphi), \tag{26}$$

$$\mathbf{E}_\theta^{\mathrm{sca}} = \sum_{n=1}^{\infty}\sum_{m=-n}^{+n}(-1)^m\left\{c_{nm}h_n^{(2)}(k_0r_1)im\tilde{\pi}_n^m(\cos\theta) + d_{nm}\frac{1}{k_0r_1}\frac{d(r_1h_n^{(2)}(k_0r_1))}{dr_1}\tilde{\tau}_n^m(\cos\theta)\right\}\exp(im\varphi), \tag{27}$$

$$\mathbf{E}_{\varphi}^{\mathrm{sca}} = \sum_{n=1}^{\infty}\sum_{m=-n}^{+n}(-1)^m\left\{-c_{nm}h_n^{(2)}(k_0r_1)\tilde{\tau}_n^m(\cos\theta) + d_{nm}\frac{1}{k_0r_1} \times \frac{d(r_1h_n^{(2)}(k_0r_1))}{dr_1}im\tilde{\pi}_n^m(\cos\theta)\right\}\exp(im\varphi). \quad (28)$$

F. Scattered Field in the Far Zone

In the far zone away from the scatterer, where $kr \gg ka$, the spherical Hankel functions reduce to spherical waves, according to

$$h_n^{(2)}(kr) \sim i^{n+1}\frac{e^{-ikr}}{kr}, \qquad \frac{dh_n^{(2)}(kr)}{d(kr)} \sim i^n\frac{e^{-ikr}}{kr}. \quad (29)$$

Inserting Eq. (29) into Eq. (26)–(28), the scattered field in the far zone degenerates to transversal spherical waves, and the nonzero components are expressed as

$$\mathbf{E}_{\theta}^{\mathrm{sca}} = i\frac{e^{-ik_0r_1}}{k_0r_1}\sum_{n=1}^{\infty}\sum_{m=-n}^{+n}[c_{nm}m\tilde{\pi}_n^m(\cos\theta) - d_{nm}\tilde{\tau}_n^m(\cos\theta)]i^{n+1}(-1)^m\exp(im\varphi), \quad (30)$$

$$\mathbf{E}_{\varphi}^{\mathrm{sca}} = \frac{e^{-ik_0r_1}}{k_0r_1}\sum_{n=1}^{\infty}\sum_{m=-n}^{+n}[-c_{nm}\tilde{\tau}_n^m(\cos\theta) + d_{nm}m\tilde{\pi}_n^m(\cos\theta)]i^{n+1}(-1)^m\exp(im\varphi). \quad (31)$$

The scattering intensity may be expressed as [4]

$$\begin{pmatrix} I_{\theta} \\ I_{\varphi} \end{pmatrix} = \frac{\lambda^2}{4\pi^2r_1^2}\begin{pmatrix} |S_2|^2 \\ |S_1|^2 \end{pmatrix}, \quad (32)$$

where

$$S_2 = \sum_{n=1}^{\infty}\sum_{m=-n}^{+n}[c_{nm}m\tilde{\pi}_n^m(\cos\theta) - d_{nm}\tilde{\tau}_n^m(\cos\theta)]i^{n+1}(-1)^m\exp(im\varphi), \quad (33)$$

$$S_1 = \sum_{n=1}^{\infty}\sum_{m=-n}^{+n}[c_{nm}\tilde{\tau}_n^m(\cos\theta) - d_{nm}m\tilde{\pi}_n^m(\cos\theta)]i^{n+1}(-1)^m\exp(im\varphi). \quad (34)$$

3. NUMERICAL RESULTS

A computer program is written in FORTRAN relying on the theoretical work stated above. Thanks to the programs published and maintained on the Internet, such as the one from Wriedt [56], it allows almost instant verification of results without costly software development for some commonly used subroutines. For instance, the required Ricatti–Bessel functions in our program are evaluated using the recursion algorithm presented by Ngo *et al.* [35]. The most significant differences between our code and the one from Ngo *et al.* are as follows. (i) Plane wave illumination is generalized to arbitrary shaped beam illumination. Specifically, the BSCs, for Gaussian beam illumination, are determined using the Modified Localized Approximation method developed by Gouesbet *et al.* [6,16,17,54]. (ii) Subroutines for evaluations of internal and near-surface field distributions are developed.

Furthermore, for the aim of developing a more convergent computer program, the associated Legendre functions are evaluated in terms of Wigner d functions, which achieve good convergence even when the order is very large [57]. The translational coefficients of the VSWFs are evaluated according to the recurrence relationship provided by Mackowski [48] instead of the one proposed by Bobbert and Vlieger [47] and used by Ngo *et al.* [35]. Although several modifications have been made, the convergent problem reported in Ngo's code [58] also exists in our code. Nevertheless, it has little influence on the analysis of field intensity distributions in the present paper.

Regarding the numerical evaluation of the elements H_{sn}^m in Eq. (18), Han *et al.* [36] calculated them (although with a different notation and presentation) by using a summation of a finite number of terms that satisfy the following four conditions: (i) $\sigma \le 0$, (ii) $\sigma \le -(m+m')$, (iii) $\sigma \le n-m$, (iv) $\sigma \le n-m'$. This was a fairly tedious procedure so that, for this paper, we use a somewhat more efficient method. Let us recall Eq. (102) in [22]; we can rewrite Eq. (18) as

$$H_{sn}^m = \left[\frac{(n-m)!(n+s)!}{(n+m)!(n-s)!}\right]^{1/2}e^{im\gamma}e^{is\alpha}d_{ms}^n, \quad (35)$$

where d_{ms}^n is the Wigner d function, which can be evaluated by a recurrence relation [57], which is given in Appendix B for the sake of convenience.

A. Numerical Test Cases

As a verification of the homemade program as well as of the theoretical derivations for an arbitrary shaped beam in an arbitrary orientation, we have compared our results with those published by Ngo *et al.* [35] in the case of plane wave illumination. All the results concerning the extinction and scattering efficiencies coincide with each other at least in four digits.

As another verification of the code, comparisons between the results obtained from our code are compared with those published by Han *et al.* [36] and Yan *et al.* [37]. As we noticed, only results for special cases of on-axis Gaussian beam illumination were presented by Yan *et al.* [37]. We prefer to present a comparison of scattered intensity distribution for a general case of off-axis Gaussian beam illumination in Fig. 2 between the results obtained from our code and those published by Han *et al.* [36]. In this comparison, parameters are adopted directly from [36]. The radii of the inclusion and of the host sphere are $0.5\,\mu$m and $1.0\,\mu$m with complex refractive indices of $1.55+0.0i$ and $1.33+0.0i$, respectively. The center–center separation distance is $d = 0.25\,\mu$m. It is illuminated by a Gaussian beam at incidence angles $\alpha = \gamma = 0.0°$, $\beta = 45.0°$, with wavelength $\lambda = 0.6328\,\mu$m and beam waist $w_0 = 1.0\,\mu$m. The location of the beam waist center is a varied parameter. Satisfactory agreements are achieved, although there may be some differences (logarithmic scales are used), especially in the forward- and backward-scattering direction.

Further verification is made by comparing spatial distributions of normalized source function for the internal and near-surface fields with published results for a sphere illuminated by plane wave [59].

Figure 4(a) shows the normalized source function distribution of the near-surface and internal fields along the z axis for a homogeneous spherical glass bead (having a complex refractive index $m = 1.5 + 0.0i$ and size parameter 20) illuminated by an x-axis direction polarized plane wave propagating along the $+z$ axis direction. The amplitude of the incident electromagnetic wave electric field has been set to unity. Spatial coordinates are normalized relative to the sphere radius. Results from our code are identical to those provided by Barber and Hill [59]. Particular values for exact checks are evaluated at points −2.5, −1.0, 1.0, and 2.5. The values obtained from our code are 0.87081, 1.4987, 59.2146, and 3.2682, respectively.

B. Numerical Results

1. Scattered Field in the Far Zone

Scattered field distributions resulting from a focused laser beam incident on a particle system are dependent on the properties of the incident electromagnetic beam (beam waist radius, location of beam waist center, wavelength, and incident orientation) as well as on the properties of the scatterer (shape, diameter, complex refractive index, etc.).

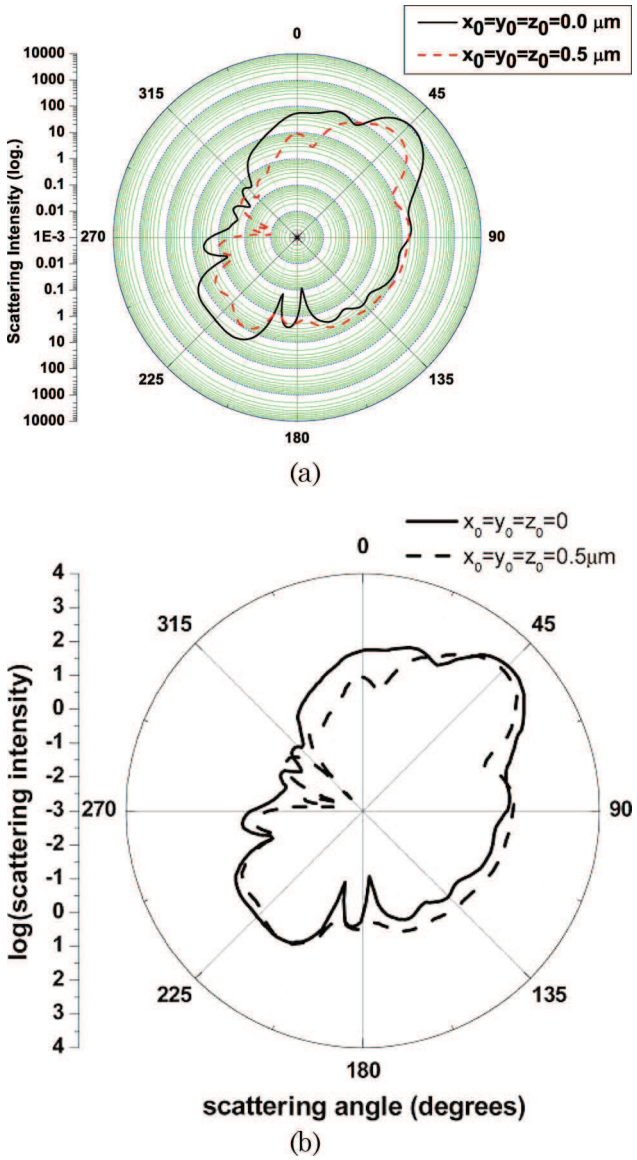

Fig. 2. (Color online) Comparison of scattered intensity distribution between the result obtained from our code and Fig. 6 published in [36].

Variations in spatial distributions of scattered field in the far zone from a spherical glass bead (having a complex refractive index $1.50 + 0.0i$) containing a spherical water inclusion (having a complex refractive index $1.33 + 0.0i$) are displayed in video format for different cases. The following parameters are applied except stated otherwise. The complex refractive index in the surrounding medium is set equal to unity. The radius of the host sphere is assumed to be $3.0\,\mu$m, and that of the inclusion is $1.50\,\mu$m. The incident electromagnetic focused Gaussian beam was assumed to be linearly polarized along the u axis at its waist with a wavelength equal to $0.6328\,\mu$m. Its beam waist center is located at the origin of the global coordinate system with $x_0 = y_0 = z_0 = 0.0\,\mu$m. The incident orientation is specified by Euler angles at $\alpha = \gamma = 0.0°$, $\beta = 90°$ so that the forward direction of the scattered field is at the center of the graphs ($\theta = 90°$, $\varphi = 0.0°$). Media 1 and Media 2 proceed along eight steps according to the scenario detailed below. The vertical axis in the movie is the zenith angle θ in degrees, and the horizontal axis is the azimuthal angle φ in degrees; scenery numbers are shown at the rightmost side to indicate the procedure of the movie. Single-frame pictures excerpted from Media 1 and Media 2 are shown in Fig. 3.

The movie begins with the inclusion situated at the center of the host sphere. The particle system is illuminated by a Gaussian beam with a pretty large beam waist, such as $w_0 = 50.0\,\mu$m; that is to say, plane wave illumination is applied. Then (i) the inclusion is translated along the z axis from the center of the host sphere $d = 0.0\,\mu$m to the edge at $d = 1.0\,\mu$m. Afterward, (ii) holding the position of the spherical inclusion constant at $d = 1.0\,\mu$m, we decrease the radius of the inclusion from $b = 1.5\,\mu$m to $b = 0.0\,\mu$m, which is followed by (iii) increasing the radius of the inclusion from $b = 0.0\,\mu$m to $b = 1.5\,\mu$m. The beam waist radius of the Gaussian beam is then (iv) decreased from $w_0 = 50.0\,\mu$m to $w_0 = 2.0\,\mu$m. That is to say, the plane wave illumination is replaced by a focused Gaussian beam illumination step-by-step, with a step of $5.0\,\mu$m in the range [$50.0\,\mu$m, $5.0\,\mu$m] and a step of $0.5\,\mu$m in the range [$5.0\,\mu$m, $2.0\,\mu$m]. Fixing the Gaussian beam waist at $w_0 = 2.0\,\mu$m and holding the position of the inclusion constant at $d = 1.0\,\mu$m, we (v) decrease the radius of the inclusion from $b = 1.5\,\mu$m to $b = 0.0\,\mu$m, which is followed by (vi) an increase from $b = 0.0\,\mu$m to $b = 1.5\,\mu$m. The inclusion then (vii) translates to the center of the host sphere with $d = 0.0\,\mu$m. At the end of the movie, (viii) we move the beam waist center of the focused Gaussian beam toward the edge of the host sphere along the z axis with $z_0 = 2.0\,\mu$m.

As we can notice from the movie, either in the illumination of a plane wave or in the illumination of a focused Gaussian beam, a second set of diffractionlike rings can be observed when the symmetry of the particle system is broken. The inclusion acts as a second radiating source, contributing to an interference structure in the scattering pattern, the spatial frequency of which varies with the location and the radius of the inclusion. A butterfly pattern is noticed growing up as the center–center separation distance increases. With a decrease in the inclusion radius, the wings of the butterfly seems to diffuse laterally (the inclusion becoming smaller, with a larger radius of curvature, throws rays away more efficiently in the lateral directions),

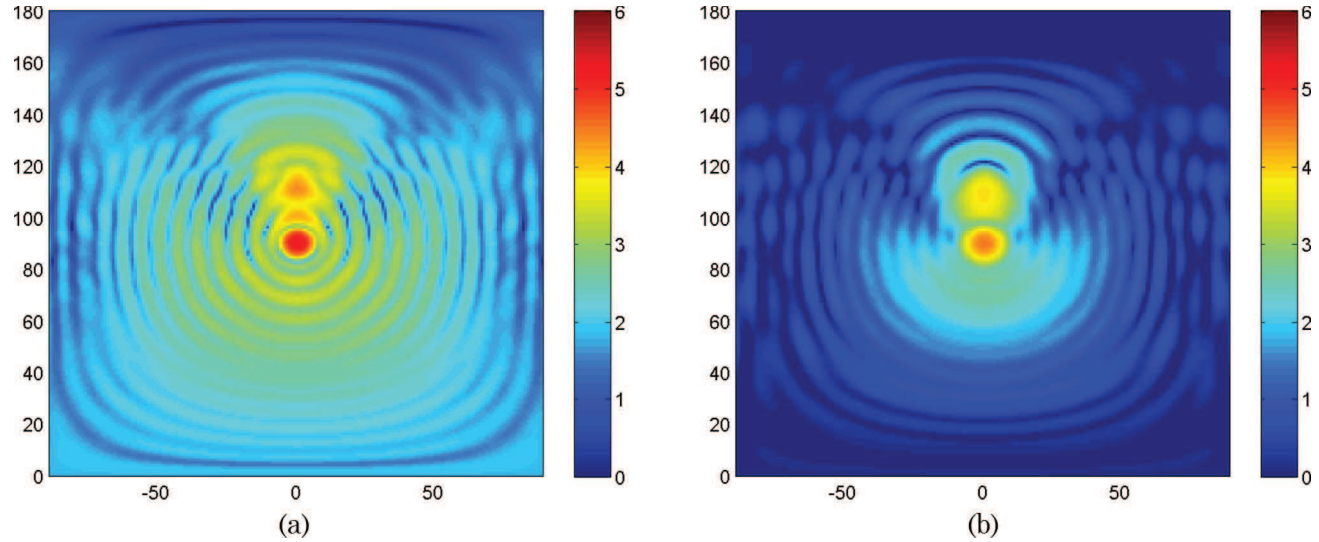

Fig. 3. (Color online) Scattered field distribution in the far zone. (a) Single-frame excerpt from Media 1 for cases of plane wave illumination. (b) Single-frame excerpt from Media 2 for cases of focused Gaussian beam illumination. The vertical axis in the movie is the zenith angle θ in degrees, and the horizontal axis is the azimuthal angle φ in degrees..

also become weaker since the inclusion is smaller, and at last disappear when the inclusion disappears.

During the procedure of plane wave illumination replaced step-by-step by Gaussian beam illumination, for most of the time we do not observe any significant variation in the scattering pattern, in accordance with the fact that the radius of the host sphere is $3.0\,\mu$m, which is much smaller than the beam waist radius, so that, for most of the time, the illumination is still essentially the one of a plane wave. When Gaussian beam effects become significant, we conversely observe a strong modification of the scattering pattern, in which an image of the inclusion in the scattering pattern becomes more and more apparent in the forward direction, while as a whole the interference pattern simplifies, with many rings progressively disappearing and much less light shed laterally.

At the last part of the movie, the inclusion is located at the center of the host sphere; such a geometry actually corresponds to the one of a coated sphere. We can observe a pattern with a maximal spherical symmetry (spherical symmetry of the scatterer, and location of the beam waist center at the center of the scatterer). When the beam waist center of the Gaussian beam is moved toward the edge of the host sphere, a progressive and eventually very significant loss of symmetry can be noticed, in which the original maximal spherical symmetry is broken. This evolution corresponds to the development of a similar butterfly pattern, but with wings stretching in the downward direction instead of in the upward directions as we saw in the first half of the movie.

2. Near-Surface Field and Internal Field

Calculations of the internal and near-surface fields of a transparent sphere could be found in the case of plane wave illumination [59] and also in the case of shaped beam illumination [8]. Large enhancement of the near-surface field located in the shadow side of the particle was found both in the on-resonance conditions and in the off-resonance conditions. In the case of shaped beam illumination, the distribution of the internal and near-surface field is strongly dependent on the location of the focal center of the laser beam, which differs significantly from the corresponding results when the exciting resource is a plane wave. Nevertheless, most efforts have been found to be devoted to spherical particles, but other shapes or composite particles are also of interest, such as a micrometer-sized particle containing a smaller eccentrically located inclusion under study in this paper. A series of calculations is then performed to demonstrate the effects of particle system geometry, orientation, and focal center location of the Gaussian beam on the spatial distributions of internal and near-surface fields.

Specifically, near-surface and internal fields distributions are calculated for a glass sphere (having a real refractive index equal to 1.50) with an eccentrically located water droplet (having a real refractive index equal to 1.33) in the case of plane wave illumination and in the case of a focused Gaussian beam illumination. The incident beam (plane wave or Gaussian beam) is originally assumed to propagate in the $+z$-axis direction with electric field vector polarized along the x axis (at the waist) with wavelength $0.6283\,\mu$m. The beam waist radius of the Gaussian beam is assumed to be $\omega_0 = 1.6\,\mu$m, which is smaller than the radius of the host sphere $a = 2.0\,\mu$m, while greater than the radius of the inclusion $b = 1.0\,\mu$m.

As aforementioned, even though the magnitude and the phase for each component of the electromagnetic field can be determined, a useful visualization of the electromagnetic field distribution can be obtained by plotting the normalized source function as a function of spatial position. Normalized source functions are calculated on a normalized square grid of dimension $2r/a \times 2r/a$. Two hundred points along the z axis and 100 points along the x axis are used in Figs. 4 and 5, due to the fact that, in these cases, the intensity variation along the x axis is much slower than that along the z axis. Nevertheless, 200 points are used both along the z axis and along the x axis in Figs. 7 and 8, which are the cases when the shaped beam is incident on the particle obliquely. It is worth mentioning that if too many points are used in the calculation of internal field distribution, the calculation of the Bessel functions may become unstable for radii near the origin, since the argument of the functions will be much smaller than the order.

Normalized source function distributions along the z axis are displayed in Fig. 4, and distributions over the equatorial

plane (x–z plane) are shown in Fig. 5 as a function of the center–center separation distance d.

In Fig. 4(a), the well-known high intensity peak in the near-surface field behind the scatterer dominates the graph, whose intensity is more than 100 times the incident beam intensity. Nevertheless, this large broad intensity peak is afterward significantly spoiled due to the existence of an inclusion, as observed in Figs. 4(b) and 4(c). Furthermore, when the plane wave illumination is replaced by a focused Gaussian beam illumination in Figs. 4(d)–4(f), the high intensity peak is also reduced greatly. In a further study (results are not shown here), we find that the narrower the Gaussian beam waist is, the lower the intensity of the high energy peak will be. Thus, we may come to the conclusion that the focusing effect caused by the curved surface of host spherical particle plays a main role in the construction of the high intensity peak in the shadow side of the host sphere, which is similar to the transmission spherical aberration caustic in the optical system. This conclusion is also supported by the fact that several intensity peaks are observed in the shadow side of the inclusion, which may mainly be due to the focusing effect of the spherical inclusion.

The other prominent feature in Fig. 4 is that a small intensity peak observed in the illuminated side of the host sphere

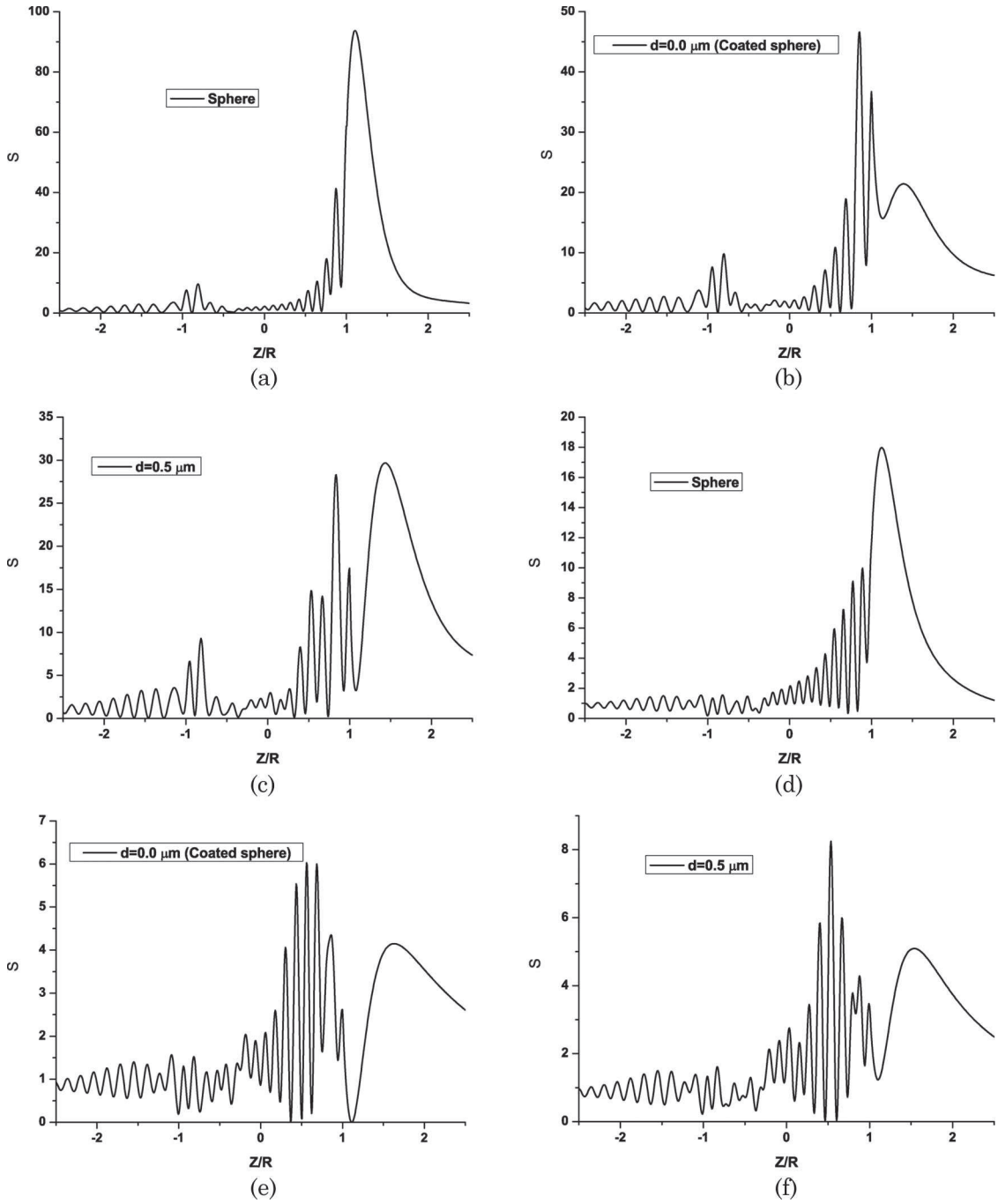

Fig. 4. Normalized source function for external and internal fields along the z axis with center–center separation distance d as the parameter. The left column [(a), (b), (c)] is for cases of plane wave illumination; the right column [(d), (e), (f)] is for cases of focused Gaussian beam illumination.

(the small peak located at approximately $z/R = -0.8$) in the case of plane wave illumination is significantly degenerated when a focused Gaussian beam illumination is applied. From a point of view of ray theory, this peak is claimed to be constructed by the crossing of the arms of the interior focusing caustic for three internal reflections [60]. And the numerical results obtained here emphasize that the construction of this peak is crucially associated with the off-axis partial waves propagating in the A zone depicted in Fig. 6.

The features found in Fig. 4 can also be observed in Fig. 5. Furthermore, if we look closely into the interior of the host sphere, three energy flows toward the shadow side of the host sphere can be apparently observed when the host sphere is illuminated by a plane wave. The main energy flows in the middle is greatly enhanced in the case of focused beam illumination, while the other two energy flows in the lateral sides are blurred or even disappear.

Spatial distributions of normalized source functions over the equatorial plane (x–z plane) are shown in Fig. 7 as a function of the incident direction of the Gaussian beam. The spherical inclusion is located on the z axis with center–center separation distance $d = 0.5$. A focused Gaussian beam illuminates the particle system with Euler angles $\alpha = \gamma = 0.0°$ and β as a parameter. The beam waist center of the Gaussian beam locates at the center of the host sphere with $x_0 = y_0 = z_0 = 0.0$.

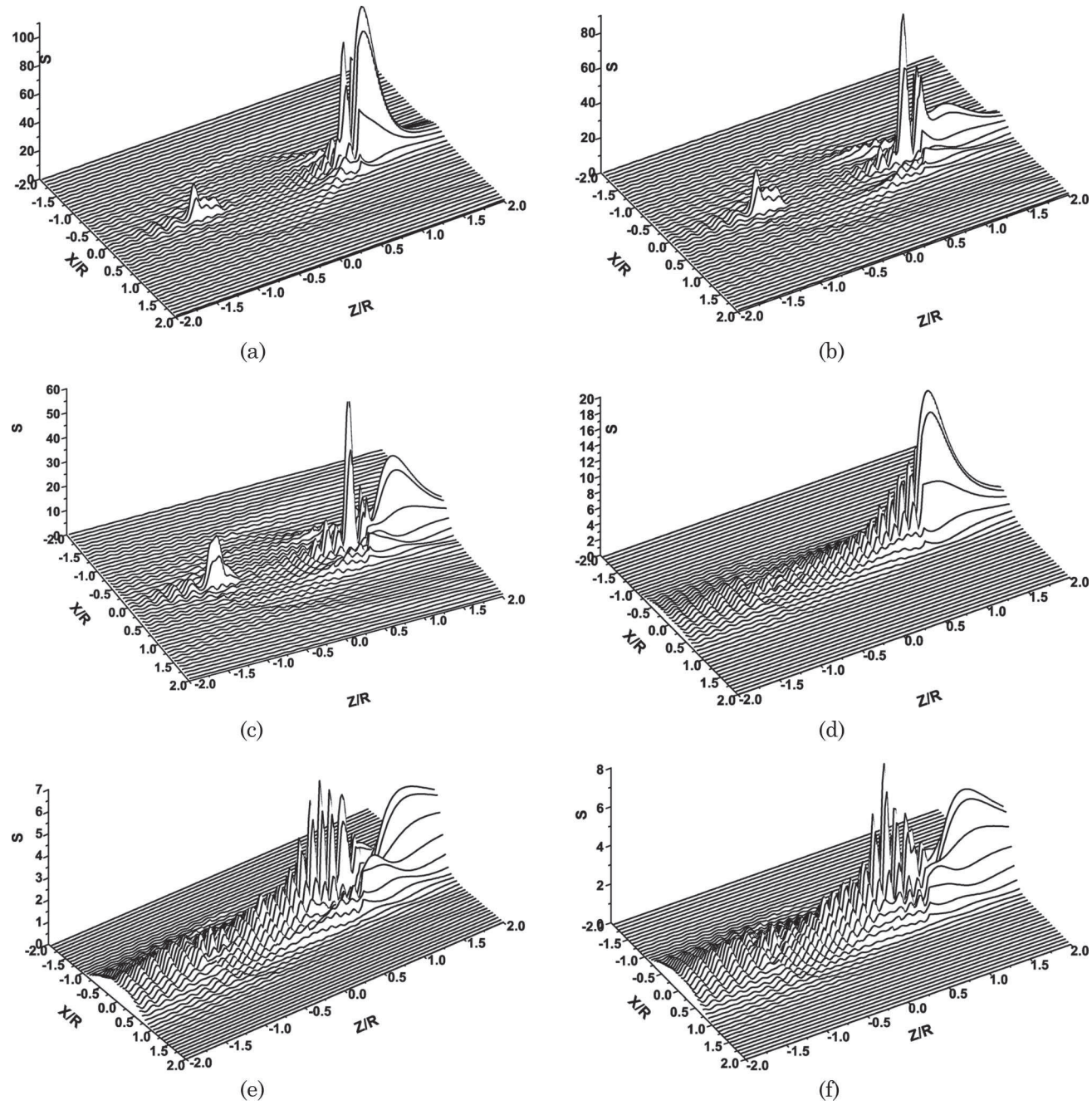

Fig. 5. Normalized source function for external and internal field over the x–z plane with center–center separation distance d as the parameter. The left column [(a), (b), (c)] is for cases of plane wave illumination; the right column [(d), (e), (f)] is for cases of focused Gaussian beam illumination.

Comparing Fig. 7(a) with Figs. 7(b)–7(d), we can observe that, when the particle system with a broken spherical symmetry is illuminated obliquely by a focused Gaussian beam, the scattered field resulting from scattering of the inclusion interferes with the incident beam, which is refracted once by the host sphere surface, to create a complex interference pattern in the internal field. This interference pattern contributes to the features that the main electromagnetic energy propagates along a different track from that of the incident beam direction; a branch of electromagnetic energy is observed to be divided from the main energy flows.

Spatial distributions of normalized source functions over the equatorial plane (x–z plane) are shown in Fig. 8, as a function of location of the Gaussian beam waist center. The spherical inclusion is located on the z axis with center–center separation distance $d = 0.5$. A focused Gaussian beam illuminates the particle system with Euler angles $\alpha = \gamma = 0.0°$ and $\beta = 90°$; that is to say, it propagates along the x axis from left to right in the figures. The position of the beam waist center of the Gaussian beam is assumed to be $x_0 = y_0 = 0.0$ and z_0 as a parameter.

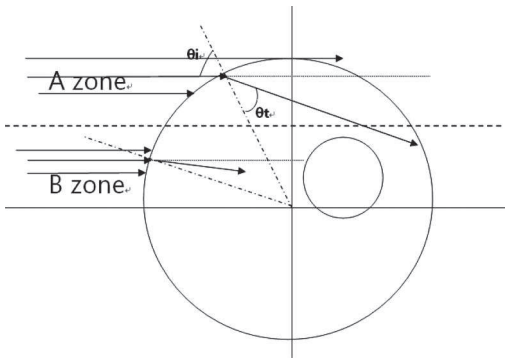

Fig. 6. Illustration of localization of partial waves in a geometric optics point of view.

Figure 8 shows the behavior of an off-axis Gaussian beam when it transmits through a host sphere with an eccentrically

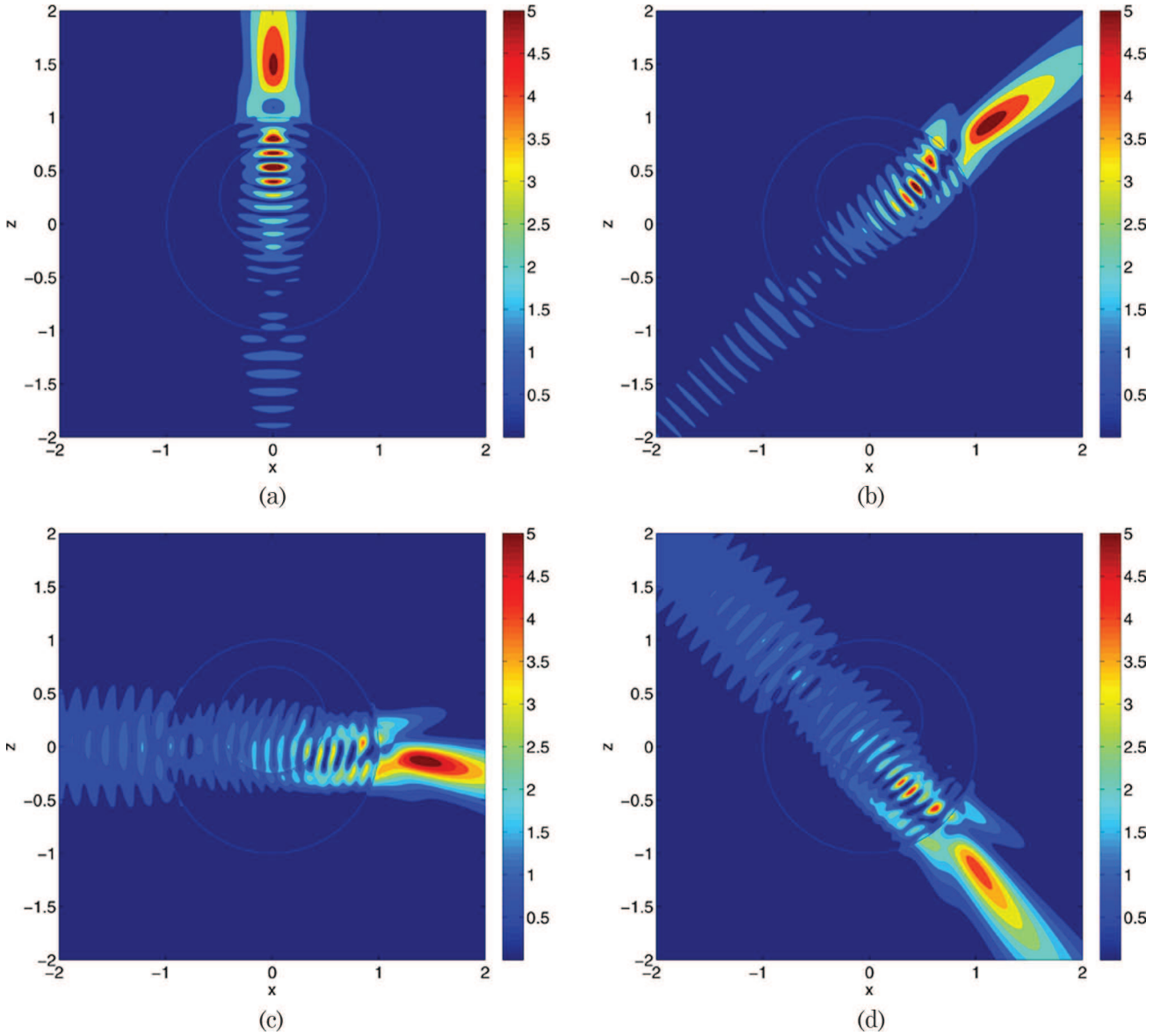

Fig. 7. (Color online) Normalized source function distribution for external and internal fields over the x–z plane with Euler angles $\alpha = \gamma = 0.0°$ and β as a parameter..

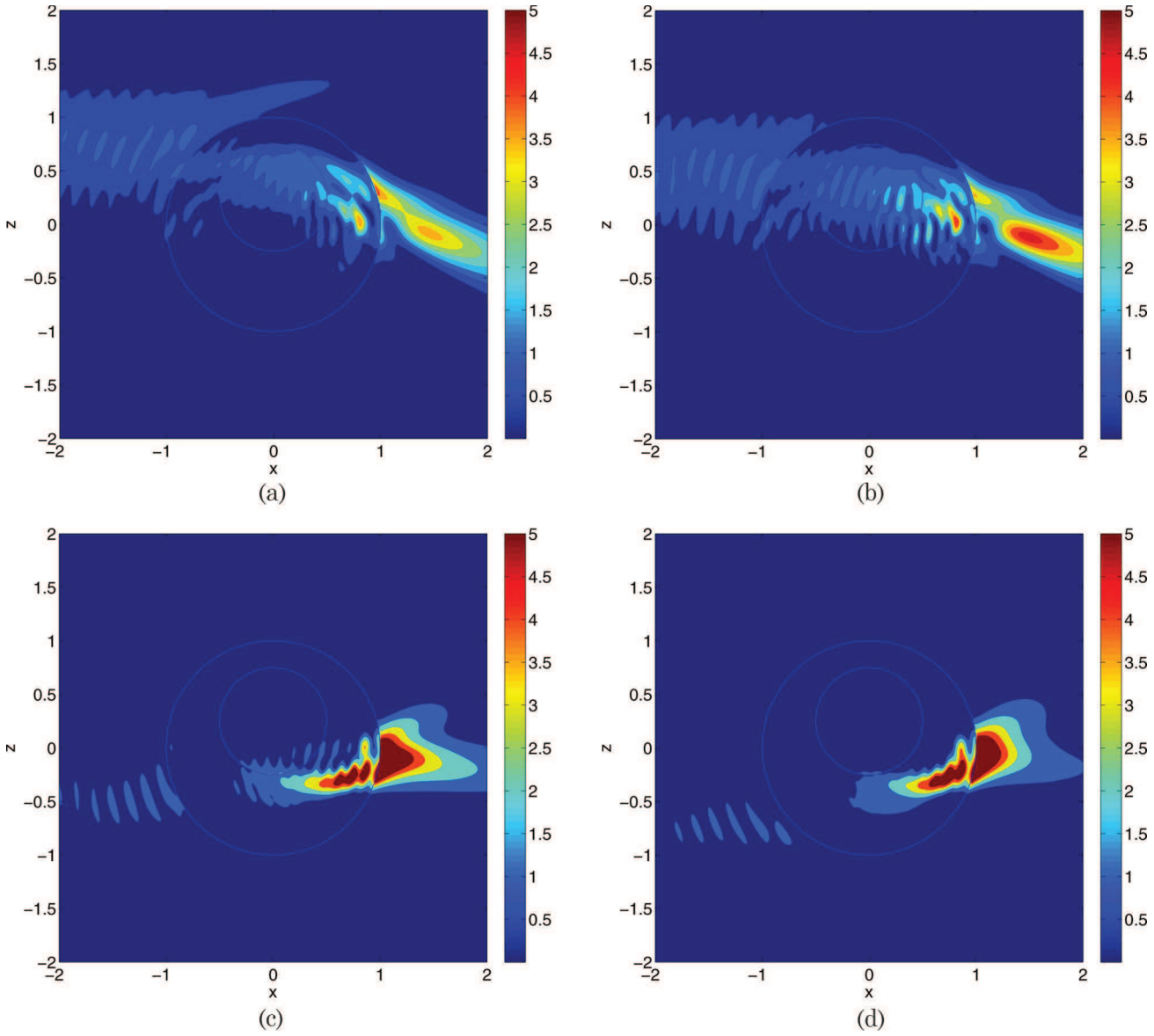

Fig. 8. (Color online) Normalized source function distribution for external and internal field over the x–z plane with location of the Gaussian beam waist center as a parameter. The Gaussian beam propagates along the x axis from left to right..

located spherical inclusion. Generally speaking, when the beam waist center of the Gaussian beam is not located at the center of the host sphere, that is to say, more partial waves with higher electromagnetic energy density become off-axis, the propagation direction of the Gaussian beam is bent toward the horizontal center-line (the x axis) due to the refraction effect at the surface of the host sphere. The farther the beam waist center is away from the host sphere center, the larger the incident angle is, which leads to a larger turning angle between the propagation direction after refraction and the original propagation direction. In the meanwhile, more energy is reflected back into the surrounding medium with the increase of the incident angle; a clear nonsymmetric interference pattern can be observed in the backward-scattering direction. These features are very similar to the case of a bunch of rays strikes on a sphere of large size parameter as shown in Fig. 6. Nevertheless, the scattering behavior becomes more complicated in the problem under study, especially the field distributions inside the particle, which is very sensitive to the relative location of the inclusion inside the host sphere.

4. CONCLUSION

Based on the recent improvements in the GLMT concerning the evaluation of BSCs [20–24], this paper presents a study on the scattering problem of a sphere with an eccentrically located spherical inclusion illuminated by an arbitrary shaped electromagnetic beam in an arbitrary orientation. A computer program is written in FORTRAN based on the theoretical work, which permits the prediction of various scattering data. Besides completing the scattering results in the far zone published in [36,37], numerical results concerning spatial distributions of the near-surface field outside of the host sphere and internal field inside the host sphere are presented for the first time in this paper for various parameter values, such as regarding orientation of the incident Gaussian beam, location of the beam waist center of the Gaussian beam, and location of the spherical inclusion.

Concerning the scattered field distributions in the far zone, when the symmetry of the problem is broken (either due to a loss of symmetry of the particle configuration or to a loss of symmetry of the location of the illuminating beam), the symmetry of the scattering pattern in the far zone is broken as well. The inclusion acts as a second radiating source, contributing to an interference structure in the scattering pattern. A second set of diffractionlike rings is observed with lower intensity relative to the main diffraction rings, whose frequency varies significantly depending on the location and radius of the inclusion. Well-apparent butterfly patterns can be observed in the movies, associated with symmetry breakings. Such symmetry breakings arise when the inclusion is more and more eccentrically located, instead of being located at the center of the host sphere (coated sphere problem), or when the beam waist center of the Gaussian beam is not situated at the center of the host sphere. Focused Gaussian beam effects have also been underlined in which radiating sources (host sphere and inclusion) appear to be more focused and brighter, with an enhancement and spreading of the interference structure, with respect to plane wave illumination.

From numerical results concerning spatial distributions of near-surface and internal fields, we can notice that the well-known high intensity peak in the near-surface field behind the scatterer, whose intensity could be more than 100 times the incident plane wave intensity, is degenerated significantly due to the existence of an inclusion or when the plane wave illumination is replaced by a focused Gaussian beam illumination. Furthermore, the narrower the Gaussian beam waist is, the lower the intensity of the high energy peak will be, indicating that the focusing effect caused by the curved surface of host spherical particle plays a significant role in the construction of the high intensity peak in the shadow side of the host sphere, which is similar to the transmission spherical aberration caustic in optical systems.

Another prominent feature is that the peak observed in the illuminated side of the host sphere in the case of plane wave illumination is significantly degenerated when a focused Gaussian beam illumination is applied, which indicates that the construction of this peak is greatly associated with the off-axis partial waves propagating in the A zone depicted in Fig. 6.

When the particle system with broken spherical symmetry is illuminated obliquely by a focused Gaussian beam, the main energy flows are observed to be out of the original track along the propagation direction of the incident beam. A branch of energy is divided from the main energy flows. Furthermore, when the beam waist center of the Gaussian beam is not located in the center of the host sphere, the incident beam is bent toward the horizontal centerline along the x axis due to the refraction effect at the surface of the host sphere. The farther the beam waist center is away from the host sphere center, the larger the turning angle between the refraction direction and the original propagation direction would be. In the meanwhile, a larger fraction of electromagnetic energy is reflected back into the surrounding medium with the increase of the incident angle; a clear nonsymmetric interference pattern can be observed in the backward scattering direction.

The original motivation of our present work lies on the future detection of the interesting optical (Hamiltonian) chaos features depicted in [39–41], which are raised by the complex optical interactions between the eccentrically located inclusion with the host sphere, in the case of loss of spherical symmetry. The study on internal and near-surface field distribution would contribute to the understanding of multiple scattering interactions between closely spaced particles or between different parts of a scattering system, such as the scattering model under study. It would also have contributions to the study of the nonlinear optical mechanisms leading to lasering in cavity quantum electrodynamic (QED) as well as to the improvement of optical sensors and imaging, such as the study of fluorescence and Raman effects. Furthermore, the work on scattered field distributions would be helpful to the improvements of relevant laser-related detecting techniques, such as in the field of particle characterization or identification of internal nonuniformities.

APPENDIX A

In general, the translational addition theorem for VSWFs can be written

$$\mathbf{M}_{nm}^{(i)}(k\mathbf{r}) = \sum_{n'=1}^{\infty}\sum_{m=-n'}^{n'} A_{m'n'}^{mn}(k\mathbf{r_0})\mathbf{M}_{n'm'}^{(i)}(k\mathbf{r_1}) + B_{m'n'}^{mn}(k\mathbf{r_0})\mathbf{N}_{n'm'}^{(i)}(k\mathbf{r_1}), \tag{A1}$$

$$\mathbf{N}_{nm}^{(i)}(k\mathbf{r}) = \sum_{n'=1}^{\infty}\sum_{m=-n'}^{n'} B_{m'n'}^{mn}(k\mathbf{r_0})\mathbf{M}_{n'm'}^{(i)}(k\mathbf{r_1}) + A_{m'n'}^{mn}(k\mathbf{r_0})\mathbf{N}_{n'm'}^{(i)}(k\mathbf{r_1}). \tag{A2}$$

If the translation is along the z axis, the double summation above reduces to a single summation over the index n'. So we obtain

$$\mathbf{M}_{nm}^{(i)}(k\mathbf{r}) = \sum_{n'=1}^{\infty} A_{nn'}^{m}(k\mathbf{r_0})\mathbf{M}_{n'm}^{(i)}(k\mathbf{r_1}) + B_{nn'}^{m}(k\mathbf{r_0})\mathbf{N}_{n'm}^{(i)}(k\mathbf{r_1}), \tag{A3}$$

$$\mathbf{N}_{nm}^{(i)}(k\mathbf{r}) = \sum_{n'=1}^{\infty} B_{nn'}^{m}(k\mathbf{r_0})\mathbf{M}_{n'm}^{(i)}(k\mathbf{r_1}) + A_{nn'}^{m}(k\mathbf{r_0})\mathbf{N}_{n'm}^{(i)}(k\mathbf{r_1}). \tag{A4}$$

For axial translations and positive values of m, the vector addition coefficients $A_{mn'}^{mn}$ and $B_{mn'}^{mn}$ can be related to the scalar addition coefficients $C_{mn'}^{mn}$:

$$A_{mn'}^{mn}(k\mathbf{z_0}) = C_{mn'}^{mn}(k\mathbf{z_0}) + \frac{kz_0}{n'+1}\sqrt{\frac{(n'-m+1)(n'+m+1)}{(2n'+1)(2n'+3)}}C_{mn'+1}^{mn}(k\mathbf{z_0}) + \frac{kz_0}{n'}\sqrt{\frac{(n'-m)(n'+m)}{(2n'+1)(2n'-1)}}C_{mn'-1}^{mn}(k\mathbf{z_0}), \tag{A5}$$

$$B_{mn'}^{mn}(k\mathbf{z_0}) = jkz_0\frac{m}{n'(n'+1)}C_{mn'}^{mn}(k\mathbf{z_0}). \tag{A6}$$

For negative values of the index m, the following symmetry relations can be used for practical calculations:

$$A^{-mn}_{-mn'}(k\mathbf{z_0}) = A^{mn}_{mn'}(k\mathbf{z_0}), \qquad B^{-mn}_{-mn'}(k\mathbf{z_0}) = -B^{mn}_{mn'}(k\mathbf{z_0}), \quad \text{(A7)}$$

$$A^{-mn}_{-mn'}(k\mathbf{z_0}) = A^{mn}_{mn'}(-k\mathbf{z_0}), \qquad B^{-mn}_{-mn'}(k\mathbf{z_0}) = B^{mn}_{mn'}(-k\mathbf{z_0}). \quad \text{(A8)}$$

The recurrence relations for the $C^{mn}_{mn'}$ coefficients are simple in the case of axial translation and positive m:

$$\begin{aligned}
&\sqrt{\frac{(n-m+1)(n+m+1)}{(2n+1)(2n+3)}}C^{mn+1}_{mn'}(k\mathbf{z_0}) \\
&\quad - \sqrt{\frac{(n-m)(n+m)}{(2n-1)(2n+1)}}C^{mn-1}_{mn'}(k\mathbf{z_0}) \\
&\quad = \sqrt{\frac{(n'-m)(n'+m)}{(2n'-1)(2n'+1)}}C^{mn}_{mn'-1}(k\mathbf{z_0}) \\
&\qquad - \sqrt{\frac{(n'-m+1)(n'+m+1)}{(2n'+1)(2n'+3)}}C^{mn}_{mn'+1}(k\mathbf{z_0}),
\end{aligned} \quad \text{(A9)}$$

$$\begin{aligned}
&\sqrt{\frac{(n-m-1)(n-m+1)}{(2n-1)(2n+1)}}C^{mn-1}_{mn'}(k\mathbf{z_0}) \\
&\quad + \sqrt{\frac{(n+m)(n+m+1)}{(2n+1)(2n+3)}}C^{mn+1}_{mn'}(k\mathbf{z_0}) \\
&\quad = \sqrt{\frac{(n'+m-1)(n'+m)}{(2n'-1)(2n'+1)}}C^{m-1n}_{m-1n'-1}(k\mathbf{z_0}) \\
&\qquad + \sqrt{\frac{(n'-m+1)(n'-m+2)}{(2n'+1)(2n'+3)}}C^{m-1n}_{m-1n'+1}(k\mathbf{z_0}).
\end{aligned} \quad \text{(A10)}$$

The convention $C^{mn}_{mn'} = 0$ for $m > n$ and $m > n'$ is assumed in the above equations.

Initial values are given:

$$\begin{aligned}
&C^{00,(1)}_{0n'}(k\mathbf{z_0}) = (-1)^{n'}\sqrt{2n'+1}j_{n'}(k\mathbf{z_0}) \\
&\text{for regular VSWFs translation,} \\
&C^{00,(3)}_{0n'}(k\mathbf{z_0}) = (-1)^{n'}\sqrt{2n'+1}h^{(1)}_{n'}(k\mathbf{z_0}) \\
&\text{for radiating VSWFs translation.}
\end{aligned} \quad \text{(A11)}$$

APPENDIX B

The recurrence relation for the Wigner d functions are given below, which can also be found in [57], Appendix B:

$$\begin{aligned}
d^{n+1}_{ms}(\beta) = &\frac{1}{n\sqrt{(n+1)^2-m^2}\sqrt{(n+1)^2-s^2}}\{(2n \\
&+1)[n(n+1)x - ms]d^n_{ms}(\beta) \\
&-(n+1)\sqrt{n^2-m^2}\sqrt{n^2-s^2}d^{n-1}_{ms}(\beta)\},
\end{aligned} \quad \text{(B1)}$$

$n \geq n_{\min}$.

Initial values are given:

$$d^{n_{\min}-1}_{ms}(\beta) = 0, \quad \text{(B2)}$$

$$\begin{aligned}
d^{n_{\min}}_{ms}(\beta) = &\xi_{ms}2^{-n_{\min}}\left[\frac{(2n_{\min})!}{(|m-s|)!|m+s|!}\right]^{1/2} \\
&\times (1-x)^{|m-s|/2}(1+x)^{|m+s|/2},
\end{aligned} \quad \text{(B3)}$$

in which

$$\xi_{ms} = \begin{cases} 1 & \text{if } s \geq m \\ (-1)^{m-s} & \text{if } s < m \end{cases}, \quad \text{(B4)}$$

$$n_{\min} = \max(|m|, |s|), \qquad x = \cos\beta. \quad \text{(B5)}$$

The Wigner d functions have real values and share the following symmetry properties:

$$d^n_{ms}(\beta) = (-1)^{m+s}d^n_{-m,-s}(\beta) = d^n_{-s,-m}(\beta), \quad \text{(B6)}$$

$$d^n_{ms}(\pi-\beta) = (-1)^{n-s}d^n_{-ms}(\beta) = (-1)^{n-m}d^n_{m,-s}(\beta). \quad \text{(B7)}$$

By specifying $s = 0$, we can obtain the associated Legendre functions in terms of the Wigner d functions:

$$d^n_{m0}(\beta) = \sqrt{\frac{(n-m)!}{(n+m)!}}P^m_n(\cos\beta), \quad \text{(B8)}$$

in which $P^m_n(\cos\beta)$ are the associated Legendre functions. With some straightforward derivations, we can obtain

$$m\tilde{\pi}^m_n(\cos\beta) = -(-1)^m\sqrt{\frac{2n+1}{2}}\frac{\sqrt{n(n+1)}}{2}[d^n_{m1}(\beta) + d^n_{m-1}(\beta)], \quad \text{(B9)}$$

$$\tilde{\tau}^m_n(\cos\beta) = -(-1)^m\sqrt{\frac{2n+1}{2}}\frac{\sqrt{n(n+1)}}{2}[d^n_{m1}(\beta) - d^n_{m-1}(\beta)], \quad \text{(B10)}$$

$$\tilde{P}^m_n(\cos\beta) = (-1)^m\sqrt{\frac{2n+1}{2}}d^n_{m0}(\beta). \quad \text{(B11)}$$

ACKNOWLEDGMENTS

The work presented in this paper is supported by the project "Bourses Doctorales en Alternance" between France and China. This work is also partially supported by the National Natural Science Foundation of China (NSFC) (grant 60771039) and by the European program INTERREG

IVa-C5: Cross-Channel Centre for Low Carbon Combustion. The authors thanks especially the two reviewers for providing several constructive comments and suggestions to the present paper.

REFERENCES

1. G. Mie, "Beiträge zur optik trüben medien speziell kolloidaler metalösungen," Ann. Phys. **25**, 377–452 (1908).
2. J. A. Lock and G. Gouesbet, "Generalized Lorenz–Mie theory and applications," J. Quant. Spectrosc. Radiat. Transfer **110**, 800–807 (2009).
3. G. Gouesbet, "Generalized Lorenz–Mie theories, the third decade: a perspective," J. Quant. Spectrosc. Radiat. Transfer **110**, 1223–1238 (2009).
4. G. Gouesbet, B. Maheu, and G. Gréhan, "Light scattering from a sphere arbitrarily located in a Gaussian beam, using a Bromwich formulation," J. Opt. Soc. Am. A **5**, 1427–1443 (1988).
5. B. Maheu, G. Gouesbet, and G. Gréhan, "A concise presentation of the generalized Lorenz–Mie theory for arbitrary location of the scatter in an arbitrary incident profile," J. Opt. **19**, 59–67 (1988).
6. G. Gouesbet, "Validity of the localized approximation for arbitrary shaped beams in the generalized Lorenz–Mie theory for spheres," J. Opt. Soc. Am. A **16**, 1641–1650 (1999).
7. L. Méès, G. Gouesbet, and G. Gréhan, "Transient internal and scattered fields from a multi-layered sphere illuminated by a pulsed laser," Opt. Commun. **282**, 4189–4193 (2009).
8. J. P. Barton, D. R. Alexander, and S. A. Schaub, "Internal and near-surface electromagnetic fields for a spherical particle irradiated by a focused laser beam," J. Appl. Phys. **64**, 1632–1639 (1988).
9. G. Gouesbet, "Interaction between an infinite cylinder and an arbitrary-shaped beam," Appl. Opt. **36**, 4292–4304 (1997).
10. G. Gouesbet and G. Gréhan, "Generalized Lorenz–Mie theory for a sphere with an eccentrically located spherical inclusion," J. Mod. Opt. **47**, 821–837 (2000).
11. Y. P. Han, G. Gréhan, and G. Gouesbet, "Generalized Lorenz–Mie theory for a spheroidal particle with off-axis Gaussian-beam illumination," Appl. Opt. **42**, 6621–6629 (2003).
12. F. Xu, K. F. Ren, G. Gouesbet, G. Gréhan, and X. Cai, "Generalized Lorenz–Mie theory for an arbitrary oriented, located, and shaped beam scattered by homogeneous spheroid," J. Opt. Soc. Am. A **24**, 119–131 (2007).
13. K. F. Ren, G. Gréhan, and G. Gouesbet, "Scattering of a Gaussian beam by an infinite cylinder in the framework of generalized Lorenz–Mie theory: formulation and numerical results," J. Opt. Soc. Am. A **14**, 3014–3025 (1997).
14. L. Méès, K. F. Ren, G. Gréhan, and G. Gouesbet, "Scattering of a Gaussian beam by an infinite cylinder with arbitrary location and arbitrary orientation: numerical results," Appl. Opt. **38**, 1867–1876 (1999).
15. G. Gouesbet and L. Méès, "Generalized Lorenz–Mie theory for infinitely long elliptical cylinders," J. Opt. Soc. Am. A **16**, 1333–1341 (1999).
16. J. A. Lock and G. Gouesbet, "Rigorous justification of the localized approximation to the beam-shape coefficients in generalized Lorenz–Mie theory. I. On-axis beams," J. Opt. Soc. Am. A **11**, 2503–2515 (1994).
17. G. Gouesbet and J. A. Lock, "Rigorous justification of the localized approximation to the beam-shape coefficients in generalized Lorenz–Mie theory. II. Off-axis beams," J. Opt. Soc. Am. A **11**, 2516–2525 (1994).
18. Y. P. Han, H. Y. Zhang, and G. X. Han, "The expansion coefficients of arbitrary shaped beam in oblique illumination," Opt. Express **15**, 735–746 (2007).
19. Y. P. Han, Y. Zhang, H. Y. Zhang, and G. X. Han, "Scattering of typical particles by beam shape in oblique illumination," J. Quant. Spectrosc. Radiat. Transfer **110**, 1375–1381 (2009).
20. G. Gouesbet, J. J. Wang, and Y. P. Han, "Transformations of spherical beam shape coefficients in generalized Lorenz–Mie theories through rotations of coordinate systems. I. General formulation," Opt. Commun. **283**, 3218–3225 (2010).
21. J. J. Wang, G. Gouesbet, and Y. P. Han, "Transformations of spherical beam shape coefficients in generalized Lorenz–Mie theories through rotations of coordinate systems. II. Axisymmetric beams," Opt. Commun. **283**, 3226–3234 (2010).
22. G. Gouesbet, J. J. Wang, and Y. P. Han, "Transformations of spherical beam shape coefficients in generalized Lorenz–Mie theories through rotations of coordinate systems. III. Special Euler angles," Opt. Commun. **283**, 3235–3243 (2010).
23. G. Gouesbet, J. J. Wang, Y. P. Han, and G. Gréhan, "Transformations of spherical beam shape coefficients in generalized Lorenz–Mie theories through rotations of coordinate systems. IV. Plane waves," Opt. Commun. **283**, 3244–3254 (2010).
24. G. Gouesbet, J. A. Lock, J. J. Wang, and G. Gréhan, "Transformations of spherical beam shape coefficients in generalized Lorenz–Mie theories through rotations of coordinate systems. V. Localized beam models," Opt. Commun. (to be published).
25. J. G. Fikioris and N. K. Uzunoglu, "Scattering from an eccentrically stratified dielectric sphere," J. Opt. Soc. Am. A **69**, 1359–1366 (1979).
26. F. Borghese, P. Denti, R. Saija, and O. I. Sindoni, "Optical properties of spheres containing several spherical inclusions," Appl. Opt. **33**, 484–493 (1994).
27. K. A. Fuller, "Morphology-dependent resonances in eccentrically stratified sphere," Opt. Lett. **19**, 1272–1274 (1994).
28. G. Videen, D. Ngo, P. Chylek, and R. G. Pinnick, "Light scattering from a sphere with an irregular inclusion," J. Opt. Soc. Am. A **12**, 922–928 (1995).
29. A. Doicu, T. Wriedt, and Y. A. Eremin, *Light Scattering by Systems of Particles: Null-Field Method with Discrete Sources: Theory and Programs* (Springer, 2006).
30. S. M. Hasheminejad and Y. Mirzaei, "Exact 3D elasticity solution for free vibrations of eccentric hollow sphere," J. Sound Vib. (to be published).
31. D. R. Secker, P. H. Kaye, R. S. Greenaway, E. Hirst, D. L. Bartley, and G. Videen, "Light scattering from deformed droplets and droplets with inclusions. I. Experimental results," Appl. Opt. **39**, 5023–5030 (2000).
32. G. Videen, W. Sun, Q. Fu, D. R. Secker, R. S. Greenaway, P. H. Kaye, E. Hirst, and D. Bartley, "Light scattering from deformed droplets and droplets with inclusions. II. Theoretical treatment," Appl. Opt. **39**, 5031–5039 (2000).
33. N. Riefler, R. Schuh, and T. Wriedt, "Investigation of a measurement technique to estimate concentration and size of inclusions in droplets," Meas. Sci. Technol. **18**, 2209–2218 (2007).
34. A. A. Riziq, M. Trainic, C. Erlick, E. Segre, and Y. Rudich, "Extinction efficiencies of coated absorbing aerosols measured by cavity ring down aerosol spectrometry," Atmos. Chem. Phys. **8**, 1823–1833 (2008).
35. D. Ngo, G. Videen, and P. Chýlek, "A FORTRAN code for the scattering of EM waves by a sphere with a nonconcentric spherical inclusion," Comput. Phys. Commun. **99**, 94–112 (1996).
36. G. X. Han, Y. P. Han, J. Y. Liu, and Y. Zhang, "Scattering of an eccentric sphere arbitrarily located in a shaped beam," J. Opt. Soc. Am. B **25**, 2064–2072 (2008).
37. B. Yan, X. Han, and K. F. Ren, "Scattering of a shaped beam by a spherical particle with an eccentric spherical inclusion," J. Opt. A Pure Appl. Opt. **11**, 015705 (2009).
38. S. Saengkaew, G. Godard, J. B. Blaisot, and G. Gréhan, "Experimental analysis of global rainbow technique: sensitivity of temperature and size distribution measurements to non-spherical droplets," Exp. Fluids **47**, 839–848 (2009).
39. G. Gouesbet, S. Meunier-Guttin-Cluzel, and G. Gréhan, "Generalized Lorenz–Mie theory for a sphere with an eccentrically located inclusion, and optical chaos," Part. Part. Syst. Charact. **18**, 190–195 (2001).
40. G. Gouesbet, S. Meunier-Guttin-Cluzel, and G. Gréhan, "Periodic orbits in Hamiltonian chaos of the annular billiard," Phys. Rev. E **65**, 016212 (2001).
41. G. Gouesbet, S. Meunier-Guttin-Cluzel, and G. Gréhan, "Morphology-dependent resonances and/or whispering gallery modes for a two-dimensional dielectric cavity with an eccentrically located circular inclusion, a Hamiltonian point of view with Hamiltonian (optical) chaos," Opt. Commun. **201**, 223–242 (2002).
42. P. T. Leung, S. W. Ng, and K. M. Pang, "Morphology-dependent resonances in dielectric spheres with many tiny inclusions," Opt. Lett. **27**, 1749–1751 (2002).

43. V. S. C. M. Rao, Gupta, and S. Dutta, "Broken azimuthal degeneracy with whispering gallery modes of microspheres," J. Opt. A Pure Appl. Opt. **7**, 279–285 (2005).
44. G. Gouesbet, "T-matrix formulation and generalized Lorenz–Mie theories in spherical coordinates," Opt. Commun. **283**, 517–521 (2010).
45. S. Stein, "Addition theorems for spherical wave functions," Quart. Appl. Math.**19**, 15–24 (1961).
46. O. R. Cruzan, "Translational addition theorems for spherical vector wave functions," Quart. Appl. Math. **20**, 33–44 (1962).
47. P. A. Bobbert and J. Vlieger, "Light scattering by a sphere on a substrate," Physica A (Amsterdam) **137**, 209–241 (1986).
48. D. W. Mackowski, "Analysis of radiative scattering from multiple sphere configurations," Proc. R. Soc. Lond. **433**, 599–614 (1991).
49. G. Gouesbet, C. Letellier, K. F. Ren, and G. Gréhan, "Discussion of two quadrature methods of evaluating beam-shape coefficients in generalized Lorenz–Mie theory," Appl. Opt. **35**, 1537–1542 (1996).
50. G. Gouesbet, G. Gréhan, and B. Maheu, "Expressions to compute the coefficients $g^m{}_n$ in the generalized Lorenz–Mie theory using finite series," J. Opt. **19**, 35 (1988).
51. K. F. Ren, G. Gouesbet, and G. Gréhan, "Integral localized approximation in generalized Lorenz–Mie theory," Appl. Opt. **37**, 4218–4225 (1998).
52. A. Doicu and T. Wriedt, "Computation of the beam-shape coefficients in the generalized Lorenz–Mie theory by using the translational addition theorem for spherical vector wave functions," Appl. Opt. **36**, 2971–2978 (1997).
53. H. Y. Zhang and Y. P. Han, "Addition theorem for the spherical vector wave functions and its application to the beam shape coefficients," J. Opt. Soc. Am. B **25**, 255–260 (2008).
54. G. Gouesbet, "Higher-order descriptions of Gaussian beams," J. Opt. **27**, 35–50 (1996).
55. J. A. Lock, "An improved Gaussian beam scattering algorithm," Appl. Opt. **34**, 559–570 (1995).
56. T. Wriedt, "The website maintained by Thomas Wriedt," http://www.scattport.org.
57. M. I. Mishchenko, J. W. Hovenier, and L. D. Travis, *Light Scattering by Nonspherical Particles: Theory, Measurements, and Applications* (Academic, 2000).
58. R. Schuh and T. Wriedt, "Computer programs for light scattering by particles with inclusions," J. Quant. Spectrosc. Radiat. Transfer **70**, 715–723 (2001).
59. P. W. Barber and S. C. Hill, *Light Scattering by Particles: Computational Methods*, Advanced Series in Applied Physics (World Scientific, 1990), Vol. 2.
60. J. A. Lock and E. A. Hovenac, "Internal caustic structure of illuminated liquid droplets," J. Opt. Soc. Am. A **8**, 1541–1552 (1991).

Optics Communications 283 (2010) 3218–3225

Contents lists available at ScienceDirect

Optics Communications

journal homepage: www.elsevier.com/locate/optcom

Transformations of spherical beam shape coefficients in generalized Lorenz–Mie theories through rotations of coordinate systems
I. General formulation

G. Gouesbet [a,*], J.J. Wang [a,b], Y.P. Han [a]

[a] Laboratoire d'Electromagnétisme des Systèmes Particulaires (LESP), Unité Mixte de Recherche (UMR) 6614, Centre National de la Recherche Scientifique (CNRS), COmplexe de Recherche Interprofessionnel en Aérothermochimie(CORIA), Université de Rouen, Institut National des Sciences Appliquées (INSA) de Rouen BP12, avenue de l'université, technopôle du Madrillet, 76801, Saint-Etienne-du Rouvray, France
[b] School of Science, Xidian University, Xi'an, China

ARTICLE INFO

Article history:
Received 3 March 2010
Received in revised form 8 April 2010
Accepted 21 April 2010

ABSTRACT

The generalized Lorenz–Mie theory in the strict sense describes the interaction between an illuminating arbitrary shaped beam and a homogeneous sphere characterized by its diameter d and its complex refractive index m. It relies on the method of separation of variables expressed in spherical coordinates. Other generalized Lorenz–Mie theories (for other kinds of scatterers) expressed in spherical coordinates are available too. In these theories, the illuminating beam is expressed by using expansions with expansion coefficients depending on some fundamental coefficients named beam shape coefficients, more specifically spherical beam shape coefficients. In this paper we present a general formulation for the transformation of spherical beam shape coefficients through rotations of coordinate systems.

1. Introduction

The generalized Lorenz–Mie theory in the strict sense describes the interaction between an illuminating arbitrary shaped beam and a homogeneous spherical particle described by its diameter d and its complex refractive index m, e.g. [1], [2] with recent reviews by Lock and Gouesbet [3] and by Gouesbet [4]. In this theory, which relies on the method of separation of variables in spherical coordinates, the electromagnetic components of the illuminating beam are described by multipole expansions over a set of basic functions. The expansion coefficients are expressed versus fundamental coefficients, usually denoted as $g^m_{n,\mathrm{TM}}$ and $g^m_{n,\mathrm{TE}}$ (n from 1 to ∞, m from $-n$ to $+n$, TM for Transverse Magnetic, TE for Transverse Electric), known as beam shape coefficients. More specifically, in the present case where we use spherical coordinates, these coefficients may also be called spherical beam shape coefficients.

There exist other generalized Lorenz–Mie theories, for other kinds of scatterers, in spherical coordinates, in which the illuminating beam is expressed by using spherical beam shape coefficients too. These other theories concern the cases of multilayered spheres [5], of spherical particles with an eccentrically located spherical inclusion [6] and of aggregates or of assemblies of spheres [7].

In any of these theories, one of the most important and complicated task, to which much effort has been devoted, is the evaluation of the beam shape coefficients. Several methods have been developed and studied, sharing various degrees of time running efficiency, or of flexibility, namely by using quadratures [8], finite series [9], localized approximations generating localized beam models [10], [11], or a hybrid method taking advantage of both quadratures and of a localized approximation, named the integral localized approximation [12].

The evaluation of beam shape coefficients has also been investigated by relying on addition theorems for translations of coordinate systems, an approach originally introduced by Doicu and Wriedt [13], and also used by Zhang and Han [14]. In the present paper, we are starting a series concerning the evaluation of beam shape coefficients by relying on addition theorems for rotations (not translations) of coordinate systems (precursors will be acknowledged later).

The specific problem to be studied may be defined as follows. Let us consider a Cartesian system of coordinates, denoted as $\mathbf{x}=(x, y,$ and $z)$, associated with usual spherical coordinates $(r, \theta,$ and $\varphi)$, called the unrotated system, and let $g^m_{n,\mathrm{TM}}$ and $g^m_{n,\mathrm{TE}}$ be the beam shape coefficients for the description of the illuminating beam in this unrotated system. Let us consider a second system of coordinates, called the rotated system, deduced from the unrotated system by a rotation defined by Euler angles $(\alpha, \beta,$ and $\gamma)$, later defined more precisely. Quantities in the rotated system are denoted by using tilde-decorations. Therefore the Cartesian coordinates of the rotated system are denoted as $\tilde{\mathbf{x}}=(\tilde{x}, \tilde{y},$ and $\tilde{z})$ and they are associated with spherical

* Corresponding author.
E-mail address: Gouesbet@coria.fr (G. Gouesbet).

0030-4018/$ – see front matter © 2010 Elsevier B.V. All rights reserved.
doi:10.1016/j.optcom.2010.04.050

coordinates ($\tilde{r}=r$, $\tilde{\theta}$, and $\tilde{\varphi}$). The beam shape coefficients in the rotated system are denoted as $\widetilde{g^m_{n,\mathrm{TM}}}$ and $\widetilde{g^m_{n,\mathrm{TE}}}$. We intend to express the beam shape coefficients in the rotated system in terms of beam shape coefficients in the unrotated system.

The previous paragraphs provided an abstract and minimal definition of the problem to be studied in the present series of papers. It is however convenient to dress this problem by introducing extra-elements. The first element concerns the definition of the unrotated system. Of course, any system may be taken as being the unrotated system and, in particular, we are free to invert the role of the unrotated and of the rotated systems, pretending that the rotated system is now to be taken as being the unrotated one and vice versa. However, to better approach the history of GLMTs and some traditional points of view taken from this history, the unrotated system will be given a specific definition as follows.

Following the description of coordinate systems given in Fig. 1 of Ref. [1], we consider a Cartesian system of coordinates, with origin O_G and coordinates (u, v, and w), attached to the illuminating beam. We take the axis O_Gw as being the main axis of propagation of the beam (particularly easy to define in the case of axisymmetric beams, such as a Gaussian beam). Next, we decide to describe the scattering phenomena by using another Cartesian coordinate, with origin O_P and coordinates (x, y, and z). We furthermore make the axes O_Px, O_Py, and O_Pz parallel to the axes O_Gu, O_Gv, and O_Gw respectively. Then, we define the coordinates (x, y, and z) as being the Cartesian coordinates of the unrotated system.

Up to now, we have only considered coordinate systems and nothing has been said concerning the nature of the scattering particles. The second element to dress the problem is concerned with the introduction of particles. These particles are such that the scattering problem they generate can be solved by using separation of variables in spherical coordinates. They are originally attached to the frame O_Pxyz which may be called the (unrotated) particle frame. When rotating this frame, the particle, which is attached to the frame, is assumed to follow the rotation of the frame, i.e. the unrotated particle frame becomes a rotated particle frame.

Let us begin by assuming that the scatterer is a homogeneous sphere defined by its diameter d and its complex refractive index m and, for the sake of simplicity, let us assume that the incident beam is a Gaussian beam or more generally what has been originally called an axisymmetric light profile [15], and later better studied under the name of axisymmetric beams [16]. We may then be facing two different situations. In the first case, the axis O_Gw of the illuminating beam coincides with the axis O_Pz of the particle frame. In other words, the center O_P of the particle is located on the axis of the beam. This is called the on-axis case. Otherwise, we are facing the off-axis case. That these two cases are deeply different may be appreciated by the following fact. In the on-axis case, it can be demonstrated that the double set $\{g^m_{n,\mathrm{TM}}, g^m_{n,\mathrm{TE}}\}$ of beam shape coefficients reduces to a single set $\{g_n\}$, $n=1\ldots\infty$, of special beam shape coefficients. Accordingly, the on-axis version of the GLMT becomes much simpler than the off-axis version. The rotation from O_Pxyz to $O_P\tilde{x}\tilde{y}\tilde{z}$ does not modify the scattering phenomena since the rotation of the attached sphere, which possesses a high degree of symmetry, does not modify the scattering problem. But it may modify deeply the computations involved to describe the phenomena. For instance, assume that we have an on-axis situation with special beam shape coefficients g_n. After the rotation, the center O_P of the particle is still located on the axis of the beam, but the axis O_Gw of the illuminating beam does not coincide any more with the axis, now denoted as $O_P\tilde{z}$, of the particle frame and, as we shall see (in Part II of this series), the description of the illuminating beam must now been made again in terms of a double set of beam shape coefficients now denoted as $\widetilde{g^m_{n,X}}$, $X=$ TM or TE. In other words, the rotation of the particle frame induces a more complicated situation without any benefit since the eventual physical results have to remain unchanged. Note however that no complication is generated by the rotation of the particle frame in the case of off-axis illumination since we need to use g^m_n-kinds of coefficients in both the rotated and unrotated systems. A similar discussion could apply to the case of multilayered spheres [5].

However, let us now consider particles which, in general, do not possess the property of invariance through rotation, although the method of separation of variables is still applied to them in spherical coordinates, e.g. [6], [7]. For being specific, let us more particularly consider the case of a sphere, with center located at O_P, with an eccentrically located spherical sphere, or inclusion [6]. Let us assume the simplest situation available, that is to say the case when the center of the inclusion is located on the axis O_Pz of the unrotated system. This may be viewed as a case of parallel illumination since the axis of the beam O_Gw is parallel to (or even coincide with) the axis of the unrotated system. Now, in contrast, in the rotated system, we are facing a quite different situation that we may call a situation of oblique illumination. It is under this name (oblique illumination) that the topic has been initiated by Han et al. [17,18]. The problem may then be expressed as the one of the evaluation of beam shape coefficients in oblique illumination in terms of beam shape coefficients in parallel illumination, providing a new method of evaluation of beam shape coefficients.

This paper is the first part of a series of papers. Part I is devoted to the general formulation and ends with a theorem which shall be used as a starting point in other subsequent parts. Part II is devoted to axisymmetric beams (particularly to on-axis axisymmetric beams), Part III to special values of Euler angles and Part IV to the case of an illuminating plane wave. A particular effort in the special cases of Parts II–IV will be devoted to the derivation of results in compact forms, rather than in terms of series (for better computer efficiency).

The present Part I is organized as follows. We begin with a few sections defining preliminary materials required for the sequel. Section 2 is devoted to vector spherical wave functions (VSWFs). Section 3 operates a conversion of the description of the incident fields, from the original Bromwich formulation used when developing the GLMT *stricto sensu* to a description in terms of VSWFs. Section 4 deals with the definition of Euler angles (α, β, and γ) allowing one to bring the unrotated system (x, y, and z) to the rotated system ($\tilde{x}$, $\tilde{y}$, and $\tilde{z}$). Section 5 deals with the rotation of VSWFs. Section 6 establishes the main result of the paper, i.e. it allows one to express the spherical beam shape coefficients in the rotated system versus those in the unrotated system. Section 7 is a conclusion in which the main result is expressed as a theorem. There is also an Appendix A devoted to a technical checking.

2. Vector spherical wave functions (VSWFs)

The vector spherical wave functions (VSWFs) used in this paper are the same than the ones which have been used in [7], [6], and [19]. They read as:

$$\mathbf{M}^{(j)}_{mn} = (-1)^m\left[imz_n(kr)\pi^m_n(\cos\theta)\exp(im\varphi)\mathbf{i}_\theta - z_n(kr)\tau^m_n(\cos\theta)\exp(im\varphi)\mathbf{i}_\varphi\right] \tag{1}$$

$$\begin{aligned}\mathbf{N}^{(j)}_{mn} = (-1)^m\Big\{&\frac{n(n+1)}{kr}z_n(kr)P^m_n(\cos\theta)\exp(im\varphi)\mathbf{i}_r \\ &+\frac{1}{kr}\left[\frac{\partial}{\partial r}rz_n(kr)\right]\tau^m_n(\cos\theta)\exp(im\varphi)\mathbf{i}_\theta \\ &+\frac{im}{kr}\left[\frac{\partial}{\partial r}rz_n(kr)\right]\pi^m_n(\cos\theta)\exp(im\varphi)\mathbf{i}_\varphi\Big\}\end{aligned} \tag{2}$$

in which $\mathbf{i}_r$, $\mathbf{i}_\theta$, and $\mathbf{i}_\varphi$ are standard unit vectors associated with the coordinates r, θ, and φ respectively of a spherical coordinate system (r, θ, and φ), k is the wave-number in the considered material, z_n designates any spherical Bessel function ($\Psi^{(j)}_n$, $j=1$, 2, 3, and 4 in the

Meixner and Schäfke notation [20], also denoted j_n, y_n, $h_n^{(1)}$ and $h_n^{(2)}$ respectively), and π_n^m, τ_n^m designate the generalized Legendre functions according to:

$$\pi_n^m(\cos\theta) = \frac{P_n^m(\cos\theta)}{\sin\theta} \tag{3}$$

$$\tau_n^m(\cos\theta) = \frac{d}{d\theta}P_n^m(\cos\theta) \tag{4}$$

in which the associated Legendre functions (often misnamed as polynomials by physicists) read as:

$$P_n^m(\cos\theta) = (-1)^m(\sin\theta)^m\frac{d^m P_n(\cos\theta)}{(d\cos\theta)^m}. \tag{5}$$

The VSWFs of Eqs. (1) and (2) may be obtained from Stratton ([21], pp. 414–416) by adding the solutions with a subscript "e" and i times the solutions with a subscript "o". They are equal to those denoted **M** and **N** by Stratton, using a more concise notation, without any subscript or superscript. However, the prefactor $(-1)^m$ does not appear in Stratton due to the fact that this author uses an alternative definition of the associated Legendre functions, namely Eq. (5) where $(-1)^m$ is dropped. The functions defined by Eqs. (1) and (2) furthermore agree with the ones used in [22], again modulo $(-1)^m$. Such prefactors may appear recurrently throughout this paper (and the other papers in the associated series).

The superscript (j) in Eqs. (1) and (2) refers to the spherical Bessel function to be used. We shall only need $\Psi_n^{(1)}$ satisfying:

$$j_n(kr)\equiv\Psi_n^{(1)}(kr) = \frac{\Psi_n(kr)}{kr} \tag{6}$$

in which Ψ_n designates Ricatti–Bessel functions.

Other classical expressions are recalled:

$$\left[\frac{d^2}{dr^2} + k^2\right]\left(r\Psi_n^{(j)}(kr)\right) = \frac{n(n+1)}{r}\Psi_n^{(j)}(kr) \tag{7}$$

$$P_n^{-m}(\cos\theta) = (-1)^m\frac{(n-m)!}{(n+m)!}P_n^m(\cos\theta). \tag{8}$$

Also, this implies:

$$P_n^m(\cos\theta) = (-1)^{\frac{m-|m|}{2}}\frac{(n-|m|)!}{(n-m)!}P_n^{|m|}(\cos\theta) \tag{9}$$

that is to say we may uniquely define $P_n^m(\cos\theta)$, $\forall m\in\mathbf{Z}$. From Eqs. (3) and (4), we deduce that a similar relation also holds for the generalized Legendre functions π_n^m and τ_n^m. Such relations are of interest because the VSWFs are expressed in terms of P_n^m, π_n^m, and τ_n^m while field expressions in the Bromwich formalism are expressed in terms of $P_n^{|m|}$, $\pi_n^{|m|}$, and $\tau_n^{|m|}$. Eq. (9), and similar relations, constitute an improvement with respect to Eq. (12) in [7] and Eq. (13) in [6].

3. Incident fields: conversion from Bromwich formulation to VSWFs

For the problem under study, we only need to deal with incident fields. We recall a basic background, extracting relevant information from [19].

The generalized Lorenz–Mie theory *stricto sensu* has originally been developed by using Bromwich scalar potentials U_{TM} and U_{TE} (TM for Transverse Magnetic and TE for Transverse Electric), for the incident, the scattered, and the internal (or sphere) waves. When the Bromwich scalar potentials are known, electric and magnetic fields of the TM and TE kinds may be obtained by using derivative rules, namely Eqs. (10)–(19) in [1]. Furthermore, from the definitions of the TM and TE waves, we have:

$$H_{r,\mathrm{TM}} = E_{r,\mathrm{TE}} = 0. \tag{10}$$

Total field components are obtained by summing TM- and TE-components. In the present paper, it is sufficient to consider electric incident field components. The Bromwich scalar potentials for the incident wave read as [1]:

$$U_{\mathrm{TM}}^{\mathrm{i}} = \frac{E_0}{k}\sum_{n=1}^{\infty}\sum_{m=-n}^{+n}c_n^{\mathrm{pw}}g_{n,\mathrm{TM}}^m\Psi_n(kr)P_n^{|m|}(\cos\theta)\exp(im\varphi) \tag{11}$$

$$U_{\mathrm{TE}}^{\mathrm{i}} = \frac{H_0}{k}\sum_{n=1}^{\infty}\sum_{m=-n}^{n}c_n^{\mathrm{pw}}g_{n,\mathrm{TE}}^m\Psi_n(kr)P_n^{|m|}(\cos\theta)\exp(im\varphi) \tag{12}$$

in which the superscript "i" stands for "incident", $g_{n,X}^m(X=\mathrm{TM,TE})$ are the beam shape coefficients, and the coefficients c_n^{pw} ("pw" standing for "plane wave") are coefficients which appear naturally in the classical Lorenz–Mie theory (expressed in the Bromwich formulation) and, for this reason, are isolated [15]. They read as:

$$c_n^{\mathrm{pw}} = \frac{1}{k}(-i)^{n+1}\frac{2n+1}{n(n+1)}. \tag{13}$$

From the expressions for the Bromwich scalar potentials, Eq. (10), and the rules of derivation of the fields given in Ref. [1], we may obtain the expressions for the components of the incident electric field. We may obtain the components of the magnetic field too, but we limit ourselves to the electric field components which are found to be:

$$E_r^i = kE_0\sum_{n=1}^{\infty}\sum_{m=-n}^{+n}c_n^{\mathrm{pw}}g_{n,\mathrm{TM}}^m\left[\Psi_n''(kr) + \Psi_n(kr)\right]P_n^{|m|}(\cos\theta)\exp(im\varphi) \tag{14}$$

$$E_\theta^i = \frac{E_0}{r}\sum_{n=1}^{\infty}\sum_{m=-n}^{+n}c_n^{\mathrm{pw}}\left[g_{n,\mathrm{TM}}^m\Psi_n'(kr)\tau_n^m(\cos\theta) + mg_{n,\mathrm{TE}}^m\Psi_n(kr)\pi_n^{|m|}(\cos\theta)\right]\exp(im\varphi) \tag{15}$$

$$E_\varphi^i = \frac{iE_0}{r}\sum_{n=1}^{\infty}\sum_{m=-n}^{+n}c_n^{\mathrm{pw}}\left[mg_{n,\mathrm{TM}}^m\Psi_n'(kr)\pi_n^{|m|}(\cos\theta) + g_{n,\mathrm{TE}}^m\Psi_n(kr)\tau_n^{|m|}(\cos\theta)\right]\exp(im\varphi) \tag{16}$$

in which a prime denotes a derivative with respect to the argument.

In terms of VSWFs, the incident field can be expressed as [23]:

$$\mathbf{E}^i = \sum_{n=1}^{\infty}\sum_{m=-n}^{+n}\left[a_{mn}\mathbf{M}_{mn}^{(1)}(k\mathbf{r}) + b_{mn}\mathbf{N}_{mn}^{(1)}(k\mathbf{r})\right]. \tag{17}$$

In particular, noting that $(\mathbf{M}_{mn}^{(1)}(k\mathbf{r}))_r$ is zero from Eq. (1) and expressing $(\mathbf{N}_{mn}^{(1)}(k\mathbf{r}))_r$ from Eq. (2), we may express the radial component E_r^i as:

$$E_r^i = \frac{1}{kr}\sum_{n=1}^{\infty}\sum_{m=-n}^{+n}(-1)^m b_{mn}n(n+1)j_n(kr)P_n^m(cos\theta)exp(im\varphi) \tag{18}$$

which must identify with Eq. (14). Using various expressions from Section 2, this identification allows one to determine b_{mn} as:

$$b_{mn} = kE_0c_n^{\mathrm{pw}}(-1)^m(-1)^{\frac{m-|m|}{2}}\frac{(n-m)!}{(n-|m|)!}g_{n,\mathrm{TM}}^m. \tag{19}$$

Similarly, working out the component E_θ^i allows one to confirm Eq. (19) and to evaluate the coefficients a_{mn} reading as:

$$a_{mn} = -ikE_0 c_n^{\mathrm{pw}} (-1)^m (-1)^{\frac{m-|m|}{2}} \frac{(n-m)!}{(n-|m|)!} g_{n,\mathrm{TE}}^m. \tag{20}$$

Dealing with E_φ^i does not provide more information, but simply confirms the expressions found for a_{mn} and b_{mn}. We have therefore established the connection between the beam shape coefficients $g_{n,X}^m$ of the original formulation of GLMT and the coefficients a_{mn} and b_{mn} of the corresponding formulation in terms of VSWFs.

4. Euler angles

The relationship between the unrotated system (x, y, and z) and the rotated system ($\tilde{x}$, $\tilde{y}$, and $\tilde{z}$) is defined by using Euler angles α, β, and γ as defined by Edmonds [24], and used by Mishchenko et al. [25], Doicu et al. [23], or Han et al. [17,18]. The definition is as follows.

(i) A first rotation, applied to the unrotated system (x, y, and z), by an angle α ($0 \le \alpha < 2\pi$) about the z-axis, brings the unrotated system to a α-rotated system with Cartesian coordinates (x_α, y_α, and z_α).
(ii) A second rotation, applied to the α-rotated system (x_α, y_α, and z_α), by an angle β ($0 \le \beta < \pi$) about the y_α-axis, brings the α-rotated system to a β-rotated system with Cartesian coordinates (x_β, y_β, and z_β).
(iii) A third rotation, applied to the β-rotated system (x_β, y_β, and z_β), by an angle γ ($0 \le \gamma < 2\pi$) about the z_β-axis, brings the β-rotated system to a γ-rotated system (simply called the rotated system) with Cartesian coordinates (x_γ, y_γ, and z_γ) better denoted as ($\tilde{x}$, $\tilde{y}$, and $\tilde{z}$).

All rotations defined above are positive (by definition, a positive rotation about a given axis is a rotation which would carry a right-handed screw in the positive direction along that axis).

Let $D(\alpha, \beta, \gamma)$ be the operator denoting the rotation with Euler angles (α, β, and γ) from coordinates $\mathbf{x}$ to coordinates $\tilde{\mathbf{x}}$. The inverse rotation is achieved by undoing successively the rotations associated with γ, β, and α in that order. Therefore, we have:

$$D^{-1}(\alpha, \beta, \gamma) = D(-\gamma, -\beta, -\alpha). \tag{21}$$

5. Rotation of VSWFs

In this section, we discuss the rotation of VSWFs (addition theorem for rotation). Because this issue is central to the present work, we shall develop it along two approaches and, thereafter, we shall show how these two approaches agree. By using two approaches, we will obtain a better understanding of the issue, useful for the sequel.

5.1. First approach, by using Wigner d-functions

The first approach relies on the use of Wigner d-functions, according to Mishchenko et al. [25]. A part of this section is devoted to some amount of translations between notations. Indeed, instead of Eq. (17), Mishchenko et al. used (p. 116):

$$\mathbf{E}^i = \sum_{n=1}^{\infty} \sum_{m=-n}^{n} \left[(a_{mn})_M Rg\mathbf{M}_{mn}(k\mathbf{r}) + (b_{mn})_M Rg\mathbf{N}_{mn}(k\mathbf{r}) \right] \tag{22}$$

in which we already introduced a few obvious changes of notations. In particular, the subscript M is used to avoid any confusion with a_{mn} and b_{mn} in Eq. (17). From Mishchenko et al. [25], Appendix C, with again a few obvious changes of notations, we have (p. 372):

$$Rg\mathbf{M}_{mn}(k\mathbf{r}) = Rg\mathbf{M}_{mn}(kr, \theta, \varphi) = \gamma_{mn} j_n(kr) \mathbf{C}_{mn}(\theta, \varphi) \tag{23}$$

in which:

$$\gamma_{mn} = \left[\frac{(2n+1)(n-m)!}{4\pi n(n+1)(n+m)!} \right]^{1/2} \tag{24}$$

and $j_n(kr)$ is defined by Eq. (6). Furthermore:

$$\mathbf{C}_{mn}(\theta, \varphi) = \left[im \frac{P_n^m(\cos\theta)}{\sin\theta} \mathbf{i}_\theta - \frac{dP_n^m(\cos\theta)}{d\theta} \mathbf{i}_\varphi \right] e^{im\varphi}. \tag{25}$$

Let us note that the definition of associated Legendre function $P_n^m(\cos\theta)$ used by Mishchenko et al. [25] is the same as ours, and therefore simultaneously different from the one used by Stratton [21]. Introducing the generalized Legendre functions π_n^m and τ_n^m, see Eqs. (3) and (4), Eq. (25) may be rewritten as:

$$\mathbf{C}_{mn}(\theta, \varphi) = e^{im\varphi} \left[im\pi_n^m(\cos\theta)\mathbf{i}_\theta - \tau_n^m(\cos\theta)\mathbf{i}_\varphi \right]. \tag{26}$$

Inserting Eq. (26) into Eq. (23), we obtain:

$$Rg\mathbf{M}_{mn}(k\mathbf{r}) = Rg\mathbf{M}_{mn}(kr, \theta, \varphi) = \gamma_{mn} j_n(kr) e^{im\varphi} \left[im\pi_n^m(\cos\theta)\mathbf{i}_\theta - \tau_n^m(\cos\theta)\mathbf{i}_\varphi \right]. \tag{27}$$

Now, from Eq. (1):

$$\mathbf{M}_{mn}^{(1)}(k\mathbf{r}) = (-1)^m j_n(kr) e^{im\varphi} \left[im\pi_n^m(\cos\theta)\mathbf{i}_\theta - \tau_n^m(\cos\theta)\mathbf{i}_\varphi \right]. \tag{28}$$

Hence, from Eqs. (27) and (28), we have:

$$\frac{Rg\mathbf{M}_{mn}}{\mathbf{M}_{mn}^{(1)}} = (-1)^m \gamma_{mn} = (-1)^m \left[\frac{(2n+1)(n-m)!}{4\pi n(n+1)(n+m)!} \right]^{1/2}. \tag{29}$$

Similarly, we readily obtain:

$$\frac{Rg\mathbf{N}_{mn}}{\mathbf{N}_{mn}^{(1)}} = \frac{Rg\mathbf{M}_{mn}}{\mathbf{M}_{mn}^{(1)}} = (-1)^m \gamma_{mn} = (-1)^m \left[\frac{(2n+1)(n-m)!}{4\pi n(n+1)(n+m)!} \right]^{1/2}. \tag{30}$$

Still from Mishchenko et al. [25], Appendix C, applying a $D(\alpha, \beta, \gamma)$-rotation to a system of coordinates $\mathbf{x} = (r, \theta, \varphi)$ leading to a new system $\tilde{\mathbf{x}} = (r, \tilde{\theta}, \tilde{\varphi})$, the VSWFs, in the version used by Mishchenko et al., transform according to (again with obvious convenient changes of notations):

$$Rg\mathbf{M}_{mn}\left(kr, \tilde{\theta}, \tilde{\varphi}\right) = \sum_{s=-n}^{n} Rg\mathbf{M}_{sn}(kr, \theta, \varphi) D_{sm}^n(\alpha, \beta, \gamma) \tag{31}$$

with a quite similar relation for **N**s, namely we could replace **M** by **K** in Eq. (31), with **K** standing both for **M** and **N**.

In agreement with Eq. (21), we conversely have:

$$Rg\mathbf{M}_{mn}(kr, \theta, \varphi) = \sum_{s=-n}^{n} Rg\mathbf{M}_{sn}\left(kr, \tilde{\theta}, \tilde{\varphi}\right) D_{sm}^n(-\gamma, -\beta, -\alpha). \tag{32}$$

In Eq. (31), we have:

$$D_{sm}^n(\alpha, \beta, \gamma) = e^{-is\alpha} d_{sm}^n(\beta) e^{-im\gamma} \tag{33}$$

in which $d^n_{sm}(\beta)$ denotes the Wigner d-functions. Mishchenko et al. [25], Appendix B, provides four different but equivalent ways to express these functions, according to:

$$\left[d^n_{sm}(\beta)\right]^{(1)} = \sqrt{(n+s)!(n-s)!(n+m)!(n-m)!} \sum_{\sigma}(-1)^{\sigma}\frac{\left(\cos\frac{\beta}{2}\right)^{2n-2\sigma+s-m}\left(\sin\frac{\beta}{2}\right)^{2\sigma-s+m}}{\sigma!(n+s-\sigma)!(n-m-\sigma)!(m-s+\sigma)!} \tag{34}$$

$$\left[d^n_{sm}(\beta)\right]^{(2)} = (-1)^{n-m}\sqrt{(n+s)!(n-s)!(n+m)!(n-m)!} \sum_{\sigma}(-1))^{\sigma}\frac{(cos\frac{\beta}{2})^{s+m+2\sigma}\left(sin\frac{\beta}{2}\right)^{2n-s-m-2\sigma}}{\sigma!(n-s-\sigma)!(n-m-\sigma)!(s+m+\sigma)!} \tag{35}$$

$$\left[d^n_{sm}(\beta)\right]^{(3)} = (-1)^{n+s}\sqrt{(n+s)!(n-s)!(n+m)!(n-m)!} \sum_{\sigma}(-1)^{\sigma}\frac{\left(\cos\frac{\beta}{2}\right)^{2\sigma-s-m}\left(\sin\frac{\beta}{2}\right)^{2n+s+m-2\sigma}}{\sigma!(n+s-\sigma)!(n+m-\sigma)!(\sigma-s-m)!} \tag{36}$$

$$\left[d^n_{sm}(\beta)\right]^{(4)} = (-1)^{s-m}\sqrt{(n+s)!(n-s)!(n+m)!(n-m)!} \sum_{\sigma}(-1)^{\sigma}\frac{\left(\cos\frac{\beta}{2}\right)^{2n-2\sigma-s+m}\left(\sin\frac{\beta}{2}\right)^{2\sigma+s-m}}{\sigma!(n-s-\sigma)!(n+m-\sigma)!(s-m+\sigma)!}. \tag{37}$$

Each of these different versions may be processed according to a certain procedure to be explained below. However, for the sake of comparison with the second approach explained in the next subsection, we remark that Han et al. [17] introduced a function $u^{(n)}_{sm}(\beta)$, which is strictly equal to a Wigner d-function $d^{(n)}_{sm}(\beta)$ introduced by Edmonds [24], reading as:

$$u^{(n)}_{sm}(\beta) = \left[\frac{(n+s)!(n-s)!}{(n+m)!(n-m)!}\right]^{1/2} \sum_{\sigma}\binom{n+m}{n-s-\sigma}\binom{n-m}{\sigma}(-1)^{n-s-\sigma}\left(\cos\frac{\beta}{2}\right)^{2\sigma+s+m}\left(\sin\frac{\beta}{2}\right)^{2n-2\sigma-s-m}. \tag{38}$$

If we compare the exponents of the functions cos and sin between Eq. (38) on one hand, and Eqs. (34)–(37), on the other hand, we see that $u^{(n)}_{sm}(\beta)$ compares favourably with the second version $[d^n_{sm}(\beta)]^{(2)}$. Indeed, we have:

$$\left[d^n_{sm}(\beta)\right]^{(2)} = (-1)^{m+s}u^{(n)}_{sm}. \tag{39}$$

For this reason, we proceed further by choosing the second version in the set of Eqs. (34)–(37). We now use Eq. (31) in which we insert Eqs. (33), (35), and (29) to obtain, after a few lines:

$$\mathrm{M}^{(1)}_{mn}\left(kr,\tilde{\theta},\tilde{\varphi}\right) = \frac{(-1)^{n+m}}{(n-m)!}\sum_{s=-n}^{n}(-1)^{m+s}(n-s)!\mathrm{M}^{(1)}_{sn}(kr,\theta,\varphi)e^{-is\alpha}e^{-im\gamma} \sum_{\sigma}(-1)^{\sigma}\binom{n+m}{n-s-\sigma}\binom{n-m}{\sigma}\left(cos\frac{\beta}{2}\right)^{2\sigma+s+m}\left(sin\frac{\beta}{2}\right)^{2n-2\sigma-s-m}. \tag{40}$$

This may be rewritten as:

$$\mathrm{M}^{(1)}_{mn}\left(kr,\tilde{\theta},\tilde{\varphi}\right) = \sum_{s=-n}^{n}G^s_{mn}(\alpha,\beta,\gamma)\mathrm{M}^{(1)}_{sn}(kr,\theta,\varphi) \tag{41}$$

in which:

$$G^s_{mn}(\alpha,\beta,\gamma) = \frac{(-1)^{n+m}}{(n-m)!}(n-s)!e^{-is\alpha}e^{-im\gamma} \sum_{\sigma}(-1)^{s+m}(-1)^{\sigma}\binom{n+m}{n-s-\sigma}\binom{n-m}{\sigma}\left(cos\frac{\beta}{2}\right)^{2\sigma+s+m}\left(sin\frac{\beta}{2}\right)^{2n-2\sigma-s-m}. \tag{42}$$

5.2. Second approach

Following Han et al. [17], we write:

$$(-1)^m P^m_n(\cos\theta)e^{im\varphi} = \sum_{s=-n}^{n}\rho(m,s,n)(-1)^s P^s_n\left(\cos\tilde{\theta}\right)e^{is\tilde{\varphi}} \tag{43}$$

$$\rho(m,s,n) = (-1)^{s+m}e^{is\gamma}\left[\frac{(n+m)!(n-s)!}{(n-m)!(n+s)!}\right]^{1/2}u^{(n)}_{sm}(\beta)e^{im\alpha} \tag{44}$$

$$u^{(n)}_{sm}(\beta) = \left[\frac{(n+s)!(n-s)!}{(n+m)!(n-m)!}\right]^{1/2}\sum_{\sigma}(-1)^{n-s-\sigma}\binom{n+m}{n-s-\sigma} \binom{n-m}{\sigma}\left(\cos\frac{\beta}{2}\right)^{2\sigma+s+m}\left(\sin\frac{\beta}{2}\right)^{2n-2\sigma-s-m}. \tag{45}$$

Eqs. (44) and (45) agree perfectly well with Eqs. (3) and (4) given by Han et al. [17]. There are however small formal differences between Eq. (43) and Eq. (2) in Han et al. [17], namely concerning the factors $(-1)^m$ in the l.h.s and $(-1)^s$ in the r.h.s. of Eq. (43). They are due to the fact that Han et al. [17] do not use our definition of the associated Legendre functions, but the alternative one from Stratton [21]. Let us note that the l.h.s of Eq. (43) concerns the unrotated system (angular variables are not tilde-decorated). Also, the subscript σ in the summation of Eq. (45) runs over all values which make the arguments of the factorials, in the binomials, non-negative (the same is true for Eqs. (34)–(37)).

Han et al. [17] claimed that they derive their formulation from Edmonds [24]. However, a missprint in Edmonds [24], appearing in Stein too [26], had to be corrected, namely the terms $e^{is\gamma}$ and $e^{im\alpha}$ in the r.h.s. of Eq. (44) were erroneously written as $e^{is\alpha}$ and $e^{im\gamma}$ respectively. It is rather easy to convince the reader that the original equations in Edmonds [24] are erroneous. Indeed, let us simply consider a rotation of angle α about the z-axis from Cartesian coordinates (x, y, and z) with associated spherical coordinates (r, θ, and φ) to an α-rotated system and observe that, under such a rotation:

$$P^m_n(\cos\theta)e^{im\varphi} = P^m_n(\cos\theta_\alpha)e^{im\varphi_\alpha}e^{im\alpha} \tag{46}$$

explicitly showing that α is associated with m, not with s. Another problem in Edmonds [24] concerns his equation 4.1.4. Afterward, using also Eqs. 4.1.10, 4.1.12, 4.1.15, we might believe that the l.h.s. of Eq. (43) concerns a rotated system, in contrast with the fact that it does concern an unrotated system. The validity of Eq. (43) may be checked by examining it for various specific values of n and m. The reader might also refer to a book by Varshalovich et al. [27] and to a thesis by Guoxia Han [28] agreeing with our Eqs. (43)–(45) that we use as the starting point for the second approach.

Let us now consider Eq. (43), multiply by $z_n(kr)$, as defined after Eqs. (1) and (2), take the gradient, and vectorially multiply on the right by $\mathbf{r}$. We obtain:

$$\left[(-1)^m\nabla z_n(kr)P^m_n(cos\theta)e^{im\varphi}\right]\mathbf{x}\mathbf{r} = \sum_{s=-n}^{+n}\rho(m,s,n)\left[(-1)^s\nabla z_n(kr)P^s_n\left(cos\tilde{\theta}\right)e^{is\tilde{\varphi}}\right]\mathbf{x}\mathbf{r}. \tag{47}$$

In order to interpret this equation, we make a detour relying on the book by Stratton. Following Stratton [21], p. 415, and recalling that our **M**s are exactly equal to those of Stratton, as pointed out in Section 2, we introduce the following equation:

$$\mathbf{M}^{(j)}_{mn}(k\mathbf{r}) = \nabla\mathbf{x}(\mathbf{i}_r u(r)\Psi_{mn}) = \mathbf{L}_{mn}\mathbf{x}\mathbf{i}_r u(r) \tag{48}$$

in which $u(r)$ is an unknown scalar function of r. We supplemented Stratton's equation with subscripts (mn) for the sake of clarity, although this may be a matter of taste. Also, in Eq. (48), we have:

$$\mathbf{L}_{mn} = \nabla\Psi_{mn} = \frac{\partial\Psi_{mn}}{\partial r}\mathbf{i}_r + \frac{1}{r}\frac{\partial\Psi_{mn}}{\partial\theta}\mathbf{i}_\theta + \frac{1}{rsin\theta}\frac{\partial\Psi_{mn}}{\partial\varphi}\mathbf{i}_\varphi \tag{49}$$

$$\Psi_{mn} = (-1)^m z_n(kr)P_n^m(cos\theta)e^{im\varphi} \tag{50}$$

in which, for the time being, the angular variables θ and φ pertain to any spherical coordinate system (rotated or unrotated). Now, let us choose $u(r)=r$, then from Eqs. (48) and (49), and using the definitions of Eqs. (3) and (4), we have:

$$\mathbf{M}_{mn}^{(j)}(k\mathbf{r}) = \mathbf{L}_{mn}\mathbf{x}\mathbf{i}_r r = \nabla\Psi_{mn}\mathbf{x}\mathbf{i}_r r =$$
$$\begin{vmatrix} \frac{\partial\Psi_{mn}}{\partial r} \\ \frac{1}{r}\frac{\partial\Psi_{mn}}{\partial\theta} \\ \frac{1}{rsin\theta}\frac{\partial\Psi_{mn}}{\partial\varphi} \end{vmatrix} \times \begin{vmatrix} r \\ 0 \\ 0 \end{vmatrix} = \begin{vmatrix} 0 \\ (-1)^m imz_n(kr)\pi_n^m(cos\theta)e^{im\varphi} \\ -(-1)^m z_n(kr)\tau_n^m(cos\theta)e^{im\varphi} \end{vmatrix}$$
$$= (-1)^m z_n(kr)e^{im\varphi}\left[im\pi_n^m(cos\theta)\mathbf{i}_\theta - \tau_n^m(cos\theta)\mathbf{i}_\varphi\right]. \tag{51}$$

Using Eqs. (50) and (51), Eq. (47) is then translated to:

$$\mathbf{M}_{mn}^{(j)}(kr,\theta,\varphi) = \sum_{s=-n}^{n}\rho(m,s,n)\mathbf{M}_{sn}^{(j)}\left(kr,\tilde{\theta},\tilde{\varphi}\right). \tag{52}$$

In particular, we shall need:

$$\mathbf{M}_{mn}^{(1)}(kr,\theta,\varphi) = \sum_{s=-n}^{n}\rho(m,s,n)\mathbf{M}_{sn}^{(1)}\left(kr,\tilde{\theta},\tilde{\varphi}\right). \tag{53}$$

Having established the rotation transformation for the **M**s, we now deal with the **N**s. From Stratton, p. 415, we have:

$$k\mathbf{N}_{mn}^{(j)} = \nabla\times\mathbf{M}_{mn}^{(j)} \tag{54}$$

for which we provide a direct check in Appendix A. This being done, we may now return to Eqs. (54) and (52), from which we immediately obtain that the **M**s and the **N**s satisfy the same transformations under rotations.

5.3. Agreement between the two approaches

We first recall what we have obtained. On one hand, from Mischenko et al. [25], we derived Eqs. (41) and (42), reading as, after a minor simplification:

$$\mathbf{M}_{mn}^{(1)}\left(kr,\tilde{\theta},\tilde{\varphi}\right) = \sum_{s=-n}^{n}G_{mn}^{s}(\alpha,\beta,\gamma)\mathbf{M}_{sn}^{(1)}(kr,\theta,\varphi) \tag{55}$$

$$G_{mn}^{s}(\alpha,\beta,\gamma) = (-1)^n\frac{(n-s)!}{(n-m)!}e^{-is\alpha}e^{-im\gamma}(-1)^s$$
$$\sum_{\sigma}(-1)^\sigma\binom{n+m}{n-s-\sigma}\binom{n-m}{\sigma}\left(cos\frac{\beta}{2}\right)^{2\sigma+s+m}\left(sin\frac{\beta}{2}\right)^{2n-2\sigma-s-m}. \tag{56}$$

On the other hand, the result of the second approach, following Han et al. [17], from Eqs. (53), (44) and (45), can be conveniently rewritten as:

$$\mathbf{M}_{mn}^{(1)}(kr,\theta,\varphi) = \sum_{s=-n}^{n}H_{mn}^{s}(\alpha,\beta,\gamma)\mathbf{M}_{sn}^{(1)}\left(kr,\tilde{\theta},\tilde{\varphi}\right) \tag{57}$$

in which:

$$H_{mn}^{s}(\alpha,\beta,\gamma) = (-1)^{m+s}\frac{(n-s)!}{(n-m)!}e^{is\gamma}e^{im\alpha}$$
$$\sum_{\sigma}(-1)^{n-s-\sigma}\binom{n+m}{n-s-\sigma}\binom{n-m}{\sigma}\left(cos\frac{\beta}{2}\right)^{2\sigma+s+m}\left(sin\frac{\beta}{2}\right)^{2n-2\sigma-s-m}. \tag{58}$$

We observe that the two approaches invert what is called the rotated system and what is called the unrotated system. To compare their results, we shall therefore have to compare, for instance, $G_{mn}^{s}(\alpha,\beta,\gamma)$ and $H_{mn}^{s}(-\gamma,-\beta,-\alpha)$. We readily have:

$$H_{mn}^{s}(-\gamma,-\beta,-\alpha) = (-1)^{m+s}(-1)^{n+m}\frac{(n-s)!}{(n-m)!}e^{-is\alpha}e^{-im\gamma}$$
$$\sum_{\sigma}(-1)^\sigma\binom{n+m}{n-s-\sigma}\binom{n-m}{\sigma}\left(cos\frac{\beta}{2}\right)^{2\sigma+s+m}\left(sin\frac{\beta}{2}\right)^{2n-2\sigma-s-m}. \tag{59}$$

We then observe that $G_{mn}^{s}(\alpha,\beta,\gamma)$ and $H_{mn}^{s}(-\gamma,-\beta,-\alpha)$ are equal, as they should. The other version of this equality is given by:

$$H_{mn}^{s}(\alpha,\beta,\gamma) = G_{mn}^{s}(-\gamma,-\beta,-\alpha) \tag{60}$$

in which $H_{mn}^{s}(\alpha,\beta,\gamma)$ will be simply denoted as H_{mn}^{s} when there is no ambiguity, in particular when we do not need to specify the values of the Euler angles.

6. Transformation of beam shape coefficients through rotations

Using the abbreviated notation H_{mn}^{s}, we now express the unrotated **M**s versus the rotated ones as:

$$\mathbf{M}_{mn}^{(1)}(kr,\theta,\varphi) = \sum_{s=-n}^{n}H_{mn}^{s}\mathbf{M}_{sn}^{(1)}\left(kr,\tilde{\theta},\tilde{\varphi}\right). \tag{61}$$

Similarly:

$$\mathbf{N}_{mn}^{(1)}(kr,\theta,\varphi) = \sum_{s=-n}^{n}H_{mn}^{s}\mathbf{N}_{sn}^{(1)}\left(kr,\tilde{\theta},\tilde{\varphi}\right). \tag{62}$$

Now, we recall Eq. (17)

$$\mathbf{E}^i = \sum_{n=1}^{\infty}\sum_{m=-n}^{+n}\left[a_{mn}\mathbf{M}_{mn}^{(1)}(kr,\theta,\varphi) + b_{mn}\mathbf{N}_{mn}^{(1)}(kr,\theta,\varphi)\right]. \tag{63}$$

We now insert Eqs. (61) and (62) into Eq. (63), yielding:

$$\mathbf{E}^i = \sum_{n=1}^{\infty}\sum_{m=-n}^{n}\sum_{s=-n}^{n}H_{mn}^{s}\left[a_{mn}\mathbf{M}_{sn}^{(1)}\left(kr,\tilde{\theta},\tilde{\varphi}\right) + b_{mn}\mathbf{N}_{sn}^{(1)}\left(kr,\tilde{\theta},\tilde{\varphi}\right)\right]. \tag{64}$$

We may interchange the names of the summation indices m and s leading to:

$$\mathbf{E}^i = \sum_{n=1}^{\infty}\sum_{m=-n}^{n}\left\{\left[\sum_{s=-n}^{n}a_{sn}H_{sn}^{m}\right]\mathbf{M}_{mn}^{(1)}\left(kr,\tilde{\theta},\tilde{\varphi}\right) + \left[\sum_{s=-n}^{n}b_{sn}H_{sn}^{m}\right]\mathbf{N}_{mn}^{(1)}\left(kr,\tilde{\theta},\tilde{\varphi}\right)\right\}. \tag{65}$$

But we may also express the electric field in terms of rotated quantities, according to:

$$\mathbf{E}^i = \widetilde{\mathbf{E}^i} = \sum_{n=1}^{\infty}\sum_{m=-n}^{n}\left[\widetilde{a_{mn}}\,\mathbf{M}_{mn}^{(1)}\left(kr,\tilde{\theta},\tilde{\varphi}\right) + \widetilde{b_{mn}}\mathbf{N}_{mn}^{(1)}\left(kr,\tilde{\theta},\tilde{\varphi}\right)\right]. \tag{66}$$

Therefore, from Eqs. (65) and (66):

$$\widetilde{a_{mn}} = \sum_{s=-n}^{n} a_{sn} H_{sn}^{m} \tag{67}$$

$$\widetilde{b_{mn}} = \sum_{s=-n}^{n} b_{sn} H_{sn}^{m}. \tag{68}$$

Finally, we invoke Eqs. (19) and (20), introduce the beam shape coefficients $\widetilde{g_{n,\mathrm{TM}}^{m}}$ and $\widetilde{g_{n,\mathrm{TE}}^{m}}$ in the rotated system, and readily obtain:

$$\widetilde{g_{n,X}^{m}} = (-1)^{m}(-1)^{\frac{m-|m|}{2}} \frac{(n-|m|)!}{(n-m)!} \sum_{s=-n}^{n} (-1)^{s}(-1)^{\frac{s-|s|}{2}} \frac{(n-s)!}{(n-|s|)!} H_{sn}^{m} g_{n,X}^{s} \tag{69}$$

in which X is TM or TE.

7. Conclusion

In this paper, we have established the law of transformation of spherical beam shape coefficients under rotations. The result obtained may be expressed as a theorem expressed below.

Let $\mathbf{x}$ and $\tilde{\mathbf{x}}$ be two systems of coordinates, named the unrotated and the rotated systems, respectively. Let $g_{n,X}^{m}$ and $\widetilde{g_{n,X}^{m}}$, with $X=$ TM or TE, be the spherical beam shape coefficients of an arbitrary shaped beam in the unrotated and in the rotated systems, respectively. Then:

$$\widetilde{g_{n,X}^{m}} = \mu_{mn} \sum_{s=-n}^{n} \frac{H_{sn}^{m}}{\mu_{sn}} g_{n,X}^{s} \tag{70}$$

in which:

$$\mu_{mn} = (-1)^{m}(-1)^{\frac{m-|m|}{2}} \frac{(n-|m|)!}{(n-m)!} \tag{71}$$

$$H_{sn}^{m} = (-1)^{n+s} \frac{(n-m)!}{(n-s)!} e^{is\alpha} e^{im\gamma} \sum_{\sigma} (-1)^{\sigma} \binom{n+s}{n-m-\sigma} \binom{n-s}{\sigma} \left(\cos\frac{\beta}{2}\right)^{2\sigma+m+s} \left(\sin\frac{\beta}{2}\right)^{2n-2\sigma-m-s} \tag{72}$$

in which (α, β, γ) are Euler angles bringing the unrotated system to the rotated system.

Appendix A

In this Annex, we provide a direct check of Eq. (54). For convenience, let us set:

$$\mathbf{R}_{mn}^{(j)} = \nabla \times \mathbf{M}_{mn}^{(j)}. \tag{73}$$

Following Stratton [21], page 52, we have:

$$\begin{aligned} \mathbf{R}_{mn}^{(j)} = {} & \frac{1}{r\sin\theta}\left[\frac{\partial}{\partial\theta}\left(\sin\theta \mathbf{M}_{mn,\varphi}^{(j)}\right) - \frac{\partial}{\partial\varphi}\mathbf{M}_{mn,\theta}^{(j)}\right]\mathbf{i}_r \\ & + \frac{1}{r}\left[\frac{1}{\sin\theta}\frac{\partial}{\partial\varphi}\mathbf{M}_{mn,r}^{(j)} - \frac{\partial}{\partial r}\left(r\mathbf{M}_{mn,\varphi}^{(j)}\right)\right]\mathbf{i}_\theta \\ & + \frac{1}{r}\left[\frac{\partial}{\partial r}\left(r\mathbf{M}_{mn,\theta}^{(j)}\right) - \frac{\partial}{\partial\theta}\mathbf{M}_{mn,r}^{(j)}\right]\mathbf{i}_\varphi \end{aligned} \tag{74}$$

in which, from Eq. (1):

$$\mathbf{M}_{mn}^{(j)} = \begin{vmatrix} \mathbf{M}_{mn,r}^{(j)} \\ \mathbf{M}_{mn,\theta}^{(j)} \\ \mathbf{M}_{mn,\varphi}^{(j)} \end{vmatrix} = \begin{vmatrix} 0 \\ (-1)^{m} im z_n(kr)\pi_n^{m}(\cos\theta)e^{im\varphi} \\ -(-1)^{m} z_n(kr)\tau_n^{m}(\cos\theta)e^{im\varphi} \end{vmatrix}. \tag{75}$$

From Eqs. (74) and (75), and invoking Eq. (2), we then readily establish:

$$\mathbf{R}_{mn,\varphi}^{(j)} = \left(\nabla \times \mathbf{M}_{mn}^{(j)}\right)_{\varphi} = (-1)^{m} \frac{im}{r}\left[\frac{\partial}{\partial r} r z_n(kr)\right]\pi_n^{m}(\cos\theta)e^{im\varphi} = k\mathbf{N}_{mn,\varphi}^{(j)} \tag{76}$$

$$\mathbf{R}_{mn,\theta}^{(j)} = \left(\nabla \times \mathbf{M}_{mn}^{(j)}\right)_{\theta} = \frac{(-1)^{m}}{r}\left[\frac{\partial}{\partial r} r z_n(kr)\right]\tau_n^{m}(\cos\theta)e^{im\varphi} = k\mathbf{N}_{mn,\theta}^{(j)}. \tag{77}$$

The derivation for $\mathbf{R}_{mn,r}^{(j)}$ is a bit more complicated. We begin by using again Eqs. (74) and (75) to obtain:

$$\mathbf{R}_{mn,r}^{(j)} = \left(\nabla \times \mathbf{M}_{mn}^{(j)}\right)_{r} = -\frac{(-1)^{m}}{r\sin\theta} z_n(kr) e^{im\varphi} A_{mn} \tag{78}$$

in which:

$$A_{mn} = \frac{d}{d\theta}\sin\theta\tau_n^{m}(\cos\theta) - m^{2}\pi_n^{m}(\cos\theta). \tag{79}$$

We may explicit rewrite A_{mn} under the form:

$$A_{mn} = \cos\theta \frac{dP_n^{m}(\cos\theta)}{d\theta} + \sin\theta \frac{d^{2}P_n^{m}(\cos\theta)}{d\theta^{2}} - m^{2}\frac{P_n^{m}(\cos\theta)}{\sin\theta}. \tag{80}$$

But we readily establish:

$$\frac{dP_n^{m}(\cos\theta)}{d\theta} = -\sin\theta \frac{dP_n^{m}(\cos\theta)}{d\cos\theta} \tag{81}$$

$$\frac{d^{2}P_n^{m}(\cos\theta)}{d\theta^{2}} = -\cos\theta \frac{dP_n^{m}(\cos\theta)}{d\cos\theta} + \sin^{2}\theta \frac{d^{2}P_n^{m}(\cos\theta)}{(d\cos\theta)^{2}}. \tag{82}$$

Inserting Eqs. (81) and (82) into Eq. (80), and rearranging, leads to:

$$\frac{A_{mn}}{\sin\theta} = -2\cos\theta \frac{dP_n^{m}(\cos\theta)}{d\cos\theta} + \sin^{2}\theta \frac{d^{2}P_n^{m}(\cos\theta)}{(d\cos\theta)^{2}} - m^{2}\frac{P_n^{m}(\cos\theta)}{\sin^{2}\theta}. \tag{83}$$

But the associated Legendre functions $P_n^{m}(\cos\theta)$ satisfy an associated Legendre equation reading as:

$$\sin^{2}\theta \frac{d^{2}P_n^{m}(\cos\theta)}{(d\cos\theta)^{2}} - 2\cos\theta \frac{dP_n^{m}(\cos\theta)}{d\cos\theta} + \left[n(n+1) - \frac{m^{2}}{\sin^{2}\theta}\right]P_n^{m}(\cos\theta) = 0. \tag{84}$$

Then, from Eqs. (83) and (84):

$$A_{mn} = -n(n+1)\sin\theta P_n^{m}(\cos\theta). \tag{85}$$

Inserting Eq. (85) into Eq. (78), and invoking Eq. (2), we finally obtain:

$$\mathbf{R}_{mn,r}^{(j)} = \left(\nabla \times \mathbf{M}_{mn}^{(j)}\right)_{r} = (-1)^{m} \frac{n(n+1)}{r} z_n(kr) P_n^{m}(\cos\theta) e^{im\varphi} = k\mathbf{N}_{mn,r}^{(j)} \tag{86}$$

as it should.

References

[1] G. Gouesbet, B. Maheu, G. Gréhan, Journal of the Optical Society of America A 5 (1988) 1427.
[2] B. Maheu, G. Gouesbet, G. Gréhan, Journal of Optics, Paris 19 (2) (1988) 59.
[3] J.A. Lock, G. Gouesbet, Journal of Quantitative Spectroscopy and Radiative Transfer 110 (2009) 800.

[4] G. Gouesbet, Journal of Quantitative Spectroscopy and Radiative Transfer 110 (2009) 1223.
[5] F. Onofri, G. Gréhan, G. Gouesbet, Applied Optics 34 (30) (1995) 7113.
[6] G. Gouesbet, G. Gréhan, Journal of Modern Optics 47 (5) (2000) 821.
[7] G. Gouesbet, G. Gréhan, Journal of Optics A: Pure and Applied Optics 1 (1999) 706.
[8] G. Gouesbet, C. Letellier, K.F. Ren, G. Gréhan, Applied Optics 35 (9) (1996) 1537.
[9] G. Gouesbet, G. Gréhan, B. Maheu, Journal of Optics, Paris 19 (1) (1988) 35.
[10] G. Gouesbet, G. Gréhan, B. Maheu, Applied Optics 27 (23) (1988) 4874.
[11] G. Gouesbet, Journal of the Optical Society of America A 16 (7) (1999) 1641.
[12] K.F. Ren, G. Gouesbet, G. Gréhan, Applied Optics 37 (19) (1998) 4218.
[13] A. Doicu, T. Wriedt, Applied Optics 36 (13) (1997) 2971.
[14] H.Y. Zhang, Y.P. Han, Journal of the Optical Society of America B 11 (2008) 255.
[15] G. Gouesbet, G. Gréhan, Journal of Optics, Paris 13 (2) (1982) 97.
[16] G. Gouesbet, Applied Optics 35 (9) (1996) 1543.
[17] Y.P. Han, H. Zhang, G. Han, Optics Express 15 (2) (2007) 735.
[18] Y.P. Han, Y. Zhang, H. Zhang, G. Han, Journal of Quantitative Spectroscopy and Radiative Transfer 110 (14–16) (2009) 1375.
[19] G. Gouesbet, Optics Communications 283 (2010) 517.
[20] L. Robin, Fonctions sphériques de Legendre et fonctions sphéroïdales, Vols 1–3, Gauthiers-Villars, 1957.
[21] J.A. Stratton, Electromagnetic Theory, McGraw-Hill Book Company, New-York, London, 1941.
[22] J.G. Fikioris, N.K. Uzunoglu, Journal of the Optical Society of America 69 (10) (1979) 1359 reprinted in 1988, SPIE, 951, Part 1, 174.
[23] A. Doicu, T. Wriedt, Y.A. Eremin, Light Scattering by Systems of Particles. Null-field Method with Discrete Sources — Theory and Programs, Springer, 2006.
[24] A.R. Edmonds, Angular Momentum in Quantum Mechanics, Princeton University Press, 1957.
[25] M.I. Mishchenko, L.D. Travis, A.A. Lacis, Scattering, Absorption, and Emission of Light by Small Particles, Cambridge University Press, 2002.
[26] S. Stein, Q. Applied Mathematics 19 (1961) 15.
[27] D.A. Varshalovich, A.N. Moskalev, V.K. Khersonskii, Quantum Theory of Angular Momentum, World Scientific, 1988.
[28] Guoxia Han. Study on the interaction of arbitrary incident Gaussian beam with eccentric sphere and bi-sphere, in Chinese. PhD thesis, Xidian University, Xi'an, China, 2009.

Optics Communications 283 (2010) 3226–3234

Contents lists available at ScienceDirect

Optics Communications

journal homepage: www.elsevier.com/locate/optcom

Transformations of spherical beam shape coefficients in generalized Lorenz–Mie theories through rotations of coordinate systems
II. Axisymmetric beams

J.J. Wang [a,b,c,d,e], G. Gouesbet [a,b,c,d,*], Y.P. Han [e]

[a] Laboratoire d'Electromagnétisme des Systèmes Particulaires (LESP), France
[b] Unité Mixte de Recherche (UMR) 6614, France
[c] Centre National de la Recherche Scientifique (CNRS), COmplexe de Recherche Interprofessionnel en Aérothermochimie (CORIA), France
[d] Université de Rouen et Institut National des Sciences Appliquées (INSA) de Rouen, BP12, avenue de l'université, technopôle du Madrillet, 76801, Saint-Etienne-du Rouvray, France
[e] School of Science, Xidian University, Xi'an, China

ARTICLE INFO

Article history:
Received 8 March 2010
Received in revised form 8 April 2010
Accepted 21 April 2010

ABSTRACT

The description of laser beams in spherical coordinates requires the introduction of expansion coefficients named beam shape coefficients, or more specifically spherical beam shape coefficients. In part I of the present series of papers, we presented a general formulation for the transformation of spherical beam shape coefficients through rotations of coordinate systems, taking the form of a theorem of transformation. The present Part II deals with the special case of axisymmetric beams, more particularly of on-axis axisymmetric beams (such as Gaussian beams in an on-axis configuration).

1. Introduction

The description of laser beams in spherical coordinates under expanded forms, which may be useful in light scattering theories, particularly for generalized Lorenz–Mie theories which describe the interaction between arbitrary shaped beams and regular particles, in spherical coordinates, e.g. [1–8], requires the evaluation of expansion coefficients known as beam shape coefficients. For these evaluations, several methods have been developed and studied, sharing various degrees of time running efficiency, or of flexibility, namely by using quadratures [9], finite series [10], localized approximations [11,12], or by a hybrid method taking advantage of both quadratures and of a localized approximation, named the integral localized approximation [13]. The evaluation of beam shape coefficients has also been investigated by relying on addition theorems for translations of coordinate systems, an approach originally introduced by Doicu and Wriedt [14], and also used by Zhang and Han [15]. The present paper pertains to a series concerning the evaluation of beam shape coefficients by relying on addition theorems for rotations (not translations) of coordinate systems, a topic initiated by Han et al [16,17].

For convenience, in particular to recall some notations, the specific problem attacked in Gouesbet et al. [18] is briefly stated again. Let us consider a Cartesian system of coordinates, denoted as $\mathbf{x}=(x, y, z)$, associated with usual spherical coordinates (r, θ, φ), called the unrotated system, and let $g^m_{n,TM}$, $g^m_{n,TE}$ be the beam shape coefficients for the description of the illuminating beam in this unrotated system. Let us consider a second system of coordinates, called the rotated system, deduced from the unrotated system by a rotation defined by Euler angles (α, β, γ), defined according to Edmonds [19], as explained in Part I [18]. Quantities in the rotated system are denoted by using tilde-decorations. Therefore the Cartesian coordinates of the rotated system are denoted as $\tilde{\mathbf{x}} = (\tilde{x}, \tilde{y}, \tilde{z})$ and they are associated with spherical coordinates $\left(\tilde{r} = r, \tilde{\theta}, \tilde{\varphi}\right)$. The beam shape coefficients in the rotated system are denoted as $\widetilde{g^m_{n,TM}}$, $\widetilde{g^m_{n,TE}}$. The problem is to express the beam shape coefficients in the rotated system in terms of beam shape coefficients in the unrotated system. A general solution to this problem has been found in Part I [18]. In some cases of significant importance, the results obtained in Part I can be further simplified, possibly receiving compact expressions, allowing one to speed up numerical computations. In the present Part II, we specify the results obtained to the case of axisymmetric beams, more particularly to the case of on-axis axisymmetric beams, such as on-axis Gaussian beams.

The paper is organized as follows. Section 2 recalls the results obtained in Part I, forming our starting point for this Part II. Section 3 recalls what are axisymmetric beams, particularly on-axis axisymmetric beams, and their properties useful for the sequel. Section 4

* Corresponding author. UMR.CNRS.6614, Université de Rouen et Institut National des Sciences Appliquées (INSA) de Rouen, BP12, avenue de l'université, technopôle du Madrillet, 76801, Saint-Etienne-du Rouvray, France.
E-mail address: Gouesbet@coria.fr (G. Gouesbet).

0030-4018/$ – see front matter © 2010 Elsevier B.V. All rights reserved.
doi:10.1016/j.optcom.2010.04.049

deals with the transformation of axisymmetric beams in expanded forms, while Section 5 deals with the same issue in compact forms. This Section 5 contains a subsection devoted to beam shape coefficients, in which the main formal results of the paper are expressed, namely by Eqs. 98, 99. Section 6 deals with the case when there is no rotation, i.e. the rotated system identifies with the unrotated system, providing a checking of our computations. Section 7 provides a discussion of the significance of the results obtained, and also serves as a conclusion.

2. General solution to the problem of the transformation of beam shape coefficients

2.1. Beam shape coefficients

In this paper, the beam shape coefficients are defined in the framework of the Bromwich formulation, as originally done in the GLMT stricto sensu, e.g. [1,2]. This framework relies on the use of two Bromwich scalar potentials U_{TM} and U_{TE} (*TM* for Transverse Magnetic and *TE* for Transverse Electric), for the incident, the scattered, and the internal (or sphere) waves. When the Bromwich scalar potentials are known, electric and magnetic fields of the *TM* and *TE* kinds may be obtained by using derivative rules, namely Eqs. (10)–(19) in [1].The Bromwich scalar potentials for the incident wave read as [1]:

$$U_{TM}^{i} = \frac{E_0}{k}\sum_{n=1}^{\infty}\sum_{m=-n}^{+n} c_n^{pw} g_{n,TM}^{m} \Psi_n(kr) P_n^{|m|}(\cos\theta)\exp(im\varphi) \tag{1}$$

$$U_{TE}^{i} = \frac{H_0}{k}\sum_{n=1}^{\infty}\sum_{m=-n}^{n} c_n^{pw} g_{n,TE}^{m} \Psi_n(kr) P_n^{|m|}(\cos\theta)\exp(im\varphi) \tag{2}$$

in which the superscript "*i*" stands for "incident". Note however that, in most of the present paper, we do not consider any scattering particle, that is to say the superscript "*i*" may rather be viewed as anticipating our results for use in GLMTs. Also, E_0 and H_0 are field strengths, and k is the wave-number in the medium in which the beam propagates. The coefficients c_n^{pw} ("*pw*" standing for "plane wave") are coefficients which appear naturally in the classical Lorenz–Mie theory and, for this reason, are isolated [20]. They read as:

$$c_n^{pw} = \frac{1}{k}(-i)^{n+1}\frac{2n+1}{n(n+1)} \tag{3}$$

The functions $\Psi_n(kr)$ are Ricatti–Bessel functions, which may be expressed in terms of spherical Bessel functions $j_n(kr)$ according to:

$$\Psi_n(kr) = krj_n(kr) \tag{4}$$

The expressions for the Bromwich scalar potentials also involve the associated Legendre functions (often misnamed as polynomials by physicists) reading as (for m non-negative):

$$P_n^m(\cos\theta) = (-1)^m(\sin\theta)^m\frac{d^m P_n(\cos\theta)}{(d\cos\theta)^m} \tag{5}$$

We also have:

$$P_n^{-m}(\cos\theta) = (-1)^m\frac{(n-m)!}{(n+m)!}P_n^m(\cos\theta) \tag{6}$$

This implies:

$$P_n^m(\cos\theta) = (-1)^{\frac{m-|m|}{2}}\frac{(n-|m|)!}{(n-m)!}P_n^{|m|}(\cos\theta) \tag{7}$$

that is to say we may uniquely define $P_n^m(\cos\theta), \forall m \in \mathbf{Z}$ [18,21].

We may then consider that Eqs. (1) and (2) serve as a definition of the beam shape coefficients $g_{n,X}^m$, with $X = TM$ or *TE*. The relationship between the scalar Bromwich formulation and a formulation in terms of vector spherical wave functions (VSWFs) is discussed elsewhere, for instance in Part I [18].

2.2. The theorem of transformation

We now know enough to express the theorem of transformation of beam shape coefficients under rotations of coordinate systems, established in Part I, reading as follows. Let $\mathbf{x}$ and $\tilde{\mathbf{x}}$ be two systems of coordinates, named the unrotated and the rotated systems, respectively. Let $g_{n,X}^m$ and $\widetilde{g_{n,X}^m}$, with $X = TM$ or *TE*, be the spherical beam shape coefficients of an arbitrary shaped beam in the unrotated and in the rotated systems, respectively. Then:

$$\widetilde{g_{n,X}^m} = \mu_{mn}\sum_{s=-n}^{n}\frac{H_{sn}^m}{\mu_{sn}}g_{n,X}^s \tag{8}$$

in which:

$$\mu_{mn} = (-1)^m(-1)^{\frac{m-|m|}{2}}\frac{(n-|m|)!}{(n-m)!} \tag{9}$$

$$H_{sn}^m = (-1)^{n+s}\frac{(n-m)!}{(n-s)!}e^{is\alpha}e^{im\gamma}\sum_{\sigma}(-1)^{\sigma}\binom{n+s}{n-m-\sigma}\binom{n-s}{\sigma} \times\left(\cos\frac{\beta}{2}\right)^{2\sigma+m+s}\left(\sin\frac{\beta}{2}\right)^{2n-2\sigma-m-s} \tag{10}$$

in which (α, β, γ) are the Euler angles bringing the unrotated system to the rotated system.

3. Definition and properties of axisymmetric beams

We are now considering a class of special beams called axisymmetric beams, discussed by Gouesbet [22], that we begin by briefly reviewing.

Let $\mathbf{S}$ be the Poynting vector, with components S_x, S_y, S_z in a Cartesian coordinate system (x, y, z) with associated spherical coordinates (r, θ, φ), and the axis z being taken as the direction of propagation of the beam. By definition, a beam is said to be generic iff (iff, i.e. if and only if) $S_z(\theta = 0)$ is not zero, that is to say iff the longitudinal component of the Poynting vector along the positive z-axis is not zero. Only generic beams are considered below.

Furthermore, we define an axisymmetric beam to be a beam for which S_z does not depend on the azimuthal angle φ, in suitably chosen coordinate systems. It is then demonstrated that the beam shape coefficients of a generic axisymmetric beam, when S_z does not depend on φ, [22], read as:

$$g_n^m = 0, |m| \neq 1 \tag{11}$$

$$g_{n,TM}^1 = \frac{1}{K}g_{n,TM}^{-1} = -i\varepsilon g_{n,TE}^1 = \frac{i\varepsilon}{K}g_{n,TE}^{-1} = \frac{g_n}{2} \tag{12}$$

The reciprocal statement is true. Eq. (12) defines a set $\{g_n\}$ of special beam shape coefficients g_n and shows that the double set $\{g_{n,TM}^m, g_{n,TE}^m\}$ of beam shape coefficients, with two subscripts (n, m) reduces to a single set $\{g_n\}$ with a single coefficient n. The parameter ε is equal to -1 $(+1)$ when the energy flux flows toward positive zs (negative zs). This parameter is therefore a property of coordinates, not a property of the beam. The parameter K is a real number and describes the state of polarization of the beam, with respect to the coordinate system used. Specifically, if S_x is proportional to $\cos\varphi$, then $K = \pm 1$. It happens that

Eq. (12) with $(\epsilon, K)=(-1,+1)$ is structurally identical with the set of equations obtained for an on-axis Gaussian beam polarized in the x direction at its focal waist, namely [1,20,23]:

$$g^{1}_{n,TM}=g^{-1}_{n,TM}=ig^{1}_{n,TE}=-ig^{-1}_{n,TE}=\frac{g_n}{2} \tag{13}$$

Note however that a beam satisfying Eqs. (11) and (13) is not necessarily a Gaussian beam. Nevertheless, an axisymmetric beam satisfying Eqs. (11) and (12) (or more specifically Eq. (13)) is called an on-axis axisymmetric beam.

4. Transformation of on-axis axisymmetric beams. Expanded forms

We now examine the theorem of transformation of beam shape coefficients under rotation when the beam, in the unrotated system, is an on-axis axisymmetric beam satisfying Eqs. (11) and (12), or more specifically Eq. (13). In this section, we provide the results using expanded forms, i.e. with series.

From Eq. (8), when Eq. (11) applies, we readily obtain:

$$\widetilde{g^{m}_{n,X}}=\mu_{mn}\left[\frac{H^{m}_{-1n}}{\mu_{-1n}}g^{-1}_{n,X}+\frac{H^{m}_{1n}}{\mu_{1n}}g^{1}_{n,X}\right] \tag{14}$$

in which, from Eq. (9):

$$\mu_{-1n}=\frac{1}{n(n+1)} \tag{15}$$

$$\mu_{1n}=-1 \tag{16}$$

Furthermore, from Eq. (10):

$$H^{m}_{-1n}=(-1)^{n+1}\frac{(n-m)!}{(n+1)!}e^{-i\alpha}e^{im\gamma}\sum_{\sigma}(-1)^{\sigma}\binom{n-1}{n-m-\sigma}\binom{n+1}{\sigma}\times\left(\cos\frac{\beta}{2}\right)^{2\sigma+m-1}\left(\sin\frac{\beta}{2}\right)^{2n-2\sigma-m+1} \tag{17}$$

Now, from Eq. (17), we extract the product of binomials:

$$B_{mn}=\binom{n-1}{n-m-\sigma}\binom{n+1}{\sigma}=\frac{(n-1)!(n+1)!}{(n-m-\sigma)!(m+\sigma-1)!\sigma!(n+1-\sigma)!} \tag{18}$$

The range of σ in Eq. (17) is defined by the fact that the arguments of the factorials in Eq. (18) should be non-negative. We may then show that this implies that the range of σ depends on m according to:

$$\begin{cases} m=0\Rightarrow\sigma=1,2,\ldots,n \\ m=j,j=1\ldots n\Rightarrow\sigma=0,1,\ldots,n-j \\ m=-j,j=1\ldots n\Rightarrow\sigma=j+1,j+2,\ldots,n+1 \end{cases} \tag{19}$$

Similarly:

$$H^{m}_{1n}=(-1)^{n+1}\frac{(n-m)!}{(n-1)!}e^{i\alpha}e^{im\gamma}\sum_{\sigma}(-1)^{\sigma}\binom{n+1}{n-m-\sigma}\binom{n-1}{\sigma}\times\left(\cos\frac{\beta}{2}\right)^{2\sigma+m+1}\left(\sin\frac{\beta}{2}\right)^{2n-2\sigma-m-1} \tag{20}$$

with:

$$\begin{cases} m=0\Rightarrow\sigma=0,1,\ldots,n-1 \\ m=j,j=1\ldots n\Rightarrow\sigma=0,1,\ldots,n-j \\ m=-j,j=1\ldots n\Rightarrow\sigma=j-1,j,\ldots,n-1 \end{cases} \tag{21}$$

We now insert Eqs. (15)–(17) and (20) into Eq. (14), considering successively the cases $m=0$, $m=j(j=1\ldots n)$ and $m=-j(j=1\ldots n)$, introducing explicitly the corresponding ranges of σ.

For $m=0$, we note that $\mu_{0n}=1$. Next, we obtain a first summation for σ ranging from 1 to n, and a second summation for σ ranging from 0 to $(n-1)$. Setting $\sigma=\sigma'+1$ in the first summation, both summations are given the same ranges. Once this is done, we observe that the products of binomials in the first and in the second summation are equal. Eventually, we obtain:

$$\widetilde{g^{0}_{n,X}}=(-1)^{n}n!(n+1)!\left[g^{1}_{n,X}e^{i\alpha}+g^{-1}_{n,X}e^{-i\alpha}\right]\times\sum_{\sigma=0}^{n-1}\frac{(-1)^{\sigma}}{(n-\sigma-1)!(n-\sigma)!\sigma!(\sigma+1)!}\left(\cos\frac{\beta}{2}\right)^{2\sigma+1}\left(\sin\frac{\beta}{2}\right)^{2n-2\sigma-1} \tag{22}$$

For $m=j$, $j=1\ldots n$, there are two summations having the same ranges for σ, and there appear two products of binomials which are not equal. The result is then readily found to be:

$$\widetilde{g^{j}_{n,X}}=\mu_{jn}\left\{(-1)^{n}\frac{(n-j)!}{(n-1)!}e^{ij\gamma}\sum_{\sigma=0}^{n-j}(-1)^{\sigma}\left(\cos\frac{\beta}{2}\right)^{2\sigma+j-1}\left(\sin\frac{\beta}{2}\right)^{2n-2\sigma-j-1}\times\left[(-1)\binom{n-1}{n-j-\sigma}\binom{n+1}{\sigma}\left(\sin\frac{\beta}{2}\right)^{2}e^{-i\alpha}g^{-1}_{n,X}+\binom{n+1}{n-j-\sigma}\binom{n-1}{\sigma}\left(\cos\frac{\beta}{2}\right)^{2}e^{i\alpha}g^{1}_{n,X}\right]\right\} \tag{23}$$

For $m=-j, j=1\ldots n$, we obtain fairly similarly (with a manipulation on indices of the first summation):

$$\widetilde{g^{-j}_{n,X}}=\mu_{-jn}\left\{(-1)^{n}\frac{(n+j)!}{(n-1)!}e^{-ij\gamma}\sum_{\sigma=j-1}^{n-1}(-1)^{\sigma}\left(\cos\frac{\beta}{2}\right)^{2\sigma-j+1}\times\left(\sin\frac{\beta}{2}\right)^{2n-2\sigma+j-3}\left[(-1)\binom{n-1}{n+j-\sigma-2}\binom{n+1}{\sigma+2}\times\left(\cos\frac{\beta}{2}\right)^{2}e^{-i\alpha}g^{-1}_{n,X}+\binom{n+1}{n+j-\sigma}\binom{n-1}{\sigma}\left(\sin\frac{\beta}{2}\right)^{2}e^{i\alpha}g^{1}_{n,X}\right]\right\} \tag{24}$$

We may afterward further specify Eqs. (22)–(24) to the case of Eq. (12), and also afterward to the case of Eq. (13). These specifications are so easy that the corresponding results are not worth to be given. As a special case of on-axis axisymmetric beams, we may also consider plane waves obtained by specifying the value of g_n to 1 [1], or more generally to a phase term $\exp(ikz_0)$ which may be viewed as irrelevant, or absorbed in the field strengths. What is however remarkable, is that the results obtained in the present section may be expressed in compact forms.

5. Transformation of on-axis axisymmetric beams. Compact forms

We are going to reach our goal by using, to begin with, preliminary steps.

5.1. Preliminaries 1

In these first preliminaries, we are going to provide specific expressions for the two following quantities:

$$mPi=2m\frac{P^{m}_{n}(\cos\beta)}{\sin\beta} \tag{25}$$

and:

$$Tau = \frac{dP_n^m(\cos\beta)}{d\beta} \tag{26}$$

in which, let us recall, P_n^m denotes the associated Legendre functions of Eqs. (5)–(7). The starting points are recurrence relations given by Stratton ([24], pages 401–402) rewritten below. It is however important to note that the definition of associated Legendre functions given by Stratton differs from ours by a factor $(-1)^m$. The recurrence relations are then written as, following closely Stratton, but with a bit of rearrangement:

$$P_n^{m+1}(cos\,\beta) + (n+m)(n-m+1)P_n^{m-1}(cos\,\beta) = -2m\,cot\,\beta P_n^m(cos\,\beta) \tag{27}$$

$$\frac{2m}{sin\,\beta}P_n^m(cos\,\beta) = -cos\,\beta\left[(n+m)(n-m+1)P_n^{m-1}(\cos\beta) + P_n^{m+1}(\cos\beta)\right] + 2m\sin\beta P_n^m(\cos\beta) \tag{28}$$

$$\frac{dP_n^m(cos\,\beta)}{d\beta} = -\sin\beta\frac{dP_n^m(\cos\beta)}{d\cos\beta} = -\frac{1}{2}\left[(n+m)(n-m+1)P_n^{m-1}(\cos\beta) - P_n^{m+1}(\cos\beta)\right] \tag{29}$$

We now insert Eq. (27) into Eq. (28), yielding:

$$\frac{2m}{\sin\beta}P_n^m(\cos\beta) = 2m\cos\beta\cot\beta P_n^m(\cos\beta) + 2m\sin\beta P_n^m(\cos\beta) \tag{30}$$

Now, from Eq. (27), we have:

$$(n+m)(n-m+1)P_n^{m-1}(\cos\beta) = -2m\cot\beta P_n^m(\cos\beta) - P_n^{m+1}(\cos\beta) \tag{31}$$

that we may insert into the third recurrence equation, namely Eq. (29), to obtain:

$$\frac{dP_n^m(\cos\beta)}{d\beta} = m\cot\beta P_n^m(\cos\beta) + P_n^{m+1}(\cos\beta) \tag{32}$$

Using well known trigonometric relations:

$$\cos\beta = 1 - 2\left(\sin\frac{\beta}{2}\right)^2 \tag{33}$$

$$\tan\frac{\beta}{2} = 2\frac{\left(\sin\frac{\beta}{2}\right)^2}{\sin\beta} \tag{34}$$

Eq. (32) is modified to:

$$\frac{dP_n^m(\cos\beta)}{d\beta} = m\frac{P_n^m(\cos\beta)}{\sin\beta} - \left[m\tan\frac{\beta}{2}P_n^m(\cos\beta) - P_n^{m+1}(\cos\beta)\right] \tag{35}$$

Let us remark that this equation establishes a relationship between the two quantities introduced at the beginning of these preliminaries, in Eqs. (25) and (26).

Now, let us consider *mPi* of Eq. (25) alone. The following trigonometric relation is valid:

$$\frac{2}{\sin\beta} = \frac{\left(\sin\frac{\beta}{2}\right)^2 + \left(\cos\frac{\beta}{2}\right)^2}{\sin\frac{\beta}{2}\cos\frac{\beta}{2}} \tag{36}$$

from which we manipulate *mPi* as follows:

$$\begin{aligned} 2m\frac{P_n^m(\cos\beta)}{\sin\beta} &= mP_n^m(\cos\beta)\frac{\left(\sin\frac{\beta}{2}\right)^2 + \left(\cos\frac{\beta}{2}\right)^2}{\sin\frac{\beta}{2}\cos\frac{\beta}{2}} \\ &= mP_n^m(\cos\beta)\left[\tan\frac{\beta}{2} + \cot\frac{\beta}{2}\right] \\ &= \left[mP_n^m(\cos\beta)\tan\frac{\beta}{2} - P_n^{m+1}(cos\,\beta)\right] \\ &\quad + \left[mP_n^m(\cos\beta)\cot\frac{\beta}{2} + P_n^{m+1}(\cos\beta)\right] \end{aligned} \tag{37}$$

Let us, for convenience, introduce:

$$A = mP_n^m(\cos\beta)\tan\frac{\beta}{2} - P_n^{m+1}(\cos\beta) \tag{38}$$

$$B = mP_n^m(\cos\beta)\cot\frac{\beta}{2} + P_n^{m+1}(\cos\beta) \tag{39}$$

We can then rewrite our results concerning *mPi* and *Tau* as follows:

$$2m\frac{P_n^m(\cos\beta)}{\sin\beta} = A + B \tag{40}$$

$$\frac{dP_n^m(\cos\beta)}{d\beta} = m\frac{P_n^m(\cos\beta)}{\sin\beta} - A = \frac{B-A}{2} \tag{41}$$

5.2. Preliminaries 2

We are now going to complete our evaluations of Eqs. (40) and (41) by expressing the results in terms of σ-summations. Recalling that Mischenko et al used the same convention as ours for associated Legendre functions, we have, from Mischenko et al ([25], Appendix, Eq.B.28):

$$d_{m0}^s(\beta) = \sqrt{\frac{(s-m)!}{(s+m)!}}P_s^m(\cos\beta) \tag{42}$$

in which $d_{m0}^s(\beta)$ is a Wigner *d*-function. Among the four expressions of the Wigner *d*-functions given by Mischenko et al, we choose B2, page 362, [25], which furthermore corresponds to the second version denoted $[d_{sm}^n(\beta)]^2$ in [18], from which we evaluate $d_{m0}^s(\beta)$ and afterward, from Eq. (42), and rearranging, we obtain:

$$P_n^m(\cos\beta) = \sum_\sigma (-1)^{n-\sigma}\frac{(n+m)!n!}{(n-\sigma)!(m+\sigma)!(n-m-\sigma)!\sigma!} \times \left(\sin\frac{\beta}{2}\right)^{2n-m-2\sigma}\left(\cos\frac{\beta}{2}\right)^{2\sigma+m} \tag{43}$$

Next, we have [26]:

$$P_n^m(-\cos\beta) = P_n^m(\cos(\pi-\beta)) = (-1)^{n+m}P_n^m(\cos\beta) \tag{44}$$

Then, from Eq. (43):

$$P_n^m(-\cos\beta) = P_n^m(\cos(\pi-\beta)) = \sum_\sigma (-1)^{n-\sigma}\frac{(n+m)!n!}{(n-\sigma)!(m+\sigma)!(n-m-\sigma)!\sigma!} \times \left(\cos\frac{\beta}{2}\right)^{2n-m-2\sigma}\left(\sin\frac{\beta}{2}\right)^{2\sigma+m} \tag{45}$$

Then, from both Eqs. (44) and (45), we obtain another expression for $P_n^m(\cos\beta)$:

$$P_n^m(\cos\beta) = \sum_\sigma (-1)^{m+\sigma} \frac{(n+m)!n!}{(n-\sigma)!(m+\sigma)!(n-m-\sigma)!\sigma!} \times \left(\cos\frac{\beta}{2}\right)^{2n-m-2\sigma} \left(\sin\frac{\beta}{2}\right)^{2\sigma+m} \tag{46}$$

Now, from Eqs. (43) and (46), we may obtain two different expressions for $P_n^{m+1}(\cos\beta)$, namely:

$$P_n^{m+1}(\cos\beta) = \sum_\sigma (-1)^{n-\sigma} \frac{(n+m+1)!n!}{(n-\sigma)!(m+1+\sigma)!(n-m-1-\sigma)!\sigma!} \times \left(\sin\frac{\beta}{2}\right)^{2n-m-1-2\sigma} \left(\cos\frac{\beta}{2}\right)^{2\sigma+m+1} \tag{47}$$

and:

$$P_n^{m+1}(\cos\beta) = \sum_\sigma (-1)^{m+1+\sigma} \frac{(n+m+1)!n!}{(n-\sigma)!(m+1+\sigma)!(n-m-1-\sigma)!\sigma!} \times \left(\cos\frac{\beta}{2}\right)^{2n-m-1-2\sigma} \left(\sin\frac{\beta}{2}\right)^{2\sigma+m+1} \tag{48}$$

We may now invoke Eqs. (46) and (48) to evaluate the quantity A, leading to, after a few standard manipulations:

$$A = mP_n^m(\cos\beta)\tan\frac{\beta}{2} - P_n^{m+1}(\cos\beta) \tag{49}$$

$$= \sum_\sigma (-1)^{m-\sigma} \frac{(n+m)!(n+1)!}{(n-\sigma-1)!(m+\sigma+1)!(n-m-\sigma)!\sigma!} \times \left(\sin\frac{\beta}{2}\right)^{2\sigma+m+1} \left(\cos\frac{\beta}{2}\right)^{2n-m-1-2\sigma}$$

We may also invoke Eqs. (43) and (47) to evaluate the quantity B, leading to, again after a few standard manipulations:

$$B = mP_n^m(\cos\beta)\cot\frac{\beta}{2} + P_n^{m+1}(\cos\beta) \tag{50}$$

$$= \sum_\sigma (-1)^{n-\sigma} \frac{(n+m)!(n+1)!}{(n-\sigma-1)!(m+\sigma+1)!(n-m-\sigma)!\sigma!} \times \left(\cos\frac{\beta}{2}\right)^{2\sigma+m+1} \left(\sin\frac{\beta}{2}\right)^{2n-m-1-2\sigma}$$

Inserting Eqs. (49) and (50) into Eq. (40), we then have:

$$2m\frac{P_n^m(\cos\beta)}{\sin\beta} = \sum_\sigma \frac{(n+m)!(n+1)!}{(n-\sigma-1)!(m+\sigma+1)!(n-m-\sigma)!\sigma!} \times \left[(-1)^{m-\sigma}\left(\sin\frac{\beta}{2}\right)^{2\sigma+m+1}\left(\cos\frac{\beta}{2}\right)^{2n-m-1-2\sigma} + (-1)^{n-\sigma}\left(\cos\frac{\beta}{2}\right)^{2\sigma+m+1}\left(\sin\frac{\beta}{2}\right)^{2n-m-1-2\sigma}\right] \tag{51}$$

Similarly, from Eq. (41):

$$2\frac{dP_n^m(\cos\beta)}{d\beta} = \sum_\sigma \frac{(n+m)!(n+1)!}{(n-\sigma-1)!(m+\sigma+1)!(n-m-\sigma)!\sigma!} \times \left[(-1)^{n-\sigma}\left(\cos\frac{\beta}{2}\right)^{2\sigma+m+1}\left(\sin\frac{\beta}{2}\right)^{2n-m-1-2\sigma} - (-1)^{m-\sigma}\left(\sin\frac{\beta}{2}\right)^{2\sigma+m+1}\left(\cos\frac{\beta}{2}\right)^{2n-m-1-2\sigma}\right] \tag{52}$$

5.3. Preliminaries 3

We now deal with the quantities H_{-1n}^m and H_{1n}^m given in Eqs. (17) and (20). Concerning H_{1n}^m of Eq. (20), it may be rewritten as:

$$H_{1n}^m = (-1)^{n+1}(n-m)!(n+1)!e^{i\alpha}e^{im\gamma} \times \sum_\sigma (-1)^\sigma \frac{\left(\cos\frac{\beta}{2}\right)^{2\sigma+m+1}\left(\sin\frac{\beta}{2}\right)^{2n-2\sigma-m-1}}{\sigma!(n-m-\sigma)!(n-1-\sigma)!(m+\sigma+1)!} \tag{53}$$

There is however an alternative way soon to be found useful. Indeed, following Mischenko et al [25], let us recall an expression already used in Part I [18], namely:

$$D_{sm}^n(\alpha,\beta,\gamma) = e^{-is\alpha}d_{sm}^n(\beta)e^{-im\gamma} \tag{54}$$

Now, among the four versions of the Wigner d-functions given by Mishchenko et al [25], instead of using the second version denoted $[d_{sm}^n]^2$ in Part I, as we have done above in the second preliminaries, let us use the fourth version denoted $[d_{sm}^n(\beta)]^4$ in Part I, and insert it into Eq. (54). This leads to:

$$D_{sm}^n(\alpha,\beta,\gamma) = (-1)^{s-m}e^{-is\alpha}e^{-im\gamma}\sqrt{(n+s)!(n-s)!(n+m)!(n-m)!} \times \sum_\sigma (-1)^\sigma \frac{\left(\cos\frac{\beta}{2}\right)^{2n-2\sigma-s+m}\left(\sin\frac{\beta}{2}\right)^{2\sigma+s-m}}{\sigma!(n-s-\sigma)!(n+m-\sigma)!(s-m+\sigma)!} \tag{55}$$

The quantity $D_{sm}^n(\alpha,\beta,\gamma)$ is used to express the transformation of vector spherical wave functions (VSWFs), from which in Part I we derived the transformation rule for beam shape coefficients, according to, following Mischenko et al [18,25]:

$$Rg\mathbf{M}_{mn}(kr,\tilde{\theta},\tilde{\varphi}) = \sum_{s=-n}^{n} Rg\mathbf{M}_{sn}(kr,\theta,\varphi)D_{sm}^n(\alpha,\beta,\gamma) \tag{56}$$

in which $Rg\mathbf{M}_{mn}$ are VSWFs which are related to other VSWFs, denoted as $\mathbf{M}_{mn}^{(1)}$, used by Stratton [24] and by ourselves in Part I, according to [18]:

$$\frac{Rg\mathbf{M}_{mn}}{\mathbf{M}_{mn}^{(1)}} = (-1)^m\left[\frac{(2n+1)(n-m)!}{4\pi n(n+1)(n+m)!}\right]^{1/2} \tag{57}$$

We now insert Eq. (55) into Eq. (56), and, by using Eq. (57), we express the result in terms of $\mathbf{M}^{(1)}$ instead of $Rg\mathbf{M}$. We then obtain a relation already provided in [18]:

$$\mathbf{M}_{mn}^{(1)}(kr,\tilde{\theta},\tilde{\varphi}) = \sum_{s=-n}^{n} G_{mn}^s(\alpha,\beta,\gamma)\mathbf{M}_{sn}^{(1)}(kr,\theta,\varphi) \tag{58}$$

in which however the quantity G^s_{mn} is given an alternative form with respect to [18], namely:

$$G^s_{mn}(\alpha,\beta,\gamma) = e^{-im\gamma}e^{-is\alpha}(n+m)!(n-s)! \times \sum_\sigma (-1)^\sigma \frac{\left(\cos\frac{\beta}{2}\right)^{2n-2\sigma-s+m}\left(\sin\frac{\beta}{2}\right)^{2\sigma+s-m}}{\sigma!(n-s-\sigma)!(n+m-\sigma)!(s-m+\sigma)!} \tag{59}$$

But the quantity H^m_{sn} involved in the theorem of transformation is given by [18]:

$$H^m_{sn} = H^m_{sn}(\alpha,\beta,\gamma) = G^m_{sn}(-\gamma,-\beta,-\alpha) \tag{60}$$

Hence, we have, from Eqs. (59), (60):

$$H^m_{sn} = (-1)^{m+s}e^{is\alpha}e^{im\gamma}(n+s)!(n-m)! \times \sum_\sigma (-1)^\sigma \frac{\left(\cos\frac{\beta}{2}\right)^{2n-2\sigma-m+s}\left(\sin\frac{\beta}{2}\right)^{2\sigma+m-s}}{\sigma!(n-m-\sigma)!(n+s-\sigma)!(m-s+\sigma)!} \tag{61}$$

In particular, for $s=-1$:

$$H^m_{-1n} = (-1)^{m-1}e^{-i\alpha}e^{im\gamma}(n-1)!(n-m)! \times \sum_\sigma (-1)^\sigma \frac{\left(\cos\frac{\beta}{2}\right)^{2n-2\sigma-m-1}\left(\sin\frac{\beta}{2}\right)^{2\sigma+m+1}}{\sigma!(n-m-\sigma)!(n-1-\sigma)!(m+1+\sigma)!} \tag{62}$$

The results of Eqs. (53) and (62) may be assembled together as follows:

$$\begin{bmatrix} H^m_{1n} \\ H^m_{-1n} \end{bmatrix} = \sum_\sigma \frac{(n-m)!}{\sigma!(n-m-\sigma)!(n-1-\sigma)!(m+1+\sigma)!} \times \begin{bmatrix} (-1)^{n+1+\sigma}(n+1)!e^{i\alpha}e^{im\gamma}\left(\cos\frac{\beta}{2}\right)^{2\sigma+m+1}\left(\sin\frac{\beta}{2}\right)^{2n-2\sigma-m-1} \\ (-1)^{m-1+\sigma}(n-1)!e^{-i\alpha}e^{im\gamma}\left(\cos\frac{\beta}{2}\right)^{2n-2\sigma-m-1}\left(\sin\frac{\beta}{2}\right)^{2\sigma+m+1} \end{bmatrix} \tag{63}$$

Let us now introduce the following short-hand notations:

$$G = \frac{1}{\sigma!(n-m-\sigma)!(n-1-\sigma)!(m+1+\sigma)!} \tag{64}$$

$$E = (-1)^{n-\sigma}\left(\cos\frac{\beta}{2}\right)^{2\sigma+m+1}\left(\sin\frac{\beta}{2}\right)^{2n-m-1-2\sigma} \tag{65}$$

$$F = (-1)^{m-\sigma}\left(\sin\frac{\beta}{2}\right)^{2\sigma+m+1}\left(\cos\frac{\beta}{2}\right)^{2n-m-1-2\sigma} \tag{66}$$

Eq. (63) can then be rewritten as:

$$\begin{bmatrix} H^m_{1n} \\ H^m_{-1n} \end{bmatrix} = \sum_\sigma \frac{-(n-m)!}{G}\begin{bmatrix} (n+1)!e^{i\alpha}e^{im\gamma}E \\ (n-1)!e^{-i\alpha}e^{im\gamma}F \end{bmatrix} \tag{67}$$

We may also rewrite Eqs. (52) and (51) as:

$$R_1 = \frac{2}{(n+m)!(n+1)!}\frac{dP^m_n(\cos\beta)}{d\beta} = \sum_\sigma \frac{E-F}{G} \tag{68}$$

$$R_2 = \frac{1}{(n+m)!(n+1)!}2m\frac{P^m_n(\cos\beta)}{\sin\beta} = \sum_\sigma \frac{E+F}{G} \tag{69}$$

From Eqs. (68) and (69):

$$\sum_\sigma \frac{E}{G} = \frac{R_1+R_2}{2} \tag{70}$$

$$\sum_\sigma \frac{F}{G} = \frac{R_2-R_1}{2} \tag{71}$$

We now rewrite Eq. (67) as:

$$\begin{bmatrix} H^m_{1n} \\ H^m_{-1n} \end{bmatrix} = \sum_\sigma \begin{bmatrix} -(n-m)!(n+1)!e^{i\alpha}e^{im\gamma}\frac{E}{G} \\ -(n-m)!(n-1)!e^{-i\alpha}e^{im\gamma}\frac{F}{G} \end{bmatrix} \tag{72}$$

We may now insert Eqs. (70), (71) into Eq. (72), and afterward invoke Eqs. (68), (69), to obtain:

$$\begin{bmatrix} H^m_{1n} \\ n(n+1)H^m_{-1n} \end{bmatrix} = (-1)\frac{(n-m)!}{(n+m)!}e^{im\gamma}\begin{bmatrix} e^{i\alpha}\left[m\frac{P^m_n(\cos\beta)}{\sin\beta}+\frac{dP^m_n(\cos\beta)}{d\beta}\right] \\ e^{-i\alpha}\left[m\frac{P^m_n(\cos\beta)}{\sin\beta}-\frac{dP^m_n(\cos\beta)}{d\beta}\right] \end{bmatrix} \tag{73}$$

that is to say:

$$\begin{bmatrix} H^m_{1n} \\ n(n+1)H^m_{-1n} \end{bmatrix} = (-1)\frac{(n-m)!}{(n+m)!}e^{im\gamma}\begin{bmatrix} e^{i\alpha}[m\pi^m_n(\cos\beta)+\tau^m_n(\cos\beta)] \\ e^{-i\alpha}[m\pi^m_n(\cos\beta)-\tau^m_n(\cos\beta] \end{bmatrix} \tag{74}$$

in which we introduced the generalized Legendre functions reading as:

$$\pi^m_n(\cos\beta) = \frac{P^m_n(\cos\beta)}{\sin\beta} \tag{75}$$

$$\tau^m_n(\cos\beta) = \frac{dP^m_n(\cos\beta)}{d\beta} \tag{76}$$

5.4. A complementary approach to compact forms

We are now going to use a complementary approach to reach the result of Eqs. (75), (76). The advantage of this second approach is that it is more concise than the previous one but with the price to pay that it is less transparent.

Recalling Eq. (21) in Part one, we take the inverse of Eq. (56), reading as:

$$Rg\mathbf{M}_{mn}(kr,\theta,\varphi) = \sum_{s=-n}^{n} Rg\mathbf{M}_{sn}\left(kr,\tilde{\theta},\tilde{\varphi}\right)D^n_{sm}(-\gamma,-\beta,-\alpha) \tag{77}$$

We now use Eq. (54), from which we derive:

$$D^n_{sm}(-\gamma,-\beta,-\alpha) = e^{is\gamma}d^n_{sm}(-\beta)e^{im\alpha} \tag{78}$$

and Eq. (57), to obtain:

$$\mathbf{M}^{(1)}_{mn}(kr,\theta,\varphi) = \sum_{s=-n}^{n}(-1)^{m+s}\left[\frac{(n-s)!}{(n+s)!}\frac{(n+m)!}{(n-m)!}\right]^{1/2} \times e^{is\gamma}e^{im\alpha}d^n_{sm}(-\beta)\mathbf{M}^{(1)}_{sn}\left(kr,\tilde{\theta},\tilde{\varphi}\right) \tag{79}$$

We now use a symmetry relation given by Mischenko et al [25], Appendix B, Eq.B.6, namely:

$$d^n_{sm}(-\beta) = (-1)^{s-m}d^n_{sm}(\beta) \tag{80}$$

rearrange, and obtain:

$$\mathbf{M}_{mn}^{(1)} = \sum_{s=-n}^{n} \left[\frac{(n-s)!}{(n+s)!}\frac{(n+m)!}{(n-m)!}\right]^{1/2} e^{is\gamma} e^{im\alpha} d_{sm}^{n}(\beta)\widetilde{\mathbf{M}_{sn}^{(1)}} \tag{81}$$

As in [18], we set:

$$\mathbf{M}_{mn}^{(1)} = \sum_{s=-n}^{n} H_{mn}^{s}\widetilde{\mathbf{M}_{sn}^{(1)}} \tag{82}$$

Therefore, from Eqs. (81) and (82), we have:

$$H_{mn}^{s} = \left[\frac{(n-s)!}{(n+s)!}\frac{(n+m)!}{(n-m)!}\right]^{1/2} e^{is\gamma} e^{im\alpha} d_{sm}^{n}(\beta) \tag{83}$$

that is to say:

$$H_{sn}^{m} = \left[\frac{(n-m)!}{(n+m)!}\frac{(n+s)!}{(n-s)!}\right]^{1/2} e^{im\gamma} e^{is\alpha} d_{ms}^{n}(\beta) \tag{84}$$

In particular, for $s=1$:

$$H_{1n}^{m} = \left[\frac{(n-m)!}{(n+m)!}\frac{(n+1)!}{(n-1)!}\right]^{1/2} e^{im\gamma} e^{i\alpha} d_{m1}^{n}(\beta) \tag{85}$$

We now invoke Eq. B.25, Appendix B, from Mischenko et al [25], rewritten under the form of two equations reading as:

$$\frac{d}{d\beta}d_{ms}^{n}(\beta) + \frac{m}{\sin\beta}d_{ms}^{n}(\beta) = \frac{s\cos\beta}{\sin\beta}d_{ms}^{n}(\beta) - \sqrt{(n-s)(n+s+1)}\,d_{ms+1}^{n}(\beta) \tag{86}$$

$$\frac{d}{d\beta}d_{ms}^{n}(\beta) - \frac{m}{\sin\beta}d_{ms}^{n}(\beta) = \frac{-s\cos\beta}{\sin\beta}d_{ms}^{n}(\beta) + \sqrt{(n+s)(n-s+1)}\,d_{ms-1}^{n}(\beta) \tag{87}$$

We now consider Eq. (86) for $s=0$, reading as:

$$\frac{d}{d\beta}d_{m0}^{n}(\beta) + \frac{m}{\sin\beta}d_{m0}^{n}(\beta) = -\sqrt{n(n+1)}\,d_{m1}^{n}(\beta) \tag{88}$$

from which we extract:

$$d_{m1}^{n}(\beta) = -\frac{1}{\sqrt{n(n+1)}}\left[\frac{d}{d\beta}d_{m0}^{n}(\beta) + \frac{m}{\sin\beta}d_{m0}^{n}(\beta)\right] \tag{89}$$

We insert this equation into Eq. (85), rearrange, and obtain:

$$H_{1n}^{m} = (-1)\left[\frac{(n-m)!}{(n+m)!}\right]^{1/2} e^{im\gamma} e^{i\alpha}\left[\frac{d}{d\beta}d_{m0}^{n}(\beta) + \frac{m}{\sin\beta}d_{m0}^{n}(\beta)\right] \tag{90}$$

But we have [25], Appendix B, Eq.B.28:

$$d_{m0}^{n}(\beta) = \sqrt{\frac{(n-m)!}{(n+m)!}}P_{n}^{m}(\cos\beta) \tag{91}$$

Inserting Eq. (91) into Eq. (90), and invoking the definitions of π_n^m and τ_n^m of Eqs. (75) and (76), we obtain:

$$H_{1n}^{m} = (-1)\frac{(n-m)!}{(n+m)!}e^{im\gamma}e^{i\alpha}\left[m\pi_{n}^{m}(\cos\beta) + \tau_{n}^{m}(\cos\beta)\right] \tag{92}$$

which identifies with the result involved in Eqs. (73) and (74).

We now specify Eq. (84) for $s=-1$ and obtain:

$$H_{-1n}^{m} = \left[\frac{(n-m)!(n-1)!}{(n+m)!(n+1)!}\right]^{1/2} e^{im\gamma} e^{-i\alpha} d_{m(-1)}^{n}(\beta) \tag{93}$$

Next, we specify Eq. (87) for $s=0$, from which we deduce:

$$d_{m(-1)}^{n}(\beta) = \frac{1}{\sqrt{n(n+1)}}\left[\frac{d}{d\beta}d_{m0}^{n}(\beta) - \frac{m}{\sin\beta}d_{m0}^{n}(\beta)\right] \tag{94}$$

Using once more Eq. (91), and the definitions of π_n^m and τ_n^m, this equation becomes:

$$d_{m(-1)}^{n}(\beta) = \frac{1}{\sqrt{n(n+1)}}\sqrt{\frac{(n-m)!}{(n+m)!}}\left[\tau_{n}^{m}(\cos\beta) - m\pi_{n}^{m}(\cos\beta)\right] \tag{95}$$

We now insert Eq. (95) into Eq. (93) and obtain:

$$H_{-1n}^{m} = \frac{1}{n(n+1)}\frac{(n-m)!}{(n+m)!}e^{im\gamma}e^{-i\alpha}\left[\tau_{n}^{m}(\cos\beta) - m\pi_{n}^{m}(\cos\beta)\right] \tag{96}$$

agreeing with Eqs. (73) and (74).

5.5. Beam shape coefficients

From Eqs. (14), (9) and (74), we may now express the beam shape coefficients in the rotated system as follows:

$$\widetilde{g_{n,X}^{m}} = (-1)^{m+1}(-1)^{\frac{m-|m|}{2}}\frac{(n-|m|)!}{(n+m)!} \times e^{im\gamma}\left\{m\pi_{n}^{m}(\cos\beta)\left[e^{-i\alpha}g_{n,X}^{-1} - e^{i\alpha}g_{n,X}^{1}\right] - \tau_{n}^{m}(\cos\beta)\left[e^{-i\alpha}g_{n,X}^{-1} + e^{i\alpha}g_{n,X}^{1}\right]\right\} \tag{97}$$

This equation may easily be specified in the case of Eq. (12). Let us better specify it for the more common form of Eq. (13). We then obtain the beam shape coefficients in the rotated system in terms of the special beam shape coefficients in the unrotated system, according to:

$$\widetilde{g_{n,TM}^{m}} = (-1)^{m}(-1)^{\frac{m-|m|}{2}}\frac{(n-|m|)!}{(n+m)!}e^{im\gamma}g_{n}\left[im\sin\alpha\pi_{n}^{m}(\cos\beta) + \cos\alpha\tau_{n}^{m}(\cos\beta)\right] \tag{98}$$

$$\widetilde{g_{n,TE}^{m}} = (-1)^{m+1}(-1)^{\frac{m-|m|}{2}}\frac{(n-|m|)!}{(n+m)!}e^{im\gamma}g_{n}\left[im\cos\alpha\pi_{n}^{m}(\cos\beta) - \sin\alpha\tau_{n}^{m}(\cos\beta)\right] \tag{99}$$

which can be further specified for the plane wave case by setting $g_n=1$, or more generally by setting it to a constant phase term of the form $\exp(ikz_0)$.

6. On-axis axisymmetric beams. Case without any rotation

Anticipating on Part III [27] which will be devoted to special values of Euler angles, we now consider the case of on-axis axisymmetric beams satisfying Eq. (97) in the case when there is no rotation, that is to say for the trivial case $\alpha=\beta=\gamma=0$. Eq. (97) then simplifies to:

$$\widetilde{g_{n,X}^{m}} = (-1)^{m+1}(-1)^{\frac{m-|m|}{2}}\frac{(n-|m|)!}{(n+m)!} \times\left\{\left[m\pi_{n}^{m}(\beta=0) - \tau_{n}^{m}(\beta=0)\right]g_{n,X}^{-1} - \left[m\pi_{n}^{m}(\beta=0) + \tau_{n}^{m}(\beta=0)\right]g_{n,X}^{1}\right\} \tag{100}$$

Let us recall Eq. (7). Then, from the definitions of π_n^m and τ_n^m, we derive similar equations reading as:

$$\begin{pmatrix} m\pi_n^m(\cos\beta) \\ \tau_n^m(\cos\beta) \end{pmatrix} = (-1)^{\frac{m-|m|}{2}} \frac{(n-|m|)!}{(n-m)!} \begin{pmatrix} m\pi_n^{|m|}(\cos\beta) \\ \tau_n^{|m|}(\cos\beta) \end{pmatrix} \tag{101}$$

We may then rewrite Eq. (100) under the following form:

$$\widetilde{g_{n,X}^m} = (-1)^{m+1} \frac{[(n-|m|)!]^2}{(n+m)!(n-m)!} \times \left\{ \left[m\pi_n^{|m|}(\beta=0) - \tau_n^{|m|}(\beta=0) \right] g_{n,X}^{-1} - \left[m\pi_n^{|m|}(\beta=0) + \tau_n^{|m|}(\beta=0) \right] g_{n,X}^{1} \right\} \tag{102}$$

But, for $m>0$ and $\beta\to 0$ (or π), we have, according to Doicu et al [28], p 257:

$$m\pi_n^m(\cos\beta) \to (-1)^m \frac{1}{2} \frac{(n+m)!}{(n-m)!(m-1)!} \left(\frac{\beta}{2}\right)^{m-1} \tag{103}$$

$$\tau_n^m(\cos\beta) \to (-1)^m \frac{1}{2} \frac{(n+m)!}{(n-m)!(m-1)!} \left(\frac{\beta}{2}\right)^{m-1} \tag{104}$$

in which we incorporate a prefactor $(-1)^m$, absent from Doicu et al [28], due to a different definition of associated Legendre functions. These relations may be rewritten as:

$$\pi_n^{|m|}(\beta\to 0) = \frac{1}{2} \frac{(-1)^{|m|}}{|m|} \frac{(n+|m|)!}{(n-|m|)!(|m|-1)!} \left(\frac{\beta}{2}\right)^{|m|-1} \tag{105}$$

$$\tau_n^{|m|}(\beta\to 0) = \frac{1}{2} (-1)^{|m|} \frac{(n+|m|)!}{(n-|m|)!(|m|-1)!} \left(\frac{\beta}{2}\right)^{|m|-1} \tag{106}$$

We insert Eqs. (105) and (106) into Eq. (102), yielding:

$$\widetilde{g_{n,X}^m} = \frac{1}{2} \left(\frac{\beta}{2}\right)^{|m|-1} (-1)^{m+1} (-1)^{|m|} \frac{(n-|m|)!(n+|m|)!}{(n-m)!(n+m)!(|m|-1)!} \times \left[\left(\frac{m}{|m|} - 1 \right) g_{n,X}^{-1} - \left(\frac{m}{|m|} + 1 \right) g_{n,X}^{1} \right] \tag{107}$$

We now consider Eq. (107) for $m>0$, becoming:

$$\widetilde{g_{n,X}^m} = \left(\frac{\beta}{2}\right)^{m-1} \frac{1}{(m-1)!} g_{n,X}^{1} \tag{108}$$

from which we deduce:

$$\widetilde{g_{n,X}^m}(m>0, m\neq 1, \beta=0) = 0 \tag{109}$$

$$\widetilde{g_{n,X}^1} = g_{n,X}^1 \tag{110}$$

Similarly, for $m<0$, Eq. (107) leads to:

$$\widetilde{g_{n,X}^m} = \left(\frac{\beta}{2}\right)^{-m-1} \frac{1}{(-m-1)!} g_{n,X}^{-1} \tag{111}$$

from which we deduce:

$$\widetilde{g_{n,X}^m}(m<0, m\neq -1, \beta=0) = 0 \tag{112}$$

$$\widetilde{g_{n,X}^{-1}} = g_{n,X}^{-1} \tag{113}$$

For $m=0$, Eq. (100) leads to:

$$\widetilde{g_{n,X}^0} = \tau_n^0(\beta=0) \left[g_{n,X}^{-1} + g_{n,X}^{1} \right] \tag{114}$$

Now, we have:

$$\tau_n^0(\cos\beta) = \frac{dP_n^0(\cos\beta)}{d\beta} = \frac{dP_n(\cos\beta)}{d\beta} = -\sin\beta \frac{dP_n(\cos\beta)}{d\cos\beta} \tag{115}$$

But $P_n(\cos\beta)$ is a polynomial of the argument $\cos\beta$. Therefore, its derivative with respect to the argument remains finite, and we then obtain:

$$\tau_n^0(\beta=0) = 0 \tag{116}$$

Hence, Eq. (114) becomes:

$$\widetilde{g_{n,X}^0} = 0 \tag{117}$$

Then, in this section, we have obtained the following result: if there is no rotation, the beam shape coefficients of on-axis axisymmetric beams in the rotated system are equal to those of the unrotated system. This is actually a rather trivial result. It does not supplement us with any new knowledge but rather provides a checking of our computations.

7. Discussion and conclusion

We now discuss the practical significance of the results obtained in this paper, a discussion which will also serve as a conclusion. To this purpose, we dress the original problem (transformation of beam shape coefficients of on-axis axisymmetric beams) with two extra-elements.

The first element concerns the definition of the unrotated system. Of course, any system may be taken as being the unrotated system and, in particular, we are free to invert the role of the unrotated and of the rotated systems, pretending that the rotated system is now to be taken as being the unrotated one and vice versa. However, to better approach the history of GLMTs and some traditional points of view taken from this history, the unrotated system will be given a specific definition as follows.

Following the description of coordinate systems given in the Fig. 1 of Gouesbet et al. [1], we consider a Cartesian system of coordinates, with origin O_G and coordinates (u, v, w) attached to the beam under discussion, now called the illuminating beam. We take the axis O_Gw as being the main axis of propagation of the beam (particularly easy to define in the present case of axisymmetric beams). Next, we decide to describe the scattering phenomena by using another Cartesian coordinate system, with origin O_P and coordinates (x,y,z). We furthermore make the axes O_Px, O_Py, and O_Pz parallel to the axes O_Gu, O_Gv, and O_Gw respectively. Then, we define the coordinates (x, y, z) as being the Cartesian coordinates of the unrotated system.

Up to now, we have only considered coordinate systems and nothing has been said concerning the nature of the scattering particles. The second element to dress the problem is concerned with the introduction of particles. These particles are such that the scattering problem they generate can be solved by using separation of variables in spherical coordinates. They are originally attached to the frame O_Pxyz which may be called the (unrotated) particle frame. When rotating this frame, the particle, which is attached to the frame, is assumed to follow the rotation of the frame.

Let us begin by assuming that the scatterer is a homogeneous sphere defined by its diameter d and its complex refractive index m. In the case of axisymmetric beams (not necessarily on-axis), we may readily define two different situations. In the first case, the axis O_Gw of

the illuminating beam coincides with the axis O_Pz of the particle frame and, therefore, the center O_P of the particle is located on the axis of the beam. This is called the on-axis case. Otherwise, we are facing the off-axis case. That these two cases are deeply different may be appreciated by the following fact. In the on-axis case, we know that the double set $\{g^m_{n,TM}, g^m_{n,TE}\}$ of beam shape coefficients reduces to a single set $\{g_n\}$, $n=1\ldots\infty$, of special beam shape coefficients, as the consequence of Eqs. (11) and 12, or 13. Accordingly, the on-axis version of the GLMT becomes much simpler than the off-axis version. The rotation from O_Pxyz to $O_P\tilde{x}\tilde{y}\tilde{z}$ does not modify the scattering phenomena since the rotation of the attached sphere, which possesses a high degree of symmetry, does not modify the scattering problem. But it may modify deeply the computations involved to describe the phenomena. For instance, in the unrotated system, we only need to use special beam shape coefficients g_n in the on-axis case. After the rotation, the center O_P of the particle is still located on the axis of the beam, but the axis O_Gw of the illuminating beam does not coincide any more with the axis, now denoted as $O_P\tilde{z}$, of the particle frame and, as we have established in this paper, the description of the illuminating beam must now been made again in terms of a double set of beam shape coefficients now denoted as $\widetilde{g^m_{n,X}}, X = TM$ or TE. In other words, the rotation of the particle frame induces a more complicated situation without any benefit since the eventual physical results have to remain unchanged. Note however that no complication is generated by the rotation of the particle frame in the case of off-axis illumination since we need to use g^m_n-kinds of coefficients in both the rotated and unrotated systems. A similar discussion could apply to the case of multilayered spheres [3].

However, let us now consider particles which, in general, do not possess the property of invariance through rotation, although the method of separation of variables may still be applied to them in spherical coordinates, e.g. [4,5]. For being specific, let us more particularly consider the case of a sphere, with center located at O_P, with an eccentrically located spherical sphere, or inclusion [5]. Let us assume the simplest situation available, that is to say the case when the center of the inclusion is located on the axis O_Pz of the unrotated system. This may be viewed as a case of parallel illumination since the axis of the beam O_Gw is parallel to the axis of the unrotated system. Now, in contrast, in the rotated system, we are facing a quite different situation that we may call a situation of oblique illumination. It is under this name (oblique illumination) that the topic has been initiated by Han et al [16,17]. The problem may then be expressed as the one of the evaluation of beam shape coefficients in oblique illumination in terms of beam shape coefficients in parallel illumination. The present paper elaborated on a solution to this problem, discussing it, in the case of on-axis axisymmetric beams. Accordingly, the main formal results of the paper are Eqs. (98), (99).

References

[1] G. Gouesbet, B. Maheu, G. Gréhan, Journal of the Optical Society of America A 5 (1988) 1427.
[2] B. Maheu, G. Gouesbet, G. Gréhan, Journal of Optics, Paris 19 (2) (1988) 59.
[3] F. Onofri, G. Gréhan, G. Gouesbet, Applied Optics 34 (30) (1995) 7113.
[4] G. Gouesbet, G. Gréhan, Journal of Optics A: Pure and Applied Optics 1 (1999) 706.
[5] G. Gouesbet, G. Gréhan, Journal of Modern Optics 47 (5) (2000) 821.
[6] G. Gouesbet, G. Gréhan, Atomization and sprays 10 (3–5) (2000) 277.
[7] J.A. Lock, G. Gouesbet, Journal of Quantitative Spectroscopy and Radiative Transfer 110 (2009) 800.
[8] G. Gouesbet, Journal of Quantitative Spectroscopy and Radiative Transfer 110 (2009) 1223.
[9] G. Gouesbet, C. Letellier, K.F. Ren, G. Gréhan, Applied Optics 35 (9) (1996) 1537.
[10] G. Gouesbet, G. Gréhan, B. Maheu, Journal of Optics, Paris 19 (1) (1988) 35.
[11] G. Gouesbet, G. Gréhan, B. Maheu, Applied Optics 27 (23) (1988) 4874.
[12] G. Gouesbet, Journal of the Optical Society of America A 16 (7) (1999) 1641.
[13] K.F. Ren, G. Gouesbet, G. Gréhan, Applied Optics 37 (19) (1998) 4218.
[14] A. Doicu, T. Wriedt, Applied Optics 36 (13) (1997) 2971.
[15] H.Y. Zhang, Y.P. Han, Journal of the Optical Society of America B 11 (2008) 255.
[16] Y.P. Han, H. Zhang, G. Han, Optics Express 15 (2) (2007) 735.
[17] Y.P. Han, Y. Zhang, H. Zhang, G. Han, Journal of Quantitative Spectroscopy and Radiative transfer 110 (14–16) (2009) 1375.
[18] G. Gouesbet, J.J. Wang, Y.P. Han, Transformations of spherical beam shape coefficients in generalized Lorenz–Mie theories through rotations of coordinate systems. I. General formulation, Optics Communications 283 (17) (2010) 3218.
[19] A.R. Edmonds, Angular Momentum in Quantum Mechanics, Princeton University Press, 1957.
[20] G. Gouesbet, G. Gréhan, Journal of Optics, Paris 13 (2) (1982) 97.
[21] G. Gouesbet, Optics Communications 283 (2010) 517.
[22] G. Gouesbet, Applied Optics 35 (9) (1996) 1543.
[23] G. Gouesbet, G. Gréhan, B. Maheu, Journal of Optics, Paris 16 (1985) 83.
[24] J.A. Stratton, Electromagnetic Theory, McGraw-Hill Book Company, New-York, London, 1941.
[25] M.I. Mishchenko, L.D. Travis, A.A. Lacis, Scattering, Absorption, and Emission of Light by Small Particles, Cambridge University Press, 2002.
[26] L. Robin, Fonctions sphériques de Legendre et fonctions sphéroïdales, Vols 1–3, Gauthiers-Villars, 1957.
[27] G. Gouesbet, J.J. Wang, Y.P. Han, Transformations of spherical beam shape coefficients in generalized Lorenz–Mie theories through rotations of coordinate systems. III. Special Euler angles, Optics Communications 283 (17) (2010) 3235.
[28] A. Doicu, T. Wriedt, Y.A. Eremin, Light scattering by systems of particles, null-field method with discrete sources—Theory and programs, Springer, 2006.

Optics Communications 283 (2010) 3235–3243

Contents lists available at ScienceDirect

Optics Communications

journal homepage: www.elsevier.com/locate/optcom

Transformations of spherical beam shape coefficients in generalized Lorenz–Mie theories through rotations of coordinate systems III. Special values of Euler angles

G. Gouesbet [a,b,c,*], J.J. Wang [a,b,c,d], Y.P. Han [d]

[a] Laboratoire d'Electromagnétisme des Systèmes Particulaires (LESP), France
[b] Unité Mixte de Recherche (UMR) 6614, Centre National de la Recherche Scientifique (CNRS), COmplexe de Recherche Interprofessionnel en Aérothermochimie (CORIA), Université de Rouen, France
[c] Institut National des Sciences Appliquées (INSA) de Rouen BP12, avenue de l'université, technopôle du Madrillet, 76801, Saint-Etienne-du Rouvray, France
[d] School of Science, Xidian University, Xi'an, China

ARTICLE INFO

Article history:
Received 8 March 2010
Received in revised form 8 April 2010
Accepted 21 April 2010

ABSTRACT

This paper is Part III of a series of papers devoted to the transformation of beam shape coefficients under rotations of coordinate systems. These coefficients are required for the expanded description of laser beams, particularly for use in the framework of generalized Lorenz–Mie theories. In Part I of this series of papers, we presented a general formulation for the transformation of spherical beam shape coefficients through rotations of coordinate systems, under the form of a theorem of transformation. Part II was devoted to the special case of axisymmetric beams, more particularly of on-axis axisymmetric beams. With this Part III, we investigate simplifications of the general formulation for special values of the Euler angles defining the rotation. As in Part II, one of the aims is to uncover compact forms of formulae useful to speed-up computations.

1. Introduction

For the sake of convenience, we recall the specific problem which is studied in this series of papers. Let us consider a Cartesian system of coordinates, denoted as $\mathbf{x}=(x,y,z)$, associated with usual spherical coordinates (r,θ,φ), called the unrotated system, and let $g^m_{n,TM}$, $g^m_{n,TE}$ be the beam shape coefficients for the description of the illuminating beam in this unrotated system. Let us consider a second system of coordinates, called the rotated system, deduced from the unrotated system by a rotation defined by Euler angles (α,β,γ), as defined in Part I [1]. Quantities in the rotated system are denoted by using tilde-decorations. Therefore the Cartesian coordinates of the rotated system are denoted as $\tilde{\mathrm{x}}=(\tilde{x},\tilde{y},\tilde{z})$ and they are associated with spherical coordinates $(\tilde{r}=r,\tilde{\theta},\tilde{\varphi})$. The beam shape coefficients in the rotated system are denoted as $\widetilde{g^m_{n,TM}}$, $\widetilde{g^m_{n,TE}}$. The problem is to express the beam shape coefficients in the rotated system in terms of beam shape coefficients in the unrotated system. A general solution to this problem has been found in Part I of the present series of papers [1]. It takes the form of a theorem of transformation from which all subsequent developments can be derived. In particular, Part II discussed the special case of axisymmetric beams, particularly of on-axis axisymmetric beams [2], which are rather common and of widespread use. The most emblematic example is a Gaussian beam interacting head-on with a spherical particle, as can be described in some Generalized Lorenz–Mies, e.g. [3–5]. In the present Part III, we deal with other special cases of Part I, namely when the Euler angles are given special values, with the aim to provide results in compact forms. Such compact forms should be useful to speed-up numerical computations in some privileged configurations.

The paper is organized as follows. Section 2 recalls a basic background from previous parts [1,2], namely the theorem of transformation, how to dress the problem (in particular when considering a host sphere containing an inclusion), and the definition of on-axis axisymmetric beams. Section 3 deals with the trivial case of no rotation, when all Euler angles are zero, and constitute a check of the formulation. Section 4 deals with the case when the inclusion introduced in the dressed problem is upside-down located. Section 5 deals with the case when the center of the inclusion is located in the "horizontal plane." Section 6 deals with the case when the center of the inclusion is located in the Cartesian vertical planes. Section 7 discusses the case of a rotation about the vertical axis, and its relationship with the case when there is no rotation at all. Section 8 is a conclusion.

2. Basic background

2.1. The theorem of transformation

The theorem of transformation, established in Part I [1], reads as follows. Let $\mathbf{x}$ and $\tilde{\mathrm{x}}$ be two systems of coordinates, named the

* Corresponding author.
E-mail address: Gouesbet@coria.fr (G. Gouesbet).

0030-4018/$ – see front matter © 2010 Elsevier B.V. All rights reserved.
doi:10.1016/j.optcom.2010.04.051

unrotated and the rotated systems, respectively. Let $g^m_{n,X}$ and $\widetilde{g^m_{n,X}}$, with $X=TM$ or TE, be the spherical beam shape coefficients of an arbitrary shaped beam in the unrotated and in the rotated systems, respectively. Then:

$$\widetilde{g^m_{n,X}} = \mu_{mn} \sum_{s=-n}^{n} \frac{H^m_{sn}}{\mu_{sn}} g^s_{n,X} \tag{1}$$

in which:

$$\mu_{mn} = (-1)^m (-1)^{\frac{m-|m|}{2}} \frac{(n-|m|)!}{(n-m)!} \tag{2}$$

$$H^m_{sn} = (-1)^{n+s} \frac{(n-m)!}{(n-s)!} e^{is\alpha} e^{im\gamma} S_\sigma(\beta) \tag{3}$$

$$S_\sigma(\beta) = \sum_\sigma (-1)^\sigma \binom{n+s}{n-m-\sigma} \binom{n-s}{\sigma} \left(\cos\frac{\beta}{2}\right)^{2\sigma+m+s} \left(\sin\frac{\beta}{2}\right)^{2n-2\sigma-m-s} \tag{4}$$

in which (α, β, γ) are Euler angles bringing the unrotated system to the rotated system.

2.2. Dressing the problem

The matter discussed in this paper, more generally in the present series of papers, just requires us to introduce two coordinate systems, an unrotated system and a rotated one. To help our mind producing concrete mental pictures, and to give us the opportunity in the sequel of this paper to use an extended language, we shall however dress the problem under discussion with two extra-elements, already extensively introduced in Part I [1], and briefly recalled in this section.

The first element concerns the definition of the unrotated system. As in the figure 1 of [3], we consider a Cartesian system of coordinates, with origin O_G and coordinates (u, v, w). attached to a beam called the illuminating beam. We take the axis O_Gw as being the main axis of propagation of the beam and we decide to describe the scattering phenomena by using another Cartesian coordinate, with origin O_P and coordinates (x, y, z). We furthermore make the axes O_Px, O_Py, O_Pz parallel to the axes O_Gu, O_Gv, O_Gw respectively. Then, we define the coordinates (x, y, z) as being the Cartesian coordinates of the unrotated system.

The second element to dress the problem is concerned with the introduction of particles. In this paper, we shall specifically consider that the particle is a sphere with an eccentrically located spherical inclusion [6]. It is originally attached to the frame O_Pxyz which may be called the (unrotated) particle frame. When rotating this frame, the particle, which is attached to the frame, is assumed to follow the rotation of the frame. We also assume that, in the unrotated system, the center of the inclusion is located on the axis Oz, and the center of the host sphere is located at the origin O_P of coordinates of the particle frame. The specification of Euler angles is then equivalent to the specification of the location of the center of the inclusion.

2.3. On-axis axisymmetric beams

We consider beams for which the beam shape coefficients satisfy the following relations [2,7]:

$$g^m_{n,X} = 0, |m| \neq 1 \tag{5}$$

$$g^1_{n,TM} = \frac{1}{K} g^{-1}_{n,TM} = -i\varepsilon g^1_{n,TE} = \frac{i\varepsilon}{K} g^{-1}_{n,TE} = \frac{g_n}{2} \tag{6}$$

Eq. (6) defines a set $\{g_n\}$ of special beam shape coefficients g_n and shows that the double set $\{g^m_{n,TM}, g^m_{n,TE}\}$ of beam shape coefficients, with two subscripts (n, m) reduces to a single set $\{g_n\}$ with a single coefficient n. The parameter ε is equal to -1 $(+1)$ when the energy flux flows toward positive zs (negative zs). The parameter K is a real number which describes the state of polarization of the beam. It happens that Eq. (6) with $(\epsilon,K)=(-1, +1)$ is structurally identical with the set of equations obtained for an on-axis Gaussian beam polarized in the x direction at its focal waist, namely [3,8,9]:

$$g^1_{n,TM} = g^{-1}_{n,TM} = ig^1_{n,TE} = -ig^{-1}_{n,TE} = \frac{g_n}{2} \tag{7}$$

A beam satisfying Eqs. (5) and (6) (or its special case of Eq. (7)) is called an on-axis axisymmetric beam.

3. No rotation

The interest of this first special case, in which the Euler angles take the special values: $\alpha=\beta=\gamma=0$, is to provide a checking. Indeed, we should not expect any new physical result from this section because the rotated beam shape coefficients, in the case of no rotation, must be equal to the original beam shape coefficients. This will be indeed the case.

We start from Eqs. (1)–(4), expressing the theorem of transformation, and we are looking for $\widetilde{g^m_{n,X}}(\alpha=\beta=\gamma=0)$. To this aim, let us examine the quantity $S_\sigma(0)$. This is different from 0 and will then contribute to Eq. (3) only when the exponent of $\sin(\beta/2)$ is 0, that is to say when:

$$\sigma = n - \frac{m+s}{2} \tag{8}$$

Hence:

$$S_\sigma(0) = \left[(-1)^\sigma \binom{n+s}{n-m-\sigma} \binom{n-s}{\sigma}\right]_{\sigma=n-\frac{m+s}{2}} \tag{9}$$

From Eqs. (4), (3) and (9), we then have:

$$H^m_{sn}(\alpha=\beta=\gamma=0) = (-1)^{n+s} \frac{(n-m)!}{(n-s)!} \left[(-1)^\sigma \binom{n+s}{n-m-\sigma} \binom{n-s}{\sigma}\right]_{\sigma=n-\frac{m+s}{2}} \tag{10}$$

We then see, from the subscript in the bracketed term, that H^m_{sn} $(\alpha=\beta=\gamma=0)$ is zero when m and s do not possess the same parity. We then have to examine two cases (i) m and s even and (ii) m and s odd.

In the first case, we set $m=2M$ and $s=2S$, and convert Eq. (10) to:

$$H^{2M}_{2S,n}(\alpha=\beta=\gamma=0) = (-1)^n \frac{(n-2M)!}{(n-2S)!} (-1)^{n-M-S} \binom{n+2S}{S-M} \binom{n-2S}{n-M-S} \tag{11}$$

This equation may be rewritten as:

$$H^{2M}_{2S,n}(\alpha=\beta=\gamma=0) = (-1)^{M+S} \frac{(n-2M)!}{(n-2S)!} \frac{(n+2S)!(n-2S)!}{(S-M)!(n+M+S)!(n-M-S)!(M-S)!} \tag{12}$$

From the factorials $(S-M)!$ and $(M-S)!$, we see that we need $M=S$, and the single contribution, after simplification, is found to be:

$$H^{2M}_{2M,n} = 1 \tag{13}$$

which, invoking Eq. (1), implies:

$$\widetilde{g^{2M}_{n,X}} = g^{2M}_{n,X} \tag{14}$$

as expected. Similarly, in the second case, we set $m=2M+1$, observe that we must have $s=2S+1$, and obtain:

$$\widetilde{g_{n,X}^{2M+1}} = g_{n,X}^{2M+1} \tag{15}$$

again as expected.

4. Inclusion upside-down

4.1. Arbitrary shaped beams

In this section, we let the Euler angle α unspecified and specify the two other Euler angles as follows:

$$\beta = \pi; \gamma = 0 \tag{16}$$

This is a situation in which the center of the inclusion is still located on the axis *Oz* but it has been brought from an upside position to a downside position. Because $\cos(\beta/2)$ is then equal to 0, the only term which remains in the summation of Eq. (4) is the one for which:

$$\sigma = -\frac{m+s}{2} \tag{17}$$

From Eq. (3), this implies that H_{sn}^{m} is 0 whenever m and s have different parities. We then begin by assuming that m and s are even, and therefore set:

$$\begin{cases} m = 2M \\ s = 2S \end{cases} \tag{18}$$

so that the only term in the S_σ-summation is for:

$$\sigma = -M-S \tag{19}$$

From Eq. (4), we then obtain:

$$S_\sigma(\beta=\pi) = (-1)^{M+S}\binom{n+2S}{n-M+S}\binom{n-2S}{-M-S} \tag{20}$$

becoming:

$$S_\sigma(\beta=\pi) = (-1)^{M+S}\frac{(n+2S)!(n-2S)!}{(n-M+S)!(M+S)!(-M-S)!(n+M-S)!} \tag{21}$$

From the two factorials $(M+S)!$ and $(-M-S)!$ in the denominator, we see that we must have $(S+M)=0$, that is to say:

$$S = -M \tag{22}$$

This implies that, in the same way that the S_σ-summation reduces to a single term, the s-summation of Eq. (1) reduces to a single term too, the one for which Eq. (22) is satisfied. We therefore have:

$$\widetilde{g_{n,X}^{2M}} = \frac{\mu_{2Mn}}{\mu_{-2Mn}} H_{-2Mn}^{2M} g_{n,X}^{-2M} \tag{23}$$

in which, from Eq. (3), with $\gamma=0$:

$$H_{-2Mn}^{2M} = (-1)^n \frac{(n-2M)!}{(n+2M)!} e^{-2iM\alpha} S_\sigma(\beta=\pi) \tag{24}$$

in which, from Eqs. (21) and (22), $S_\sigma(\beta=\pi)$ reduces exactly to (1). From these results, and invoking also Eq. (2), we obtain:

$$\widetilde{g_{n,X}^{2M}} = \frac{(n-|2M|)!}{(n-|-2M|)!}(-1)^n e^{-2iM\alpha} g_{n,X}^{-2M} \tag{25}$$

simplifying to, whatever M:

$$\widetilde{g_{n,X}^{2M}} = (-1)^n e^{-2iM\alpha} g_{n,X}^{-2M} \tag{26}$$

We now deal with the odd case: $m=2M+1$, with $s=2S+1$. From Eq. (1), we have:

$$\widetilde{g_{n,X}^{2M+1}} = \mu_{2M+1,n} \sum_{s=-n,\, s=2S+1}^{n} \frac{H_{2S+1,n}^{2M+1}}{\mu_{2S+1,n}} g_{n,X}^{2S+1} \tag{27}$$

But, from Eq. (3):

$$H_{2S+1,n}^{2M+1}(\beta=\pi,\gamma=0) = (-1)^{n+1}\frac{(n-2M-1)!}{(n-2S-1)!} e^{i(2S+1)\alpha} S_\sigma(\beta=\pi) \tag{28}$$

in which, according to Eq. (4):

$$S_\sigma(\beta=\pi) = \sum_\sigma (-1)^\sigma \binom{n+s}{n-m-\sigma}\binom{n-s}{\sigma} \left(\cos\frac{\pi}{2}\right)^{2\sigma+m+s}\left(\sin\frac{\pi}{2}\right)^{2n-2\sigma-m-s} \tag{29}$$

$$\text{for } m=2M+1, s=2S+1, \sigma = -\frac{m+s}{2} = -M-S-1$$

becoming:

$$S_\sigma(\beta=\pi) = (-1)^{M+S+1}\binom{n+2S+1}{n-M+S}\binom{n-2S-1}{-M-S-1} \tag{30}$$

leading to:

$$S_\sigma(\beta=\pi) = (-1)^{M+S+1}\frac{(n+2S+1)!}{(n-M+S)!(S+M+1)!}\frac{(n-2S-1)!}{(-M-S-1)!(n-S+M)!} \tag{31}$$

The factorials $(S+M+1)!$ and $(-M-S-1)!$ in the denominator imply that we must have:

$$S = -M-1 \tag{32}$$

Therefore, there is only one term remaining in the summation of Eq. (27), involving $H_{-2M-1,n}^{2M+1}$. Also, accounting for Eq. (32), we readily have, from Eq. (31):

$$S_\sigma(\beta=\pi) = 1 \tag{33}$$

so that we obtain, from Eqs. (28) and (33):

$$H_{-2M-1,n}^{2M+1} = (-1)^{n+1}\frac{(n-2M-1)!}{(n+2M+1)!} e^{-i(2M+1)\alpha} \tag{34}$$

Now, Eq. (27) simplifies to:

$$\widetilde{g_{n,X}^{2M+1}} = \frac{\mu_{2M+1,n}}{\mu_{-2M-1,n}} H_{-2M-1,n}^{2M+1} g_{n,X}^{-2M-1} \tag{35}$$

We now recall Eq. (2) and obtain:

$$\mu_{2M+1,n} = (-1)^{2M+1}(-1)^{\frac{2M+1-|2M+1|}{2}}\frac{(n-|2M+1|)!}{(n-2M-1)!} \tag{36}$$

$$\mu_{-2M-1,n} = (-1)^{-2M-1}(-1)^{\frac{-2M-1-|-2M-1|}{2}}\frac{(n-|-2M-1|)!}{(n+2M+1)!} \tag{37}$$

We then readily establish:

$$R_{Mn} = \frac{\mu_{2M+1,n}}{\mu_{-2M-1,n}} = (-1)^{1+\frac{-|2M+1|+|-2M-1|}{2}} \frac{(n-|2M+1|)!}{(n-2M-1)!} \frac{(n+2M+1)!}{(n-|-2M-1|)!} \tag{38}$$

that we examine for $M>0$ and $M<0$. In both cases, the result is:

$$R_{mn} = -\frac{(n+2M+1)!}{(n-2M-1)!} \tag{39}$$

We afterward insert Eqs. (34) and (39) into (35), leading to:

$$\widetilde{g_{n,X}^{2M+1}} = (-1)^n e^{-i(2M+1)\alpha} g_{n,X}^{-2M-1} \tag{40}$$

4.2. On-axis axisymmetric beams

We now specify the results obtained in the previous sub-section to the case of on-axis axisymmetric beams. Inserting Eq. (5) into Eqs. (26) and (40) leads to:

$$\widetilde{g_{n,X}^{2M}} = 0 \tag{41}$$

$$\widetilde{g_{n,X}^{2M+1}} = 0 \text{ but for } M = 0, -1 \tag{42}$$

We then readily obtain:

$$\widetilde{g_{n,X}^{1}} = (-1)^n e^{-i\alpha} g_{n,X}^{-1} \tag{43}$$

$$\widetilde{g_{n,X}^{-1}} = (-1)^n e^{i\alpha} g_{n,X}^{1} \tag{44}$$

for $M=0,-1$ respectively. We may then specify these results for Eqs. (6) or (7). Let us do it for Eq. (7). We obtain:

$$\widetilde{g_{n,TM}^{1}} = \frac{1}{2}(-1)^n e^{-i\alpha} g_n \tag{45}$$

$$\widetilde{g_{n,TE}^{1}} = \frac{i}{2}(-1)^n e^{-i\alpha} g_n \tag{46}$$

$$\widetilde{g_{n,TM}^{-1}} = \frac{1}{2}(-1)^n e^{i\alpha} g_n \tag{47}$$

$$\widetilde{g_{n,TE}^{-1}} = \frac{-i}{2}(-1)^n e^{i\alpha} g_n \tag{48}$$

These relations do not share the same simplicity as the ones displayed for instance in Eq. (7). In particular, $\widetilde{g_{n,TM}^{1}} / \widetilde{g_{n,TM}^{-1}}$ is equal to $\exp(-2i\alpha)$ which is different from (1), except for $\alpha=0$, in contrast with $g_{n,TM}^{1}/{g_{n,TM}}^{-1}$ which in Eq. (7) is always equal to 1. Nevertheless, from a physical point of view, the value of α is irrelevant. Indeed, the value $\alpha=0$ defines the same upside-down physical situation than any other value, and could have been specified in Eq. (16), in the same way than we have set γ equal to 0. For $\alpha=0$ however, the relations above can be pleasantly summarized as follows:

$$\widetilde{g_{n,TM}^{1}} = \widetilde{g_{n,TM}^{-1}} = -i\widetilde{g_{n,TE}^{1}} = i\widetilde{g_{n,TE}^{-1}} = \frac{1}{2}(-1)^n g_n \tag{49}$$

which may be interestingly compared with Eq. (7), or more interestingly, with Eq. (6). Both equations then formally identify with $(-1)^n g_n$ changed to g_n, with $K=1$, and $\varepsilon=+1$. This value of ε is in agreement with the fact that the case under study makes the beam flowing toward negative z,s.

As a checking, we should recover these particular results for on-axis axisymmetric beams from the compact forms obtained for this case, given in [2], specified for $\beta=\pi$, $\gamma=0$, reading as:

$$\begin{aligned}\widetilde{g_{n,X}^{m}} = {} & (-1)^{m+1}(-1)^{\frac{m-|m|}{2}} \frac{(n-|m|)!}{(n+m)!} \\ & \times\Big\{m\pi_n^m(cos\beta=-1)\Big[e^{-i\alpha}g_{n,X}^{-1} - e^{i\alpha}g_{n,X}^{1}\Big] \\ & -\tau_n^m(cos\beta=-1)\Big[e^{-i\alpha}g_{n,X}^{-1} + e^{i\alpha}g_{n,X}^{1}\Big]\Big\}\end{aligned} \tag{50}$$

in which $\pi_n^m(\cos\beta)$ and $\tau_n^m(\cos\beta)$ are the generalized Legendre functions defined as:

$$\pi_n^m(cos\beta) = \frac{P_n^m(cos\beta)}{sin\beta} \tag{51}$$

$$\tau_n^m(cos\,\beta) = \frac{dP_n^m(cos\beta)}{d\beta} \tag{52}$$

For convenience, just playing with arguments in a looser way, we better rewrite Eq. (50) as:

$$\begin{aligned}\widetilde{g_{n,X}^{m}} = {} & (-1)^{m+1}(-1)^{\frac{m-|m|}{2}} \frac{(n-|m|)!}{(n+m)!} \\ & \times\Big\{m\pi_n^m(\beta=\pi)\Big[e^{-i\alpha}g_{n,X}^{-1} - e^{i\alpha}g_{n,X}^{1}\Big] \\ & -\tau_n^m(\beta=\pi)\Big[e^{-i\alpha}g_{n,X}^{-1} + e^{i\alpha}g_{n,X}^{1}\Big]\Big\}\end{aligned} \tag{53}$$

To deal with this expression, we start with a bit of preparation. From Doicu et al. [10], p 257, we have, for $m>0$:

$$m\pi_n^m(\theta\to 0,\pi) = (-1)^m \frac{1}{2}\frac{(n+m)!}{(n-m)!(m-1)!}\left(\frac{\theta}{2}\right)^{m-1} \tag{54}$$

$$\tau_n^m(\theta\to 0,\pi) = (-1)^m \frac{1}{2}\frac{(n+m)!}{(n-m)!(m-1)!}\left(\frac{\theta}{2}\right)^{m-1} \tag{55}$$

in which the prefactor $(-1)^m$, which does not appear in Doicu et al. [10], is due to the fact than Doicu et al. used an alternative definition for the associated Legendre functions. With our convention, let us recall that these associated Legendre functions may be given a unique form, whatever $m\in\mathbf{Z}$, reading as [1]:

$$P_n^m(cos\theta) = (-1)^{\frac{m-|m|}{2}} \frac{(n-|m|)!}{(n-m)!} P_n^{|m|}(cos\theta) \tag{56}$$

Next, from the definitions of π_n^m and τ_n^m, Eq. (56) implies that, whatever the value of $m\in\mathbf{Z}$:

$$m\pi_n^m(cos\theta) = (-1)^{\frac{m-|m|}{2}} \frac{(n-|m|)!}{(n-m)!} m\pi_n^{|m|}(cos\theta) \tag{57}$$

$$\tau_n^m(cos\theta) = (-1)^{\frac{m-|m|}{2}} \frac{(n-|m|)!}{(n-m)!} \tau_n^{|m|}(cos\theta) \tag{58}$$

We now set:

$$\theta = \pi-\beta \tag{59}$$

so that, in the present case where $\beta=\pi$, we have $\theta=0$.

We also have from Doicu et al. [10], p 260:

$$\pi_n^m(\beta) = (-1)^{n-m}\pi_n^m(\pi-\beta) \tag{60}$$

$$\tau_n^m(\beta) = (-1)^{n-m+1}\tau_n^m(\pi-\beta) \tag{61}$$

Inserting Eqs. (60) and (61) into Eq. (53), and using Eq. (59), we obtain:

$$\begin{aligned}\widetilde{g_{n,X}^m} = {} & (-1)^{n+1}(-1)^{\frac{m-|m|}{2}}\frac{(n-|m|)!}{(n+m)!} \\ & \times\{\left[m\pi_n^m(\theta=0)+\tau_n^m(\theta=0)\right]e^{-i\alpha}g_{n,X}^{-1} \\ & +\left[\tau_n^m(\theta=0)-m\pi_n^m(\theta=0)\right]e^{i\alpha}g_{n,X}^{1}\}\end{aligned} \tag{62}$$

We now introduce Eqs. (57) and (58) into Eq. (62) and obtain:

$$\begin{aligned}\widetilde{g_{n,X}^m} = {} & (-1)^{n+1}(-1)^{m-|m|}\frac{(n-|m|)|)!}{(n+m)!}\frac{(n-|m|)|)!}{(n-m)!} \\ & \times\left\{\left[m\pi_n^{|m|}(\theta=0)+\tau_n^{|m|}(\theta=0)\right]e^{-i\alpha}g_{n,X}^{-1}\right. \\ & \left.+\left[\tau_n^{|m|}(\theta=0)-m\pi_n^{|m|}(\theta=0)\right]e^{i\alpha}g_{n,X}^{1}\right\}\end{aligned} \tag{63}$$

Eqs. (54) and (55) then imply that $\widetilde{g_{n,X}^m}$ is proportional to $(\theta/2)^{|m|-1}$, with $\theta=0$, that is to say, with the case $m=0$ excluded:

$$\widetilde{g_{n,X}^m} = 0, |m|\neq 1, m\neq 0 \tag{64}$$

Afterward, from Eqs. (54), (55) and (63), we obtain:

$$\widetilde{g_{n,X}^1} = (-1)^n e^{-i\alpha}g_{n,X}^{-1} \tag{65}$$

$$\widetilde{g_{n,X}^{-1}} = (-1)^n e^{i\alpha}g_{n,X}^{1} \tag{66}$$

that is to say, we have recovered Eqs. (43) and (44), as required.

We still have to deal with the case $m=0$. Specifying Eq. (62) for this case, we have:

$$\widetilde{g_{n,X}^0} = (-1)^{n+1}\tau_n^0(\theta=0)\left[e^{-i\alpha}g_{n,X}^{-1}+e^{i\alpha}g_{n,X}^{1}\right] \tag{67}$$

However, from Eq. (52):

$$\tau_n^0(cos\theta) = \frac{dP_n^0(cos\theta)}{d\theta} = \frac{dP_n(cos\theta)}{d\theta} = -sin\theta\frac{dP_n(cos\theta)}{dcos\theta} \tag{68}$$

But $P_n(\cos\theta)$ is a polynomial of the argument $\cos\theta$. Therefore, its derivative with respect to the argument remains finite, and we then obtain:

$$\tau_n^0(\theta=0) = 0 \tag{69}$$

leading to:

$$\widetilde{g_{n,X}^0} = 0 \tag{70}$$

so that Eq. (64) can be extended to the case $m=0$.

5. Inclusion in the horizontal plane

We now consider the case when the Euler angle α is free, specifying the two other Euler angles to:

$$\beta = \pi/2; \gamma = 0 \tag{71}$$

In the dressed problem, with the center of the inclusion in the unrotated system located on the z-axis, called the vertical axis, Eq. (71) corresponds to the case when the center of the inclusion is located in the horizontal plane containing the center of the host sphere.

5.1. Expanded forms: arbitrary shaped beams

We specify Eq. (4) expressing $S_\sigma(\beta)$ for $\beta=\pi/2$, that is to say for:

$$cos\frac{\beta}{2} = cos\frac{\pi}{4} = \frac{\sqrt{2}}{2} = sin\frac{\beta}{2} = sin\frac{\pi}{4} \tag{72}$$

We then obtain:

$$S_\sigma(\beta=\pi/2) = \frac{1}{2^n}\sum_\sigma(-1)^\sigma\binom{n+s}{n-m-\sigma}\binom{n-s}{\sigma} \tag{73}$$

This can be rewritten as:

$$S_\sigma(\beta=\pi/2) = \frac{1}{2^n}(n+s)!(n-s)!T_\sigma(n,m,s) \tag{74}$$

in which:

$$T_\sigma(n,m,s) = \sum_\sigma\frac{(-1)^\sigma}{(n-m-\sigma)!(m+\sigma+s)!(\sigma)!(n-s-\sigma)!} \tag{75}$$

Let us now consider the general result of Eq. (1) in which we insert the expressions for μ_{mn} and μ_{sn} given by Eq. (2), and the expression for H_{sn}^m given by Eq. (3), all these specified for $\beta=\pi/2$, $\gamma=0$, with $S_\sigma(\beta)$ available from Eqs. (74), (75), eventually leading to:

$$\begin{aligned}\widetilde{g_{n,X}^m}(\beta=\pi/2,\gamma=0) = {} & (-1)^{n+m}(-1)^{\frac{m-|m|}{2}}(n-|m|)!\frac{1}{2^n} \\ & \sum_{s=-n}^{n}(-1)^{\frac{s-|s|}{2}}e^{is\alpha}\frac{(n+s)!(n-s)!}{(n-|s|)!}T_\sigma(n,m,s)g_{n,X}^s\end{aligned} \tag{76}$$

It may be convenient to rewrite this expression as:

$$\widetilde{g_{n,X}^m}(\beta=\pi/2,\gamma=0) = A_n^m(S_0+S_+ +S_-) \tag{77}$$

in which:

$$A_n^m = (-1)^{n+m}(-1)^{\frac{m-|m|}{2}}(n-|m|)!\frac{1}{2^n} \tag{78}$$

and S_0 (corresponding to the term for $s=0$), S_+ (corresponding to the terms for positive values of s) and S_- (corresponding to the terms for negative values of s) can be given the following forms:

$$S_0 = n!T_\sigma(n,m,0)g_{n,X}^0 \tag{79}$$

$$S_+ = \sum_{s=1}^{n}e^{is\alpha}(n+s)!T_\sigma(n,m,s)g_{n,X}^s \tag{80}$$

$$S_- = \sum_{s=-n}^{-1}(-1)^s e^{is\alpha}(n-s)!T_\sigma(n,m,s)g_{n,X}^s \tag{81}$$

Although a bit contradicting the title of this sub-section, we are now going to provide an explicit compact expression for $T_\sigma(n,m,0)$ involved in S_0, reading as:

$$T_\sigma(n,m,0) = \sum_\sigma \frac{(-1)^\sigma}{(n-m-\sigma)!(m+\sigma)!\sigma!(n-\sigma)!} \tag{82}$$

For this, we recall that we have demonstrated, in [2]:

$$P_n^m(cos\beta) = \sum_\sigma (-1)^{n-\sigma} \frac{(n+m)!n!}{(n-\sigma)!(m+\sigma)!(n-m-\sigma)!\sigma!} \times\left(sin\frac{\beta}{2}\right)^{2n-m-2\sigma}\left(cos\frac{\beta}{2}\right)^{2\sigma+m} \tag{83}$$

We specify this equation for $\beta=\pi/2$ and we obtain:

$$P_n^m(0) = \frac{(-1)^n}{2^n}(n+m)!n!T_\sigma(n,m,0) \tag{84}$$

that is to say:

$$T_\sigma(n,m,0) = \frac{(-1)^n 2^n}{(n+m)!n!}P_n^m(0) \tag{85}$$

But [11]:

$$\begin{cases} P_n^m(0) = 0, (n-m)\,\text{odd} \\ P_n^m(0) = (-1)^{\frac{n+m}{2}} \dfrac{(n+m-1)!!}{2^{\frac{n-m}{2}}\left(\frac{n-m}{2}\right)!}, (n-m)\,\text{even} \end{cases} \tag{86}$$

in which:

$$\begin{cases} n!! = 1.3.5...n \\ (-1)!! = 1 \end{cases} \tag{87}$$

We afterward insert Eq. (86) into Eq. (85) to obtain:

$$\begin{cases} T_\sigma(n,m,0) = 0, (n-m)\,\text{odd} \\ T_\sigma(n,m,0) = \dfrac{(-1)^n 2^n}{(n+m)!n!}(-1)^{\frac{n+m}{2}} \dfrac{(n+m-1)!!}{2^{\frac{n-m}{2}}\left(\frac{n-m}{2}\right)!}, (n-m)\,\text{even} \end{cases} \tag{88}$$

Hence, inserting this relation into Eq. (79) we have:

$$\begin{cases} S_0 = 0, (n-m)\,\text{odd} \\ S_0 = \dfrac{(-1)^n 2^n}{(n+m)!}(-1)^{\frac{n+m}{2}} \dfrac{(n+m-1)!!}{2^{\frac{n-m}{2}}\left(\frac{n-m}{2}\right)!} g_{n,X}^0, (n-m)\,\text{even} \end{cases} \tag{89}$$

Inserting Eqs. (78), (80), (81), and (89) into Eq. (77), we may write our result under the following form:

$$\begin{aligned} \widetilde{g_{n,X}^m} = (-1)^{n+m}(-1)^{\frac{m-|m|}{2}}(n-|m|)!\frac{1}{2^n} \\ \times\Bigg\{\frac{(-1)^n 2^n}{(n+m)!}(-1)^{\frac{n+m}{2}} \frac{(n+m-1)!!}{2^{\frac{n-m}{2}}\left(\frac{n-m}{2}\right)!} g_{n,X}^0 \delta_{\text{par}(2)\text{par}(n-m)} \\ + \sum_{s=1}^{n} e^{is\alpha}(n+s)!T_\sigma(n,m,s)g_{n,X}^s \\ + \sum_{s=-n}^{-1}(-1)^s e^{is\alpha}(n-s)!T_\sigma(n,m,s)g_{n,X}^s\Bigg\} \end{aligned} \tag{90}$$

in which par(i) is the parity of i.

5.2. Expanded forms: on-axis axisymmetric beams

In the case of on-axis axisymmetric beams, we may apply Eq. (5) to Eq. (90) which dramatically simplifies to:

$$\begin{aligned} \widetilde{g_{n,X}^m} = (-1)^{n+m}(-1)^{\frac{m-|m|}{2}}(n-|m|)!\frac{1}{2^n} \\ \times\left\{e^{i\alpha}(n+1)!T_\sigma(n,m,1)g_{n,X}^1 - e^{-i\alpha}(n+1)!T_\sigma(n,m,-1)g_{n,X}^{-1}\right\} \end{aligned} \tag{91}$$

We now specify Eq. (91) to Eq. (7). This readily leads to the following results:

$$\begin{aligned} \widetilde{g_{n,TM}^m} = (-1)^{n+m}(-1)^{\frac{m-|m|}{2}}(n-|m|)!\frac{(n+1)!}{2^{n+1}}g_n \\ \times\left[T_\sigma(n,m,1)e^{i\alpha} - T_\sigma(n,m,-1)e^{-i\alpha}\right] \end{aligned} \tag{92}$$

$$\begin{aligned} \widetilde{g_{n,TE}^m} = -i(-1)^{n+m}(-1)^{\frac{m-|m|}{2}}(n-|m|)!\frac{(n+1)!}{2^{n+1}}g_n \\ \times\left[T_\sigma(n,m,1)e^{i\alpha} + T_\sigma(n,m,-1)e^{-i\alpha}\right] \end{aligned} \tag{93}$$

5.3. Concise form: arbitrary shaped beams

Let us rewrite Eq. (4) under the following form:

$$\begin{aligned} S_\sigma(\beta) = \sum_\sigma (-1)^\sigma \frac{(n+s)!(n-s)!}{(n-m-\sigma)!(s+m+\sigma)!\sigma!(n-s-\sigma)!} \\ \times\left(cos\frac{\beta}{2}\right)^{2\sigma+m+s}\left(sin\frac{\beta}{2}\right)^{2n-2\sigma-m-s} \end{aligned} \tag{94}$$

Now, in [1], we have introduced four versions of Wigner d-functions, following Mishchenko et al. [12]. One of them reads as:

$$\begin{aligned} d_{ms}^n(\beta) = (-1)^{n-s}\sqrt{(n+m)!(n-m)!(n+s)!(n-s)!} \\ \sum_\sigma (-1)^\sigma \frac{\left(cos\frac{\beta}{2}\right)^{s+m+2\sigma}\left(sin\frac{\beta}{2}\right)^{2n-s-m-2\sigma}}{\sigma!(n-m-\sigma)!(n-s-\sigma)!(m+s+\sigma)!} \end{aligned} \tag{95}$$

from which we deduce:

$$S_\sigma(\beta) = (-1)^{n+s}\left[\frac{(n+s)!}{(n+m)!}\frac{(n-s)!}{(n-m)!}\right]^{1/2} d_{ms}^n(\beta) \tag{96}$$

We then use Eqs. (74) and (96), to obtain:

$$T_\sigma(n,m,s) = \frac{(-1)^{n+s}2^n}{\sqrt{(n+s)!(n-s)!(n+m)!(n-m)!}} d_{ms}^n\left(\beta=\frac{\pi}{2}\right) \tag{97}$$

At the present step, the expression for the d-function still however contains a σ-summation, so that the effective gain is not obvious. This σ-summation is simply made explicit when we use the original notation for $S_\sigma(\beta)$. However, the d-function can also be evaluated by using a recurrence relation in [12] (Appendix B, p 365) so that Eq. (97) may actually be viewed as being more efficient than an expanded form. Nevertheless, we shall not call it a compact form, but a concise form. Concise forms for beam shape coefficients may afterward been readily obtained by using Eqs. (96), (3), (2) and (1).

5.4. Compact forms: on-axis axisymmetric beams

Genuine compact forms may however been obtained in the case of on-axis axisymmetric beams, by elaborating more on Eq. (91) which

involves the quantities $T_\sigma(n,m,1)$ and $T_\sigma(n,m,-1)$. Indeed, from Eq. (97):

$$T_\sigma(n,m,1) = \frac{(-1)^{n+1}2^n}{\sqrt{(n+1)!(n-1)!(n+m)!(n-m)!}} d^n_{m1}\left(\beta=\frac{\pi}{2}\right) \quad (98)$$

$$T_\sigma(n,m,-1) = \frac{(-1)^{n+1}2^n}{\sqrt{(n-1)!(n+1)!(n+m)!(n-m)!}} d^n_{m(-1)}\left(\beta=\frac{\pi}{2}\right) \quad (99)$$

We insert Eqs. (98) and (99) into (91), yielding:

$$\widetilde{g^m_{n,X}} = (-1)^{m+1}(-1)^{\frac{m-|m|}{2}} \frac{(n-|m|)!\sqrt{(n+1)!}}{\sqrt{(n-m)!(n+m)!(n-1)!}} \times\left[e^{i\alpha}d^n_{m1}\left(\beta=\frac{\pi}{2}\right)g^1_{n,X} - e^{-i\alpha}d^n_{m(-1)}\left(\beta=\frac{\pi}{2}\right)g^{-1}_{n,X}\right] \quad (100)$$

We now invoke Eq. (B25), Appendix B, from Mishchenko et al. [12], rewritten under the form of two equations reading as:

$$\frac{d}{d\beta}d^n_{ms}(\beta) + \frac{m}{sin\beta}d^n_{ms}(\beta) = \frac{s\,cos\beta}{sin\beta}d^n_{ms}(\beta) - \sqrt{(n-s)(n+s+1)}d^n_{ms+1}(\beta) \quad (101)$$

$$\frac{d}{d\beta}d^n_{ms}(\beta) - \frac{m}{sin\beta}d^n_{ms}(\beta) = \frac{-s\,cos\beta}{sin\beta}d^n_{ms}(\beta) + \sqrt{(n+s)(n-s+1)}d^n_{ms-1}(\beta) \quad (102)$$

We specify these equations for $s=0$ and readily obtain:

$$d^n_{m1}(\beta) = \frac{-1}{\sqrt{n(n+1)}}\left[\frac{d}{d\beta}d^n_{m0}(\beta) + \frac{m}{sin\beta}d^n_{m0}(\beta)\right] \quad (103)$$

$$d^n_{m(-1)}(\beta) = \frac{+1}{\sqrt{n(n+1)}}\left[\frac{d}{d\beta}d^n_{m0}(\beta) - \frac{m}{sin\beta}d^n_{m0}(\beta)\right] \quad (104)$$

We insert Eqs. (103) and (104) into Eq. (100), leading to:

$$\widetilde{g^m_{n,X}} = \left\{(-1)^m(-1)^{\frac{m-|m|}{2}}\frac{(n-|m|)!}{\sqrt{(n-m)!(n+m)!}} \times\left[e^{i\alpha}g^1_{n,X}\left(\frac{d}{d\beta}d^n_{m0}(\beta) + \frac{m}{sin\beta}d^n_{m0}(\beta)\right) + e^{-i\alpha}g^{-1}_{n,X}\left(\frac{d}{d\beta}d^n_{m0}(\beta) - \frac{m}{sin\beta}d^n_{m0}(\beta)\right)\right]\right\}_{\beta=\frac{\pi}{2}} \quad (105)$$

But we have, from Mishchenko et al. [12], Appendix B, Eq. (B.28):

$$d^n_{m0}(\beta) = \sqrt{\frac{(n-m)!}{(n+m)!}}P^m_n(cos\beta) \quad (106)$$

By using this relation, and the definitions of π^m_n and τ^m_n, Eq. (105) can be rewritten as:

$$\widetilde{g^m_{n,X}} = (-1)^m(-1)^{\frac{m-|m|}{2}}\frac{(n-|m|)!}{(n+m)!} \times[e^{i\alpha}g^1_{n,X}(\tau^m_n(cos\beta) + m\pi^m_n(cos\beta) + e^{-i\alpha}g^{-1}_{n,X}(\tau^m_n(cos\beta) - m\pi^m_n(cos\beta)]_{\beta=\frac{\pi}{2}} \quad (107)$$

This may be further simplified. For this, we use Eqs. (86), (87) and recall [11]:

$$\left[\frac{dP^m_n(cos\beta)}{dcos\beta}\right]_{\beta=\frac{\pi}{2}} = \begin{cases} 0 \text{ for } (n-m) \text{ even} \\ (-1)^{\frac{n+m-1}{2}}\dfrac{(n+m)!!}{2^{\frac{n-m-1}{2}}\left(\frac{n-m-1}{2}\right)!} \text{ for } (n-m) \text{ odd} \end{cases} \quad (108)$$

Next, we have:

$$\left[\pi^m_n(cos\beta)\right]_{\beta=\frac{\pi}{2}} = \pi^m_n(0) = \left[\frac{P^m_n(cos\beta)}{sin\beta}\right]_{\beta=\frac{\pi}{2}} = P^m_n(0) \quad (109)$$

$$\left[\tau^m_n(cos\beta)\right]_{\beta=\frac{\pi}{2}} = \tau^m_n(0) = \left[\frac{dP^m_n(cos\beta)}{d\beta}\right]_{\beta=\frac{\pi}{2}} = \left[-sin\beta\frac{dP^m_n(cos\beta)}{dcos\beta}\right]_{\beta=\frac{\pi}{2}} = -\left[\frac{dP^m_n(cos\beta)}{dcos\beta}\right]_{\beta=\frac{\pi}{2}} \quad (110)$$

Inserting these results into Eq. (107), we obtain the following beam shape coefficients compact forms:

$$\widetilde{g^m_{n,X}}(n-m,\text{even}) = \frac{(-1)^m(-1)^{\frac{m-|m|}{2}}(-1)^{\frac{n+m}{2}}}{2^{\frac{n-m}{2}}}\frac{m(n-|m|)!(n+m-1)!!}{(n+m)!\left(\frac{n-m}{2}\right)!} \times\left[e^{i\alpha}g^1_{n,X} - e^{-i\alpha}g^{-1}_{n,X}\right] \quad (111)$$

$$\widetilde{g^m_{n,X}}(n-m,\text{odd}) = \frac{(-1)^{m+1}(-1)^{\frac{m-|m|}{2}}(-1)^{\frac{n+m-1}{2}}}{2^{\frac{n-m-1}{2}}}\frac{(n-|m|)!(n+m-1)!!}{(n+m)!\left(\frac{n-m-1}{2}\right)!} \times\left[e^{i\alpha}g^1_{n,X} - e^{-i\alpha}g^{-1}_{n,X}\right] \quad (112)$$

These two last equations can readily be specified for Eqs. (6) or (7). Equivalently, we could start from the results obtained for on-axis axisymmetric beams in Part II [2] and specify them for the case under study.

6. Inclusion in the Cartesian vertical planes

After having considered the case, call it case H, when the center of the inclusion is located in the plane xOy (the horizontal plane), we might naturally consider the cases when the center of the inclusion is located in what we call in this paper the Cartesian vertical planes, namely either in the plane yOz (case V1) or in the plane $x0z$ (case V2). We shall be content with a discussion of the case V1.

According to the definition of Euler angles, we must have $0 \le \beta < \pi$. Therefore, case V1 requires us to consider two different cases:

(i) $\alpha = 3\pi/2$, β current, $\gamma = 0$. In this case, the inclusion runs along a half-circle on the left of the plane (x, z), crossing the negative y-axis.

(ii) $\alpha = \pi/2$, β current, $\gamma = 0$. In this case, the inclusion runs along a half-circle on the right of the plane (x, z), crossing the positive y-axis.

We insert Eq. (96) into Eq. (3) to obtain:

$$H^m_{sn}(\beta) = \left[\frac{(n+s)!(n-m)!}{(n-s)!(n+m)!}\right]^{1/2} e^{is\alpha}e^{im\gamma}d^n_{ms}(\beta) \quad (113)$$

We now consider the case (i) with $\alpha=3\pi/2$ and $\gamma=0$. With these values of the Euler angles, Eq. (113) simplifies to:

$$H_{sn}^{m}(\beta)=(-i)^{s}\left[\frac{(n+s)!(n-m)!}{(n-s)!(n+m)!}\right]^{1/2}d_{ms}^{n}(\beta) \tag{114}$$

For case (ii), when $\alpha=\pi/2$, $\gamma=0$, we similarly obtain:

$$H_{sn}^{m}(\beta)=i^{s}\left[\frac{(n+s)!(n-m)!}{(n-s)!(n+m)!}\right]^{1/2}d_{ms}^{n}(\beta) \tag{115}$$

These are what we have called concise forms (not compact forms). Concise expressions for the beam shape coefficients may afterward be obtained by using Eq. (1).

We now discuss the case of on-axis asymmetric beams, recalling a compact form obtained in Part II [2] for on-axis axisymmetric beams in the rotated system:

$$\begin{aligned}\widetilde{g_{n,X}^{m}}=&(-1)^{m+1}(-1)^{\frac{m-|m|}{2}}\frac{(n-|m|)!}{(n+m)!}e^{im\gamma}\\&\times\{m\pi_{n}^{m}(cos\beta)\left[e^{-i\alpha}g_{n,X}^{-1}-e^{i\alpha}g_{n,X}^{1}\right]-\tau_{n}^{m}(cos\beta)\\&\times\left[e^{-i\alpha}g_{n,X}^{-1}+e^{i\alpha}g_{n,X}^{1}\right]\}\end{aligned} \tag{116}$$

In case (i), Eq. (116) simplifies to:

$$\begin{aligned}\widetilde{g_{n,X}^{m}}=&i(-1)^{m+1}(-1)^{\frac{m-|m|}{2}}\frac{(n-|m|)!}{(n+m)!}\\&\times\left\{m\pi_{n}^{m}(cos\beta)\left[g_{n,X}^{-1}+g_{n,X}^{1}\right]-\tau_{n}^{m}(cos\beta)\left[g_{n,X}^{-1}-g_{n,X}^{1}\right]\right\}\end{aligned} \tag{117}$$

When Eq. (7) is satisfied, this equation leads to:

$$\widetilde{g_{n,TM}^{m}}=i(-1)^{m+1}(-1)^{\frac{m-|m|}{2}}\frac{(n-|m|)!}{(n+m)!}m\pi_{n}^{m}(cos\beta)g_{n} \tag{118}$$

$$\widetilde{g_{n,TE}^{m}}=(-1)^{m+1}(-1)^{\frac{m-|m|}{2}}\frac{(n-|m|)!}{(n+m)!}\tau_{n}^{m}(cos\beta)g_{n} \tag{119}$$

in agreement with results already obtained in Part II [2].

In case (ii), Eq. (116) simplifies to:

$$\begin{aligned}\widetilde{g_{n,X}^{m}}=&i(-1)^{m}(-1)^{\frac{m-|m|}{2}}\frac{(n-|m|)!}{(n+m)!}\\&\times\left\{m\pi_{n}^{m}(cos\beta)\left[g_{n,X}^{-1}+g_{n,X}^{1}\right]+\tau_{n}^{m}(cos\beta)\left[g_{n,X}^{1}-g_{n,X}^{-1}\right]\right\}\end{aligned} \tag{120}$$

Specifying Eq. 7, we then obtain:

$$\widetilde{g_{n,TM}^{m}}=i(-1)^{m}(-1)^{\frac{m-|m|}{2}}\frac{(n-|m|)!}{(n+m)!}m\pi_{n}^{m}(cos\beta)g_{n} \tag{121}$$

$$\widetilde{g_{n,TE}^{m}}=(-1)^{m}(-1)^{\frac{m-|m|}{2}}\frac{(n-|m|)!}{(n+m)!}\tau_{n}^{m}(cos\beta)g_{n} \tag{122}$$

Specifying Eq. (7), we then obtain in: agreement with results already obtained in Part II [2].

It is worthwhile to note that Eqs. (121), (122) agree with Eqs. (118), (119), except for a phase term equal to (-1).

Concerning V2, let us just mention that, due to the constraint $0\leq\beta<\pi$, we have to separately consider two cases (i) $\alpha=\gamma=0$ (ii) $\alpha=\pi$, $\gamma=0$. The rest is left to the reader.

7. Rotation about the vertical axis

This case corresponds to $\beta=0$, and will allow us an interesting discussion on physics. With the axis Oz being taken as the vertical axis, this is a case when the only rotation involved is a rotation about the vertical axis. We have actually already considered a special case of it, namely the case of no rotation: $\alpha=\beta=\gamma=0$. We begin by discussing the relationship between these two special cases.

For $\beta=0$, Eq. (3) becomes:

$$H_{sn}^{m}(\beta=0)=(-1)^{n+s}\frac{(n-m)!}{(n-s)!}e^{is\alpha}e^{im\gamma}S_{\sigma}(0) \tag{123}$$

In the case of no rotation, this reduces to:

$$H_{sn}^{m}(\text{norotation})=(-1)^{n+s}\frac{(n-m)!}{(n-s)!}S_{\sigma}(0) \tag{124}$$

that is to say:

$$\frac{H_{sn}^{m}(\beta=0)}{H_{sn}^{m}(\text{no rotation})}=e^{is\alpha}e^{im\gamma} \tag{125}$$

In terms of beam shape coefficients, this implies:

$$\widetilde{g_{n,X}^{m}}(\beta=0)=\mu_{mn}e^{im\gamma}\sum_{s=-n}^{n}e^{is\alpha}\frac{H_{sn}^{m}(\text{no rotation})}{\mu_{sn}}g_{n,X}^{s} \tag{126}$$

with the reciprocal relation:

$$\widetilde{g_{n,X}^{m}}(\text{no rotation})=\mu_{mn}e^{-im\gamma}\sum_{s=-n}^{n}e^{-is\alpha}\frac{H_{sn}^{m}(\beta=0)}{\mu_{sn}}g_{n,X}^{s} \tag{127}$$

Nevertheless, for $\beta=0$, any rotation $(\alpha, 0, \gamma)$ is equivalent to a single rotation Γ such as $\Gamma=(\alpha+\gamma)$, that is to say of the kind $(0, 0, \Gamma)$. Starting from Eq. (127) (or 126), we then physically obtain the interesting relation:

$$\widetilde{g_{n,X}^{m}}(\text{no rotation})=e^{-im\Gamma}\widetilde{g_{n,X}^{m}}(\beta=0) \tag{128}$$

Both kinds of beam shape coefficients are simply related by a phase factor, involving a single angle of rotation Γ around the original z-axis. A similar discussion is also valid in the special case of on-axis axisymmetric beams, although in this case only H_{1n}^{m} and H_{-1n}^{m} intervene.

Also, let us extend the discussion by considering a problem dressed with a spherical inclusion having its center located on the axis Oz. Then, both cases (no rotation, rotation about the vertical axis) are equivalent and the phase angle Γ should be physically irrelevant.

We now mathematically elaborate on these remarks. The issue is that we should be able to derive Eq. (128) mathematically (and not physically) from Eq. (127). To this purpose, we start from Eq. (96), with $\beta=0$:

$$S_{\sigma}(\beta=0)=(-1)^{n+s}\left[\frac{(n+s)!(n-s)!}{(n+m)!(n-m)!}\right]^{1/2}d_{ms}^{n}(\beta=0) \tag{129}$$

But, from Mischenko et al. [12], Appendix B, p 363, Eq. (B6), we have:

$$d_{ms}^{n}(\beta=0)=\delta_{ms} \tag{130}$$

Inserting Eq. (130) into Eq. (129) readily leads to:

$$S_{\sigma}(\beta=0)=(-1)^{n+s}\delta_{ms} \tag{131}$$

We now insert Eq. (131) into Eq. (123), yielding:

$$H_{sn}^{m}(\beta = 0) = e^{im\gamma}e^{is\alpha}\delta_{ms} \tag{132}$$

Similarly, inserting Eq. (131) into Eq. (124), we obtain:

$$H_{sn}^{m}(\text{no rotation}) = \delta_{ms} \tag{133}$$

Inserting Eqs. (132) and (133) into Eq. (126) and afterward into Eq. (127), we obtain:

$$\widetilde{g_{n,X}^{m}}(\beta = 0) = e^{im(\gamma + \alpha)}g_{n,X}^{m} \tag{134}$$

$$\widetilde{g_{n,X}^{m}}(\text{no rotation}) = g_{n,X}^{m} \tag{135}$$

From these two last equations, we recover Eq. (128). Let us remark also that Eq. (135) is already known to us from the section devoted to the case of no rotation. It has here been obtained in a way which is faster, albeit less transparent.

8. Conclusion

This paper pertains to a series devoted to the study of the transformation of spherical beam shape coefficients under rotations of coordinate systems, for use in some generalized Lorenz–Mie theories expressed in terms of spherical coordinates. Such a study provides a new means to the evaluation of beam shape coefficients of arbitrary shaped beams. After Part I devoted to the general formulation of the problem, Part II was devoted to the special case of on-axis axisymmetric beams. The present Part III investigated special values of Euler angles, with a special effort due to the search of compact forms which, presumably, should allow one to speed up the numerical computations of beam shape coefficients in cases when such compact forms have been obtained. The formal manipulations involved in this search also allow one to deepen our understanding of the mathematics and physics involved in the issue. Part IV will be devoted to a specific study of plane waves in unrotated and rotated systems.

References

[1] G. Gouesbet, J.J. Wang, Y.P. Han, Transformations of spherical beam shape coefficients in generalized Lorenz–Mie theories through rotations of coordinate systems, I. General formulation, Optics Communications 283 (17) (2010) 3218–3225.
[2] J.J. Wang, G. Gouesbet, Y.P. Han, Transformations of spherical beam shape coefficients in generalized Lorenz–Mie theories through rotations of coordinate systems, II. Axisymmetricbeams, Optics Communications 283 (17) (2010) 3226–3234.
[3] G. Gouesbet, B. Maheu, G. Gréhan, Journal of the Optical Society of America A 5 (1988) 1427–1443.
[4] B. Maheu, G. Gouesbet, G. Gréhan, Journal of Optics, Paris 19 (2) (1988) 59–67.
[5] F. Onofri, G. Gréhan, G. Gouesbet, Applied Optics 34 (30) (1995) 7113–7124.
[6] G. Gouesbet, G. Gréhan, Journal of Modern Optics 47 (5) (2000) 821–837.
[7] G. Gouesbet, Applied Optics 35 (9) (1996) 1543–1555.
[8] G. Gouesbet, G. Gréhan, Journal of Optics, Paris 13 (2) (1982) 97–103.
[9] G. Gouesbet, G. Gréhan, B. Maheu, Journal of Optics, Paris 16 (1985) 83–93.
[10] A. Doicu, T. Wriedt, Y.A. Eremin, Light scattering by systems of particles, Null-field Method with Discrete Sources — Theory and Programs, Springer, 2006.
[11] L. Robin, Fonctions sphériques de Legendre et fonctions sphéroïdales, Vols 1–3, Gauthiers-Villars, 1957.
[12] M.I. Mishchenko, L.D. Travis, A.A. Lacis, Scattering, Absorption, and Emission of Light by Small Particles, Cambridge University Press, 2002.

Optics Communications 283 (2010) 3244–3254

Contents lists available at ScienceDirect

Optics Communications

journal homepage: www.elsevier.com/locate/optcom

Transformations of spherical beam shape coefficients in generalized Lorenz–Mie theories through rotations of coordinate systems. IV. Plane waves

G. Gouesbet [a,*], J.J. Wang [a,b], Y.P. Han [b], G.Grehan [a]

[a] Laboratoire d'Electromagnétisme des Systèmes Particulaires (LESP), Unité Mixte de Recherche (UMR), 6614 du Centre National de la Recherche Scientifique (CNRS), Complexe de Recherche Interprofessionnel en Aérothermochimie (CORIA), Université de Rouen, et Institut National des Sciences Appliquées (INSA) de Rouen, BP12, avenue de l'université, technopôle du Madrillet,76801, Saint-Etienne-du Rouvray, France
[b] School of Science, Xidian University, Xi'an, China

ARTICLE INFO

Article history:
Received 8 March 2010
Received in revised form 8 April 2010
Accepted 21 April 2010

ABSTRACT

This paper is the fourth of a series devoted to the transformation of beam shape coefficients through rotations of coordinate systems. These coefficients are required to express electromagnetic fields of laser beams in expanded forms, for instance for use in some generalized Lorenz–Mie theories. The main result of Part I has been the theorem of transformation of beam shape coefficients under rotations. Part II dealt with the special case of on-axis axisymmetric beams. Part III dealt with other special cases, namely when the Euler angles specifying the rotation are given some special values. The present Part IV studies another special case, namely the one of plane waves viewed as special on-axis axisymmetric beams, and can therefore be viewed as a special case of Part II. Unexpectedly, it is found that, in general, although plane waves are fairly trivial, their expansions require using non trivial beam shape coefficients, exactly as required when dealing with arbitrary shaped beams.

1. Introduction

This paper is the fourth one of a series of papers devoted to the study of the transformation of beam shape coefficients, under the rotation of coordinate systems. These coefficients are required to express the electromagnetic fields of laser beams in expanded form, and therefore play an essential role in generalized Lorenz–Mie theories describing the interaction between electromagnetic arbitrary shaped beams and some regular particles. The specific problem under study in this series may be recalled as follows. Let us consider a Cartesian system of coordinates, denoted as $\mathbf{x}=(x, y, z)$, with spherical coordinates (r, θ, φ), called the unrotated system, and let $g^m_{n,\mathrm{TM}}$, $g^m_{n,\mathrm{TE}}$ be the beam shape coefficients for the description of the illuminating beam in this unrotated system. Let us consider a second system of coordinates, called the rotated system, deduced from the unrotated system by a rotation defined by Euler angles (α, β, γ), defined as in [1]. Quantities in the rotated system are denoted by using tilde-decorations. Therefore the Cartesian coordinates of the rotated system are denoted as $\tilde{\mathbf{x}}=(\tilde{x}, \tilde{y}, \tilde{z})$, with spherical coordinates $(\tilde{r}=r, \tilde{\theta}, \tilde{\varphi})$. The beam shape coefficients in the rotated system are denoted as $\tilde{g}^m_{n,\mathrm{TM}}, \tilde{g}^m_{n,\mathrm{TE}}$. The problem is to express the beam shape coefficients in the rotated system in terms of beam shape coefficients in the unrotated system. A general solution to this problem has been found in Part I of the present series of papers [1]. Part II discussed the special case of on-axis axisymmetric beams [2]. In Part III [3], we dealt with the case when the Euler angles are given special values. With this Part IV we return to plane waves, viewed as special cases of on-axisymmetric beams described in Part II. One of the unexpected results of this paper is that these plane waves, in general, i.e. in the case of oblique illumination, requires the use of beam shape coefficients, exactly as in the case of arbitrary shaped beams. This means that they have to be expressed in a framework pertaining to generalized Lorenz–Mie theories.

The paper is organized as follows. Section 2 recalls a few miscellaneous basic ingredients required for the sequel, namely the definition of beam shape coefficients, with some basic mathematical expressions, the definition of on-axis axysimmetric beams, the expressions of electric and fields components in the rotated system, the expressions of electric and magnetic fields in the unrotated system for on-axis axisymmetric beams, various expressions for plane waves under expanded and non-expanded (compact) forms. Section 3 deals with a plane wave in the unrotated system. Section 4 similarly discusses the much more difficult case of plane waves in the rotated system. Section 5 provides a discussion which will also serve as a conclusion.

2. Basic ingredients

2.1. Beam shape coefficients

In this paper, the beam shape coefficients are defined in the framework of the Bromwich formulation, as originally done in the

* Corresponding author.
E-mail address: Gouesbet@coria.fr (G. Gouesbet).

0030-4018/$ – see front matter © 2010 Elsevier B.V. All rights reserved.
doi:10.1016/j.optcom.2010.04.053

GLMT *stricto sensu*, e.g. [4,5]. The incident field is expressed by two Bromwich scalar potentials U^i_{TM} and U^i_{TE} (TM for Transverse Magnetic and TE for Transverse Electric), reading as [4]:

$$U^i_{\mathrm{TM}} = \frac{E_0}{k}\sum_{n=1}^{\infty}\sum_{m=-n}^{+n} c_n^{\mathrm{pw}} g^m_{n,\mathrm{TM}} \Psi_n(kr) P_n^{|m|}(\cos\theta)\exp(im\varphi) \tag{1}$$

$$U^i_{\mathrm{TE}} = \frac{H_0}{k}\sum_{n=1}^{\infty}\sum_{m=-n}^{n} c_n^{\mathrm{pw}} g^m_{n,\mathrm{TE}} \Psi_n(kr) P_n^{|m|}(\cos\theta)\exp(im\varphi) \tag{2}$$

in which the superscript "*i*" stands for "incident". Also, E_0 and H_0 are field strengths, and k is the wave-number in the medium in which the beam propagates. The coefficients c_n^{pw} ("pw" standing for "plane wave") are coefficients which appear naturally in the classical Lorenz–Mie theory and, for this reason, are isolated [6]. They read as:

$$c_n^{\mathrm{pw}} = \frac{1}{k}(-i)^{n+1}\frac{2n+1}{n(n+1)} \tag{3}$$

The functions $\Psi_n(kr)$ are Ricatti–Bessel functions, which may be expressed in terms of spherical Bessel functions $j_n(kr)$ according to:

$$\Psi_n(kr) = krj_n(kr) \tag{4}$$

Let us recall, for further use, that the spherical Bessel functions satisfy:

$$\left[\frac{d^2}{dr^2} + k^2\right](rj_n(kr)) = \frac{n(n+1)}{r} j_n(kr) \tag{5}$$

The expressions for the Bromwich scalar potentials also involve the associated Legendre functions defined as (for m non-negative):

$$P_n^m(\cos\theta) = (-1)^m(\sin\theta)^m\frac{d^m P_n(\cos\theta)}{(d\cos\theta)^m} \tag{6}$$

in which P_n's are Legendre polynomials. They may be uniquely defined, $\forall m\ \mathbf{Z}$, according to [1]:

$$P_n^m(\cos\theta) = (-1)^{\frac{m-|m|}{2}}\frac{(n-|m|)!}{(n-m)!}P_n^{|m|}(\cos\theta) \tag{7}$$

We may then consider that Eqs. (1) and (2) serve as a definition of the beam shape coefficients $g^m_{n,X}$, with $X=$TM or TE. The relationship between the scalar Bromwich formulation and a formulation in terms of vector spherical wave functions (VSWFs) is discussed elsewhere, for instance in Part I [1].

2.2. Beam shape coefficients for on-axis axisymmetric beams and plane waves

On-axis axisymmetric beams satisfy the following relations [2,7]:

$$g^m_{n,X} = 0, |m|\neq 1 \tag{8}$$

$$g^1_{n,\mathrm{TM}} = \frac{1}{K}g^{-1}_{n,\mathrm{TM}} = -i\varepsilon g^1_{n,\mathrm{TE}} = \frac{i\varepsilon}{K}g^{-1}_{n,\mathrm{TE}} = \frac{g_n}{2} \tag{9}$$

Eq. (9) defines a set $\{g_n\}$ of special beam shape coefficients g_n and shows that the double set $\{g^m_{n,\mathrm{TM}}, g^m_{n,\mathrm{TE}}\}$ of beam shape coefficients, with two subscripts (n,m) reduces to a single set $\{g_n\}$ with a single coefficient n. It happens that Eq. (9) with $(\varepsilon, K)=(-1,+1)$ is structurally identical with the set of equations obtained for an on-axis Gaussian beam polarized in the x direction at its focal waist [4,6,8]. We then have:

$$g^1_{n,\mathrm{TM}} = g^{-1}_{n,\mathrm{TM}} = ig^1_{n,\mathrm{TE}} = -ig^{-1}_{n,\mathrm{TE}} = \frac{g_n}{2} \tag{10}$$

The case of on-axis axisymmetric beams is assumed to hold for the unrotated system (before applying Euler angles (α, β, γ)). In the rotated system, the special beam shape coefficients g_n of Eqs. (9) and (10), give birth to a new set of beam shape coefficients $\left\{\widetilde{g^m_{n,\mathrm{TM}}}, \widetilde{g^m_{n,\mathrm{TE}}}\right\}$. We then have the following relationships [2]:

$$\widetilde{g^m_{n,\mathrm{TM}}} = (-1)^m(-1)^{\frac{m-|m|}{2}}\frac{(n-|m|)!}{(n+m)!}e^{im\gamma}g_n \left[im\sin\alpha\pi_n^m(\cos\beta) + \cos\alpha\tau_n^m(\cos\beta)\right] \tag{11}$$

$$\widetilde{g^m_{n,\mathrm{TE}}} = (-1)^{m+1}(-1)^{\frac{m-|m|}{2}}\frac{(n-|m|)!}{(n+m)!}e^{im\gamma}g_n \left[im\cos\alpha\pi_n^m(\cos\beta) - \sin\alpha\tau_n^m(\cos\beta)\right] \tag{12}$$

in which π_n^m and τ_n^m are generalized Legendre functions reading as:

$$\pi_n^m(\cos\beta) = \frac{P_n^m(\cos\beta)}{\sin\beta} \tag{13}$$

$$\tau_n^m(\cos\beta) = \frac{dP_n^m(\cos\beta)}{d\beta} \tag{14}$$

Let us now assume that we are dealing with plane waves. Then, the special beam shape coefficients g_n may be taken equal to 1 or, more generally, are equal to phase factors of the form $\exp(ikz_0)$.e.g. [4,6]. In any case, they are constant terms which do not depend any more on the subscript n. Therefore, we may make the change: $gn\rightarrow g$.

Furthermore, from Eq. (7), we have:

$$\begin{pmatrix}\pi_n^m(\cos\beta)\\ \tau_n^m(\cos\beta)\end{pmatrix} = (-1)^{\frac{m-|m|}{2}}\frac{(n-|m|)!}{(n-m)!}\begin{pmatrix}\pi_n^{|m|}(\cos\beta)\\ \tau_n^{|m|}(\cos\beta)\end{pmatrix} \tag{15}$$

Inserting Eq. (15) into Eq. (11), we obtain, for a plane wave:

$$\widetilde{g^m_{n,\mathrm{TM}}} = g(-1)^m\frac{[(n-|m|)!]^2}{(n+m)!(n-m)!}e^{im\gamma} \left[im\sin\alpha\pi_n^{|m|}(\cos\beta) + \cos\alpha\tau_n^{|m|}(\cos\beta)\right] \tag{16}$$

But we have:

$$\frac{[(n-|m|)!]^2}{(n+m)!(n-m)!} = \frac{(n-|m|)!}{(n+|m|)!} \tag{17}$$

Hence, Eq. (16) simplifies to:

$$\widetilde{g^m_{n,\mathrm{TM}}} = g(-1)^m\frac{(n-|m|)!}{(n+|m|)!}e^{im\gamma} \left[im\sin\alpha\pi_n^{|m|}(\cos\beta) + \cos\alpha\tau_n^{|m|}(\cos\beta)\right] \tag{18}$$

Similarly, Eq. (12) becomes:

$$\widetilde{g^m_{n,\mathrm{TE}}} = g(-1)^{m+1}\frac{(n-|m|)!}{(n+|m|)!}e^{im\gamma} \left[im\cos\alpha\pi_n^{|m|}(\cos\beta) - \sin\alpha\tau_n^{|m|}(\cos\beta)\right] \tag{19}$$

Eqs. (18) and (19) exhibit a somewhat unexpected result announced in the Introduction, namely that, in general, the description of the plane wave in the rotated system requires the use of beam shape coefficients

(a double set of beam shape coefficients), as for arbitrary shaped beams, in contrast with the easy degenerated description in the unrotated system.

2.3. Electric and magnetic fields in the rotated system

The electric and magnetic fields, in expanded forms, in the rotated system are exactly the ones obtained in the general framework of spherical GLMTs, although, from a notational point of view, the beam shape coefficients are tilde-decorated in the rotated system. Relevant references are [4] and [9]. The most efficient one is [10]. Electric field components are also explicitly given in [11].The expressions read as:

$$E_r^i = kE_0 \sum_{n=1}^{\infty} \sum_{m=-n}^{n} c_n^{\mathrm{pw}} \widetilde{g_{n,\mathrm{TM}}^m} \left[\Psi_n''(kr) + \Psi_n(kr)\right] P_n^{|m|}(\cos\theta) e^{im\varphi} \tag{20}$$

$$E_\theta^i = \frac{E_0}{r} \sum_{n=1}^{\infty} \sum_{m=-n}^{n} c_n^{\mathrm{pw}} [\widetilde{g_{n,\mathrm{TM}}^m} \Psi_n'(kr) \tau_n^{|m|}(\cos\theta) + m\widetilde{g_{n,\mathrm{TE}}^m} \Psi_n(kr) \pi_n^{|m|}(\cos\theta)] e^{im\varphi} \tag{21}$$

$$E_\varphi^i = \frac{iE_0}{r} \sum_{n=1}^{\infty} \sum_{m=-n}^{n} c_n^{\mathrm{pw}} [m\widetilde{g_{n,\mathrm{TM}}^m} \Psi_n'(kr) \pi_n^{|m|}(\cos\theta) + \widetilde{g_{n,\mathrm{TE}}^m} \Psi_n(kr) \tau_n^{|m|}(\cos\theta)] e^{im\varphi} \tag{22}$$

$$H_r^i = kH_0 \sum_{n=1}^{\infty} \sum_{m=-n}^{n} c_n^{\mathrm{pw}} \widetilde{g_{n,\mathrm{TE}}^m} \left[\Psi_n''(kr) + \Psi_n(kr)\right] P_n^{|m|}(\cos\theta) e^{im\varphi} \tag{23}$$

$$H_\theta^i = \frac{H_0}{r} \sum_{n=1}^{\infty} \sum_{m=-n}^{n} c_n^{\mathrm{pw}} \left[\widetilde{g_{n,\mathrm{TE}}^m} \Psi_n'(kr) \tau_n^{|m|}(\cos\theta) - m\widetilde{g_{n,\mathrm{TM}}^m} \Psi_n(kr) \pi_n^{|m|}(\cos\theta)\right] e^{im\varphi} \tag{24}$$

$$H_\varphi^i = \frac{iH_0}{r} \sum_{n=1}^{\infty} \sum_{m=-n}^{n} c_n^{\mathrm{pw}} \left[m\widetilde{g_{n,\mathrm{TE}}^m} \Psi_n'(kr) \pi_n^{|m|}(\cos\theta) - \widetilde{g_{n,\mathrm{TM}}^m} \Psi_n(kr) \tau_n^{|m|}(\cos\theta)\right] e^{im\varphi} \tag{25}$$

in which the tilde-decorated beam shape coefficients $\widetilde{g_{n,X}^m}$ are expressed by Eqs. (11) and (12) in terms of special beam shape coefficients g_n when the beam in the unrotated system is an on-axis axisymmetric beam, and by Eqs. (18) and (19) in terms of a degenerated special beam shape coefficient g when the beam in the unrotated system is a plane wave. The other quantities in the set of equations have been defined previously, see Eqs. (3), (4), (6), (13) and (14).

2.4. Electric and magnetic fields in the unrotated system

For the time being, we assume that the beam in the unrotated system is an on-axis axisymmetric beam, expressed in terms of special beam shape coefficients g_n (not tilde-decorated) satisfying Eq. (10). The electric and magnetic field components may then have been derived from Eqs. (20)–(25) above (tilde-decorations removed), and are also available from elsewhere, e.g. [7]. They read as:

$$E_r^i = \frac{E_0}{r} \cos\varphi \sum_{n=1}^{\infty} c_n^{\mathrm{pw}} g_n n(n+1) j_n(kr) P_n^1(\cos\theta) \tag{26}$$

$$E_\theta^i = \frac{E_0}{r} \cos\varphi \sum_{n=1}^{\infty} c_n^{\mathrm{pw}} g_n \left[\frac{dr j_n(kr)}{dr} \tau_n(\cos\theta) - ikr j_n(kr) \pi_n(\cos\theta)\right] \tag{27}$$

$$E_\varphi^i = -\frac{E_0}{r} \sin\varphi \sum_{n=1}^{\infty} c_n^{\mathrm{pw}} g_n \left[\frac{dr j_n(kr)}{dr} \pi_n(\cos\theta) - ikr j_n(kr) \tau_n(\cos\theta)\right] \tag{28}$$

$$H_r^i = \frac{H_0}{r} \sin\varphi \sum_{n=1}^{\infty} c_n^{\mathrm{pw}} g_n n(n+1) j_n(kr) P_n^1(\cos\theta) \tag{29}$$

$$H_\theta^i = \frac{H_0}{r} \sin\varphi \sum_{n=1}^{\infty} c_n^{\mathrm{pw}} g_n \left[\frac{dr j_n(kr)}{dr} \tau_n(\cos\theta) - ikr j_n(kr) \pi_n(\cos\theta)\right] \tag{30}$$

$$H_\varphi^i = \frac{H_0}{r} \cos\varphi \sum_{n=1}^{\infty} c_n^{\mathrm{pw}} g_n \left[\frac{dr j_n(kr)}{dr} \pi_n(\cos\theta) - ikr j_n(kr) \tau_n(\cos\theta)\right] \tag{31}$$

in which $\pi_n = \pi_n^1$ and $\tau_n = \tau_n^1$.

Let us remark that these expressions satisfy:

$$\frac{E_r^i}{H_r^i} = \frac{E_\theta^i}{H_\theta^i} = \frac{E_0 \cos\varphi}{H_0 \sin\varphi} \tag{32}$$

$$\frac{E_\varphi^i}{H_\varphi^i} = -\frac{E_0 \sin\varphi}{H_0 \cos\varphi} \tag{33}$$

These relations however are not valid in the general case (in particular in the rotated system).

2.5. Plane wave expressions

Here is an expression for the expansion of a general plane wave $e^{i\mathbf{k}\cdot\mathbf{r}}$ [12]:

$$e^{i\mathbf{k}\cdot\mathbf{r}} = 4\pi \sqrt{\frac{\pi}{2}} \frac{1}{k} \sum_{n=0}^{\infty} \sum_{m=-n}^{n} i^n Y_n^{m*}(\theta_k, \varphi_k) \varphi_{knm}^{(0)}(\mathbf{r}) \tag{34}$$

in which the star denotes a complex conjugation, θ_k, φ_k denote polar angles in the wave-number space, Y_n^m's are spherical harmonics, and:

$$\varphi_{knm}^{(0)}(\mathbf{r}) = \sqrt{\frac{2}{\pi}} k j_n(kr) Y_n^m(\theta, \varphi) \tag{35}$$

are free spherical waves.

Eq. (34) can be rewritten as:

$$e^{i\mathbf{k}\cdot\mathbf{r}} = 4\pi \sum_{n=0}^{\infty} \sum_{m=-n}^{n} i^n j_n(kr) Y_n^{m*}(\theta_k, \varphi_k) Y_n^m(\theta, \varphi) \tag{36}$$

Rather than $e^{i\mathbf{k}\cdot\mathbf{r}}$, we shall actually need $e^{-i\mathbf{k}\cdot\mathbf{r}}$, reading as:

$$e^{-i\mathbf{k}\cdot\mathbf{r}} = 4\pi \sum_{n=0}^{\infty} \sum_{m=-n}^{n} (-i)^n j_n(kr) Y_n^m(\theta_k, \varphi_k) Y_n^{m*}(\theta, \varphi) \tag{37}$$

In the same way that there is a unique form to express P_n^m, $\forall m \in \mathbf{Z}$, there is a unique form to express the spherical harmonics, reading as:

$$Y_n^m(\theta, \varphi) = (-1)^{\frac{m-|m|}{2}} \sqrt{\frac{2n+1}{4\pi}} \sqrt{\frac{(n-|m|)!}{(n+|m|)!}} P_n^{|m|}(\cos\theta) e^{im\varphi} \tag{38}$$

that can be established from the unique form for P_n^m together with the definition of the spherical harmonics.

Inserting Eq. (38) into Eq. (37), we obtain:

$$e^{-i\mathbf{k}\cdot\mathbf{r}} = \sum_{n=0}^{\infty} \sum_{m=-n}^{n} (-i)^n (2n+1) \frac{(n-|m|)!}{(n+|m|)!} j_n(kr) P_n^{|m|}(\cos\theta_k) P_n^{|m|}(\cos\theta) e^{im\varphi_k} e^{-im\varphi} \tag{39}$$

For further use, it is convenient to make a change of subscript ($m \to -m$) leading to:

$$e^{-i\mathbf{k}\cdot\mathbf{r}} = \sum_{n=0}^{\infty} \sum_{m=-n}^{n} (-i)^n (2n+1) \frac{(n-|m|)!}{(n+|m|)!} j_n(kr) P_n^{|m|}(\cos\theta_k) P_n^{|m|}(\cos\theta) e^{-im\varphi_k} e^{im\varphi} \tag{40}$$

It is important to remark, for further use, that the term ($n=0$) in this summation is equal to $j_0(kr) = \sin(kr)/(kr)$, see [13], i.e. does not

depend on any angular coordinate. Therefore, it does not play any role in any derivation with respect to an angular variable.

We shall also need another form for $\exp(-i\mathbf{k}\cdot\mathbf{r})$, i.e. a non-expanded one. Let us set:

$$\mathbf{k} = \left(k_x, k_y, k_z\right) \tag{41}$$

in Cartesian coordinates in the wave-number space and, in spherical coordinates in the wave-number space:

$$\mathbf{k} = (k, \theta_k, \varphi_k) = (k, \beta, \gamma_k) \tag{42}$$

in which we have conveniently introduced, for further use, the change of variables: $\theta_k \to \beta$, $\varphi_k \to \gamma_k$.

We have:

$$\left.\begin{aligned} k_x &= k\sin\beta\cos\gamma_k \\ k_y &= k\sin\beta\sin\gamma_k \\ k_z &= k\cos\beta \end{aligned}\right\} \tag{43}$$

In the physical space, we have:

$$\left.\begin{aligned} x &= r\sin\theta\cos\varphi \\ y &= r\sin\theta\sin\varphi \\ z &= r\cos\theta \end{aligned}\right\} \tag{44}$$

So that:

$$e^{-i\mathbf{k}\cdot\mathbf{r}} = \exp\{-ikr[\sin\beta\sin\theta(\cos\gamma_k\cos\varphi + \sin\gamma_k\sin\varphi) + \cos\beta\cos\theta]\} \tag{45}$$

Furthermore, with the change of notations just introduced above, and isolating the $(n=0)$-term, Eq. (40) becomes:

$$\begin{aligned} e^{-i\mathbf{k}\cdot\mathbf{r}} = {} & \frac{\sin kr}{kr} \\ & + \sum_{n=1}^{\infty}\sum_{m=-n}^{n}(-i)^n(2n+1)\frac{(n-|m|)!}{(n+|m|)!}j_n(kr) \\ & P_n^{|m|}(\cos\beta)P_n^{|m|}(\cos\theta)e^{-im\gamma_k}e^{im\varphi} \end{aligned} \tag{46}$$

As an interesting special case, we may consider Eq. (45) for $\beta=0$. We then have [14]:

$$\begin{aligned} e^{-ikr\cos\theta} &= \sum_{n=0}^{\infty}(-i)^n(2n+1)j_n(kr)P_n(\cos\theta) \\ &= \frac{\sin kr}{kr} + \sum_{n=1}^{\infty}(-i)^n(2n+1)j_n(kr)P_n(\cos\theta) \end{aligned} \tag{47}$$

which can also be rewritten as:

$$e^{-ikr\cos\theta} = \sum_{n=0}^{\infty} c_n^{\mathrm{pw}} n(n+1)ikj_n(kr)P_n(\cos\theta) \tag{48}$$

in which we have used Eq. (3).

3. Plane wave in the unrotated system

3.1. Compact forms

In the unrotated system $\mathbf{x}=(x, y, z)$ with spherical coordinates (r, θ, φ), we consider a plane wave. This plane wave, and many expressions below, can be obtained from a Gaussian beam with a beam radius going to infinite studied in [8,15].

In Cartesian coordinates, the plane wave is described by the following relations:

$$\left.\begin{aligned} E_x^i &= E_0 e^{-ikz} & H_x^i &= 0 \\ E_y^i &= 0 & H_y^i &= H_0 e^{-ikz} \\ E_z^i &= 0 & H_z^i &= 0 \end{aligned}\right\} \tag{49}$$

in which H_0/E_0 is a certain physical constant that we do not need to define (see [15]).

The components in spherical coordinates then read as, in compact forms:

$$E_r^i = E_0\cos\varphi\sin\theta e^{-ikr\cos\theta} \tag{50}$$

$$E_\theta^i = E_0\cos\varphi\cos\theta e^{-ikr\cos\theta} \tag{51}$$

$$E_\varphi^i = -E_0\sin\varphi e^{-ikr\cos\theta} \tag{52}$$

$$H_r^i = H_0\sin\varphi\sin\theta e^{-ikr\cos\theta} \tag{53}$$

$$H_\theta^i = H_0\sin\varphi\cos\theta e^{-ikr\cos\theta} \tag{54}$$

$$H_\varphi^i = H_0\cos\varphi e^{-ikr\cos\theta} \tag{55}$$

3.2. Expanded forms

The corresponding expanded forms are given by Eqs. (38)–(43) in [15], with the proviso that we have to replace the special beam shape coefficients g_n by a constant g, i.e. a constant phase term of the form $\exp(ikz_0)$ that we may conveniently take equal to 1, or absorb in E_0 and H_0. From Eqs. (38)–(43) in [15], and using also Eqs. (3) and (5), the expanded forms can be rewritten as:

$$E_{r*}^i = \frac{E_0}{r}\cos\varphi\sum_{n=1}^{\infty} c_n^{\mathrm{pw}} n(n+1)j_n(kr)P_n^1(\cos\theta) \tag{56}$$

$$E_{\theta*}^i = \frac{E_0}{r}\cos\varphi\sum_{n=1}^{\infty} c_n^{\mathrm{pw}}\left[\frac{drj_n(kr)}{dr}\tau_n(\cos\theta) - ikrj_n(kr)\pi_n(\cos\theta)\right] \tag{57}$$

$$E_{\varphi*}^i = -\frac{E_0}{r}\sin\varphi\sum_{n=1}^{\infty} c_n^{\mathrm{pw}}\left[\frac{drj_n(kr)}{dr}\pi_n(\cos\theta) - ikrj_n(kr)\tau_n(\cos\theta)\right] \tag{58}$$

$$H_{r*}^i = \frac{H_0}{r}\sin\varphi\sum_{n=1}^{\infty} c_n^{\mathrm{pw}} n(n+1)j_n(kr)P_n^1(\cos\theta) \tag{59}$$

$$H_{\theta*}^i = \frac{H_0}{r}\sin\varphi\sum_{n=1}^{\infty} c_n^{\mathrm{pw}}\left[\frac{drj_n(kr)}{dr}\tau_n(\cos\theta) - ikrj_n(kr)\pi_n(\cos\theta)\right] \tag{60}$$

$$H_{\varphi*}^i = \frac{H_0}{r}\cos\varphi\sum_{n=1}^{\infty} c_n^{\mathrm{pw}}\left[\frac{drj_n(kr)}{dr}\pi_n(\cos\theta) - ikrj_n(kr)\tau_n(\cos\theta)\right] \tag{61}$$

Eqs. (56)–(61) are, coherently, special cases of Eqs. (26)–(31) with $g_n \to 1$. Also, we used a star subscript to distinguish compact and expanded forms. Due to the coherence of the Bromwich formalism and to the fact that plane waves exactly satisfy Maxwell's equations (which is generically not the case for the description of arbitrary shaped beams, e.g. [15]), corresponding compact and expanded forms must be strictly equal. This is most easy to demonstrate for radial components (the privileged ones since they are sufficient to determine the beam shape coefficients, e.g. [4]), but more tricky for angular components, as we are going to see. The sequel of this section will also provide us with a training for the more complicated case of fields in the rotated system.

3.3. Equality between compact and expanded radial components

For the radial electric component, let us start from Eq. (56). We then use $P_n^1 = \mathrm{d}P_n/\mathrm{d}\theta$, Eqs. (3) and (47) to readily establish:

$$E_{r*}^i = \frac{-iE_0}{kr}\cos\varphi\frac{\partial}{\partial\theta}e^{-ikr\cos\theta} = E_0\cos\varphi\sin\theta e^{-ikr\cos\theta} = E_r^i \tag{62}$$

as it should.

Similarly, starting from Eq. (59), we readily establish:

$$H_{r*}^i = \frac{-iH_0}{kr}\sin\varphi\frac{\partial}{\partial\theta}e^{-ikr\cos\theta} = H_0\sin\varphi\sin\theta e^{-ikr\cos\theta} = H_r^i \tag{63}$$

3.4. Equality between compact and expanded angular components

Let us now consider the electric θ–component. We must have:

$$E_{\theta*}^i = E_\theta^i \tag{64}$$

that is to say, from Eqs. (57) and (51):

$$\sum_{n=1}^{\infty} c_n^{\mathrm{pw}}\left[\frac{drj_n(kr)}{dr}\tau_n(\cos\theta) - ikrj_n(kr)\pi_n(\cos\theta)\right] = r\cos\theta e^{-ikr\cos\theta} \tag{65}$$

To prove this equality, we use a technique similar to the one previously invented in [15]. Let us rewrite Eq. (65) under the form:

$$A_\theta + B_\theta = R_\theta \tag{66}$$

in which:

$$A_\theta = \sum_{n=1}^{\infty} c_n^{\mathrm{pw}}\frac{drj_n(kr)}{dr}\tau_n(\cos\theta) \tag{67}$$

$$B_\theta = -ikr\sum_{n=1}^{\infty} c_n^{\mathrm{pw}} j_n(kr)\pi_n(\cos\theta) \tag{68}$$

$$R_\theta = r\cos\theta e^{-ikr\cos\theta} \tag{69}$$

Now, we derive A_θ with respect to r, and use Eq. (5), yielding:

$$\frac{\partial A_\theta}{\partial r} = \sum_{n=1}^{\infty} c_n^{\mathrm{pw}}\frac{n(n+1)}{r}j_n(kr)\tau_n(\cos\theta) - k^2\sum_{n=1}^{\infty} c_n^{\mathrm{pw}} rj_n(kr)\tau_n(\cos\theta) \tag{70}$$

In the first term of the r.h.s., we express τ_n versus P_n, according to $\tau_n = \mathrm{d}P_n^1/\mathrm{d}\theta = \mathrm{d}^2P_n/\mathrm{d}\theta^2$, invoke Eq. (48) and obtain:

$$\frac{\partial A_\theta}{\partial r} = \frac{1}{ikr}\frac{\partial^2}{\partial\theta^2}e^{-ikr\cos\theta} - k^2\sum_{n=1}^{\infty} c_n^{\mathrm{pw}} rj_n(kr)\tau_n(\cos\theta) \tag{71}$$

Deriving again with respect to r, we obtain:

$$\frac{\partial^2 A_\theta}{\partial r^2} = \frac{1}{ik}\frac{\partial}{\partial r}\frac{1}{r}\frac{\partial^2}{\partial\theta^2}e^{-ikr\cos\theta} - k^2 A_\theta \tag{72}$$

This implies:

$$\left(\frac{\partial^2}{\partial r^2} + k^2\right)A_\theta = \left(ik + k^2 r\cos\theta - 2ik\cos^2\theta - k^2 r\cos^3\theta\right)e^{-ikr\cos\theta} \tag{73}$$

For B_θ, we derive it immediately twice with respect to r, use Eq. (5), express π_n versus P_n^1 and afterward P_n^1 versus P_n, invoke Eq. (48), and obtain:

$$\left(\frac{\partial^2}{\partial r^2} + k^2\right)B_\theta = -ike^{-ikrcos\theta} \tag{74}$$

For R_θ, we readily have:

$$\left(\frac{\partial^2}{\partial r^2} + k^2\right)R_\theta = -k\cos\theta\left(-kr + 2i\cos\theta + kr\cos^2\theta\right)e^{-ikr\cos\theta} \tag{75}$$

Next, from Eqs. (73), (74), and (75), we may check that:

$$\left[\frac{\partial^2}{\partial r^2} + k^2\right](A_\theta + B_\theta - R_\theta) = 0 \tag{76}$$

We therefore have:

$$A_\theta + B_\theta = R_\theta + F_\theta \tag{77}$$

in which $F_\theta = F(r,\theta)$ satisfies the following differential equation:

$$\left(\frac{\partial^2}{\partial r^2} + k^2\right)F(r,\theta) = 0 \tag{78}$$

The general solution of Eq. (78) reads as:

$$F(r,\theta) = C(\theta)\cos kr + S(\theta)\sin kr \tag{79}$$

Eq. (77) may therefore be rewritten as:

$$\sum_{n=1}^{\infty} c_n^{\mathrm{pw}}\left[\frac{drj_n(kr)}{dr}\tau_n(\cos\theta) - ikrj_n(kr)\pi_n(\cos\theta)\right] = r\cos\theta e^{-ikr\cos\theta} + C(\theta)\cos kr + S(\theta)\sin kr \tag{80}$$

We are now going to prove that $C(\theta) = S(\theta) = 0$, therefore establishing the validity of Eq. (65). We begin by considering the limit of Eq. (80) when $(kr) = 0$. We have the fact that [13,16]:

$$j_n(0) = 0, n > 0 \tag{81}$$

Furthermore, the derivatives of $j_n(kr)$ with respect to (kr) are finite. Therefore:

$$\left[\frac{drj_n(kr)}{dr}\right]_{r=0} = \left[j_n(kr) + r\frac{dj_n(kr)}{dr}\right]_{r=0} = j_n(0) = 0, n > 0 \tag{82}$$

Then, for $r = 0$, Eq. (80) implies:

$$C(\theta) = 0 \tag{83}$$

To deal with $S(\theta)$, we derive Eq. (80) with respect to r, take advantage of our previous result of Eq. (83), and obtain:

$$\sum_{n=1}^{\infty} c_n^{\mathrm{pw}}\left[\frac{d^2rj_n(x)}{dr^2}\tau_n(\cos\theta) - i\frac{drj_n(kr)}{dr}\pi_n(\cos\theta)\right] = \frac{\cos\theta}{k}e^{-ikr\cos\theta}(1 - ikr\cos\theta) + kS(\theta)\cos kr \tag{84}$$

We afterward use Eq. (5) rewritten under the form:

$$\frac{d^2rj_n(kr)}{dr^2} = \frac{n(n+1)}{kr}j_n(kr) - krj_n(kr) \tag{85}$$

and substitute it into Eq. (84). The l.h.s of the obtained result reads as:

$$LHS = \sum_{n=1}^{\infty} c_n^{\mathrm{pw}} \left\{ \left[\frac{n(n+1)}{kr} - kr \right] j_n(kr)\tau_n(\cos\theta) - i\left[j_n(kr) + r\frac{dj_n(kr)}{dr} \right] \pi_n(\cos\theta) \right\} \tag{86}$$

becoming, for $r=0$:

$$(LHS)_{r=0} = \sum_{n=1}^{\infty} c_n^{\mathrm{pw}} \left[\frac{n(n+1)}{kr} j_n(kr)\tau_n(\cos\theta) \right]_{r=0} \tag{87}$$

We express τ_n versus P_n, invoke Eq. (48), and obtain:

$$\begin{aligned}(LHS)_{r=0} &= \left[\frac{-i}{k^2 r}\frac{\partial^2}{\partial\theta^2} e^{-ikr\cos\theta} \right]_{r=0} \\ &= \frac{-i}{k}\left\{ \left[i\cos\theta - kr + kr\cos^2\theta \right] e^{-ikr\cos\theta} \right\}_{r=0} \\ &= \frac{\cos\theta}{k}\end{aligned} \tag{88}$$

This is to be compared with the r.h.s. of Eq. (84), for $r=0$, reading as:

$$RHS = \frac{\cos\theta}{k} + kS(\theta) \tag{89}$$

Hence:

$$S(\theta) = 0 \tag{90}$$

so that we are done. The electric φ–component would be treated quite similarly. And, for magnetic field components, it is easy to show that the problems they raise are equivalent to the ones solved for the electric components.

We end this section with a remark on strategy: in the case of radial components, we have been able to go from a known expanded form to a compact form, without the need to know the compact form. Conversely, in what we have done above for the angular components, we have shown the validity of equations relating an expanded form and a compact one, both forms having to be known. This difference of strategy is to be kept in mind because it will be preserved in the next section.

4. Plane wave in the rotated system

We now examine the plane wave in the rotated system. Insofar as there will not be any ambiguity, we conveniently omit the tilde-decorations. We essentially follow the same line of exposition than in the previous section, but are dealing with more complicated calculations which, most often, should better be made by using a symbolic computation software. In the previous section, computations could be hand-made, serving as exercises for the present section, beside its own interest.

4.1. Compact forms

In the original unrotated system, the field components given by Eq. (49) may be rewritten as:

$$\mathbf{E}^i = E_0 e^{-i\mathbf{k}\cdot\mathbf{r}}\mathbf{x} \tag{91}$$

$$\mathbf{H}^i = H_0 e^{-i\mathbf{k}\cdot\mathbf{r}} y \tag{92}$$

in which $\mathbf{x}$ and $\mathbf{y}$ are unit vectors along the x- and y-directions of the unrotated Cartesian system (x, y, z). Also, note that $\mathbf{k}\cdot\mathbf{r}$ is an invariant (a scalar product) whose expression in the unrotated system is kz but which is now convenient to express in its invariant form.

After the first rotation by an angle α (revise the definition of Euler angles in [1]), the vector $\mathbf{x}$ is transformed as:

$$\mathbf{x} = \cos\alpha\mathbf{x}_\alpha - \sin\alpha\mathbf{y}_\alpha \tag{93}$$

in which $\mathbf{x}_\alpha$ and $\mathbf{y}_\alpha$ are unit vectors along the x_α- and y_α-directions of the Cartesian coordinate system $(x_\alpha, y_\alpha, z_\alpha)$ generated by the α-rotation. Inserting Eq. (93) into Eq. (91), the electric field becomes:

$$\mathbf{E}^i = E_0(\cos\alpha\mathbf{x}_\alpha - \sin\alpha\mathbf{y}_\alpha)e^{-i\mathbf{k}\cdot\mathbf{r}} \tag{94}$$

Carrying out the second rotation with an angle β, the unit vectors $\mathbf{x}_\alpha$ and $\mathbf{y}_\alpha$ are transformed according to:

$$\mathbf{x}_\alpha = \cos\beta\mathbf{x}_\beta + \sin\beta\mathbf{z}_\beta \tag{95}$$

$$\mathbf{y}_\alpha = \mathbf{y}_\beta \tag{96}$$

in which $\mathbf{x}_\alpha$, $\mathbf{y}_\alpha$, and $\mathbf{z}_\alpha$ are unit vectors defined in the now obvious way. The electric field now reads as:

$$\mathbf{E}^i = E^i_{x_\beta}\mathbf{x}_\beta + E^i_{y_\beta}\mathbf{y}_\beta + E^i_{z_\beta}\mathbf{z}_\beta \tag{97}$$

in which:

$$E^i_{x_\beta} = E_0\cos\alpha\cos\beta e^{-i\mathbf{k}\cdot\mathbf{r}} \tag{98}$$

$$E^i_{y_\beta} = -E_0\sin\alpha e^{-i\mathbf{k}\cdot\mathbf{r}} \tag{99}$$

$$E^i_{z_\beta} = E_0\cos\alpha\sin\beta e^{-i\mathbf{k}\cdot\mathbf{r}} \tag{100}$$

We now proceed to the third rotation for which:

$$\mathbf{x}_\beta = \cos\gamma\mathbf{x}_\gamma - \sin\gamma\mathbf{y}_\gamma \tag{101}$$

$$\mathbf{y}_\beta = \sin\gamma\mathbf{x}_\gamma + \cos\gamma\mathbf{y}_\gamma \tag{102}$$

$$\mathbf{z}_\beta = \mathbf{z}_\gamma \tag{103}$$

and establish, similarly as before:

$$\mathbf{E}^i = E^i_{x_\gamma}\mathbf{x}_\gamma + E^i_{y_\gamma}\mathbf{y}_\gamma + E^i_{z_\gamma}\mathbf{z}_\gamma \tag{104}$$

in which:

$$E^i_{x_\gamma} = E_0(\cos\alpha\cos\beta\cos\gamma - \sin\alpha\sin\gamma)e^{-i\mathbf{k}\cdot\mathbf{r}} \tag{105}$$

$$E^i_{y_\gamma} = -E_0(\sin\alpha\cos\gamma + \cos\alpha\cos\beta\sin\gamma)e^{-i\mathbf{k}\cdot\mathbf{r}} \tag{106}$$

$$E^i_{z_\gamma} = E_0\cos\alpha\sin\beta e^{-i\mathbf{k}\cdot\mathbf{r}} \tag{107}$$

Omitting tilde-decorations for the rotated system, we may then evaluate the electric radial field component in the rotated system, from Eqs. (105)–(107), according to:

$$E^i_r = E^i_{x_\gamma}\cos\varphi\sin\theta + E^i_{y_\gamma}\sin\varphi\sin\theta + E^i_{z_\gamma}\cos\theta \tag{108}$$

leading to:

$$E_r^i = E_0 e^{-i\mathbf{k}\cdot\mathbf{r}}\{\sin\alpha\sin\theta[-\sin\gamma\cos\varphi-\cos\gamma\sin\varphi] - \cos\alpha\sin\theta\cos\beta[\sin\gamma\sin\varphi-\cos\gamma\cos\varphi] + \cos\alpha\sin\beta\cos\theta\} \quad (109)$$

Similarly, the angular components of the electric field are found to be:

$$E_\theta^i = E_{x_\gamma}^i\cos\varphi\cos\theta + E_{y_\gamma}^i\sin\varphi\cos\theta - E_{z_\gamma}^i\sin\theta \quad (110)$$

becoming:

$$E_\theta^i = E_0 e^{-i\mathbf{k}\cdot\mathbf{r}}[\cos\alpha\cos\beta\cos\theta(\cos\gamma\cos\varphi-\sin\gamma\sin\varphi) - \sin\alpha\cos\theta(\sin\gamma\cos\varphi+\sin\varphi\cos\gamma] - \cos\alpha\sin\beta\sin\theta] \quad (111)$$

and:

$$E_\varphi^i = -E_{x_\gamma}^i\sin\varphi + E_{y_\varphi}^i\cos\varphi \quad (112)$$

becoming:

$$E_\varphi^i = -E_0 e^{-i\mathbf{k}\cdot\mathbf{r}}[\cos\alpha\cos\beta(\cos\gamma\sin\varphi+\sin\gamma\cos\varphi) + \sin\alpha(\cos\gamma\cos\varphi-\sin\gamma\sin\varphi)] \quad (113)$$

For the radial magnetic field, we may proceed similarly as for the radial electric field, starting from Eq. (92), and obtain:

$$H^i = H_{x_\gamma}^i\mathbf{x}_\gamma + H_{y_\gamma}^i\mathbf{y}_\gamma + H_{z_\gamma}^i\mathbf{z}_\gamma \quad (114)$$

in which:

$$H_{x_\gamma}^i = H_0(\sin\alpha\cos\beta\cos\gamma+\cos\alpha\sin\gamma)e^{-i\mathbf{k}\cdot\mathbf{r}} \quad (115)$$

$$H_{y_\gamma}^i = H_0(\cos\alpha\cos\gamma-\sin\alpha\cos\beta\sin\gamma)e^{-i\mathbf{k}\cdot\mathbf{r}} \quad (116)$$

$$H_{z_\gamma}^i = \sin\alpha\sin\beta e^{-i\mathbf{k}\cdot\mathbf{r}} \quad (117)$$

Afterward, we have:

$$H_r^i = H_{x_\gamma}^i\cos\varphi\sin\theta + H_{y_\gamma}^i\sin\varphi\sin\theta + H_{z_\gamma}^i\cos\theta \quad (118)$$

that is to say:

$$H_r^i = H_0 e^{-i\mathbf{k}\cdot\mathbf{r}}\{\cos\alpha\sin\theta[\sin\gamma\cos\varphi+\cos\gamma\sin\varphi] + \sin\alpha\sin\theta\cos\beta[\cos\gamma\cos\varphi-\sin\gamma\sin\varphi] + \sin\alpha\sin\beta\cos\theta\} \quad (119)$$

For the angular components, we find:

$$H_\theta^i = H_{x_\gamma}^i\cos\varphi\cos\theta + H_{y_\gamma}^i\sin\varphi\cos\theta - H_{z_\gamma}^i\sin\theta \quad (120)$$

$$H_\theta^i = H_0 e^{-i\mathbf{k}\cdot\mathbf{r}}[\sin\alpha\cos\beta\cos\theta(\cos\gamma\cos\varphi-\sin\gamma\sin\varphi) + \cos\alpha\cos\theta(\sin\gamma\cos\varphi+\cos\gamma\sin\varphi) - \sin\alpha\sin\beta\sin\theta] \quad (121)$$

$$H_\varphi^i = -H_{x_\gamma}^i\sin\varphi + H_{y_\gamma}^i\cos\varphi \quad (122)$$

$$H_\varphi^i = H_0 e^{-i\mathbf{k}\cdot\mathbf{r}}[\cos\alpha(\cos\gamma\cos\varphi-\sin\gamma\sin\varphi) - \sin\alpha\cos\beta(\sin\gamma\cos\varphi+\cos\gamma\sin\varphi)] \quad (123)$$

4.2. Radial electric field

We start from Eq. (20), and will once again omit the tilde-decorations. The bracket term is modified by using Eqs. (5) and (4), leading to:

$$\left[\psi_n''(kr)+\psi_n(kr)\right] = \frac{n(n+1)}{kr}j_n(kr) \quad (124)$$

Furthermore, we insert the expression of c_n^{pw}, i.e. Eq. (3), leading to:

$$E_r^i = \frac{-iE_0}{kr}\sum_{n=1}^{\infty}\sum_{m=-n}^{n}(-i)^n(2n+1)g_{n,\mathrm{TM}}^m j_n(kr)P_n^{|m|}(\cos\theta)e^{im\varphi} \quad (125)$$

Inserting Eq. (18) for $g_{n,\mathrm{TM}}^m$ into Eq. (125), we obtain:

$$E_r^i = \frac{-iE_0}{kr}\sum_{n=1}^{\infty}\sum_{m=-n}^{n}(-i)^n(2n+1)j_n(kr)P_n^{|m|}(\cos\theta)e^{im\varphi}(-1)^m\frac{(n-|m|)!}{(n+|m|)!}e^{im\gamma}\left[im\sin\alpha\pi_n^{|m|}(\cos\beta)+\cos\alpha\tau_n^{|m|}(\cos\beta)\right] \quad (126)$$

in which the constant g has been set equal to 1 (or absorbed into E_0).

This may be rewritten as a sum of two terms, in which $\pi_n^{|m|}$ and $\tau_n^{|m|}$ are expressed versus the associated Legendre functions, according to:

$$E_r^i = \left(E_r^i\right)_1 + \left(E_r^i\right)_2 \quad (127)$$

$$\left(E_r^i\right)_1 = \frac{E_0}{kr}\frac{\sin\alpha}{\sin\beta}\sum_{n=1}^{\infty}\sum_{m=-n}^{n}(-i)^n(-1)^m(2n+1)\frac{(n-|m|)!}{(n+|m|)!} j_n(kr)P_n^{|m|}(\cos\theta)e^{im\varphi}e^{im\gamma}mP_n^{|m|}(\cos\beta) \quad (128)$$

$$\left(E_r^i\right)_2 = \frac{-iE_0}{kr}\cos\alpha\frac{\partial}{\partial\beta}\sum_{n=1}^{\infty}\sum_{m=-n}^{n}(-i)^n(-1)^m(2n+1)\frac{(n-|m|)!}{(n+|m|)!} j_n(kr)P_n^{|m|}(\cos\theta)e^{im\varphi}e^{im\gamma}P_n^{|m|}(\cos\beta) \quad (129)$$

We modify again these results by introducing:

$$\gamma_k = -(\pi+\gamma) \quad (130)$$

implying:

$$(-1)^m e^{im\gamma} = e^{-im\gamma_k} \quad (131)$$

Hence:

$$\left(E_r^i\right)_1 = \frac{E_0}{kr}\frac{\sin\alpha}{\sin\beta}\sum_{n=1}^{\infty}\sum_{m=-n}^{n}(-i)^n(2n+1)\frac{(n-|m|)!}{(n+|m|)!} j_n(kr)P_n^{|m|}(\cos\theta)e^{im\varphi}e^{-im\gamma_k}mP_n^{|m|}(\cos\beta) \quad (132)$$

$$\left(E_r^i\right)_2 = \frac{-iE_0}{kr}\cos\alpha\frac{\partial}{\partial\beta}\sum_{n=1}^{\infty}\sum_{m=-n}^{n}(-i)^n(2n+1)\frac{(n-|m|)!}{(n+|m|)!} j_n(kr)P_n^{|m|}(\cos\theta)e^{im\varphi}e^{-im\gamma_k}P_n^{|m|}(\cos\beta) \quad (133)$$

Now, from Eq. (46):

$$\frac{\partial}{\partial\varphi}e^{i\mathbf{k}\cdot\mathbf{r}} = i\sum_{n=1}^{\infty}\sum_{m=-n}^{n}(-i)^n(2n+1)\frac{(n-|m|)!}{(n+|m|)!}j_n(kr) \\ P_n^{|m|}(\cos\beta)P_n^{|m|}(\cos\theta)e^{-im\gamma_k}me^{im\varphi} \tag{134}$$

Hence:

$$\left(E_r^i\right)_1 = \frac{-iE_0}{kr}\frac{\sin\alpha}{\sin\beta}\frac{\partial}{\partial\varphi}e^{-i\mathbf{k}\cdot\mathbf{r}} \tag{135}$$

Using Eq. (45), this becomes:

$$\left(E_r^i\right)_1 = E_0\sin\alpha\sin\theta[\cos\gamma_k\sin\varphi - \sin\gamma_k\cos\varphi]e^{-i\mathbf{k}\cdot\mathbf{r}} \tag{136}$$

which, by using Eq. (130), implies:

$$\left(E_r^i\right)_1 = -E_0\sin\alpha\sin\theta[\cos\gamma\sin\varphi + \sin\gamma\cos\varphi]e^{-i\mathbf{k}\cdot\mathbf{r}} \tag{137}$$

Similarly, we establish:

$$\left(E_r^i\right)_2 = \frac{-iE_0}{kr}\cos\alpha\frac{\partial}{\partial\beta}e^{-i\mathbf{k}\cdot\mathbf{r}} \tag{138}$$

leading to:

$$\left(E_r^i\right)_2 = E_0\cos\alpha[\cos\beta\sin\theta(\cos\gamma\cos\varphi - \sin\gamma\sin\varphi) + \sin\beta\cos\theta]e^{-i\mathbf{k}\cdot\mathbf{r}} \tag{139}$$

Summing up $(E_r^i)_1$ of Eq. (137) and $(E_r^i)_2$ of Eq. (139), we recover Eq. (109), as it should.

4.3. Radial magnetic field

We start from Eq. (23) and proceed similarly as for the electric field, to obtain:

$$H_r^i = \left(H_r^i\right)_1 + \left(H_r^i\right)_2 \tag{140}$$

in which:

$$\left(H_r^i\right)_1 = \frac{iH_0}{kr}\frac{\cos\alpha}{\sin\beta}\sum_{n=1}^{\infty}\sum_{m=-n}^{n}(-i)^n(2n+1)\frac{(n-|m|)!}{(n+|m|)!} \\ j_n(kr)P_n^{|m|}(\cos\beta)P_n^{|m|}(\cos\theta)e^{-im\gamma_k}ime^{im\varphi} \tag{141}$$

which is translated to:

$$\left(H_r^i\right)_1 = \frac{iH_0 g}{kr}\frac{\cos\alpha}{\sin\beta}\frac{\partial}{\partial\varphi}e^{-i\mathbf{k}\cdot\mathbf{r}} \tag{142}$$

becoming:

$$\left(H_r^i\right)_1 = H_0\cos\alpha\sin\theta[\cos\gamma\sin\varphi + \sin\gamma\cos\varphi]e^{-i\mathbf{k}\cdot\mathbf{r}} \tag{143}$$

Let us remark that:

$$\frac{\left(E_r^i\right)_1}{\left(H_r^i\right)_1} = -\frac{E_0\sin\alpha}{H_0\cos\alpha} \tag{144}$$

Concerning $(H_r^i)_2$, it is readily found to read as:

$$\left(H_r^i\right)_2 = -\frac{iH_0}{kr}\sin\alpha\frac{\partial}{\partial\beta}e^{-i\mathbf{k}\cdot\mathbf{r}} \tag{145}$$

leading to:

$$\left(H_r^i\right)_2 = H_0\sin\alpha[\cos\beta\sin\theta(\cos\gamma\cos\varphi - \sin\gamma\sin\varphi) + \sin\beta\cos\theta]e^{-i\mathbf{k}\cdot\mathbf{r}} \tag{146}$$

Let us remark that:

$$\frac{\left(E_r^i\right)_2}{\left(H_r^i\right)_2} = \frac{E_0\cos\alpha}{H_0\sin\alpha} \tag{147}$$

As a whole, summing $(H_r^i)_1$ and $(H_r^i)_2$, we recover Eq. (119), as it should.

4.4. Electric field, θ–component

On one hand, the electric field component E_θ^i is given, in compact form, by Eq. (111). On the other hand, for the expanded form version, we start from Eq. (21), omit the tilde-decorations, insert Eqs. (3), (4), (18) and (19), and write it as the sum of four terms, according to:

$$E_\theta^i = A_{\theta1} + A_{\theta2} + B_{\theta1} + B_{\theta2} \tag{148}$$

in which:

$$A_{\theta1} = \frac{-iE_0}{kr}\cos\alpha\sum_{n=1}^{\infty}\sum_{m=-n}^{n}(-i)^n\frac{2n+1}{n(n+1)}\frac{(n-|m|)!}{(n+|m|)!} \\ \frac{drj_n(kr)}{dr}\tau_n^{|m|}(\cos\beta)\tau_n^{|m|}(\cos\theta)e^{-im\gamma_k}e^{im\varphi} \tag{149}$$

$$A_{\theta2} = \frac{E_0}{kr}\sin\alpha\sum_{n=1}^{\infty}\sum_{m=-n}^{n}(-i)^n\frac{2n+1}{n(n+1)}\frac{(n-|m|)!}{(n+|m|)!} \\ \frac{drj_n(kr)}{dr}m\pi_n^{|m|}(\cos\beta)\tau_n^{|m|}(\cos\theta)e^{-im\gamma_k}e^{im\varphi} \tag{150}$$

$$B_{\theta1} = \frac{-E_0}{kr}\cos\alpha\sum_{n=1}^{\infty}\sum_{m=-n}^{n}(-i)^n\frac{2n+1}{n(n+1)}\frac{(n-|m|)!}{(n+|m|)!} \\ krj_n(kr)m\pi_n^{|m|}(\cos\beta)m\pi_n^{|m|}(\cos\theta)e^{-im\gamma_k}e^{im\varphi} \tag{151}$$

$$B_{\theta2} = \frac{-iE_0}{kr}\sin\alpha\sum_{n=1}^{\infty}\sum_{m=-n}^{n}(-i)^n\frac{2n+1}{n(n+1)}\frac{(n-|m|)!}{(n+|m|)!} \\ krj_n(kr)\tau_n^{|m|}(\cos\beta)m\pi_n^{|m|}(\cos\theta)e^{-im\gamma_k}e^{im\varphi} \tag{152}$$

Rather than testing Eq. (148), we shall more conveniently test this equation multiplied by r. We then introduce the notation:

$$\varepsilon_\theta = rE_\theta^i \tag{153}$$

and similar notations for $\mathcal{X}_{\theta i} = rX_{\theta i}^i$, in which X is A or B, and the subscript i is 1 or 2.

To process $\mathcal{A}_{\theta1}$, we derive it once with respect to r, invoke Eq. (5), explicit one of the terms obtained in terms of derivatives of $e^{-i\mathbf{k}\cdot\mathbf{r}}$, and rederive once again with respect to r, to obtain:

$$\hat{D}\mathcal{A}_{\theta1} = \frac{-iE_0}{k}\cos\alpha\frac{\partial}{\partial r}\frac{1}{r}\frac{\partial}{\partial\beta}\frac{\partial}{\partial\theta}e^{-i\mathbf{k}\cdot\mathbf{r}} \tag{154}$$

in which we introduced the operator:

$$\hat{D} = \left(\frac{\partial^2}{\partial r^2} + k^2\right) \tag{155}$$

The term $\mathcal{A}_{\theta 2}$ is processed quite similarly, leading to:

$$\hat{D}\mathcal{A}_{\theta 2} = \frac{-iE_0 \sin\alpha}{k \sin\beta} \frac{\partial}{\partial r} \frac{1}{r} \frac{\partial}{\partial \varphi} \frac{\partial}{\partial \theta} e^{-i\mathbf{k}\cdot\mathbf{r}} \tag{156}$$

For $\mathcal{B}_{\theta 1}$ and $\mathcal{B}_{\theta 2}$, we simply apply the operator $\hat{D}$, invoke Eq. (5), and establish:

$$\hat{D}\mathcal{B}_{\theta 1} = \frac{E_0 \cos\alpha}{r \sin\beta \sin\theta} \frac{\partial^2}{\partial \varphi^2} e^{-i\mathbf{k}\cdot\mathbf{r}} \tag{157}$$

$$\hat{D}\mathcal{B}_{\theta 2} = \frac{-E_0 \sin\alpha}{r \sin\theta} \frac{\partial}{\partial \beta} \frac{\partial}{\partial \varphi} e^{-i\mathbf{k}\cdot\mathbf{r}} \tag{158}$$

For $\mathcal{E}_\theta$ of Eq. (153), we invoke E^i_θ of Eq. (111), and also Eq. (45) for $e^{-i\mathbf{k}\cdot\mathbf{r}}$, write it under the form:

$$\mathcal{E}_\theta = rE_0 \mathcal{D} e^{-ikrC} \tag{159}$$

and establish:

$$\hat{\mathcal{D}}\mathcal{E}_\theta = -kE_0 \mathcal{D}\left(-kr + 2i\mathcal{C} + kr\mathcal{C}^2\right) e^{-i\mathbf{k}\cdot\mathbf{r}} \tag{160}$$

Using the form of Eq. (45) for $e^{-i\mathbf{k}\cdot\mathbf{r}}$, we afterward obtain, from Eqs. (154), (156)–(158), and (160), without forgetting to recall $\gamma_k = -(\pi+\gamma)$ of Eq. (130):

$$\hat{D}(\mathcal{A}_{\theta 1} + \mathcal{A}_{\theta 2} + \mathcal{B}_{\theta 1} + \mathcal{B}_{\theta 2}) = \hat{D}\mathcal{E}_\theta \tag{161}$$

In other words, we obtain the same result when the operator $\hat{D}$ is applied to the expanded and to the compact forms of rE^i_θ. This means that these two forms are equal within a function F satisfying $\mathcal{D}F = 0$. The general form for F is therefore:

$$F = C_{E\theta} \cos kr + S_{E\theta} \sin kr \tag{162}$$

in which $C_{E\theta}$ and $S_{E\theta}$ do not depend on r.

Hence:

$$\mathcal{A}_{\theta 1} + \mathcal{A}_{\theta 2} + \mathcal{B}_{\theta 1} + \mathcal{B}_{\theta 2} = \mathcal{E}_\theta + C_{E\theta} \cos kr + S_{E\theta} \sin kr \tag{163}$$

Now, from Eqs. (149)–(152), and using Eq. (81), we have:

$$(\mathcal{A}_{\theta 1})_{r=0} = (\mathcal{A}_{\theta 2})_{r=0} = (\mathcal{B}_{\theta 1})_{r=0} = (\mathcal{B}_{\theta 2})_{r=0} = (\mathcal{E}_\theta)_{r=0} = 0 \tag{164}$$

which, inserted into Eq. (163), implies:

$$C_{E\theta} = 0 \tag{165}$$

Next, we consider the derivative with respect to r of Eq. (163), knowing Eq. (165), in the limit $r = 0$:

$$\left[\frac{\partial}{\partial r}(\mathcal{A}_{\theta 1} + \mathcal{A}_{\theta 2} + \mathcal{B}_{\theta 1} + \mathcal{B}_{\theta 2})\right]_{r=0} = \left(\frac{\partial \mathcal{E}_\theta}{\partial r}\right)_{r=0} + kS_{E\theta} \tag{166}$$

We afterward evaluate, in a now fairly obvious way:

$$\left(\frac{\partial \mathcal{A}_{\theta 1}}{\partial r}\right)_{r=0} = \left(\frac{-iE_0}{kr} \cos\alpha \frac{\partial}{\partial \beta} \frac{\partial}{\partial \theta} e^{-i\mathbf{k}\cdot\mathbf{r}}\right)_{r=0} \tag{167}$$

$$\left(\frac{\partial \mathcal{A}_{\theta 2}}{\partial r}\right)_{r=0} = \left(\frac{-iE_0}{kr} \frac{\sin\alpha}{\sin\beta} \frac{\partial}{\partial \varphi} \frac{\partial}{\partial \theta} e^{-i\mathbf{k}\cdot\mathbf{r}}\right)_{r=0} \tag{168}$$

$$\left(\frac{\partial \mathcal{B}_{\theta 1}}{\partial r}\right)_{r=0} = \left(\frac{\partial \mathcal{B}_{\theta 2}}{\partial r}\right)_{r=0} = 0 \tag{169}$$

After evaluation of Eqs. (167), (168) and of $(\partial \mathcal{E}_\theta / \partial r)_{r=0}$, Eq. (166) implies:

$$S_{E\theta} = 0 \tag{170}$$

ending the demonstration of the equality between compact and expanded forms.

4.5. Electric field, φ–component

The study of this component is quite parallel to the study of the previous one, so that we shall expose it in a somewhat more concise way. The electric field component E^i_φ in the rotated system is given, in compact form, by Eq. (113). We then use the notation ε_φ to denote rE^i_φ. The expanded form of ε_φ is written as the sum of four terms reading as:

$$\mathcal{A}_{\varphi 1} = \frac{iE_0}{k} \sin\alpha \sum_{n=1}^{\infty} \sum_{m=-n}^{n} (-i)^n \frac{2n+1}{n(n+1)} \frac{(n-|m|)!}{(n+|m|)!} \frac{dr j_n(kr)}{dr} m\pi_n^{|m|}(\cos\beta) m\pi_n^{|m|}(\cos\theta) e^{-im\gamma_k} e^{im\varphi} \tag{171}$$

$$\mathcal{A}_{\varphi 2} = \frac{E_0}{k} \cos\alpha \sum_{n=1}^{\infty} \sum_{m=-n}^{n} (-i)^n \frac{2n+1}{n(n+1)} \frac{(n-|m|)!}{(n+|m|)!} \frac{dr j_n(kr)}{dr} \tau_n^{|m|}(\cos\beta) m\pi_n^{|m|}(\cos\theta) e^{-im\gamma_k} e^{im\varphi} \tag{172}$$

$$\mathcal{B}_{\varphi 1} = \frac{-iE_0}{k} \cos\alpha \sum_{n=1}^{\infty} \sum_{m=-n}^{n} (-i)^n \frac{2n+1}{n(n+1)} \frac{(n-|m|)!}{(n+|m|)!} kr j_n(kr) m\pi_n^{|m|}(\cos\beta) \tau_n^{|m|}(\cos\theta) e^{-im\gamma_k} e^{im\varphi} \tag{173}$$

$$\mathcal{B}_{\varphi 2} = \frac{E_0}{k} \sin\alpha \sum_{n=1}^{\infty} \sum_{m=-n}^{n} (-i)^n \frac{2n+1}{n(n+1)} \frac{(n-|m|)!}{(n+|m|)!} kr j_n(kr) \tau_n^{|m|}(\cos\beta) \tau_n^{|m|}(\cos\theta) e^{-im\gamma_k} e^{im\varphi} \tag{174}$$

We afterward establish:

$$\hat{D}\mathcal{A}_{\varphi 1} = \frac{-iE_0 \sin\alpha}{k \sin\beta \sin\theta} \frac{\partial}{\partial r} \frac{1}{r} \frac{\partial^2}{\partial \varphi^2} e^{-i\mathbf{k}\cdot\mathbf{r}} \tag{175}$$

$$\hat{D}\mathcal{A}_{\varphi 2} = \frac{-iE_0 \cos\alpha}{k \sin\theta} \frac{\partial}{\partial r} \frac{1}{r} \frac{\partial}{\partial \beta} \frac{\partial}{\partial \varphi} e^{-i\mathbf{k}\cdot\mathbf{r}} \tag{176}$$

$$\hat{D}\mathcal{B}_{\varphi 1} = \frac{-E_0 \cos\alpha}{r \sin\beta} \frac{\partial}{\partial \theta} \frac{\partial}{\partial \varphi} e^{-i\mathbf{k}\cdot\mathbf{r}} \tag{177}$$

$$\hat{D}\mathcal{B}_{\varphi 2} = \frac{E_0 \sin\alpha}{r} \frac{\partial}{\partial \beta} \frac{\partial}{\partial \theta} e^{-i\mathbf{k}\cdot\mathbf{r}} \tag{178}$$

Writing $\mathcal{E}_\varphi$ under the form:

$$\mathcal{E}_\varphi = rE_0 \mathcal{F} e^{-ikrC} \tag{179}$$

We also have:

$$\hat{D}\mathcal{E}_\varphi = -kE_0 \mathcal{F}\left(-kr + 2i\mathcal{C} + kr\mathcal{C}^2\right) e^{-i\mathbf{k}\cdot\mathbf{r}} \tag{180}$$

We afterward establish:

$$\hat{D}\left(\mathcal{A}_{\varphi 1} + \mathcal{A}_{\varphi 2} + \mathcal{B}_{\varphi 1} + \mathcal{B}_{\varphi 2}\right) = \hat{D}\mathcal{E}_\varphi \tag{181}$$

implying:

$$\mathcal{A}_{\varphi 1} + \mathcal{A}_{\varphi 2} + \mathcal{B}_{\varphi 1} + \mathcal{B}_{\varphi 2} = \mathcal{E}_{\varphi} + C_{E\varphi}\cos kr + S_{E\varphi}\sin kr \tag{182}$$

Proceeding in the same way than for the component E_θ^i, we afterward establish:

$$\left(\frac{\partial \mathcal{A}_{\varphi 1}}{\partial r}\right)_{r=0} = \left(\frac{-iE_0\sin\alpha}{kr\sin\beta\sin\theta}\frac{\partial^2}{\partial\varphi^2}e^{-ik\cdot r}\right)_{r=0} \tag{183}$$

$$\left(\frac{\partial \mathcal{A}_{\varphi 2}}{\partial r}\right)_{r=0} = \left(\frac{-iE_0\cos\alpha}{kr\sin\theta}\frac{\partial}{\partial\beta}\frac{\partial}{\partial\varphi}e^{-ik\cdot r}\right)_{r=0} \tag{184}$$

$$\left(\frac{\partial \mathcal{B}_{\varphi 1}}{\partial r}\right)_{r=0} = \left(\frac{\partial \mathcal{B}_{\varphi 2}}{\partial r}\right)_{r=0} = 0 \tag{185}$$

and find:

$$C_{E\varphi} = S_{E\varphi} = 0 \tag{186}$$

4.6. Magnetic field, angular components

For the θ–component, the compact form H_θ^i is given by Eq. (121). Being still more concise than for the previous component, we find that the quantity $\mathcal{H}_\theta = rH_\theta^i$, in the expanded form, is the sum of four terms according to:

$$\mathcal{H}_\theta = \mathcal{C}_{\theta 1} + \mathcal{C}_{\theta 2} + \mathcal{D}_{\theta 1} + \mathcal{D}_{\theta 2} \tag{187}$$

Working out each of these terms, we find that they may be expressed as:

$$\begin{pmatrix}\mathcal{C}_{\theta 1}\\ \mathcal{D}_{\theta 2}\end{pmatrix} = \frac{-H_0\cos\alpha}{E_0\sin\alpha}\begin{pmatrix}\mathcal{A}_{\theta 2}\\ \mathcal{B}_{\theta 2}\end{pmatrix} \tag{188}$$

$$\begin{pmatrix}\mathcal{C}_{\theta 2}\\ \mathcal{D}_{\theta 1}\end{pmatrix} = \frac{H_0\sin\alpha}{E_0\cos\alpha}\begin{pmatrix}\mathcal{A}_{\theta 1}\\ \mathcal{B}_{\theta 1}\end{pmatrix} \tag{189}$$

We afterward establish:

$$\hat{D}(\mathcal{C}_{\theta 1} + \mathcal{C}_{\theta 2} + \mathcal{D}_{\theta 1} + \mathcal{D}_{\theta 2}) = \hat{D}\mathcal{H}_\theta \tag{190}$$

implying:

$$\mathcal{C}_{\theta 1} + \mathcal{C}_{\theta 2} + \mathcal{D}_{\theta 1} + \mathcal{D}_{\theta 2} = \mathcal{H}_\theta + C_{H\theta}\cos kr + S_{H\theta}\sin kr \tag{191}$$

Afterward, proceeding in the same way than for the electric components, we establish:

$$C_{H\theta} = S_{H\theta} = 0 \tag{192}$$

For the φ–component, the compact form H_φ^i is given by Eq. (123). The quantity $\mathcal{H}_\varphi = r\mathcal{H}_\varphi^i$, in the expanded form, is the sum of four terms according to:

$$\mathcal{H}_\varphi = \mathcal{C}_{\varphi 1} + \mathcal{C}_{\varphi 2} + \mathcal{D}_{\varphi 1} + \mathcal{D}_{\varphi 2} \tag{193}$$

Working out each of these terms, we find that they may be expressed as:

$$\begin{pmatrix}\mathcal{C}_{\varphi 1}\\ \mathcal{D}_{\varphi 2}\end{pmatrix} = \frac{-H_0\cos\alpha}{E_0\sin\alpha}\begin{pmatrix}\mathcal{A}_{\varphi 1}\\ \mathcal{B}_{\varphi 2}\end{pmatrix} \tag{194}$$

$$\begin{pmatrix}\mathcal{C}_{\varphi 2}\\ \mathcal{D}_{\varphi 1}\end{pmatrix} = \frac{H_0\sin\alpha}{E_0\cos\alpha}\begin{pmatrix}\mathcal{A}_{\varphi 2}\\ \mathcal{B}_{\varphi 1}\end{pmatrix} \tag{195}$$

We afterward establish:

$$\hat{D}\left(\mathcal{C}_{\varphi 1} + \mathcal{C}_{\varphi 2} + \mathcal{D}_{\varphi 1} + \mathcal{D}_{\varphi 2}\right) = \hat{D}\mathcal{H}_\varphi \tag{196}$$

implying:

$$\mathcal{C}_{\varphi 1} + \mathcal{C}_{\varphi 2} + \mathcal{D}_{\varphi 1} + \mathcal{D}_{\varphi 2} = \mathcal{H}_\varphi + C_{H\varphi}\cos kr + S_{H\varphi}\sin kr \tag{197}$$

Afterward, proceeding in the same way than for the previous components, we establish:

$$C_{H\varphi} = S_{H\varphi} = 0 \tag{198}$$

5. Discussion and conclusion

In a series of papers devoted to the transformation of spherical beam shape coefficients (for use in generalized Lorenz–Mie theories in spherical coordinates) under the rotation of coordinate systems, this paper discusses the case of plane waves viewed as a special case of on-axis axisymmetric beams. The description in the unrotated system is taken as simple as possible. The corresponding description in the rotated system is far more complicated and it might seem that, for plane waves, the interest of rotations is suspicious.

Nevertheless, to better understand the issue, let us now dress the problem by attaching a scattering particle to the unrotated system, and assuming that this particle follows any rotation of it. If the particle is a homogeneous spherical particle defined by its diameter and its complex refractive index, as in the GLMT *stricto sensu* [4], then any rotation lets the physics invariant. There is therefore no interest indeed to choose working with the rotated system which complicates the intermediary calculations without any benefit. The same is true when the scattering particle is a multilayered sphere [17].

However, let us now assume that the scatterer is a spherical particle with an eccentrically located spherical inclusion [18]. Let us locate the center of the inclusion on the "vertical" axis *Oz* of the unrotated system, and the center of the host sphere at the origin *O* of the Cartesian coordinate system. The plane wave in the unrotated system propagates along the axis *Oz* and we are facing a rather easy geometry of the scattering problem. Everything now becomes more complicated after rotation, when the plane wave is still propagating along *Oz* but the center of the inclusion is no more located on this axis. This may be viewed as a case of oblique illumination. This terminology (oblique illumination) is the one which has indeed been used by Han et al. [19,20] when they initiated the issue. We then have discussed a new way of calculating the beam shape coefficients of plane waves under oblique illumination, and took this opportunity to investigate the mathematical behavior of these waves. A similar discussion is valid for assemblies of spheres and aggregates [21], for instance in the case of several spheres aligned along an axis. Such scatterers are currently under study, e.g. [22,23].

A last remark of importance is also to be recalled. Eqs. (18) and (19) indeed exhibit a somewhat unexpected result, namely that, in general, the description of the plane wave in the rotated system requires the use of beam shape coefficients (a double set of beam shape coefficients), as for arbitrary shaped beams, in contrast with the easy degenerated description in the unrotated system.

References

[1] G. Gouesbet, J.J. Wang, Y.P. Han, Transformations of spherical beam shape coefficients in generalized Lorenz–Mie theories through rotations of coordinate systems. I. General formulation, Optics Communications 283 (17) (2010) 3218.
[2] J.J. Wang, G. Gouesbet, Y.P. Han, Transformations of spherical beam shape coefficients in generalized Lorenz–Mie theories through rotations of coordinate systems. II. Axisymmetric beams, Optics Communications 283 (17) (2010) 3226.

[3] G. Gouesbet, J.J. Wang, Y.P. Han, Transformations of spherical beam shape coefficients in generalized Lorenz–Mie theories through rotations of coordinate systems. III. Special Euler angles, Optics Communications 283 (17) (2010) 3235.
[4] G. Gouesbet, B. Maheu, G. Gréhan, Journal of the Optical Society of America A 5 (1988) 1427.
[5] B. Maheu, G. Gouesbet, G. Gréhan, Journal of Optics, Paris 19 (2) (1988) 59.
[6] G. Gouesbet, G. Gréhan., Journal of Optics, Paris 13 (2) (1982) 97.
[7] G. Gouesbet, Applied Optics 35 (9) (1996) 1543.
[8] G. Gouesbet, G. Gréhan, B. Maheu, Journal of Optics, Paris. 16 (1985) 83.
[9] G. Gouesbet, G. Gréhan, G. Gouesbet., in: N. Chigier (Ed.), Generalized Lorenz–Mie Theory and Applications to Optical Sizing, Hemisphere Publishing Corporation, 1991, p. 339, chapter Ten.
[10] G. Gouesbet and G. Gréhan. *Book on generalized Lorenz-Mie theories, in preparation, to be published by Springer-Verlag.*
[11] G. Gouesbet, Optics Communications 283 (2010) 517.
[12] C. Cohen-Tannoudji, B. Diu, F. Laloë, Mécanique Quantique, Tomes 1 et 2, Hermann, 1973.
[13] G.B. Arfken, H.J. Weber, Mathematical Methods for Physicists, Sixth edition. Academic Press, 2005.
[14] L. Robin, Fonctions sphériques de Legendre et fonctions sphéroïdales, Vols. 1–3, Gauthiers-Villars, 1957.
[15] G. Gouesbet, B. Maheu, G. Gréhan, Journal of Optics, Paris 16 (5) (1985) 239.
[16] P.M. Morse, H. Feshbach, Methods of Theoretical Physics, McGraw-Hill Book Company, 1953.
[17] F. Onofri, G. Gréhan, G. Gouesbet, Applied Optics 34 (30) (1995) 7113.
[18] G. Gouesbet, G. Gréhan, Journal of Modern Optics 47 (5) (2000) 821.
[19] Y.P. Han, H. Zhang, G. Han, Optics Express 15 (2) (2007) 735.
[20] Y.P. Han, Y. Zhang, H. Zhang, G. Han, Journal of Quantitative Spectroscopy and Radiative transfer 110 (14-16) (2009) 1375.
[21] G. Gouesbet, G. Gréhan, Journal of Optics A: Pure and Applied Optics 1 (1999) 706.
[22] G. Han, Y.P. Han, H. Liu, Y. Zhang, Journal of Optical Society of America B 25 (12) (2008) 2064.
[23] B. Yan, X. Han, K.F. Ren, Journal of Optics A: Pure and Applied Optics 11 (2009) 015705 paper.

Optics Communications 284 (2011) 411–417

Contents lists available at ScienceDirect

Optics Communications

journal homepage: www.elsevier.com/locate/optcom

Transformations of spherical beam shape coefficients in generalized Lorenz–Mie theories through rotations of coordinate systems. V. Localized beam models

G. Gouesbet [a,*], J.A. Lock [b], J.J. Wang [a,c], G. Gréhan [a]

[a] Laboratoire d'Electromagnétisme des Systèmes Particulaires (LESP), Unité Mixte de Recherche (UMR) 6614 du Centre National de la Recherche Scientifique (CNRS), COmplexe de Recherche Interprofessionnel en Aérothermochimie (CORIA), Université de Rouen et Institut National des Sciences Appliquées (INSA) de Rouen BP12, avenue de l'université, technopôle du Madrillet, 76801, Saint-Etienne-du Rouvray, France
[b] Department of Physics, Cleveland State University, Cleveland, OH, 44115, USA
[c] School of Science, Xidian University, Xi'an, China

ARTICLE INFO

Article history:
Received 9 August 2010
Accepted 31 August 2010

ABSTRACT

This paper is the fifth of a series of papers devoted to the transformation of beam shape coefficients through rotations of coordinate systems. These coefficients are required to express electromagnetic fields of laser beams in expanded forms, for use in some generalized Lorenz–Mie theories, or in other light scattering approaches such as Extended Boundary Condition Method. Part I was devoted to the general formulation. Parts II, III, IV were devoted to special cases, namely axisymmetric beams, special values of Euler angles, and plane waves respectively. The present Part V is devoted to the study of localized approximation and localized beam models, and of their behavior under the rotation of coordinate systems.

1. Introduction

Many approaches to light scattering, such as generalized Lorenz–Mie theories in spherical coordinates (for homogeneous spheres [1,2], multilayered spheres [3], spheres with spherical inclusions [4], assemblies of spheres and aggregates [5], with recent reviews in Refs. [6,7]), or Extended Boundary Condition Method, also called Null-Field Method [8,9], most often misleadingly named T-matrix method [10], require the evaluation of expansion coefficients known as beam shape coefficients.

These beam shape coefficients may be evaluated by using various methods, namely quadratures [11], finite series [12], localized approximations generating localized beam models [13,14], or a hybrid method taking advantage of both quadratures and of a localized approximation, named the integral localized approximation [15]. The evaluation of beam shape coefficients has also been investigated by relying on addition theorems for translations of coordinate systems, an approach originally introduced by Doicu and Wriedt [16], and also used by Zhang and Han [17].

In the previous papers of this series [18–21], we have developed another approach, initiated by Han et al. [22,23], to the evaluation of beam shape coefficients, relying on addition theorems for rotations (not for translations) of coordinate systems. This approach takes the form of a theorem of transformation which expresses the beam shape coefficients in a rotated system in terms of beam shape coefficients in an unrotated system.

The present paper is devoted to the study of a synthetical question, concerning both the use of localized approximations, and the use of rotational addition theorems, to the evaluation of beam shape coefficients. It happens that the use of a localized approximation, to evaluate beam shape coefficients, provides the most efficient method, with regards to computational times, by orders of magnitudes with respect to other methods such as by using quadratures. It is also the most appealing from a physical point of view because it provides many physical insights on the interpretation of beam models.

Then, let us consider an original system of coordinates, called the unrotated system, in which we possess compact (non-expanded expressions), to describe an electromagnetic field. Most usually, this description does not exactly satisfy Maxwell's equations, this being called a non-Maxwellian description, a feature having deep consequences in light scattering theories [24–27]. Nevertheless, by using a localized approximation, we may obtain, in the unrotated system, an expanded beam description, called a localized beam model, which is Maxwellian, i.e. which exactly satisfies Maxwell's equations. By using the theorem of transformation previously mentioned, we may then obtain a localized beam model in a rotated system in terms of the localized beam model in the unrotated system. This procedure to obtain a localized beam model in the rotated system is called the *RL*-procedure. It is achieved by applying the localization in the unrotated system (operator *L*) followed by a rotation (operator *R*) to the rotated system, in short: localize and afterward rotate.

Alternatively, we may start from the non-Maxwellian beam description in the unrotated system, rotate it to the rotated system,

* Corresponding author. Tel.: +33 2 35 52 83 92; fax: +33 2 35 52 83 90.
E-mail address: Gouesbet@coria.fr (G. Gouesbet).

0030-4018/$ – see front matter © 2010 Elsevier B.V. All rights reserved.
doi:10.1016/j.optcom.2010.08.082

and afterward apply a localized approximation in the rotated system. This is called the *LR*-procedure, i.e. first rotate and afterward localize.

In general, since we are working with non-Maxwellian descriptions of beams, we should not expect that the operators R and L commute: $RL \neq LR$, but we expect that they nearly commute, that is to say that the results of applying the *RL*- or the *LR*-procedures, although different, are close enough in some sense. In the light of this expectation, we were quite surprised to find that the operators R and L do not commute, not only for non-Maxwellian beams, but for Maxwellian beams as well. The aim of this paper is to demonstrate these unexpected statements, to explain why it is so, and to draw consequences.

The paper is organized as follows. In Section 2, a few basic ingredients required for the sequel are recalled. They concern the definitions of beam shape coefficients and of Euler angles, a theorem of transformation of beam shape coefficients through rotations of coordinate systems, and the modified localized approximation procedure for arbitrary shaped beams, in its current form. Section 3 discusses the *RL*-procedure, while Section 4 discusses the *LR*-procedure. Section 5 is a conclusion. A concise Appendix is devoted to a small technicality.

2. Basic ingredients

2.1. Beam shape coefficients

The beam shape coefficients that are considered in the present series of papers are denoted as $g^m_{n,\,TM}$ and $g^m_{n,\,TE}$ (n from 1 to ∞, m from $-n$ to $+n$, *TM* for Transverse Magnetic, *TE* for Transverse Electric), e.g. Refs [1,2] in which they are used in the framework of a generalized Lorenz–Mie theory describing the interaction between an electromagnetic arbitrary shaped beam and a homogeneous sphere defined by its diameter and its complex refractive index. There are various ways to define them. An expedient one might be to write down the expression for the radial electric field component according to Ref. [18]:

$$E_r = \frac{1}{kr}\sum_{n=1}^{\infty}\sum_{m=-n}^{+n}(-1)^m b_{mn} n(n+1) j_n(kr) P_n^m(\cos\upsilon)\exp(im\eta) \tag{1}$$

in which k is the wave number in the space where the wave (an illuminating wave in the framework of a scattering problem) propagates, (r, υ, η) are spherical coordinates, j_n designates spherical Bessel functions of the first kind, and P_n^m are associated Legendre functions. The expansion coefficients b_{mn} read as:

$$b_{mn} = kE_0 c_n^{pw}(-1)^m(-1)^{\frac{m-|m|}{2}}\frac{(n-m)!}{(n-|m|)!}g^m_{n,\,TM} \tag{2}$$

in which E_0 is a field strength which, without any loss of generality, will be taken equal to 1 in the sequel (similarly, when required, the magnetic field strength H_0 is taken equal to 1 as well), and c_n^{pw} are coefficients appearing naturally in the Bromwich version of the Lorenz–Mie theory. The *TE*-beam shape coefficients $g^m_{n,\,TE}$ will not be considered in this paper. They would be similarly defined, in terms of the radial magnetic field component H_r, instead of E_r, and any statement we shall make for the *TM*-coefficients would apply, *mutatis mutandis,* to the *TE*-coefficients as well.

2.2. Euler angles

Let us consider an unrotated frame of reference with Cartesian coordinates (x, y, z) and spherical coordinates (r, θ, φ). We then apply to this frame a rotation defined by Euler angles (α, β, γ) leading to a rotated frame of reference with Cartesian coordinates $(\tilde{x}, \tilde{y}, \tilde{z})$ and spherical coordinates $\left(\tilde{r}=r,\ \tilde{\theta},\ \tilde{\varphi}\right)$, in which tilde-decorations are used to denote quantities in the rotated system. The definitions of the Euler angles are given in Ref. [18], but it is most convenient to repeat these definitions here.

(i) A first rotation, applied to the unrotated system (x, y, z), by an angle α $(0\leq\alpha<2\pi)$ about the z-axis, brings the unrotated system to an α–rotated system with Cartesian coordinates $(x_\alpha, y_\alpha, z_\alpha)$.

(ii) A second rotation, applied to the α–rotated system $(x_\alpha, y_\alpha, z_\alpha)$, by an angle β $(0\leq\beta<\pi)$ about the y_α–axis, brings the α–rotated system to a β–rotated system with Cartesian coordinates $(x_\beta, y_\beta, z_\beta)$.

(iii) A third rotation, applied to the β–rotated system $(x_\beta, y_\beta, z_\beta)$, by an angle γ $(0\leq\gamma<2\pi)$ about the z_β–axis, brings the β–rotated system to a γ–rotated system (simply called the rotated system) with Cartesian coordinates $(x_\gamma, y_\gamma, z_\gamma)$ better denoted as $(\tilde{x}, \tilde{y}, \tilde{z})$.

All rotations defined above are positive (by definition, a positive rotation about a given axis is a rotation which would carry a right-handed screw in the positive direction along that axis).

2.3. The theorem of transformation

We now know enough to state the theorem of transformation demonstrated in Ref. [18].

Let x and $\tilde{\mathrm{x}}$ be two systems of coordinates, named the unrotated and the rotated systems, respectively. Let $g^m_{n,X}$ and $\widetilde{g^m_{n,X}}$, with $X = TM$ or *TE*, be the spherical beam shape coefficients of an arbitrary shaped beam in the unrotated and in the rotated systems, respectively. Then:

$$\widetilde{g^m_{n,X}} = \mu_{mn}\sum_{s=-n}^{n}\frac{H^m_{sn}}{\mu_{sn}}g^s_{n,X} \tag{3}$$

in which:

$$\mu_{mn} = (-1)^m(-1)^{\frac{m-|m|}{2}}\frac{(n-|m|)!}{(n-m)!} \tag{4}$$

$$H^m_{sn} = (-1)^{n+s}\frac{(n-m)!}{(n-s)!}e^{is\alpha}e^{im\gamma}\sum_{\sigma}(-1)^{\sigma}\binom{n+s}{n-m-\sigma}\binom{n-s}{\sigma}\left(\cos\frac{\beta}{2}\right)^{2\sigma+m+s}\left(\sin\frac{\beta}{2}\right)^{2n-2\sigma-m-s} \tag{5}$$

in which (α,β,γ) are Euler angles bringing the unrotated system to the rotated system, defined in the previous subsection.

We shall be more specifically concerned with beams pertaining to a class of beams, named on-axis axisymmetric beams, e.g. Ref. [28]. They may be defined by beam shape coefficients taking the following values:

$$g^m_{n,X} = 0, |m|\neq 1 \tag{6}$$

$$g^1_{n,\,TM} = \frac{1}{K}g^{-1}_{n,\,TM} = -i\varepsilon g^1_{n,\,TE} = \frac{i\varepsilon}{K}g^{-1}_{n,\,TE} = \frac{g_n}{2} \tag{7}$$

in which $K\in\mathbf{R}$, and $\varepsilon = \pm 1$, are parameters. Eqs. (6) and (7) show that, for this class of beams under consideration, the double set of beam shape coefficients $\{g^m_{n,TM}, g^m_{n,TE}\}$ reduces to a single $\{g_n\}$ of coefficients, named special beam shape coefficients. A particular interesting case is when $(K,\varepsilon) = (1,-1)$. Then, Eq. (7) reduces to:

$$g^1_{n,\,TM} = g^{-1}_{n,\,TM} = ig^1_{n,\,TE} = -ig^{-1}_{n,\,TE} = \frac{g_n}{2} \tag{8}$$

This is in particular valid in the case of an on-axis Gaussian beam polarized in the x-direction at its focal waist, e.g. Refs. [1,29,30]. When

both Eqs. (6) and (8) are valid, the theorem of transformation for the *TM*-beam shape coefficients reduces to a simple enough expression [19]:

$$\widetilde{g^{m}_{n,\,TM}} = (-1)^{m}(-1)^{\frac{m-|m|}{2}}\frac{(n-|m|)!}{(n+m)!}e^{im\gamma}g_n\left[im\,\sin\alpha\pi^{m}_{n}(\cos\beta) + \cos\alpha\tau^{m}_{n}(\cos\beta)\right] \quad (9)$$

in which π^{m}_{n} and τ^{m}_{n} are generalized Legendre functions reading as:

$$\pi^{m}_{n}(\cos\beta) = \frac{P^{m}_{n}(\cos\beta)}{\sin\beta} \quad (10)$$

$$\tau^{m}_{n}(\cos\beta) = \frac{dP^{m}_{n}(\cos\beta)}{d\beta} \quad (11)$$

2.4. Modified localized approximation

We now recall the modified localized approximation procedure for arbitrary shaped beams such as exposed and justified in Ref. [14]. Following Ref. [14], we decompose the radial electric component expressed in a spherical coordinate system (r,υ,η) into *m*-modes according to:

$$E_r(R,\upsilon,\eta) = \sum_{m=-\infty}^{\infty} E^{m}_{r}(R,\upsilon,\eta) \quad (12)$$

$$E^{m}_{r}(R,\upsilon,\eta) = \left\{e^{-iR\cos\upsilon}\sin\upsilon e^{im\eta}\right\}\mathcal{E}^{m}_{r}(R,\upsilon) \quad (13)$$

The *TM*-beam shape coefficients are then given by:

$$\overline{g^{m}_{n,\,TM}} = \left(\frac{-i}{L^{1/2}}\right)^{|m|-1}\mathcal{E}^{m}_{r}\left(L^{1/2},\pi/2\right) \quad (14)$$

in which the overbar denotes "localization" and:

$$L = (n-|m|)(n+|m|+1) = (n+1/2)^2-(|m|+1/2)^2. \quad (15)$$

In these equations, we introduced the notation $R=kr$. Furthermore, in the unrotated system, we have: $(\upsilon,\eta)=(\theta,\varphi)$ and, in the rotated system: $(\upsilon,\eta) = \left(\tilde{\theta},\tilde{\varphi}\right)$.

To decrease the amount of actual computations in the case of complicated structures, it is however convenient to rewrite the above procedure in a different way. Let us introduce the notation:

$$\overline{\overline{F}} = \overline{\overline{F(\upsilon)}} = F(\upsilon=\pi/2). \quad (16)$$

We may then rewrite the modified localized approximation procedure as:

$$\overline{\overline{E_r}} = E_r(R,\pi/2,\eta) = \sum_{m=-\infty}^{\infty}\overline{\overline{E^{m}_{r}}} = \sum_{m=-\infty}^{\infty}E^{m}_{r}(R,\pi/2,\eta) \quad (17)$$

$$\overline{\overline{E^{m}_{r}}} = e^{im\eta}\overline{\overline{\mathcal{E}^{m}_{r}}}(R) = e^{im\eta}\mathcal{E}^{m}_{r}(R,\pi/2) \quad (18)$$

$$\overline{g^{m}_{n,\,TM}} = \left(\frac{-i}{L^{1/2}}\right)^{|m|-1}\overline{\overline{\mathcal{E}^{m}_{r}}}\left(L^{1/2}\right) \quad (19)$$

3. The *RL*-procedure

We are now going to evaluate beam shape coefficients in the rotated system by using a *RL*-procedure, that is to say we first apply a localization operator (or procedure) and afterward a rotation. To be specific, we shall assume that the beam is a first-order Davis beam taken as an approximation to a Gaussian beam.

3.1. Beam description in the unrotated system

The beam description in the unrotated system is taken to be the one of a Gaussian beam in the first-order Davis approximation, when the location parameters are $x_0=y_0=z_0=0$. It is defined by the following equations, e.g. Refs. [1,31] and references therein:

$$E_y = H_x = 0 \quad (20)$$

$$E_x = \Psi_0\exp(-ikz) \quad (21)$$

$$E_z = -\frac{2Q}{l}xE_x \quad (22)$$

$$H_y = \Psi_0\exp(-ikz) \quad (23)$$

$$H_z = -\frac{2Q}{l}yH_y \quad (24)$$

$$\Psi_0 = iQ\exp\left(-iQ\frac{x^2+y^2}{w_0^2}\right) \quad (25)$$

$$Q = \frac{1}{i+2\frac{z}{l}}. \quad (26)$$

The radial electric field component E_r, which is the only one required to evaluate the *TM*-beam shape coefficients, then reads as:

$$E_r = \Psi_0\cos\varphi\sin\theta\left(1-2\frac{Q}{l}r\cos\theta\right)\exp(-ikr\cos\theta) \quad (27)$$

with, now:

$$\Psi_0 = iQ\exp\left(-iQ\frac{r^2\sin^2\theta}{w_0^2}\right) \quad (28)$$

$$Q = \frac{1}{i+2\frac{r\cos\theta}{l}}. \quad (29)$$

We also recall that the diffraction length *l* is given by:

$$l = kw_0^2 \quad (30)$$

and that we have the beam confinement factor *s* given by:

$$s = \frac{1}{kw_0} \quad (31)$$

in which w_0 is the beam waist radius.

An interesting special case which will be used in the next section is when $w_0=\infty$, that is to say when $s=0$, which is equivalent to the consideration of only $O(s^0)$–contributions in series expansions of the first-order Davis beam description presented above. The Gaussian beam has then become a plane wave which, from the above equations, is found to read as:

$$E_x = \exp(-ikz), E_y = E_z = 0. \quad (32)$$

3.2. Beam shape coefficients in the unrotated system

As an exercise, let us evaluate the *TM*-beam shape coefficients of this plane wave, in the unrotated system, by using the modified

localized approximation procedure. The radial electric field component for this case is readily found to be:

$$E_r = \cos\varphi \sin\theta \exp(-ikr\cos\theta) = \frac{e^{i\varphi}+e^{-i\varphi}}{2}\sin\theta\exp(-ikr\cos\theta). \quad (33)$$

Hence:

$$\overline{\overline{E_r}} = \frac{e^{i\varphi}+e^{-i\varphi}}{2} \quad (34)$$

leading to:

$$\overline{\overline{E_r^m}} = \overline{\overline{\mathcal{E}_r^m}} = 0, |m|\neq 1 \quad (35)$$

$$\overline{\overline{E_r^1}} = e^{i\varphi}/2, \overline{\overline{E_r^{-1}}} = e^{-i\varphi}/2 \quad (36)$$

$$\overline{\overline{\mathcal{E}_r^1}} = \overline{\overline{\mathcal{E}_r^{-1}}} = 1/2 \quad (37)$$

$$g_{n,\ TM}^{m} = 0, |m|\neq 1 \quad (38)$$

$$g_{n,TM}^{1} = g_{n,\ TM}^{-1} = 1/2. \quad (39)$$

Eqs. (38) and (39) agree with Eqs. (6) and (8) as it should since the plane wave under study is a special case of an on-axis axisymmetric beam [28]. All the associated special beam shape coefficients, namely g_n, see Eq. (8), for this plane wave are furthermore equal to 1, a result known to us since a long time, e.g. Refs. [1,29].

This exercise being done, we now turn our attention to the values of the beam shape coefficients for the first-order Davis beam previously described (with $s\neq 0$). This first-order Davis beam is an on-axis axisymmetric beam [28]. Therefore, beam shape coefficients reduce to special beam shape coefficients. We may use a localized approximation, a modified localized approximation, or a standard beam (all of them being variants of localized approximations), to express these special beam shape coefficients [31]. There is however a unified description, according to the following formulas [32]:

$$g_n = \sum_{l=0}^{\infty} G_{2l} s^{2l} \quad (40)$$

$$G_{2l} = \sum_{k=0}^{l} \alpha_{lk}[n(n+1)]^k \quad (41)$$

in which it has to be noted that the coefficients G_{2l} also depend on the partial wave number n, although this is not explicitly specified in the notation.

For the localized approximation, we have:

$$g_n = \exp\left[-(n+1/2)^2 s^2\right] \quad (42)$$

leading to:

$$G_{2l} = \frac{(-1)^l}{l!}(n+1/2)^{2l} \quad (43)$$

$$\alpha_{lk} = \frac{(-1)^l}{k!(l-k)!}\left(\frac{1}{4}\right)^{l-k}. \quad (44)$$

For the modified localized approximation, we have:

$$g_n = \exp\left[-(n-1)(n+2)s^2\right] \quad (45)$$

leading to:

$$G_{2l} = \frac{(-1)^l}{l!}[(n-1)(n+2)]^l \quad (46)$$

$$\alpha_{lk} = \frac{(-1)^k}{k!(l-k)!}2^{l-k}. \quad (47)$$

For the standard beam, we have:

$$g_n = \sum_{l=0}^{\infty} \frac{(-1)^l}{l!} n_l s^{2l} \quad (48)$$

in which:

$$n_0 = 1 \quad (49)$$

$$n_l = (n-l)(n-l+1)\ldots(n-1)(n+2)\ldots(n+l+1), l>0. \quad (50)$$

This leads to:

$$G_{2l} = \frac{(-1)^l}{l!} n_l. \quad (51)$$

There is however no compact expression for the coefficients α_{lk}, although they can be readily evaluated.

3.3. Beam shape coefficients in the rotated system

To obtain the beam shape coefficients in the rotated system, in the *RL*-approach, we apply the theorem of transformation for the case of axisymmetric beams [19], recalled in Eq. (9). To denote the fact that we first generated a localized beam, and afterward rotated, the *TM*-beam shape coefficients are denoted as $\widetilde{\overline{g_{n,\ TM}^m}}$, in which the overbar denotes the localization, and the tilde denotes the rotation. We then readily obtain:

$$\widetilde{\overline{g_{n,\ TM}^m}} = (-1)^m(-1)^{\frac{m-|m|}{2}}\frac{(n-|m|)!}{(n+m)!}e^{im\gamma}\left[im\sin\alpha\pi_n^m(\cos\beta) + \cos\alpha\tau_n^m(\cos\beta)\right]\sum_{l=0}^{\infty} G_{2l}s^{2l} \quad (52)$$

which is valid for the unified description encompassing the localized approximation, the modified localized approximation, and the standard beam description. For the modified localized approximation, Eq. (52) specifically becomes, using Eq. (45):

$$\widetilde{\overline{g_{n,\ TM}^m}} = (-1)^m(-1)^{\frac{m-|m|}{2}}\frac{(n-|m|)!}{(n+m)!}e^{im\gamma}\left[im\sin\alpha\pi_n^m(\cos\beta) + \cos\alpha\tau_n^m(\cos\beta)\right]\exp\left[-(n-1)(n+2)s^2\right]. \quad (53)$$

At $0(s^0)$, or equivalently in the plane wave case of Eq. (32):

$$\widetilde{\overline{g_{n,\ TM}^m}} = (-1)^m(-1)^{\frac{m-|m|}{2}}\frac{(n-|m|)!}{(n+m)!}e^{im\gamma}\left[im\sin\alpha\pi_n^m(\cos\beta) + \cos\alpha\tau_n^m(\cos\beta)\right]. \quad (54)$$

4. The *LR*-procedure

In this procedure, we first apply a rotation of coordinates, express the original first-order Davis beam in this system of coordinates and, afterward, apply the modified localized approximation procedure to the obtained result. When this is done, it is observed that the beam shape coefficients in the rotated system obtained either by the *RL*- or the *LR*-procedures severely disagree. In other words, *R* and *L* do not commute. This happens even for $O(s^0)$–contribution, that is to say for

the plane wave that we have previously considered. Hence, we shall be content in applying the *LR*-procedure to it. Furthermore, it will be sufficient to consider a rotation with Euler angles α and β, with however $\gamma=0$. The result of the *RL*-procedure is then, from Eq. (54), with $\gamma=0$:

$$\widetilde{\overline{g^{m}_{n,\,TM}}} = (-1)^{m}(-1)^{\frac{m-|m|}{2}}\frac{(n-|m|)!}{(n+m)!}\left[im\sin\alpha\pi_n^m(\cos\beta) + \cos\alpha\tau_n^m(\cos\beta)\right]. \tag{55}$$

4.1. Rotation of Cartesian field components

Let $\hat{x},\hat{y},\hat{z}$ be unit vectors along the directions x,y,z of the unrotated system, respectively. Let $\widehat{x_\alpha}$, $\widehat{y_\alpha}$, $\widehat{z_\alpha}$ be unit vectors along the directions $x_\alpha,y_\alpha,z_\alpha$ of the α–rotated system, respectively. The relationship between these unit vectors through the α–rotation is given by:

$$\begin{pmatrix}\hat{x}\\ \hat{y}\\ \hat{z}\end{pmatrix} = \begin{pmatrix}\cos\alpha & -\sin\alpha & 0\\ \sin\alpha & \cos\alpha & 0\\ 0 & 0 & 1\end{pmatrix}\begin{pmatrix}\widehat{x_\alpha}\\ \widehat{y_\alpha}\\ \widehat{z_\alpha}\end{pmatrix}. \tag{56}$$

Let $\widehat{x_\beta}=\hat{\tilde{x}}$, $\widehat{y_\beta}=\hat{\tilde{y}}$, $\widehat{z_\beta}=\hat{\tilde{z}}$ the unit vectors along the directions $x_\beta=\tilde{x},y_\beta=\tilde{y},z_\beta=\tilde{z}$, of the β–rotated system (identifying with the rotated system since there is no third rotation of angle γ), respectively. The relationship between unit vectors through this second (and final) rotation is given by:

$$\begin{pmatrix}\widehat{x_\alpha}\\ \widehat{y_\alpha}\\ \widehat{z_\alpha}\end{pmatrix} = \begin{pmatrix}\cos\beta & 0 & \sin\beta\\ 0 & 1 & 0\\ -\sin\beta & 0 & \cos\beta\end{pmatrix}\begin{pmatrix}\widehat{x_\beta}=\hat{\tilde{x}}\\ \widehat{y_\beta}=\hat{\tilde{y}}\\ \widehat{z_\beta}=\hat{\tilde{z}}\end{pmatrix}. \tag{57}$$

4.2. Rotation of coordinates

We shall also need to relate the unrotated coordinates (x,y,z) and the rotated coordinates $(\tilde{x},\tilde{y},\tilde{z})$.

For the first rotation:

$$\begin{pmatrix}x\\ y\\ z\end{pmatrix} = \begin{pmatrix}\cos\alpha & \varepsilon\sin\alpha & 0\\ -\varepsilon\sin\alpha & \cos\alpha & 0\\ 0 & 0 & 1\end{pmatrix}\begin{pmatrix}x_\alpha\\ y_\alpha\\ z_\alpha\end{pmatrix} \tag{58}$$

in which ε is either $(+1)$ or (-1). For the time being, we let the value of ε undetermined because our conclusion will not depend on it. In order to avoid distracting the attention of the reader from the main issue, the actual value of ε is better discussed in a small accessory Appendix.

Similarly, for the second rotation:

$$\begin{pmatrix}x_\alpha\\ y_\alpha\\ z_\alpha\end{pmatrix} = \begin{pmatrix}\cos\beta & 0 & -\varepsilon\sin\beta\\ 0 & 1 & 0\\ \varepsilon\sin\beta & 0 & \cos\beta\end{pmatrix}\begin{pmatrix}x_\beta=\tilde{x}\\ y_\beta=\tilde{y}\\ z_\beta=\tilde{z}\end{pmatrix}. \tag{59}$$

And, as a whole, we obtain:

$$\begin{pmatrix}x\\ y\\ z\end{pmatrix} = \mathbf{R}\begin{pmatrix}\tilde{x}\\ \tilde{y}\\ \tilde{z}\end{pmatrix} \tag{60}$$

in which the rotation matrix $\mathbf{R}$ reads as:

$$\mathbf{R} = \begin{pmatrix}R_{11} & R_{12} & R_{13}\\ R_{21} & R_{22} & R_{23}\\ R_{31} & R_{32} & R_{33}\end{pmatrix} = \begin{pmatrix}\cos\alpha\cos\beta & \varepsilon\sin\alpha & -\varepsilon\cos\alpha\sin\beta\\ -\varepsilon\sin\alpha\cos\beta & \cos\alpha & \sin\alpha\sin\beta\\ \varepsilon\sin\beta & 0 & \cos\beta\end{pmatrix} \tag{61}$$

4.3. Rotation of the electric radial field component

The determination of the *TM*-beam shape coefficients in the rotated system relies on the expression for the electric radial field component E_r in the rotated system that is established and discussed in this subsection. Using Eqs. (56) and (57), $\mathbf{E}=E_x\hat{x}$, with $E_x=\exp(-ikz)$, is found to become:

$$\mathbf{E} = E_x\left[\cos\alpha\cos\beta\hat{\tilde{x}} - \sin\alpha\hat{\tilde{y}} + \cos\alpha\sin\beta\hat{\tilde{z}}\right] \tag{62}$$

Therefore:

$$E_{\tilde{x}} = \cos\alpha\cos\beta\exp(-ikz) \tag{63}$$

$$E_{\tilde{y}} = -\sin\alpha\exp(-ikz) \tag{64}$$

$$E_{\tilde{z}} = \cos\alpha\sin\beta\exp(-ikz) \tag{65}$$

The radial field component reads as:

$$E_r = E_{\tilde{x}}\cos\tilde{\varphi}\sin\tilde{\theta} + E_{\tilde{y}}\sin\tilde{\varphi}\sin\tilde{\theta} + E_{\tilde{z}}\cos\tilde{\theta}. \tag{66}$$

Inserting Eqs. (63)–(65) into Eq. (66), we obtain:

$$E_r = \left[\sin\tilde{\theta}(\cos\alpha\cos\beta\cos\tilde{\varphi} - \sin\alpha\sin\tilde{\varphi}) + \cos\alpha\sin\beta\cos\tilde{\theta}\right]\exp(-ikz). \tag{67}$$

According to the second version of the modified localized approximation procedure, rather than E_r, we preferably use $\overline{\overline{E_r}}$ reading as:

$$\overline{\overline{E_r}} = E_r\left(\tilde{\theta}=\pi/2\right) = \left(\cos\alpha\cos\beta\frac{e^{i\tilde{\varphi}}+e^{-i\tilde{\varphi}}}{2} - \sin\alpha\frac{e^{i\tilde{\varphi}}-e^{-i\tilde{\varphi}}}{2i}\right)\overline{\overline{\exp(-ikz)}}. \tag{68}$$

Expressing z in terms of $\tilde{x},\tilde{y},\tilde{z}$ by using Eq. (60), and afterward $\tilde{x},\tilde{y},\tilde{z}$ in terms of spherical coordinates $\tilde{r}=r,\tilde{\theta},\tilde{\varphi}$, we obtain:

$$kz = R\left(R_{31}\sin\tilde{\theta}\cos\tilde{\varphi} + R_{32}\sin\tilde{\theta}\sin\tilde{\varphi} + R_{33}\cos\tilde{\theta}\right) \tag{69}$$

leading to:

$$\overline{\overline{\exp(-ikz)}} = \exp\left[iB\cos\tilde{\varphi}\right] \tag{70}$$

in which we have implemented the values of $R_{31}=\varepsilon\sin\beta, R_{32}=0$, and introduced the quantity:

$$B = -\varepsilon R\sin\beta. \tag{71}$$

Since $\overline{\overline{\exp(-ikz)}}$ is 2π–periodic with respect to $\tilde{\varphi}$, we may express it as a Fourier transform, according to:

$$\overline{\overline{\exp(-ikz)}} = \sum_{l=-\infty}^{+\infty}\frac{A_l}{2\pi}e^{il\tilde{\varphi}}. \tag{72}$$

Let us apply the operator $\int_0^{2\pi}d\tilde{\varphi}e^{-im\tilde{\varphi}}$ to both Eqs. (70) and (72).

First, we have:

$$\int_0^{2\pi} d\tilde{\varphi}\frac{A_l}{2\pi}e^{i(l-m)\tilde{\varphi}} = \begin{cases} 0, l\neq m \\ A_m, l=m \end{cases}. \quad (73)$$

Hence, from Eq. (72):

$$\int_0^{2\pi} d\tilde{\varphi}e^{-im\tilde{\varphi}}\sum_{l=-\infty}^{+\infty}\frac{A_l}{2\pi}e^{il\tilde{\varphi}} = \sum_{l=-\infty}^{+\infty}\int_0^{2\pi} d\tilde{\varphi}\frac{A_l}{2\pi}e^{i(l-m)\tilde{\varphi}} = A_m = MD. \quad (74)$$

This term, named *MD*, must be equal to *MG* given by:

$$MG = \int_0^{2\pi} d\tilde{\varphi}e^{iB\cos\tilde{\varphi}-im\tilde{\varphi}}. \quad (75)$$

But we have in Ref. ([33], p 690):

$$J_n(x) = \frac{i^{-n}}{2\pi}\int_0^{2\pi} e^{i(x\cos\theta + n\theta)}d\theta \quad (76)$$

so that:

$$MG = \frac{2\pi}{i^m}J_{-m}(B) \quad (77)$$

which is equal to $MD = A_m$, implying:

$$A_m = \frac{2\pi}{i^m}J_{-m}(B). \quad (78)$$

Inserting this result in Eq. (72):

$$\overline{\overline{\exp(-ikz)}} = \sum_{m=-\infty}^{+\infty}(-1)^m i^m J_{-m}(B)e^{im\tilde{\varphi}}. \quad (79)$$

But we have in Ref. ([33], p 677):

$$J_{-m}(B) = (-1)^m J_m(B) \quad (80)$$

Hence:

$$\overline{\overline{\exp(-ikz)}} = \sum_{m=-\infty}^{+\infty} i^m J_m(B)e^{im\tilde{\varphi}}. \quad (81)$$

We may then rewrite Eq. (68) as:

$$\overline{\overline{E_r}} = \left(f_+e^{i\tilde{\varphi}} + f_-e^{-i\tilde{\varphi}}\right)\sum_{m=-\infty}^{+\infty} i^m J_m(B)e^{im\tilde{\varphi}}. \quad (82)$$

in which:

$$f_+ = \frac{1}{2}(\cos\alpha\cos\beta + i\sin\alpha) \quad (83)$$

$$f_- = \frac{1}{2}(\cos\alpha\cos\beta - i\sin\alpha) \quad (84)$$

In Eq. (82), we have a sum of two terms. In the first term, we make a change of subscript $m+1\rightarrow m$. In the second term, we make a change of subscript $m-1\rightarrow m$. It then happens that $\overline{\overline{E_r}}$ may be rewritten as:

$$\overline{\overline{E_r}} = \sum_{m=-\infty}^{+\infty} i^{m+1}e^{im\tilde{\varphi}}\left[f_-J_{m+1}(B) - f_+J_{m-1}(B)\right]. \quad (85)$$

As a check, we may set $\alpha=\beta=0$. Then, using ([33], p 676):

$$\begin{cases} J_m(0) = 0, m\neq 0 \\ J_0(0) = 1 \end{cases}. \quad (86)$$

It is afterward readily established that we recover Eq. (34) from Eq. (85).

4.4. Rotated beam shape coefficients and discussion

We may then apply the modified localized approximation procedure to obtain the *TM*-beam shape coefficients in the rotated system. The *m*-modes are found to read as:

$$\overline{\overline{E_r^m}} = i^{m+1}e^{im\tilde{\varphi}}\left[f_-J_{m+1}(B) - f_+J_{m-1}(B)\right] \quad (87)$$

leading to:

$$\overline{\overline{\mathcal{E}_r^m}} = i^{m+1}\left[f_-J_{m+1}(B) - f_+J_{m-1}(B)\right] \quad (88)$$

Hence:

$$\overline{\overline{g_{n,TM}^m}} = \left(\frac{-i}{L^{1/2}}\right)^{|m|-1} i^{m+1}\left[f_-J_{m+1}\left(-\varepsilon L^{1/2}\sin\beta\right) - f_+J_{m-1}\left(-\varepsilon L^{1/2}\sin\beta\right)\right] \quad (89)$$

in which the coefficients are decorated in such a way as to recall that we first rotate, and afterward localize, in contrast with the coefficients in Eq. (55) in which the coefficients are decorated differently. We then observe that Eqs. (89) and (55) do not agree, i.e. as announced, the operations *R* (rotation) and *L* (localization) do not commute.

To vividly illustrate this lack of commutativity, let us consider the following special case: $n=1$, $m=0$, $\alpha=0$, $\beta=\pi/2$. Then, from Eq. (55), we obtain:

$$\overline{\overline{g_{1,TM}^0}} = \cos(\alpha=0)\left[\frac{dP_1(\cos\beta)}{d\beta}\right]_{\beta=\pi/2} = -\cos(\alpha=0)\sin(\beta=\pi/2) = -1. \quad (90)$$

But, for $\alpha=0$, $\beta=\pi/2$, we have, from Eqs. (83) and (84):

$$f_+(\alpha=0,\ \beta=\pi/2) = f_-(\alpha=0,\ \beta=\pi/2) = 0 \quad (91)$$

Hence:

$$\overline{\overline{g_{1,TM}^0}} = 0 \neq \overline{\overline{g_{1,TM}^0}}. \quad (92)$$

5. Conclusion

We have convincingly established that the current modified localized approximation for arbitrary shaped beams does not commute with rotations of coordinate systems, and more importantly that the exhibited lack of commutativity is harsh, a somewhat unexpected feature. The reason why it is however simple to identify, namely the modified localized approximation derived in Ref. [14] is indeed valid for arbitrary shaped beams propagating along the *z*-axis or parallel to it, but it is not valid for arbitrary shaped beams AND for arbitrary orientation of the beam. The orientation required for the beam of Eq. (9) in Ref. [14] will thereafter be called the standard orientation.

Therefore, at the present time, if we want to obtain a localized beam model under an orientation which is "not standard", we have to use the first procedure we have used in this paper, that is to say the *RL*-procedure in which we first localize and afterward rotate. As a consequence, we now have the most interesting question to know whether one can design a new localized approximation which would be, in one step only, valid for both arbitrary shaped beams AND arbitrary orientation of the beam. We are currently pursuing this line of investigation.

Appendix A

There are two different points of view available when dealing with rotations.

The first point of view is the one which is taken in this series of papers: we make a rotation of an original unrotated system of coordinates but we let the laser beam unrotated. Then, to secure the value of ε, let us consider the unrotated system (x,y,z) and the rotated system $(x_\alpha,y_\alpha,z_\alpha)$ obtained from a rotation of angle α about the axis z. Let us next consider the point P on the axis x_α (that can be thought as being a point attached to the laser beam to which no rotation is applied), lying in the first quadrant of the (x,y) plane, and let us take its coordinates in the rotated system as being $(x_\alpha(P),y_\alpha(P),z_\alpha(P))=(1,0,0)$. Since the point P is taken in the first quadrant of the (x,y) plane, it has $x>0$ and $y>0$. By using Eq. (58), we however obtain $(x(P),y(P),z(P))=(\cos\alpha,-\varepsilon\sin\alpha,0)$. To retrieve $y(P)>0$, we therefore must have $\varepsilon=-1$.

In the second point of view (which is not the one taken in this series of papers), the laser beam is rotated. Let us consider a vector $\overrightarrow{OM}$ attached to the unrotated system (and to the laser beam), defined as $\overrightarrow{OM}=X\hat{x}+Y\hat{y}$. When rotating the laser beam, this vector would be rotated too, becoming $\overrightarrow{OM}'=X\hat{\tilde{x}}+Y\hat{\tilde{y}}$, i.e. the rotation does not affect the length of the components which are X and Y in both the unrotated and in the rotated systems, but affects the orientation of the unit vectors. Then, as readily demonstrated in elementary textbooks dealing with rotations, we would have $\varepsilon=+1$.

Finally, the values of ε given above are valid for positive rotations used in this paper. In the case of negative rotations, they would have to be interchanged.

References

[1] G. Gouesbet, B. Maheu, G. Gréhan, Journal of the Optical Society of America A 5 (1988) 1427.
[2] B. Maheu, G. Gouesbet, G. Gréhan, Journal of Optics, Paris 19 (2) (1988) 59.
[3] F. Onofri, G. Gréhan, G. Gouesbet, Applied Optics 34 (30) (1995) 7113.
[4] G. Gouesbet, G. Gréhan, Journal of Modern Optics 47 (5) (2000) 821.
[5] G. Gouesbet, G. Gréhan, Journal of Optics A : Pure and Applied Optics 1 (1999) 706.
[6] J.A. Lock, G. Gouesbet, Journal of Quantitative Spectroscopy and Radiative Transfer 110 (2009) 800.
[7] G. Gouesbet, Journal of Quantitative Spectroscopy and Radiative Transfer 110 (2009) 1223.
[8] M.I. Mishchenko, L.D. Travis, A.A. Lacis, Scattering, Absorption, and Emission of Light by Small Particles, Cambridge University Press, 2002.
[9] A. Doicu, T. Wriedt, Y.A. Eremin, Light Scattering by Systems of Particles. Null-field Method with Discrete Sources—Theory and Programs, Springer, 2006.
[10] G. Gouesbet, Optics Communications 283 (2010) 517.
[11] G. Gouesbet, C. Letellier, K.F. Ren, G. Gréhan, Applied Optics 35 (9) (1996) 1537.
[12] G. Gouesbet, G. Gréhan, B. Maheu, Journal of Optics, Paris 19 (1) (1988) 35.
[13] G. Gouesbet, G. Gréhan, B. Maheu, Applied Optics 27 (23) (1988) 4874.
[14] G. Gouesbet, Journal of the Optical Society of America A 16 (7) (1999) 1641.
[15] K.F. Ren, G. Gouesbet, G. Gréhan, Applied Optics 37 (19) (1998) 4218.
[16] A. Doicu, T. Wriedt, Applied Optics 36 (13) (1997) 2971.
[17] H.Y. Zhang, Y.P. Han, Journal of the Optical Society of America B 11 (2008) 255.
[18] G. Gouesbet, J.J. Wang, Y.P. Han, Optics Communications 283 (2010) 3218.
[19] J.J. Wang, G. Gouesbet, Y.P. Han, Optics Communications 283 (2010) 3226.
[20] G. Gouesbet, J.J. Wang, Y.P. Han, Optics Communications 283 (2010) 3235.
[21] G. Gouesbet, J.J. Wang, Y.P. Han, G. Gréhan, Optics Communications 283 (2010) 3244.
[22] Y.P. Han, H. Zhang, G. Han, Optics Express 15 (2) (2007) 735.
[23] Y.P. Han, Y. Zhang, H. Zhang, G. Han, Journal of Quantitative Spectroscopy and Radiative Transfer 110 (14–16) (2009) 1375.
[24] J.A. Lock, G. Gouesbet, Journal of the Optical Society of America A 11 (9) (1994) 2503.
[25] G. Gouesbet, J.A. Lock, Journal of the Optical Society of America A 11 (9) (1994) 2516.
[26] G. Gouesbet, J.A. Lock, G. Gréhan, Applied Optics 34 (12) (1995) 2133.
[27] G. Gouesbet, Journal of the Optical Society of America A 13 (12) (1996) 2434.
[28] G. Gouesbet, Applied Optics 35 (9) (1996) 1543.
[29] G. Gouesbet, G. Gréhan, Journal of Optics, Paris 13 (2) (1982) 97.
[30] G. Gouesbet, G. Gréhan, B. Maheu, Journal of Optics, Paris 16 (1985) 83.
[31] G. Gouesbet, J.A. Lock, G. Gréhan. Journal of Quantitative Spectroscopy and Radiative Transfer (in press).
[32] G. Gouesbet, Journal of Optics, Paris 27 (1) (1996) 35.
[33] G.B. Arfken, H.J. Weber, Mathematical Methods for Physicists, Sixth Edition, Academic Press, 2005.

附录A Wigner函数，广义球谐函数，连带勒让德函数

Wigner函数，广义球谐函数是联系相当紧密的两类函数，它们被广泛应用在量子物理，群论等研究领域，可以很有效地表征与空间旋转相关的变量。Wigner d函数有以下几个表达式：

$$d_{ms}^{n}(\beta)=\sqrt{(n+m)!(n-m)!(n+s)!(n-s)!}\times\sum_{\sigma}(-1)^{\sigma}\frac{(\cos\frac{\beta}{2})^{2n-2\sigma+m-s}(\sin\frac{\beta}{2})^{2\sigma-m+s}}{\sigma!(n+m-\sigma)!(n-s-\sigma)!(s-m+\sigma)!} \tag{A. 1}$$

$$d_{ms}^{n}(\beta)=(-1)^{n-s}\sqrt{(n+m)!(n-m)!(n+s)!(n-s)!}\times\sum_{\sigma}(-1)^{\sigma}\frac{(\cos\frac{\beta}{2})^{2\sigma+m+s}(\sin\frac{\beta}{2})^{2n-2\sigma-m-s}}{\sigma!(n-m-\sigma)!(n-s-\sigma)!(m+s+\sigma)!} \tag{A. 2}$$

$$d_{ms}^{n}(\beta)=(-1)^{n+m}\sqrt{(n+m)!(n-m)!(n+s)!(n-s)!}\times\sum_{\sigma}(-1)^{\sigma}\frac{(\cos\frac{\beta}{2})^{2\sigma-m-s}(\sin\frac{\beta}{2})^{2n-2\sigma+m+s}}{\sigma!(n+m-\sigma)!(n+s-\sigma)!(\sigma-m-s)!} \tag{A. 3}$$

$$d_{ms}^{n}(\beta)=(-1)^{m-s}\sqrt{(n+m)!(n-m)!(n+s)!(n-s)!}\times\sum_{\sigma}(-1)^{\sigma}\frac{(\cos\frac{\beta}{2})^{2n-2\sigma-m+s}(\sin\frac{\beta}{2})^{2\sigma+m-s}}{\sigma!(n-m-\sigma)!(n+s-\sigma)!(m-s+\sigma)!} \tag{A. 4}$$

其中 n,m,s 为整数，$\beta\in[0,\pi]$。要求 $n\geq 0$ 以及 $-m\leq n$，$s\leq n$。

根据上述Wigner d函数的数学表达式，可以推导出以下对称关系，这些对称关系将大大简化相关的数值计算：

$$d_{ms}^{n}(\beta)=(-1)^{m-s}d_{-m-s}^{n}(\beta)=(-1)^{m-s}d_{sm}^{n}(\beta)=d_{-s-m}^{n}(\beta) \tag{A. 5}$$

$$d_{ms}^{n}(-\beta)=(-1)^{m-s}d_{ms}^{n}(\beta)=d_{sm}^{n}(\beta),\quad d_{ms}^{n}(0)=d_{sm}^{n}(0)=\delta_{ms} \tag{A. 6}$$

$$d_{ms}^{n}(\pi-\beta)=(-1)^{n-s}d_{-ms}^{n}(\beta)=(-1)^{n-m}d_{m-s}^{n}(\beta),\quad d_{ms}^{n}(\pi)=(-1)^{n-m}\delta_{-ms} \tag{A. 7}$$

Wigner d函数可用以下递推公式来进行数值计算：

$$d_{ms}^{n+1}(x)=\frac{1}{n\sqrt{(n+1)^2-m^2}\sqrt{(n+1)^2-s^2}}\Big\{(2n+1)[n(n+1)x-ms]d_{ms}^{n}(x)$$
$$-(n+1)\sqrt{n^2-m^2}\sqrt{n-s^2}d_{ms}^{n-1}(x)\Big\},\qquad n\geq n_{\min} \tag{A. 8}$$

初始值为：

$$d_{ms}^{n_{\min}-1}(x)=0$$
$$d_{ms}^{n_{\min}}(x)=\xi_{ms}2^{-n_{\min}}\sqrt{\frac{(2n_{\min})!}{(|m-s|)!(|m+s|)!}}(1-x)^{|m-s|/2}(1+x)^{|m+s|/2} \tag{A. 9}$$

其中：

$$\xi_{ms}=\begin{cases}1 & s\geq m\\ (-1)^{m-s} & s\leq m\end{cases} \tag{A. 10}$$

广义球函数是另外一个很重要的数学函数集，它与Wigner d函数之间有关系：

$$d_{ms}^{n}(\beta)=i^{s-m}P_{ms}^{n}(\cos\beta) \tag{A. 11}$$

因此对于广义球谐函数，我们可以得到类似于Wigner d函数的递推关系：

$$P_{ms}^{n+1}(x)=\frac{1}{n\sqrt{(n+1)^2-m^2}\sqrt{(n+1)^2-s^2}}\Big\{(2n+1)[n(n+1)x-ms]P_{ms}^{n}(x)$$
$$-(n+1)\sqrt{n^2-m^2}\sqrt{n-s^2}P_{ms}^{n-1}(x)\Big\},\qquad n\geq n_{\min} \tag{A. 12}$$

相应初始值为：

$$P_{ms}^{n_{\min}-1}(x)=0 \tag{A. 13}$$

$$P_{ms}^{n_{\min}}(x)=(-i)^{|m-s|}2^{-n_{\min}}\sqrt{\frac{(2n_{\min})!}{(|m-s|)!(|m+s|)!}}(1-x)^{|m-s|/2}(1+x)^{|m+s|/2} \tag{A. 14}$$

广义球谐函数和Wigner d函数分别由以下归一化等式：

$$\int_0^{\pi}\sin\beta d\beta d_{ms}^{n}(\beta)d_{ms}^{n'}(\beta)=\frac{2}{2n+1}\delta_{nn'} \tag{A. 15}$$

$$\int_{-1}^{1}dxP_{ms}^{n}(x)P_{ms}^{n'}(x)=(-1)^{m+s}\frac{2}{2n+1}\delta_{nn'} \tag{A. 16}$$

当$s=0$时，Wigner d函数退化为连带勒让德函数，即：

$$d_{m0}^{n}(\beta)=\sqrt{\frac{(n-m)!}{(n+m)!}}P_{n}^{m}(\cos\beta) \tag{A. 17}$$

其中

$$P_{n}^{m}(\cos\beta)=(-1)^{m}(\sin\beta)^{m}\frac{d^{m}P_{n}(\cos\beta)}{(d\cos\beta)^{m}} \tag{A. 18}$$

另外我们有以下数学关系式：

$$\frac{d}{d\beta}d_{ms}^{n}(\beta)+\frac{m}{\sin\beta}d_{ms}^{n}(\beta)=\frac{s\cos\beta}{\sin\beta}d_{ms}^{n}(\beta)-\sqrt{(n-s)(n+s+1)}d_{ms+1}^{n}(\beta) \tag{A. 19}$$

$$\frac{d}{d\beta}d_{ms}^{n}(\beta)-\frac{m}{\sin\beta}d_{ms}^{n}(\beta)=\frac{-s\cos\beta}{\sin\beta}d_{ms}^{n}(\beta)+\sqrt{(n+s)(n-s+1)}d_{ms-1}^{n}(\beta) \tag{A. 20}$$

当$s=0$时，我们可以得到：

$$\frac{d}{d\beta}d_{m0}^{n}(\beta)+\frac{m}{\sin\beta}d_{m0}^{n}(\beta)=-\sqrt{n(n+1)}d_{m1}^{n}(\beta) \tag{A. 21}$$

$$\frac{d}{d\beta}d_{m0}^{n}(\beta)-\frac{m}{\sin\beta}d_{m0}^{n}(\beta)=\sqrt{n(n+1)}d_{m-1}^{n}(\beta) \tag{A. 22}$$

将关系式(A.17)代入式(A.21)-(A.22)，并引入：

$$\tau_{n}^{m}(\cos\beta)=\frac{d}{d\beta}P_{n}^{m}(\cos\beta),\qquad \pi_{n}^{m}(\cos\beta)=\frac{P_{n}^{m}(\cos\beta)}{\sin\beta} \tag{A. 23}$$

可以得到：

$$\sqrt{\frac{(n-m)!}{(n+m)!}}\left[\tau_{n}^{m}(\cos\beta)+m\pi_{n}^{m}(\cos\beta)\right]=-\sqrt{n(n+1)}d_{m1}^{n}(\beta) \tag{A. 24}$$

$$\sqrt{\frac{(n-m)!}{(n+m)!}}\left[\tau_{n}^{m}(\cos\beta)-m\pi_{n}^{m}(\cos\beta)\right]=\sqrt{n(n+1)}d_{m-1}^{n}(\beta) \tag{A. 25}$$

则有：

$$m\pi_{n}^{m}(\cos\beta)=-\sqrt{\frac{(n+m)!}{(n-m)!}}\frac{\sqrt{n(n+1)}}{2}\left[d_{m1}^{n}(\beta)+d_{m-1}^{n}(\beta)\right] \tag{A. 26}$$

$$\tau_{n}^{m}(\cos\beta)=-\sqrt{\frac{(n+m)!}{(n-m)!}}\frac{\sqrt{n(n+1)}}{2}\left[d_{m1}^{n}(\beta)-d_{m-1}^{n}(\beta)\right] \tag{A. 27}$$

对连带勒让德函数进行完全归一化：

$$\int_{-1}^{1}dx\widetilde{P_{n}^{m}}(x)=1 \tag{A. 28}$$

则归一化连带勒让德函数与连带勒让德函数的关系式为：

$$\widetilde{P_{n}^{m}}(x)=c_{n}^{m}P_{n}^{m}(x) \tag{A. 29}$$

其中有：

$$c_{n}^{m}=(-1)^{m}\sqrt{\frac{2n+1}{2}\frac{(n-m)!}{(n+m)!}} \tag{A. 30}$$

则有：

$$\widetilde{P_{n}^{m}}(x)=(-1)^{m}\sqrt{\frac{2n+1}{2}}d_{m0}^{n}(\beta) \tag{A. 31}$$

$$m\widetilde{\pi}_n^m(\cos\beta) = -(-1)^m \sqrt{\frac{2n+1}{2}} \frac{\sqrt{n(n+1)}}{2} \left[d_{m1}^n(\beta) + d_{m-1}^n(\beta) \right] \tag{A. 32}$$

$$\widetilde{\tau}_n^m(\cos\beta) = -(-1)^m \sqrt{\frac{2n+1}{2}} \frac{\sqrt{n(n+1)}}{2} \left[d_{m1}^n(\beta) - d_{m-1}^n(\beta) \right] \tag{A. 33}$$

附录B 球矢量波函数平移加法定理

如图B.1所示，坐标系 $Oxyz$ 和 $O_1x_1y_1z_1$ 平行，其中原点 O_1 在坐标系 $Oxyz$ 中的矢径为 $\mathbf{r}_0$。设空间中任意一点M在坐标系 $Oxyz$ 和 $O_1x_1y_1z_1$ 中的矢径分别为 $\mathbf{r}$ 和 $\mathbf{r}_1$。则有简单的数学关系式：$\mathbf{r}=\mathbf{r}_0+\mathbf{r}_1$。

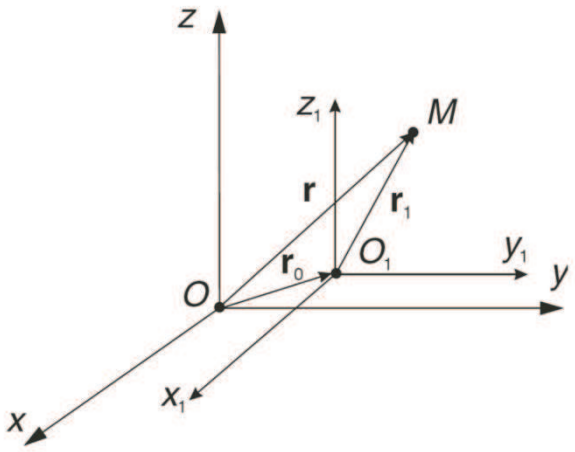

图B.1 直角坐标系的平行移动示意图

对于一般的坐标系平移情况，我们有以下关系式：

$$\begin{aligned}\mathbf{M}_{mn}^{(j)}(k\mathbf{r})&=\sum_{\nu=1}^{\infty}\sum_{\mu=-\nu}^{\nu}[A_{\mu\nu}^{mn,p}(k\mathbf{r}_0)\mathbf{M}_{\mu\nu}^{(j)}(k\mathbf{r}_1)+B_{\mu\nu}^{mn,p}(k\mathbf{r}_0)\mathbf{N}_{\mu\nu}^{(j)}(k\mathbf{r}_1)]\\ \mathbf{N}_{mn}^{(j)}(k\mathbf{r})&=\sum_{\nu=1}^{\infty}\sum_{\mu=-\nu}^{\nu}[B_{\mu\nu}^{mn,p}(k\mathbf{r}_0)\mathbf{M}_{\mu\nu}^{(j)}(k\mathbf{r}_1)+A_{\mu\nu}^{mn,p}(k\mathbf{r}_0)\mathbf{N}_{\mu\nu}^{(j)}(k\mathbf{r}_1)]\end{aligned}\tag{B. 1}$$

如果坐标系沿 z 轴方向移动，则双重积分退化成一重积分：

$$\begin{aligned}\mathbf{M}_{mn}^{(j)}(k\mathbf{r})&=\sum_{\nu=1}^{\infty}[A_{m\nu}^{mn,p}(k\mathbf{r}_0)\mathbf{M}_{m\nu}^{(j)}(k\mathbf{r}_1)+B_{m\nu}^{mn,p}(k\mathbf{r}_0)\mathbf{N}_{m\nu}^{(j)}(k\mathbf{r}_1)]\\ \mathbf{N}_{mn}^{(j)}(k\mathbf{r})&=\sum_{\nu=1}^{\infty}[B_{m\nu}^{mn,p}(k\mathbf{r}_0)\mathbf{M}_{m\nu}^{(j)}(k\mathbf{r}_1)+A_{m\nu}^{mn,p}(k\mathbf{r}_0)\mathbf{N}_{m\nu}^{(j)}(k\mathbf{r}_1)]\end{aligned}\tag{B. 2}$$

对于收敛性正则球谐函数，我们有：

$$\begin{aligned}\mathbf{M}_{mn}^{(1)}(k\mathbf{r})&=\sum_{\nu=1}^{\infty}[A_{m\nu}^{mn,1}(k\mathbf{r}_0)\mathbf{M}_{m\nu}^{(1)}(k\mathbf{r}_1)+B_{m\nu}^{mn,1}(k\mathbf{r}_0)\mathbf{N}_{m\nu}^{(1)}(k\mathbf{r}_1)]\\ \mathbf{N}_{mn}^{(1)}(k\mathbf{r})&=\sum_{\nu=1}^{\infty}[B_{m\nu}^{mn,1}(k\mathbf{r}_0)\mathbf{M}_{m\nu}^{(1)}(k\mathbf{r}_1)+A_{m\nu}^{mn,1}(k\mathbf{r}_0)\mathbf{N}_{m\nu}^{(1)}(k\mathbf{r}_1)]\end{aligned}\tag{B. 3}$$

对于发散性球谐函数，在$r_1 \geq r_0$的情况下，我们有：

$$\begin{aligned}\mathbf{M}_{mn}^{(3)}(k\mathbf{r}) &= \sum_{\nu=1}^{\infty}[A_{m\nu}^{mn,1}(k\mathbf{r}_0)\mathbf{M}_{m\nu}^{(3)}(k\mathbf{r}_1) + B_{m\nu}^{mn,1}(k\mathbf{r}_0)\mathbf{N}_{m\nu}^{(3)}(k\mathbf{r}_1)] \\ \mathbf{N}_{mn}^{(3)}(k\mathbf{r}) &= \sum_{\nu=1}^{\infty}[B_{m\nu}^{mn,1}(k\mathbf{r}_0)\mathbf{M}_{m\nu}^{(3)}(k\mathbf{r}_1) + A_{m\nu}^{mn,1}(k\mathbf{r}_0)\mathbf{N}_{m\nu}^{(3)}(k\mathbf{r}_1)]\end{aligned} \tag{B. 4}$$

在$r_1 < r_0$的情况下，我们有：

$$\begin{aligned}\mathbf{M}_{mn}^{(3)}(k\mathbf{r}) &= \sum_{\nu=1}^{\infty}[A_{m\nu}^{mn,3}(k\mathbf{r}_0)\mathbf{M}_{m\nu}^{(1)}(k\mathbf{r}_1) + B_{m\nu}^{mn,3}(k\mathbf{r}_0)\mathbf{N}_{m\nu}^{(1)}(k\mathbf{r}_1)] \\ \mathbf{N}_{mn}^{(3)}(k\mathbf{r}) &= \sum_{\nu=1}^{\infty}[B_{m\nu}^{mn,3}(k\mathbf{r}_0)\mathbf{M}_{m\nu}^{(1)}(k\mathbf{r}_1) + A_{m\nu}^{mn,3}(k\mathbf{r}_0)\mathbf{N}_{m\nu}^{(1)}(k\mathbf{r}_1)]\end{aligned} \tag{B. 5}$$

矢量平移因子$(A_{m\nu}^{mn,p}, B_{m\nu}^{mn,p})$可以通过求解标量平移因子$C_{m\nu}^{mn}$的迭代求解方法来计算：

$$\begin{aligned}A_{mn'}^{mn}(kz_0) = C_{mn'}^{mn}(kz_0) &+ \frac{kz_0}{n'+1}\sqrt{\frac{(n'-m+1)(n'+m+1)}{(2n'+1)(2n'+3)}}C_{mn'+1}^{mn}(kz_0) \\ &+ \frac{kz_0}{n'}\sqrt{\frac{(n'-m)(n'+m)}{(2n'+1)(2n'-1)}}C_{mn'-1}^{mn}(kz_0)\end{aligned} \tag{B. 6}$$

$$B_{mn'}^{mn}(kz_0) = jkz_0\frac{m}{n'(n'+1)}C_{mn'}^{mn}(kz_0) \tag{B. 7}$$

对于m为负数的情况，我们可以利用以下对称关系来计算：

$$A_{-mn'}^{-mn}(kz_0) = A_{mn'}^{mn}(kz_0), \quad B_{-mn'}^{-mn}(kz_0) = -B_{mn'}^{mn}(kz_0) \tag{B. 8}$$

$$A_{-mn'}^{-mn}(kz_0) = A_{mn'}^{mn}(-kz_0), \quad B_{-mn'}^{-mn}(kz_0) = B_{mn'}^{mn}(-kz_0) \tag{B. 9}$$

关于标量平移因子$C_{m\nu}^{mn}$的计算：

$$\begin{aligned}&\sqrt{\frac{(n-m+1)(n+m+1)}{(2n+1)(2n+3)}}C_{mn'}^{mn+1}(kz_0) - \sqrt{\frac{(n-m)(n+m)}{(2n-1)(2n+1)}}C_{mn'}^{mn-1}(kz_0) \\ &= \sqrt{\frac{(n'-m)(n'+m)}{(2n'-1)(2n'+1)}}C_{mn'-1}^{mn}(kz_0) - \sqrt{\frac{(n'-m)(n'+m)}{(2n'-1)(2n'+1)}}C_{mn'+1}^{mn}(kz_0)\end{aligned} \tag{B. 10}$$

$$\begin{aligned}&\sqrt{\frac{(n-m-1)(n-m+1)}{(2n-1)(2n+1)}}C_{mn'}^{mn-1}(kz_0) + \sqrt{\frac{(n+m)(n+m+1)}{(2n+1)(2n+3)}}C_{mn'}^{mn+1}(kz_0) \\ &= \sqrt{\frac{(n'+m-1)(n'+m)}{(2n'-1)(2n'+1)}}C_{m-1n'-1}^{m-1n}(kz_0) + \sqrt{\frac{(n'-m+1)(n'-m+2)}{(2n'+1)(2n'+3)}}C_{m-1n'+1}^{m-1n}(kz_0)\end{aligned} \tag{B. 11}$$

初始化值：

$$C_{0n'}^{00,(1)}(kz_0) = (-1)^{n'}\sqrt{2n'+1}j_{n'}(kz_0) \tag{B. 12}$$

$$C_{0n'}^{00,(3)}(kz_0) = (-1)^{n'}\sqrt{2n'+1}h_{n'}^{(1)}(kz_0) \tag{B. 13}$$